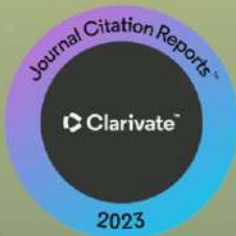


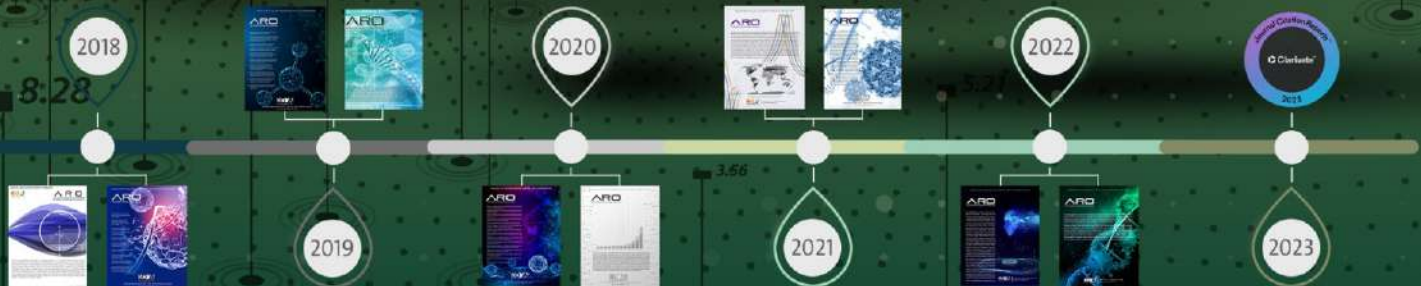
ARO

The Scientific Journal of Koya University

IMPACT
FACTOR
0.6



20¹³₂₃
THE 10th
ANNIVERSARY
ISSUE



ARO-The Scientific Journal of Koya University

ARO, meaning "Today" in Hewramí Kurdish, is an esteemed international scientific journal proudly published by Koya University with the following identifiers: p-ISSN: 2410-9355, e-ISSN: 2307-549X, and DOI: 10.14500/2307-549X. As a reputable open-access peer-reviewed journal, ARO is dedicated to publishing original scientific research, global news, and insightful commentary. Recognized for its impact in the academic community, ARO Journal has been awarded an Impact Factor by WoS-ESCI and covers diverse areas of Multidisciplinary Sciences, welcoming both original research articles and review articles. Notably, ARO Journal is committed to providing free access to its content and proudly boasts the absence of both APC (Article Processing Charges) and ASC (Article Submission Charges) fees.



ARO Executive Publisher

Dr. Mohammed H. Zangana; President of Koya University and the Executive Publisher of ARO.

ARO Editor-in-Chief

Dr Dilan Majid Rostam is the Editor-in-Chief and member of the member Senior Executive Editorial Board.

ARO Editorial Board

ARO takes pride in its robust and dedicated Editorial Board, comprising a distinguished twelve-member Senior Executive Editorial Board and a dynamic six-member Associate Editorial Board, both instrumental in shaping journal policies and ensuring editorial excellence. Additionally, ARO benefits from a highly esteemed Board of Reviewing Editors, consisting of over 250 prominent scientists from diverse fields. Their invaluable expertise and rigorous peer-review process contribute to the high standards and credibility of ARO, making it a leading platform for disseminating original scientific research, global news, and insightful commentary. The ARO editorial group consists of.

Senior Executive Editors

Dilan M. Rostam, Salah I. Yahya, Basim M. Fadhil, Fahmi F. Muhammad, Wali M. Hamad, Jorge Correia, Fouad Mohammed, Jacek Binda, Nadhir Al-Ansari, Howri Mansurbeg, Tara F. Tahir and Yazen A. Khaleel.

Associate Editors

Hamed M. Jassim, Iqbal M.G. Tahir, Saddam T. Ahmad, Sahar B. Mahmood and Layth I. Abd Ali and Mohammad Gh. Faraj.

This Issue Reviewers

Abbas Rezaei, Abdalkareem Abbas, Abdolhamid Zahedi, Abdulbasit K. Al-Talabani, Ali F. Almehemdi, Asaad H. Ismail, Ashish Srivastava, Bahman O. Taha, Bayan S. Al-Numan, BlnD Mohammed, Bushra K. Oleiwi, Dhifaf J. Sadeq, Diyar J. Dhannoon, Dr.Raja Kumar Parabathina, Ehsan Nazemi, Fakhri Hamdullah Ibraheem, Faleh H. Mohammed, Faris R. Ahmed, Faten A. Chaqmaqchee, Halgurd S. Maghdid, Hanaa A. Muhammad, Hayder M. Issa, Hedi Rasul, Hussein Almalikee, Ibrahim N. Qader, Ismail M. Maulood, Ismail S. Ibrahim, Jamal I. Kakrasul, Katan S. Ali, Kayhan Zrar, Khalid N. Sediq, Lafta R. Al-Khazraji, Laith A. Najam, Maryam Toliat, Mehmet C. Kiziltas, Miran H. Baban, Mohammad B. Jamshidi, Mohammed F. Mohammed Sabri, Mohammed Q. Ali, Nashwan K. Abdulkareem, Noor Ibraheem, Omed G. Abdullah, Rabar M. Abdulrahman, Rafid Kadhim Abbas, Salah I. Yahya, Shilan Sameen, Xinghua Li.

ARO Editorial Web and New Media: Dilan M. Rostam and Salah I. Yahya

Managing Editor: Salah I. Yahya

Secretarial Office of the Journal: Haneen H. Falah

Journal Cover Designer: Othman K. Ibrahim

ARO is a distinguished online open access scientific journal that releases hardcopies biannually. All published articles are freely accessible online under the Creative Commons Attribution License (CC-BY-NC-SA 4.0). It is important to note that the responsibility for the content lies solely with the authors and not with ARO or Koya University.

ARO the Scientific Journal Office

Koya University, University Park
Danielle Mitterrand Boulevard, Koya KOY45
Kurdistan Region - F.R. Iraq

E-mail: aro.journal@koyauniversity.org

url: aro.koyauniversity.org

June 2023

ARO

The Scientific Journal of Koya University

Vol XI, No 1(2023)

Contents

Aro Editorial Words	iii
Sazan M. Talaat	01
Role of Cinnamon Supplementation on Glycemic Markers, Lipid Profile and Weight Status in Patients with Type II Diabetes	
Soran S. Badawi	10
Using Multilingual Bidirectional Encoder Representations from Transformers on Medical Corpus for Kurdish Text Classification	
Subasini Uthirapathy	16
Cytostatic Effects of Avocado Oil Using Single-cell Gel Electrophoresis (Comet Assay): An Evaluation	
Abbas Rezaei, Salah I. Yahya, Leila Nouri	22
A Comprehensive Review on Microstrip Couplers: Structure, Design Method and Performance	
Niaz H. Hamad, Mohammad G. Faraj, Akram H. Taha	32
Structural and Optical Properties of Cadmium Sulfide-doped Silver Deposited on Glass and Polymer Substrates by Chemical Spray Pyrolysis	
Saman M. Omer, Kayhan Z. Ghafoor , Shavan K. Askar	38
Plant Disease Diagnosing Based on Deep Learning Techniques:A Survey and Research Challenges	
Muzafar K. Omar, Hanaa A. Muhammad, Sawan M. Mirkhan	48
Effects of Crude Plant Extracts from Five Parts of Melia azedarach on Tribolium confusum	
Sheelan A. Ahmed	52
Effect of Hot Glue Additive on the Rheological Properties of Asphalt Cement and Mixtures Performance	
Twana N. Hassan, Saif T. Manji	60
Simulating Combined Cycle and Gas Turbine Power Plant under Design Condition using Open-Source Software DWSIM A Comparative Study	
Nabaz S. Hussein, Rahel Kh. Ibrahim	72
Fresh and Mechanical Properties of Concrete Containing Oil-Well Cutting Material	

Varoujan K. Sissakian, Lanja H. Abdullah, Balanbo N. Abdulkareem	79
Geomorphic Indicators of Folds Lateral Growth Using Satellite Images: Sulaimaniyah Vicinity in Kurdistan Region of Iraq	
Shavan K. Askar	88
Deep Forest Based Internet of Medical Things System for Diagnosis of Heart Disease	
Yasmin A. Hassan, Abdul Monem S. Rahma	99
The Most Common Characteristics of Fragile Video Watermarking: A Review	
Barham K. Rahim, Peshawa O. Amin, Fahmi F. Muhammadsharif, Salah R. Saeed,	105
Kamal A. Ketuly	
Optical and Optoelectronic Studies of Binary and Ternary Films of Poly(L-Tryptophane), Poly(5-hydroxy-L-tryptophane), and P(TER-CO-TRI) Doped with Sudan Dye	
Mani D. Fadaee, Farzin Shama, Mohammad S. Feali, Maryam S. Gilan	116
A Miniaturized wide Stopband Low-pass Filter using T and Modified L Shapes Resonators	
Zakariya A. Hussein	121
Radiation Detection and Heavy Metals Measurements in Powdered Blood Sample of Leukemia Patients	
Trifa S. Othman, Saman M. Abdullah	126
An Intelligent Intrusion Detection System for Internet of Things Attack Detection and Identification Using Machine Learning	
Pshtiwan T. Jaf, Jafar A. Ali, Ayad A. A. Razzaq	138
Drilling Pipe Corrosion Reduction Using Natural, Biodegradable, and Environmentally Friendly Additive to the Drilling Fluid	
Jihan M. Qasim	143
The Overshot Gate as a Flow-Measuring Device	
Sarwar S. Ismael, Faris R. Ahmed	149
Seismic Fragility Curves for Reinforced Concrete Dual System Buildings: Pearl Tower as Case Study	
The 10th Anniversary of ARO: 2013-2023	157

ARO Editorial Words

Dear esteemed readers,

It is with great pleasure that we present the 20th issue of ARO, the Scientific Journal of Koya University (KOU), marking our momentous 10th anniversary. This milestone highlights the remarkable journey of ARO, an internationally recognized scientific journal, as it continues to contribute to the academic landscape in the Kurdistan Region of Iraq.

We are thrilled and delighted to announce that ARO has achieved a remarkable Impact Factor of 0.6, as officially announced by Clarivate Analytics in June 2023. This prestigious recognition is a testament to the unwavering commitment of the executives and the collective effort of our esteemed authors, reviewers, and editorial team in realising the globally set mission of ARO. We are proud to welcome new editorial members who share our pioneering vision and contribute to ARO's journey of international distinction.

As we embark on our 11th year, our vision is to further enhance ARO's impact and visibility within the scholarly community. In line with this commitment, we are currently being considered for inclusion in the esteemed Science Citation Index Expanded™ (SCIE) by Clarivate Analytics. This evaluation underscores our dedication to maintaining and promoting excellence in scientific publishing.

ARO persists in its mission of providing valuable resources, support, and guidance to researchers throughout the publication process, while also advocating for open access to scientific research. We are proud to have been awarded the DOAJ Seal listing, a testament to our commitment to trusted high-quality open access publishing.

We acknowledge the challenges in finding dependable and proficient reviewers, and we continue to strive to enhance this crucial aspect of our journal. We are grateful for the overwhelming response from researchers, academics, and professionals over the past decade, which has led us to expand our Editorial Board to accommodate the growing number of manuscript submissions.

In this issue, you will find original research papers spanning various fields, demonstrating the multidisciplinary nature of ARO. We extend our deepest gratitude to the authors who have placed their trust in ARO and submitted their groundbreaking research for publication. We also express our appreciation to all peer reviewers from esteemed universities worldwide who have dedicated their time and expertise to ensure the quality of this issue.

As we set our sights on the future, we remain dedicated to upholding the highest standards of scientific publishing and providing a valuable resource for researchers worldwide. Your unwavering support and constructive feedback are of utmost importance to us as we strive to establish Aro as a platform that fosters scientific excellence and knowledge dissemination. Together, let us embark on this exciting journey of growth and innovation.

With warm regards,

Dilan M. Rostam
Editor-in-Chief

Mohammed H. S. Zangana
Executive Publisher

Salah I. Yahya, Basim M. Fadhil, Fahmi F. Muhammad, Wali M. Hamad, Jorge Correia, Fouad Mohammed, Jacek Binda, Nadhir Al-Ansari, Howri Mansurbeg, Tara F. Tahir and Yazen A. Khaleel.
Executive Editorial Board

Role of Cinnamon Supplementation on Glycemic Markers, Lipid Profile and Weight Status in Patients with Type II Diabetes

Sazan M. Talaat

School of Biosciences, Faculty of Science,
University of Nottingham, UK

Abstract—Type II diabetes has been on the rise for the past few decades and the current management plan of diabetes is challenging to individuals in keeping their blood glucose levels within normal limits. There is a constant search of new ways to tackle these challenges. Cinnamon is suggested to have antihyperglycemic and lipid lowering effect and has been proposed to be utilized in type II diabetes. The aim behind this review is to explore the role of cinnamon in improving the glycemic status, lipid profile, and weight status of patients with type II diabetes. PubMed and ScienceDirect databases have been searched for eligible studies conducted until February 2022, the outcomes measured were glycemic markers as primary outcome and lipid profile and weight status as secondary outcomes. A total of ten trials involving 861 patients were included in the study. Five studies have demonstrated reductions in glycemic markers (ranging between -0.56 and -1.9 mmol/L for fasting blood sugar and between -0.21% and -0.93% for glycated hemoglobin) whereas the remaining four did not show any significant reduction. The most improvements in glycemic markers are seen in patients with poorly controlled diabetes and patients with higher body mass index (BMI) values. The majority of the studies did not record improvement in lipid profile. Changes in weight status are only observed in overweight patient category (BMI between 25 and 30). Overall, there is no coherent evidence to decide about antihyperglycemic, lipid lowering, and weight reducing effects of cinnamon in type II diabetes. Further trials are needed to reach a definitive verdict.

Index Terms—Cinnamon, Glycated hemoglobin, Lipid profile, Type II diabetes.

I. INTRODUCTION

Type II diabetes mellitus cases have been on constant rise globally, especially in the 21st century. According to international diabetes federation, as of 2021, 1 in 10 adults is suffering from the disease (536 million people worldwide) and this number is expected to further rise to 783 million by

2045 (*IDF Diabetes Atlas 2021 | IDF Diabetes Atlas, 2022; Sun, et al., 2022*).

These growing rates translate to massive costs in terms of lives lost and money spent for example only in 2021, diabetes was responsible for 6.7 million deaths. In the same year, health spending due to diabetes has reached 966 billion dollars, which is more than a threefold increase over the past 15 years (*IDF Diabetes Atlas 2021 | IDF Diabetes Atlas, 2022*).

Due to this overwhelming growth of diabetes globally, there is an urgent need to enhance the diagnosis and management of the disease (Khan, et al., 2014). At present, the main goal in managing diabetic patients is to control blood sugar levels (target glycated hemoglobin [HbA1c] $<7\%$) as any prolonged deviation from normal ranges can lead to macro and microvascular complications. Moreover, due to the increased risk of cardiovascular disease in diabetic patients, it is also important to keep blood pressure and lipid levels at normal ranges (Allen, et al., 2013).

In the attempt of maintain multiple variables at check, several challenges arise, polypharmacy can be considered as one of the major ones in type II diabetics. Polypharmacy can be defined as taking more than five medications per day and is currently the case in 57–84% of diabetic patients. (Alwhaibi, et al., 2018). This in turn, could be responsible for increased burden on the patients (mixing up of drugs and forgetting to properly take their medications) that result in decreased compliance and adherence to the treatment regimen.

Poor medication adherence is regarded as one of the major factors affecting glycemic control and is associated with increased morbidity and mortality. At best, 45% of all type II diabetic patients fail to achieve glycemic control (HbA1c $<7\%$) (Polonsky and Henry, 2016). In addition, polypharmacy also puts patients at risk of developing drug related adverse effects (Bui, et al., 2021).

To tackle the current challenges, researchers have been in continuous search of alternative ways to manage the disease. There is increasing interest in herbal remedies to be incorporated into the care protocol of diabetic patients. Many herbs are thought to possess hypoglycemic effects and researches focusing on this topic have been constantly on the rise (Governa, et al., 2018; Sharma, et al., 2020). One of the herbs of interest is cinnamon.

ARO-The Scientific Journal of Koya University
Vol. XI, No. 1 (2023), Article ID: ARO.11041. 9 pages
DOI: 10.14500/aro.11041

Received: 01 August 2022; Accepted: 31 December 2022

Review paper: Published: 15 January 2023

Corresponding author's e-mail: stxst21@nottingham.ac.uk

Copyright © 2023 Sazan M. Talaat. This is an open access article distributed under the Creative Commons Attribution License.



Cinnamon is a widely used culinary spice that can be generally divided into two species, Ceylon (or true) cinnamon (botanical name: *Cinnamomum verum*) or the more common *Cinnamomum cassia*. Both belong to lauraceae family. Cinnamon is available in a variety of forms including bark (or quills), powders, or extracts from cinnamon powder. Different forms of cinnamon have different phytochemicals and bioavailability. Volatile oils constitute 1–4% of various cinnamon products, and include 60–80% cinnamaldehyde; 10% eugenol; 5–10% trans-cinnamic acid; 5–10% phenolic compounds; and 4–10% of other compounds, and traces of coumarin (Costello, et al., 2016).

Both *in vitro* and *in vivo* evidences show that cinnamon may have benefits in enhancing insulin sensitivity and glycemic control (Governa, et al., 2018). The exact compound that is responsible for hypoglycemic actions of cinnamon is still under investigation (Costello, et al., 2016), but it has been suggested that this effect is due to cinnamaldehyde or phenolic compounds content (Governa, et al., 2018; Mandal, et al., 2021).

Cinnamaldehyde concentrations vary according to the species and form of cinnamon. *c. cassia* has a higher concentration than *C. verum* yet the high concentration of coumarin (a potential toxin) in *c. cassia* (as compared to *C. verum*) limits its use in large quantities. Considering this potential toxicity, *C. verum* might be the better choice for the management of long term conditions such as type II diabetes mellitus (Governa, et al., 2018).

Up to the present time, none of the authoritative bodies recommend any specific indication for cinnamon in diabetes management. Despite the availability of a fair amount of research on cinnamon, the evidence is not coherent and it is still controversial whether or not cinnamon possesses adequate glucose lowering effect to be incorporated in the treatment regimen of type II diabetes (Governa, et al., 2018).

There is a couple of review articles published on the effect of cinnamon on blood sugar levels in humans (Akilen, et al., 2012; Allen, et al., 2013; Namazi, et al., 2019). But since then, there have been several RCTs published on this topic, that is why a more recent overview is needed with the inclusion of the findings from the more recent studies to give a more up to date insight of the effect of cinnamon on blood sugar parameters.

Hence, the aim behind conducting this literature review is to gather evidence to find out where does exactly cinnamon stand in the management of diabetic patients in terms of its effect on blood sugar levels as well as if it has any influence on optimizing lipid profile and weight status in patients with type II diabetes.

II. METHODOLOGY

Through utilizing PICO model, the research question that is intended to be addressed in this review is “in adult type II diabetic patients, does the use of cinnamon cause a change/improvement in the glycemic control compared to similar patients that do not incorporate cinnamon in their treatment

regimen? and if there is improvement, is it clinically significant?”

The PICO analysis components, that is, the population, intervention, comparator, outcome, and setting criteria used to perform this review are shown in the following Table I:

A. Selection of Papers

For the purpose of generating this literature review, PubMed and ScienceDirect databases were searched with several keywords to identify relevant studies to be included. The keywords used were the following:

1. Cinnamon
2. *Cinnamomum zeylanicum*
3. *C. cassia*
4. Type 2 diabetes mellitus
5. Fasting blood sugar (FBS)
6. HbA1c
7. Glycemic =control

The primary outcome measure was the blood sugar levels (either FBS or HbA1c or serum insulin) whereas changes in weight status and patients’ lipid profile were secondary outcomes of interest.

The inclusion and exclusion criteria were designed in a way that would make it possible to precisely answer the research question. Since we are intending to evaluate the effect of an intervention in our literature review, the study design offering the most reliable and strong evidence would be randomized controlled clinical trials (RCTs), therefore full text clinical trials which were published till November 2022 involving adult patients and measuring changes in blood sugar levels as their primary outcome were searched for to be included.

Exclusion criteria were animal studies, studies not measuring outcomes of interest, studies done on non-diabetic adults, and systematic reviews. Studies involving pediatric and adolescent populations were also excluded from the study.

No limits were set for language or year of publication to gather most of the available evidence.

For the purpose of evaluation of outcomes, statistical significance was considered to be achieved when $p < 0.05$ and clinically significant changes were considered to be the following cutoff points for each of the variables:

TABLE I
PICO ANALYSIS

PICOs	Criteria
Population	Type II diabetic patients (adults)
Intervention	Cinnamon powder consumption
Comparator	Placebo/control group
Outcome	Primary outcomes: glycemic markers (FBS, HbA1c, serum insulin) Secondary outcomes: Body weight (BMI), lipid profile (TC, TG, LDL, HDL)
Setting	Randomized controlled trials

FBS: Fasting blood sugar, HbA1c: Glycated hemoglobin, BMI: Body mass index, TC: Total cholesterol, TG: Triglycerides, LDL: Low-density lipoprotein, HDL: High-density lipoprotein

- a. 0.5% reduction on HbA1c levels.(Lameijer, et al., 2020)
- b. 10% reduction in low-density lipoprotein (LDL) levels.
- c. 10% increase in high-density lipoprotein levels.
- d. 30% reduction in triglyceride levels (Bradley, et al., 2009).

B. Data Extraction

Data extracted from each of the included studies for authors, year of publication, study design, region where study is carried out, number of participants, participant gender and age distribution, oral medication use, duration of diabetes, insulin use, outcomes measured, amount and form of cinnamon used, duration of cinnamon intake, blood sugar readings, lipid profile values, and weight changes.

C. Quality Assessment of the Studies

The quality of the RCTs was assessed using the Jadad scale (Jadad, et al., 1996), based on three components, randomization, double blinding, and description of withdrawals with scores ranging from 0 to 5. Trials scoring three or greater were considered to be high in quality, whereas scores of two or less indicated low quality. Detailed description and the checklist of Jadad scale are shown in Appendix 1.

III. RESULTS

A. Search Results, Study Characteristics and Quality Assessment

As a result of the initial searches, 44 clinical trials were identified from both PubMed and ScienceDirect databases, 12

of which were duplicates. By limiting the search to *in vivo* studies carried out on adults and screening the abstract of the studies against the remaining inclusion and exclusion criteria, ten studies were eligible to be included in this review.

The detailed strategy of study inclusion can be depicted in the following flowchart (Fig. 1).

B. Quality Assessment of Included Studies

According to Jadad scoring scheme, nine of the ten included studies were regarded to be high in quality, while the remaining one study being low in quality. The detailed scoring scheme of each study is shown in Table II.

C. Characteristics and Findings of Included Studies

The sample sizes among the studies ranged from 44 to 140 and collectively involved 861 diabetic patients. The studies were carried out across four continents in the following countries: Iran (n = 3), USA (n = 2), Brazil (n = 1), UK (n = 1), China (n = 1), Germany (n = 1), and Pakistan (n = 1).

Nine studies measured changes in FBS and HbA1c levels and five studies measured serum insulin levels. In terms of secondary outcome measures, seven studies measured lipid profile readings while only four studies looked into measuring body mass index (BMI) of the study subjects.

Four studies utilized *C. cassia* as their cinnamon species, whereas one study used *cinnamomum verum* species. The remaining studies did not mention what species they have used. Regarding the form of the cinnamon, the majority of studies used the powder form (n = 8) whereas the other

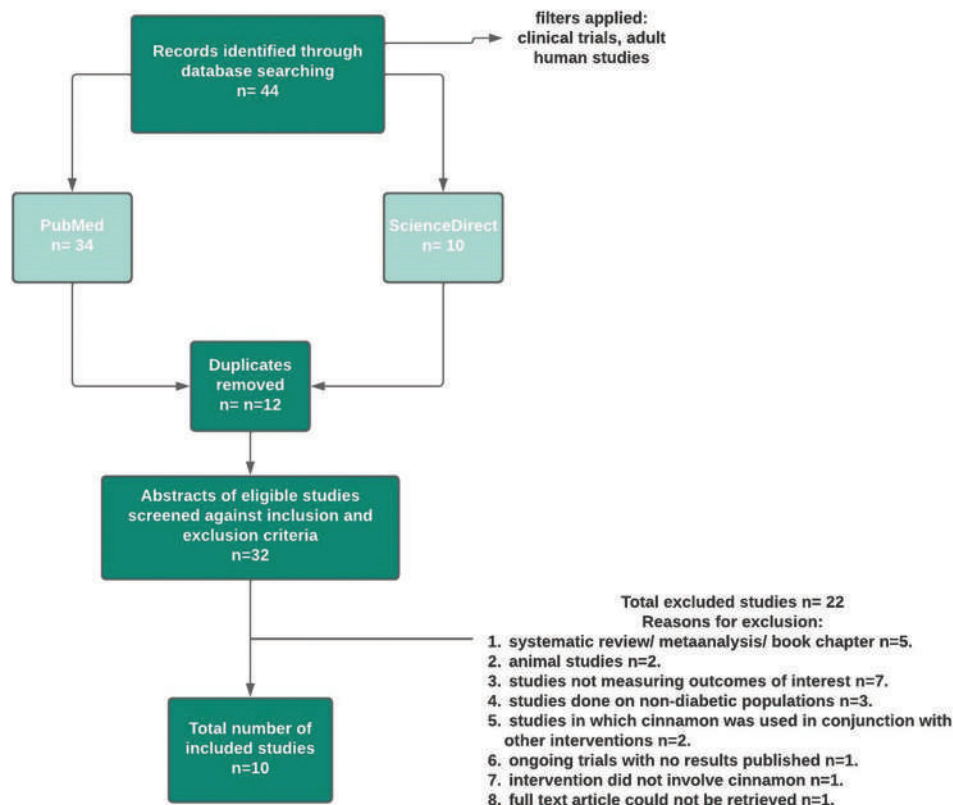


Fig. 1. The search strategy and identification of papers of interest.

ones used extracts ($n = 2$) with varying doses. The time of the interventions ranged from just over a month to up to 4 months, with most studies conducting their intervention over a period of 3 months. The full characteristics of the included studies and their main findings are depicted in Tables III and IV, respectively.

D. Effect of Cinnamon on Glycemic Control (Primary Outcome Measures)

FBS

Of the nine studies that measured FBS levels, the intake of cinnamon was successful in producing statistically significant reductions in five studies only. The reductions ranged between -0.56 and -1.9 mmol/L with most reductions being obtained from the study done by Khan, et al. in Pakistan (Khan, et al., 2003), in contrast, the four remaining studies

only recorded none to very modest reductions that did not reach statistical significance.

Only two studies explored the intervention with cinnamon in different dosages, Khan, et al. have looked into three different quantities of cinnamon powder in their study, the patients showed similar reductions in FBS regardless of which dose was used (Khan et al., 2003). Conversely, Lu, et al. who have used cinnamon extract in their intervention, found that a greater reduction in FBS was observed when a higher dose of cinnamon was used (Lu, et al., 2012).

HbA1c

Similar to FBS values, HbA1c measured in five studies brought about significant reductions ranging between -0.21% and -0.93% as compared to the pre-intervention values, the remaining four studies failed to demonstrate significant changes in HbA1c levels. Only one study has tested the

TABLE II
QUALITY ASSESSMENT OF INCLUDED STUDIES BY JADAD SCALE.

Study	Was the study randomized (0/1)	Was the randomization appropriate (0/1)	Was the study double blinded (0/1)	Was double blinding method appropriate (0/1)	Description of withdrawals and dropouts	Total score
(Khan, et al., 2003)	1	0	0	0	0	1
(Mang, et al., 2006)	1	0	1	1	1	4
(Blevins, et al., 2007)	1	0	1	1	1	4
(Crawford, 2009)	1	1	0	0	1	3
(Akilen, et al., 2010)	1	1	1	1	1	5
(Lu, et al., 2012)	1	0	1	1	1	4
(Mirfeizi, et al., 2016)	1	1	1	1	1	5
(Talaie, et al., 2017)	1	0	1	1	1	4
(Zare, et al., 2019)	1	1	1	1	1	5
(Lira Neto, et al., 2021)	1	1	1	1	1	5

TABLE III
CHARACTERISTICS OF INCLUDED STUDIES

Author/Year of publication	Country	Study design	No. of participants	Mean age/ Gender	Oral medication use for diabetes	Insulin use	Duration of diabetes	Outcomes measured
Khan, et al., 2003	Pakistan	RCT	60	52.2 50% female	Yes	No	7 years	FBS TC, TG, LDL, HDL
Mang, et al., 2006	Germany	RCT	79	63.25 32% female	Some patients took oral medications	No	7 years	FBS, HbA1c TC, TG, LDL, HDL
Blevins, et al., 2007	USA	RCT	57	Not given 51% female	Yes	No	Not mentioned	FBS, HbA1c TC, TG, LDL, HDL, serum insulin
Crawford, 2009	USA	RCT	109	60.3 42% female	Yes	Some patients used insulin	Not mentioned	HbA1c
Akilen et al., 2010	UK	RCT	58	54.9 57% female	Yes	No	Not mentioned	FBS, HbA1c TC, TG, LDL, HDL WC, BMI
Lu, et al., 2012	China	RCT	69	62 62% female	Yes	No	Not mentioned	FBS, HbA1c TC, TG, LDL, HDL
Mirfeizi, et al., 2016	Iran	RCT	105	54 77% female	Yes	No	Not mentioned	FBS, HbA1c TC, TG, LDL, HDL, serum insulin, BMI
Talaie, et al., 2017	Iran	RCT	44	57.6 61.5% female	Yes	Some patients used insulin	<8 years	FBS, HbA1c Serum insulin
Zare, et al., 2019	Iran	RCT	140	52.5 46% female	Yes	No	Not mentioned	FBS, HbA1c TC, TG, LDL, HDL, serum insulin, BMI
Lira Neto, et al., 2021	Brazil	RCT	140	61.3 69.3% female	Yes	No	Not mentioned	FBS, HbA1c, serum insulin

FBS: Fasting blood sugar, TC: Total cholesterol, TG: Triglycerides, LDL: Low-density lipoprotein, HDL: High-density lipoprotein, BMI: Body mass index.

TABLE IV
MAIN FINDINGS OF INCLUDED STUDIES

Author/Year of publication	Form of cinnamon used	Amount of cinnamon consumed	Duration of cinnamon use	Glycaemic status	Lipid profile (all units in mmol/L)	Weight status
Khan, et al., 2003	<i>C. cassia</i> powder	1 g 3 g 6 g	40 days	FBS 1 g: -1.9 mmol/L 3 g: -1.5 mmol/L 6 g: -1.6 mmol/L (p<0.05)	TG: 1g: -0.58, 3g: -0.59, 6g: 0.41 TC: 1 g: -0.82, 3 g: -1.48, 6 g: 0.44 LDL: 1 g: -0.31, 3 g: -0.8, 6 g: 0.15 HDL: Significant changes only in 3 g group	N/A
Mang, et al., 2006	Aqueous cinnamon extract	1 g	4 months	FBS: -1.11 mmol/L (p<0.05) HbA1c: NS	TC, TG, LDL, HDL: NS	N/A
Blevins, et al., 2007	<i>C. cassia</i> powder	1 g	3 months	FBS, HbA1c, serum insulin: NS	TG, TC, LDL, HDL: NS	BMI: NS
Crawford, 2009	<i>C. cassia</i> powder	1 g	3 months	HbA1c: -0.83% (p<0.05)	N/A	N/A
Akilen, et al., 2010	<i>C. cassia</i> powder	2 g	3 months	FBS: NS HbA1c: -0.36%(p=0.002)	TC, TG, LDL, HDL: NS	BMI: NS
Lu, et al., 2012	Cinnamon extract	Low dose: 120 mg (from 4.8 g cinnamon) High dose: 360 mg (from 14.4 g cinnamon)	3 months	FBS: Low dose: -1.02 mmol/L (p<0.01) High dose: -1.62 mmol/L (p<0.01) HbA1c: Low dose: -0.67% (p<0.01) High dose: -0.93% (p<0.01)	TG reduced in low dose group only (-0.78 mmol/L) TC, LDL, HDL: NS	N/A
Mirfeizi, et al., 2016	Cinnamon powder	1 g	3 months	FBS: NS HbA1C: NS Serum insulin: NS	TG, TC, LDL, HDL: NS	BMI: -0.6 kg/m ² (p=0.026)
Talaei, et al., 2017	Cinnamon powder	3 g	2 months	FBS: NS HbA1c: NS Serum insulin :NS	N/A	N/A
Zare, et al., 2019	Cinnamon powder	1 g	3 months	FBS: -0.73 mmol/L (p<0.001) HbA1c: -0.27% (p<0.001) Serum insulin: -1.77 mIU/L (p<0.001)	TG: NS TC: -0.41 (p<0.001) LDL: -0.15 (p=0.018) HDL: +0.03 (p=0.038)	BMI: -0.53 kg/m ² (p<0.001)
Lira Neto, et al., 2021	Cinnamomun verum powder	3 g	3 months	FBS: -0.56 mmol/L (p=0.001) HbA1c: -0.21% (p=0.001) Serum insulin: NS	N/A	N/A

NS: Non-significant

effect of different doses of cinnamon on HbA1c levels and has found a dose response relationship i.e. as the dose of cinnamon increased, a greater reduction of HbA1c value was observed (Lu, et al., 2012). Zare, et al. have found that baseline BMI value of the subjects influenced the reduction in HbA1c levels by cinnamon, subjects with BMI higher than 27 had better HbA1c reductions as compared to lower BMI subjects (Zare, et al., 2019).

Serum insulin

The majority of the studies (four out of five) have failed to find any role of cinnamon in reducing serum insulin levels. On the contrary, in the study by Zare, et al., cinnamon was successful in reducing serum insulin by -1.77 mIU/L (Zare, et al., 2019).

E. Effect of Cinnamon on Secondary Outcome Measures

Lipid profile

The vast majority of studies failed to show significant changes in lipid profile values for cinnamon intervention. Merely in the studies of Khan, et al. and Zare, et al., cinnamon had a significant effect on lipid profile (Khan, et al., 2003; Zare, et al., 2019). Similar to HbA1c status, Zare, et al. have noticed that the efficacy of cinnamon in decreasing lipid parameters was also influenced by baseline BMI of the subjects, subjects with a BMI of 27 or more had greater reductions in lipid profile as compared to subjects with BMI lower than 27 (Zare, et al., 2019). In regards to clinical significance, only the study done by Khan, et al. had satisfactory reduction percentages to indicate clinically significant results (Khan, et al., 2003).

Weight status (BMI)

Four studies have explored the role of cinnamon in controlling weight status in diabetic subjects. Blevins, et al. and Akilen, et al. whose subjects had a baseline BMI in the obese category (BMI > 30 kg/m²) did not record a significant decrease in BMI in their interventions (Blevins, et al., 2007; Akilen, et al., 2010). Conversely, Mirfeizi, et al. and Zare, et al. have demonstrated a positive impact of cinnamon on BMI levels of their subjects, it is worth to mention that the subjects in both studies had a baseline BMI in the overweight category (BMI between 25 and 30 kg/m²) (Mirfeizi, et al., 2016; Zare, et al., 2019).

IV. DISCUSSION

This literature review aimed to explore the effect of cinnamon on the glycemic status of diabetic patients as well as its effect on lipid profile and weight status.

A. Effect of Cinnamon on Glycemic Control

Overall, from the data available, it is difficult to draw a definite conclusion about the effect of cinnamon in improving glycemic control in type II diabetic patients. The conflicting results obtained from the different studies may have been due to the different sources, doses, and forms of which cinnamon was used in each study as well as the different patient profile including their age, diabetes status, and baseline values. Another reason would be the variability of diet, exercise patterns, pharmacotherapy and poor drug compliance of the patients among the studies, all those could have acted as confounders that led to dissimilar results.

The number and type of antihyperglycemic medications taken by study subjects were highly variable among the studies despite the attempt of some studies to control that by distributing subjects with similar medication number and type to both intervention and control groups, and excluding subjects that had a medication type/dosage change. This may have acted as a confounding factor in influencing the final outcomes.

Looking into the findings of all studies, its noticeable than Khan, et al. have recorded the highest reductions in FBS. The population of Khan's study compared to all other studies had very high baseline FBS levels indicating that their diabetes was poorly controlled, this may have been the reason why such great reductions were observed after intervention with cinnamon. This is an indication that cinnamon may be more effective in reducing FBS in poorly controlled diabetic patients rather than patients with well controlled diabetes. However, the findings from Khan et al. should be interpreted with caution because of the poor methodological and reporting quality of the study (Jadad score = 1) as the dropouts and exclusion rates of the subjects was not reported, the adherence of the subjects to take cinnamon tablets were not assessed, and the study was not blinded. All of these issues may have given rise to various biases and affected the outcomes of the study (Khan, et al., 2003).

Several mechanisms have been proposed to explain the antihyperglycemic effect of cinnamon. Studies have

shown that cinnamon can act as an insulin secretagogue stimulating insulin release as well as activating enzymes that are responsible for glucose metabolism, glycolysis, and gluconeogenesis. It also enhances glucose uptake by the cells, all of which contribute to its hypoglycemic effect (Gupta Jain, et al., 2017; Governa, et al., 2018).

A systematic review and meta-analysis which was carried out in 2012, has shown cinnamon to be effective in significantly reducing FBS by -0.84 mmol/L and HbA1c by 0.09% (Akilen, et al., 2012), they have stated that cinnamon could be a promising adjunct in diabetes management. However, since 2012, there have been several RCTs published in this field and if taken into account, may alter their final conclusions. Furthermore, from a clinical point of view, a decrease of 0.09% is much <0.5% cut off value and is unlikely to induce much improvement clinically.

Similarly, in another systematic review of 10 RCTs, Allen, et al. have found that cinnamon had a significant effect on reducing FBS whereas they could not find any influence of cinnamon on the long term control of blood sugar levels as they could not detect any significant changes in HbA1c levels (Allen, et al., 2013).

Conversely, according to a more recent review, cinnamon was ineffective in having any effect on glycemic markers (FBS and HbA1c) (Mandal, et al., 2021). The major drawback from this review was the sole inclusion of studies using whole cinnamon or its powder, studies utilizing cinnamon extracts as well as studies using *C. zeylanicum* species as their cinnamon were excluded from their analysis.

B. Effect of Cinnamon on Lipid Profile

Close to the findings of glycemic status, cinnamon intervention also had conflicting outcomes in its influence of lipid profile parameters. In the seven studies measuring lipid profile, three have shown that cinnamon had an effect in reducing triglyceride (TG) levels and two only were successful to show an impact on total cholesterol (TC) and low-density lipoprotein (LDL).

One of the factors that may have possibly affected this dissimilarity is the baseline lipid profiles of the patients. In three studies, lipid profile values were either within the normal ranges or very near to normal levels to begin with, and this may have been the reason that cinnamon had no effect in improving the lipid profile readings (Blevins, et al., 2007; Akilen, et al., 2010; Mirfeizi, et al., 2016).

A recent systematic review and meta-analysis of 19 RCTs have showed significant lipid lowering effect (TG, TC, and LDL-C) of cinnamon in type II diabetes patients (Jamali, et al., 2020). However, they have shown this effect to be more pronounced in studies that have lasted for <2 months. This may be a reason why our results are not in alignment with their findings as most of the included studies in this review have durations of more than 2 months.

In vitro studies have demonstrated lipid lowering activity of cinnamon and it has been attributed to its cinnamate content, which is a phenolic compound found in the inner bark. Cinnamate has reduced cholesterol levels in rats by

inhibiting HMG Co-A reductase enzyme activity as well as suppressing lipid peroxidation through enhancing the activity of hepatic antioxidant enzyme (Lee, et al., 2003; Amin and Abd El-Twab, 2009).

Only a few systematic reviews have been carried out to assess the effectivity of cinnamon in improving lipid profile in diabetic patients. A review by Allen et al. have concluded that cinnamon had no significant effect on lipid profile in patients with type II diabetes (Allen, et al., 2013). In 2018, another systematic review was carried out and the added evidence from randomized controlled trials carried out in that 5 year gap were still unsuccessful in showing an overall improvement in lipid profile (Santos and da Silva, 2018).

C. Effect of Cinnamon on Weight Status (BMI)

Tackling obesity in patients with type II diabetes not only improves their glycemic control, but also lowers their risk of morbidity and mortality; therefore, weight management is an integral part in the management plan of type II diabetes (Ross, et al., 2011).

Zare, et al. and Mirfeizi, et al. have found similar reductions in BMI values in their interventions (-0.53 kg/m² and -0.6 kg/m², respectively). These results come in alignment with the findings of a systematic review of 12 trials which has quantified the decrease of BMI value due to cinnamon supplementation to be -0.51 kg/m² (Mousavi, et al., 2020).

Cinnamaldehyde, the compound that gives cinnamon its flavor, is thought to be responsible of the antiobesogenic effect of cinnamon (Camacho, et al., 2015). The antiobesogenic effect of cinnamon has been explained by several mechanisms. Animal studies have shown that cinnamon could inhibit the differentiation of adipocytes, induce fatty acid oxidation, act as an antagonist at cannabinoid receptors, and may also affect intestinal lipid absorption (Mollazadeh and Hosseinzadeh, 2016).

D. Strengths and Limitations

The main strength of the study is its inclusiveness, no time or language limits were set in including the studies for this review, and this allowed for the most relevant evidence to be collected. Furthermore, the included studies are divided across four continents which enhance the diversity of the population and make the finding more generalizable/applicable to the global population.

Quality wise, as it is also evident from the Jadad scores, the majority of the studies were of very high quality, hence their findings can be depended upon to assess the impact of cinnamon in type II diabetes. Additionally, the greater part of the included studies had robust follow-up strategies to ensure that all their subjects adhered to the intervention for the full duration. They have excluded any subject who have been incompliant to efficiently reflect the impact of the intervention.

This review is not void from limitations, starting with addressing the stage of diabetes, most of the studies did not mention for how long their subjects had diabetes, also

patients with complications or on insulin therapy were mostly excluded. Another limitation was that none of the interventions assessed the long term effectivity of cinnamon nor its safety in prolonged use.

V. CONCLUSION AND RECOMMENDATIONS

There is no coherent evidence to decide about the antihyperglycemic, lipid lowering, and weight reducing effects of cinnamon in type II diabetic patients. Cinnamon has been effective in improving glycemic markers only in patients with poor baseline values, cinnamon also achieved better results in patients with higher BMI (>27) compared to the lower BMI (<27).

We recommend further studies to be carried out in different stages of diabetes to draw definite conclusions about the effect of cinnamon in glycemic control. In addition, studies with longer durations are required to determine the long-term effect and toxicity of cinnamon supplementation in type II diabetes.

REFERENCES

- Akilen, R., Tsiami, A., Devendra, D. and Robinson, N., 2010. Glycated haemoglobin and blood pressure-lowering effect of cinnamon in multi-ethnic Type 2 diabetic patients in the UK: A randomized, placebo-controlled, double-blind clinical trial. *Diabetic Medicine*, 27(10), pp.1159-1167.
- Akilen, R., Tsiami, A., Devendra, D. and Robinson, N., 2012. Cinnamon in glycaemic control: Systematic review and meta analysis. *Clinical Nutrition*, 31(5), pp.609-615.
- Allen, R.W., Schwartzman, W., Baker, W.L., Coleman, C.I. and Phung, O.J., 2013. Cinnamon use in Type 2 diabetes: An updated systematic review and meta-analysis. *Annals of Family Medicine*, 11(5), pp.452-459.
- Alwhaibi, M., Balkhi, B., Alhawassi, T.M., Alkofide, H., Alduhaim, N., Alabdulali, R., Drweesh, H. and Sambamoorthi, U., 2018. Polypharmacy among patients with diabetes: A cross-sectional retrospective study in a tertiary hospital in Saudi Arabia. *BMJ Open*, 8(5), p.e020852.
- Amin, K.A. and Abd El-Twab, T.M., 2009. Oxidative markers, nitric oxide and homocysteine alteration in hypercholesterolemic rats: Role of atorvastatin and cinnamon. *International Journal of Clinical and Experimental Medicine*, 2, pp.254-265.
- Blevins, S.M., Leyva, M.J., Brown, J., Wright, J., Scofield, R.H. and Aston, C.E., 2007. Effect of cinnamon on glucose and lipid levels in non insulin-dependent Type 2 diabetes. *Diabetes Care*, 30(9), pp.2236-2237.
- Bradley, R., Kozura, E., Buckle, H., Kaltunas, J., Tais, S. and Standish, L.J., 2009. Description of clinical risk factor changes during naturopathic care for Type 2 diabetes. *Journal of Alternative and Complementary Medicine*, 15(6), pp.633-638.
- Bui, D.H.T., Nguyen, B.X., Truong, D.C., Meyrowitsch, D.W., Søndergaard, J., Gammeltoft, T., Bygbjerg, I.C. and Jannie, N., 2021. Polypharmacy among people living with Type 2 diabetes mellitus in rural communes in Vietnam. *PLoS One*, 16(4), p.e0249849.
- Camacho, S., Michlig, S., de Senarclens-Bezençon, C., Meylan, J., Meystre, J., Pezzoli, M., Markram, H. and Le Coutre, J., 2015. Anti-obesity and antihyperglycemic effects of cinnamaldehyde via altered ghrelin secretion and functional impact on food intake and gastric emptying. *Scientific Reports*, 5(1), p.7919.
- Costello, B.R., Dwyer, J.T., Saldanha, L., Bailey, R.L., Merkel, J. and Wambog, E., 2016. Do cinnamon supplements have a role in glycemic control

- in Type 2 diabetes-a narrative review? *Journal of the Academy of Nutrition and Dietetics*, 116(11), p.1794.
- Crawford, P., 2009. Effectiveness of cinnamon for lowering hemoglobin A1C in patients with Type 2 diabetes: A randomized, controlled trial. *Journal of the American Board of Family Medicine*, 22(5), pp.507-512.
- Diabetesatlas., 2022. *IDF Diabetes Atlas 2021. IDF Diabetes Atlas*. Available from: <https://www.diabetesatlas.org/atlas/tenth-edition> [Last accessed on 2022 Mar 14].
- Governa, P., Bainsi, G., Borgonetti, V., Cettolin, G., Giachetti, D., Magnano, A.R., Miraldi, E. and Biagi, M., 2018. Phytotherapy in the management of diabetes: A review. *Molecules*, 23(1), p.105.
- Gupta Jain, S., Puri, S., Misra, A., Gulati, S. and Mani, K., 2017. Effect of oral cinnamon intervention on metabolic profile and body composition of Asian Indians with metabolic syndrome: A randomized double-blind control trial. *Lipids in Health and Disease*, 16(1), p.113.
- Jadad, A.R., Moore, R.A., Carroll, D., Jenkinson, C., Reynolds, D.J., Gavaghan, D.J. and McQuay, H.J., 1996. Assessing the quality of reports of randomized clinical trials: Is blinding necessary? *Controlled Clinical Trials*, 17(1), pp.1-12.
- Jamali, N., Kazemi, A., Saffari-Chaleshtori, J., Samare-Najaf, M., Mohammadi, V. and Clark, C.C.T., 2020. The effect of cinnamon supplementation on lipid profiles in patients with Type 2 diabetes: A systematic review and meta-analysis of clinical trials. *Complementary Therapies in Medicine*, 55, p.102571.
- Khan, A., Safdar, M., Khan, M.M.A., Khattak, K.N. and Anderson, R.A., 2003. Cinnamon improves glucose and lipids of people with Type 2 diabetes. *Diabetes Care*, 26(12), pp.3215-3218.
- Khan, N.M., Ahmad, A., Tiwari, R.K., Kamal, M.A., Mushtaq, G. and Ashraf, G.M., 2014. Current challenges to overcome in the management of Type 2 diabetes mellitus and associated neurological disorders. *CNS Neurological Disorders Drug Targets*, 13(8), pp.1440-1457.
- Lameijer, A., Fokkert, M.J., Edens, M.A., Slingerland, R.J., Bilo, H.J.G. and van Dijk, P.R., 2020. Determinants of HbA1c reduction with FreeStyle Libre flash glucose monitoring (FLARE-NL 5). *Journal of Clinical and Translational Endocrinology*, 22, p.100237.
- Lee, J.S., Jeon, S.M., Park, E.M., Huh, T.L., Kwon, O.S., Lee, M.K. and Choi, M.S., 2003. Cinnamate supplementation enhances hepatic lipid metabolism and antioxidant defense systems in high cholesterol-fed rats. *Journal of Medicinal Food*, 6(3), pp.183-191.
- Lira Neto, J.C.G., Damasceno, M.M.C., Ciol, M.A., de Freitas, R.W.J.F., de Araújo, M.F.M., de Souza Teixeira, C.R., Carvalho, G.C.N., Lisboa, K.W.S.C., Marques, R.L.L., Alencar, A.M.P.G. and Zanetti, M.L., 2021. Efficacy of cinnamon as an adjuvant in reducing the glycemic biomarkers of Type 2 diabetes mellitus: A three-month, randomized, triple-blind, placebo-controlled clinical trial. *Journal of the American College of Nutrition*, 41, pp.266-274.
- Lu, T., Sheng, H., Wu, J., Cheng, Y., Zhu, J. and Chen, Y., 2012. Cinnamon extract improves fasting blood glucose and glycosylated hemoglobin level in Chinese patients with Type 2 diabetes. *Nutrition Research*, 32(6), pp.408-412.
- Mandal, A., Sharma, S., Rani, R., Ranjan, S., Kant, R. and Mirza, A., 2021. Impact of cassia bark consumption on glucose and lipid control in Type 2 diabetes: An updated systematic review and meta-analysis. *Cureus*, 13(7), p.e16376.
- Mang, B., Wolters, M., Schmitt, B., Kelb, K., Lichtinghagen, R., Stichtenoth, D.O. and Hahn, A., 2006. Effects of a cinnamon extract on plasma glucose, HbA1c, and serum lipids in diabetes mellitus Type 2. *European Journal of Clinical Investigation*, 36(5), pp.340-344.
- Mirfeizi, M., Tourzani, Z.M., Mirfeizi, S.Z., Jafarabadi, M.A., Rezvani, H.R. and Afzali, M., 2016. Controlling Type 2 diabetes mellitus with herbal medicines: A triple-blind randomized clinical trial of efficacy and safety. *Journal of Diabetes*, 8(5), pp.647-656.
- Mollazadeh, H. and Hosseinzadeh, H., 2016. Cinnamon effects on metabolic syndrome: A review based on its mechanisms. *Iranian Journal of Basic Medical Sciences*, 19(12), pp.1258-1270.
- Mousavi, S.M., Rahmani, J., Kord-Varkaneh, H., Sheikhi, A., Larijani, B. and Esmailzadeh, A., 2020. Cinnamon supplementation positively affects obesity: A systematic review and dose-response meta-analysis of randomized controlled trials. *Clinical Nutrition*, 39(1), pp.123-133.
- Namazi, N., Khodamoradi, K., Khamechi, S.P., Heshmati, J., Ayati, M.H. and Larijani, B., 2019. The impact of cinnamon on anthropometric indices and glycemic status in patients with Type 2 diabetes: A systematic review and meta-analysis of clinical trials. *Complementary Therapies in Medicine*, 43, pp.92-101.
- Polonsky, W.H. and Henry, R.R., 2016. Poor medication adherence in Type 2 diabetes: Recognizing the scope of the problem and its key contributors. *Patient Preference and Adherence*, 10, p.1299-1307.
- Ross, S.A., Dzida, G., Vora, J., Khunti, K., Kaiser, M. and Ligthelm, R.J., 2011. Impact of weight gain on outcomes in Type 2 diabetes. *Current Medical Research and Opinion*, 27(7), pp.1431-1438.
- Santos, H.O. and da Silva, G.A.R., 2018. To what extent does cinnamon administration improve the glycemic and lipid profiles? *Clinical Nutrition ESPEN*, 27, pp.1-9.
- Sharma, S., Mandal, A., Kant, R., Jachak, S. and Jagzape, M., 2020. Is cinnamon efficacious for glycaemic control in Type-2 diabetes mellitus? *The Journal of the Pakistan Medical Association*, 70(11), pp.2065-2069.
- Sun, H., Saeedi, P., Karuranga, S., Pinkepank, M., Ogurtsova, K., Duncan, B.B., Stein, C., Basit, A., Chan, J.C.N., Mbanya, J.C., Pavkov, M.E., Ramachandaran, A., Wild, S.H., James, S., Herman, W.H., Zhang, P., Bommer, C., Kuo, S., Boyko, E. and Magliano, D.J., 2022. IDF diabetes atlas: Global, regional and country-level diabetes prevalence estimates for 2021 and projections for 2045. *Diabetes Research and Clinical Practice*, 183, p.109119.
- Talaei, B., Amouzegar, A., Sahranavard, S., Hedayati, M., Mirmiran, P. and Azizi, F., 2017. Effects of cinnamon consumption on glycemic indicators, advanced glycation end products, and antioxidant status in Type 2 diabetic patients. *Nutrients*, 9, p.991.
- Zare, R., Nadjarzadeh, A., Zarshenas, M.M., Shams, M. and Heydari, M., 2019. Efficacy of cinnamon in patients with Type II diabetes mellitus: A randomized controlled clinical trial. *Clinical Nutrition*, 38(2), pp.549-556.

APPENDIX

Jadad score for assessing the quality of randomized controlled trials (RCT)

The Jadad scale is calculated using the seven items in the table below. The first five items are indications of good quality, and each counts as one point towards an overall quality score. The final two items indicate poor quality, and a point is subtracted for each if its criteria are met. The range of possible scores is 0–5.

1. Was the study described as randomized (this includes words such as randomly, random, and randomization)?
Yes=1, No=0
2. Was the method used to generate the sequence of randomisation described and appropriate (table of random numbers, computer-generated, etc.)?
Yes=1, No=0
3. Was the study described as double blind?
Yes=1, No=0
4. Was the method of double blinding described and appropriate (identical placebo, active placebo, dummy, etc.)?
Yes=1, No=0
5. Was there a description of withdrawals and dropouts?
Yes=1, No=0
6. Deduct one point if the method used to generate the sequence of randomization was described and it was inappropriate (for example, patients were allocated alternately, or according to date of birth, and hospital number).
Described but inappropriate = -1, Described and appropriate = 0

7. Deduct one point if the study was described as double blind but the method of blinding was inappropriate (for example, comparison of tablet vs. injection with no double dummy).
Described but inappropriate = -1, Described and appropriate = 0

Randomization

A method to generate the sequence of randomization will be regarded as appropriate if it allowed each study participant to have the same chance of receiving each intervention and the investigators could not predict which treatment was next. Methods of allocation using date of birth, date of admission, hospital number or alternation should be not regarded as appropriate.

Double blinding

A study must be regarded as double blind if the word “double blind” is used. The method will be regarded as appropriate if it is stated that neither the person doing the assessments nor the study participant could identify the intervention being assessed, or if in the absence of such a statement the use of active placebos, identical placebos or dummies is mentioned.

Withdrawals and dropouts

Participants who were included in the study but did not complete the observation period or who were not included in the analysis must be described. The number and the reasons for withdrawal in each group must be stated. If there were no withdrawals, it should be stated in the article. If there is no statement on withdrawals, this item must be given no point.

Using Multilingual Bidirectional Encoder Representations from Transformers on Medical Corpus for Kurdish Text Classification

Soran S. Badawi

Charmo Center for Scientific Research and Consulting – Language and Linguistic Center, Charmo University
Chamchamal, Sulaimani, Kurdistan region - F.R. Iraq

Abstract—Technology has dominated a huge part of human life. Furthermore, technology users use language continuously to express feelings and sentiments about things. The science behind identifying human attitudes toward a particular product, service, or topic is one of the most active fields of research, and it is called sentiment analysis. While the English language is making real progress in sentiment analysis daily, other less-resourced languages, such as Kurdish, still suffer from fundamental issues and challenges in Natural Language Processing (NLP). This paper experiments with the recently published medical corpus using the classical machine learning method and the latest deep learning tool in NLP and Bidirectional Encoder Representations from Transformers (BERT). We evaluated the findings of both machine learning and deep learning. The outcome indicates that BERT outperforms all the machine learning classifiers by scoring (92%) in accuracy, which is by two points higher than machine learning classifiers.

Index Terms—Bidirectional Encoder Representations from Transformers, Deep learning, Machine learning, Natural language processing, Sentiment analysis, Transformers.

I. INTRODUCTION

The text classification method in natural language processing (NLP) is one of the approaches of identifying the emotions in text. The field has gained more popularity since the emergence of social platforms such as Twitter and Facebook (Hoang, Bihorac, and Rouces, 2019). It has been tackled very well in the English Language. Conversely, the work done in the Kurdish language remains in its infancy; thus, more cooperation and contributions are required from research communities to offer a mature sentiment analysis system in Kurdish. The previous Kurdish sentiment analysis works mostly centered on classical machine learning classifiers. In general, these classical methods are considered to be super-fast and simple. Due to feature engineering, their

performance firmly hangs on the feature selection before training.

Later on, deep learning was developed as a popular alternative to traditional machine learning methods because of its excellence in NLP tasks like text classifications (Collobert, et al., 2011). The main idea of deep learning algorithms is the automated extraction of representations from data (LeCun, et al., 2015).

The previous methods, for instance, a bag-of-words (BOW) and a Term Frequency Inverse Document Frequency (TF-IDF) approach, statistically represent word frequency in documents. Therefore, they could not recognize the relationship between different keywords in a document as inherently statistical methods. Consequently, Word Embedding methods emerged to help solve this issue by representing words as mathematical vectors in a multidimensional space. Usually, these vectors provide vital information about the associations between words. Numerous studies on word embedding proved that pre-trained word embedding models, such as word2vec (Mikolov, et al., 2013) and GloVe (Pennington, Socher, and Manning, 2014) and Bidirectional Encoder Representations from Transformers (BERT) (Devlin, 2018), can significantly enhance text classification and other NLP tasks.

BERT is based on a multi-layer bidirectional transformer (Vaswani, et al., 2017). BERT is pre-trained on a large corpus of multilingual data in a self-supervised pattern, which implies that it was only pre-trained on the raw text independence of humans, labeling them in any way. It uses an automatic process to generate inputs and labels from those texts. Google Search Team has pre-trained BERT with 12 layers and 768 hidden dimensions per single token. Bert's total parameter equals 110 million parameters (Devlin, 2018).

In this study, we use BERT to classify Kurdish texts. We begin by comparing the BERT's performance with traditional machine learning methods that have been extensively utilized in earlier publications. The rest of this paper is structured in this way. We examine the literature on classifying Kurdish texts in the next part. Then, we apply a customized BERT-Multilingual model to the medical corpus and compare the outcomes with text categorization methods based on machine learning. The conclusion of this study will be included in the final section.

ARO-The Scientific Journal of Koya University
Vol. XI, No. 1 (2023), Article ID: ARO.11088. 6 pages
Doi: 10.14500/aro.11088

Received: 10 October 2022; Accepted: 29 December 2022

Regular research paper: Published: 15 January 2023.

Corresponding author's e-mail: Soran.sedeeq@charmouniversity.org

Copyright © 2023 Soran S. Badawi. This is an open access article distributed under the Creative Commons Attribution License.



II. RELATED WORKS

Kurdish language has more than 30 million speakers around the globe and is categorized as one of the less-resourced languages, particularly in the field of NLP (Esmaili, 2012). Unlike English, mountainous works have been done in different areas of NLP; the sentiment analysis process in Kurdish is still in its early stages. So far, only one research study has been carried out in this direction. Two Kurdish researchers, Salam Abdulla and Mzhda Hiwa Hama, carried out the work. Their work entitled "Sentiment Analyses for Kurdish Social Network Texts using Naive Bayes Classifier" (2015)". Their data contained 15k tweets containing positive and negative labels, distributed half for each tag. The result was achieved using Naive Bayes (0.66) (Abdulla and Hama, 2015). In addition to this, the corpus is not available online. Moreover, their corpus was not trained in deep learning tools.

III. BERT ARCHITECTURE

BERT, which stands for Bidirectional Encoder Representations from Transformers, is a transformers model pre-trained on a large corpus of multilingual data in a self-supervised fashion, which means that it was pre-trained on the raw texts only, independence of humans labeling them in any way with an automatic process to generate inputs, and labels from those texts. Google Search Team has pre-trained BERT with 12 layers and 768 hidden dimensions per single token. Bert's total parameter equals 110 million parameters (Devlin, 2018). The architecture of the model is displayed in Fig. 1.

Moreover, BERT requires its input token sequence to have a specific format. The first token of every sequence should be assigned as (CLS) (classification token), and there should be a (SEP) token (separation token) after every sentence to achieve the same format (Ling, 2020). To construct an input representation for a token, a sum is applied to its token, segment, and position embeddings. An illustration of this construction is shown in Fig. 2.

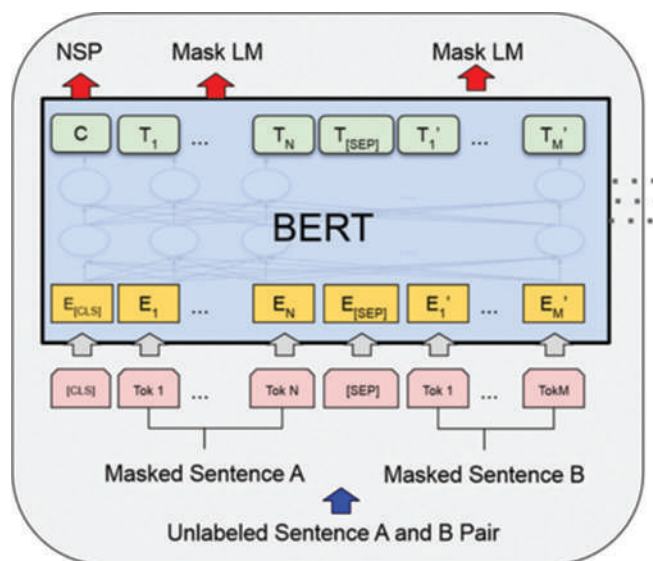


Fig. 1. The architecture of the model.

BERT is widely implemented in text classification for other resourceful languages. Since it gives high accuracy compared to traditional machine learning algorithms due to having many layers, as shown in Fig. 3.

As illustrated in Fig. 3, the first is called Input, the input layer. This layer accepts the initial word embedding and delivers it into BERT. The second part is BERT which is the pre-trained BERT model. The output of this part is the final word embedding of each input token. The last part is predict. In this part, the hidden representation is passed to a dense layer followed by *softmax*. The *softmax* is applied along the dimension of the sequence. Mathematically, the *softmax* function takes input as a vector of K real numbers and normalizes it into a probability distribution consisting of K probabilities proportional to the exponentials of the input numbers. The output is the probabilities of each label (Ling, 2020)

IV. METHODOLOGY

The dataset used in this paper contains social media comments written in the Kurdish language. Because many users used Arabic-supported keyboards built-in on their mobile devices when commenting on videos, posts, and pictures. For example, in the Arabic letter "ز" is absent. If users intend to type words that have the letter "ز," they write "خوش" instead of "خۆش." This dictation error causes the machine learning classifiers, BOW and Bert, which use the tokenization process to understand those two words when they are a single word.

Pre-processing is an essential phase of machine learning and deep learning. The pre-processing helps the classifiers to provide better results. From a morphological perspective, Kurdish is a language with numerous attachments, such as Arabic and Persian. Knowing the extension might give information about the pronouns, the plurality, and the location pre-positionally (Cieliebak, et al., 2017). Thus, pre-processing would be challenging since the language has progressed in NLP. Luckily, we could use the python KLPT toolkit developed by Ahmadi (2020). The libraries on KLPT helped us with normalization, standardization, and tokenization. It is essential to know that there are no special libraries to point out stop-words in the Kurdish language. We created the stop-word lists and implemented them on the corpus. The dataset includes a collection of raw comments from Kurdish social media users. The initial cleaning of the dataset included the removal of URLs, not-Kurdish alphabetical, emojis, and numbers. However, there are no mentions of using software or a library to accomplish this. We used the KLPT library to perform the following process;

1. Normalization for unifying dialects and scripts based on different encodings
For example
Unnormalized texts - "دكتور كيان ٤٥ رۆزه نهشته ركه ريم كردوه"
Normalized text "دكتور كيان 45 روزه نهشته ركه ريم كردوه"
2. Standardization – When given a normalized text, it returns standardized Kurdish text according to Sorani's recommendations.

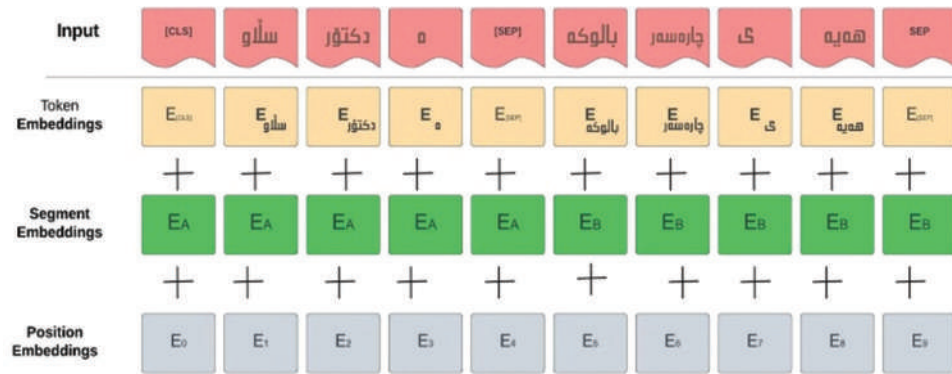


Fig. 2. Input representation of BERT.

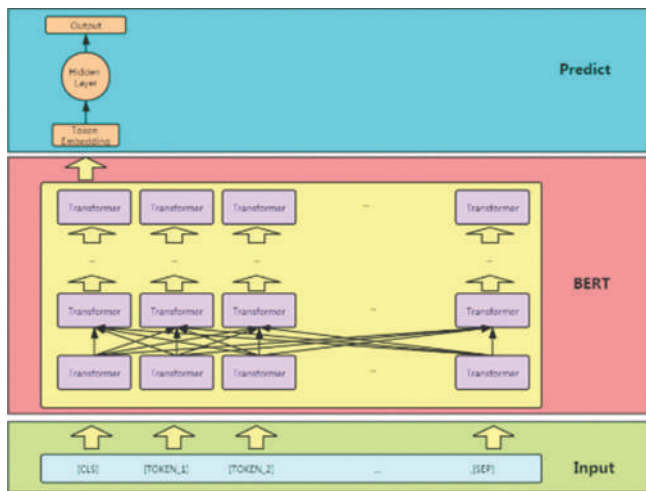


Fig. 3. BERT layers for text classification.

For instance

Unstandardized text - "دکتۆر گیان 45 رۆژه نهشتهرکهیم کردوه"
 Standardized text- "دکتۆر گیان 45 رۆژه نهشتهرکهیم کردوه"

3. Tokenization refers to slicing sentences into words and putting them in a list.

For example, the tokenization of the example above is ['دکتۆر', ' _گیان_ ', '45', 'رۆژه', 'نهشتهرکهیم', 'کردوه']

Luckily, the library’s documentation would help us construct a scientific set of vocabulary, which would be crucial to the machine learning classifiers when using BOW and for Bert to find the tokens of each language in the pre-trained model.

We implement HuggingFace, a BERT-multilingual tokenizer, and its model on the input data. Our data are tokenized before being used for training by fine-tuning the BERT model. The process of fine-tuning Bert begins with stacking multilingual-BERT with five multilingual-BERT layers. We add a dense layer with a softmax activation function in the next step. A binary cross-entropy loss function was also used to minimize the errors while training our models (Zahera, et al., 2019). Compared to the original BERT, the fine-tuned model requires much less time to train. Furthermore, fine-tuning BERT assists us with training a model to good performance on a much smaller amount of training data. Finally, this simple fine-tuning procedure (typically adding one fully connected

layer on top of BERT and training for a few epochs) was shown to achieve a state of the art results with minimal task-specific adjustments for a wide variety of tasks: Classification, language inference, semantic similarity, question answering, etc. Rather than implementing custom and sometimes obscure architecture shown to work well on a specific task, simply fine-tuning BERT is shown to be a better (or at least equal) alternative. We reduce the max length to 128 for the BERT tokenizer, the batch size to 8, as shown in Fig. 4, and the training epochs to 3.

We experiment with decision tree and support vector machine (SVM) classifiers, multinomial stochastic gradient descent (SGD), k-nearest neighbor (kNN), SVM, Random Forest, and Logistic Regression. We compare their results with BERT, as shown in Table I. We also use a Count Vectorizer with a mixture of unigrams, bi-grams, and tri-gram representations of words for our machine-learning methods, because of the nature of our corpus. Usually, medical texts contain many keywords with low frequency (e.g., a disease’s name or a medicine’s name). The disease or medicine names have been transliterated into Kurdish language, as displayed in Fig. 5. These words contribute heavily to the classification since they are often less frequent; their importance would be lost in a BOW approach because of their low frequency, which only counts the word frequency in documents. Furthermore, we notice that the majority of medical texts include words such as “دکتۆر، عیاده، فیتامین، مرههه، لیزهر، فیلمه، پیسته”

Data-splitting is an essential step. The method used for splitting the data predominantly affects the model’s outcome. Since our dataset is not very big, we used holdout to split our data. In the first phase, we used (the 80% train-20% test) technique. Moreover, we split the trainset using the Holdout technique to create a validation set. Having a validation set is vital, particularly in the case of deep learning.

V. RESULTS AND DISCUSSION

This work’s database comprises 6756 samples distributed between two labels (medical and non-medical). The number of medical texts equals 3076, while the number of non-medical texts is 3680 (Saeed, 2022), as shown in Fig. 6.

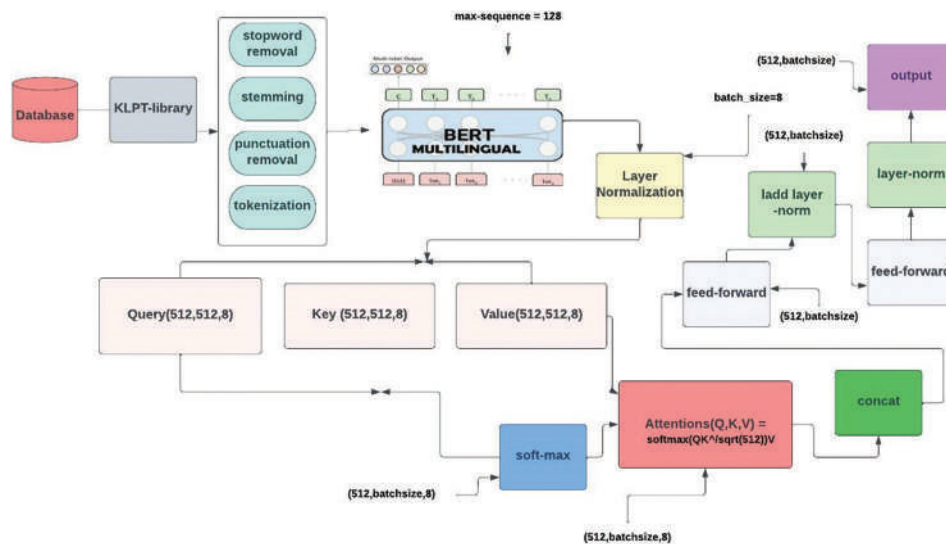


Fig. 4. The design of the full fine-tuned (proposed) model.

من سالیگ عهه‌مه‌لایات کراوم له کاته‌وه بیستم هیشک ده‌بیت	medical
سلاو من ده م‌وجاوم خالی قاوه‌ی یه جی باشه یزه حمه ت	medical
سه رکه وتوبیت	notmedical
رجیم له ره مه زان زه ره ر‌نینه	medical
سلاو دک‌تورگیان من‌برجم زور ده‌وره‌ئ	medical
ده‌ست خو‌ش بی‌ت دک‌توره	medical
دک‌تور من بیستم زور چوره	medical
من لیوم زور ووشک ابیت به لام لی‌تر او‌خۆمه وه رۆزانه ج بکه م‌دایم جه وری اکه م‌سودی نیبه	medical
سلاو دک‌توره بی زه‌حمت مره‌می اک‌زیمای ده‌ست جی باشه	medical
ئه‌ی ده‌ست خو‌ش سو‌باس	notmedical
چاره‌سه‌ری گوشتی پ‌شتی جاو‌به‌جی له کریت پ‌ئولی جاو	medical
سلاو دک‌تور سه‌رم نوک ده‌وره‌ئ	medical
زایانی زور‌ترت یاخود سود	medical
ب‌یستی دم جاوم سوره زوده سونی وشک‌یش ج‌بیکه م‌ته مه‌نم سال	medical
وشک بو‌نی بیستم ده‌ست خورانی زور	medical
دک‌توره ف‌یس بوک ناو‌نیشان	medical
سلاو دک‌تور شو‌ئینی ز‌بیکه چۆن لاده‌ج‌یت	medical
سلاو ب‌ستی ده‌سم وشک له‌ی خورانی زوره چۆن چاره‌سه‌ره‌که‌ری	medical

Fig. 5. Sample texts in the corpus.

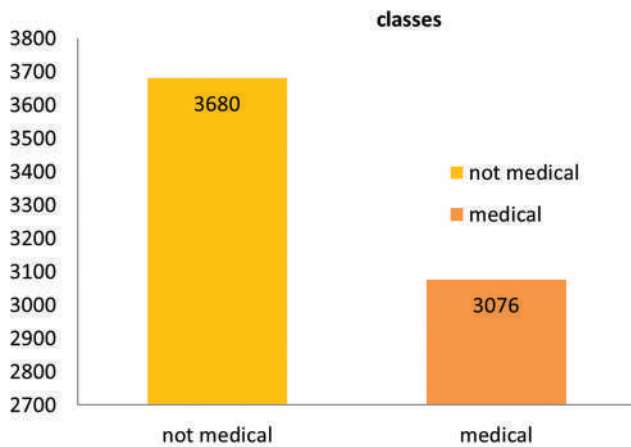


Fig. 6. The amount of data in the corpus.

We separate (4324 texts) for training and validation (1081 texts) and keep the rest (1352 texts) for testing. A shuffling technique was implemented to block the model from learning the specific order of words and inputs and provide a more

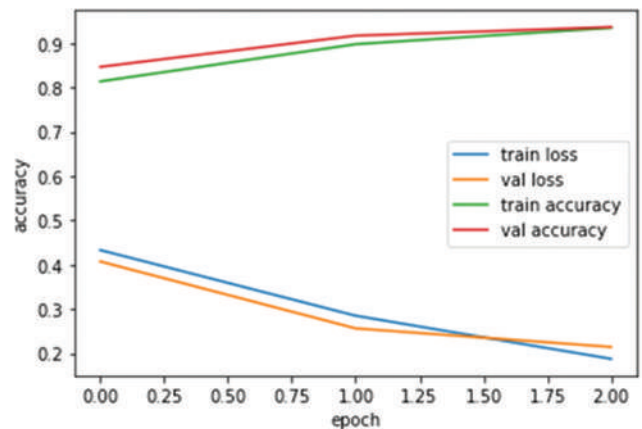


Fig. 7. The accuracy PER 2 epochs.

TABLE 1
THE SCORE OF (PRECISION, RECALL, ACCURACY, AND F1_SCORE) METRICS QF EACH CLASSIFIER

Classifier	Precision	Recall	Accuracy	F1_score
Multinomial	0.91	0.90	0.90	0.90
SGD	0.90	0.89	0.89	0.88
Decision tree	0.85	0.85	0.85	0.85
Random forest	0.90	0.89	0.89	0.89
SVM	0.82	0.82	0.82	0.82
KNN	0.33	0.57	0.57	0.42
Logistic regression	0.89	0.88	0.88	0.87
Bert multilingual	0.92	0.92	0.92	0.92

SVM: Support vector machines, kNN: k-nearest neighbor, SGD: Stochastic gradient descent

realistic result. Table I shows the scores achieved from training on the classifiers.

The corpus works well with machine learning and deep learning classifiers, except for KNN, with the lowest score of 0.57. In terms of precision, the multinomial classifier outperforms other classical classifiers with a score of 0.91. Moreover, the second-best classifiers are SGD and

random forest, scoring 0.90. The rest of the classifiers stay between 0.80 and 0.89. Similarly, multinomial yields a more significant result than other ML classifiers for recall which is 0.90. SGD and random forest come second by scoring one point lower than multinomial.

Regarding deep learning, BERT outperforms the classical classifier by scoring the highest point in all measurements, which is 0.92. the model was merely trained for ten epochs. It is essential to state that training the model on a higher number helps the model achieve a score closer to 100% for all measurements, as shown in Fig. 7. Furthermore, the validation loss decreases significantly, guaranteeing a higher accuracy score.

Training loss is a metric to evaluate how well a deep-learning model fits the training data. On the other hand, validation loss specifies how well a deep learning model performs when evaluated against validation data. Moreover, the validation and training accuracy measure the model's overfitting. Overfitting refers to a statistical modeling error that occurs when a function is too closely aligned with a limited set of data points. Thus, the model is only helpful for its initial data set and not any other data sets. Since the gap between training loss and validation loss is too narrow, as illustrated in Fig. 7, it indicates that our model is fully optimized and has zero overfitting cases.

In the next phase, We attempt to compare our model with another state-of-the-art model in the Kurdish language. Unfortunately, this matter has yet to be tackled by researchers in the language. Therefore, we sought other language models which are close to the English language. We discovered a Bert-based model in the persian language known as ParsBert. Moreover, we compared our fine-tuned BERT model with the latest ParsBert model (Farahani, et al., 2021). ParBert is a recent state-of-the-art model developed for persian languages. The pre-trained model is used for numerous tasks such as text classification, question-answering, and named entity recognition. We trained our dataset on the pre-trained model; the results are displayed (Table II).

Overall, it can be noted that our fine-tuned model works slightly better than ParsBert, particularly in the case of precision and F1_score. The main reason behind this is that the Persian language is close to the Kurdish language, particularly in the sense of having nearly similar alphabetical letters and many standard vocabularies that existed in our corpus, as shown in Table III. Naturally, these similarities helped ParsBert find the tokens for most of the lexicons in our corpus, which ultimately yielded high results for ParsBert.

It is worth noting that having such a model is crucial to the Kurdish language. Even though this is the first time, the Kurdish language is introduced to a pre-trained model like BERT. The model outperformed the state-of-the-art by fine-tuning and using widespread softmax activation. The outcome achieved can add another source for the Kurdish language and prevent it from being labeled a less-resourced language. Moreover, the model can be utilized on Kurdish clinical websites or social media pages to separate medical and nonmedical questions. They can answer medical questions and serve their users, guaranteeing more customers. This is because our model can recognize non-medical text with high accuracy.

TABLE II

THE SCORE OF (PRECISION, RECALL, ACCURACY, AND F1_SCORE) METRICS QF MULTILINGUAL AND PARSBERT

Model	Precision	Recall	Accuracy	F1_score
BERT-multilingual	92	92	92	92
ParsBert	91	92	92	91

TABLE III

SAMPLE OF COMMON WORDS BETWEEN KURDISH AND PERSIAN

Kurdish	Persian	English meaning
دكتور	دکتر	Doctor
(مو(قز	مو	Hair
سەر	سر	Head
دهست	دست	Hand
عیلاج	عیلاج	Treatment
گوشت	گوشت	Meat

VI. CONCLUSION

In this paper, we experimented with the recently published medical corpus for the Kurdish language using machine learning and deep learning (BERT) to classify texts. We removed the stop words and irrelevant texts in the pre-processing stage. We compared the performances of the deep learning method with the conventional machine learning classifiers. Our experiments indicate that the BERT-multilingual model achieved higher accuracy of 0.92 in the text classification task and showed at least +0.2 improvement over the traditional machine learning methods. For future work, we suggest using augmentation techniques by lemmatizing and giving the stem of the keywords in the input data, as this yielded higher results in other languages.

REFERENCES

- Abdulla, S. and Hama, M. H., 2015. Sentiment analyses for kurdish social network texts using naive bayes classifier. *Journal of University of Human Development*, 1(4), pp. 393-397.
- Ahmadi, S., 2020. *KLPT-Kurdish Language Processing Toolkit*. In: Proceedings of Second Workshop for NLP Open Source Software (NLP-OSS), pp. 72-84.
- Cieliebak, M., Deriu, J.M., Egger, D. and Uzdilli, F., 2017. *A Twitter Corpus and Benchmark Resources for German Sentiment Analysis*. In: Proceedings of the Fifth International Workshop on Natural Language Processing for Social Medias. pp. 45-51.
- Collobert, R., Weston, J., Bottu, L., Karlen, M., Kavukcuoglu, K. and Kuksa, P., 2011. Natural language processing (almost) from scratch. *Journal of Machine Learning Research*, 12, pp. 2493-2537.
- Devlin, J., Chang, M.W., Lee, K. and Toutanova, K., 2018. BERT: Pre-training of deep bidirectional transformers for language understanding. Available from: <http://arxiv.org/abs/1810.04805>
- Esmaili, K., 2012. Challenges in Kurdish text processing. arXiv preprint arXiv:1212.0074.
- Farahani, M., Gharachorloo, M., Farahani, M. and Manthouri, M., 2021. Parsbert: Transformer-based model for persian language understanding. *Neural Processing Letters*, 53(6), pp. 3831-3847.
- Hoang, M., Bihorac, O.A. and Rouces, J., 2019. *Aspect-Based Sentiment Analysis Using Bert*. In: Proceedings of the 22nd Nordic Conference on Computational Linguistics. pp. 187-196.

LeCun, Y., Bengio, Y. and Hinton, G., 2015. Deep learning. *Nature*, 521(7553), pp. 436-444.

Ling, J., 2020. *Coronavirus Public Sentiment Analysis with BERT Deep Learning*. Dalarna University, Sweden.

Mikolov, T., Sutskever, I., Chen, K., Corrado, G. and Dean, J. 2013. Distributed representations of words and phrases and their compositionality. In: Proc. Advances in Neural Information Processing Systems. 26, pp.3111–3119.

Pennington, J., Socher, R. and Manning, C., 2014. *Glove: Global vectors for word representation*. In: Proceedings of the 2014 Conference on Empirical Methods

in Natural Language Processing (EMNLP), pp. 1532-1543.

Saeed, A.M., Hussein, S. R., Ali, C.M. and Rashid, T. A., 2022. Medical dataset classification for Kurdish short text over social media. *Data Brief*, 42, p.108089.

Vaswani, A., Shazeer, N., Parmar, N., Uszkoreit, J., Jones, L., Gomez, A.N., Kaiser, L. and Polosukhin, I., 2017. Attention is all you need. In: *Advances in Neural Information Processing Systems*, Vol. 30. NeurIPS Proceedings.

Zahera, H. M. Elgendy, I., Jalota, R. and Sherif, M.A., 2019. *Fine-tuned BERT Model for Multi-Label Tweets Classification*. The Real Estate Company, Mumbai. pp. 1-7.

Cytostatic Effects of Avocado Oil Using Single-cell Gel Electrophoresis (Comet Assay): An Evaluation

Subasini Uthirapathy

Department of Pharmacology, Faculty of Pharmacy, Tishk International University,
Erbil, Kurdistan Region, Iraq

Abstract—The goal of this paper is to assess the mutagenic and genotoxic potentials of avocado oil made from the fruit pulp of *Persea Americana*, a member of the *Lauraceae* family. Michigan Cancer Foundation-7 (MCF-7) cells are used in the 3-4,5 dimethylthiazol-2yl-2,5-diphenyl tetrazolium bromide (MTT) test to examine the possible antiproliferative and cytostatic qualities of different doses of avocado oil, and MCF-7 cells are used in the comet assay to examine the potential cytostatic effects of avocado oil extracted from the avocado fruit. DNA in human breast cancer cells is partially damaged by avocado oil. However, DNA damage at low, medium, and high levels was discovered in the positive control. Without positive control, the DNA damage level falls in the low, middle, and high ranges. The MTT assay shows that avocado oil exerts a dose-dependent cytostatic impact on human breast cancer MCF-7 cells with an IC_{50} value of 379.2 $\mu\text{g/mL}$, which is the IC_{50} value that causes genotoxicity in the comet assay.

Index Terms—Avocado oil, *Persea Americana*, Genotoxicity, Mutagenic, Cytostatic

I. INTRODUCTION

In a multistage process that involves moving from a precancerous lesion to a malignant tumor state, cancer develops when normal cells undergo the change into tumor cells. The interaction of a person's genetic characteristics with environmental elements such as ultraviolet radiation, chemical elements such as cigarettes and asbestos, and biological elements such as viruses and bacteria leads to these alterations (Cragg and Newman, 2009). Deregulation of one or more cellular mechanisms, such as cell division and apoptosis, which are necessary for the healthy cells' normal growth and proliferation, leads to the development of cancer (Elmore, 2007). The main aim of medication development and candidate screening is to identify the differences in regulatory mechanism at play in cancer cells responsible for transformation and particularly target that mechanism (Wiman and Zhivotovsky, 2017) *Persea americana*, often called avocado or gator pear,

stands out among the fruits with exceptional dietary and therapeutic properties. According to earlier studies, the total lipid content of fruit was higher than that of seed (Matsuoka and Yashiro, 2018, Imran, et al., 2017).

P. americana, avocado or alligator pear, has excellent nutritional and medical applications. Avocado oil is a nutritious oil that is rich in the unsaturated fat oleic acid. It aids in the body's absorption of other fat-soluble vitamins and contains vitamin E. It has been shown to lower low-density lipoprotein cholesterol and raise high-density lipoprotein cholesterol since it is a good source of monounsaturated fat. It contains high amount of fats, proteins, fibers, as well as vitamins and minerals such as phosphorus, sodium, magnesium, potassium, iron, and zinc (Orhevba and Jinadu, 2011; Oluwole, et al., 2013). The bioactive compounds separated from *P. americana* such as linoleic acid, linolenic acid, and oleic acid are all present in abundance in avocado oil that is derived from the fruit's pulp. In addition, it has minerals, vitamins A, C, D, and E, as well as -sitosterol, -carotene, and lecithin (IsabelleSantana, et al., 2019).

Decoctions of avocado seeds have been used in ethnopharmacological investigations of the Aztec and Maya cultures to treat gastrointestinal irregularities, diabetes, inflammation, and mycotic and parasite illnesses. Insecticidal, antibacterial, antidiabetic, and blood pressure-lowering properties of avocado seeds are highlighted in our prior review (Dabas, et al., 2011). Avocado seeds are abundant in polyphenols and have a wide variety of compounds in them. The ethanolic extract of avocado seeds contains a triterpenoid component, and Michigan Cancer Foundation-7 (MCF-7) breast cells were used to study the seed's cytotoxic effects (Abubakar, Achmadi and Suparto, 2017). Dabas, et al., in 2013, discovered that the IC_{50} values for the triterpenoid fractions were 80.1 g/mL and 99.7 g/mL, whereas the IC_{50} values for the total extract were 560.2 g/mL and 107.2 g/mL, respectively. Kristanty, et al., in 2014, discovered that the cytotoxicity of aqueous and ethanolic extract of avocado seeds suppressed T47D breast cancer cell line. Using the comet test or single-cell gel electrophoresis (SCGE), one can evaluate DNA damage and repair in individual cells in a flexible, sensitive, easy-to-use, and affordable manner. In the fields of genotoxicity, pharmacology, and molecular investigations, it is necessary to detect DNA damage at the level of eukaryotic cells. The comet assay is useful for measuring DNA breaks at

ARO-The Scientific Journal of Koya University
Vol. XI, No. 1 (2023), Article ID: ARO.11073. 21 pages
DOI: 10.14500/aro.11073

Received: 19 September 2022; Accepted: 31 December 2022

Regular research paper: Published: 15 January 2023

Corresponding author's e-mail: subasini.uthirapathy@tiu.edu.iq

Copyright © 2023 Subasini Uthirapathy. This is an open access article distributed under the Creative Commons Attribution License.



apurinic and apyrimidinic locations, particularly single-strand DNA breaks. Cells with DNA crosslinks, base-pair damage, and apoptotic nuclei (Nandhakumar, et al., (2011).

Ostling and Johnson, in 1984, provided an explanation of DNA migration from nuclei exposed to an electric field under neutral conditions. Singh, et al., in 1988, significantly improved the specificity and repeatability of this method by modifying and refining it in alkaline conditions. The comet test has since gained popularity and developed into a widely used method for assessing DNA damage. The alkaline comet assay is the method that is most frequently used to evaluate DNA damage (Kaur, et al., 2011).

A quick, easy, visible, and sensitive method for determining and assessing DNA breakage in mammalian cells is the single-cell electrophoresis test, sometimes referred to as the comet assay (Tice, et al., 2000, Kaur, et al., 2011, Collins, 2003). The primary goal of the current study is to assess the anticancer potential of *P. Americana* avocado oil, on human breast MCF-7 cancer cell line using a variety of assay methodologies, including morphological investigations, cell viability tests, and comet assays.

II. MATERIALS AND METHODS

A. Chemicals and Consumables

The human breast cancer cell line MCF-7 was bought from NCCS Pune in India. Fetal bovine serum (FBS), Dulbecco's Modified Eagle's Medium (DMEM), the antibiotic solution was from Gibco (USA), dimethyl sulfoxide (DMSO), 3-4,5 dimethylthiazol-2-yl-2,5-diphenyl tetrazolium bromide (MTT) was from Sigma, USA, 1X PBS was from Himedia, 96-well tissue culture plate, and wash beaker were purchased from Tarson Products Pvt Ltd, Kolkata, India.

Agarose low melting and normal melting gels, sodium chloride (analytical grade-AR), potassium chloride (AR), disodium hydrogen phosphate (AR), disodium EDTA, trichloroacetic acid, zinc sulfate, sodium carbonate, ammonium nitrate (AR), potassium dihydrogen phosphate (AR), triton X 100, glycerol, and formaldehyde. Glass measuring cylinders, beakers, conical flasks, staining troughs, straining boxes, micropipettes, and tubes for microcentrifugation.

B. Isolation of Avocado Oil Extracted from a Pulp of Avocados by Cold-pressed Method

Avocado fruits were obtained a local grocery store in Erbil, Iraq. The following is the steps involved in making Avocado oil. After washing the avocados, cut them into two halves, then using a spoon collect the flesh of the avocado such that they will come out having a paste like consistency. Spread the avocado paste on a tray and spread with medium layer in thickness such that the layer is not too thick and not too thin. The tray is placed in a warm shady and airy area in the house. Avoiding placing the tray directly in the sun. After 4 h, the top layer of the avocado paste it has a dark brownish color. At this stage use a spoon and mix the paste such that the upper layer mixes well with the layer using the spoon,

the upper layer and lower layer of the paste are mixed well gently. After mixing the avocado paste is spread back on the tray and kept it in an airy, warm, and shady corner in the house. We repeat this procedure whenever we notice that the upper layer of the avocado has a dark brownish color. After the procedure is repeated, whenever noticed that the upper layer of the avocado became a dark brownish color. Once more, the mixture will include almost no avocado paste and only oil. Now take the avocado mixture out of the avocado.

Avoiding too dry paste may lead to difficulty in removing it from the tray and difficult to press out the oil. The oil using cheese cloth is ready and the bowl that use in collecting the oil. Then hold the cloth together and squeeze out the oil, there is so much oil coming out. The oil will be kept in an aseptic area.

C. MTT Assay

The MTT test was used to evaluate the possible cytotoxic and antiproliferative effects of avocado oil on human MCF-7 cells (human breast cancer) cell lines. Al-Qubaisi, et al., in 2011, used the MTT experiment with a few minor modifications. According to the methodology, MCF-7 cell lines were grown in liquid DMEM supplemented with 10% FBS, 100 g/mL streptomycin, and 100 g/mL penicillin. These conditions were kept at 37°C in a 5% CO₂ atmosphere.

Trypsinization was used to harvest the cultivated MCF-7 cells, which were, then, gathered in a 15 mL tube. The cells were, then, seeded into a 96-well tissue culture plate at a density of 1×10^5 cells/mL cells/well (200 μ L) in DMEM media with 10% FBS and 1% antibiotic solution for 24–48 h at 37°C. In a serum-free DMEM medium, the wells were cleaned with sterile PBS before being treated with various doses of avocado oil. The cells were incubated for 24 h at 37°C in a humidified 5% CO₂ incubator, with each sample being replicated three times.

The cells were, then, treated for a further 2–4 h with MTT (20 μ L of 5 mg/mL) until purple precipitates were plainly visible under an inverted microscope. The medium and MTT (220 μ L) were then aspirated out of the wells and rinsed with 1X PBS (200 μ L). In addition, DMSO (100 μ L) was added, and the plate was agitated for 5 min to dissolve the formazan crystals.

With the use of a fluorescence multi-detection reader, the optical density (OD) was measured at 570 nm (Thermo Fisher Scientific, USA). Cells that had not been treated served as a control. Measurements were made, and a graphic representation of the concentration needed to reduce viability by 50% was obtained. The drug concentration was plotted in the X-axis using the standard GraphPad prism 6.0 program, with the relative cell viability being represented on the Y-axis.

$$\text{Cell viability (\%)} = \frac{\text{OD test}}{\text{OD control}} \times 100$$

D. Comet Assay (SCGE)

“Human MCF-7 breast cancer cells were used in the comet test”. In a 24-well plate, at a density of 10,000 MCF-7 cells were planted, and they were then cultured for 24 h at 37°C in a humidified 5% CO₂ incubator (Nandakumar, et al., 2011). The wells were treated with 379.2 μ g/mL of avocado oil sample in a serum-free DMEM medium for 24 h in a CO₂

incubator after being treated with sterile PBS. Following incubation, the cells were collected using trypsinization in a 1.5 mL tube, and the comet assay was carried out using, with a few minor modifications of Nandhakumar, et al., (2011) techniques. First, 200 μ L of 0.75% normal melting agarose and then 100 μ L of 0.5% low melting agarose were progressively applied onto the microscopic slides. The following phase involved adding 20 μ L of cell suspension to 60 μ L of 0.5% low melting agarose, which served as the third layer on the slides.

After that, the slides were kept at 4°C overnight in cell lysis buffer (2.5 M NaCl, 0.2 M NaOH, 100 mM Na₂EDTA, 10 mM Tris-HCl, 1% Triton X-100, and 10% dimethyl sulfoxide, pH = 10.0). The slides were then three times submerged in double-distilled water, followed by a 20-min incubation with an unwinding solution (3M NaOH). Slides were, then, put into a horizontal gel electrophoresis tank with electrophoresis solution (1 mM Na₂EDTA and 300 mM NaOH, pH = 13). For 25 min, the electrophoresis was carried out at 25 V (1 V/cm, 300 mA). The slides were, then, exposed for 10 min to neutralization buffer (0.4 M Tris-HCl, pH = 7.5), immersed 3 times in ultrapure water, and allowed to air dry.

III. RESULTS AND DISCUSSION

The purpose of this study was to look into the cytostatic effects of genuine avocado oil on MCF-7 human breast cancer cells. With the prevalence of malignancies, many herbal plant species demonstrate cytostatic activities (Parasuraman, Raveendran and Kesavan, 2010). Therefore, it is crucial to comprehend the possible toxicity of herbal plants. Some traditional medicinal herbs have secondary metabolite components that have the potential to cause cancer and/or be genotoxic. In developing nations, the majority of medicinal plants are used for homemade medicines. They provide a variety of nutrients and biomolecules important to human health (Nadin, Vargas-Roig and Ciocca, 2001). Five avocado fruits were used in the cold-pressed extraction of avocado oil from the fruit's pulp, yielding more than 20 mL of dark greenish essential oil. Linoleic acid, linolenic acid, and oleic acid are all present in abundance in avocado oil that is derived from the fruit's pulp. In addition, it has minerals, vitamins A, C, D, and E, as well as sitosterol, carotene, and lecithin (IsabelleSantana, et al., 2019). Sterols and hydrocarbons made up the majority of *P. americana* fruits. The smallest components in the fruit other than that seed of *P. americana* were derivatives of other types of sterols, including campesterol, stigmasterol, and sitosterol.

Lipid components are the avocado fruit's most significant attributes. Five to six fatty acids are present in substantial concentrations in avocado fruits. These acids include the monounsaturated fatty acids (MUFA) oleic acid and palmitoleic acid, the polyunsaturated fatty acids (PUFA) linoleic acid and linolenic acid, as well as the saturated fatty acids (SFA) palmitic acid and stearic acid. Oleic acid, which was the most prevalent MUFA at both sites, makes up more than 50% of the total lipids. According to McDaniel, et al., (2008), "avocados have been found to have a fruit oil that

is high in MUFAs (MUFA), PUFA, and SFAs, with 71% MUFA, 13% PUFA, and 16% SFAs."

A. MTT Assay

MCF-7 cells were tested using the MTT assay to determine their cytotoxicity against human breast cancer cells. Human breast MCF-7 cells' ability to proliferate was decreased by avocado oil. Fig. 1 shows the MTT assay findings. Within 24 h, the proliferation of cells toward MCF-7 cells was inhibited at different concentrations (31.25–1000 μ g/mL). The IC₅₀ value of avocado oil for MCF-7 cell lines at 24 h was 379.2 μ g/ml. MTT was a water-soluble substance that the live cell can take up. For calorimetric measurement, a water-insoluble blue formazan that was the reduction product of MTT must be dissolved. Effects of avocado oil on human breast cancer cells that suppress cancer cell growth (MCF-7), it exhibited the most cytotoxic effects. Due to the oil's bioactive components, particularly MUFA such as oleic acid and linoleic acid, the antiproliferative properties of avocado oil are enhanced. Avocado oil has an IC₅₀ of 379.2 μ g/mL, with MCF-7 cells being the most sensitive. MCF-7 cells were used in this experiment due to their sensitivity to growth inhibition caused by avocado oil. To find out how normal, non-tumorigenic cells respond to avocado oil in terms of growth.

As shown in Fig. 2a, the untreated MCF-7 cells maintained their original morphology and close closeness to one another even when the incubation time was extended to 24 h. In contrast, after being exposed to avocado oil for 24 h, MCF-7 cells started to lose their normal shape. The MCF-7 cells' characteristic elongated spindle-shaped morphology was no longer visible. When the treatment was extended to 48 h, dead cells were discovered; more were discovered at 24 h (Fig. 2b-g). The results of the present study show that avocado essential oil possesses cytostatic properties. The same observational results agreed with those published by Sahranavard, Naghibi and Ghafari (2012) and Jayaprakash, et al. (2010). Numerous natural compounds have been shown to be able to cause apoptosis in different tumor cells with human origin (Aigner, 2002; Shiezadeh, et al., 2013). Apoptotic inducers originating from plants must be thoroughly screened, whether they were

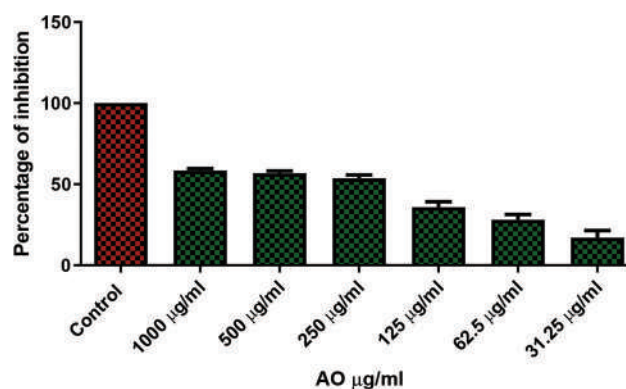


Fig. 1. Cytostatic effect assessed by 3-4,5 dimethylthiazol-2yl-2,5-diphenyl tetrazolium bromide assay of Avocados oil (data were presented as the mean of triplicate determinations \pm standard deviation).

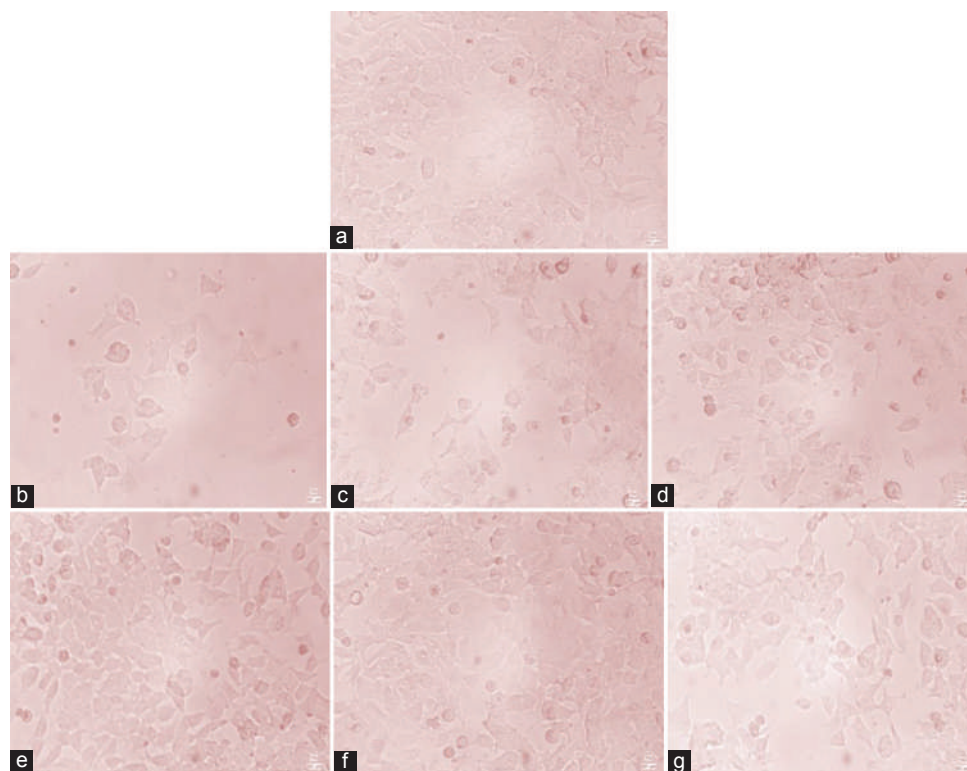


Fig. 2. Cytostatic produced by essential oil of Avocados against human breast cancer MCF-7 cells. Where, figure (a) control cells; and figure (b-g) essential oils of Avocados fruits (conc. 31.25–1000 µg/mL, respectively).

TABLE I
GENOTOXICITY OF AVOCADO OIL IN HUMAN BREAST CANCER CELL LINE IN THE COMET ASSAY

S. No	Test sample	Number of comet events								DNA damage events (%)		
		Class 0	Class 1	Class 2	Class 3	Class 4	Class 0	Class 1	Class 2		Class 3	Class 4
1.	Control	100	100	0	0	0	0	0	0	0	0	0
2.	Treated 79.2 µg/mL of AO	61	58	20	26	7	5	10	8	2	3	40.5%
3.	Average	59.5	23	6	9	2.5						

raw extracts or part of components that have been extracted from their original natural plant sources (Taraphdar, Roy and Bhattacharya, 2001).

B. Comet Assay (SCGE)

At a concentration of 379.2 µg/mL of avocado oil, 59.5% of cells (Class 0) showed no damage, 23% of cells (Class 1) showed light damage, and 9% of cells (Class 1) showed medium damage (Class 3). Cells in 6 and 2.5 were severely damaged by avocado oil (Class 2 and Class 4). The results are shown in Table I. The cells were stained with 50 µL of ethidium bromide (5 mg/L), then viewed under a fluorescence microscope. Fluorescent slides are used to see ethidium bromide dyed slides. The utilization of a fluorescent microscope with a ×200 magnification and an excitation filter of 590 nm allows for the observation of ethidium bromide-stained slides. All procedures were done in low light to prevent extra DNA damage (Nadin, Vargas-Roig and Ciocca, 2001).

C. Evaluation of DNA Damage

Using an ocular scale affixed to the microscope’s eyepiece, the length of the comet tail can be measured. Alternatively, the degree of damage can be visually graded from Class 0–4 based on how the comet appears Fig. 3. Additional option is to use image analysis tools to quantify other DNA damage characteristics as the percentage of DNA damage in the head and tail, the length of the tail movement, the area of the tail, etc. Per sample, a total of 50–70 randomly chosen cells are examined. Comets must be chosen at random to encompass the entire gel. Comets observed in overlaps, air bubbles, and edges are discarded. Fig. 4a-c and Fig. 5 shows the comet’s length, tail length, head diameter, and % of DNA content in the head, tail, and tail movement (Collins, 2003). Twenty fatty acids were found in avocado oil, of which six compounds could be isolated from them, whereas 14 fatty acids remained unrecognized. According to their percentages of 8.87%, 44.61% and 6.40%, respectively, the discovered fatty acids were categorized as saturated, monounsaturated, and polyun SFAs. The discovered fatty acids were categorized as saturated, monounsaturated, and polyun SFAs. The main MUFA from the saponifiable materials that could be isolated was oleic acid methyl ester (Louw, 2012). Other secondary metabolic phytoconstituents such as flavonoids, alkaloids, triterpenes, glycosides, tannins, and steroids are among the phytochemicals found in avocado oil (McDaniel, et al., 2008, Cardoso, et al., 2004).

The IC₅₀ value of avocado oil data showed that there was low, medium, and high damage at concentrations of 379.2 g/mL in comet assay; this may be related to variations in cell physiology, such as cell cycle (Jayaprakash, et al., 2010,

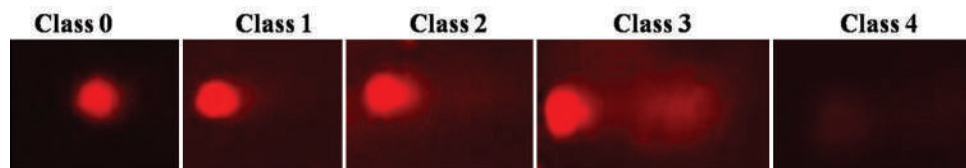


Fig. 3. Visual scoring of DNA damage from Class 0–4 according to comet appearance. Magnification $\times 200$.

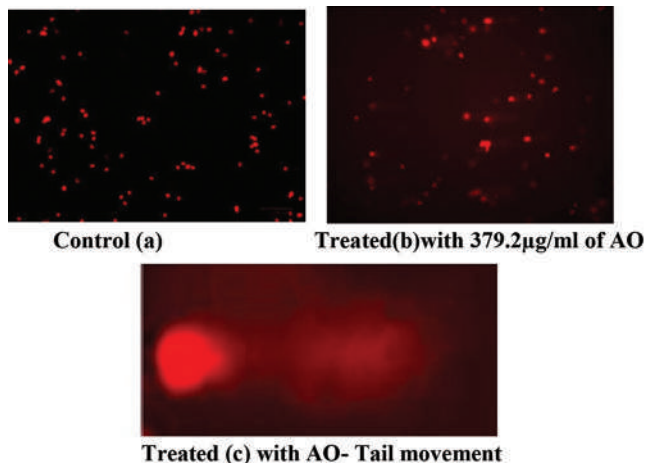


Fig. 4. Photomicrographs of stained DNA human breast cancer cell (MCF-7) for alkaline COMET assay. (a) Untreated showing no DNA damage, (b) treated with Avocado oil (379.2 $\mu\text{g}/\text{mL}$) showing DNA damage, (c) tail movement.



Fig. 5. Various comet parameters - CL: Comet length, TL: Tail length, HD: Head diameter - Magnification $\times 200$.

Kaskoos, et al., 2021). Results showed that there was a decrease in cell damage compared with control group, there was less cell damage. However, a different study using the MTT test showed that avocado oil exhibits a strong cytostatic impact in a dose-dependent manner (JavedAhmad, et al., 2021). Avocado essential oil has medicinal properties and has been used for many years to treat many ailments. With the COMET assay (Kaur, et al., 2011, Jakobsen, et al., 2009, Barakat, et al., 2013), it did not demonstrate total DNA damage. The results of this study show that genotoxicity is caused in Comet assay and MTT assay models by the original essential oil from avocado fruits. Despite the fact that it has antimutagenic properties, more research on molecular signaling pathways is needed. Barakat, et al., in 2013, proved that the water extract of avocado exhibited small IC_{50} values of 13.3 $\mu\text{g}/\text{mL}$ in HepG-2 and 22 $\mu\text{g}/\text{mL}$ in HT-29 cell lines. MTT assay and COMET assay, which are very sensitive tests for estimating DNA damage and which directly identify

single or double strand breaks in individual cells, were used to evaluate the cytotoxicity and genotoxicity of avocado oil in human breast cancer cell lines.

IV. CONCLUSION

Avocado oil is an herb with medicinal characteristics, compared to lipid extract from the seeds, the oil from *P. americana's* fruit displayed surprisingly prominent antioxidant, anti-inflammatory, and anticancer properties. This could be explained by the substantial amounts of sterols, hydrocarbons, and un SFAs. This study's MTT and COMET assay were used to assess the cytostatic and genotoxic effects of avocado oil at various concentrations. These findings imply that the real avocado oil exhibited low, medium, and high levels of DNA damage. The DNA was not completely damaged, though. These show that the actual avocado oils are mutagenic.

ACKNOWLEDGMENT

I gratefully acknowledge the Tishk International University, Erbil, Iraq, for providing research facilities and also acknowledge Trichy Research Institute of Biotechnology Pvt. Ltd., Trichy, Tamil Nadu, India, for conducting anticancer cell line study.

REFERENCES

- Abubakar, A.N.F., Achmadi, S.S. and Suparto, I.H., 2017. Triterpenoid of avocado (*Persea Americana*) seed and its cytotoxic activity toward breast MCF-7 and liver HepG2 cancer cells. *Asian Pacific Journal of Tropical Biomedicine*, 7(5), pp.397-400.
- Aigner, T., 2002. Apoptosis, necrosis, or whatever: How to find out what really happens? *Journal of Pathology*, 198(1), pp.1-4.
- Al-Qubaisi, M., Rozita, R., Yeap, S.K., Omar, A.R., Ali, A.M. and Alitheen, N.B., 2011. Selective cytotoxicity of goniothalamin against hepatoblastoma HepG2 cells. *Molecules*, 16(4), pp.2944-2959.
- Barakat, H.S., El-Hallouty, S., Khalifa, N.S. and Salem, D., 2013. Effect of the water extracts of avocado fruit and cherimoya leaf on four human cancer cell lines and *Vicia faba* root tip cells. *Journal of Agricultural Science*, 5(7), p.245.
- Cardoso, C.R.B., Souza, M.A., Ferro, E.A.V., Favoreto, S. Jr. and Pena, J.D.O., 2004. Influence of topical administration of n-3 and n-6 essential and n-9 nonessential fatty acids on the healing of cutaneous wounds. *Wound Repair and Regeneration*, 12(2), pp.235-243.
- Collins, A.R., 2003. The comet assay. Principles, applications, and limitations. *Methods in Molecular Biology*, 203, pp.163-167.
- Cragg, G. and Newman, D.J., 2009. Nature: A vital source of leads for anticancer drug development. *Phytochemistry Reviews*, 8, pp.313-331.

- Dabas, D., Elias, R.J., Lambert, J.D. and Ziegler, G.R., 2011. A colored avocado seed extract as a potential natural colorant. *Journal of Food Science*, 76(9), pp.C1335-C1341.
- Dabas, D., Shegog, R.M., Ziegler, G.R. and Lambert J.D., 2013. Avocado (*Persea Americana*) seed as a source of bioactive phytochemicals. *Current Pharmaceutical Design*, 19(4), pp.6133-6140.
- Elmore, S., 2007. Apoptosis: A review of programmed cell death. *Toxicologic Pathology*, 35, pp.495-516.
- Imran, A., Qamar, H.Y., Ali, Q., Naeem, H., Riaz, M., Amin, S., Kanwal, N., Ali, F., Saba, M.F. and Nasir I.A., 2017. Role of molecular biology in cancer treatment. A review article. *Iranian Journal of Public Health*, 46(11), pp.1475-1485.
- IsabelleSantana, I., Castelo-Branco, V.N., Guimarães, B.M., de Oliveira Silva, L., Di Sarli Peixoto, V.O., Cabral, L.M.C., Freitas, S.P. and Torres, A.G., 2019. Hass avocado (*Persea Americana* Mill.) oil enriched in phenolic compounds and tocopherols by expeller-pressing the unpeeled microwave dried fruit. *Food Chemistry*, 286, pp.354-361.
- Jakobsen, M.U., O'Reilly, E.J., Heitmann, B.L., Pereira, M.A., Bälter, K., Fraser, G.E., Goldbourt, U., Hallmans, G., Knekt, P., Liu, S., Pietinen, P., Spiegelman, D., Stevens, J., Virtamo, J., Willett, W.C., Ascherio, A., 2009. Major types of dietary fat and risk of coronary heart disease: A pooled analysis of 11 cohort studies. *American Journal of Clinical Nutrition*, 89(5), pp.1425-1432.
- JavedAhmad, J., Uthirapathy, S., Ameen, M.S.M. and Anwer, E.T., 2020. Essential oil composition and antidiabetic, anticancer activity of *Rosmarinus officinalis* L. leaves from Erbil (Iraq). *Journal of Essential Oil Bearing Plants*, 22(6), pp.1544-1553.
- Jayaprakash, T., RamachandraRao, K., Bhat, B.V., Chand, P. and Kumar, S.N., 2010. DNA damage studies in cases of trisomy 21 using comet assay. *Current Pediatric Research*, 14, pp.1-4.
- Kaskoos, R.A., Ahmad, J. and Uthirapathy, S., 2021. Chemical composition and cytotoxic activity of *Pistacia atlantica* var. *kurdica* fruits. *ARO The Scientific Journal of Koya University*, 9(2), pp.91-95.
- Kaur, R., Kaur, S. and Lata, M., 2011. Evaluation of DNA damage in agricultural workers exposed to pesticides using single cell gel electrophoresis (comet) assay. *Indian Journal of Human Genetics*, 17(3), pp.179-187.
- Kristanty, R.E., Suriawati, J. and Sulistiyo, J., 2014. Cytotoxic activity of avocado seeds extracts (*Persea Americana* mill.) on t47d cellines. *International Research Journal of Pharmacy*, 5(7), pp.557-559.
- Louw, L., 2012. Effects of conjugated linoleic acid and high oleic acid safflower oil in the treatment of children with HPV-induced laryngeal papillomatosis: A randomized, double-blinded and crossover preliminary study. *Lipids Health and Disease*, 11, p.136.
- Matsuoka, T. and Yashiro, M., 2018. Biomarkers of gastric cancer: Current topics and future perspective. *World Journal of Gastroenterology*, 24(26), pp.2818-2832.
- McDaniel, J.C., Belury, M., Ahijevych, K. and Blakely, W., 2008. Omega-3 fatty acids effect on wound healing. *Wound Repair and Regeneration*, 16(3), pp.337-345.
- Nadin, S.B., Vargas-Roig, L.M. and Ciocca, D.R., 2001. A silver staining method for single-cell gel assay. *Journal of Histochemistry Cytochemistry*, 9, pp.1183-1186.
- Nandhakumar, S., Parasuraman, S., Shanmugam, M.M., Rao, K.R., Chand, P. and Bhat B.V., 2011. Evaluation of DNA damage using single-cell gel electrophoresis (comet assay). *Journal of Pharmacology Pharmacotherapeutics*, 2, pp.107-111.
- Oluwole, S., Yusuf, K., Fajana, O. and Olanian, D., 2013. Qualitative studies on proximate analysis and characterization of oil from *Persea Americana* (Avocado pear). *Journal of Natural Science Research*, 3(2), pp.68-73.
- Orhevba, B.A. and Jinadu, A.O., 2011. Determination of physico-chemical properties and nutritional contents of Avocado pear (*Persea Americana* M.). *Academic Research International*, 1(3), p.372.
- Ostling, O. and Johanson, K.J., 1984. Microelectrophoretic study of radiation-induced DNA damage in individual mammalian cells. *Biochemical and Biophysical Research Communications*, 123(1), pp.291-298.
- Parasuraman, S., Raveendran, R. and Kesavan, R., 2010. Blood sample collection in small laboratory animals. *Journal of Pharmacology Pharmacotherapeutics*, 1(2), pp.87-93.
- Sahranavard, S., Naghibi, F. and Ghafari, S., 2012. Cytotoxic activity of extracts and pure compounds of *Bryoniaia aspera*. *International Journal of Pharmacy and Pharmaceutical Sciences*, 4(3), pp.541-543.
- Shiezadeh, F., Mousavi, S.H., Amiri, M.S., Iranshahi, M., Tayarani-Najaran, Z. and Karimi G., 2013. Cytotoxic and apoptotic potential of rheum turkestanicum Janisch root extract on human cancer and normal cells. *Iranian Journal of Pharmaceutical Research*, 12(4), pp.811-819.
- Singh, N.P., McCoy, M.T., Tice, R.R. and Schneider, E.L., 1988. A simple technique for quantitation of low levels of DNA damage in individual cells. *Experimental Cell Research*, 175(1), pp.184-191.
- Taraphdar, A.K., Roy, M. and Bhattacharya, R.K. 2001. Natural products as inducers of apoptosis: Implication for cancer therapy and prevention. *Current Science*, 80(11), pp.1388-1896.
- Tice, R.R., Agurell, E., Anderson, D., Burlinson, B., Hartmann, A., Kobayashi, A., Miyamae, Y., Rojas, E., Ryu, J.C. and Sasaki, Y.F., 2000. Single cell gel/comet assay: Guidelines for *in vitro* and *in vivo* genetic toxicology testing. *Environmental and Molecular Mutagenesis*, 35(3), pp.206-221.
- Wiman, K.G. and Zhivotovsky, B., 2017. Understanding cell cycle and cell death regulation provides novel weapons against human diseases. *Journal of Internal Medicine*, 281(5), pp.483-495.

A Comprehensive Review on Microstrip Couplers: Structure, Design Method, and Performance

Abbas Rezaei¹, Salah I. Yahya^{2,3}, and Leila Nouri^{4,5}

¹Department of Electrical Engineering, Kermanshah University of Technology, Kermanshah, Iran

²Department of Communication and Computer Engineering, Cihan University-Erbil, Erbil, Iraq

³Department of Software Engineering, Faculty of Engineering, Koya University, Koya KOY45, Iraq

⁴Institute of Research and Development, Duy Tan University, Da Nang 550000, Vietnam

⁵Faculty of Electrical – Electronic Engineering, Duy Tan University, Da Nang 550000, Vietnam

Abstract—In this paper, several types of microstrip couplers are investigated in terms of structure, performance, and design methods. These planar 4-ports passive devices transmit a signal through two different channels. Designers' competition has always been in miniaturizing and improving performance of couplers. Proposing a novel structure is an advantage of some previously reported couplers. A high-performance coupler should have high isolation and low losses at both channels. The common port return loss in the pass band should have a low value. Among the couplers, those with balanced amplitude and phase are more popular. The popular mathematical analysis methods are even/odd mode analysis, extracting the information from the ABCD matrix and analyzing the equivalent LC circuit of a simple resonator. According to the phase shift value, couplers are classified as 90° and correct multiples of 90°, where a microstrip 0° coupler can be used as a power divider. Some couplers have filtering and harmonic elimination features that are superior to other couplers. However, few designers paid attention to suppressing the harmonics. If the operating frequency is set in according to the type of application, the coupler becomes particularly valuable.

Index Terms—ABCD matrix, Branch-line, Coupler, Directional, Microstrip

I. INTRODUCTION

In classification, microstrip couplers can be divided into two main categories: branch-line and directional couplers. The

other types of couplers are ring couplers, rat race couplers, etc., which have been less reported. Microstrip branch-line couplers (BLCs) are a type of quadrature hybrid. Many BLCs, Ring and rat-race couplers, have been reported using different microstrip structures. In (Chi, et al., 2012) interdigital radial cells (ring structure), in (Salehi, Noori and Abiri, 2015; Salehi and Noori, 2014; Rezaei, Noori and Hosseini, 2018) high/low impedance sections (branch-line structures), in (Sun, et al., 2005) discontinuous microstrip lines, in (Lai and Ma, 2013) interdigital series structures (rat-race structure), in (Tian, et al., 2019) composite planar transmission lines, and in (Maheswari and Jayanthi, 2022) a simple hollow rectangle is utilized to obtain the microstrip couplers. To miniaturize, the simple conventional rectangle of the branch-line coupler is loaded by T-shape inner stubs in (Lalbakhsh, et al., 2021). By bending the transmission lines in a compact space (instead of the conventional rectangle) a new multi-channel branch-line coupler is designed in (Tang and Chen, 2009). A 3-dB BLC is introduced in (Abouelnaga and Mohra, 2017) with good isolation and large negative common port return loss in dB. However, it has not a filtering frequency response. To achieve the bandpass filtering couplers, coupled lines are a good choice which have been used in (Nie, et al., 2019; Arriola, Lee and Kim, 2021; Noori and Rezaei, 2018; Shi, et al., 2016). To suppress the harmonics, the couplers with low-pass filtering frequency responses are designed in (Khan, Mehdi and Zhao, 2019; Roshani, et al., 2022; Kim and Kong, 2010). Two series rectangles (2-section) in (Shukor and Seman, 2016; Mojarrad and Basharat, 2015) and four series rectangles (4-section) in (Tang, et al., 2006) are used to design BLCs. Interestingly, where two rectangles are in series, there are two transmission poles (TPs) (Shukor and Seman, 2016; Mojarrad and Basharat, 2015) and where four

ARO-The Scientific Journal of Koya University
Vol. XI, No. 1 (2023), Article ID: ARO.11108. 10 pages
DOI: 10.14500/aro.11108

Received: 02 November 2022; Accepted: 24 December 2022

Review paper: Published: 15 January 2023

Corresponding author's e-mail: leilanouri@duytan.edu.vn

Copyright © 2023 Abbas Rezaei, Salah I. Yahya and Leila Nouri.

This is an open access article distributed under the Creative Commons Attribution License.



rectangles become series, four TPs have been created in the passband (Tang, et al., 2006). Similarly, several rectangular loops (multi-section) have been integrated in series to create several TPs in the bandpass in (Tang, Tseng and Hsu, 2014), but it occupies a large area. To reach a novel structure, the conventional rectangle arms are carved in (Abdulbari, et al., 2021). For suppressing the harmonics up to the 14th, a new ring coupler is introduced in (Zhang and Zhang, 2019) which is a precious achievement. A 90° hybrid coupler, with a large size, inspired by the structure of 2-section BLC is introduced in (Chiu, et al., 2014). A BLC with balanced magnitude and phase is indicated in (Velan and Kanagasabai, 2016) which is obtained by a little change in the proposed structure in (Tang and Chen, 2009). Triple-channel BLC with tunable operating frequencies is presented in (Liou, et al., 2009). A 3-dB BLC is designed in (Alhalabi, et al., 2018) to operate at 2.45 GHz for wireless local area networks (WLANs). Having very good isolation and return loss is two advantages of this work. Two 3-dB and 6-dB broadband BLCs working at 2 GHz with chebyshev frequency responses have been designed in (Smolarz, Wincza and Gruszczynski, 2020). Another 90° microstrip hybrid coupler with a wide fractional bandwidth (FBW) of 84.3% is presented in (Sun, et al., 2019) which has no isolation port. The fractional bandwidth of amplitude can be calculated using the upper and lower cutoff frequencies S_{21} and S_{31} . A BLC is designed in (Shukor and Seman, 2020) based on analyzing the substrate. This coupler works at 26 GHz which makes it suitable for fifth-generation (5G) applications. The other types of branch-line and rat-race couplers are designed in (Chen, Sim and Wu, 2016; Kao and Chen, 2000; Santiko, Saputera and Wahyu, 2016; Wang, et al., 2007; Shamsinejad, Soleimani and Komjani, 2018; Li, Qu and Xue, 2007).

Conventionally, a directional coupler comprises two parallel couple lines with four ports. A well-designed directional coupler should have high directivity, where, directivity is the ratio of forward power to reverse power. An ideal directional coupler will have an infinite value of directivity. To sample an RF signal passing in a microstrip transmission line the directional couplers are useful devices. It is utilized to couple the waves in one direction. They have been demanded by microwave circuits such as balanced mixers, antenna feeds and modulators (March, et al., 1982). A coupled-line capacitive-loaded directional coupler is designed in (Dydyk, et al., 1999). If a coupler structure is symmetric, the even/odd-mode phase velocities help to improve the isolation. According to this, a symmetric directional coupler using a pair of simple coupled lines similar to (Dydyk, et al., 1999) is proposed and analyzed (in terms of even/odd modes) in (Kim, et al., 2004). To realize a high directivity in (Kumar, et al., 2020), the structure of the conventional directional coupler is changed a little. Four coupled lines have been utilized in (Tripathi, et al., 2018) to improve the performance. The advantages of this coupler are a filtering frequency response with good directivity. Some directional couplers with high directivity have been reviewed in (Yaduvanshi and Bhatia, 2016) to show the main reason for poor performance. In (Kim, et al., 2001), the coupled parallel lines are bent in the middle and a u-shaped structure

is created to obtain a directional coupler with good isolation and directivity. In (Sanna, et al., 2018) a directional coupler with high isolation and tight coupling is proposed. Another directional coupler is designed by creating a bend in the coupled parallel lines in (Hong and Lancaster, 2001).

In this work, we will review several types of microstrip couplers in terms of branch-line couplers, directional couplers, ring couplers, etc. The size and substrate of some couplers will be reviewed. Moreover, we will investigate the various structures of couplers which lead to reach the different types of frequency responses. A perfect comparison of the couplers performance will be down. The comparison parameters are coupling factor, return loss, insertion loss, magnitude and phase balance, filtering response, and harmonics suppression. Furthermore, the operating frequency and applications of couplers will be studied. To compare the performance of directional couplers, directivity will also be added. A summary of the useful mathematical design methods is presented too.

II. BRANCH-LINE, RING, AND RAT-RACE COUPLERS

The layout of microstrip conventional branch-line coupler is presented in Fig. 1. This coupler works at 1 GHz which is suitable for GSM applications. As presented, it occupies a large implementation area. Designers of branch-line couplers are always competing to make this basic structure smaller. A Rogers_RT_Duroid 5880 with $\epsilon_r = 2.22$ is used to simulate the conventional structure. The frequency response of this coupler for two different thicknesses of substrate layer is depicted in Fig. 1b and c, which is clear for $h = 0.381$ mm it has the better isolation (S_{41}) and common port return loss (S_{11}). Not having a filtering frequency response is one of the most important problems of this conventional structure. The bandpass filtering response is usually created using coupled lines. However, if a low-pass filter (LPF) structure is used on the conventional coupler arms, a low-pass filtering response will be produced and subsequently, the harmonics can be suppressed (Roshani, et al., 2022).

Some structures of the BLCs with their substrate properties and advantages are presented in Table I. As shown, the structures of couplers in (Rezaei, Noori and Hosseini, 2018; Tang and Chen, 2009; Roshani, et al., 2022) are novel. However, the complexity of the proposed structures in (Rezaei, Noori and Hosseini, 2018) and (Roshani, et al., 2022) leads to hard fabrication and subsequently, the possibility of manufacturing error will be high. Contrary to these structures, a very simple structure is proposed in (Maheswari and Jayanthi, 2022) In (Lalbahksh, et al., 2021), six stubs were loaded inside a thin rectangular which led to create a low-pass filtering frequency response. The designed coupler in (Abouelnaga and Mohra, 2017) is built on a Teflon substrate. It has a relatively simple structure with good isolation and common port return loss. The structures reported in (Nie, et al., 2019) and (Khan, Mehdi and Zhao, 2019) are very similar and the dielectric constants in both structures are 2.2. This makes both of them able to suppress the harmonics. In (Arriola, Lee and Kim, 2021), the coupling used in the input/output ports leads to a filtering frequency

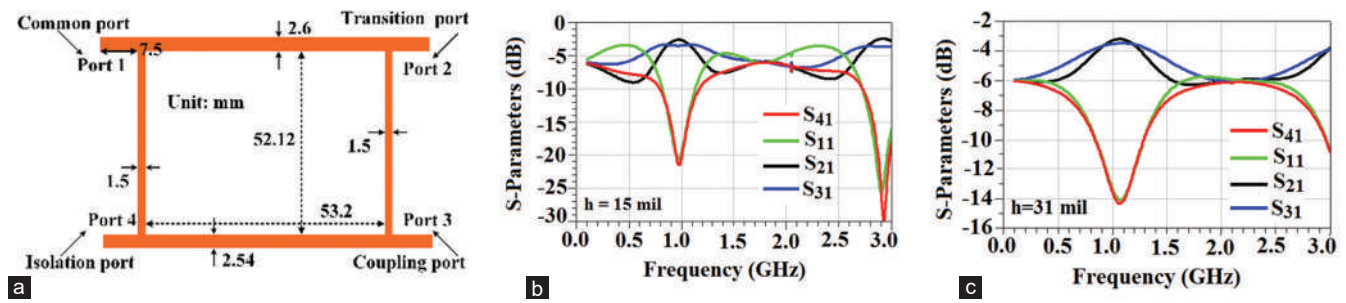


Fig. 1. Conventional branch-line coupler (a) layout of microstrip, (b) frequency response for $h = 0.381$ mm, and (c) frequency response for $h = 0.7874$ mm.

TABLE I
LAYOUT, SUBSTRATE AND ADVANTAGE OF SOME BLCs

References	Layout of BLCs	Substrate	ϵ_r	Thickness	Advantages
Rezaei, Noori and Hosseini, 2018		Rogers_RT_Duroid 5880	2.22	0.7874 mm	1. Low phase shift 2. Novel structure
Maheswari and Jayanthi, 2022		FR4	4.4	1.6 mm	1. Less design complexity and easy fabrication
Lalbaksh, et al., 2021		RT/Duroid	2.2	0.508 mm	1. Balanced magnitude 2. Filtering frequency response 3. Suppressed harmonics
Tang and Chen, 2009		Rogers RO4003	3.38	0.508 mm	1. Novel structure 2. High isolation 3. Good common port return loss 4. Multipassband
Abouelnaga and Mohra, 2017		Teflon	2.2	0.7874 mm	1. High isolation 2. Good common port return loss
Nie, et al., 2019		---	2.2	0.508 mm	1. Filtering frequency response 2. Suppressed harmonics
Arriola, Lee and Kim, 2021		Chukoh	2.6	0.5 mm	1. Filtering frequency response 2. Wide passband
Khan, Mehdi and Zhao, 2019		F4BM-2	2.2	0.8 mm	1. Filtering frequency response 2. Suppressed harmonics
Roshani, et al., 2022		RT-Duroid	2.2	0.508 mm	1. Compact size 2. Novel structure 3. Filtering frequency response 4. Suppressed harmonics

BLCs: Branch-line couplers

response and subsequently the harmonics will be suppressed. As a result, the RT-Duroid substrate with $\epsilon_r = 2.2$ is popular in designing the BLCs.

The frequency responses of some BLCs (presented in Table I) are shown in Figs. 2a-g, where the vertical and horizontal axes show S-parameters in dB and frequency in GHz, respectively. The operating frequency of the designed BLC in (Rezaei, Noori and Hosseini, 2018) is near 2.4GHz which is shown in Fig. 2a. Therefore, this coupler is appropriate for WLAN applications. Fig. 2b depicts an image of the scattering parameters in the narrow-band, while

in the wide-band view, the harmonics are well suppressed. Fig. 2c shows the multi-channel frequency response of the BLC designed in (Tang and Chen, 2009) whereas we can see the good values of return loss and isolation. As shown in Figs. 2d, e and g, the lowpass filtering frequency responses are obtained by (Nie, et al., 2019; Khan, Mehdi and Zhao, 2019; Roshani, et al., 2022). The relatively good values of isolation and return loss are indicated in the frequency response in (Abouelnaga and Mohra, 2017) (Fig. 3f).

The parameters of microstrip couplers can be calculated using the following formulas:

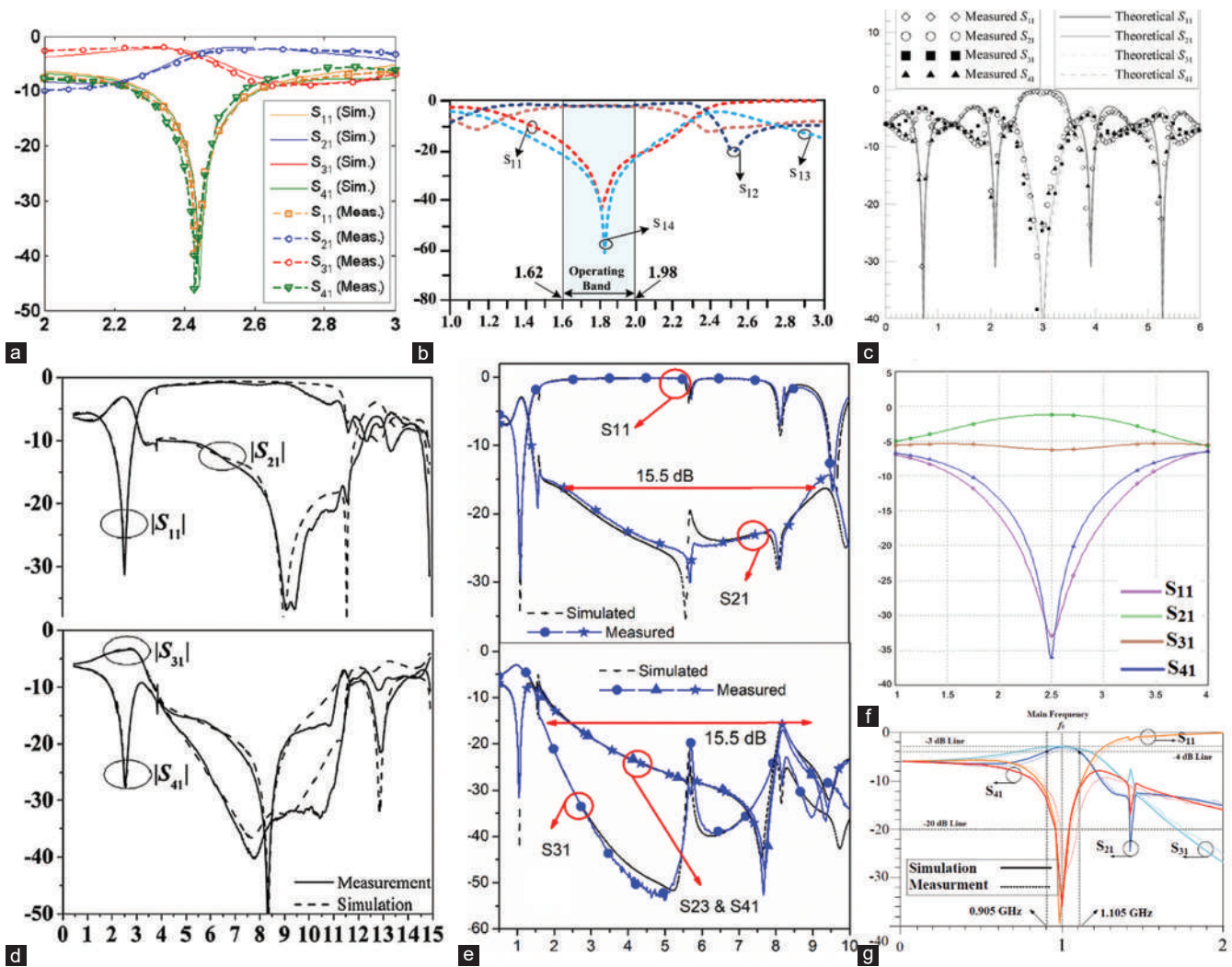


Fig. 2. Frequency response of some branch-line couplers in Table 1, (a) (Rezaei, Noori and Hosseini, 2018), (b) (Lalbahksh, et al., 2021), (c) (Tang and Chen, 2009), (d) (Nie, et al., 2019), (e) (Khan, Mehdi and Zhao, 2019), (f) (Abouelnaga and Mohra, 2017), and (g) (Roshani, et al., 2022).

$$\begin{aligned}
 IL (dB) &= -20 \log(|S_{21}|) \\
 RL (dB) &= -20 \log(|S_{11}|) \\
 CF (dB) &= -20 \log(|S_{31}|) \\
 I (dB) &= -20 \log(|S_{41}|)
 \end{aligned} \tag{1}$$

Where IL, RL, CF, and I are insertion loss, common port return loss, coupling factor, and isolation respectively. However, we do not need to calculate these parameters. Because the EM simulator of Advanced Design System (and HFSS software) can give them to us from simulation results.

For designing most of BLCs mathematical theory, methods have been presented. Design methods sometimes include calculating the transfer matrix and extracting the necessary information from it (Salehi and Noori, 2014; Rezaei, Noori and Hosseini, 2018; Abouelnaga and Mohra, 2017; Nie, et al., 2019; Khan, Mehdi and Zhao, 2019; Kim and Kong, 2010; Smolarz, Wincza and Gruszczynski, 2020). In some cases, the LC equivalent circuit of a small part of the couplers is presented and analyzed (Chi, et al., 2012; Rezaei, Noori and Hosseini, 2018; Sun, et al., 2005; Lai and Ma, 2013; Lalbahksh, et al., 2021; Noori and Rezaei, 2018; Roshani,

et al., 2022; Abdulbari, et al., 2021; Chiu, et al., 2014; Liou, et al., 2009). Furthermore, even and odd modes have been analyzed for some symmetrical structures in (Abouelnaga and Mohra, 2017; Arriola, Lee and Kim, 2021; Tang, Tseng and Hsu, 2014; Sun, et al., 2019). In (Chi, et al., 2012), an equivalent LC circuit of a unit cell is proposed. Then unit-cell phase response is calculated using this LC circuit. In (Salehi, Noori and Abiri, 2015), even/odd modes analysis is done using the input impedance of a basic resonator. The analysis of the proposed BLC in (Salehi and Noori, 2014) is based on the ABCD matrix and the calculation of the reflection coefficient (Γ). It is important to note that we can extract, the insertion loss, return loss, and Γ from the ABCD matrix as follows (Salehi and Noori, 2014; Chen, et al., 2013):

$$\begin{aligned}
 IL &= -20 \log \left(\left| \frac{A+B/Z_0 - CZ_0 - D}{A+B/Z_0 + CZ_0 + D} \right| \right) \\
 RL &= -20 \log \left(\left| \frac{2}{A+B/Z_0 + CZ_0 + D} \right| \right) \\
 \Gamma &= \frac{A+B - C - D}{A+B + C + D}
 \end{aligned} \tag{2}$$

Where Z_0 is the impedance of terminals. The condition of having perfect impedance matching is obtained in (Rezaei, Noori and Hosseini, 2018), using ABCD matrix where $\Gamma = 1$. Under this condition the losses will be decreased significantly. Moreover, in (Rezaei, Noori and Hosseini, 2018), the resonance frequency is calculated under the perfect matching. In (Sun, et al., 2005), the phase velocity of a discontinuous transmission line is obtained based on an equivalent ladder LC circuit as follows:

$$v_p = \frac{1}{\sqrt{LC}} \quad (3)$$

Where C and L are the inductance and capacitance of the ladder LC circuit. The analysis of BLC in (Lai and Ma, 2013) is based on finding the frequencies of transmission zeros. In (Maheswari and Jayanthi, 2022), the length of each arm (L_{arm}) is equal to $\lambda/4$, which is expressed as follows:

$$L_{arm} = \frac{\lambda}{4} = \frac{300}{4f(\text{GHz})\sqrt{\epsilon_{re}}} \quad (4)$$

$$\text{where: } \epsilon_{re} = \frac{1 + \epsilon_r}{2} + \frac{1 - \epsilon_r}{2} \left(\frac{1}{\sqrt{1 + 12h/w}} \right) \text{ for } w/h \geq 1$$

In Equation (4), L_{arm} is in mm, w is the width of the arm in mm, and f is the frequency in GHz. Therefore, based on a predetermined target frequency and the value of the effective dielectric constant (ϵ_{re}), the length of each arm will be determined. The transfer function of an LC equivalent of a resonator in (Lalbakhsh, et al., 2021) is calculated. This LC circuit is a LPF that the authors calculated its cutoff frequency based on the values of lumped elements. In (Tang and Chen, 2009), the resonance frequencies of all passbands are calculated as some functions of the admittances of microstrip cells. To calculate the S-parameters in (Abouelnaga and Mohra, 2017), the even and odd modes ABCD matrices have been calculated, where the vector amplitudes of the signals emerging from the four ports are estimated as follows:

$$\begin{aligned} P_1 &= 0.5(\Gamma_{Even} + \Gamma_{Odd}) \\ P_2 &= 0.5(T_{Even} + T_{Odd}) \\ P_3 &= 0.5(T_{Even} - T_{Odd}) \\ P_4 &= 0.5(\Gamma_{Even} - \Gamma_{Odd}) \end{aligned} \quad (5)$$

Where Γ and T are the reflection and transmission coefficients respectively. Moreover, the transmission parameters S_{21} and S_{31} are derived as follows:

$$\begin{aligned} S_{21} &= 0.5(T_{Even} + T_{Odd}) \\ S_{31} &= 0.5(T_{Even} - T_{Odd}) \end{aligned} \quad (6)$$

The transition matrix of a quarter-wavelength transmission line, with an impedance of Z and 90° electrical length, is written in (Nie, et al., 2019) as follows:

$$M_{\lambda/4} = \begin{bmatrix} 0 & jZ \\ \frac{j}{Z} & 0 \end{bmatrix} \quad (7)$$

The ABCD matrix in Equation (7) can be also used for the conventional branch-line coupler (Khan, Mehdi and Zhao, 2019). The ABCD matrix of a stub loaded transmission line presented in Fig. 3 is calculated as follows (Nie, et al., 2019):

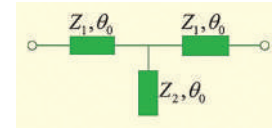


Fig. 3. Stub loaded transmission line where θ_0 is the electrical length.

$$M_{SLR} = \begin{bmatrix} \cos^2\theta_0 - \sin^2\theta_0 \left(1 + \frac{Z_1}{Z_2}\right) & jZ_1 \left(2 \sin\theta_0 \cos\theta_0 - j \frac{Z_1^2}{Z_2} \sin^2\theta_0 \tan\theta_0\right) \\ \frac{j}{Z_1} 2 \sin\theta_0 \cos\theta_0 \left(1 + \frac{Z_1}{Z_2}\right) & \cos^2\theta_0 - \sin^2\theta_0 \left(1 + \frac{Z_1}{Z_2}\right) \end{bmatrix} \quad (8)$$

To match another transmission line to this stub-loaded line, the ABCD matrices of them should be equal. In (Shi, et al., 2016), for a coupling structure the coupling coefficients M_{12} and external quality factor are written as follows (Kumar, Tannous and Danshin, 1995):

$$\begin{aligned} M_{12} &= \frac{\text{Fractional Bandwidth}}{\sqrt{g_1 g_2}} \\ Q_e &= \frac{g_1 g_2}{\text{Fractional Bandwidth}} \end{aligned} \quad (9)$$

Where g -values are the lumped element values of the low-pass prototype filter with a cutoff frequency of 1 GHz. It should be noted that the coupler designed in (Shi, et al., 2016) has a bandpass filtering response so that we can define the external quality factor for it. In general, the quality factor is the ratio of the primary energy stored in the resonator to the energy lost in one radian of a oscillation cycle. For analyzing the proposed BLC in (Shukor and Seman, 2020; Chen, et al., 2013) the Q-factor due to the dielectric, Q_d is expressed as the following Equation:

$$Q_d = \frac{\epsilon_{re} \sqrt{(\epsilon_r - 1)}}{\epsilon_r (\epsilon_{re} - 1) \sqrt{\lambda_0} \tan\delta} \quad (10)$$

Where λ_0 and $\tan\delta$ are the wavelength in the air and the loss tangent, respectively. The value of ϵ_{re} can be calculated from Equation (4). Fig. 4 depicts the equivalent of the branch line with the ABCD matrix calculated in (Roshani, et al., 2022) as the following Equations:

$$T_{branch-line} = \begin{bmatrix} \cos 2\theta_a - b \sin 2\theta_a & \\ jZ_a (\sin 2\theta_a - b(1 - \cos 2\theta_a)) & \\ jY_a (\sin 2\theta_a + b(1 + \cos 2\theta_a)) & \\ \cos 2\theta_a - b \sin 2\theta_a & \end{bmatrix}$$

where :

$$b = \frac{Z_a}{2Z_b} (\tan\theta_{b1} + \tan\theta_{b2}) \quad (11)$$

Since the ABCD-matrix of a quarter-wave line is written in Eq. (7), we can calculate the transition matrix of the conventional BLC, from Equation (10) as below (Kim and Kong, 2010):

$$T_{conventional} = \begin{bmatrix} 0 & jZ_a \tan\theta_a \\ jYa \cot\theta_a & 0 \end{bmatrix} \quad (12)$$

The equivalent of a 2-section branch-line coupler is indicated in Fig. 5, where a, b, c, and d are the characteristic impedances of lines with electrical lengths of θ . From (Shukor and Seman, 2016; Kumar, Tannous and Danshin, 1995) we can write that:

$$a = d \frac{\sqrt{\frac{Z_{O2}}{Z_{O1}} \left(1 + \left| -j \frac{cd}{b^2} Z_{O1} \left(\frac{1}{a} + \frac{1}{d} - \frac{b^2}{abc}\right) \right|^2\right)} - 1}{\sqrt{\frac{Z_{O2}}{Z_{O1}} \left(1 + \left| -j \frac{cd}{b^2} Z_{O1} \left(\frac{1}{a} + \frac{1}{d} - \frac{b^2}{abc}\right) \right|^2\right)} - \frac{Z_{O2}}{Z_{O1}}} \quad (13)$$

To show the advantages and disadvantages of the reported coupler, we compared them in Tables II and III. The return loss (RL), insertion loss (IL), coupling factor (CF), isolation (I), and phase imbalance (PI) of single-band couplers have been compared in Table II, where the RL, IL, CF, and I are best values of S_{11} , S_{21} , S_{31} , and S_{41} in dB inside the passbands. The summarized comparison results show that, the best values of RL, IL, CF, I, and PI are obtained in (Chi, et al., 2012; Rezaei, Noori and Hosseini, 2018; Tian, et al., 2019; Lalbakhsh, et al., 2021; Noori and Rezaei, 2018), respectively. Meanwhile, the most compact size is achieved in (Tian, et al., 2019) which is only $0.0044 \lambda_g^2$, where λ_g is the calculated guided wavelength in the operating frequency in mm. The frequency response types, harmonic suppression, operating frequency (f_o), and applications of some single-band microstrip couplers are depicted in Table III. As written in Table III, the majority of them cannot suppress the harmonics. The best harmonic suppression is achieved in (Zhang and Zhang, 2019), where it could attenuate up to the 14th harmonic.

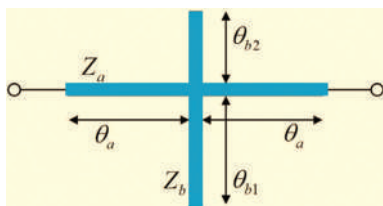


Fig. 4. Branch-Line equivalent.

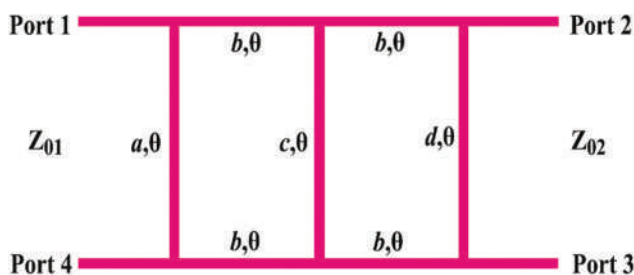


Fig. 5. Equivalent of 2-section branch-line coupler.

III. DIRECTIONAL COUPLERS

A directional coupler may be composed of two parallel coupled lines with four ports. In the performance evaluation of directional couplers, in addition to the important parameters explained for other types of couplers, directivity parameter is important. This parameter is presented by D which can be calculated as $D = -20 \text{Log}(|S_{23}|)$ (Kim, et al., 2004). The layout structures, substrate features, and advantages of some directional couplers are presented in Table IV. The radial stubs have been used in (March, et al., 1982) to obtain a wide channel. The GaAs substrate with $\epsilon_r = 12.9$, and $h = 0.1$ mm is used to design a simple directional coupler in (Kim, et al., 2004). Using a high dielectric constant will increase the normalized size. Therefore, in (Kim, et al., 2004), the value of the dielectric constant is decreased to 2.5. As written in Table IV, high directivity is achieved in (Tripathi, et al., 2018) and (Kim, et al., 2001) where high isolation is an achievement of (Kim, et al., 2004) and (Hong and Lancaster, 2001). Please note that the reported directional couplers are less than BLCs. The conventional directional coupler is presented in (Dydyk, et al., 1999).

Fig. 6 depicts the frequency response of the directional coupler in (Tripathi, et al., 2018), where they have been obtained for different values of the space between coupled lines. Based on this method, we can select the best values of the space between coupled lines. As shown in Fig. 6, by decreasing the space between coupled lines, the passband will be improved. Because, it leads to create two transition poles and reach the better value of insertion losses at the coupled and trough ports (S_{31} and S_{21}) whereas the best common port return loss is obtained under this condition. Since the coupling structure is an inseparable section from directional couplers, their frequency responses may be able to filter the undesired frequencies. Having a filtering response is a big advantage when harmonics are suppressed.

The performance and size of some directional couplers are compared in Table V. The reported coupler in (March, et al., 1982) works at 2.4 GHz for WLANs. Since the couplers in (Kim, et al., 2004) and (Tripathi, et al., 2018) work at 1.75 GHz and 1 GHz, they are suitable for GSM. Only, the introduced coupler in (Tripathi, et al., 2018) has a filtering frequency response, whereas it occupies a small area. The best values of directivity and isolation are obtained in (Kim, et al., 2001) and (Kim, et al., 2004), respectively. However, the proposed coupler in (Kim, et al., 2004) has an undesired coupling factor.

The number of rat race couplers is few. Therefore, it is not possible to draw a general conclusion about their phase behaviors. However, both rat race couplers given by (Lai and Ma, 2013) and (Lalbakhsh, et al., 2021) are 0° . It seems that the position of the output ports has an effect on this matter. Meanwhile, there are 0° (or 180°) and 90° (or 270°) branch-line couplers some couplers with asymmetric structures have been reported. The structures of the couplers presented in (Shi, et al., 2016), (Sun, et al., 2019) and (Kao and Chen, 2000) are asymmetric. Comparing the frequency response of these couplers shows that the symmetry or asymmetry does not have a significant effect on obtaining the filtering frequency response and the suppressing the harmonics. In general, it can

TABLE II
COMPARISON OF SINGLE-BAND MICROSTRIP COUPLERS IN TERMS OF RL, I, PI AND SIZE







Ref.	RL	S_{21} (dB)	S_{31} (dB)	I	PI	Size (λ_g^2)	Size (mm ²)	FBW
Chi, et al., 2012	16.99	1.38	8.11	20.33	7.1°	---	---	---
Salehi, Noori and Abiri, 2015	18.2	3.1	3.1	19.3	0.8°	0.0425	55.8	---
Salehi and Noori, 2014	21.4	3.3	3.3	42.9	0.094°	0.023	175.12	---
Rezaei, Noori and Hosseini, 2018	29	3	3.08	30	0.037°	0.037	345.75	---
Sun, et al., 2005	35	---	---	35	0.5°	---	---	---
Lai and Ma, 2013	23.8	3.28	3.28	28.5	0.2°	0.0231	97.99	18.8%
Tian, et al., 2019	43.7	3.07	3.04	15	3.8°	0.00444	1600	---
Maheswari and Jayanthi, 2022	16.6	3.54	3.57	20.8	2.15°	0.285 ^a	560.7 ^a	---
Lalbahsh, et al., 2021	35	3.06	3.07	60	0.8°	0.0392	504.03	22%
Abouelnaga and Mohra, 2017	---	---	---	---	---	0.152 ^a	1161.37 ^a	---
Arriola, Lee and Kim, 2021	20	3.6±0.5	3.6±0.5	20	---	0.2379 ^a	1157.52	49%
Noori and Rezaei, 2018	29.5	3.3	2.8	31.3	0.97°	0.0754	534.36	---
Shi, et al., 2016	---	---	---	20	3°	0.138	---	3.5%
Khan, Mehdi and Zhao, 2019	29	3.5	3.02	29.7	2.1°	0.027	1287	30%
Roshani, et al., 2022	28	3	3	29	0.5°	0.008	428.49	20%
Kim and Kong, 2010	24	3.3	3.7	32	---	---	700	12.5%
Shukor and Seman, 2016	10	3±2	3±1.6	10	5°	---	1071.2	34.3%
Mojarrad and Basharat, 2015	20	3.25±0.1	3.25±0.1	20	1°	---	---	58%
Tang, et al., 2006	---	---	---	15	1°	---	---	40%
Tang, Tseng and Hsu, 2014	18.33	3.15	3.15±0.1	---	---	---	---	70%
Abdulbari, et al., 2021	30.69	2.97	3.65	29.28	3.6°	0.0432	432	30.22%
Zhang and Zhang, 2019	---	3.12	3.1	---	1.5°	0.039	630.12	24%
Chiu, et al., 2014	10	---	---	13	3°	---	4107	87%
Velan and Kanagasabai, 2016	19.43	3.49	3.68	22.98	0.08°	---	3584	37.8%
Liou, et al., 2009	15	---	---	15	5°	0.448	994.7	---
Alhalabi, et al., 2018	25.5	2.9	3.9	27.5	1°	---	338.3	---
Shukor and Seman, 2020	12	3±1	3±0.8	12	3°	0.307 ^a	595.01	---

^aWe calculate this using the information in the references. RL: Return loss, I: Isolation, PI: Phase imbalance, FBW: Fractional bandwidth

TABLE III
COMPARISON BETWEEN BLCS IN TERMS OF THE FILTERING FREQUENCY RESPONSE, HARMONICS, OPERATING FREQUENCY AND APPLICATIONS

References	Filtering response	Frequency of the last attenuated harmonic	N th suppressed harmonic	f _o (GHz)	Application
Chi, et al., 2012	Yes	No	No	2.4	WLANs
Salehi, Noori and Abiri, 2015	No	No	No	5.7	WLANs
Salehi and Noori, 2014	No	No	No	2.4	WLANs
Rezaei, Noori and Hosseini, 2018	No	No	No	2.4	WLANs
Sun, et al., 2005	No	No	No	1	GSM
Lai and Ma, 2013	Yes	7.2	3 rd	2.4	WLANs
Tian, et al., 2019	No	No	No	0.5	Wireless Networks
Maheswari and Jayanthi, 2022	No	No	No	3.5	Wi-Max
Lalbahsh, et al., 2021	Yes	12.6 GHz	7 th	1.8	GSM
Abouelnaga and Mohra, 2017	No	No	No	2.5	Wireless Networks
Noori and Rezaei, 2018	Yes	15.1 GHz	5 th	2.82	Wireless Networks
Shi, et al., 2016	Yes	2.3 GHz	1 st	1.87	GSM
Khan, Mehdi and Zhao, 2019	Yes	10 GHz	9 th	1	GSM
Roshani, et al., 2022	Yes	9 GHz	9 th	1	GSM
Kim and Kong, 2010	Yes	2 GHz	2 nd	1	GSM
Shukor and Seman, 2016	No	No	No	3.5	Wi-Max
Mojarrad and Basharat, 2015	No	No	No	2.4	WLANs
Tang, et al., 2006	No	No	No	2.4	WLANs
Tang, Tseng and Hsu, 2014	No	No	No	2.4	WLANs and Ultra-Wideband
Abdulbari, et al., 2021	No	No	No	3.55	Wi-Max and 5G
Zhang and Zhang, 2019	Yes	7 GHz	14 th	0.5	Wireless Networks
Chiu, et al., 2014	No	No	No	1	GSM
Velan and Kanagasabai, 2016	No	No	No	0.433	Wireless Networks
Alhalabi, et al., 2018	No	No	No	2.45	WLANs
Smolarz, Wincza and Gruszczynski, 2020	No	No	No	2	Wireless Networks
Sun, et al., 2019	No	No	No	3	Wireless Networks

TABLE IV
LAYOUT OF DIRECTIONAL COUPLERS, SUBSTRATE FEATURES AND THEIR ADVANTAGES

Refs	Layout of BLCs	Substrate	ϵ_r	Thickness	Advantages
March, et al., 1982		Duroid	10.5	1.27 mm	1. Balanced phase 2. Wide channel
Dydyk, et al., 1999		GaAs	12.9	0.1 mm	1. Good RL
Kim, et al., 2004		---	2.5	0.7874 mm	1. High isolation
Tripathi, et al., 2018		FR-4	4.4	1.59 mm	1. High directivity 2. Filtering response 3. Novel structure
Kim, et al., 2001		---	---	---	1. High directivity 2. Novel structure
Hong and Lancaster, 2001		---	---	---	1. High isolation

BLCs: Branch-line couplers

TABLE V
COMPARISON AMONG PREVIOUS REPORTED DIRECTIONAL COUPLERS

References	Return loss (dB)	S_{21} (dB)	S_{31} (dB)	Isolation (dB)	Directivity (dB)	f_o (GHz)	Filtering responses
March, et al., 1982	25	3.55 ± 0.5	3.55	35	---	2.4	No
Kim, et al., 2004	---	---	20.2	47	26	1.75	No
Tripathi, et al., 2018	24.5	2.22	6.2	38	44	1.01	Yes
Kim, et al., 2001	---	---	3	---	68	2.5	No
Sanna, et al., 2018	30	---	3.15	30	32	2	No
Hong and Lancaster, 2001	---	5.8^*	2.9	40	30	10.5	No

*Approximate value

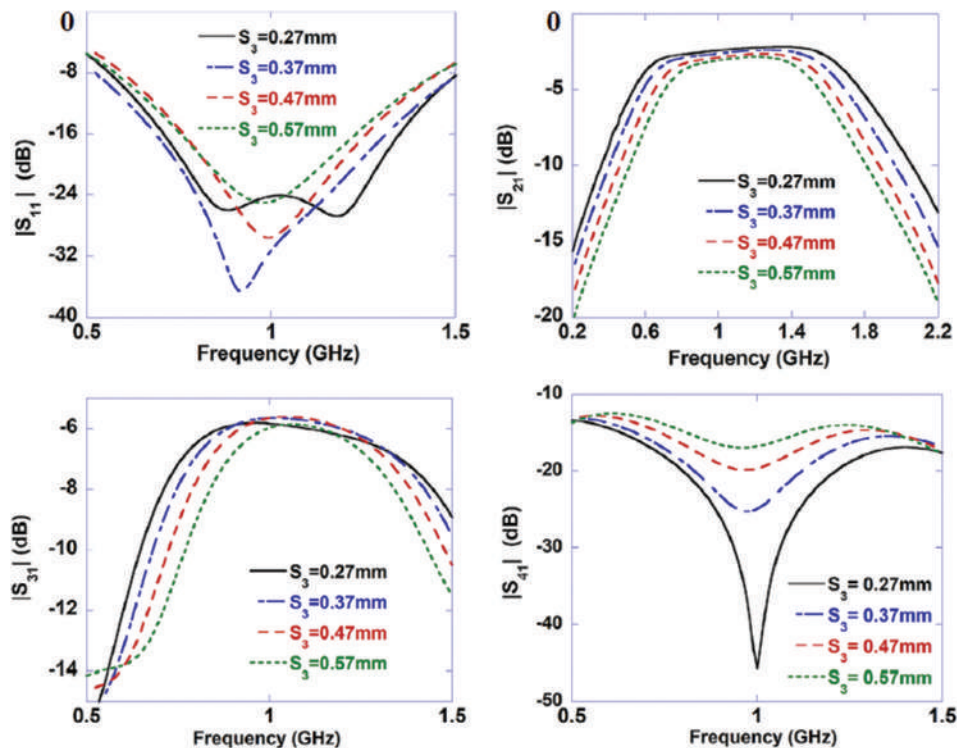


Fig. 6. Scattering parameters of the directional coupler in (Tripathi, et al., 2018), where S_3 is the gap between two upper (and two lower) coupled lines.

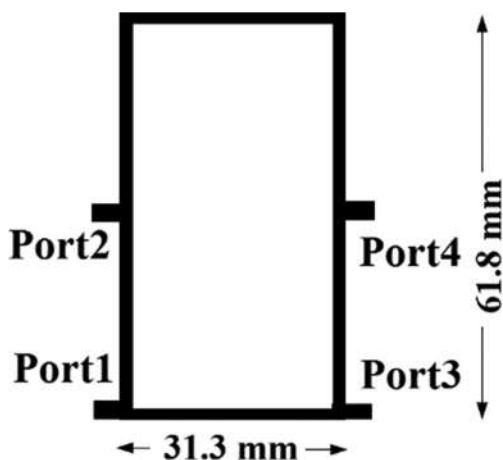


Fig. 7. The layout of conventional rat race coupler.

be said that the use of these asymmetric structures increases the size of some couplers. The conventional rat race coupler is depicted in Fig. 7. As shown in this figure, it occupies a large size of 1934.34 mm^2 ($0.5 \lambda_g \times 0.25 \lambda_g$), where λ_g is the guided wavelength calculated at its 1.8 GHz operational frequency. The insertion losses of the conventional rat race couplers are $<0.3 \text{ dB}$ (Lalbakhsh, et al., 2021).

Three dual-band couplers are proposed by (Feng, et al., 2020), (Chang, et al., 2022) and (Jia, Zhang and Zhang, 2020) with the overall dimensions of $0.162 \lambda_g^2$, $0.078 \lambda_g^2$, and $0.156 \lambda_g^2$, respectively. The dimensions of dual-band and multi-band couplers are usually larger than the dimensions of the single-band couplers. Designing multi-band couplers is much more difficult (Liou, et al., 2009). The multi-band coupler presented by (Liou, et al., 2009) occupies a large area of $0.448 \lambda_g^2$ whereas it has a weak phase balance. The dual-band coupler designed by (Feng, et al., 2020) operates at 0.9/1.8 GHz which makes it suitable for GSM applications. The phase difference between two output ports of this coupler is 89.6° and 90.7° at the lower and upper channel, respectively, whereas these values for (Chang, et al., 2022) are 89.5° and 91.6° . The fractional bandwidths at the upper and lower channels of (Jia, Zhang and Zhang, 2020) are 34.7% and 14.9%, respectively. Two other special types of couplers are Lange and Bagley-polygon couplers. The Lange coupler is a four-port structure developed by Dr. Julius Lange in 1969. In order to design it, the interdigital cells have been used. Its structure is relatively similar to the coupler presented in (Tripathi, et al., 2018). Bagley-polygon couplers are another type of couplers that have a triangular structure, in which three ports are located on three vertices. Port 1 is located between ports 2, 3 on a side of the triangle. To achieve a better frequency response, the structure of this triangle can be optimized. As an example, we can change the width of the sides or load some blocks inside it.

IV. CONCLUSION

Several types of microstrip couplers including branch-lines, directional, rate-races, and rings are reviewed in this

work. The structure, substrate, performance, advantages, and disadvantages of some of them were explained. The size and performance, in terms of insertion loss, return loss, coupling factor, isolation, directivity and phase balance, of these couplers are compared and reviewed. Moreover, the useful and popular mathematical design methods that presented in some reported works are investigated in this paper. We conclude that the even/odd mode analysis, extracting the main parameters from the ABCD matrix and analyzing the LC circuits are the favorite design methods.

FUNDING

This research was funded by the Kermanshah University of Technology, Iran, grant No. S/P/T/1439.

REFERENCES

- Abdulbari, A.A., Rahim, S.K.A., Aziz, M.Z.A.A., Tan, K.G., Noordin, N.K., and Nor, M.Z.M., 2021. New design of wideband microstrip branch line coupler using T-shape and open stub for 5G application. *International Journal of Electrical and Computer Engineering*, 11(2), pp.1346-1355.
- Abouelnaga, T.G., and Mohra, A.S., 2017. Reconfigurable 3 6 dB novel branch line coupler. *Open Journal of Antennas and Propagation*, 5, pp.7-22.
- Alhalabi, H., Issa, H., Pistono, E., Kaddour, D., Podevin, F., Abouchahine, S., and Ferrari, P., 2018. Miniaturized branch-line coupler based on slow-wave microstrip lines. *International Journal of Microwave and Wireless Technologies*, 10(10), pp.1-4.
- Arriola, W.A., Lee, J.Y., and Kim, I.S., 2021. Wideband 3 dB branch line coupler based on $\lambda/4$ open circuited coupled lines. *IEEE Microwave and Wireless Components Letters*, 21(9), pp.486-488.
- Chang, H., Lim, T., Dimitrov, K.C., and Lee, Y., 2022. Dual-band branch-line coupler based on crossed lines for arbitrary power-split ratios. *Sensors*, 22, pp. 5527.
- Chen, C.C., Sim, C.Y.D., and Wu, Y.J., 2016. Miniaturised dual-band rat-race coupler with harmonic suppression using synthetic transmission line. *Electronics Letters*, 52(21), pp.1784-1786.
- Chen, C.F., Huang, T.Y., Shen, T.M., and Wu, R.B., 2013. Design of miniaturized filtering power dividers for system-in-a-package. *IEEE Transactions on Microwave Theory and Techniques*, 3(10), pp.1663-1672.
- Chi, P.L., 2012. Miniaturized ring coupler with arbitrary power divisions based on the composite right/left-handed transmission lines. *Microwave and Wireless Component Letters*, 22(4), pp.170-172.
- Chiu, L., 2014. Wideband microstrip 90° hybrid coupler using high pass network. *International Journal of Microwave Science and Technology*, 2014, pp.1-6.
- Dydyk, M., 1999. Microstrip directional couplers with ideal performance via single-element compensation. *IEEE Transactions on Microwave Theory and Techniques*, 47(6), pp.956-964.
- Feng, W., Duan, X., Shi, Y., Zhou, X.Y., and Che, W., 2020. Dual-band branch-line couplers with short/open-ended stubs. *IEEE Transactions on Circuits and Systems II*, 67(11), pp.2497-2501.
- Hong, J.S., and Lancaster, M.J., 2001. *Microstrip Filters for RF/Microwave Applications*. John Wiley and Sons, Hoboken.
- Jia, L., Zhang, L., and Zhang, C., 2020. A dual-band and wide-band branch-line coupler with a large frequency ratio. *Microwave and Optical Technology Letters*, 63(1), pp.146-151.

- Kao, C.W., and Chen, C.H., 2000. Novel uniplanar 180° hybrid-ring couplers with spiral-type phase inverters. *IEEE Microwave and Guided Wave Letters*, 10(10), pp.412-414.
- Khan, Z.B., Mehdi, G., and Zhao, H., 2019. Design of a compact hybrid branch line coupler with 2-D implementation of stepped impedance transmission lines of high impedance ratio for wide range of harmonic suppression. *ACES Journal*, 34(8), pp.1211-1218.
- Kim, C.S., Kim, Y.T., Song, S.H., Jung, W.S., Kang, K.Y., Park, J.S., and Ahn, D., 2001. A Design of Microstrip Directional Coupler for High Directivity and Tight Coupling. In: *Microwave Conference*. European.
- Kim, C.S., Lim, J.S., Kim, D.Y., and Ahn, D., 2004. A design of single and multi-section microstrip directional coupler with the high directivity. *IEEE MTT-S International Microwave Symposium Digest*, 3, pp.1895-1898.
- Kim, J.S., and Kong, K.B., 2010. Compact branch-line coupler for harmonic suppression. *Progress in Electromagnetics Research*, 16, pp.233-239.
- Kumar, M., Islam, S.N., Sen, G., and Parui, S.K., 2020. Design of filtering directional coupler with improved performance. *International Journal of RF and Microwave Computer Aided Engineering*, 30(2), e22224.
- Kumar, S., Tannous, C., and Danshin, T., 1995. A multisection broadband impedance transforming branch-line hybrid. *IEEE Transactions on Microwave Theory and Techniques*, 43(11), pp.2517-2523.
- Lai, C.H., and Ma, T.G., 2013. Miniaturised rat-race coupler with second and third harmonic suppression using synthesised transmission lines. *Electronics Letters*, 49(22), pp.1394-1396.
- Lalbahksh, A., Mohamadpour, G., Roshani, S., Ami, M., Roshani, S., Sayem, A.S., Alibakhshikenari, M., and Koziel, S., 2021. Design of a compact planar transmission line for miniaturized rat-race coupler with harmonics suppression. *IEEE Access*, 9, pp.129207-129217.
- Li, J.L., Qu, S.W., and Xue, Q., 2007. Microstrip directional coupler with flat coupling and high isolation. *Electronics Letters*, 43(4), pp.228-229.
- Liou, C.Y., Wu, M.S., Yeh, J.C., Chueh, Y.Z., and Mao, S.G., 2009. A novel triple-band microstrip branch-line coupler with arbitrary operating frequencies. *IEEE Microwave and Wireless Components Letters*, 19(11), pp.683-685.
- Maheswari, S., and Jayanthi, T., 2022. Design of compact branch-line coupler for Wi-max applications. *International Journal of Microwave and Optical Technology*, 17(1), pp.68-73.
- March, S.L., 1982. Phase velocity compensation in parallel-coupled microstrip. *IEEE MTT-S International Microwave Symposium Digest*, 82(1), pp.410-412.
- Mojarrad, S., and Basharat, H., 2015. Modified double box branch line coupler by utilizing quasi T-shape stub. *International Journal of Innovative Science Engineering and Technology*, 2(11), pp.390-393.
- Nie, W., Xu, K.D., Zhou, M., Xie, L.B., and Yang, X.L., 2019. Compact narrow/wide band branch-line couplers with improved upper-stopband. (*AEÜ*) *International Journal of Electronics and Communications*, 98, pp.45-50.
- Noori, L., and Rezaei, A., 2018. A microstrip hybrid coupler with wide stop-band using symmetric structure for wireless applications. *Journal of Microwaves Optoelectronics and Electromagnetic Applications*, 17(1), pp.23-31.
- Rezaei, A., Noori, L., and Hosseini, S.M., 2018. Novel microstrip branch-line coupler with low phase shift for WLANs. *Analog Integrated Circuits and Signal Processing*, 98, pp.377-383.
- Roshani, S., Yahya, S.I., Roshani, S., Farahmand, A.H., and Hemmati, S., 2022. Design of a modified compact coupler with unwanted harmonics suppression for L-band applications. *Electronics*, 11(11), 1747.
- Salehi, M., and Noori, L., 2014. Novel 2.4 GHz branch-line coupler using microstrip cells. *Microwave and Optical Technology Letters*, 56(9), pp.2110-2113.
- Salehi, M.R., Noori, L., and Abiri, E., 2015. Novel tunable branch-line coupler for WLAN applications. *Microwave and Optical Technology Letters*, 57(5), pp.1081-1084.
- Sanna, G., Montisci, G., Jin, Z., Fanti, A., and Casula, G.A., 2018. Design of a low-cost microstrip directional coupler with high coupling for a motion detection sensor. *Electronics*, 7(2), p.25.
- Santiko, A.B., Saputera, Y.P., and Wahyu, Y., 2016. Design and Implementation of Three Branch Line Coupler at 3.0 GHz Frequency for S-Band Radar System. In: *The 22nd Asia-Pacific Conference on Communications*. IEEE, Indonesia, pp.315-318.
- Shamsinejad, S., Soleimani, M., and Komjani, N., 2008. Novel enhanced and miniaturized 90° coupler for 3G EH mixers. *Progress in Electromagnetics Research Letters*, 3, pp.43-50.
- Shi, J., Qiang, J., Xu, K., Wang, Z.B., Lin, L., Chen, J.X., Liu, W., and Zhang, X.Y., 2016. A balanced filtering branch-line coupler. *IEEE Microwave and Wireless Components Letters*, 26(2), pp.119-121.
- Shukor, N.A.M., and Seman, N., 2016. Enhanced design of two-section microstrip-slot branch line coupler with the overlapped k/4 open circuited lines at ports. *Wireless Personal Communications*, 88(3), pp.467-478.
- Shukor, N.A.M., and Seman, N., 2020. 5G planar branch line coupler design based on the analysis of dielectric constant, loss tangent and quality factor at high frequency. *Scientific Reports*, 10, 16115.
- Smolarz, R., Wincza, K., and Gruszczynski, S., 2020. Chebyshev-response branch-line couplers with enhanced bandwidth and arbitrary coupling level. *Electronics*, 9(11), 1828.
- Sun, K.O., Ho, S.J., Yen, C.C., and Weide, D., 2005. A compact branch-line coupler using discontinuous microstrip lines. *IEEE Microwave and Wireless Components Letters*, 15(8), pp.519-520.
- Sun, P., Chen, Q., Han, R., and Lu, A.Z., 2019. Analysis and design of wideband 90° microstrip hybrid coupler. *IEEE Access*, 7, pp.186409-186416.
- Tang, C.W., and Chen, M.G., 2009. Design of multipassband microstrip branch-line couplers with open stubs. *IEEE Transactions on Microwave Theory and Techniques*, 57(1), pp.196-204.
- Tang, C.W., Chen, M.G., Lin, Y.S., and Wu, J.W., 2006. Broadband microstrip branch-line coupler with defected ground structure. *Electronics Letters*, 42(25), pp.1458-1460.
- Tang, C.W., Tseng, C.T., and Hsu, K.C., 2014. Design of wide passband microstrip branch-line couplers with multiple sections. *IEEE Transactions on Components Packaging and Manufacturing Technology*, 4(7), pp.1222-1227.
- Tian, H., Chung, K.L., Liu, R., Dai, M., and Tang, W., 2019. Miniaturised quadrature hybrid coupler using composite planar transmission lines. *Electronics Letters*, 55(19), pp.1049-1051.
- Tripathi, N., 2018. Review paper on microstrip directional coupler with high directivity. *International Research Journal of Engineering and Technology (IRJET)*, 5(5), pp.4149-4152.
- Velan, S., and Kanagasabai, M., 2016. Compact microstrip branch-line coupler with wideband quadrature phase balance. *Microwave and Optical Technology Letters*, 58(6), pp.1369-1374.
- Wang, J., Wang, B.Z., Guo, Y.X., Ong, L.C., and Xiao, S., 2007. A compact slow-wave microstrip branch-line coupler with high performance. *IEEE Microwave and Wireless Components Letters*, 17(7), pp.501-503.
- Yaduvanshi, B., and Bhatia, D., 2016. Stub-Based Design of Coupled Line Directional Couplers. In: *2016 International Conference on Micro-Electronics and Telecommunication Engineering*, IEEE, Ghaziabad.
- Zhang, H., and Zhang, Z., 2019. Miniaturized microstrip branch-line coupler with good harmonic suppression based on radial stub loaded resonators. *Progress in Electromagnetics Research Letters*, 87, pp.15-20.

Structural and Optical Properties of Cadmium Sulfide-doped Silver Deposited on Glass and Polymer Substrates by Chemical Spray Pyrolysis

Niaz H. Hamad, Mohammad G. Faraj, and Akram H. Taha

Department of Physics, Faculty of Science and Health, Koya University,
Koya, KOY45, Kurdistan Region – F.R. Iraq

Abstract—This process of this paper is carried out using the chemical spraying method to produce homogeneous thin films of pure cadmium sulfide-doped with silver at different percentages of 1%, 3%, and 5% on glass and polyimide plastic substrates at 300°C. The aim is to study the optical and structural properties of the samples and the effect of the silver doping rate on films produced with these properties. Due to X-ray diffraction studies, all films created had a hexagonal phase, and it was noticed that they had a very precise structure free of holes or cracks. The obtained crystal size ranged between 22.74 nm and 55.05 nm for different substrates, and the prominent plane was (002). From the optical properties, all films exhibited transmission higher than 60%, thus showing a low absorption, which makes them be used as light-permeable layers in the Solar Cell system. In addition, emission peaks were revealed by photo luminescence spectra examination at wavelengths ranging between (542.94 nm) and (546.02 nm), which led to calculate the energy gap (E_g) of the produced films, ranged between (2.27 eV) and (2.28 eV) for the different substrates.

Index Terms—Cadmium sulfide-Ag, Chemical spray technique, X-ray diffraction pattern, Photo luminescence studies.

I. INTRODUCTION

Recent advances in thin film nanotechnology (Ahmed, et al., 2021b) offer a possible method for solar energy applications to lessen the environmental crisis brought on by energy use. Because solar energy is one of the most significant renewable energy sources, scientists have created or modified several semiconductor thin films to optimize high solar cell efficiencies at cheap cost (Ahmed, et al., 2020). Due to its broad bandgap (2.42 eV) at ambient temperature, chalcogenides of cadmium, notably cadmium sulfide (CdS), are one of the most actively researched topics among

material scientists (Islam, et al., 2013, Shkir, et al., 2020c). The II-VI semiconductor family such as (CdS) has received much attention for its tunable optical and electrical properties (Mahmood, et al., 2018, Shkir, et al., 2020d).

Bulk CdS, one of the most significant window layer materials for solar cell devices, typically transmits energy in the low energy region of the visible solar spectrum. However, by adding a suitable amount of impurity, particularly transition metal ions, it is possible to re-engineer CdS to transmit the entire visible spectrum. Due to their capacity to alter the bandgap, noble metals, including gold (*Au*), copper (*Cu*), and silver (*Ag*), have been regarded as the most promising possibilities among these (Bora, et al., 2021) and reduce resistivity while also produce structural changes. A crucial factor for solar cell window layer materials is low resistance and good transmission when combined with p-type semiconductor absorber thin films such as *CdTe*, *Cu₂S* (Ojeda-Barrero, et al., 2018), *CuInSe₂* (Rahman, Hossain and Ismail, 2020), *CdSe*, and *PbS* (Aboud, et al., 2019). CdS is well known for its n-type wide band gap, which makes it an appropriate window layer counterpart for solar cell applications (Manthrammel, et al., 2020, Nazir, et al., 2014).

Thus, CdS has wide applications in optoelectronic device technologies, including optical filters, LEDs (Ahmed, et al., 2021a), lasers (Ikhmayies, 2020), photocatalysis (Manthrammel, et al., 2020), photodetectors (Mohammed, et al., 2021), nonlinear integrated optical devices (Rahman, Hossain and Ismail, 2020), and multicolor optical switches (Shkir, et al., 2020b).

A novel feature of the ongoing work is the fabrication and characterization of films fabricated on polyimide (PI) plastic substrates using chemical spray pyrolysis techniques with varying Ag ratios. In this respect, the use of flexible polymer substrates is of great interest (Faraj, Ibrahim and Salhin Ali, 2012, Faraj, Pakhuruddin and Taboada, 2017). It has important advantages such as light weight, high impact resistance, and scalable roll-to-roll manufacturing process.

Many methods are employed to prepare CdS thin films, including vacuum evaporation (Shaban, et al., 2021), chemical deposition (Shkir, et al., 2020b), sputtering (Yadav, Barote and Masumdar, 2010), successive ionic layer adsorption and reaction (SILAR) (Deshmukh, Kheraj and

ARO-The Scientific Journal of Koya University
Vol. XI, No. 1 (2023), Article ID: ARO.11097. 6 pages
DOI: 10.14500/aro.11097

Received: 23 October 2022; Accepted: 07 January 2023
Regular research paper: Published: 15 January 2023

Corresponding author's e-mail: niazhamakhan25@gmail.com
Copyright © 2023 Niaz H. Hamad, Mohammad G. Faraj, and Akram H. Taha. This is an open access article distributed under the Creative Commons Attribution License.



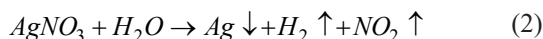
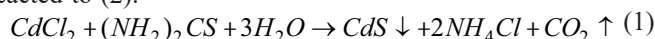
Panchal, 2018, Taghizadeh Chari and Fadavieslam, 2019), printing (An, et al., 2021), laser ablation (Wada, 2022), electrodeposition (Valencia and Baena, 2015), chemical bath techniques (Kakhaki, et al., 2022), solgel (Mohammed, et al., 2021), and chemical spray pyrolysis CSP (Vishwas, Shamala and Gandla, 2022). The characteristics of thin films and powders of CdS at the nanoscale depend on the dopant type, concentration, method of preparation/deposition, and pH application (Shkir, et al., 2020a).

In the present work, CdS and CdS -Ag thin films were fabricated with a chemical spray pyrolysis method and deposited on different substrates, glass, and PI plastic, with different ratios of doping. A comparative study of the optical properties before and after Ag layer deposition on the surface of the CdS has been performed, highlighting the strong reduction in the energy gap and increase in transmission.

II. EXPERIMENTAL PROCEDURE

A. Preparation of CdS Solutions

A thermal chemical spraying solution of CdS was prepared first without doping and then by doping with different weight ratios (1%, 3%, and 5%) of silver with molar weights of cadmium chloride and silver nitrate to obtain the mentioned ratios. The weight of each of the cadmium chlorides ($CdCl_2 \cdot H_2O$) ($CdCl_2 \cdot H_2O$) was approximately 0.91653 g (as a source of cadmium ions), and thiourea [$(NH_2)_2CS$]. Approximately 0.38032 g (source of sulfur ions) to obtain (CdS). The solutions are reacted according to (1) to obtain (CdS) doped with silver, silver nitrate with masses (0.0129, 0.3878, and 0.0648) g was used to obtain the ratios mentioned above. All solutions were prepared with a fixed titer of molarities of (0.1 M). All weights were wholly dissolved in distilled water in a 250 mL volumetric vial. Then, the mixture was mixed well at a temperature slightly more significant than room temperature with sufficient times using a magnetic stirrer to obtain a clear, suspended liquid. The solutions are reacted to (2):



All the products of the above reactions are gases except for CdS and Ag, which are impurities.

B. Substrate Cleaning

The substrates used in this paper are glass and PI plastic, which were cleaned using methanol solution and immersed in it for more than 15 min to eliminate contaminants. The substrate was cleaned with distilled water after cleaning (DI water). This was followed by drying with warm, dry air.

C. Experience

After many attempts using chemical spray pyrolysis technique, a device used is shown in Fig. 1a and b, and the following optimization conditions were noticed: the



Fig. 1. (a) Spray pyrolysis technique. (b) The amplified section of the device.

substrate temperature was kept at 300°C. During deposition, the distance between the nozzle and the substrate was approximately 29 cm, the deposition rate time was approximately (3–5) s, the spraying rate was 1 spray, and the carrier gas was air. The above-mentioned solutions were sprayed on different substrates with the weight mentioned above ratios. The obtained films were adherent.

III. CHARACTERIZATION TECHNIQUE

X-ray diffraction (XRD) analysis (PANalytical-Typenr: 94 30 060 03002-S/N: DY1376-MFG) Technique was used to study and investigate the structural properties of thin film models. An X-ray diffractometer was used with a wide diffraction angle (2θ) range of (5°-80°) degrees. (UV-VIS) double beam spectrometer of type (PerkinElmer precisely Lambda 25-Shelton, CT 06484 USA-Part No. L600000B-Serial No. 101N8022902) was also used to determine and measure the optical transmittance in the wavelength range of 400 and 800 nm. Finally, a photo luminescence (PL) device (instrument Cary Elipse-instrument serial number: MY131500007) with an excitation wavelength of fluorescein (400 nm) was used to calculate the direct energy gap of the film.

IV. RESULTS AND DISCUSSION

A. Structural Studies

The crystal structures of CdS and Ag-doped thin films on different substrates were investigated using XRD. Moreover, in both cases the thin films were deposited on glass and PI substrates. The prominent 2θ peaks are shown in Table I for glasses and PI substrates.

The prominent peaks for the sample CdS pure on the glass substrate marked in Fig. 2 are 24.87°, 26.53°, 28.25°, 36.64°, 43.86°, and 48.08°, with the corresponding diffraction planes (100), (002), (101), (110), (103), and (113). This is the same for the CdS doping Ag ratios, with the difference shown in Fig. 2 due to the different impurity percentages. The mean

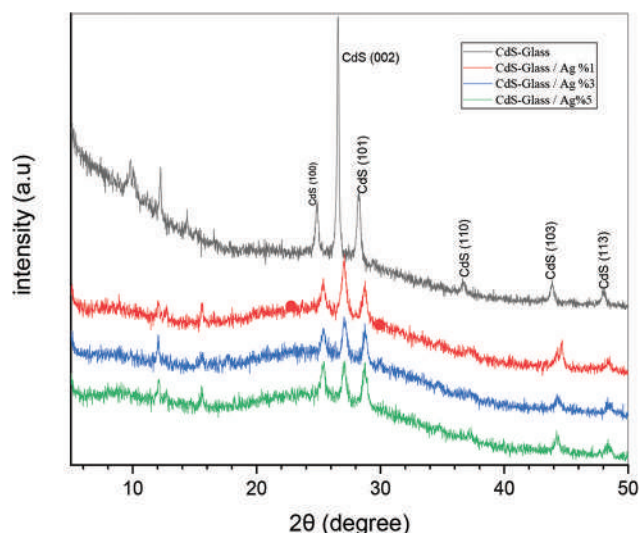


Fig. 2. X-ray diffraction patterns of cadmium sulfide and Ag-doped thin films deposited on glass substrates.

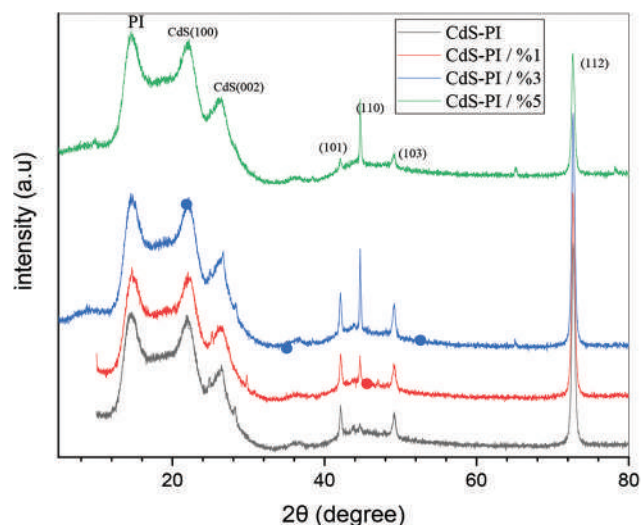


Fig. 3. X-ray diffraction pattern of cadmium sulfide and Ag-doped thin film deposited on polyimide substrate.

peak is 26.53° , and its corresponding plane is (002), roughly the same as the other samples. These measured diffraction peaks are highly in agreement with the standard XRD data of JPDFS (Card no. 41–1049) for hexagonal wurtzite structures and indicate the formation of CdS films with those structures, as reported in (Mahmood, et al., 2018, Yang, et al., 2018). However, the prominent peaks for the sample CdS pure on the PI substrate marked in Fig. 3 had six diffraction peaks at 2θ values of 22.11° , 26.43° , 42.10° , 44.63° , 49.16° , and 72.43° corresponding to their diffraction planes (100), (002), (101), (110), (103), and (112). This is the same for CdS doping of Ag on PI, with the difference due to the different impurity percentages, as shown in Fig. 3. The mean peak in Fig. 3 is 26.43° , and its corresponding plane is (002), roughly the same as the other samples. These diffraction peaks support the conventional XRD data JCPD6-314 for hexagonal wurtzite structures, which indicate the formation of CdS films with such structures as reported in (Faraj, Pakhuruddin and Taboada, 2017, Mensah, et al., 2021), in which hexagonal-structured thin films are preferred for solar cell applications (Taghizadeh Chari and Fadavieslam, 2019). In both cases, by comparing the above data in Figs. 2 and 3, there is a difference between the peaks obtained due to the different substrates. The average crystallite size was estimated from the X-ray diffraction pattern using the prominent peak, depending on Scherrer's equation:

$$D = \frac{0.9\lambda}{\beta \cos\theta} \quad (3)$$

Where D is the crystallite size, λ is the X-ray wavelength (1.54 \AA), β is the full width at half maximum (FWHM) in radians, and θ is the center of the diffraction peak angle value in radians. The FWHM value (2θ) and peaks were calculated using the XRD data peak program, as shown in Table I.

With the use of Scherrer's formula, the particle size values are determined. Compared to natural crystallite sizes, the value derived from Scherrer's equation is different. In

TABLE I
CRYSTAL SIZE AND (2θ) FOR CdS PURE AND AG-DOPED ON PI AND GLASS SUBSTRATES

Sample	(2θ) degree	FWHM	D nm
CdS -Glass	26.53	0.12	55.05
CdS -Glass-Ag 1%	27.06	0.25	37.17
CdS -Glass-Ag 3%	27.06	0.25	37.17
CdS -Glass-Ag 5%	27.12	0.17	55.05
CdS pure-PI	27.12	0.17	55.05
CdS -PI-Ag 1%	25.19	0.15	65.77
CdS -PI-Ag 3%	26.68	0.17	55.01
CdS -PI-Ag 5%	26.40	0.40	22.7

CdS: Cadmium sulfide, PI: Polyimide

XRD analysis, peak broadening often results from physical parameters such as crystallite size and lattice strain as well as instrumental broadening. Physical factors are represented by the FWHM of each diffraction peak as a linear combination of the contributions from lattice strain and crystallite size calculated using Scherrer's equation and the actual crystallite size. Table 1 lists the parameters, which are different, and it has been found that unit cell size increases for some samples and decreases for others with increasing concentrations of Ag in CdS. As the unit cell decreases evident volume, this confers a suggestion regarding incorporating Ag dopant in CdS matrix or due to intrinsic defects. This may also be explained by Vegard's law (Shkir, et al., 2020a). Vegard's law states that if doping takes place at interstitial or substitutional positions in the matrix, the lattice will increase or decrease, respectively. Hence, both possibilities exist.

B. Optical Characterization

UV-visible spectra

Figs. 4 and 5 show the optical transmission spectra of the CdS thin films with varying Ag ratios on glass and PI substrates. All the films show more than 60% transmission for wavelengths longer than 500 nm. As the Ag ratios increased, the sample optical transmittance increased within

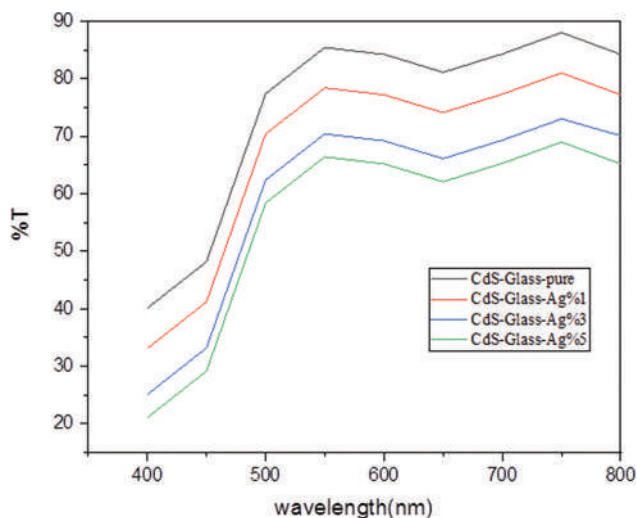


Fig. 4. Transmission spectra of cadmium sulfide pure and Ag-doped with ratios of (1%, 3%, and 5%) on a glass substrate.

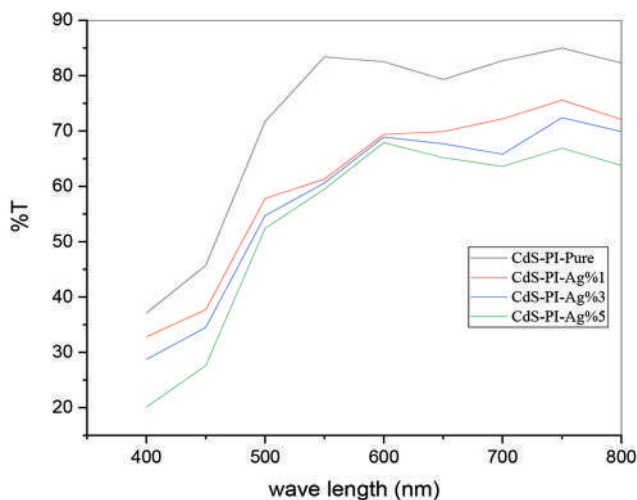


Fig. 5. Transmission spectra of cadmium sulfide pure and Ag-doped with ratios of (1%, 3%, and 5%) on polyimide substrate.

a (400–800) nm wavelength region. In the CdS films, the optical transmittance spectra increased as the Ag doping ratios increased. This occurred because the addition of silver enhanced the crystal structure and reduced surface roughness; similar behavior in the transmission spectra of the CdS films has been reported in (Manthrammel, et al., 2020). Thus, showing a low absorption, it can be used as a light-permeable layer in the Solar Cell system.

PL studies

PL studies help understanding the various transitions inside the samples when light incident on. Because of the vacancies of Cd and S and the interstitial locations of Cd and S, CdS is well known for its wide emission spectra in the UV, blue, green, yellow, and red spectra. According to reports in (Manthrammel, et al., 2020), these inherent flaws may function as luminous centers and provide a wide defect allied PL spectrum. Figs. 6 and 7 represent the PL spectra of CdS pure and doped Ag with different weight ratios on

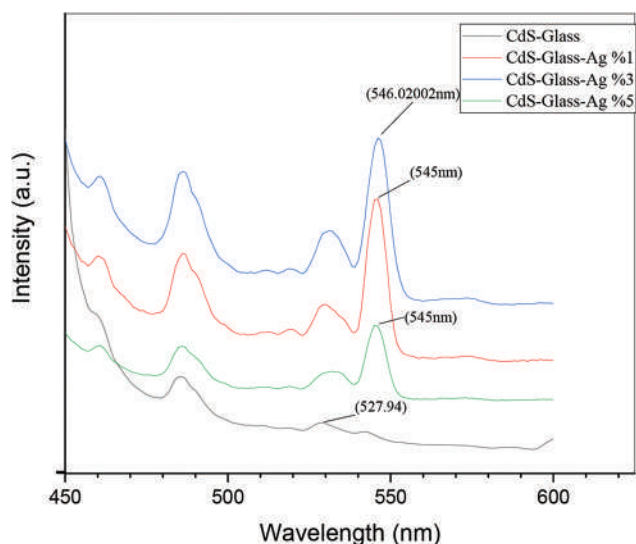


Fig. 6. Cadmium sulfide photo luminescence spectra and Ag-doped with different concentrations on a glass substrate.

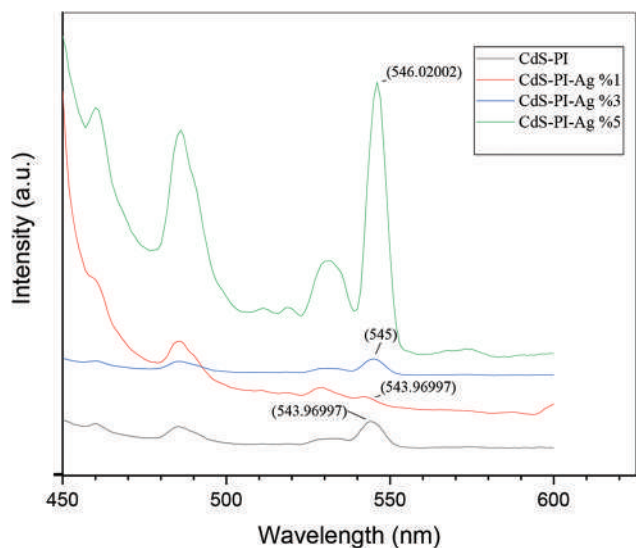


Fig. 7. Cadmium sulfide photo luminescence spectra and Ag-doped with different concentrations on polyimide substrate.

glass and PI substrates at constant temperature 300°C. Thin films excited at 400 nm. The intense peak in both cases is the glass substrate and polyamide plastic, and in all models, it ranges from 542.94 nm to 546.02 nm, see Fig. 6, Fig. 7 and recorded in Table II. Other weak peaks appear in the Figs. 6 and 7, and these weak peaks indicate the transition from one band to another and that the emission is related to defects. However, it is also noticed that the values of the wavelengths of the models change slightly change the long wavelengths due to the increase in the doping ratio, which indicates that the defect level is due to low interstitial defects. As the wavelength increases, the frequency decreases, so the energy gap decreases, and this is proportional to the facts as in (Ikhmayies, 2020). To calculate the energy gap, based on Planck’s law in all models, used (4), and the results are recorded in Table II.

TABLE II
ENERGY GAP FOR CdS PURE AND Ag-DOPED WITH DIFFERENT
CONCENTRATIONS ON GLASS AND PI SUBSTRATES

Sample	Wavelength (nm)	Energy gap (eV)
CdS-Glass	527.94	2.34
CdS-Glass-Ag 1%	545	2.27
CdS-Glass-Ag 3%	546.02	2.27
CdS-Glass-Ag 5%	545	2.27
CdS pure-PI	543.97	2.27
CdS-PI-Ag 1%	543.97	2.27
CdS -PI-Ag 3%	545	2.27
CdS -PI-Ag 5%	546.02	2.27

CdS: Cadmium sulfide, PI: Polyimide

$$E_g = h\nu \quad (4)$$

Where E_g is the energy gap in a unit (eV), h is Planck's constant ($6.63 \times 10^{-34} \text{ J.s}$) and ν is the frequency of visible light in Hz . $\nu = \frac{c}{\lambda}$ where c is $\left(3 \times 10^8 \frac{\text{m}}{\text{s}}\right)$. λ is the visible light wavelength in nm.

Then, equation (4) can be reformed as:

$$E_g = \frac{1240}{\lambda_{nm}} \text{ (eV)} \quad (5)$$

The energy gap was calculated according to (5). The energy gap values show that they are 2.34 eV and 2.27 eV for pure CdS samples in glass and PI plastic substrates, respectively. A very small difference is observed between them, perhaps due to the different substrates. Since the theoretical E_g value of CdS is 2.42 eV, compared with the practical results, a slight difference between them is found at approximately 0.08 eV. This may be due to film deposition.

For the other samples, which were impregnated with silver in different proportions, in both cases, the glass substrates and polyamide plastics showing clear differences in the value of the energy gap, as recorded in Table II. As the percentage of doping increases, the value of the energy gap decreases, which makes CdS films used in solar cells and leads to an increase in electrical conductivity and ease to charge carriers, moving quickly from the valence band to the conduction band by absorbing less energy from visible light, which approaches the color of yellow as acceptable with advance reports (Shkir, et al., 2020a).

V. CONCLUSION

Recent studies on the CdS deposition method using chemical spray pyrolysis and CdS doped Ag thin films onto glass have attracted much attention because of its low cost, ease of use, and capacity for mass production. In this study, CdS thin films were deposited by chemical spray pyrolysis onto glass and PI substrates at various Ag ratios (1%, 3%, and 5%). Following deposition, the effect of the Ag ratio on the structure and film optical properties was studied. The XRD pattern confirmed the proper phase formation of the films. The crystalline size varied between 22.74 nm and 55.05 nm. The optical transmissions of all films were <60% for wavelengths longer than 500 nm. The CdS film optical

transmittance spectra increased as the Ag doping ratios increased. The energy band gap of all films was determined by PL measurement. The values ranged between 2.27 eV and 2.28 eV.

ACKNOWLEDGMENT

The authors would like to thank Koya University for the permission granted to conduct their research activities.

REFERENCES

- Aboud, A.A., Mukherjee, A., Revaprasadu, N., and Mohamed, A.N., 2019. The effect of Cu-doping on CdS thin films deposited by the spray pyrolysis technique. *Journal of Materials Research and Technology*, 8(2), pp.2021-2030.
- Ahmed, A.A.A., Al-Hesni, N.M., Al-Osta, A.H., Al-Salmi, M.L., Manssor, K.A., Ja'adan, S.M., Al-Asbahi, B.A., Qaid, S.M.H., Ghaithan, H.M., and Farooq, W.A., 2021a. Influence of single and dual doping (Ag and Co) on the optical properties of CdS quantum dot thin films for solar application. *Optik*, 246, p.167824.
- Ahmed, M.A., Ahmed, E.H., Sabri, M.M., and Abed, W.R., 2020. The performance of high-efficiency perovskite solar cell (PSC) by using capacitance simulator. *Journal of Physics Conference Series*, 1530, p.012149.
- Ahmed, M.A., Sabri, M.F.M., and Abed, W.R., 2021b. The study of optical and electrical properties of nanostructured silicon carbide thin films grown by pulsed-laser deposition. *Aro Scientific Journal of Koya University*, 9(2), pp.46-50.
- An, B.G., Kim, H.R., Chang, Y.W., Park, J.G., and Pyun, J.C., 2021. Photosensors-based on cadmium sulfide (CdS) nanostructures: A review. *Journal of the Korean Ceramic Society*, 58(6), pp.631-644.
- Bora, J., Borthakur, A., Arandhara, G., and Saikia, P.J., 2021. Effect of Ag doping on the optical and structural properties of CdS/polyvinyl alcohol thin films by thermolysis process. *Thin Solid Films*, 734(2), p.138847.
- Deshmukh, S.G., Kheraj, V., and Panchal, A.K., 2018. Preparation of nanocrystalline CdS thin film by successive ionic layer adsorption and reaction (SILAR) method. *Materials Today Proceedings*, 5(10), pp.21322-21327.
- Faraj, M.G., Ibrahim, K., and Salhin Ali, A., 2012. Fabrication and characterization of thin-film Cu (In, Ga) Se₂ solar cells on a PET plastic substrate using screen printing. *Materials Science in Semiconductor Processing*, 15(2), pp.165-173.
- Faraj, M.G., Pakhuruddin, M.Z., and Taboada, P., 2017. Structural and optical properties of cadmium sulfide thin films on flexible polymer substrates by chemical spray pyrolysis technique. *Journal of Materials Science Materials in Electronics*, 28(9), pp.6628-6634.
- Ikhmayies, S.J., 2020. *Advances in Energy Materials*. 1sted., Springer International Publishing, United States of America.
- Islam, M.A., Hossain, M.S., Aliyu, M.M., Chelvanathan, P., Huda, Q., Karim, M.R., Sopian, K., and Amin, N., 2013. Comparison of structural and optical properties of CdS thin films grown by CSVT, CBD and sputtering techniques. *Energy Procedia*, 33, pp.203-213.
- Kakhaki, Z.M., Youzbashi, A.A., Sangpour, P., Naderi, N., and Orooji, Y., 2022. Influence of Cd salt concentration on the photoconductivity of CdS thin films prepared by chemical bath technique. *Materials Science in Semiconductor Processing*, 148, p.106773.
- Mahmood, W., Ali, J., Thomas, A., Awan, S.U., Jackman, M., Haq, A.U., Hassan, M.U., and Shah, N.A., 2018. Role of Ag¹⁺ substitutional defects on the electronic and optical properties of n-type CdS thin films semiconductor for sustainable and stable window layer in solar cells technology. *Optical Materials*, 85, pp.143-152.
- Manthrammel, M.A., Shkir, M., Shafik, S., Anis, M., and Alfaiy, S., 2020. A systematic investigation on physical properties of spray pyrolysis-fabricated CdS thin films for opto-nonlinear applications: An effect of Na doping. *Journal*

of *Materials Research*, 35(4), pp.410-421.

Mensah, M.B., Awudza, J.A., Revaprasadu, N., and O'Brien, P., 2021. Synthesis of CdS and PbS nanoparticles by the thermal decomposition of ethyl xanthate complexes in castor oil using the heat-up technique. *Materials Science in Semiconductor Processing*, 122, p.105493.

Mohammed, I.M.S., Gubari, G.M.M., Sonawane, M.E., Kasar, R.R., Patil, S.A., Mishra, M.K., Kutwade, V.V., and Sharma, R., 2021. Influence of pH on the physical properties of CdS thin film and its photosensor application. *Applied Physics A*, 127(8), p.597.

Nazir, A., Toma, A., Shah, N.A., Panaro, S., Butt, S., Sagar, R.R., Raja, W., Rasool, K., and Maqsood, A., 2014. Effect of Ag doping on opto-electrical properties of CdS thin films for solar cell applications. *Journal of Alloys and Compounds*, 609, pp.40-45.

Ojeda-Barrero, G., Oliva-Avilés, A., Oliva, A., Maldonado, R.D., Acosta, M., and Alonzo-Medina, G.M., 2018. Effect of the substrate temperature on the physical properties of sprayed-CdS films by using an automatized perfume atomizer. *Materials Science in Semiconductor Processing*, 79, pp. 7-13.

Rahman, M.F., Hossain, J., and Ismail, A.B., 2020. Structural, surface morphological and optical properties and their correlation with the thickness of spin coated superior quality CdS thin film synthesized using a novel chemical route. *SN Applied Sciences*, 2(12), p.1956.

Shaban, Z.M., Khlati, J.A., Khadayeir, A.A., Habubi, N.F., and Chiad, S.S., 2021. Structural, morphology and optical properties of Ag-doped nanostructured CdS thin films. *Journal of Physics Conference Series*, 1999(1), p.012063.

Shkir, M., Ashraf, I.M., Alfaify, S., El-Toni, A.M., Ahmed, M., and Khan A., 2020a. A noticeable effect of Pr doping on key optoelectrical properties of CdS thin films prepared using spray pyrolysis technique for high-performance photodetector applications. *Ceramics International*, 46(4), pp.4652-4663.

Shkir, M., Ashraf, I.M., Chandekar, K.V., Yahia, I.S., Khan, A., Algarni, H., and

Alfaify, S., 2020b. A significant enhancement in visible-light photodetection properties of chemical spray pyrolysis fabricated CdS thin films by novel Eu doping concentrations. *Sensors and Actuators A Physical*, 301, p.111749.

Shkir, M., Ashraf, I.M., Khan, A., Khan, M.T., El-Toni, A.M., Alfaify, S., 2020c. A facile spray pyrolysis fabrication of Sm: CdS thin films for high-performance photodetector applications. *Sensors and Actuators A Physical*, 306, p.111952.

Shkir, M., Khan, Z.R., Anis, M., Shaikh, S.S., and Alfaify, S., 2020d. A comprehensive study of opto-electrical and nonlinear properties of Cu@CdS thin films for optoelectronics. *Chinese Journal of Physics*, 63, pp.51-62.

Taghizadeh Chari, F., and Fadavieslam, M.R., 2019. Microstructural, optical and electrical properties of CdS thin films grown by spray pyrolysis technique as a function of substrate temperature. *Optical and Quantum Electronics*, 51(2), pp.1-16.

Valencia, D.E.J., and Baena, O.J.R., 2015. Portland cement clinker formation: High temperature equilibria and phase composition prediction. In: *TMS 2015 144th Annual Meeting and Exhibition*. Springer, Germany. pp.879-886.

Vishwas, M., Shamala, K.S., and Gandla, S., 2022. Comparison of optical properties of CdS thin films synthesized by spray pyrolysis and thermal evaporation method. *Journal of Optics*, 51(1), pp.1-5.

Wada, H., 2022. Preparation of functional nanoparticles by laser process in liquid and their optical applications. In: *High-energy Chemistry and Processing in Liquids*. Springer, Germany. pp.237-259.

Yadav, A.A., Barote, M.A., and Masumdar, E.U., 2010. Studies on nanocrystalline cadmium sulphide (CdS) thin films deposited by spray pyrolysis. *Solid State Sciences*, 12(7), pp.1173-1177.

Yang, F., Tian, X., Zhang, K., Zhang, X., and Liu, L., 2018. The morphology-property effect and synergetic catalytic effect of cds as electrocatalysts for dyesensitized solar cells. *ECS Journal of Solid State Science and Technology*, 7, pp.311-316.

Plant Disease Diagnosing Based on Deep Learning Techniques: A Survey and Research Challenges

Saman M. Omer^{1,2}, Kayhan Z. Ghafoor^{3,4}, Shavan K. Askar¹

¹Department of Technical Information System Engineering, Erbil Technical Engineering College, Erbil Polytechnic University, Erbil, Kurdistan Region – F.R. Iraq

²Department of Computer Science, College of Basic Education, University of Raparin, Ranya, Kurdistan Region – F.R. Iraq

³Department of Computer Science, Knowledge University, Erbil 44001, Kurdistan Region – F.R. Iraq

⁴Department of Software and Informatics Engineering, Salahaddin University-Erbil, Erbil 44001, Kurdistan Region – F.R. Iraq

Abstract—Agriculture crops are highly significant for the sustenance of human life and act as an essential source for national income development worldwide. Plant diseases and pests are considered one of the most imperative factors influencing food production, quality, and minimize losses in production. Farmers are currently facing difficulty in identifying various plant diseases and pests, which are important to prevent plant diseases effectively in a complicated environment. The recent development of deep learning techniques has found use in the diagnosis of plant diseases and pests, providing a robust tool with highly accurate results. In this context, this paper presents a comprehensive review of the literature that aims to identify the state of the art of the use of convolutional neural networks (CNNs) in the process of diagnosing and identification of plant pest and diseases. In addition, it presents some issues that are facing the models performance, and also indicates gaps that should be addressed in the future. In this regard, we review studies with various methods that addressed plant disease detection, dataset characteristics, the crops, and pathogens. Moreover, it discusses the commonly employed five-step methodology for plant disease recognition, involving data acquisition, preprocessing, segmentation, feature extraction, and classification. It discusses various deep learning architecture-based solutions that have a faster convergence rate of plant disease recognition. From this review, it is possible to understand the innovative trends regarding the use of CNN's algorithms in the plant diseases diagnosis and to recognize the gaps that need the attention of the research community.

Index Terms—Deep learning, Plant disease diagnosis, Plant disease detection, Plant disease recognition.

ARO-The Scientific Journal of Koya University
Vol. XI, No. 1 (2023), Article ID: ARO.11080. 10 pages
DOI: 10.14500/aro.11080

Received: 03 October 2022; Accepted: 15 January 2023
Reviewing paper: Published: 02 February 2023.

Corresponding author's e-mail: saman.muhammad@uor.edu.krd
Copyright © 2023 Saman M. Omer¹, Kayhan Z. Ghafoor,
Shavan K. Askar. This is an open access article distributed under the
Creative Commons Attribution License.



I. INTRODUCTION

Plants are a crucial part of life on Earth as they provide humans with breathable oxygen, food, etc. Furthermore, they provide food for insects and other animals, facilitate weather change, provide clean air, balance the ecosystem, and regulate flooding. In most countries, agriculture crops have become the chief source of economic development. Agriculture plant or crop cultivation has quickly developed in terms of quantity and quality of food production. However, a wide range of factors affect agriculture production such as occurrence of pests and diseases on crops, which, in turn, requires increasing food security. Unfortunately, such diseases are not always detected at an early stage (Fina, et al., 2013).

Plants have been reported to have the following organs: leaf, stem, root, fruit, and flower. In agricultural plants, leaves are an important organ of plants for providing information about the amount and nature of gardening crop (Saleem, et al., 2020). Numerous studies have been conducted on plant leaves as a comparative tool for different purposes such as classification and identification. This is because leaves are often the basis for identification and can be easily perceived, as they are usually green and flattened. Plant diseases can be understood as an unusual state that can interrupt usual plant growth (Shruthi, Nagaveni and Raghavendra, 2019). Plant disease prevention and control have been broadly discussed, because plants are susceptible to diseases and are affected by their outer environment. Normally, plant disease diagnoses have a significant role in monitoring farming systems accurately (Sun, Jia and Geng, 2018).

Plant disease identification is an important mechanism for preventing plant diseases in a complicated environment. Farmers often recognize the symptoms of plant diseases using traditional means, for example, by making naked eye observations and referring to the information in books and internet. (Shruthi, Nagaveni and Raghavendra, 2019). Furthermore, traditional methods such as microscope and DNA sequencing-based approaches have been used to

classify and detect various types of diseases. Such methods, however, necessitate experienced experts in farming, and many farmers are not even permitted to use advanced tools, though most of them own a smartphone for capturing images (Amara, Bouaziz and Algergawy, 2017; Lu, et al., 2017).

The agriculture domain has witnessed massive developments with the aid of technology. Image processing and object detection methods have been used for detecting the infected region in the plant. In addition to their simplicity and accuracy, such techniques are fast (Shruthi, Nagaveni and Raghavendra, 2019; Panigrahi, et al., 2020). Hence, advancements in computer and internet technology can help address the problem of automatic plant disease recognition. Such developments are essential in scientific research for classifying and detecting the symptoms of plant diseases automatically using innovative and intelligent techniques (Saleem, et al., 2020; Bashish, Braik and Bani-Ahmad, 2011).

One of the branches of machine learning is deep learning, which is based on a set of algorithms (Benuwa, et al., 2016). Numerous state-of-the-art deep learning architectures have been used for plant disease detection and recognition. Deep learning algorithms have also been modified by some researchers to enhance the recognition performance of the disease in numerous plant types (see Section II). This paper reviews and compares the methodologies and performances of various deep learning models for the task of plant disease recognition and classification. The remainder of this paper is organized as follows: Section II overviews the extant literature on automated plant disease recognition and discusses the state-of-the-art deep learning methods for data acquisition, preprocessing, segmentation, feature extraction, and classification of plant diseases. Section III discusses research challenges in the said domain. Finally, Section IV summarizes and concludes the current work.

II. LITERATURE REVIEW

Many approaches have been used in agriculture domain for automatic plant disease recognition in various plant parts such as fruit, root, stem, and leaf. A general plant disease detection and classification system using image processing includes five different stages, namely, data acquisition, preprocessing, segmentation, feature extraction, and classification. Fig. 1 depicts this five-step procedure (Panigrahi, et al., 2020).

A. Data Acquisition

The first step in plant disease classification and detection system is image acquisition. A wide variety of devices such as digital camera and smart phone camera can be used to capture images of healthy and diseased plants.

B. Data Preprocessing

The preprocessing step in machine learning or deep learning is important for building an efficient dataset to develop generalizability of the model. In deep learning, a huge amount of data must be collected from different sources such as physical devices, tools, software programs such as

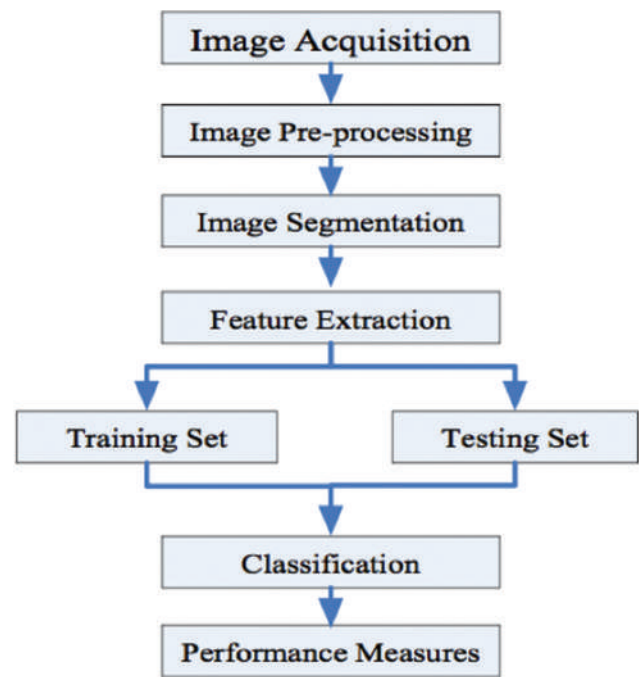


Fig. 1. Flow diagram of the classification process (Panigrahi, et al., 2020).

web crawlers and manual surveys. The model performance may be affected during data collection due to hardware faults, software problems, tool failures, noise, and human errors. Data preprocessing might solve problems such as data not fitting into memory and local storage. It may also help visualize and accelerate the process.

Data preprocessing has an important effect on the performance of a supervised machine learning model. It can solve several kinds of problems on data using transformation, cleaning, normalization, feature extraction, and feature selection before being fed as input to the machine learning or deep learning model (Kotsiantis, Kanellopoulos and Pintelas, 2006). Removing background noise and suppressing undesired distortions have been shown to advance some image features and make the input suitable for further processing (Shruthi, Nagaveni and Raghavendra, 2019; Oo and Htun, 2018). For instance, to boost the reliability of their model, Sladojevic, et al. preprocessed input images by cropping them manually, thereby highlighting region of interest by creating the square around the leaves (Sladojevic, et al., 2016).

In another study, Lu, et al. resized an image from 5760×3840 into 512×512 RGB image to reduce the running time and dimension of training data (Lu, et al., 2017). In another work, Ashqar, Abu-Nasser and Abu-Naser, 2019 preprocessed input images by resizing them to 128×128 pixels, normalizing the pixel values to a $[0,1]$ range, and balancing dissimilar classes (Ashqar, Abu-Nasser and Abu-Naser, 2019). In (Chen, et al., 2020), Photoshop tools have been used to equally process images into RGB model for computations, and then, these images are resized to 224×224 pixels. Table I shows different studies following various approaches for image preprocessing.

TABLE I
INVESTIGATION OF PRE-PROCESSING TECHNIQUES APPLIED IN PLANT IDENTIFICATION

Authors	Pre-processing methods/Purposes
Amara, Bouaziz and Algergawy, 2017	Image were resized and converted into grayscale
Lu, et al., 2017	Images were resized to smaller size to reduce a running time and dimensions
Sladojevic, et al., 2016	Cropping all images manually and draw a square around the region of interest leaves
Ashqar, Abu-Nasser and Abu-Naser, 2019	Resizee, normalized, and balance dissimilar class of image
Chen, et al., 2020	Photoshop tool used to equally processed images and resized images
Nagasubramanian, et al., 2019	RGB images transformed to HSV color spaces

C. Data Segmentation

Computer vision and pattern recognition tasks require intelligent segmentation to recognize the content of an image and to facilitate image analysis. Image segmentation process divides the visual input into slices, which are denoted as entities or parts of entities and involve a set of pixels. Segmentation analyzes image data to identify boundaries in images, simplify the illustration of image, and extract meaningful information for further processing. It has a significant role in recognition and categorization of various plant diseases. Deep learning models can be usually applied directly on images to eliminate the process of segmentation.

Several studies have been conducted on automatic segmentation using various techniques. For example, Barbedo realized that image segmentation might be beneficial to separate the region, where the symptoms are located. The accuracy obtained by a convolutional neural network (CNN) trained with localized symptom lesion regions (87%) was found to be higher than original image (76%) (Barbedo, 2018). Moreover, a threshold metric of segmentation can be employed for RGB wavebands of the charcoal rot stem hyperspectral image (Nagasubramanian, et al., 2019). The authors of (Arnal Barbedo, 2019) segmented images into separate spots and lesions, which increased image number and data diversity as well as made it feasible to recognize numerous diseases in the same leaf, where single symptoms were being considered. About 12% accuracy was achieved, which is greater than the case when raw images were used. The authors of (Mohanty, Hughes and Salathé, 2016) segmented leaves to remove unnecessary background information. They opted a method based on a set of masks made by studying the color, saturation constituents, and lightness of a series of image parts. They showed that segmented images perform better than grayscale images but worse than colored images. Table II summarizes various segmentation processes.

D. Feature Extraction

In pattern recognition, image features play a significant role and are part of an object in image to identify it. Features, most generally, describe image properties such as corners, edges, regions of interest points, and ridges. In plant disease

TABLE II
SUMMARIZES VARIOUS SEGMENTATION PROCESS AND ADVANTAGES

Authors	Segmentation process	Advantages
Nagasubramanian, et al., 2019	A threshold metrics of segmentation used for RGB wavebands	Employed for RGB wavebands of the charcoal rot stem hyperspectral image
Barbedo, 2018	Symptom segmentation used to separate the region of the symptoms are located	The accuracy obtained with localized symptom lesion regions higher than original image
Arnal Barbedo, 2019	Separate spots and lesions were segmented in the images	Image number and data diversity increases and recognizing a numerous diseases in the same leaf is feasible
Mohanty, Hughes and Salathé, 2016	All extra background information are removed from leaves based on a set of masks that made by study of the color, saturation constituents, and lightness	It has better performance than using images of a gray-scale, and less than colored images

recognition, color, shape, and texture have been used as characteristic descriptors to discriminate between plant object (foreground), and other unrelated objects (background). Image texture feature defines how the patterns of color are dispersed in an image. Image color feature is used to discriminate one disease from another. Moreover, due to diseases that have different shape features which are area, axis, and angle, they used to discriminate diseases (Panigrahi, et al., 2020).

Usually, machine learning datasets include a very huge or high dimensional data, which might contain correlated features, which can be misleading or redundant, which increases space size and makes data processing complex. Dimensionality reduction is a technique that can reduce the dimension of a set of features. Applying dimensionality reduction can represent data using a decreased group of features (Dara and Tumma, 2018; Karthikayani and Arunachalam, 2020).

Whereas traditional pattern recognition approaches adopt handcrafted features, deep learning automatically adapts features in a better and modernized way from a huge dataset (Karthikayani and Arunachalam, 2020). Fig. 2 illustrates a simple way to compare traditional and deep learning methods. The latter is categorized as a group of machine learning algorithms, wherein input layers are basically mapped onto output layers (Mohanty, Hughes and Salathé, 2016). Such methods involve various layers of non-linear processing units for extracting and adapting features. All sequential layers use the previous layer's output as an input (Benuwa, et al., 2016).

In a CNN, dimensionality reduction and the classification process are combined in the same model. CNNs use multiple feature extraction stages and avoid the complicated feature extraction procedure, and to learn the task specific features more efficiently.

Dimensionality reduction techniques can be broadly categorized into two types, namely, feature extraction and feature election (Karthikayani and Arunachalam, 2020), such as shown in Fig. 3 (Uddin, Mamun and Hossain, 2020). In machine learning, feature extraction is an important technique

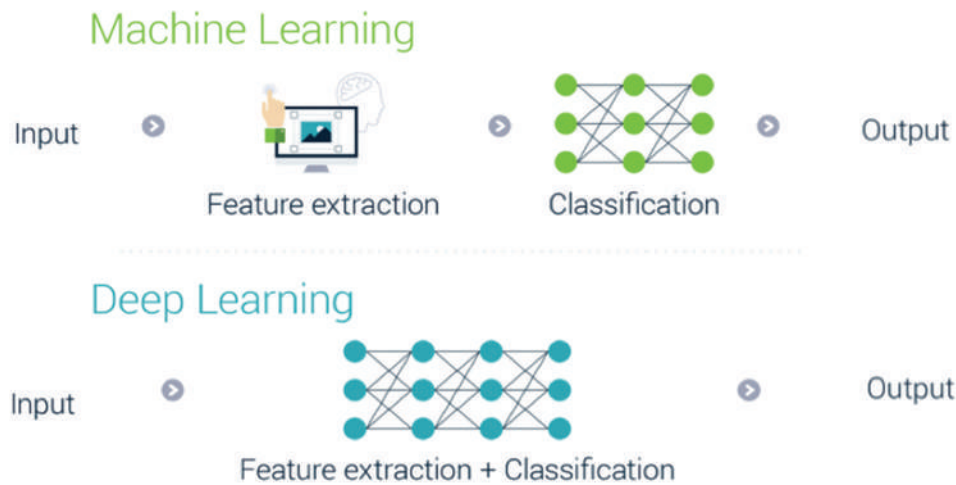


Fig. 2. Feature extraction between a traditional machine and deep learning.

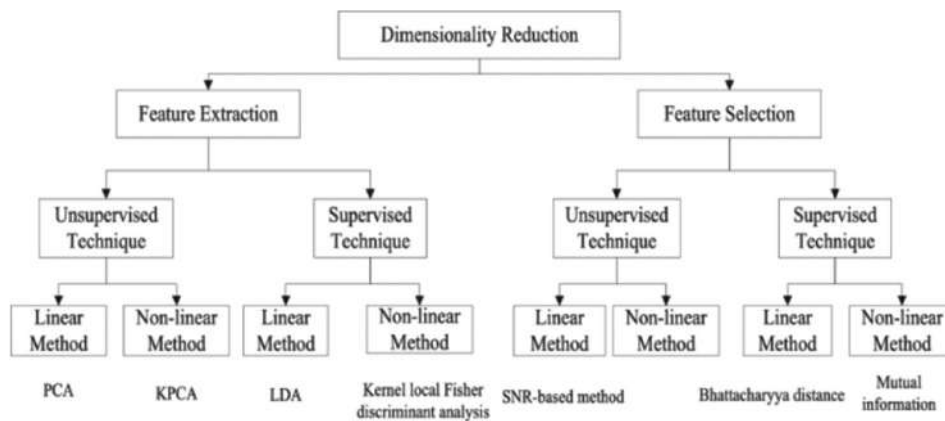


Fig. 3. Dimensionality reduction techniques (Uddin, Mamun and Hossain, 2020).

for converting an input image into a set of features (Dara and Tumma, 2018) and for reducing the dimensionality of feature space (Karthikayani and Arunachalam, 2020). Feature extraction can decrease the number of features needed to define a huge input dataset (Dara and Tumma, 2018) and to delete the data that are less significant (Karthikayani and Arunachalam, 2020). It affects the learning algorithm accuracy for processing the data in a least amount of time (Karthikayani and Arunachalam, 2020).

The second type of technique for dimensionality reduction is feature selection, which aims to find the best features among the whole obtained features. It selects the most important and preferable features among all features from the original dataset. These features can provide relevant information about the data and enable accurate prediction at output stage (Dara and Tumma, 2018; Karthikayani and Arunachalam, 2020).

A CNN is a stack of non-linear transformation functions and can automatically learn representations from the data, to use the numerous feature extraction steps (Khan, et al., 2020; Reyes, Caicedo and Camargo, 2015). It is a specific type of feed-forward neural network (information is fed from layer to layer without reversing) (Zbakh, et al., 2019) and is motivated by biological processes that occur in the visual cortex in the living beings of mind. In the 1980s, CNNs

were initially proposed for digit recognition (LeCun, et al., 1989). Recently, CNN-based deep learning architectures have enabled huge-scale object recognition tasks.

CNNs are capable of extracting features hierarchically and classifying them (Khan, et al., 2020). A CNN has several layers that hierarchically calculate features from images as an input. Deep CNNs have been used for large-scale image classification for the 1st time in (Krizhevsky, Sutskever and Hinton, 2017) and exhibited remarkable performance. CNN architecture consists of convolution layers, a pooling layer, an activate function layer, dropout layers, and a fully connected layer at the end, as shown in Fig. 4.

Convolutional and pooling layers act as feature extractors (Amara, Bouaziz and Algerawy, 2017). The Convolutional layer keeps the outcomes of the convolution of filters or kernels of the preceding layer (Durmus, Gunes and Kirci, 2017). These filters or kernels to be learned contain weights and biases; all filters are restricted spatially but expand with comprehensive depth of input volume (Dara and Tumma, 2018). In addition, convolution layers produce a feature map by extracting features of an input image using a filter or kernel (Ibrahim, Sabri and Isa, 2018). The kernel (window) slides over the entire image step by step. The result is taken from summation over the entire image (Zbakh, et al., 2019). Different feature maps yield from

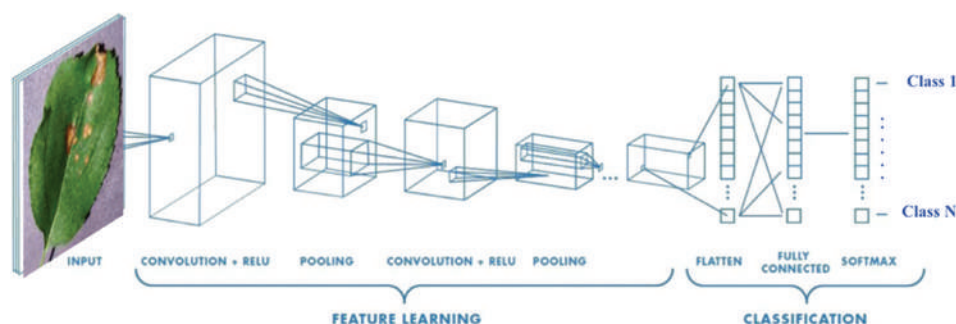


Fig. 4. Convolutional neural network architecture.

multiple convolutional layers and different filters to ensure complete extraction of various features.

The activation function has a significant role in the learning process, and thus, selecting a proper activation function would affect the training dynamics and task performance (Ramachandran, Zoph and Le, 2017). Various activation functions have been used to inculcate non-linear combination of features (e.g., ReLU, sigmoid, tanh, and maxout) (Khan, et al., 2020) and to increase non-linearity of the network (Durmus, Gunes and Kirci, 2017). The most commonly used function is ReLU, which is a piecewise linear function, in which all negative pixel values are replaced by zero, whereas positive pixel values are retained (FatihahSahidan, et al., 2019; Gu, et al., 2018).

The pooling layer works independently over the entire input depth to rescale it. Hence, the feature matrix is decreased (Dara and Tumma, 2018). Pooling layer has a significant concept after activation function to obtain a strong feature versus noise and distortion (Saufi, et al., 2018). It is used to decrease the connection numbers between convolutional layers, reduce the sampling size, and decrease the dimensionality of feature mapping (Ibrahim, Sabri and Isa, 2018; Gu, et al., 2018), reduce neuron size, and reduce overfitting (Durmus, Gunes and Kirci, 2017). Commonly used pooling methods include max, average, mixed, and stochastic pooling. Dropout layers are used to avoid overfitting, which randomly shuts down the neurons in the network (Durmus, Gunes and Kirci, 2017).

E. Classification

Classification is generally accomplished using fully connected layer with an activation function softmax, in which computer program uses learned features from input data to categorize the same into predefined classes (Amara et al., 2017) and uses various collections of features (Dara and Tumma, 2018). Many classification techniques have been used in agricultural domain for investigating plant diseases. Traditional machine learning methods have been extensively implemented in agricultural arena. In addition, the deep CNN techniques have been applied for object identification and plant disease categorization and have witnessed tremendous developments in past years. Deep learning has been extensively considered for computer vision tasks in current years, and thus, a huge number of related techniques have been developed. Although it has been proven to be effective

in different classification and detection problems, it is very challenging to grasp unknown objects due to the different shape and posture of objects (Jiang, et al., 2021). For example, LeNet model as a CNN has been used in (Amara, Bouaziz and Algergawy, 2017) to classify two banana leaf diseases, namely, banana speckle and sigatoka. The authors of (Liu, et al., 2017) designed a novel deep CNN architecture for accurately classifying four different types of apple diseases such as mosaic, rust, brown spot, and Alternaria leaf spot. They used a dataset of 13,689 images of unhealthy apple leaves and obtained overall accuracy of 97.62%. Lu, et al. developed an innovative CNN-based identification method to categorize ten common rice diseases. Using this model, they attained an accuracy of 95.48% on a dataset including 500 images of unhealthy and healthy rice leaves and stems (Lu, et al., 2017). The authors of (Ashqar, Abu-Nasser and Abu-Naser, 2019) selected a CNN (ConvNet-based) approach for classifying plant seedlings with a dataset containing approximately 5000 images belonging to 12 different species.

Transfer learning is the process of reusing a pretrained model for solving a new problem that is different from scratch, which involves learning or training data from basic. For instance, the authors of (Chen, et al., 2020) studied transfer learning of deep CNN to classify diseased leaves. They chose VGGNet and inception models for improving the learning capability of small lesion signs. The authors of (Arnal Barbedo, 2019) used a pretrained CNN that employed GoogLeNet architecture to study the use of separate spot and lesions, instead of using whole leaves and classified various plant infections. They concluded that the accuracy attained from separate lesions and spots was 94%. Mohanty, et al. evaluated and focused on two famous deep CNN models, namely, AlexNet and GoogLeNet, trained using scratch and transfer learning, to classify 14 crop classes and 26 diseases. They noted that GoogLeNet reliably performs better classification based on training transfer learning on images of unhealthy and healthy leaves, and attained an accuracy of 99.35% (Mohanty, Hughes and Salathé, 2016). In addition, Nagasubramanian, et al. improved a technique named a supervised 3D-CNN for learning the spectral and spatial information of hyperspectral images of healthy leaves and charcoal rot disease categorization examples in soybean stems. They explained the significance of specific hyperspectral wavelengths in categorization using a saliency map-based visualization technique and obtained a 95.73% classification

accuracy (Nagasubramanian, et al., 2019). A state-of-the-art CNN model from scratch proposed in (Omer, Ghafoor and Askar, 2022) to diagnosis five cucumber leaf diseases and one healthy leaf. A comparative experiments were conducted based on applying pretrained models (AlexNet, Inception-V3, and ResNet-50) to prove the authenticity of the proposed CNN.

In general, most studies in the extant literature are dedicated to plant disease classification. However, plant disease identification (both localization and classification) is a complicated task. Some deep learning techniques have been developed for the purpose of plant disease detection. Deep learning meta-architectures such as Faster Region-based CNN (Faster R-CNN), Region-based Fully Convolutional Network (R-FCN), and Single Shot Multibox Detector (SSD) have been used as a detector for categorization and localization of plant leaves disease (Saleem, et al., 2020), and they have been used in (Fuentes, et al., 2017) for detecting tomato diseases and pests, with suitable performance.

The authors of (Durmus, Gunes and Kirci, 2017) used AlexNet and SqueezeNet models to detect tomato diseases from leaf images and found that the former performed slightly better than the latter in terms of accuracy. Sladojevic, et al. developed an innovative technique based on deep CNN for detecting plant diseases automatically and classified 13 different kinds of plant diseases from the healthy leaf images using CaffeNet CNN architecture. The authors achieved an average accuracy of 96.3% (Sladojevic, et al., 2016). In addition, Hernández and López proposed a method for detecting plant diseases based on a probabilistic programming using Bayesian deep learning procedures (Hernández and López, 2020). Ferentinos used five CNN models, namely, AlexNet, AlexNetOWTBn, GoogLeNet, Overfeat, and VGG to detect plant illnesses using images of healthy and

unhealthy leaves. They reported VGG to be a successful model with a 99.53% success rate on test dataset containing 17,548 images (Ferentinos, 2018). In another study, Ramcharan, et al. applied transfer learning for training a deep CNN Inception v3 to detect three cassava diseases and two kinds of pest damage (Ramcharan, et al., 2017). Table III, summarized that several algorithms had been carried out for plant leaf disease classification.

F. Dataset

In the previous studies, various datasets have been used for plant disease classification and detection tasks. Some of those datasets are PlantVillage dataset, which contains healthy and diseased images of five crops, namely, apple (Liu, et al., 2017), corn, grape, potato, and tomato (FatihahSahidan, et al., 2019; Ramcharan, et al., 2017). In addition, the authors of (Ramcharan, et al., 2017) used cassava disease dataset, whereas the authors of (Saleem, et al., 2020) used ImageNet dataset. The authors of (Amara, Bouaziz and Algergawy, 2017) used a real banana disease dataset, in which they derived from the PlantVillage dataset. Several steps are required for the implementation of deep learning algorithms, as shown in Fig. 5 (Saleem, et al., 2020) that start from data collection to visualization mappings.

We can infer from this section that, even though some deep learning models have been developed for image classification in the application of plant disease diagnosis and detection, this is still a fertile area of research and should result in improvements for better recognition of plant diseases in various situations, such as different lighting conditions and taking real background into consideration. It also concluded that leaf is the most commonly used plant organ for classifying plant diseases, as its image can be easily

TABLE III
SUMMARIZES VARIOUS STUDIES FOR PLANT DISEASE CLASSIFICATION

Authors	Methods	Dataset	Accuracy
Saleem, et al., 2020	Faster R-CNN, R-FCN with ResNet , and SSD with Inception	PlantVillage	73.07%
Amara, Bouaziz and Algergawy, 2017	LeNet	PlantVillage (2 types of banana leaves diseases)	0.9757
Lu, et al., 2017	CNN	rice diseases (10 common diseases)	95.48%
Sladojevic, et al., 2016	CNN (CaffeNet)	PlantVillage (13 different diseases)	96.3%
Ashqar, Abu-Nasser and Abu-Naser, 2019	CNN (ConvNet)	Plant seedling dataset	99.48%
Chen, et al., 2020	VGGNet and Inception	Rice plant images	92.00%
Nagasubramanian, et al., 2019	Supervised 3D-CNN	4 soybean genotypes were selected from soybean stem samples	95.73%
Barbedo, 2018	CNN (GoogLeNet)	Freely available dataset contains almost 50,000 images	94%. from separate lesions and spots
Mohanty, Hughes and Salathé, 2016	AlexNet and GoogLeNet	PlantVillage	99.35% from GoogLeNet
Durmus, Gunes and Kirci, 2017	AlexNet and SqueezeNet	PlantVillage (tomato leaves)	0.9565 from AlexNet
Liu, et al., 2017	CNN (Goo- gLeNet)	Apple images (4 common types of apple disease)	97.62%
Fuentes, et al., 2017	Faster R-CNN, R-FCN, and SSD with ResNet	PlantVillage (tomato leaves)	88.20% from RFCN with ResNet 50
Ferentinos, 2018	AlexNet, Overfeat, AlexNetOWTBn, GoogLeNet, and VGG	Openly available database contains 87,848 images	99.53% from VGG

SSD: Single Shot Multibox Detector

collected, and it is green and smooth during all four seasons. Another finding is that it presents that the PlantVillage dataset was used in the majority of the studies. It includes a simple background and several photos of various plant spices with their diseases. However, the actual environment needs to be taken into account for a realistic scenario.

III. RESEARCH CHALLENGES

Nowadays, deep learning models have attained good performance and promising results in various domains, such as image classification and detection, speech recognition, and object detection. Such models are advanced enough to deal with complicated tasks. Different architectural models have been used in deep learning recently to obtain significant performance and efficiency. Despite the developments and improvements that have been applied to deep learning models in various research studies, especially in plant disease classification and detection, numerous significant research gaps and challenges still need to be addressed before implementing different deep learning architectures for plant disease recognition. Research issues and challenges that have been recognized in this paper are hyperparameter tuning, model overfitting, plant organs, unavailability of plant disease dataset, and different plant diseases.

A. Hyperparameter Tuning

The state-of-the-art models automatically learn features from images and classify on the basis of these learned features. Traditional machine learning models, on the other hand, manually extract features and tune them, which can be time consuming. Throughout the training and testing of the model, a set of parameters, for learning process, known as hyperparameters, are used. A large set of hyperparameters are used in various deep learning architectures (Hutter, Lücke and Schmidt-Thieme, 2015).

In every dataset, hyperparameter tuning has a significant effect on training the model to obtain a good performance and

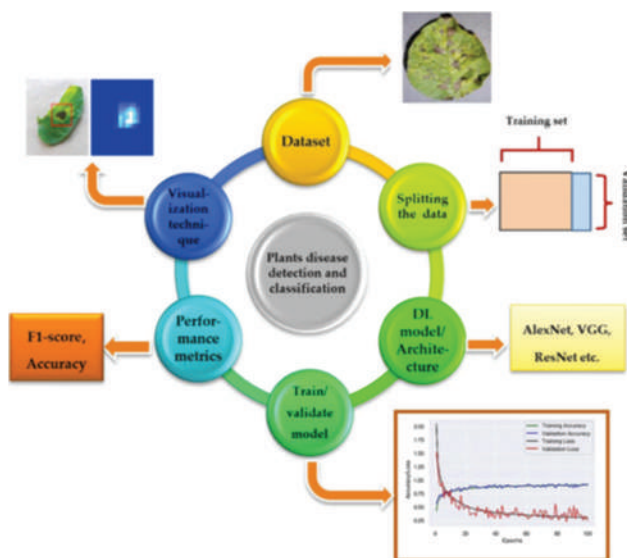


Fig. 5. Flow diagram of deep learning implementation [2].

develops validation errors (Victoria and Maragatham, 2021). Hyperparameters include the parameters of (i) regularization, (ii) network architecture, such as layer numbers and sigmoid transfer function kinds, (iii) sample numbers and learning rates, (iv) preprocessing, such as reducing dimensionality and normalization, and (v) initialization weight parameters. Theoretically, several methods have been treated using hyper-prior and manually using optimization techniques.

Some of these hyperparameters pose a greater challenge of grounded mathematical treatment (Hutter, Lücke and Schmidt-Thieme, 2015). In such instances, hyperparameter tuning of a deep learning architecture is an issue that must be addressed based on empirical data using improving theoretical background and evaluating the performance of the network (Angelov and Sperduti, 2016), such as shown in Fig. 6 (Analytics vidhya, 2020).

For instance, a simplified system or improved technique would require less hyperparameters. On the other hand, a complex system can be customized automatically using hyperparameter optimization algorithms in a given application for optimal performance (Hutter, Lücke and Schmidt-Thieme, 2015). Victoria and Maragatham proposed a Bayesian hyperparameter optimization technique for improving model performance, where all hyperparameter values are optimized (Angelov and Sperduti, 2016).

B. Model Overfitting

Overfitting is an issue facing machine learning algorithms, especially deep learning models, in which errors or random noise occur rather than the underlying relationship described in the model (Liu, et al., 2017). Overfitting has been shown to have a negative effect on robust performance of the training set across multiple datasets such as ImageNet, CIFAR-10, CIFAR-100, and SVHN (Rice, Wong and Kolter, 2020), such as shown in Fig. 7. Liu, et al. employed several techniques to avoid overfitting. They used dataset augmentation operations such as mirror symmetry, image rotation, PCA jittering, and brightness adjustment to increase the diversity of training images and enhance the generalizability of their model (Liu, et al., 2017).

The authors of (Rice, Wong and Kolter, 2020) studied data augmentation and regularization techniques to

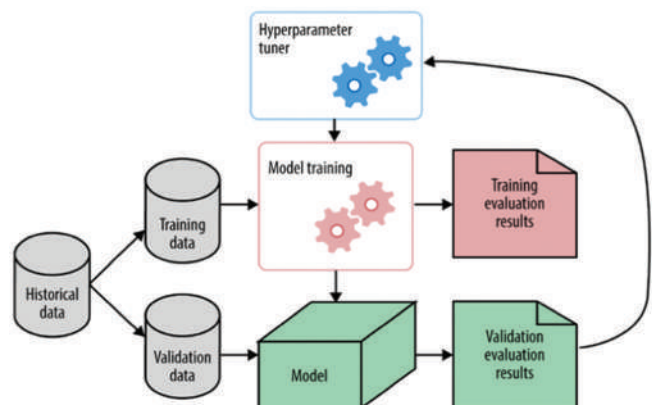


Fig. 6. Hyperparameter tuning process [43].

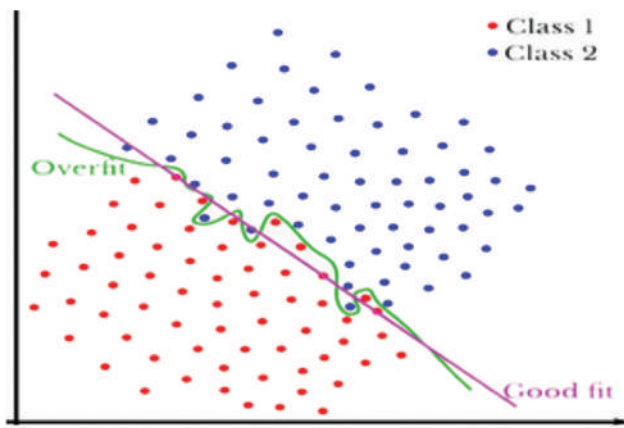


Fig. 7. Overfitting in machine learning.

remedy overfitting. Their experimental testing showed that regularization methods do not robustly prevent overfitting and tend to make the model over-regularized. Furthermore, the authors of (Arsenovic, et al., 2019) used two different augmentation algorithms to prevent overfitting, namely, traditional augmentation methods, like pixel-wise changes or rotations, and training using generative adversarial network. They used local normalization obtained using response-normalization layers and used convolution layers instead of some fully connected layers (Liu, et al., 2017). Furthermore, another way to prevent the model from overfitting using transfer learning is by retraining the last few layers and freezing the first layer (Barbedo, 2018). The authors of (Mohanty, Hughes and Salathé, 2016) changed the data ratio of train and test sets. In addition, two different methods such as training the network model using more examples and changing network complexity like changing structure and parameters of the network have been used to reduce overfitting (Brownlee, 2018). In neural network, dropout means removing units from the network temporarily along with outgoing and incoming connections during training process. Srivastava, et al. used the dropout algorithm for resolving the overfitting problem. They noted that this technique can provide a significant development over regularization algorithms and markedly reduce overfitting (Srivastava, et al., 2014).

C. Plant Organs

Plants have various organs that have been used as a characteristic to be studied by researchers in various fields, especially in disease recognition and detection task.

Based on this review paper, leaf plant organ had been mostly used by researchers such as in (Saleem, et al., 2020; Amara, Bouaziz and Algergawy, 2017; Ashqar, Abu-Nasser and Abu-Naser, 2019; Nagasubramanian, et al., 2019; Dara and Tumma, 2018; FatihahSahidan, et al., 2019; Ferentinos, 2018; Ramcharan, et al., 2017; Victoria and Maragatham, 2021; and Angelov and Sperduti, 2016), for the purpose of classifying and detecting plant diseases. In (Arnal Barbedo, 2019), instead of using entire leaf, separate spot and lesions have been used.

However, many diseases have been better categorized in other organs using their symptoms. For instance, the stem has

been used in (Lu, et al., 2017; Barbedo, 2018). Furthermore, in Ashqar, Abu-Nasser and Abu-Naser (2019) seeding has been used for classification. Hence, a comprehensive plant image dataset must be constructed to incorporate images of other plant organs and better classify plant diseases.

D. Challenges Associated with Constructing Large Datasets

In deep learning, a huge dataset with a wide variety is required. However, constructing such a dataset involves challenges. Barbedo realized that plant species, disease variety, variety of conditions in capturing image, and sample numbers in each class of the dataset affect and prevent deep learning models more widely to be used in practice (Barbedo, 2018). Data annotation is one of the important tasks that require expert assistance to label an input image accurately (Kamilaris and Prenafeta-Boldú, 2018).

Researchers have used different datasets in their studies to train deep learning models. For instance, a publicly available PlantVillage dataset is mostly used to calculate the accuracy and performance, which contains many different healthy and diseased images with simple plain background. Yet, most researchers have used similar architectural design and obtained a quite redundant result from their experiments on the dataset such as (Amara, Bouaziz and Algergawy, 2017; Dara and Tumma, 2018; Victoria and Maragatham, 2021; Brahimi, Boukhalfa and Moussaoui, 2017; and Cruz, et al., 2017). Although they have used several aspects of the model for training and testing the system for plant disease recognition, they have still not gained enough new information. Thus, new tests should be considered with supplementary interesting datasets (Barbedo, 2018). Some researchers have also constructed a synthetic dataset (Sladojevic, et al., 2016). However, many challenges still needed to be addressed.

In general, in agriculture field, there is not an enough available dataset to researchers. For this purpose, researchers are required to improve and build a new dataset that includes some different plant organs and different leaf diseases.

E. Challenges of Plant Diseases

Plant disease management and pathology are faced with ever-growing challenges. On the one hand, agricultural productivity has reduced due to depleting natural resources and diminishing arable lands. On the other hand, due to increasing global population, requests for high quality and varied food have increased. In addition, the evolution and epidemics of plant diseases have globally increased due to intensification, resources such as water, fertilizer, and pesticides (He, Zhan and Xie, 2016). Plant diseases and pests are the major reason that lead to substantial economic losses and reduced plant yields. In technological advancements, the theories of plant diseases and pest diagnoses such as detection and classification have been developed from symptoms and signs of the diseases (Balodi, et al., 2017).

In the future, plant disease management plans, such as an accurate plant disease recognition, are important and must be emphasized more for societal development, food security globalization, climate change, and disease prevention. In the field of plant pathology advancements, some new avenues

for specific and sensitive plant diagnosis procedures have been developed that are coupled with molecular biology, bioinformatics, and biotechnology (He, Zhan and Xie, 2016; Balodi, et al., 2017).

IV. CONCLUSION

In agriculture farming, plant diseases and pests affect the food loss production if sufficient care is not given. Therefore, an automatic diagnosis plant disease and detection system is essential, as it has many benefits to people in the field of agriculture, pharmaceutical industry, etc. The automated plant disease diagnosis systems combine the expertise of phytopathology experts with the capacity to extract symptomatic features using CNN algorithms to identify and classify plant diseases and pests. This paper is a review and summarized techniques of the deep CNN-based plant disease diagnosis and detection. It also presents some issues and challenges regarding the plant disease classification, detection and dataset characteristics, due to the diversity of problems and the specificities of real-world scenarios that increase the difficulty to semantically catalog the data in representative datasets. In addition, this review investigated some deep learning architectures, this is still a fertile area of research for researchers to address gaps in different agricultural domains by integrating image processing and machine learning, especially CNN-based approaches. Another finding is, deep learning models should be effective for many illumination conditions; therefore, the datasets should include images from a variety of field scenarios in addition to those that depict the real environment. One can conclude from the review, that the CNN models are a widely used in diagnosis and detecting plant disease and pests, for which an accurate and fast model is necessary. In addition, to comprehend the variables influencing the identification of plant disease, such as the classes and quantity of datasets, learning rate, illumination, and similar aspects, a comprehensive study is necessary.

ACKNOWLEDGMENT

The authors would like to thank University of Raporin and Erbil Polytechnique University for their support during the preparation of the work. Many thanks for the reviewers for their valuable comments and suggestions on the manuscript which improved the performance of the paper.

REFERENCES

- Amara, J., Bouaziz, B. and Algergawy, A., 2017. *A Deep Learning-based Approach for Banana Leaf Diseases Classification*. Available from: <https://dl.gi.de/handle/20.500.12116/944> [Last accessed on 2021 Jul 05].
- Analytics vidhya, 2020. *Hyperparameter Tuning Using Optuna*. Available from: <https://www.analyticsvidhya.com/blog/2020/11/hyperparameter-tuning-using-optuna> [Last accessed: 5on 2021 Jul 05].
- Angelov, P. and Sperduti, A., 2016. 'Challenges in Deep Learning'. Available from: <https://eprints.lancs.ac.uk/id/eprint/134273> [Last accessed on 2021 Jun 12].
- Arnal Barbedo, J. G., 2019 Plant disease identification from individual lesions and spots using deep learning. *Biosystems Engineering*, 180, pp. 96-107.
- Arsenovic, M., Karanovic, M., Sladojevic, S., Anderla, A. and Stefanovic, D., 2019. Solving current limitations of deep learning based approaches for plant disease detection. *Symmetry*, 11(7), p. 939.
- Ashqar, B.A.M., Abu-Nasser, B.S. and Abu-Naser, S.S., 2019. *Plant Seedlings Classification Using Deep Learning*. Available from: <https://www.ijeais.org/ijaisr> [Last accessed on 2021 Jun 11].
- Balodi, R., Bisht, S., Ghatak A. and Rao, K.H., 2017. Plant disease diagnosis: Technological advancements and challenges. *Indian Phytopathology*, 70, pp. 275-281.
- Barbedo, J.G.A., 2018. Factors influencing the use of deep learning for plant disease recognition. *Biosystems Engineering*, 172, pp. 84-91.
- Bashish, D.A., Braik, M. and Bani-Ahmad, S., 2011. Detection and classification of leaf diseases using K-means-based segmentation and neural-networks-based classification. *Information Technology Journal*, 10(2), pp. 267-275.
- Benywa, B.B., Zhan, Y., Ghansah, B., Wornyo, D.K. and Kataka, F.B., 2016. A review of deep machine learning. *International Journal of Engineering Research in Africa*, 24, pp. 124-136.
- Brahimi, M., Boukhalfa, K. and Moussaoui, A., 2017. Deep learning for tomato diseases: Classification and symptoms visualization. *Applied Artificial Intelligence*, 31(4), pp. 299-315.
- Brownlee, J. 2018. *Better Deep Learning: Train Faster, Reduce Overfitting, and Make Better Predictions*. Available from: <https://books.google.com/books?hl=en&lr=&id=T1-nDwAAQBAJ&oi=fnd&pg=PP1&dq=Better+Deep+Learning,+Train+Faster,+Reduce+Overfitting,+and+Make+Better+Predictions,+Machine+Learning+Mastery+With+Python&ots=tDPNdk15EZ&sig=fVvGLaGFhLu5H7ktaeHCX8US49E> [Last accessed on 2021 Jun 12].
- Chen, J., Chen, J., Zhang, D., Sun, Y. and Nanekkarana, Y.A., 2020. Using deep transfer learning for image-based plant disease identification. *Computers and Electronics in Agriculture*, 173, p. 105393.
- Cruz, A.C., Luvisi, A., De Bellis, L. and Ampatzidis, Y., 2017. X-FIDO: An effective application for detecting olive quick decline syndrome with deep learning and data fusion. *Frontiers in Plant Science*, 8, p. 1741.
- Dara, S. and Tumma, P., 2018. Feature Extraction by Using Deep Learning: A Survey. In: *Proceedings of the 2nd International Conference on Electronics, Communication and Aerospace Technology, ICECA 2018*. Institute of Electrical and Electronics Engineers Inc., United States, pp. 1795-1801.
- Durmus, H., Gunes, E.O. and Kirci, M., 2017. Disease Detection on the Leaves of the Tomato Plants by Using Deep Learning. In: *2017 6th International Conference on Agro-Geoinformatics, Agro-Geoinformatics 2017*. Institute of Electrical and Electronics Engineers Inc., United States.
- FatihahSahidan, N., Juha, A.K., Mohammad, N. and Ibrahim, Z., 2019. Flower and leaf recognition for plant identification using convolutional neural network. *Indonesian Journal of Electrical Engineering and Computer Science*, 16(2), pp. 737-743.
- Ferentinos, K.P., 2018. Deep learning models for plant disease detection and diagnosis. *Computers and Electronics in Agriculture*, 145, pp. 311-318.
- Fina, F., Birch, P., Young, R., Obu, J., Faithpraise, B. and Chatwin, C., 2013. Automatic plant pest detection and recognition using k-means clustering algorithm and correspondence filters. *International Journal of Advanced Biotechnology and Research*, 4, 189-199.
- Fuentes, A., Yoon, S., Kim, S.C. and Park, D.S., 2017. A robust deep-learning-based detector for real-time tomato plant diseases and pests recognition. *Sensors (Switzerland)*, 17(9), p. 2022.
- Gu, J., Wang, Z., Kuen, J., Ma, L., Shahroudy, A., Shuai, B., Liu, T., Wang, X., Wang, G., Cai, J. and Chen, T., 2018. Recent advances in convolutional neural networks. *Pattern Recognition*, 77, pp. 354-377.
- He, D.C., Zhan, J.S. and Xie, L.H., 2016. Problems, challenges and future of plant disease management: From an ecological point of view. *Journal of Integrative Agriculture*, 15(4), pp. 705-715.

- Hernández, S. and López, J.L., 2020. Uncertainty quantification for plant disease detection using Bayesian deep learning. *Applied Soft Computing Journal*, 96, p. 106597.
- Hutter, F., Lücke, J. and Schmidt-Thieme, L., 2015. Beyond manual tuning of hyperparameters. *KI-Kunstliche Intelligenz*, 29(4), pp. 329-337.
- Ibrahim, Z., Sabri, N. and Isa, D., 2018. Multi-maxpooling Convolutional Neural Network for Medicinal Herb Leaf Recognition. In: *Proceedings of the 6th IIAE International Conference on Intelligent Systems and Image Processing 2018*. The Institute of Industrial Applications Engineers, Japan.
- Jiang, D., Li, G., Sun, Y., Hu, J., Yun, J. and Liu, Y., 2021. Manipulator grabbing position detection with information fusion of color image and depth image using deep learning. *Journal of Ambient Intelligence and Humanized Computing*, 12(12), pp. 10809-10822.
- Kamilaris, A. and Prenafeta-Boldú, F.X., 2018. Deep learning in agriculture: A survey. *Computers and Electronics in Agriculture*, 147, pp. 70-90.
- Karthikayani, K. and Arunachalam, A.R., 2020. A survey on deep learning feature extraction techniques. In: *AIP Conference Proceedings*. American Institute of Physics Inc., College Park, Maryland.
- Khan, A., Sohail, A., Zahoor, U. and Qureshi, A.S., 2020. A survey of the recent architectures of deep convolutional neural networks. *Artificial Intelligence Review*, 53(8), pp. 5455-5516.
- Kotsiantis, S.B., Kanellopoulos, D. and Pintelas, P.E., 2006. Data preprocessing for supervised learning. *International Journal of Computer Science*, 1, pp.111-117.
- Krizhevsky, A., Sutskever, I. and Hinton, G.E., 2017. ImageNet classification with deep convolutional neural networks. *Communications of the ACM*, 60(6), pp. 84-90.
- LeCun, Y., Boser, B., Denker, J.S., Henderson, D., Howard, R.E., Hubbard, W. and Jackel, L.D., 1989. Backpropagation applied to handwritten zip code recognition. *Neural Computation*, 1(4), pp. 541-551.
- Liu, B., Zhang, Y., He, D. and Li, Y., 2017. Identification of apple leaf diseases based on deep convolutional neural networks. *Symmetry*, 10, p. 11.
- Lu, Y., Yi, S., Zeng, N., Liu, Y. and Zhang, Y., 2017. Identification of rice diseases using deep convolutional neural networks. *Neurocomputing*, 267, pp. 378-384.
- Mohanty, S.P., Hughes, D.P. and Salathé, M., 2016. Using deep learning for image-based plant disease detection. *Frontiers in Plant Science*, 7, p. 1419.
- Nagasubramanian, K., Jones, S., Singh, A.K., Sarkar, S., Singh, A. and Ganapathysubramanian, B., 2019. Plant disease identification using explainable 3D deep learning on hyperspectral images. *Plant Methods*, 15(1), p. 98.
- Omer, S.M., Ghafoor, K.Z. and Askar, S.K., 2022. 'An intelligent system for cucumber leaf disease diagnosis based on the tuned convolutional neural network algorithm. *Mobile Information Systems*, 2022, p. 8909121.
- Oo, Y.M. and Htun, N.C., 2018. Plant leaf disease detection and classification using image processing. *International Journal of Research and Engineering*, 5(9), pp. 516-523.
- Panigrahi, K.P., Das, H., Sahoo, A.K. and Moharana, S.C., 2020. Maize leaf disease detection and classification using machine learning algorithms. In: *Advances in Intelligent Systems and Computing*. Springer, Germany, pp. 659-669.
- Ramachandran, P., Zoph, B. and Le, Q.V., 2017. Searching for Activation Functions. *6th International Conference on Learning Representations, ICLR 2018-Workshop Track Proceedings*. Available from: <http://arxiv.org/abs/1710.05941> [Last accessed on 2021 Jun 11].
- Ramcharan, A., Baranowski, K., McCloskey, P., Ahmed, B., Legg, J. and Hughes, D.P., 2017. Deep learning for image-based cassava disease detection. *Frontiers in Plant Science*, 8, p. 1852.
- Reyes, A.K., Caicedo, J.C. and Camargo, J.E., 2015. *Fine-tuning Deep Convolutional Networks for Plant Recognition*. pp. 467-475. Available from: <https://ceur-ws.org/Vol-1391/121-CR.pdf> [Last accessed on 2021 Jul 05].
- Rice, L., Wong, E. and Kolter, J.Z., 2020. Overfitting in Adversarially Robust Deep Learning. In: *Proceedings of Machine Learning Research*. Available from: <https://github.com> [Last accessed on 2021 Jun 12].
- Saleem, M.H., Khanchi, S., Potgieter, P. and Arif, K.M., 2020. Image-based plant disease identification by deep learning meta-architectures. *Plants*, 9(11), pp. 1451.
- Saufi, M.M., Zamanhuri, M.A., Mohammad, N. and Ibrahim, Z., 2018. Deep learning for roman handwritten character recognition. *Indonesian Journal of Electrical Engineering and Computer Science*, 12(2), pp. 455-460.
- Shruthi, U., Nagaveni, V. and Raghavendra, B.K., 2019. A Review on Machine Learning Classification Techniques for Plant Disease Detection. In: *2019 5th International Conference on Advanced Computing and Communication Systems, ICACCS 2019*. Institute of Electrical and Electronics Engineers Inc., United States, pp. 281-284.
- Sladojevic, S., Arsenovic, M., Anderla, A., Culibrk, D. and Stefanovic, D., 2016. Deep neural networks based recognition of plant diseases by leaf image classification. *Computational Intelligence and Neuroscience*, 2016, p. 3289801.
- Srivastava, N., Hinton, G., Krizhevsky, A., Sutskever, I. and Salakhutdinov, R., 2014. Dropout: A simple way to prevent neural networks from overfitting. *Journal of Machine Learning Research*, 15, pp. 1929-1958.
- Sun, G., Jia, X. and Geng, T., 2018. Plant diseases recognition based on image processing technology. *Journal of Electrical and Computer Engineering*, 2018, p. 6070129.
- Uddin, M.P., Mamun, M.A. and Hossain, M.A., 2020. 'PCA-based feature reduction for hyperspectral remote sensing image classification. In: *IETE Technical Review (Institution of Electronics and Telecommunication Engineers, India)*. Taylor and Francis Ltd., United Kingdom.
- Victoria, A.H. and Maragatham, G., 2021. Automatic tuning of hyperparameters using Bayesian optimization. *Evolving Systems*, 12(1), pp. 217-223.
- Zbakh, A., Mdaghri, Z.A., Benyoussef, A., Kenz, A. El and Yadari, M. El, et al. 2019. Spectral classification of a set of hyperspectral images using the convolutional neural network, in a single training. *International Journal of Advanced Computer Science and Applications IJACSA*. Vol. 10, No. 6, Available from: <https://hal.science/hal-02172017> [Last accessed on 2023 Jan 29]

Effects of Crude Plant Extracts from Five Parts of *Melia azedarach* on *Tribolium confusum*

Muzafar K. Omar, Hanaa A. Muhammad, and Sawan M. Mirkhan

Department of Biology, Faculty of Science and Health, Koya University,
Danielle Mitterrand Boulevard, Koya KOY45, Kurdistan Region – F.R. Iraq

Abstract—*Tribolium confusum* is one of the most common pests of many commodities, especially cereals and their products. These pests are known for being the most destructive insect pests attacking and infesting stored flour and grain in soil, warehouses, grocery stores, and homes. Therefore, this study aims to control these pests with an environmentally friendly, healthier, and cost-effective pesticide instead of the common artificial chemicals to practice the current management of cereal storage pest control in the Kurdistan Region of Iraq. For this to be achieved, the toxicity effect of crude plant extracts from five different parts of *Melia azedarach* in tap water with concentrations of 50%, 60%, 70%, 80%, and 90% at different times (2, 4, 6, 8, and 10 h) against stored-product insect was tested. The toxicity effect of these extracts varied based on the crude plant part extracts, concentrations, and exposure period according to the SAS system investigation on the mortality rate of *T. confusum* adults (Duncan test). The extracts' compatibility with treated adults of *T. confusum* in the clear petri dish was noted. Besides, the number of dead adults was measured by loss of motion.

Index Terms—Crude plant extract, *Melia azedarach*, *Tribolium confusum*, Mortality.

I. INTRODUCTION

The quantitative and qualitative agricultural saved yields are important sources of world food. They are getting lost by the attack of more than 600 species of beetle pests (Rajendran, 2002; Kostyukovsky and Trostanetsky, 2006; Meena, Suhag and Prates, 2006; Stejskal, et al., 2015). Confused flour beetle Species (*Tribolium confusum*), Family: Tenebrionidae, and Order: Coleoptera is one of the most common beetles that have a crucial impact on different types of stored cereal (Soomro and Sultana, 2018; and Gharsan, et al., 2018). Since different types of control for insect contamination are a major problem in food commodities of food industries (Isman, 2006), many different materials are tested on protecting cereal yields against insect pests in storage (Adler, Ojimeelukwe

and Tapondjou, 2000; Weaver and Subramanyam, 2000; Isman, 2006).

Chemical materials are commonly used as pesticides in crop protection, which cause environmental pollutants and have undesirable effects on animals and human beings. Thus, bioinsecticides have been used as various strategies for controlling insect pests in recent years (Khambay, et al., 2002; Hashim and Devi, 2003; and Nathan, et al., 2005).

The method of insect control with plant extracts has a great impact on insects, including ovicidal, repellent, antifeedant, sterilization, and toxic effects in insects, for instance, the toxicity may happen through contact, and ingestion, or through fumigant action (Isman, 2006). The extract compounds from some chemotypes of the common Name: Bead Tree, Kurdish Name: Zehre Masi, Species: *Melia azedarach*, Family: Meliaceae, and Order: Sapindales have been reported to be toxic to insects (Kanver, Rao and Batra, A., 2014).

The present study aimed to test the natural plant extract of *M. azedarach* in different concentrations and times against the severe crop-product pest (*T. confusum*).

II. MATERIALS AND METHODS

A. Plant Extract

First, fresh plant parts of *M. azedarach*, such as a premature leaf, mature leaf, flower, pre-mature fruit, and mature fruit were collected from Koya town. Then, plant parts are washed with water, dark-shade dried, and grind to powder using an electric blender. Followed by, about 20 g of each plant part's powder being soaked in 100ml of tap water in different glass bottles. After 1 day, the solutions were filtered using filter paper and stored in a glass container in a refrigerator (4°C) (Negahban, Moharrampour and Sefidkon, 2007). Finally, plant part extracts were tested to determine the mortality percentage of *T. confusum* adults.

B. Insect Collection

Two to three weeks old adults of confused flour beetle (*T. confusum*) were collected and separated from the contaminated flour and rice (Mohamed, Zaitoun and Singer, 2013). The insect was reared in a hot place approximately at 30°C before the test.

ARO-The Scientific Journal of Koya University
Vol. XI, No. 1 (2023), Article ID: ARO.11038. 4 pages
DOI: 10.14500/aro.11038

Received: 20 July 2022; Accepted: 28 January 2023
Regular research paper: Published: 10 February 2023

Corresponding author's e-mail: hanaa.muhammad@koyauniversity.org
Copyright © 2023 Muzafar K. Omar, Hanaa A. Muhammad,
Sawan M. Mirkhan. This is an open access article distributed under
the Creative Commons Attribution License.



C. Mortality Test

The extracted parts of the plant were used to test the adult mortality rate of *T. confusum*. The extracts were mixed with tap water to make different concentrations (50%, 60%, 70%, 80%, and 90%). The filter paper was placed inside the petri dish (6 cm diameter) and then 10 adults of the insect were released into each petri dish. After that, they were sprayed with each concentration from each part of the plant until the insect body was rushed. The same number of insects was treated with tap water and used as a control in the test. Four replications were done for each concentration and control in each part of the plant (Sahaf, Moharramipour and Meshkatalasadat, 2008). The adult confused flour beetle mortality was recorded at 2, 4, 6, 8, and 10 h after the treatment. The number of insect mortality was measured using direct observation with naked eyes, and when the insect has no motion, the insect was considered dead (Muhammad, 2008).

III. RESULTS AND DISCUSSION

This study was conducted to determine the insecticidal activity of chemical materials in the crude plant part extracts of *M. azedarach*, they were used on the adult of *T. confusum*. The different rates of insect mortality were caused by the

impact of different crude plant part extracts of *M. azedarach* regarding different concentrations and times.

The relation between five crud plant extracts (A) of *M. azedarach*, which was prepared into five different concentrations with control (B) at five different periods of exposure (C) on the adult of Confused Flour Beetle (*T. confusum*) is presented in Table I. The efficiency of crude plant extract of the pre-mature leaf was tested against concentrations of 50% and 60%. The concentration of 50% for mature leaf crude plant extracts showed the lowest effect on the mortality rate of *T. confusum* adult after 2 h, which was about 0.00%. However, the highest mortality rate at the same period of exposure was raised to 40% for mature fruit crude plant extract at 90% concentration. After 4 h treatments, the value of minimum mortality rate was recorded, which was 2.50% against 50%, 60%, and 70% concentration for the immature leaf crude plant extract determined for confused flour beetle adult and the loftiest mortality rate was 77.50% at a concentration of 90% was found for crude plant extract of the mature fruit. The minimum toxicity effects of mortality rate for the crude plant part extracts against *T. confusum* were about 2.50% after 6 h at concentrations of 50% and 60%. However, the maximum mortality rate was escalated to 92.00% after 6 h treatments

TABLE I
ILLUSTRATE THE INTERACTIONS BETWEEN CRUDE PLANT PART EXTRACTS (A), CRUDE PLANT PART EXTRACT CONCENTRATE (B) AND MEAN MORTALITY % OF ADULT TRIBOLIUM CONFUSUM AT DIFFERENT EXPOSURE PERIODS (H) (C)

Crude plant part extract (A)	The concentration of plant part extract (B)	Mean mortality % of adult <i>Tribolium confusum</i> at different exposure periods (h) (C)					
		(2) h	(4) h	(6) h	(8) h	(10) h	p value
Pre-mature leaf	C	0.00±0.00	0.00±0.00	0.00±0.00	0.00±0.00	0.00±0.00	non
	50	0.00±0.00	0.00±0.00	2.50±2.50	2.50±2.50	2.50±2.50	0.7362
	60	0.00±0.00	2.50±2.50	5.00±2.88	5.00±2.88	7.50±2.50	0.2837
	70	5.00±2.88	5.00±2.88	5.00±2.88	10.00±2.88	20.00±4.08	0.0092
	80	12.50±2.50	15.00±2.88	20.00±4.08	25.00±2.88	35.00±2.88	0.0009
	90	15.00±2.88	17.50±4.78	30.00±4.08	37.50±4.78	52.50±4.78	0.0001
Mature leaf	C	0.00±0.00	0.00±0.00	2.50±2.50	2.50±2.50	5.00±2.88	0.4146
	50	0.00±0.00	5.00±2.88	5.00±2.88	10.00±4.08	10.00±4.08	0.1916
	60	5.00±2.88	7.50±2.50	15.00±2.88	15.00±2.88	17.50±2.50	0.0226
	70	7.50±2.50	12.50±2.50	15.00±2.88	17.50±2.50	27.50±2.50	0.001
	80	17.50±2.50	27.50±2.50	32.50±2.50	37.50±2.50	47.50±6.29	0.0014
	90	20.00±4.08	35.00±6.45	42.50±4.78	52.50±2.50	62.50±4.78	0.0001
Flower	C	2.50±2.50	2.50±2.50	2.50±2.50	5.00±2.88	5.00±2.88	0.8961
	50	15.00±5.00	17.50±2.50	22.50±4.78	22.50±4.78	22.50±4.78	0.6519
	60	15.00±5.00	17.50±2.50	22.50±4.78	22.50±4.78	22.50±4.78	0.6519
	70	22.50±2.50	37.50±4.78	45.00±5.00	47.50±6.29	52.50±4.78	0.0084
	80	40.00±4.08	57.50±4.78	65.00±5.00	72.50±4.78	72.50±4.78	0.001
	90	45.00±2.88	67.50±2.50	77.50±6.29	77.50±6.29	77.50±6.29	0.0016
Pre-mature fruit	C	0.00±0.00	2.50±2.50	2.50±2.50	2.50±2.50	2.50±2.50	0.9052
	50	10.00±4.08	20.00±7.07	27.50±10.30	37.50±8.53	42.50±6.29	0.0522
	60	15.00±2.88	20.00±4.08	27.50±4.78	35.00±6.29	37.50±6.29	0.0313
	70	12.50±4.78	30.00±7.07	32.50±8.53	45.00±6.45	45.00±6.45	0.0227
	80	27.50±2.50	35.00±2.88	47.50±4.78	50.00±7.07	55.00±6.45	0.0091
	90	35.00±6.45	47.50±2.50	55.00±2.88	65.00±2.88	75.00±6.45	0.0002
Mature fruit	C	2.50±2.50	2.50±2.50	2.50±2.50	2.50±2.50	5.00±2.88	0.9413
	50	10.00±4.08	22.50±4.78	32.50±4.78	37.50±2.50	40.00±4.08	0.0007
	60	12.50±4.78	27.50±2.50	40.00±4.08	50.00±4.08	55.00±6.45	0.0001
	70	32.50±7.50	47.50±7.50	50.00±5.77	60.00±5.77	62.50±4.78	0.0326
	80	42.50±4.78	57.50±2.50	70.00±8.16	77.50±6.29	82.50±4.78	0.001
	90	60.00±4.08	77.50±4.78	97.50±2.50	100	100	0.00

with 90% concentrations for mature fruit crude plant extract against the adult of *T. confusum*. The mortality of adult insects that were affected by *M. azedarach* crude plant extract of pre-mature leaf was recorded at the lowest rate of about 5.00% after 8 h at concentrations of 50% and 60%. On the other hand, at the same time, the highest mortality rate was elevated to 100% at 90% concentration for mature fruit crude plant extracts. Finally, after 10 h of treatment, the lowest mortality rate was 5.00% with 50% concentration against the adult of *T. confusum* which was fixed for pre-mature leaf crude plant extract, while the highest mortality rate of 100% after 10 h was found at 90% concentrations of mature fruit crude plant extract of *M. azedarach*. This study investigated the activity of the crude plant extract of the fruit of the Argentinian *M. azedarach* L. (Meliaceae). The use of these plant extracts as a pesticide has an effective potential impact on pest control programs (Mariäa, et al., 2003). The obtained data from the Crude plant extract of *M. azedarach* fruit contributes to a better understanding of the toxicity action as a bio-insecticide (Al-Mehmadi and Al-Khalaf, 2010).

Overall, the results from this investigation indicate that the mature fruit crude plant extract was able to induce more than three-fourths mortality at 4 h, and reached its maximum value of 100 at 8 h of treatment. The results for the other crude plant part extracts against the adult of *T. confusum* show encouraging results that agree with the study that was done by Ali and Mohammed in 2013, who showed that the effect of the extracts as a pesticide was raised with the exposure time with increasing concentration. Besides, it was established that there were mortality rates in all concentrations and times for extracts of five crude plant part extracts of *M. azedarach* on the adult of *T. confusum* compare to the controls. Sensitive species of Coleoptera seem to be affected particularly by this crude plant extract to a point that in many cases toxicity defunct values are as high as 90–100% (Mariäa, et al., 2003).

IV. CONCLUSION

Using this natural fast-acting insecticide, we may have a sustainable strategy for improving the insecticide's ability to control *T. confusum* adults as it is cost-effective, and environmentally friendly to human beings and the rest of the ecosystem. Notably, the most active part of the *M. azedarach* plant was the mature fruit crude plant part extracted from the procured mortality data; hence, *T. confusum* can be controlled using this method.

From the results, the effectiveness of crude plant extracts from the five plant parts of *M. azedarach* as an insecticide, the following can be concluded:

1. The crude plant extracts can be used to control the adults of *T. confusum*, especially the mature fruit of the plant.
2. Reducing the environmental impact which otherwise could be caused by dangerous artificial pesticides.
3. This fast-acting insecticide is cost-effective.

REFERENCES

- Adler, C., Ojimekwe, P. and Taponjju, A.L., 2000. Utilisation of phytochemicals against stored product insects. In: Adler, C., Schoeller, M. Eds. In: *Proceedings of the Meeting of the OILB Working Group "Integrated Protection in Stored Products"*. vol. 23. IOBC/WPRS Bulletin, Berlin, Germany, pp. 169-175.
- Ali, W.K. and Mohammed, H.H., 2013. Toxic effect of some plant extracts on the mortality of flour beetle *Tribolium confusum* (duval) (Coleoptera: Tenebrionidae). *Entomology, Ornithology Herpetology*, 2, p.1000115.
- Al-Mehmadi, R.M. and Al-Khalaf, A.A., 2010. Larvicidal and histological effects of *Melia azedarach* extract on *Culex quinquefasciatus* say. Larvae (Diptera: Culicidae). *Journal of King Saud University Science*, 22, pp.77-85.
- Carpinella, C.C., Defago, M.T., Valladares, G. and Palacios, S.M., 2003. Antifeedant and insecticide properties of a limonoid from *Melia azedarach* (Meliaceae) with potential use for pest management. *Journal of Agriculture and Food Chemistry*, 51, pp.369-374.
- Gharsan, F., Jubara, N., Alghamdi, L., Almakady, Z. and Basndwh, E., 2018. Toxicity of five plant oils to adult *Tribolium castaneum* (Coleoptera: Tenebrionidae) and *Oryzaephilus surinamensis* (Coleoptera: Silvanidae). *Florida Entomologist*, 101, pp.592-596.
- Hashim, M.S. and Devi, K.S., 2003. Insecticidal action of the polyphenolic rich fractions from the stem bark of *Streblus asper* on *Dysdercus cingulatus*. *Fitoterapia*, 74, pp.670-676.
- Isman, M.B., 2006. Botanical insecticides, deterrents, and repellents in modern agriculture and an increasingly regulated world. *Annual Review of Entomology*, 51, pp.45-66.
- Kanver, S.K., Rao, D.V. and Amla, B., 2014. Phyto-morphological overview of medicinal plant: *Melia azedarach* Linn. *Journal of Functional and Environmental Botany*, 4(1), pp.10-21.
- Khambay, B.P., Beddie, D.G. and Simmonds, M.S., 2002. An insecticidal mixture of tetramethylcyclohexenedione isomers from *Kunzea ambigua* and *Kunzea baxterii*. *Phytochemistry*, 59, pp.69-71.
- Kostyukovsky, M. and Trostanetsky, A., 2006. The effect of a new chitin synthesis inhibitor, novaluron, on various developmental stages of *Tribolium castaneum* (Herbst). *Journal of Stored Products Research*, 42, pp.136-148.
- Meena, R., Suhag, P. and Prates, H.T., 2006. Evaluation of ethanolic extract of *Baccharis genistelloides* against stored grain pests. *Journal of Stored Products Research*, 34, pp.243-249.
- Mohamed, H.M., Zaitoun, A.A. and Singer, F.A., 2013. Repellent and toxicity of crude plant extracts on saw-toothed grain beetle (*Oryzaephilus surinamensis*) (L.). *Journal of Food Agriculture and Environment*, 11, pp.381-384.
- Muhammad, H.H., 2008. Toxicity effect of four plants extracts against the oak leaf cut worm *Euproctis melania* staud. (*Lymantriidae: Lepidoptera*) Zanko. *Zanco Journal of Pure and Applied Sciences*, 20, pp.83-88.
- Nathan, S.S., Kalaivani, K., Murugan, K. and Chung, P.G., 2005. The toxicity and physiological effect of neem limonoids on *Cnaphalocrocis medinalis* (Guene'e), the rice leafhopper. *Pesticide Biochemistry and Physiology*, 81, pp.113-122.
- Negahban, M., Moharrampour, S. and Sefidkon, F., 2007. Fumigant toxicity of essential oil from *Artemisia sieberi* Besser against three stored-product insects. *Journal of Stored Products Research*, 43(2), pp.123-128.
- Rajendran, S., 2002. Postharvest pest losses. In: Pimentel, D., Ed. *Encyclopedia of Pest Management*. Marcel Dekker, Inc., New York. pp.654-656.
- Sahaf, B.Z., Moharrampour, S. and Meshkatsadat, M.H., 2008. Fumigant toxicity of essential oil from *Vitex pseudo-negundo* against *Tribolium castaneum* (Herbst) and *Sitophilus oryzae* (L.). *Journal of Asia Pacific Entomology*, 11, pp.175-179.
- Soomro, F.D. and Sultana, R., 2018. Incidence of darkling beetles (Coleoptera: Tenebrionidae) from lower Sindh Tando Jam Hyderabad. *Journal of Entomology*

and Zoology Studies, 6, 2560-2562.

Stejskal, V., Hubert, J., Aulicky, R. and Kucerova, Z., 2015. Overview of present and past and pest-associated risks in stored food and feed products: European perspective. *Journal of Stored Products Research*, 64(Part B),

pp.122-132.

Weaver, D.K. and Subramanyam, B., 2000. Botanicals. In: Subramanyam, B. and Hagstrum, D.W. Eds. *Alternatives to Pesticides in Stored-product IPM*. Kluwer Academic Publishers, Massachusetts, United States of America. pp.303-320.

Effect of Hot Glue Additive on the Rheological Properties of Asphalt Cement and Mixtures Performance

Sheelan A. Ahmed

Department of Civil Engineering, Koya University
Daniel Mitterrand Boulevard, Koya KOY45 AB64, Kurdistan Region – Iraq

Abstract—In general, the physical and rheological properties of asphalt binder are directly affecting the resistance of asphalt mix to the permanent deformation (rutting), water damage, and thermal cracking. The degradation in these properties leads to severe distresses that appear in the pavement and, consequently, make the repair and maintenance very expensive. Since the modified-asphalt cement may help to minimize such aforementioned distresses, this research is established for this purpose. It aims to investigate the physical and rheological properties of modified-asphalt cement with silicone, dense silicone rubber, and ethylene propylene diene monomer rubber. Five contents for each type of hot glue are investigated; 0.4, 0.8, 1.2, 1.6, and 2% of the asphalt cement weight. Conventional asphalt cement tests such as penetration, softening point, dynamic viscosity, and ductility tests are conducted to evaluate the hot glue-modified asphalt cement properties. Moreover, the Marshall and indirect tensile strength tests are conducted to examine the effect of hot glue on the performance of the asphalt mixtures at concentrations of 0.8 and 1.6% of the asphalt cement weight. The results show that the hot glue-modified asphalt cement leads to an increase in the hardness and consistency, and a reduction in the temperature susceptibility of asphalt cement. These features lead to better Marshall stability and tensile strength ratio, as compared with the standard asphalt cement mixture.

Index Terms—Hot glue, Silicone, Dense silicone rubber, Ethylene propylene diene monomer rubber, Modified asphalt cement, Indirect tensile strength, Marshall Stiffness.

I. INTRODUCTION

In Iraq, the asphalt pavement has significant distress due to both climatic conditions and the growing traffic volume of heavy trucks; accumulation of these factors with inadequate maintenance has caused distresses on pavement surface in recent years. Due to this, it is essential to modify asphalt

cement with materials that can help achieve the best performance of the asphalt to improve its qualities.

Lewandowski (1994) summarized the main reasons that led to the modification of asphalt cement with various types of additives that play a role in obtaining softer mixtures to resist cracking at low temperatures or stiffer blends to reduce rutting at high temperatures or to improve the fatigue resistance of mixtures or to increase the stability and strength of mixtures. According to King and King (1986), the selection of an asphalt cement modifier for a given project may be influenced by various other factors such as cost, availability, expected performance, and workability.

Fernando and Guirguis (1983) found that rubber is a great organic polymer for blending with asphalt cement to modify the type of road binder due to its inherently chemical components. The resulting binder has improved durability, distortion resistance, flexibility at low temperatures, and viscosity at high temperatures. On the other hand, Tayebali, et al. (1992) concluded that using reclaimed rubber obtained from used tires, polyethylene in the form of low density (LDPE) for asphalt cement modification performed satisfactorily. Similarly, Khodary Moalla Hamed (2010) investigated how scrap tires (Crumb rubber) affected the rheological characteristics and fatigue resistance of asphalt mixtures, comparing them to commercial polymers such as styrene-butadiene-styrene (SBS). The outcomes show a significant enhancement in the fatigue behavior of all used modifier types compared to conventional mixtures.

Kumar, Choudhary and Kumar (2019) researched the use of ethylene-propylene-diene-monomer (EPDM) rubber waste from scrapped automotive rubber parts other than tires to modify asphalt binder. The results showed that EPDM-modified binders perform better than the control (unmodified) binders in terms of rutting, fatigue, and cracking. In addition, the results of the mix performance displayed that mixtures with modified EPDM binders have enhanced stiffness, stability, and resistance to moisture damage. Al-Ani (2009) experimentally investigated rubber silicones' asphalt mixture performance. Rubber-silicone was added to asphalt cement in four different percentages (1%, 2%, 3%, and 5%). The findings indicated that Rubber-Silicone has great effects on the performance of asphalt mixture by increasing the Marshall stability and the

ARO-The Scientific Journal of Koya University
Vol. XI, No. 1 (2023), Article ID: ARO.11055. 8 pages
DOI: 10.14500/aro.11055

Received: 26 August 2022; Accepted: 02 February 2023
Regular research paper: Published: 20 February 2023

Corresponding author's e-mail: sheelan.abdulwahid@koyauniversity.org

Copyright © 2023 Sheelan A. Ahmed. This is an open access article distributed under the Creative Commons Attribution License.



flexibility properties of the mix, which appears by reducing the permanent deformation by about (30–70) %.

Zhang, Yu, and Wu (2010) verified that using the polymer to enhance the asphalt binder can reduce temperature susceptibility, permanent deformation (rutting), and fatigue cracking. However, the viscosity and stiffness of the asphalt mixture are increased by adding the polymer, which lowers its workability.

II. EXPERIMENTAL PROGRAM

A. Materials Characterization

The materials used in this study are locally available and currently used in road construction in Iraq.

Asphalt cement

One type of asphalt cement with a penetration grade of (40–50) was used in this study, brought from the Hal band oil refinery in northern Iraq. The qualities of asphalt must meet the parameters laid out in the Iraqi specifications. To find out the penetration, ductility, specific gravity, softening point, Flash point, and Fire point, tests were carried out. The physical properties of the asphalt samples are given in Table I.

Hot melt glue sticks

Silicones are renowned for their retention of flexibility and low compression set characteristics within one of the elastomers' widest working temperature ranges. Three different types of hot glue sticks were used in this study.

A silicone rubber rod is a round bar that made of solid silicone rubber, see the Fig.1. The red glue sticks are used to provide high levels of compressibility across a broad temperature range, have a non-stick, watertight surface, and perform well against weathering. The advantages of silicone rubber rods are unmatched by the other types of rubber. Silicone rubbers have great heat and cold resistance, fine electrical characteristics, strong chemical stability, and flame retardancy. The properties of the silicone rubber rod are given in Table II (adopted from Alibaba.com).

The black glue sticks are used for all types of weather. EPDM cords shown in the Fig.2 are highly popular due to their suitability for use in a wide variety of applications and working environments. Due to their versatility for usage in a wide range of applications and working situations, EPDM cords are very common largely due to the material's ability to combine mechanical strength with resistance, and it is widely known for its excellent resistance to weathering. This enables the EPDM solid rubber cord to deliver constant performance in both indoor and exterior applications. In addition, the tensile strength, tear resistance, and flexibility of EPDM cables are well-balanced, guaranteeing that the cord is durable and easy to use. The properties of the EPDM cords are given in Table III (adopted from the rubber company).

Transparent hot glue sticks as shown in the Fig.3 work with heat guns. It is perfect for gluing wood, paper, pottery, fabric, and other items. It dries instantly, providing a strong binding between the components. The properties of the transparent sticks are given in Table IV (adopted from Polymax Group).

TABLE I
PHYSICAL PROPERTIES OF ASPHALT CEMENT

Properties	Unit	ASTM	Test results
Penetration at (25°C, 100 g, 5 s)	0.1 mm	D5	45
Specific gravity at 25° C	-	D70	1.02
Softening point (ring and ball)	°C	D36	56.4
Ductility (25°C, 5 cm/min)	Cm	D113	138
Flash point	°C	D92	270
Fire point	°C	D92	318

TABLE II
RED HOT GLUE STICKS PROPERTIES

Properties	Test results	Unit
Material	Dense Silicone Rubber Material	
Standard hardness	60±5	Shore A
Viscosity	9500 @ 193°C	Centipoises
Minimum temperature	-40	°C
Maximum temperature	+220	°C
Softening point	81	°C
Working time	70	S

TABLE III
BLACK HOT GLUE STICKS PROPERTIES

Properties	Test results	Unit
Material	Ethylene Propylene Diene Monomer Rubber	
Standard hardness	70±5	Shore A
Viscosity	12000 @ 193°C	Centipoises
Minimum temperature	-30	°C
Maximum temperature	+150	°C
Softening point	85	°C
Working time	40	S

TABLE IV
TRANSPARENT HOT GLUE STICKS PROPERTIES

Properties	Test results	Unit
Material	Silicone (VMQ)	
Standard hardness	60±5	Shore A
Viscosity	6000 @ 193°C	Centipoises
Minimum temperature	-60	°C
Maximum temperature	+230	°C
Softening point	88	°C
Working time	15	S

Aggregates

This study used the 12.5 mm maximum size dense gradation in the hot asphalt concrete wearing course mix based on the State Corporation of Roads and Bridges specifications (SORB, 2007). The coarse and fine aggregate utilized in this investigation was brought from the Darbande Zeoi quarry near Sulaymaniyah and mechanically crushed at Tanjero hot mix asphalt plant. The specification limits and selected gradation of manufactured asphalt mixtures are shown in Table V. An ordinary Portland cement with a specific gravity of (3.15) was used as a mineral filler.

B. Laboratory Specimen Preparation and Test Methods

Penetration test

The penetration test is the method used most frequently worldwide to categorize asphalt cement. The test includes

TABLE V
SELECTED COMBINED GRADATION OF AGGREGATE AND FILLER ACCORDING TO
SORB SPECIFICATIONS

Sieve size	Specification range	Selected gradation
1/2"	100	100
3/8"	90–100	95
No. 4	55–85	70
No. 8	32–67	50
No. 50	7–23	15
No. 200	4–10	7

measuring the vertical penetration of a standard steel needle into a bitumen sample at 25°C temperature to determine the consistency of the bitumen. 100 g of needle weight is loaded over 5 s. The needle penetration depth in the bitumen sample is 0.1 mm; therefore, the penetration unit is 0.1 mm. The penetration is a numerical representation of the bitumen's reaction to temperature changes. ASTM D5 explains how to conduct the test.

Softening point test

The asphalt cement softening point provides a measure of its thermal stability. The asphalt cement softening point is evaluated using the ring and ball method. The softening point determines the temperature at which the asphalt cement starts to flow and becomes soft enough to no longer support the weight of a metal ball. The rings and assembly are submerged to a depth of 105 ± 3 mm in a water bath, each specimen is centered on a 9.5 mm steel ball bearing weighing 3.50 ± 0.05 g, and the temperature is raised at a rate of $5 \pm 0.5^\circ\text{C}/\text{min}$. The average of two temperatures at which the two balls fall and touch the base plate is recorded as the softening point. The test procedure is described in ASTM D36.

Ductility test

The asphalt cement ductility test is one of the most important tests that must be performed when constructing the road. A material's ductility refers to its ability for plastic deformation (permanent deformation) before material rupture. When two ends of a briquet specimen of the material are pulled apart at a speed of $5 \text{ cm}/\text{min} \pm 0.5$ and at a temperature of $25 \pm 0.5^\circ\text{C}$, the ductility of asphalt cement is determined by the length in centimeters (cm) to which the asphalt cement sample will stretch before breaking. The test procedure is described in ASTM D113.

Dynamic viscosity test

The viscosity test of the asphalt cement sample is one of the crucial tests on asphalt cement to be conducted before road construction. Viscosity measures the degree of fluidity of the asphalt cement sample to ensure the quality of the asphalt cement used as a binder by giving a measure of fluidity at a particular temperature. The ASTM D2171 test method describes the steps for using capillary viscometers under vacuum at 60°C to measure the dynamic viscosity of asphalt cement.

Flash and fire point test

To determine the safe mixing and application temperature ranges for a specific asphalt cement grade, the flash and fire point test is applied to asphalt cement. Using the Pensky-



Fig. 1. Red hot glue sticks.

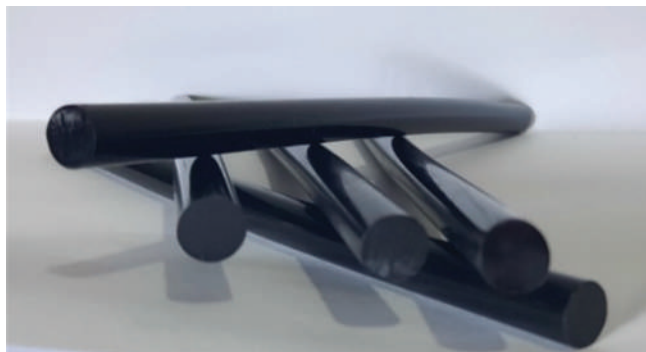


Fig. 2. Black hot glue sticks.



Fig. 3. Transparent hot glue sticks.

Martens closed cup tester, the flash and fire point of the asphalt binder were determined. The ideal rate of heating the bitumen should be $5^\circ\text{C}/\text{min}$. When the sample ignites and flashes, note the temperature at that time, which is the bitumen's Flash point. Then, heat the sample further at the same pace and apply the test flame for every 2°C rise. Note the temperature at this moment, which is the bitumen fire point, when the material catches fire and burns for at least 5 s. The test procedure is described in ASTM D92.

Resistance to plastic flow (Marshall method)

The method covers the measurement of the resistance to plastic flow of cylindrical specimens of bituminous paving mixture loaded on the lateral surface by means of the Marshall apparatus according to (ASTM D1559). The prepared mixture is placed in preheated mold (4 in) (101.6 mm) in diameter by (3 in) (76.2 mm) in height, and compacted with a hammer of 10 lb. (4.536 kg) sliding weight, and a free fall of (18

in) (457.2 mm) on the top and bottom of each specimen. The specimens are then left to cool at room temperature for 24 h. Marshall stability and flow tests are performed on each specimen according to the method described by ASTM D-1559. The cylindrical specimen is placed in a water bath at 60°C for 30–40 min, then compressed on the lateral surface at a rate of 2 in/min (50.8 mm/min) until the maximum load resistance and corresponding flow value is recorded. Three specimens for each combination are prepared and the average results are reported. The bulk specific gravity is determined for each specimen in accordance with ASTM D-2726.

Indirect tensile strength

Indirect tensile testing was performed to evaluate the moisture susceptibility of asphalt mixtures according to AASHTO T283 test procedure. Six specimens of each mix were prepared and divided into two groups. The first group of specimens was placed at 25°C for 2 h to measure the tensile strength at dry conditions. The indirect tensile strength is the maximum tensile stress calculated from the peak load applied at break and the dimensions of the specimen according to the following equation:

$$\sigma_{IDT} = \frac{2000 P_{max}}{2tD} \quad (1)$$

Where σ_{IDT} is indirect tensile strength (kPa), P_{max} is peak load (N), t is specimen thickness (mm), and D is specimen diameter (mm).

The second group of specimens was put in a water bath of 60°C for 24 h before being conditioned in a 25°C of water bath for 2 h. The indirect tensile strength is the maximum tensile stress calculated from the peak load applied at break and the dimensions of the specimen according to the following equation:

$$T.S.R = \frac{\sigma_{IDT-Wet}}{\sigma_{IDT-dry}} \quad (2)$$

Where $\sigma_{IDT-Wet}$ is the indirect tensile strength at wet condition (kPa), and $\sigma_{IDT-dry}$ is the indirect tensile strength at dry condition (kPa).

C. Testing Methodology

To achieve the objectives of this study, three different types of hot glue sticks were added with five different content (0.4%, 0.8%, 1.2%, 1.6%, and 2.0%) to the asphalt cement, the research methodology has been divided and performed into two stages: first, evaluation of asphalt cement properties with different types and contents of hot glue, and second, evaluation of the mixture performance, such as Marshall stability flow and stiffness of asphalt cement with optimum hot glue content for each type. The research methodology of the present study is presented stepwise in the form of the flowchart, as shown in Fig. 4.

III. RESULTS AND DISCUSSION

A. Evaluation of Asphalt Cement Properties

Three types of hot glues (transparent sticks made from silicone, red sticks made from silicone dense silicone

rubber, and black sticks made from ethylene propylene diene monomer rubber) were added with five different percentages (0.4, 0.8, 1.2, 1.6, and 2.0%) to the asphalt cement. The influence of adding hot glue on the physical properties of asphalt cement samples was instigated. Fig. 5 is representing the relationship between the penetration values and hot glue content. It is observed that a decrease in penetration values with increasing hot glue content, this dramatic decrease was due to the base asphalt cement becoming stiffer with an increase in the hot glue content. Furthermore, it is noted in Fig. 6 that adding hot glue enhances the softening point of asphalt cement.

The ductility of asphalt cement at a temperature of 25°C drops sharply with increased hot glue content, as shown in Fig. 7. This can be attributed to the hot glue reducing the homogeneity of the structure and thereby weakening the ductility of asphalt cement, whereas the dynamic viscosity of the asphalt cement becomes greater with an increase in the hot glue content at test temperature (60°C), as shown in Fig. 8. The increase in viscosity is a result of the hardening

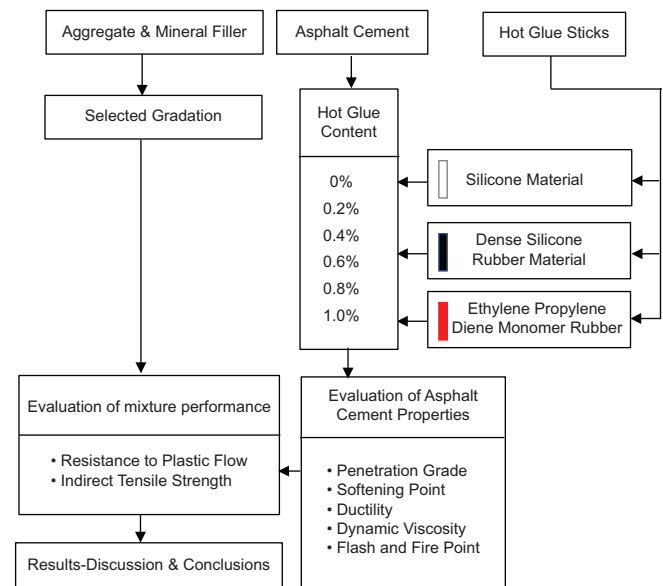


Fig. 4. The flow chart of the study

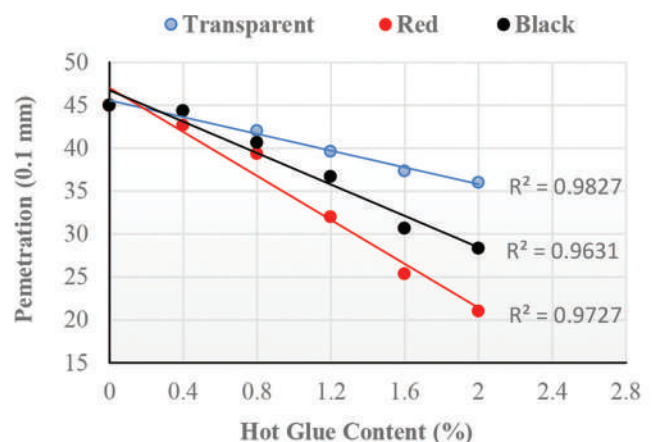


Fig. 5. Effect of hot glue content on penetration of asphalt cement.

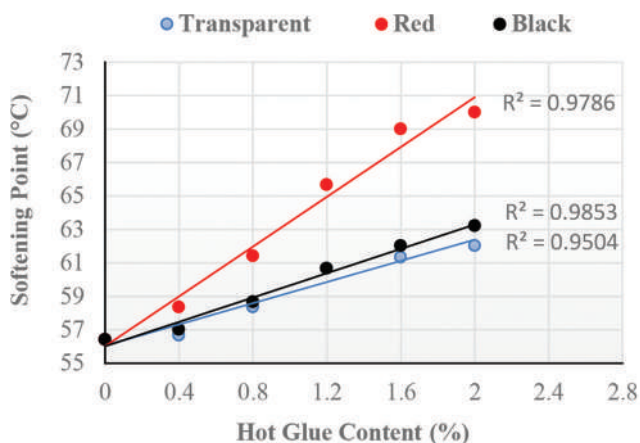


Fig. 6. Effect of hot glue content on softening point of asphalt cement.

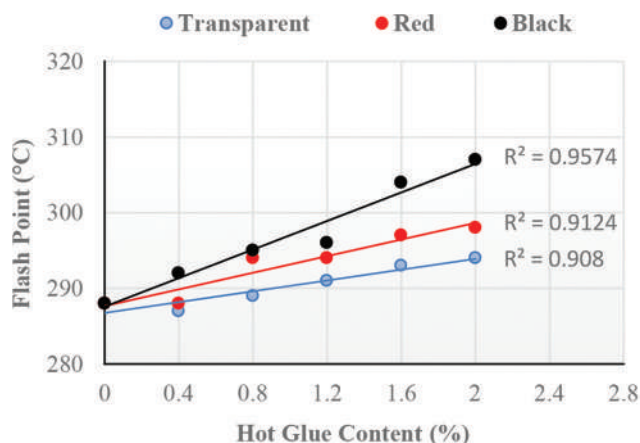


Fig. 9. Effect of hot glue content on flash point of asphalt cement.

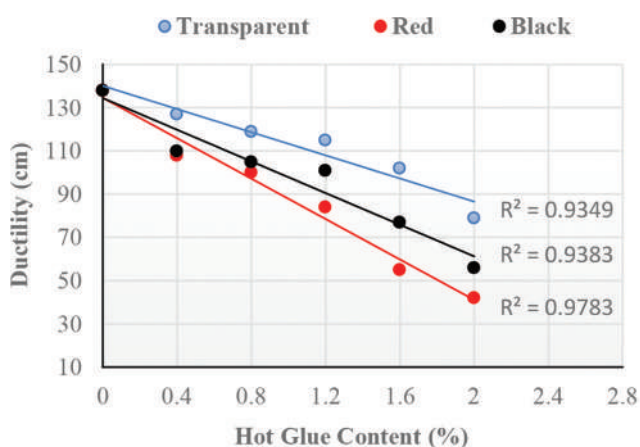


Fig. 7. Effect of hot glue content on ductility of asphalt cement.

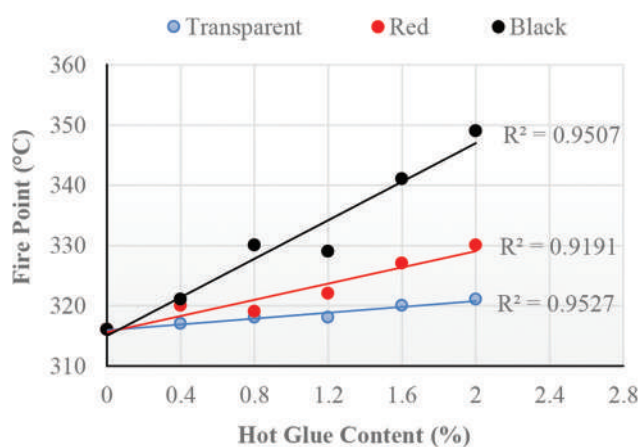


Fig. 10. Effect of hot glue content on fire point of asphalt cement.

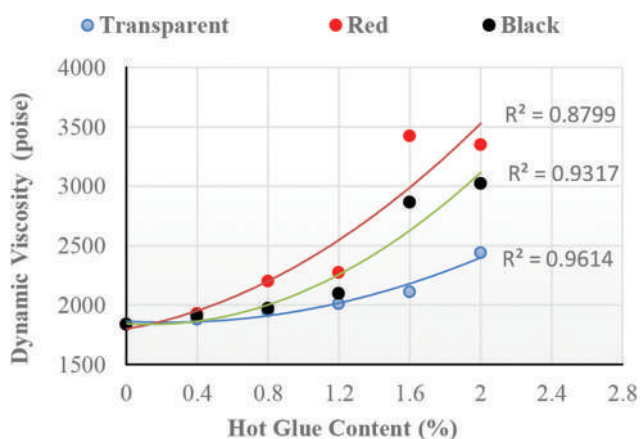


Fig. 8. Effect of hot glue content on dynamic viscosity of asphalt cement.

due to adding the hot glue. The increased viscosity of asphalt cement might be due to the better dispersion of the hot glue in the asphalt cement, which increases the bonding strength by restricting the flow of asphalt and making it harder.

The flash and fire points of asphalt cement samples with various hot glue content are shown in Figs. 9 and 10, respectively. The results showed that when the hot glue content in the asphalt cement increased, the flash, and fire

TABLE VI
MARSH ALL TEST RESULTS

Marshall properties	Units	Asphalt content %				
		4.0	4.5	5.0	5.5	6.0
Marshall stability	KN	8.57	9.857	11.921	12.28	11.479
Marshall flow	mm	2.935	2.988	3.019	3.532	5.882
Bulk density	g/cm ³	2.202	2.290	2.311	2.318	2.280
Air voids	%	5.865	5.681	4.367	3.412	2.012
Marshall stiffness	KN/mm	2.868	3.259	3.822	3.477	1.952

points increased as compared with the conventional samples of the asphalt cement. This is because some of the asphalt cement was replaced by hot glue, indicating that more heat will be needed to release the volatile components in the modified asphalt cement.

B. Evaluation of Mixture Performance

According to the adopted gradation, several specimens were prepared using various percentages of asphalt cement content ranging from (4–6) % at an increment of 0.5% blended with the aggregates and Portland cement filler. The Marshall test has determined the properties of asphalt mixtures such as the Marshall stability, flow value, percentage of air voids, and Marshall Stiffness. The results are represented in Table VI

which showed the optimum asphalt contents equal to 5.2%.

The effect of hot glue on the performance of hot mix asphalt (HMA) was evaluated using the optimum asphalt content mixed with three different types of hot glue sticks (Silicone, Dense silicone rubber, and Ethylene propylene diene monomer rubber) added by two contents (0.8% and

1.6%) of the total weight of the asphalt cement. The results of the Marshall test are shown in Figs. 11-14. According to the results, the performance of the mixtures for all types of hot glue showed improvement in Marshall stability, Marshall flow, and Marshall stiffness, whereas the air voids increased

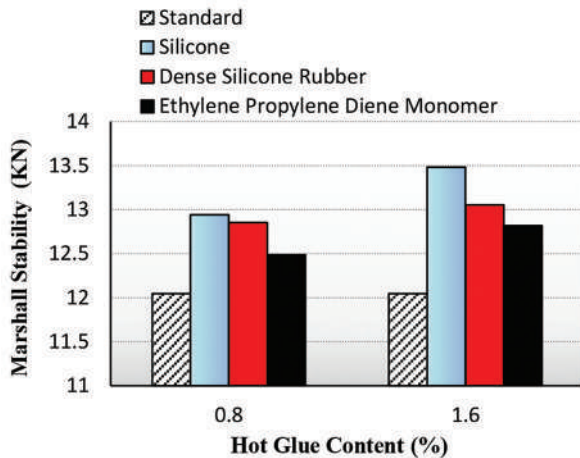


Fig. 11. Effect of hot glue types on Marshall stability of the mixture.

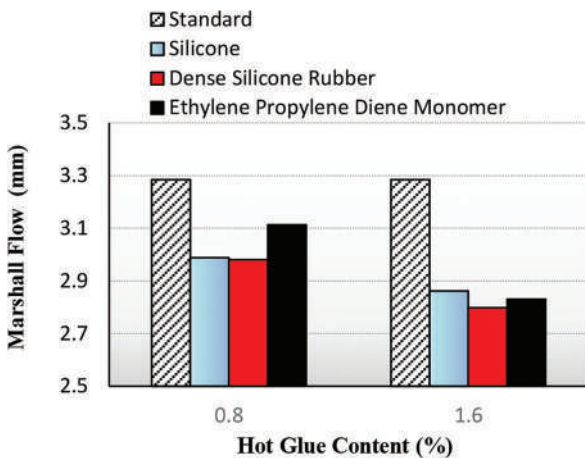


Fig. 12. Effect of hot glue types on Marshall flow of the mixture.

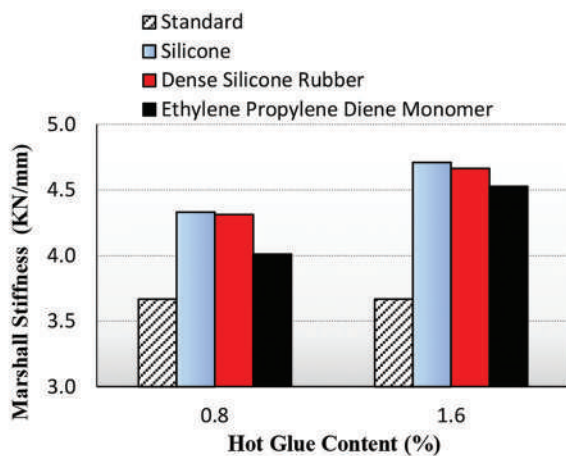


Fig. 13. Effect of hot glue types on Marshall stiffness of the mixture.

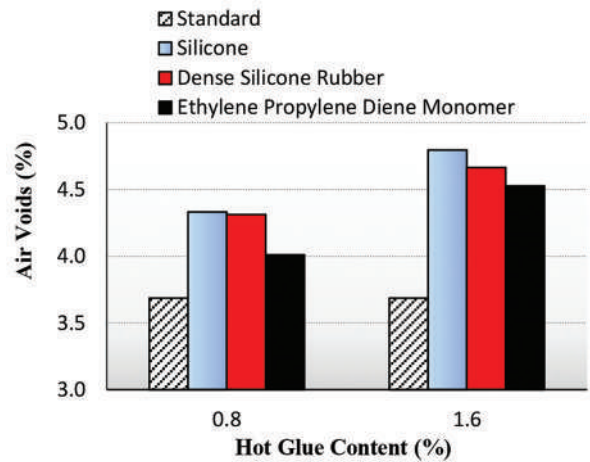


Fig. 14. Effect of hot glue types on air voids of the mixture.

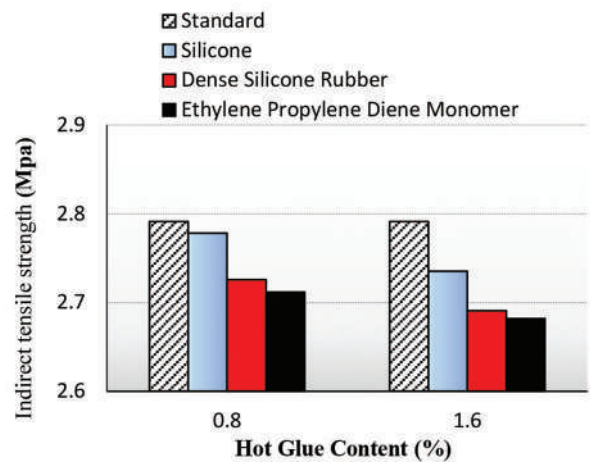


Fig. 15. Effect of hot glue types on indirect tensile strength (unconditioned).

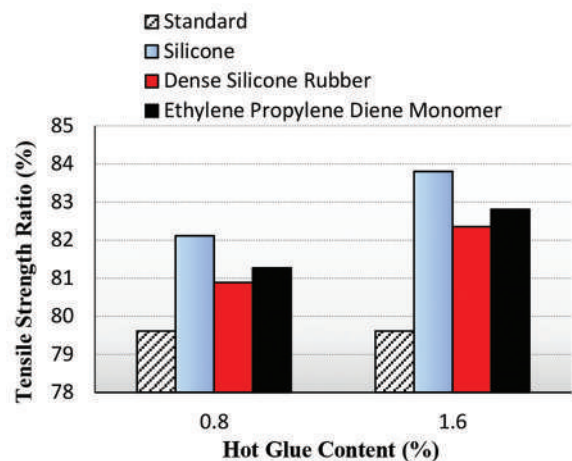


Fig. 16. Effect of hot glue types on tensile strength ratio.

TABLE VII
INDIRECT TENSILE STRENGTH RESULTS FOR DIFFERENT TYPES AND CONTENTS OF HOT GLUE

Hot glue content %	Properties	Standard	Hot glue type		
			Silicone	Dense silicone rubber	Ethylene propylene diene monomer rubber
0.8%	Indirect tensile strength – Unconditioned (MPa)	2.791	2.778	2.726	2.712
	Indirect tensile strength – Conditioned (MPa)	2.222	2.281	2.205	2.204
	Tensile strength ratio (%)	79.61	82.11	80.89	81.27
1.6%	Indirect tensile strength – Unconditioned (MPa)	2.791	2.735	2.691	2.682
	Indirect tensile strength – Conditioned (MPa)	2.222	2.292	2.216	2.221
	Tensile strength ratio (%)	79.61	83.80	82.35	82.81

as compared with the standard mixture. This can be due to an increase in viscosity which resulted from the hardening effect of hot glue. This increase in viscosity reduces softening and bleeding problems for asphalt materials at high temperatures, and also, it helps strengthen adhesion with aggregates and increases the stability of the mixture.

The indirect tensile test results are represented in Figs. 15 and 16. The findings indicated that the addition of the hot glue decreased the tensile behavior of the mixture. This can be attributed to the presence of hot glue resulted in decreasing the ability of modified asphalt cement to stretch. Since the hot glue is typically water-resistant, the mixture's tensile strength ratio improved reasonably compared to the standard mixture. The results of the indirect tensile strength for conditioned and unconditioned cases are shown in Table VII.

IV. CONCLUSIONS

In this study, the evaluation of the asphalt cement was presented according to the conventional physical and rheological properties of asphalt cement by adding hot glue sticks (silicone, dense silicone rubber, and ethylene propylene diene monomer rubber). Test data obtained from the testing program yields the following outcomes:

1. Results of physical properties showed that the addition of silicone, dense silicone rubber, and ethylene propylene diene monomer rubber into asphalt cement led to a decrease in penetration measurements, whereas the flash and softening points increased, implying the improvement of temperature susceptibility and the consistency asphalt cement.
2. The modified asphalt cement with dense silicone rubber, ethylene propylene diene monomer rubber up to a percentage of 0.8%, and silicone modified asphalt cement up to a percentage of 1.6%, demonstrated significant high adhesion performance and acceptable ductility values.
3. The addition of hot glue into asphalt cement resulted in a significant increase in dynamic viscosity, indicating an improvement in the stiffness and hardness of the modified asphalt cement.
4. The Marshall stability and Marshall stiffness improved by 12% and 28%, respectively, in asphalt cement modified by 1.6% silicon content, which had the best performance of the asphalt mixture as compared with the other types of hot glue.
5. Even though the indirect tensile strength decreased by adding 0.8% and 1.6% of hot glue into modified mixtures,

the tensile strength ratio was slightly enhanced compared with the standard mixture.

V. RECOMMENDATIONS

1. Further work is required to investigate the effect of chemical compositions of the different types of hot glues on the performance of hot mix asphalt.
2. Additional research is needed to study the effect of hot glue properties on the resistance of the mixture to low-temperature cracking, rutting, and fatigue.

REFERENCES

- AASHTO T283-03., 2016. *Standard Method of Test for Resistance of Compacted Asphalt Mixtures to Moisture-Induced Damage*. AASHTO T283-03, Washington, DC.
- Al-Ani, T.M.A., 2009. Modification of asphalt mixture performance by rubber-silicone additive. *Anbar Journal for Engineering Sciences*, 2(1), pp. 71-81.
- ASTM International., 2003, *Standard Test Method for Resistance to Plastic Flow of Bituminous Mixtures Using Marshall Apparatus: Annual Book of ASTM Standards USA*. ASTM D1559-89, Pennsylvania, United States.
- ASTM International., 2015. *Standard Test Method for Ductility of Bituminous Materials: Annual Book of Standards American Society for Testing and Materials*. ASTM D113, Pennsylvania, United States.
- ASTM International., 2015. *Standard Test Method for Flash and Fire Points by Cleveland Open Cup Tester: Annual Book of Standards American Society for Testing and Materials*. ASTM D92, Pennsylvania, United States.
- ASTM International., 2015. *Standard Test Method for Penetration of Bituminous Materials: Annual Book of Standards American Society for Testing and Materials*. ASTM D5, Pennsylvania, United States.
- ASTM International., 2015. *Standard Test Method for Softening Point of Bitumen (Ring-and-Ball Apparatus): Annual Book of Standards American Society for Testing and Materials*. ASTM D36, Pennsylvania, United States.
- ASTM International., 2018. *Standard Test Method for Viscosity of Asphalts by Vacuum: Annual Book of Standards American Society for Testing and Materials*. ASTM D2171, Pennsylvania, United States.
- Fernando, M.J. and Guirguis, H.R., 1983. *Rubberized Asphalt in Pavement Technology for Hot Climates*. Vol. 3. Association of Asia and Australasia (REAAA), Malaysia. pp. 25-43.
- Khodya Moalla Hamed, F., 2010. *Evaluation of Fatigue Resistance for Modified Asphalt Concrete Mixtures Based on Dissipated Energy Concepts*. Department of Civil Engineering and Geodesy, Technische Universitat Darmstadt, Germany.
- King, G.N. and King, H.W., 1986. *Polymer Modified Asphalts, an Overview*.

American Society of Civil Engineering, Virginia, United States. pp. 240-254.

Kumar, A., Choudhary, R. and Kumar, A., 2019. *Utilization of Waste Ethylene-Propylene-Diene-Monomer (EPDM) Rubber Modified Binder in Asphalt Concrete Mixtures Conference*. In: 5th Conference of the Transportation Research Group of India (CTRG-2019), Bhopal, India.

Lewandowski, L.H., 1994. Polymer Modification of Paving Asphalt Binders. *Rubber Chemistry and Technology*, 67, pp. 435-447.

Alibaba.com. Available from: <https://www.therubbercompany.com/extrusions-profiles/solid-sponge-rubber-cords/epdm-solid-rubber-cord> [Last accessed 2022 Jul 28].

The Rubber Company. Available from: https://www.alibaba.com/product-detail/Rubber-Solid-Rods-High-Temperature%20Resistant_1600069572471.html [Last accessed 2022 Jul 28].

Polymax Group. Available from: <https://www.polymax.co.uk/silicone/silicone-rubber-cord-solid/translucent-silicone-cord> [Last accessed 2022 Jul 28].

State Organization of Road and Bridges (SORB), 2007. *Section R9, Hot-Mix Asphalt Concrete Pavement, Revised Edition by Consultant Civil Engineer Nuraddin Saeed Hussain (Issued in Iraq 1986)*.

Tayebali, A.A., Goodrich, J.I., Sousa, J.B. and Monismith, C.I., 1992. Influence of rheological properties of modified asphalt binders on the load deformation characteristics of the binder-aggregate mixture. In: Wardlaw, K.R. and Shuler, S., editors. *ASTM STP 1108: Polymer Modified Asphalt Binders*. ASTM International, United States. pp. 77-96.

Zhang, F., Yu, J. and Wu, S., 2010. Effect of aging on rheological properties of storage-stable SBS/sulfur-modified asphalts. *Journal of Hazardous Materials*, 182, p. 507-517.

Simulating Combined Cycle and Gas Turbine Power Plant under Design Condition using Open-Source Software DWSIM: A Comparative Study

Twana N. Hassan and Saif T. Manji

Department of Chemical Engineering, Faculty of Engineering, Koya University,
Koya KOY45, Iraq

Abstract—Nowadays, clean and high-power generation is essential matters worldwide. To be improved and optimized, power plants require accurate models that can be introduced to process simulators. There is various commercial software for industrial simulation which is not accessible to everyone. The open-source DWSIM process simulator is the first chemical engineering code that offers many tools for the better study of industrial plants. In this paper, we employ DWSIM software to simulate a combined cycle gas turbine (CCGT) power plant under design conditions for three cases. The generic models are predicted for multistage compressors and compressor maps. In the first case, two models developed in ASPEN HYSYS and GateCycle will be considered. The achieved results by DWSIM are acceptably comparable for thermal efficiency and power generation. The DWSIM result is 3.5% lower than the ASPEN HYSYS for thermal efficiency, and the power generation is completely the same. In the second case, rigorous simulation was carried out using actual field data from the local CCGT power plant. The DWSIM outcomes are very close to the practical data. The power generation of GT and CC is very close; the variety is nearly 0.45%. In the third case, the simulation of CCGT with a cogeneration system is precisely accomplished, and the outcomes of DWSIM are shown in excellent agreement. The DWSIM prediction shows lower values by 0.26%, 4.79%, and 0.72% for the HP turbine, LP turbine, and plant net power, respectively.

Index Terms—Combined cycle gas turbine, Heat recovery steam generator, Megawatt generation, Open-source code DWSIM, Thermal efficiency.

I. INTRODUCTION

Electric power is mainly generated through fuel combustion (coal, diesel oil, and natural gas). As electric power demand increases, CO₂ emissions also increase because of the combustion of hydrocarbon fuels. Combined cycle gas turbine (CCGT) is one of the investigative and alternative sources of

providing electrical power because of their ability to reduce CO₂ emissions, high efficiency, excellent adjustability, faster service, and good control power (Polyzakis, Koroneos and Xydis, 2008) and (Boyce, 2012).

The GT follows the Bryton cycle, in which ambient air is compressed to reach high pressure and mixed with fuel (natural gas). When the mixture is sparked in the combustion chamber to form high-pressure and high-temperature flue gas. The hot flue gas will expand in the turbine and convert its kinetic energy to mechanical energy, then to power through the generator (Cengel and Boles, 2008). The thermal efficiency of GT is generally between 35% and 40% (Ahmed, Elhosseini and Arafat Ali, 2018). When the heat recovery steam generator and steam turbine are combined, the high temperature from the GT's exhaust is sent to a heat recovery steam generator (HRSG) unit, which uses deionized water to make high-temperature and high-pressure steam. This steam runs the steam turbine.

Modelling and simulation are modern ways to consider and refine procedures to satisfy the rising requirements for performance, protection, and the climate. Simulation has evolved into a critical enabler in judgment, engineering, and operations, spanning the entire life cycle of a manufacturing device. Simulation can depict how the model changes over time under various circumstances.

There are commercial codes appropriate for designing CCGT, such as (GateCycle, EBSILON Professional, and Thermoflow). Ordys, et al. (1994) described Modeling and Simulation of Power Generation Plants. Griffin, et al., (1996) stated a power plant simulation software for optimizing thermodynamic and financial plant operation. The MATLAB®/Simulink®/SimPowerSystems® environment has been successfully implemented for CCGT, the simulation findings show that the created model is a valuable tool for studying and analyzing the majority of electrical oscillation phenomena that occur when a CCGT is linked to a power system grid (Ibrahim and Hamarash, 2008). Seifi, et al. (2008) also used MATLAB® and SIMULINK® to create a simulation toolbox for a combined-cycle power plant. Zabre, et al. (2009) developed a Simulator of a combined cycle power plant for operator training. Vieira, et al. (2010) described the effective integrated thermo economic improvement of the

ARO-The Scientific Journal of Koya University
Vol. XI, No. 1 (2023), Article ID: ARO.11098. 12 pages
DOI: 10.14500/aro.11098

Received: 23 October 2022; Accepted: 07 February 2023
Regular research paper: Published: 20 February 2023

Corresponding author's e-mail: twana.najih@koyauniversity.org
Copyright © 2023 Twana N. Hassan, Saif T. Manji. This is an open access article distributed under the Creative Commons Attribution License.



profitability of a complicated combined cycle cogeneration plant working under a variety of economic scenarios by using THERMO FLEX. A performance model for CCGT plants was created in MATLAB/Simulink by (Hasan, Rai and Arora, 2014), and the effect of changing various factors on efficiency was investigated. Saddiq, et al. (2015) utilized Aspen HYSYS software to investigate a simple gas turbine and gas turbine exhaust in a variety of configurations. GateCycle[®] (version 6.1.2) as a commercial modeling program was used by Oh, Lee and Kwak. (2017) to analyze the thermodynamic properties of a 300-MW combined cycle power plant. Liu and Karimi (2018) in a commercial simulator proposed a technique and the essential connections for simulating the part-load operation of a common CCGT plant through (GateCycle). The researchers modeled and evaluated the part-load performance of the CCGT system while considering the off-design behavior of all units. They presented a simulation-based optimization technique that generates an ideal operating strategy for every part-load to enhance overall plant efficiency. A 420MW CCGT power plant and thermal energy storage dynamic model have been created in Aspen Plus (Li, et al., 2017). Achimnole, Orhorhoro and Onogbotsere (2017) used the Aspen HYSYS software simulation for the performance evaluation of a gas turbine with and without a cooling system. Liu and Karimi (2018a) introduced a novel operating technique termed EGR-IGVC to increase a CCGT plant's part-load performance. Reveillere, Longeon and Rossi (2019) they employed Simcenter Amesim software to generate dynamic models of all subsystems and their interconnections in combined cycle power plants. Wiguno, Tetrisyanda and Wibawa (2020) used the Aspen Hysys V9 process simulator to investigate the impact of gas composition, air intake cooling, and steam injections on combined cycle power plant (CCPP) efficiency.

Because commercial software is very costly, finding open-source codes to simulate the CCGT power plant process is very needed to achieve plant analysis.

DWSIM is the only open-source simulation code in chemical engineering that can be used professionally that was created by Daniel Wagner Oliveira de Medeiros, a chemical engineer and software developer (DWSIM, 2004). DWSIM has proved its reliability in the past few years. The main advantage of adopting DWSIM in this work is its flexibility since it supports a wide variety of unit operations and makes user-defined unit operations and uses them. Another advantage of DWSIM over other chemical engineering simulation codes is its ease of use and free download from the internet. It also enables us to do studies and evaluate data using sophisticated models and processes. DWSIM contains the essential capability for steady-state mass and energy balances, as well as the ability to investigate component performance and setup conditions. It is simple to use, straightforward to report on, and has high convergence speeds. Tangsriwong, et al. (2020) show a comparative study between Aspen plus and DWSIM of Booster and sale gas compression. DWSIM was proven capable of adequately simulating chemical processes, and calculating thermodynamics and chemical characteristics, particularly for gas products. Andreasen (2022) presents

a thorough analysis of the free and open-source process simulator DWSIM. The outcomes of DWSIM are examined to a commercial process simulator that is often used in the sector using a simulation model of an oil and gas separation plant that has already been reported. Compared outcomes are within 1% of one another. The outcomes positive and offer validity for the utilizing the examined open-sourced process simulation software in a professional setting. DWSIM was used to simulate the operation of reducing nitrobenzene to produce aniline. After careful consideration and evaluating viability, every component operation's numerous thermodynamic data were included. The simulation produced promising findings that improved our understanding of the relationship between the reaction's kinetics and thermodynamics (Halageri and Pauls, 2015).

This research aims to study the CCGT power plant and use open-source simulation code DWSIM which accessible to everyone to simulate the process under design conditions for different cases.

In this study, a generic model proposes for various cases under design conditions for CCGT simulation. The generic model predicts a multistage compressor with an intercooler between stages and estimates compressor maps. The various units of each plant were simulated using DWSIM unit operations, including the simulation of CCGT, in which heat is recovered directly from GT exhaust to produce high-temperature steam via HRSG. The results were compared with published results in ASPEN HYSYS and GateCycle. The simulation was also validated by comparing DWSIM results with actual field data for CCGT. The CCGT simulation is also carried out for both with and without a cogeneration system, and the outcomes are contrasted to published data.

II. METHODOLOGY OF CCGT SIMULATION

A very efficient electric generation cycle is created by combining the gas turbine cycle with the HRSG and steam turbine. A compressor, combustion chamber, and turbine are the three basic components of a gas turbine cycle power generation, and a series of heat exchangers is the main component of a steam cycle, which is followed by a steam turbine. Because the open-source process simulator DWSIM was not quite ready to simulate CCGT, we used a general model to help us deal with the challenges we encountered. From ambient conditions, air is filtered by air filter which is simulated using a valve in DWSIM and its pressure drop is defined by equation (1) (Liu and Karimi, 2018b).

$$\Delta P = \Delta P_d \left(\frac{m}{m_d} \right)^{1.84} \left(\frac{T}{T_d} \right) \left(\frac{P}{P_d} \right)^{-1} \quad (1)$$

ΔP_d is the design pressure drop, M_d is the design mass flow rate, T_d is the design inlet temperature, P_d is the design inlet pressure, M is the inlet mass flow rate, T is the design inlet temperature, and P is the design inlet pressure.

Gas turbine compressors consist of a multistage compressor with an intercooler in between. Because of the unavailability of multistage compressors in DWSIM codes, we predicted

our gas turbine compressor into two stages of compressors. The pressure ratio for each compressor is predicted from the equation (2) (Sarathy, 2021).

$$R = \left[\frac{P_{Last}}{P_{First}} \right]^{1/n} \quad (2)$$

R is the compressors pressure ratio, P_{First} is the compressors inlet pressure, P_{Last} is the compressors outlet pressure, and n is the compressor stages.

When the pressure of the first compressor increases, its discharge temperature also increases, so we need to cool down its temperature to prevent the second stage compressor blade from exceeding temperature and use cooled air to control turbine temperature through the (rotor and stator) cooling stream. When the first compressor outlet temperature is cooled down through an intercooler to near ambient temperature, it causes a water vapor droplet to form due to the air humidity that should be removed to prevent the second compressor from corrosion. In this case, we installed a gas-liquid separator to remove water droplets. When the compressed air leaves the separator, it goes to a second compressor to be compressed to the right pressure.

Compressors work following the compressor map. We employ the general relativized compressor map as in Fig. 1., which is proposed by (Liu and Karimi, 2018b). In our case study, all parameters (mass flow, speed, pressure ratio, and isentropic efficiency) for each case are calculated depending on their design condition data through using equation (3), (4), (5), and (6) (Liu and Karimi, 2018).

$$m_{cor,r} = \left(\frac{m_{in} \sqrt{T_{in}}}{P_{in}} \right) / \left(\frac{m_{in,d} \sqrt{T_{in,d}}}{P_{in,d}} \right) \quad (3)$$

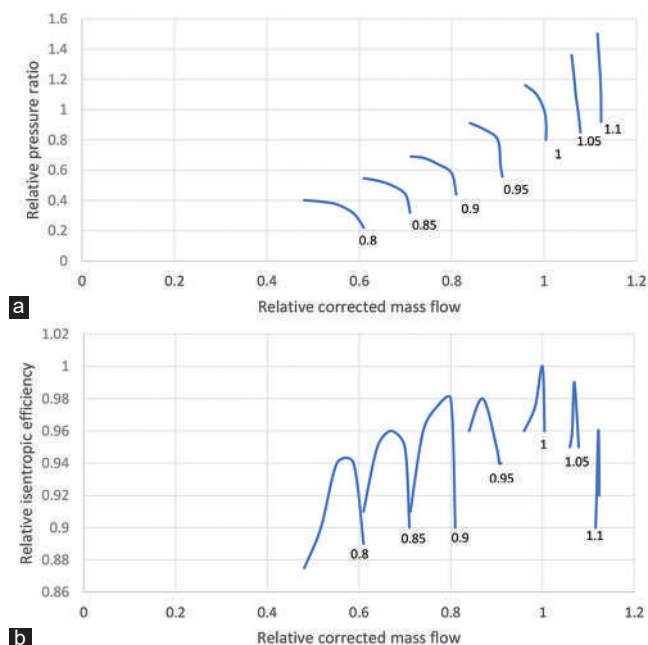


Fig. 1. General relativized compressor map: (a) Relative corrected mass flow versus relative pressure ratio, (b) relative corrected mass flow versus relative isentropic efficiency.

$m_{cor,r}$ is the relative corrected mass flow, m_{in} is refer to the compressor inlet mass flow, P_{in} refer to the compressor inlet pressure, T_{in} is refer to the compressor inlet temperature, and d denotes to the parameter at design condition.

$$PR_r = \frac{PR-1}{PR_d-1} \quad (4)$$

PR_r refer to the relative pressure ratio and PR is referred to the pressure ratio.

$$\eta_r = \frac{\eta}{\eta_d} \quad (5)$$

η_r refer to the relative efficiency and η is refer to the efficiency.

$$N_{cor,r} = \left(\frac{N}{\sqrt{T_{in}}} \right) / \left(\frac{N_d}{\sqrt{T_{in,d}}} \right) \quad (6)$$

Where $N_{cor,r}$ refer to the compressor corrective reactive speed, which are specify under each curve on the map.

After second compressor, the air is divided into three parts for stator cooling, rotor cooling, and combustion air. The hot flue gas from the combustion chamber expanded in the turbine to generate power while and the turbine inlet temperature was controlled by stator cooling. The following are the proposed CCGT case studies:

A. Case 1 (CCGT power plant using HYSYS data)

Fig. 2. shows the flow sheet diagram of the GT plants which are predicted under our generic model, designed condition data of CCGT is stated in Table I.

From ambient conditions, air is filtered by an air filter AFT, which is simulated by using a valve in DWSIM. Air is compressed to form high-pressure air, which is designed and settled by the compressor unit in DWSIM unit operation. The compressor maps of both compressors in case 1 are stated in Fig. 3. In case 1, we predicted the intercooler outlet temperature as 30°C. From compressor discharge, some of the air is split for cooling purposes (stator cooling and rotor cooling) by split-01. Natural gas is used as a fuel source for the combustion chamber, which the conversion reactor in DWSIM is used as a combustion chamber for burning natural gas. CTRL-01 is used as a controller to prevent the gas turbine from exceeding its temperature. DWSIM offers an expander for turbine simulation, which appears in Fig. 2. as TURB. Hot flue gas from the combustion chamber exit is expanded in the TURB to generate the desired megawatt MW. As stated in Fig. 4, the HRSG of CCGT contains three stages of pressure: low pressure (LP), intermediate pressure (IP), and high pressure (HP).

HRSG consists of a series of Shell and Tube Heat Exchanger as its shell is merged by GT exhaust flue gas and its tube serves three-stage pressure of steam production, LP economizer receives water from the LP pump which feeds the recirculation pump (RCP) to preheat the inlet water. For each stage of the HRSG a water pump is installed followed by the economizers, LP economizer receives water from LP pump (S22) and mix in (MIX3) with the RCP outlet (S27) to preheat

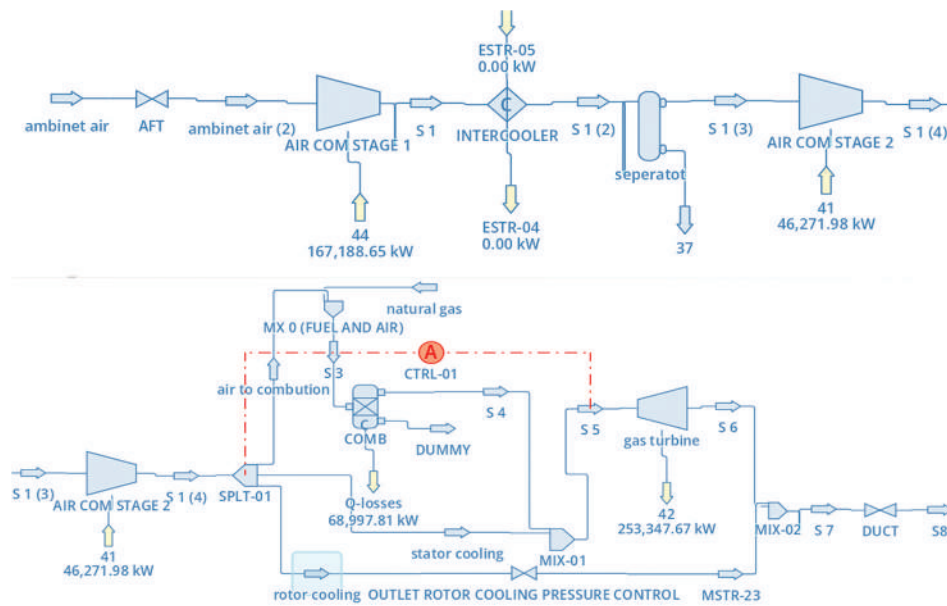


Fig. 2. Gas turbine process flow diagram for case 1.

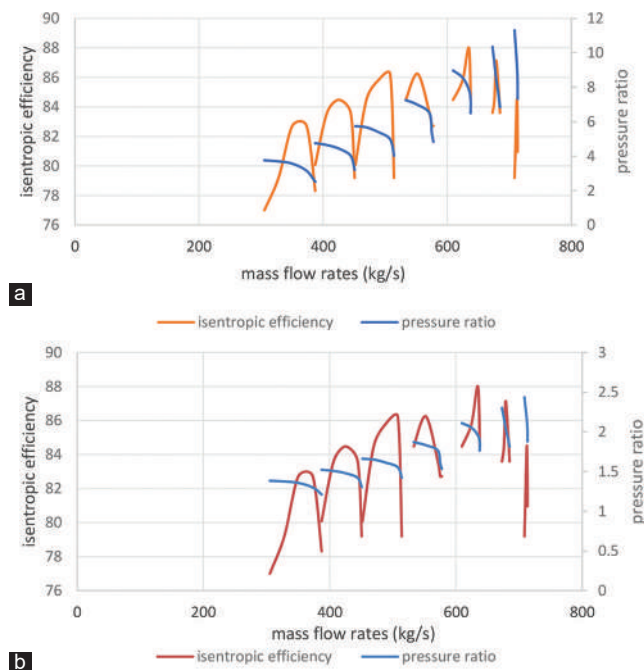


Fig. 3. Compressor map for GT case 1: (a) Stage 1 compressor map, (b) stage 2 compressor map.

condensate water then its outlet splits into two parts (SPLT2) first one recirculated to RCP (S25) and second part (S28) feed into the LP DRUM, liquid from LP drum bottom (S29) is splits (SPLT3) into three parts first stream (S30a) recirculated into the LP boiler to form water-steam mixture second stream (S34) feed water to the IPP and third stream (S43) feed water to the HPP. HRSG stages steam production work similarly so we take the HP line as an example to explain their process of steam production. HPP discharge is split into two parts first one sends water to the de-superheater one (DeSHT1) to prevent HPSPT1 from exceeding temperature and the second part feeds

water into the HP economizers (HPECO1, HPECO2, and HPECO3), respectively. After water absorbed the required temperature from economizers feed it into the HP drum then from the HP drum water recirculates into the HP boiler to form water-steam mixtures after that it feeds back to the HP drum to separate water-steam mixture, both recycle streams (R16 and R3) are control amount of the steam leaves the drum. Steam leaves the HP drum the passes through (HPSPH1 and HPSPH2), respectively, to produce dry superheated steam as a stream (S55).

Fig. 5 shows the schematic diagram of the steam turbines and condensate units. HP superheated steam (S55) feeds into the HP turbine to produce power, then mixes in the (MIX4) with IP superheated steam then feed into the reheater one (RHT1) to absorb extra heat or reheating, then (DeSHT2) is installed to prevent the IP turbine from exceeding temperature, then reaches RHT2 and feeds to the IP turbine. The outlet IP turbine mixes in (MIX5) with the LP superheated steam, which then feeds into the LP turbine. The exhaust stream (S63) from the LP turbine is condensed through COND and recirculated into the LPP.

All economizers, evaporators, superheaters, and condensate are simulated in DWSIM using heat exchangers, DRUMs are simulated by the gas-liquid separator in DWSIM, PUMPs are simulated by pressure change using a pump, steam turbines and gas turbines are installed through expanders. Design variable of CCGT is stated in Table I (Liu and Karimi, 2018b).

B. Case 2 (CCGT power plant using field data from Sulaymaniyah CCGT Power Plant) (Sulaymaniyah CCGT Power Plant, 2022).

The proposed GT plant of actual field data case 2 is also designed under our general model and similar to Fig. 2. and Case 1 except its inlet data will change as stated in Table II. The data has been collected from one of the local companies

TABLE I
DESIGN VARIABLE OF CCGT PLANT CASE 1

Variable	Value
Ambient condition	
Pressure	1.013 bar
Temperature	15°C
Molar fraction	77.30% N ₂ , 20.74% O ₂ , 1.01% H ₂ O, 0.03% CO ₂ , 0.92% Ar
Fuel condition	
Pressure	30 bar
Temperature	10°C
Molar fraction	87.08% CH ₄ , 7.83% C ₂ H ₆ , 2.94% C ₃ H ₈ , 1.47% N ₂ , 0.68% CO ₂
Gas turbine	
Inlet airflow	635 kg/s
Inlet air pressure loss	0.5 (%)
Compressor pressure ratio	15.4
Compressor isentropic efficiency	88%
Compressor mechanical efficiency	99%
Fuel flow	14.74 kg/s
Combustor efficiency	99.50%
Combustor pressure loss	3.50%
Combustor exit temperature	1405°C
Turbine inlet temperature	1328°C
Turbine exhaust temperature	615°C
HRSG	
HP/IP/LP steam temperatures	565.0/297.0/295°C
HP/IP/LP pinch point temperatures	10.0/10.0/10.0°C
HP/IP/LP approach point temperatures	8.0/10.0/16.4°C
HP SPHT 1 steam outlet temperature	510°C
RHT 1/2 steam outlet temperature	520.0/565.0°C
HP ECON 1/2 water outlet temperature	208.0/280.0°C
Pressure losses on gas/water/steam sides	1.5/5.0/3.0%
Steam turbines (STs)	
HP/IP/LP ST inlet pressure	98.8/24.0/4.0 bar
HP/IP/LP ST isentropic efficiency	87.0/91.0/89.0%
Shaft speed 3000	3000 rpm

°C: Cellules, kg: Kilo gram, s: Second, rpm: Revolution per minute, kpa: Kilo pascal, CCGT: Combined cycle gas turbine, HRSG: Heat recovery steam generator

in the Kurdistan region. The plant includes four gas turbines, which are followed by four HRSG. The superheated steam from all HRSGs is combined to form main steam, which is then merged to the steam turbines. The components and simulation procedure are similar to those of the GT turbines in cases 1, except that it is designed for lower MW generation. The predicted compressor stage maps are stated in Fig. 6.

The combined cycle in case 2 containing two-stages (HP and LP) of pressure PFD diagram of CC is shown in Fig. 7. CC includes one preheater, one LP economizer, two HP economizers, one LP evaporator, one HP evaporator, one LP superheater, two HP superheaters, one LP DRUM, one HP DRUM, and two steam turbines (HP and LP). When the steam leaves the LP turbine, its condensate goes through an air-cooling cycle (ACC) and is mixed with makeup demineralized water and then collected in the condensate collection tank, condensate pump feeds water into the four HRSG because all HRSGs similarly. We take one HRSG as an example for our methodology. The preheater receives water from two streams which are mixed in (MIX3).

TABLE II
DESIGN VARIABLE OF CCGT PLANT CASE 2

Variable	Value
Ambient condition	
Pressure	101.3 kPa
Temperature	13.3°C
Molar fraction	77.30% N ₂ , 20.74% O ₂ , 1.01% H ₂ O, 0.03% CO ₂ , 0.92% Ar
Fuel condition	
Pressure	23.8 bar
Temperature	40°C
Molar fraction	88.8% CH ₄ , 8.84% C ₂ H ₆ , 1.48% C ₃ H ₈ , 0.175% N ₂ , 0.093% CO ₂
Gas turbine	
Inlet air flow	458.2 kg/s
Inlet air after pressure loss of filter house	0.82
Compressor pressure ratio	13
Compressor isentropic efficiency	91.10%
Fuel flow	6.9 kg/s
Combustor efficiency	99%
Combustor pressure loss	0.1
Combustor exit temperature	1390°C
Turbine inlet temperature	1050°C
Turbine exhaust temperature	547°C
Gas turbine thermal efficiency	32.20%
Heat recovery steam generator (HRSG)	
LP EVA outlet pressure	8.16 bar
HP EVA outlet pressure	72.8 bar
HP/LP steam temperatures	525.1/223.1 (°C)
HP SUPHT 1 steam outlet temperature	497.3 (°C)
HP ECON 1/2 water outlet temperature	120/284.2 (°C)
Steam turbines (STs)	Turbines (STs)
HP/LP ST inlet pressure	67.15/6.04 (bar)
HP/LP ST isentropic efficiency	90/65 (%)
Shaft speed 3000	3000 (rpm)

°C: Cellules, kg: Kilo gram, s: Second, rpm: Revolution per minute, kpa: Kilo pascal, CCGT: Combined cycle gas turbine, HRSG: Heat recovery steam generator

The first stream (HRSG5 PREHEATER) comes from the condensate pump and the second stream (S21) comes from the recirculation discharge pump. The warm water from the outlet of the preheater is split (SPLT3) into two streams. The first stream recirculates to the RCP and the second stream (HRSG5 COND PREH) feeds into the deaerator. The deaerator works as a gas-liquid separator to remove dissolved gases. The bottom of the deaerator collects water and feeds warmed water to the BFP. BFP pumps include two stages of pressure (HP and LP) because both stages work similarly, so we take only the HP line to explain our methodology. High pressure water from BFP feeds water into (HPECO1 and HPECO2) then feeds into the HP drum. From the bottom of the HP drum, warmed water recirculated (R5) (S30) into the HP evaporator (HP EVAP) that turns warmed liquid water into water-vapor mixture and returns into the HP drum to separate water-vapor mixture, (R1 and R5) recalculate the steam flow amount that leaves the HP drum, then feeds into the (HP1SUPHTR) to make dry superheater steam. Its outlet mixes with the (HP DESUPERHEATER) stream which comes from BFP discharges to prevent superheated steam from exceeding

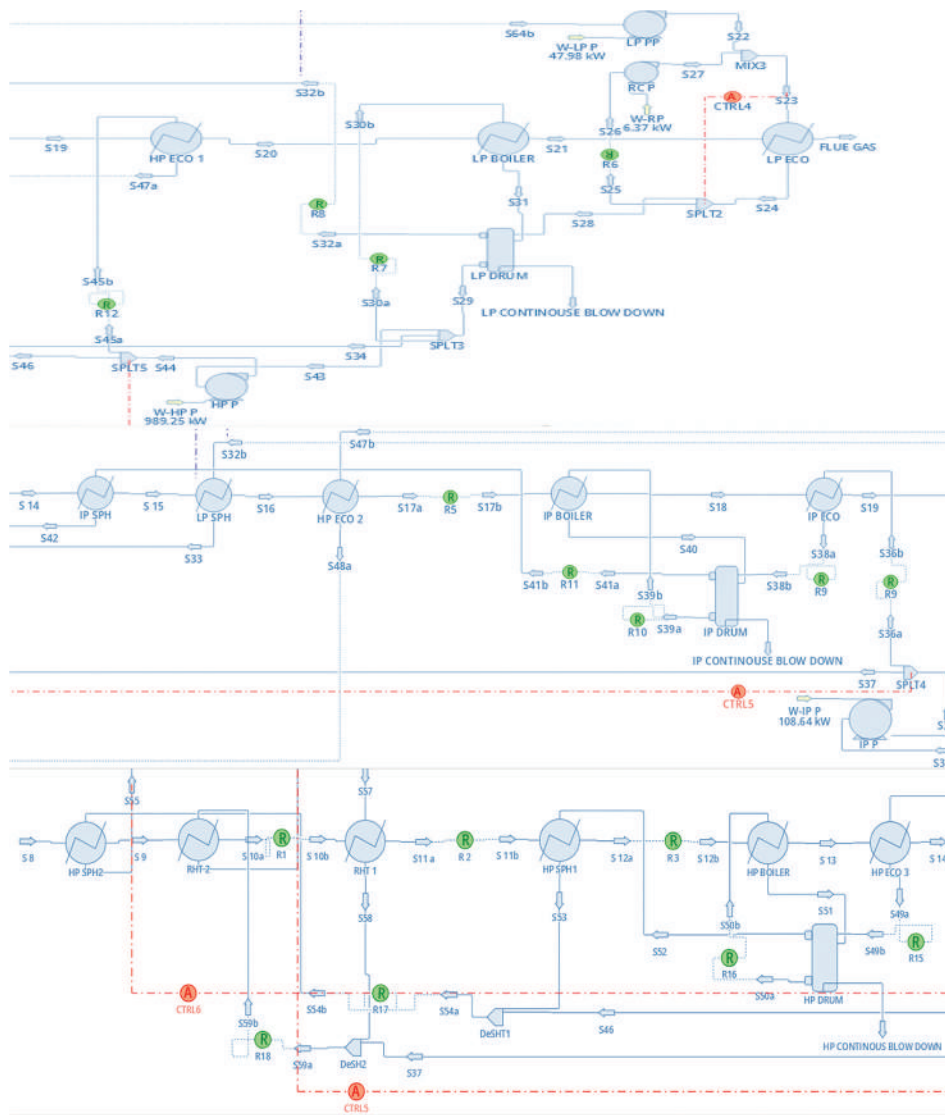


Fig. 4. Heat recovery steam generator process flow diagram for case 1.

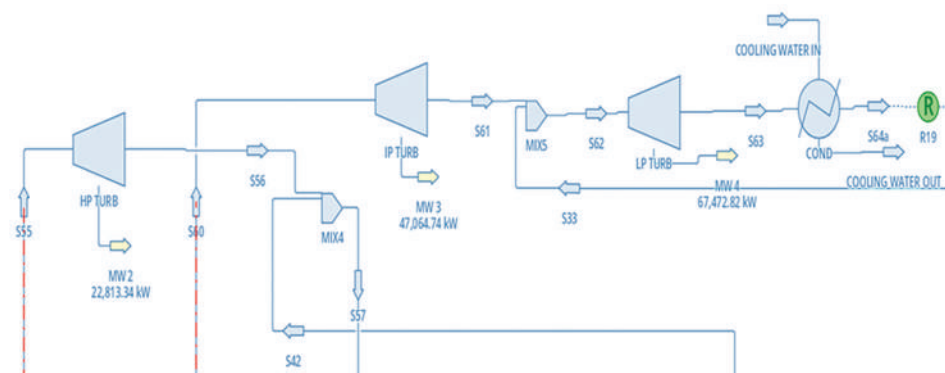


Fig. 5. Steam turbine process flow diagram of case 1.

temperature. Then feeds into the (HP2SUPHTR) to increase steam temperature and prepare it for feeding the HP steam turbine.

All HRSG HP superheated steam mixes to form an HP HEADER, which then feeds into the HP turbine to generate

the required power. All LP superheated steam from all HRSG is mixed to form LP HEADER and fed to the LP turbine to generate the required power, exhaust of the LP turbine condensate through (ACC). The PFD diagram of the main superheated steam, steam turbines, and condensate system

stated in Fig. 8. and the design condition of CCGT case 2 are shown in Table II.

All preheaters, economizers, superheaters, and evaporators are simulated in DWSIM by heat exchangers. All drums and

deaerators are simulated by gas-liquid separators in DWSIM. The main steam valve and filter house are simulated by the valve and also the pump in the unit operation in DWSIM.

C. Case 3

The project includes two parts of operation CCGT and CCGT with a district heat system (DH). CCGT can be engaged with a DH system to produce auxiliary heat which provided to the companies that need heat and for heating purpose especially in the coldest country and seasons. The required heat can be obtained through utilizing heat exchanger that use HP turbine outlet and mixed with LP superheater to warm the water and obtain the required heat.

CCGT without cogeneration

The simulation of GT with and without cogenerations is proposed similarly as our general model except its parameter values are changed, which is stated in Table III (Lee, Kim and Kim, 2017). The predicted compressor maps are shown in Fig. 9. The HRSG simulation model is stated in Fig. 10, and steam turbines are shown in Fig. 11.

In this case, because the authors did not mention the required details of the process, we predicted each unit for our simulation. This model contains two gas turbines and HRSG. Demineralized water is fed to the preheater through an LP feed water pump to raise the water temperature, HP pump receives water from the preheater outlet and then feeds water into two stages of pressure in our HRSG. Because both lines work similarly, we only describe the HP line in our

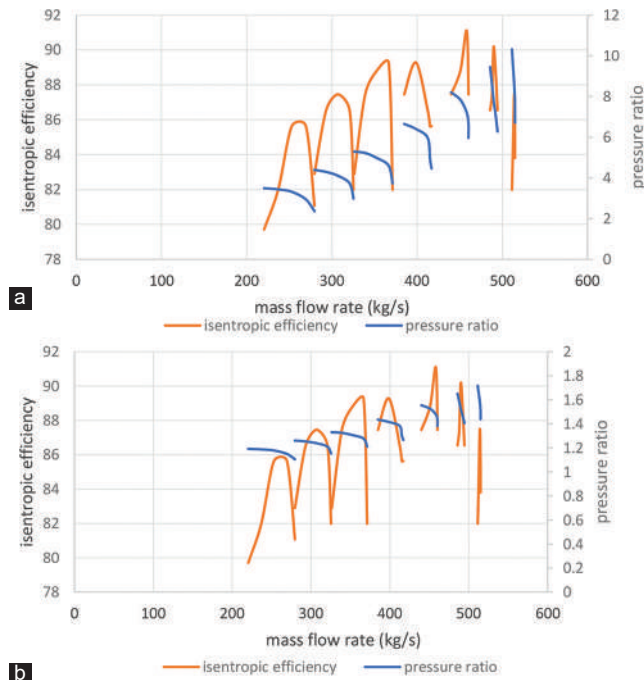


Fig. 6. Compressor maps for GT case 2: (a) Compressor stage1 map, (b) compressor stage2 map.

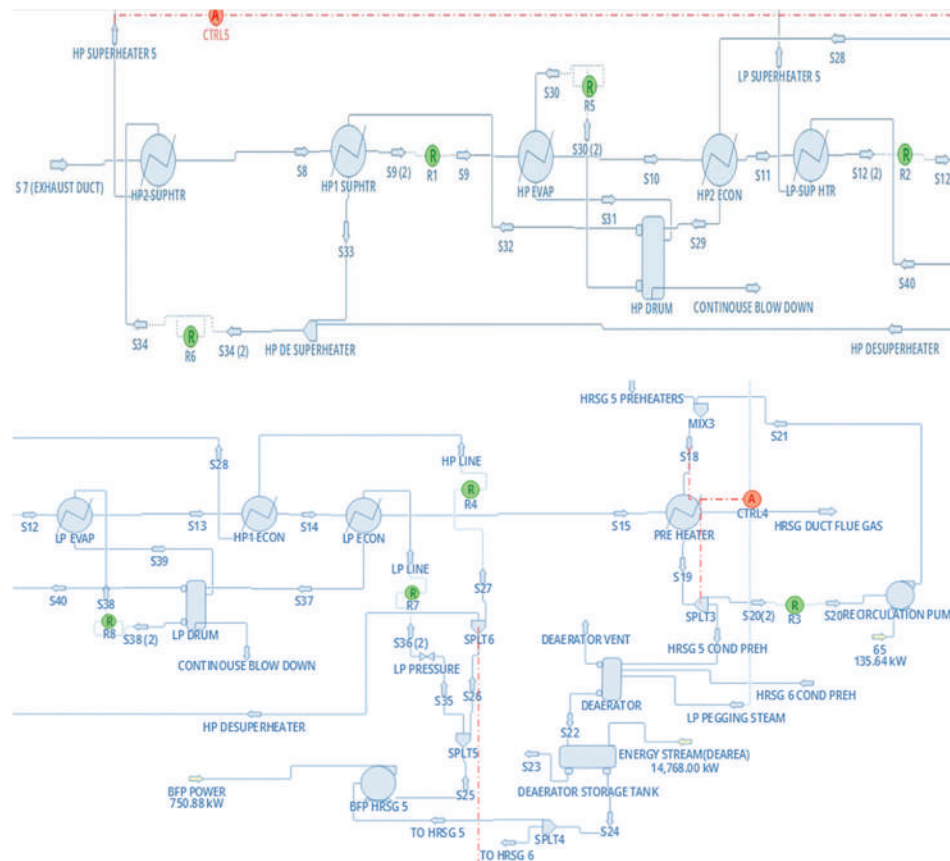


Fig. 7. Process flow diagram of combined cycle for case 2.

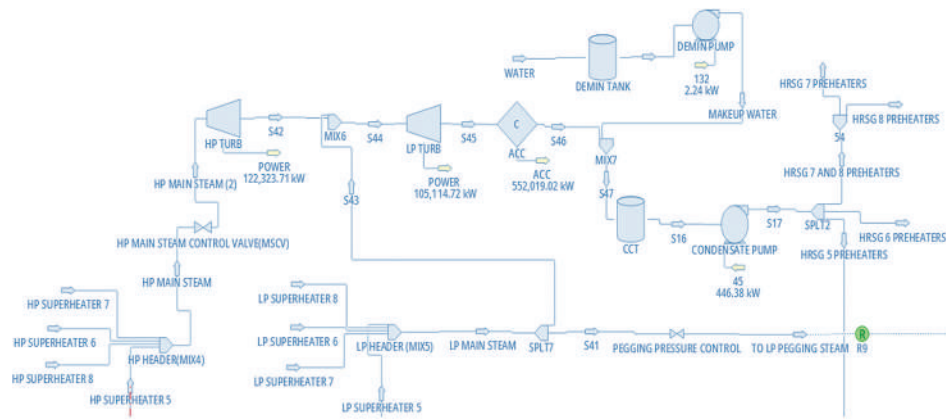


Fig. 8. PFD diagram of superheated main steams, steam turbines, and condensate system.

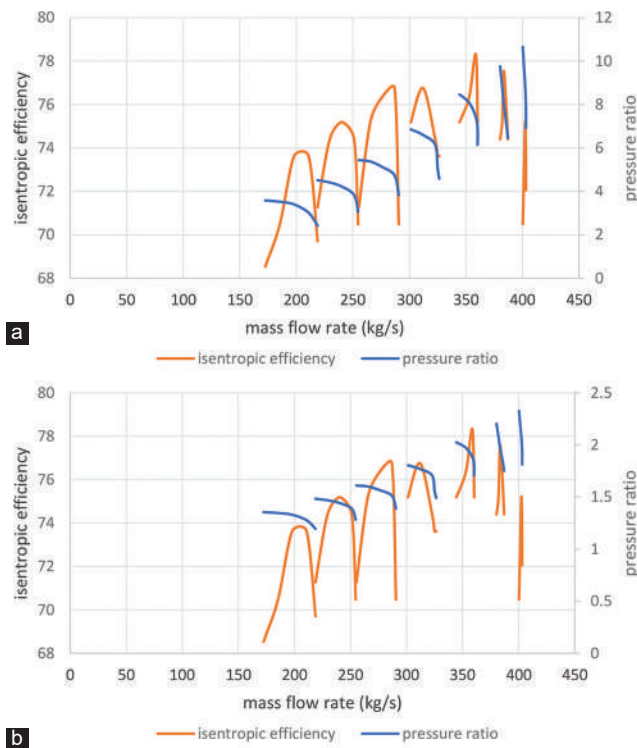


Fig. 9. Compressors maps for GT case 3: (a) Compressor stage 1 map, (b) compressor stage 2 map.

procedures. (S9) from the HP pump will be the inlet of the HP economizer for absorbing required heat then enters the HP drum. From the HP drum bottom, warmed water leaves and is recirculated (R4) into the HP boiler to absorb required heat to form water-steam mixtures, then returned into the HP drum to separate water-steam mixtures. From the HP drum top, a steam stream leaves the drum which is calculated by (R4 and R5) then feeds into the HP superheater.

In this case, the steam turbine receives steam from two HRSG to form HP superheated main steam, which then feeds into the HP steam turbine. The outlet of the HP turbine is mixed in (HP and LP MIXER) with the LP main steam stream, which then enters the LP turbine to generate the required power. Table III shows design variables of CCGT without cogeneration for case 3.

TABLE III
DESIGN PARAMETER OF CCGT CASE 3

Parameter	Value
Air temperature	15°C
Air pressure	101.325 kPa
Fuel flow rate	6.39 kg/s
Compressor pressure ratio	14
Compressor outlet temperature	376.73°C
Compressor efficiency	78.32%
Turbine inlet temperature	1140°C
Turbine exhaust temperature	533°C
Exhaust gas flow rate	365.08 kg/s
Gross power output	100 MW
Gas turbine	
Gross efficiency	30.35%
Inlet gas temperature	533°C
Outlet gas temperature	112.88°C
HRSG	
HP steam temperature	505°C
HP steam pressure	78.06 bar
HP steam flow rate	87.8 kg/s
LP steam temperature	147.2°C
LP steam pressure	4.41 bar
LP steam flow rate	27.44 kg/s
HP feed water temperature	89.39°C
LP feed water temperature	88.62°C
Steam Turbine	
HP turbine power	53.09 MW
HP turbine efficiency	85.89%
HP turbine outlet pressure	6 bars
LP turbine power	54.83 MW
LP turbine efficiency	76.74%
LP turbine outlet pressure	0.08 bar

°C: Cellules, kg: Kilo gram, s: Second, rpm: Revolution per minute, kpa: Kilo pascal, CCGT: Combined cycle gas turbine, HRSG: Heat recovery steam generator

CCGT with DH system

The simulation of GT and HRSG with DH is the same as the previous model, steam turbine with DH simulation PFD is stated in Fig. 12. The design condition of the GT and HRSG is as the previous model and steam turbines with DH parameters are stated in Table IV.

The simulation of both is the same as above, except in this model the LP turbine did not serve to generate power. The superheated steam feeds into the HP turbine to make

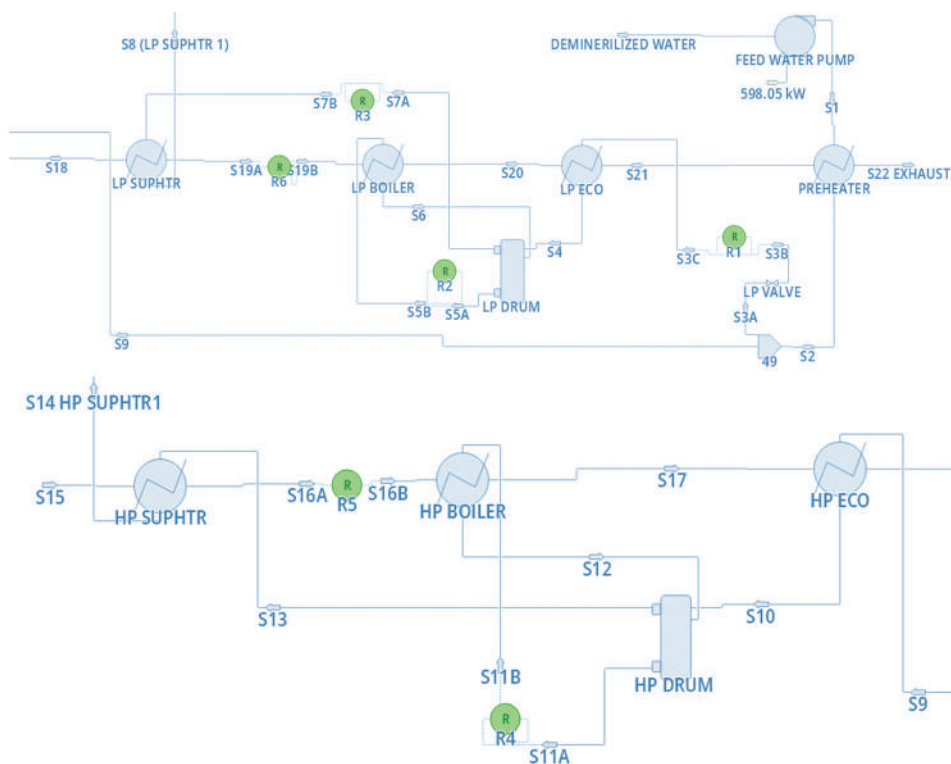


Fig. 10. Heat recovery steam generator process flow diagram for case 3.

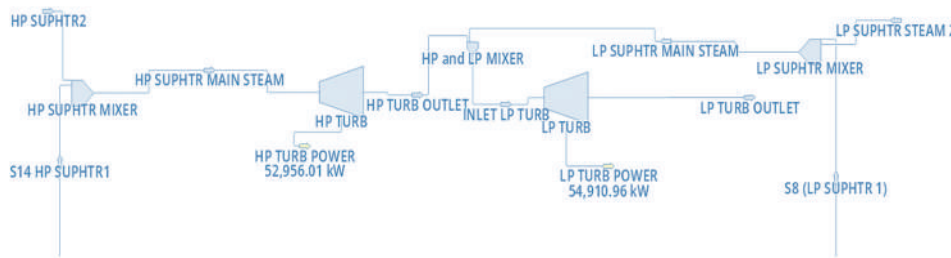


Fig. 11. Steam turbines process flow diagram for case 3.

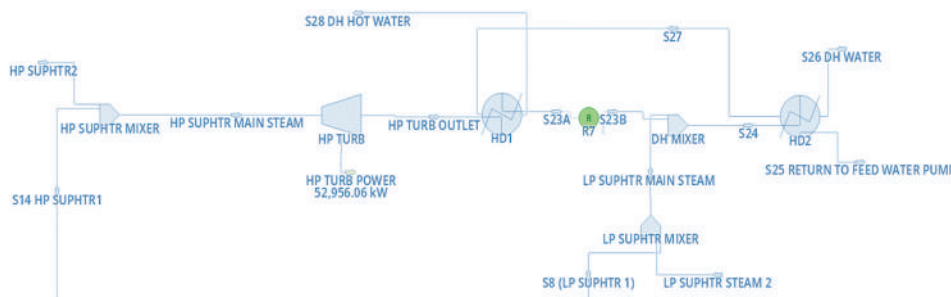


Fig. 12. Steam turbine with a district heat system.

TABLE IV
DESIGN PARAMETER OF DISTRICT HEATING

Parameter	Value
DH water temperature	120°C
DH return water temperature	65°C
System DH water flow rate	1206.06 kg/s
Thermal efficiency	80.50%

°C: Cellules, kg: Kilo gram, s: Second

the required power, then leaves the HP turbine, then feeds into the HD1 to maintain required heat into the cold stream from the other side of the HD1 heat exchanger. After this, it leaves HD1 and mixes with LP superheated main steam and enters HD2 of the district heat system to maintain heat on the cold side of the HD2 heat exchanger. From the cold side of the HD2 heat exchanger, water is fed (S26 DH WATER)

into the HD2 to absorb heat from the hot side, then enters HD1 to absorb extra heat and finally leaves (S28 DH HOT WATER) district heat system at 120°C that can be used for district systems.

III. RESULTS AND DISCUSSION

A. Case 1

The DWSIM open-source simulation software is used to simulate the design condition of the CCGT plant. The results of the simulation are compared with published results of ASPEN HYSYS and GateCycle (Liu and Karimi, 2018b) as shown in Fig. 13.

Fig. 13 compares the performance of ASPEN HYSYS, GateCycle, and DWSIM in modeling the CCGT plant under design circumstances.

The power generation of simulating GT turbines in DWSIM is in good agreement with HYSYS. The heat rate of DWSIM results is completely the same as ASPEN HYSYS and 1.55% higher than GateCycle results. These results are good agreement for DWSIM CCGT simulation.

The thermal efficiency of both ASPEN HYSYS and GateCycle is nearly the same, but in DWSIM the value is less by about 3.5%. HYSYS and GateCycle support a multistage compressor and turbine, and in practically all GT work with the multistage compressor, the cooling air from the compressor is taken from the compressor stages depending on the target position of the cooling area, but DWSIM does not support a multistage compressor yet. As a result, exhaust GT simulation temperature also indicates excellent agreement as all three software's are nearly the same around 615°C, which helps us simulate our combined cycle.

Conducting an HRSG simulation under DWSIM is quite similar to that in commercial codes since all unit operations are available (heat exchangers, expanders, separator for drum purpose, pumps, recycle, and controllers) and the designed parameters (pressure, temperature, isentropic efficiency, and flow) are set as Table I and the outcome is very similar and agreed. The MW generation by expanders is very close to the commercial software, which is 1.77%. DWSIM achieves MW lower than HYSYS result, and the DWSIM exhaust temperature through HRSG is practically accepted because it is higher than 100°C, which is higher than the NO_x dewpoint. Plant efficiency in DWSIM shows higher result than HYSYS by 5% this is because DWSIM steam cycle efficiency is higher than HYSYS this variety result is coming from lack of DWSIM multistage compressor that change its outlet temperature.

B. Case 2

The simulation of the CCGT plant carried out for actual field data from one of the Kurdistan region's companies. Because of the operating company and manufacturer privacy some data cannot be given, GT is mostly working at part-load operation so using a compressor map becomes very essential for covering part-load operation and testing inlet condition parameters on the CCGT plant during design and part-load operations, because there is no actual compressor map data from practical even from literature and because of lack of multistage compressor in our open source code DWSIM we forced to make few assumptions.

As for case 1, we divided the air compressor into two stages with an intercooler in between. Because the GT performance

is heavily dependent on compressor performance, and some of the air comes from various stages in the compressor (for cooling and valve opening or closing), we are unable to reach the desired cooling temperature of the cooling streams from the compressor's final stages due to high temperatures.

Fig. 14 shows that there is a lot of acceptance and response to the use of DWSIM software to simulate CCGT field data and assumptions.

The power generation of GT and CC is very close. The variety is about 0.45%. Besides the equality of the GT exhaust temperature, which in field operation is about 547°C, there is a variety of GT thermal efficiency of about -1% because there is a variation in the heat rate between DWSIM and field data and there are no required data from the field, especially for turbine inlet temperature. Fig. 14 shows an excellent agreement between field results and DWSIM results for net power, gas turbine heat rate, and overall cycle heat rates.

C. Case 3

CCGT without cogeneration

Comparisons of CCGT in DWSIM and CCGT by the predicted model of the used reference are stated in Fig. 15.

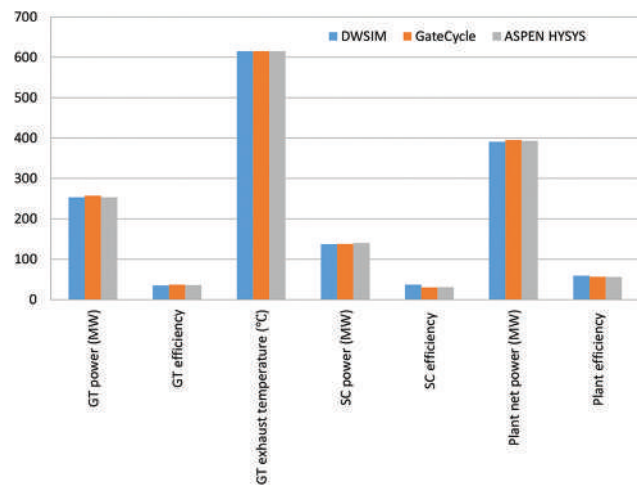


Fig. 13. Design performance comparison between ASPEN HYSYS, GateCycle, and DWSIM for case 1.

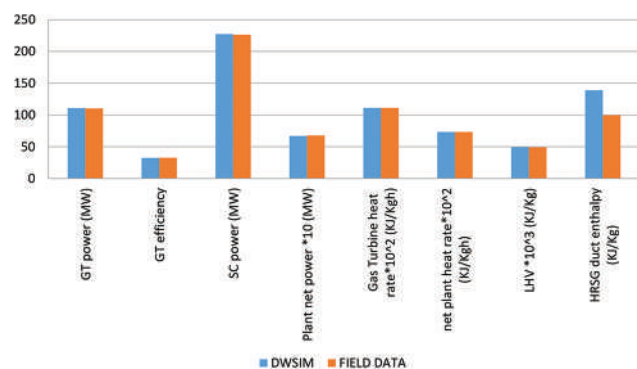


Fig. 14. Design performance comparisons between field and DWSIM results.

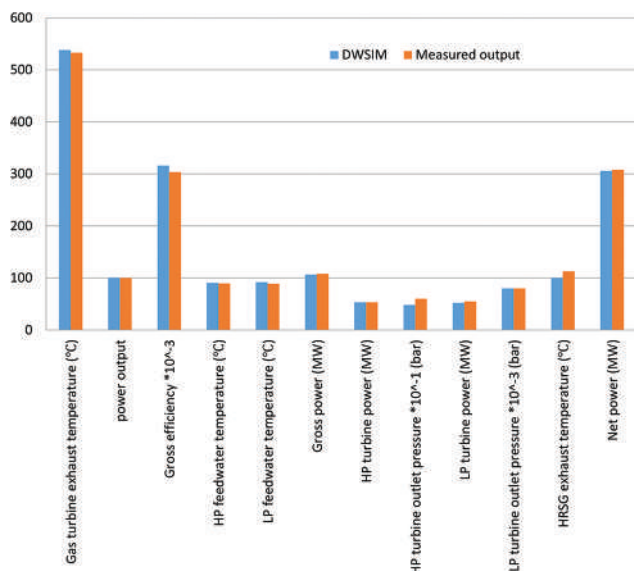


Fig. 15. Comparison results between DWSIM and measured output of combined cycle gas turbine without cogeneration system.

The generic model is applied to the GT of the CC power plant, which is designed to work without a cogeneration system. As in previous cases, due to unavailability of the multistage compressor, we used two cooling systems for gas turbine cooling. As with the compressor discharge, two lines are separate for cooling the gas turbine's rotor and stator. The model is run so as to simulate the desired CCGT and achieve desirable results.

We obtained gas turbine MW generation closely same as a predicted measure in the used reference as the difference is only about 0.27% which excellent gaining of DWSIM for simulating GT, in additional gas turbine exhaust temperature also very reasonable and have good agreement compared to the used reference its error about 0.96% higher than reference result, the thermal efficiency of the simulated gas turbine in DWSIM is higher about 4.11% than predicted reference because of assumed generic model of cooling air system and unavailability of compressor and turbine multistage.

The HRSG simulation of DWSIM shows very close outcomes compared to the predicted model. The outlet temperature of both stages of pressure is close to the same as HP feed water outlet temperature has 1.19% error and LP feed water outlet temperature has 3.6% error. The exhaust temperature of the DWSIM simulator is 11.4% lower than the predicted reference temperature, which is (100°C and 112.99°C), respectively. This difference occurs because the model is predicted and the reference did not state required information about heat exchangers and their condition, but practically we can observe that the result is highly agreed. The power generation of both models has extremely similar outcomes as DWSIM prediction shows lower values of 0.26%, 4.79%, and 0.72% for HP turbine, LP turbine, and plant net power, respectively. The higher error of LP turbine power generation occurs because of steam separation in the LP drum, which produces lower flow of steam by 21.5%,

but the results indicate that DWSIM software has excellent response for combine cycle simulation design.

CCGT with district heat system

In the cogeneration mode, the LP turbine did not serve for MW generation, but the HP turbine and gas turbines remained in the previous mode for power generations that became 253.5 MW of net power in the DWSIM model. As a result, DWSIM net power is higher by 0.16% than predicted using the used reference. The cogeneration system in the DWSIM simulation shows excellent agreement as simulated under the same conditions in the predicted used reference.

IV. CONCLUSION

In this paper, DWSIM an open-source process simulator has been used to study and simulate CCGT power plants operated under design conditions. DWSIM had proved to be a reliable process simulator in the past few years and is continuously being improved and optimized with each version.

DWSIM's simulations capabilities were put to test against prominent commercial codes such as Aspen HYSYS and GateCycle and power plant data to see whether it is a viable choice to simulate and investigate CCGTs plants. For this purpose, a generic model for a CCGPT plant has been prepared and slightly modified for each case study as required. This model is capable of simulating a multistage compression with a compressor map as well as includes a rigorous model for the HRSG.

Three case studies have been adopted for the validation of the generic model: two simulations conducted in Aspen HYSYS and GateCycle and plant data. The parameters of each case were introduced to the generic model and the DWSIM's obtained results (power generation, thermal efficiency, and heat rates) show very good agreement with the case studies results and the adoption of the relativized compressor map has proved to be successful. The results deviation from the respective case can be summarized as a maximum of 5% for the plant efficiency in Case 1 whereas it is much less for the power generation, GT exhaust temperature.etc., in Case 2, the agreement is more apparent whereas in Case 3 only without cogeneration condition the exhaust temperature is lower than expected by about 11% that has shown to largest deviation in this case. The main source of error of in the covered cases can be ascribed to the lack of crucial data such as the compressor's multistage conditions.

For the final conclusion about the use and importance of DWSIM in CCGT plant simulation, we found that in light of the promising results that DWSIM is quite reliable in CCGT plants simulations under design conditions for applications such as operators training, academic studies, or process optimization given.

It is worth noting that CCGT plants usually operate under part-load or off-design conditions and it is imperative to investigate how DWSIM is capable of simulating such cases but due to the complexity of part-load design simulations it was chosen be done in a future work.

REFERENCES

- Achimnole, E.N., Orhororo, E.K. and Onogbotsere, M.O., 2017. Simulation of gas turbine power plant using high pressure fogging air intake cooling system, online. *International Journal of Emerging Engineering Research and Technology*, 4, pp. 691-696.
- Ahmed, A.S.E., Elhosseini, M.A. and Arafat Ali, H., 2018. Modelling and practical studying of heat recovery steam generator (HRSG) drum dynamics and approach point effect on control valves. *Ain Shams Engineering Journal*, 9(4), pp. 3187-3196.
- Andreasen, A., 2022. Evaluation of an open-source chemical process simulator using a plant-wide oil and gas separation plant flowsheet model as basis. *Periodica Polytechnica Chemical Engineering*, 66(3), pp. 503-511.
- Boyce, M., 2012. *Gas Turbine Engineering Handbook*. 4th ed. Butterworth-Heinemann, United Kingdom.
- Cengel, Y.A. and Boles, M.A., 2006. *Thermodynamics: An Engineering Approach*. 5th ed. McGraw-Hill, New York. p. 962.
- Daniel Wagner Oliveira de Medeiros., 2004. DWSIM (7.5.1). [DWSIM] [2022]. Available from: <https://dwsim.org/index.php/download> [Last accessed on 2022 Apr 02].
- Griffin, P.R., Elmasri, M., Chen, G.T., Kamppila, S. and Basile, F., 1996. *Power Plant Simulation Software For Optimizing Thermodynamic and Financial Plant Operation*. Available from: <http://asmedigitalcollection.asme.org/GT/proceedings-pdf/GT1996/78750/V004T11A003/4216106/v004t11a003-96-gt-277.pdf> [Last accessed on 1996 Jun 10].
- Halageri, A. and Pauls, G., 2015. *Production of Aniline by Hydrogenation of Nitrobenzene*. Available from: <https://www.studocu.com/in/document/indian-institute-of-technology-roorkee/thermodynamics-and-chemical-kinetics/aniline-synthesis-from-nitrobenzen/22854448>.
- Hamarash, I.I., 2008. Modeling and Simulation of the Perdawd CCGS Connected to the Kurdistan Regional Power System of Iraq Using Simulink. In: Ao, S.I. and International Association of Engineers., Ed. *World Congress on Engineering: WCE 2008: 2-4 July, 2008*. Newseod Ltd., International Association of Engineers, Imperial College London, London, UK.
- Hasan, N., Rai, J.N. and Arora, B.B., 2014. Optimization of CCGT power plant and performance analysis using MATLAB/Simulink with actual operational data. *SpringerPlus*, 3(1), pp. 1-9.
- Li, D., Hu, Y., He, W. and Wang, J., 2017. *Dynamic Modelling and Simulation of a Combined-Cycle Power Plant Integration with Thermal Energy Storage*. 23rd International Conference on Automation and Computing (ICAC).
- Liu, Z. and Karimi, I.A., 2018. Simulation and optimization of a combined cycle gas turbine power plant for part-load operation. *Chemical Engineering Research and Design*, 131, pp. 29-40.
- Liu, Z. and Karimi, I.A., 2018a. New operating strategy for a combined cycle gas turbine power plant. *Energy Conversion and Management*, 171, pp. 1675-1684.
- Liu, Z. and Karimi, I.A., 2018b. Simulating combined cycle gas turbine power plants in Aspen HYSYS. *Energy Conversion and Management*, 171, pp. 1213-1225.
- Oh, H.S., Lee, Y. and Kwak, H.Y., 2017. Diagnosis of combined cycle power plant based on thermoeconomic analysis: A computer simulation study. *Entropy*, 19(12), 643.
- Ordys, A., Katebi, R., Johnson, M. and Grimble, M., 1994. *Modelling and Simulation of Power Generation Plants*. Springer-Verlag, London, Great-Britain.
- Polyzakis, A.L., Koroneos, C. and Xydis, G., 2008. Optimum gas turbine cycle for combined cycle power plant. *Energy Conversion and Management*, 49(4), pp. 551-563.
- Reveillere, A., Longeon, M. and Rossi, I., 2019, *Dynamic Simulation of a Combined Cycle for Power Plant Flexibility Enhancement in E3S Web of Conferences*. EDP Sciences, Les Ulis, France.
- Saddiq, H.A., Perry, S., Ndagana, S.F. and Mohammed, A., 2015. Modelling of gas turbine and gas turbine exhaust and its utilisation as combined cycle in utility system. *International Journal of Scientific and Engineering Research*, 6(4), pp. 925-933.
- Seifi, A.R., Salehi, A., Eng, M. and Safavi, A.A., 2008. *Combined-Cycle Plant Simulation Toolbox for Power Plant Simulator*, 9(1), pp. 97-109.
- Sarathy, J.V., 2021. Gas compression stages-design & optimization. *Engineering Practice Magazine*, 8(24), pp. 15-18.
- Sulaymaniyah CCGT Power Plant., 2022. *Sulaymaniyah Combine Cycle Power Plant*. Mass Company, Sulaymaniyah, Iraq.
- Tangsrirong, K., Lapchit, P., Kittijungjit, T., Klamrassamee, T., Sukjai, Y. and Laonual, Y., 2020. Modeling of chemical processes using commercial and open-source software: A comparison between Aspen plus and DWSIM. In: *IOP Conference Series: Earth and Environmental Science*. Institute of Physics Publishing, Bristol, United Kingdom.
- Vieira, L.S., Matt, C.F., Guedes, V.G., Cruz, M.E. and Castellões, F.V., 2010. Maximization of the profit of a complex combined-cycle cogeneration plant using a professional process simulator. *Journal of Engineering for Gas Turbines and Power*, 132(4), pp. 418011-4180110.
- Wiguno, A., Tetrisyanda, R. and Wibawa, G., 2020. The effect of gas composition, air intake cooling, and steam injection on combined cycle power plant performance. In: *AIP Conference Proceedings*. American Institute of Physics Inc., Maryland.
- Zabre, E., Roldán-Villasana, E.J., Romero-Jiménez, G., Cruz, R., 2009. Combined Cycle Power Plant Simulator for Operator's Training. In: Ao, S.I. and International Association of Engineers., Ed. *World Congress on Engineering and Computer Science : WCECS 2009 : 20-22 October, 2009*. Newseod Ltd., International Association of Engineers San Francisco, USA.

Fresh and Mechanical Properties of Concrete Containing Oil-Well Cutting Material

Nabaz S. Hussein, Rahel Kh. Ibrahim

Department of Civil Engineering, Faculty of Engineering, Koya University,
Koya KOY45, Kurdistan region – F.R. Iraq

Abstract—Oil-well cutting material (OWCM) is a waste generated during the process of oil-well drilling. Its disposal is costly and harmful to the environment. The chemical makeup for the material implies that it might be used as a partial cement replacement in concrete. It is high in calcium oxide, silica, and aluminum oxide, which are the main oxides found in raw materials used to produce cement. Replacing a part of cement by OWCM in concrete mixtures can directly reduce the quantity of the cement used which leads to decreasing the emission of carbon dioxide and solving the disposal problems for the OWCM as well. This process can be considered as a significant step in producing environmentally friendly concrete. This study focuses on investigating the fresh and mechanical properties of different concrete mixes that have different strength grades, containing different percentages of OWCM as a cement replacement. For this purpose, different concrete mixes containing 10%, 15%, 20%, 25%, 30%, 35%, and 40% of OWCM as a cement replacement, besides the control Portland cement for the three different concrete strength grades, were prepared. After performing the slump and flow tests, cube specimens were cast and moist-cured for 3, 28, and 90 days and subjected to compression test, whereas 28-day moist-cured cylinder specimens were subjected to splitting tensile test. The test results have revealed that in spite of small reduction in strength with replacing cement by up to 20% of OWCM, the strength of the concrete remains within the designed strength grade ranges.

Index Terms—Oil-well cutting material, Fresh properties, Compressive strength, Splitting tensile strength, Environment-friendly concrete.

I. INTRODUCTION

The use of environment friendly materials in the engineering sector is a huge challenge. The environment is a major issue that must be addressed in all sectors, particularly engineering, because it has a direct impact on our lives.

Oil-well cutting material is formed during the drilling procedure of an oil-well. It has oil, heavy metals, biological

materials, and dirt in it. Thousands of cubic meters of oil-well cutting material can be created during the drilling operation of a single well (Ghazi, et al., 2011). The majority of drilling businesses keep this trash in open yards with no treatment. Environmental standards require cutting storage to be isolated to prevent pollution of surface and subsurface water. As a result, oil-well cutting material waste management has become an environmental issue with an accompanying expense for oil corporations.

Oil-well cutting materials, which are high in calcium oxide, silicon oxide, and aluminum oxide, might be used as a raw material in cement production. Furthermore, the oil content may aid in the reduction of fuel consumption during the calcination and clinkerization processes (Al Dhamri and Rashid, 2019). The cement industry accounts for roughly 5% of worldwide man-made CO₂ emissions, with the chemical process accounting for 50% and fuel combustion accounting for 40% (Mahasenan, Smith and Humphreys, 2003, Andrew, 2018). The cement industry emits about 900 kg of CO₂ for every 1000 kg of cement produced (Mehta, 2001, Rubenstein, 2012, Benhelal, et al., 2013).

The environmental friendliness of concrete cannot be fully appreciated without taking into account that the cement and concrete industries can provide ideal homes for using enormous quantities of waste produced from other industries. The cement and concrete industries are uniquely positioned to eliminate many wastes from the environment whereas receiving significant economic and technical benefits. The use of industrial by-products as replacements for natural materials is widely encouraged in construction, thus allowing residual materials to be recycled and valorized, whereas at the same time-saving natural resources and energy. In cement production, residual materials can be used as substitute fuels, raw materials, and supplementary cementing materials that replace by cement (Al Dhamri and Rashid, 2019).

Fly ash, ground granulated blast furnace slag, and silica fume are the most commonly used by-product materials in concrete as a cement replacement (Sata, Jaturapitakkul and Kiattikomol, 2007). The optimum percentage of these materials used in concrete as a cement replacement for obtaining best mechanical properties are 20%, 35%, and 15%, respectively (Mohamed and Najm, 2017) and (Hannesson, et al., 2012). The use of these by product materials in Portland cement concrete improves the performance of the concrete in

ARO-The Scientific Journal of Koya University
Vol. XI, No. 1 (2023), Article ID: ARO.10962. 7 pages
DOI: 10.14500/aro.10962

Received: 19 April 2022; Accepted: 26 January 2023

Regular research paper: Published: 25 February 2023

Corresponding author's e-mail: nabaz.salih@koyauniversity.org

Copyright © 2023 Nabaz S. Hussein, Rahel Kh. Ibrahim. This is

an open access article distributed under the Creative Commons Attribution License.



both the fresh and hardened states (Zabihi-Samani, Mokhtari and Raji 2018). Moreover, the other purpose of utilizing byproduct materials in concrete is to save money and getting environmental benefits. Using these materials in concrete mixtures will directly reduce the quantity of the cement used which leads to decreasing the emission of carbon dioxide and solving the disposal problems (Neville and Brooks, 1987) and (Chen, et al., 2010).

Petroleum and oil drilling companies manufacture many types of drilling fluid muds, which are employed as a carrier of rock cuttings from the earth layers during the drilling operation. This fluid mud's primary function is to pull cuttings to the surface for disposal during the drilling process, allowing the drilling operation to proceed deeper. Once the cuttings have been gathered at the surface, the combination of drilling fluid and earth cuttings is separated to remove the cuttings and allow the fluid to be reused in the drilling operation. This stage of segregation is repeated until the fluid can no longer be treated and must be discarded (Young, et al., 1991).

The disposed mud is known as oil-well cuttings material and collected in a mud waste dump. Because oil-well cutting material cuttings include oil, they are hazardous waste that should not be discharged into the environment without treatment and purification (Eldridge, 1996).

The cuttings include calcium, silica, and alumina, all of which are necessary components in the production of cement. Furthermore, the oil component provides the cuttings a calorific value, which may assist minimize fuel use during cement manufacturing. The use of these cuttings in cement would give an environmentally appropriate waste management. The extracted oil-well cutting material cannot be utilized directly in cement; yet, some pre-processing is necessary. The oil-well cutting material from drilling operations is wet material that contains a lot of water and maybe some oil. The cutting is initially transported to an especially designed-landfill. The cutting is first moved to a constructed landfill, which is open, exposed to direct sunlight, and generally located in the desert. First, the oil-well cutting material is simply let to dry in direct sunshine and high temperatures, and then, the sludge is transported to a semi-dry lined pit (Al-Maqbali, et al., 2016). The previous research focused on the use of oil-well cutting material beside the raw materials in the cement production process, whereas till the writing of the current research few published researches were existing regarding the use of oil-well cutting material as a cement replacement in concrete.

The current research focuses on replacing cement with oil-well cutting material which is a waste material produced from drilling Oil Wells to save the environment from this waste material from one side and to produce concrete that is friendlier to the environment than conventional concrete from the other side.

II. MATERIALS AND METHODS

Ordinary Portland cement type I (42.5 MPa) obtained from Mass Company was used in this research. The physical

properties and chemical composition of the cement used were summarized in Tables I and II, respectively.

The fine aggregate that was used in this research was natural river sand with a specific gravity of 2.7. Gravel with a maximum size of 12.5 mm and specific gravity of 2.67 was used as a coarse aggregate. The hyper plasticizer used in this research was polycarboxylate based under the trade name of Sika Viscocrete 5930.

The oil-well cutting material was obtained from Shewashok oil-well near Koya city/Erbil (Fig. 1a). The air-dried oil-well cutting material was milled in a rotary steel ball mill and sieved on sieve No. 200 (75 μ m) (Fig. 1b). Then, the sieved powder was burned at a temperature of 600°C, as shown in Fig. 1c for the calcination purposes and burning the organic materials. The chemical composition of the oil-well cutting material is shown in Table III.

The concrete mixture containing seven different percentages of oil-well cutting material as cement replacement (10%, 15%, 20%, 25%, 30%, 35%, and 40%) was prepared beside the control mixture for three different concrete strength grade range mixes A (25MPa), B (35MPa), and C (55MPa) having water-cement ratios (w/c) of 0.5, 0.4, and 0.32, respectively. All the mixes were designed according to (ACI211, 2011), after that trial mixes were made and corrected material quantities were determined.

The hyper plasticizer in the mixes having 0.4 and 0.32 water/cement ratio was used for maintaining proper

TABLE I
PHYSICAL PROPERTIES FOR THE USED CEMENT (MASSCOMPANY, 2021)

Physical properties	Test results
Fineness (specific surface) (cm ² /g)	3320
Specific gravity	3.17
Initial setting time (min)	100
Final setting time (min)	230
3 days compressive strength (MPa)	23
7 days compressive strength (MPa)	-
28 days compressive strength (MPa)	46.1

TABLE II
CHEMICAL COMPOSITIONS FOR THE USED CEMENT (MASSCOMPANY, 2021)

Chemical composition of the cement used.	Content (%)
SiO ₂	19.2
Al ₂ O ₃	4.6
Fe ₂ O ₃	2.6
CaO	61.5
MgO	3.5
SO ₃	2.5
K ₂ O	0.7
Na ₂ O	0.2
Equivalent Alkalies (Na ₂ O+0.658 K ₂ O)	0.66
Loss on ignition (L.O.I)	2.7
Lime saturation factor (L.S.F)	98.1
Free Lime (%)	1.0
Main compounds (Bogue's equations)	
C ₃ S	58.4
C ₂ S	11.1
C ₃ A	7.8
C ₄ AF	7.9

TABLE III
CHEMICAL COMPOSITIONS OF OIL-WELL CUTTING MATERIALS

Chemical compositions	Mass percentage
BaO	30.5
SO ₃	18.1
SiO ₂	15.4
TiO ₂	9.54
CaO	7.19
Al ₂ O ₃	3.26
Fe ₂ O ₃	2.83
MgO	2.74
ZrO ₂	2.48
V ₂ O ₅	1.98
Cl	1.22
K ₂ O	1.2
Other	3.56

workability. The mix proportions for 1 m³ of concrete for the mixes having a water-to-cement ratio of 0.5, 0.4, and 0.32 are shown in Tables IV-VI, respectively. The slump and flow tests were performed for all the mixes in accordance to (ASTM C143/C143M –05a) and (BS 1881: Part 105: 1984), respectively (ASTMC143, 2021) (BS1881, 1984).

From each concrete mix 9 (100*100*100) mm cubes and 3 (100*200 mm), cylinders were prepared. The cube specimens were immersed in water for 3, 28, and 90 days, whereas the cylinders were only immersed for 28 days. The compression test was carried out under the BS 1881: PART 116: 83, (BS1881:116, 1984), whereas the indirect tension was carried out under the (C78, 2002) standard. The experimental process for this study was carried out at the materials of construction laboratory of the Faculty of Engineering, Koya University. The trial mix and the sample preparation (cubes and cylinders) for compression and splitting tensile tests are shown in Fig. 2a-c, respectively.

III. RESULTS AND DISCUSSIONS

A. Workability

The slump and flow values for w/c ratios 0.5, 0.4, and 0.32 are shown in Tables VII-IX, respectively. The slump for the control mixes of 0.5, 0.4, and 0.32 w/c ratio was 200 mm, 210 mm, and 220 mm, whereas the flow values were 550, 553, and 560 mm, respectively. By adding Oil-well cutting material, a slight promotion in a slump was recorded. The slump promotion became more significant in higher rates of replacement for cement by oil-well cutting material. To remain the slump in a constant range for the concrete mixes, a hyper plasticizer was used. The slump increase in the mixtures containing oil-well cutting material can be attributed to the large particle size diameter of oil-well cutting materials which were larger than cement particles. As oil-well cutting material particles have a lower surface area than cement particles, lower water is needed for wetting the surface area; hence, excessive water can contribute to increasing the slump values for the concrete mixes. For the concrete mixes of (0.32 w/c ratio), the slump values were almost constant, whereas the flow showed a slight reduction. This behavior is due to

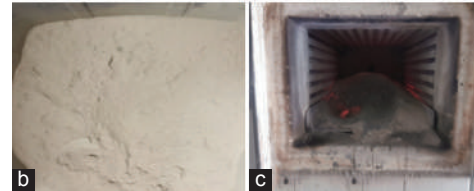


Fig. 1. (a) Oil-well cutting material (OWCM), (b) sieved OWCM, and (c) OWCM at the furnace.



Fig. 2. (a) Trial mix, (b) cube sample for compressive strength, and (c) cylinder sample for splitting tensile strength.

the technique of the flow test which depends on raising the flow table and dropping it, that the lower cohesiveness of the concrete mixes with higher replacement rates of oil-well cutting material plays the role.

B. Mechanical Properties

Compressive strength

Figs. 3-5 display the compressive strength results for grade A, B, and C concrete cubes having w/c ratios of 0.5, 0.4, and 0.32 and moist cured for 3, 28, and 90 days, respectively. The results show that the addition of oil-well cutting materials reduces compressive strength for all curing regimes when compared to the control specimen. The decrease in strength rises when the amounts of oil-well cutting materials are increased. By extending the curing period, all of the specimens achieve greater strength results. The strength reduction for grade A (0.5 w/c ratio) concrete at 3 days with 10%, 15%, 20%, 25%, 30%, 35%, and 40% of oil-well cutting materials as a cement replacement were 4.3%, 5%, 11.5%, 15%, 24.6%, 29%, and 39%, respectively. For 28 days, the strength reductions with 10%, 15%, 20%,

TABLE IV
MIX PROPORTIONS FOR 1 M³ CONCRETE FOR WATER CEMENT RATIO 0.5 GRADE A

Sample name	% Oil-well cutting materials	Water (Kg)	Superplasticizer	Cement (Kg)	Oil-well cutting materials (Kg)	Sand (Kg)	Gravel (Kg)
A0	0	200	0	400	0	640	1000
A10	10	200	0	360	40	640	1000
A15	15	200	0	340	60	640	1000
A20	20	200	0	320	80	640	1000
A25	25	200	0	300	100	640	1000
A30	30	200	0	280	120	640	1000
A35	35	200	0	260	140	640	1000
A40	40	200	0	240	160	640	1000

TABLE V
MIX PROPORTIONS FOR 1 M³ CONCRETE FOR WATER CEMENT RATIO 0.4 GRADE B

Sample name	% Oil-well cutting materials	Water (Kg)	Superplasticizer	Cement (Kg)	Oil-well cutting materials (Kg)	Sand (Kg)	Gravel (Kg)
B0	0	180	1.35	450	0	500	1130
B10	10	180	1.35	405	45	500	1130
B15	15	180	1.35	382.5	67.5	500	1130
B20	20	180	1.35	360	90	500	1130
B25	25	180	1.35	337.5	112.5	500	1130
B30	30	180	1.35	315	135	500	1130
B35	35	180	1.35	292.5	157.5	500	1130
B40	40	180	1.35	270	180	500	1130

TABLE VI
MIX PROPORTIONS FOR 1 M³ CONCRETE FOR WATER CEMENT RATIO 0.32 GRADE C

Sample name	% Oil-well cutting materials	Water (Kg)	Superplasticizer (kg)	Cement (Kg)	Oil-well cutting materials (Kg)	Sand (Kg)	Gravel (Kg)
C0	0	160	3.6	500	0	560	1150
C10	10	160	3.6	450	50	560	1150
C15	15	160	3.6	425	75	560	1150
C20	20	160	3.6	400	100	560	1150
C25	25	160	3.6	375	125	560	1150
C30	30	160	3.6	350	150	560	1150
C35	35	160	3.6	325	175	560	1150
C40	40	160	3.6	300	200	560	1150

TABLE VII
SLUMP AND FLOW VALUES FOR MIXES WITH 0.5 w/c RATIO

Sample	% oil-well cutting materials	Slump (mm)	Flow (mm)
A0	0	200	550
A10	10	200	550
A15	15	200	550
A20	20	200	550
A25	25	200	550
A30	30	215	560
A35	35	215	560
A40	40	215	570

TABLE IX
SLUMP VALUE FOR MIXES WITH 0.32 w/c RATIO

Sample	% oil-well cutting materials	Slump (mm)	Flow (mm)
C0	0	220	570
C10	10	210	550
C15	15	210	550
C20	20	210	550
C25	25	220	530
C30	30	220	530
C35	35	220	530
C40	40	220	530

TABLE VIII
SLUMP VALUE FOR MIXES WITH 0.4 w/c RATIO

Sample	% oil-well cutting materials	Slump (mm)	Flow (mm)
B0	0	210	553
B10	10	220	560
B15	15	210	570
B20	20	210	570
B25	25	210	570
B30	30	210	570
B35	35	210	570
B40	40	210	560

25%, 30%, 35%, and 40% of oil-well cutting materials as a cement replacement were 1.7%, 6%, 15.8%, 18.8%, 29.4%, 30.46%, and 44.1%, respectively. However, the compressive strength reductions after 90 days of moist curing with 10%, 15%, 20%, 25%, 30%, 35%, and 40% of oil-well cutting materials as a cement replacement were 3.65%, 10.85%, 16%, 23.78%, 25.7%, 34.39%, and 42.2%, respectively.

For grade B concrete that has a 0.4 w/c ratio, the strength reduction at 3 days with 10%, 15%, 20%, 25%, 30%, 35%, and 40% of oil-well cutting materials as a cement

replacement were 7.8%, 11.8%, 21.8%, 29.2%, 39.68%, 44.24%, and 44%, respectively. For 28 days, the strength reductions with 10%, 15%, 20%, 25%, 30%, 35%, and 40%

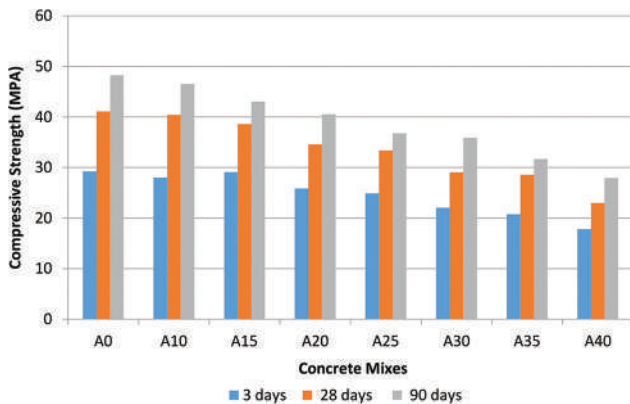


Fig. 3. Compressive strength for grade A concrete containing different percentages of oil-well cutting material made with 0.5 w/c ratio and moist cured for 3, 28, and 90 days.

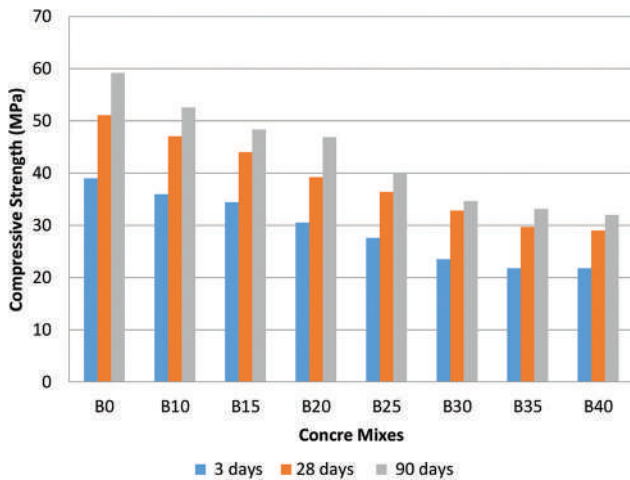


Fig. 4. Compressive strength for grade B concrete containing different percentages of oil-well cutting material made with 0.4 w/c ratio and moist cured for 3, 28, and 90 days.

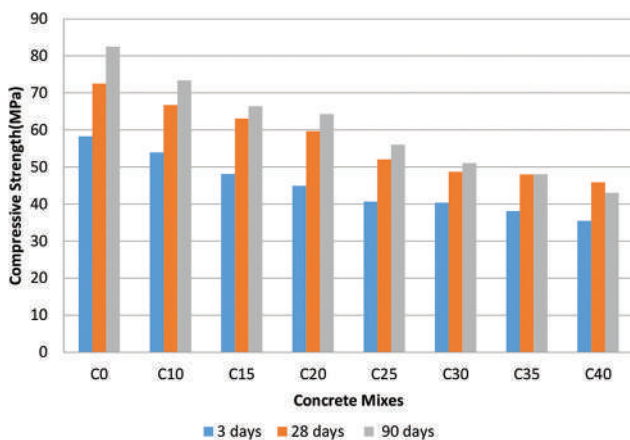


Fig. 5. Compressive strength for grade C concrete containing different percentages of oil-well cutting material made with 0.32 w/c ratio and moist cured for 3, 28, and 90 days.

of oil-well cutting materials as a cement replacement were 7.9%, 13.9%, 23.3%, 28.8%, 35.8%, 41.5%, and 43.1%, respectively. However, the compressive strength reductions at 90 days with 10%, 15%, 20%, 25%, 30%, 35%, and 40% of oil-well cutting materials as a cement replacement were 11%, 18%, 20.8%, 32%, 41%, 44%, and 45.5%, respectively.

The strength reduction for grad C concrete with 0.32 w/c ratio after 3 days of moist curing with 10%, 15%, 20%, 25%, 30%, 35%, and 40% of oil-well cutting materials as a cement replacement were 7.5%, 17.5%, 23%, 30.27%, 30.8%, 34.67%, and 39.1%, respectively. For 28 days, the strength reductions with 10%, 15%, 20%, 25%, 30%, 35%, and 40% of oil-well cutting material as a cement replacement were 7.9%, 13%, 17.72%, 28.24%, 32.57%, 33.86%, and 36.72%, respectively. However, the compressive strength reductions at 90 days with 10%, 15%, 20%, 25%, 30%, 35%, and 40% of oil-well cutting materials as a cement replacement were 11%, 19.5%, 22%, 32%, 38%, 41.74%, and 47.8%, respectively.

The reduction in compressive strength was less pronounced for lower replacement ranges in all concrete strength grades. The lower strength grades showed lower strength reduction than the higher strength grades. The higher the w/c ratio the lower reduction was recorded, in a way that with up to 25% replacement percentages, the strength remained within the designed strength grade range. The previous behavior of concrete is because the oil-well cutting material is working only as filler in concrete without having any pozzolanic activity for enhancing the compressive strength.

Tensile strength

The splitting tensile strength results for 28 days of moist cured cylinders are shown in Figs. 6-8, respectively. When compared to the control specimen, all of the specimens containing oil-well cutting materials have a lower splitting tensile strength. When the replacement percentages are raised, the loss in strength becomes more pronounced. For 0.5 water-cement ratio, the tensile strength reduction with 10%, 15%, 20%, 25%, 30%, 35%, and 40% of oil-well cutting materials as a cement replacement were 7%, 20.2%, 22.65%, 23.53%, 25.8%, 26.2%, and 27%, respectively.

For 0.4 water-cement ratio, the tensile strength reduction with 10%, 15%, 20%, 25%, 30%, 35%, and 40% of oil-well

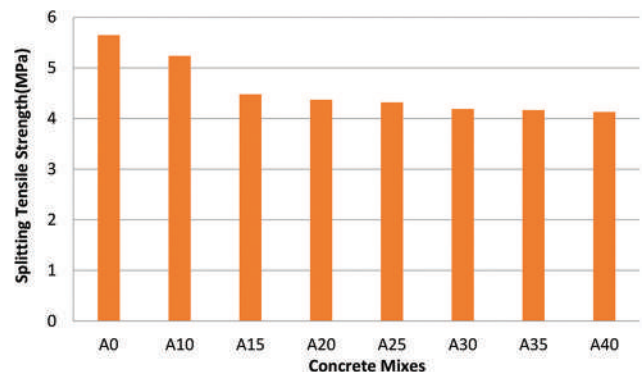


Fig. 6. Splitting tensile strength of Grade A concrete containing different percentages of oil-well cutting material made with 0.5 w/c ratio and moist cured for 28 days.

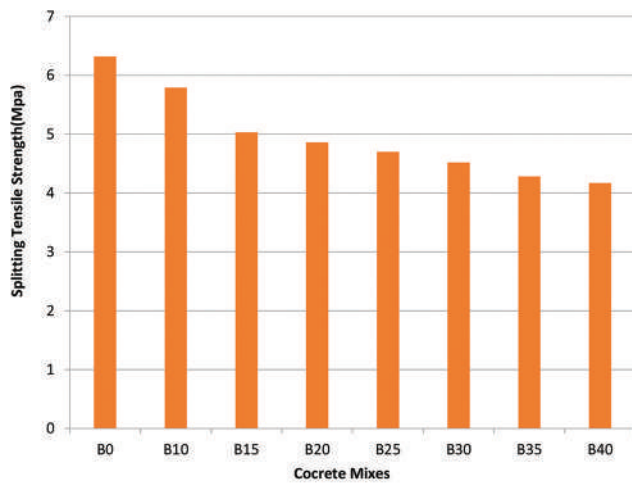


Fig. 7. Splitting tensile strength of Grade B concrete containing different percentages of oil-well cutting material made with 0.4 w/c ratio and moist cured for 28 days.

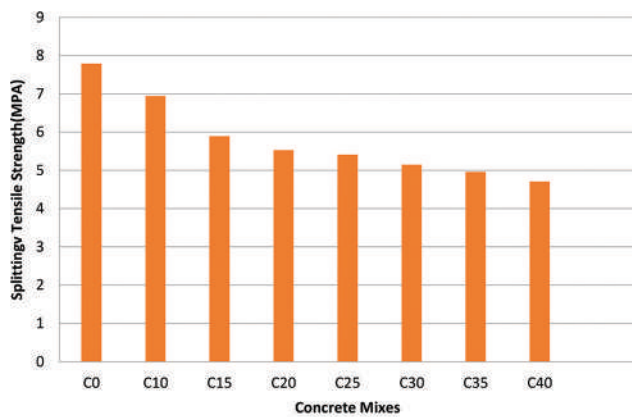


Fig. 8. Splitting tensile strength of Grade C concrete containing different percentages of oil-well cutting material made with 0.32 w/c ratio and moist cured for 28 days.

cutting materials as a cement replacement were 8%, 20%, 23%, 23.53%, 28%, 33.5%, and 34%, respectively.

For the 0.32 water-cement ratio, the tensile strength reduction with 10%, 15%, 20%, 25%, 30%, 35%, and 40% of oil-well cutting materials as a cement replacement were 11%, 24%, 29%, 30%, 34%, 36%, and 49%, respectively.

The reduction in splitting tensile strength rates was almost the same for grade A and B concretes, whereas grade C concrete showed somewhat less reduction rates. The reduction rates in splitting tensile strength were lower than that of compressive strength in higher replacement percentages.

IV. CONCLUSION

This research focuses on replacing cement with oil-well cutting material which is a waste material produced from drilling oil wells to save the environment from this waste material and produce concrete that is friendlier to the environment than the conventional concrete. From the

experiment performed and the results obtained, the following conclusions can be drawn:

- Oil-well cutting material can be used in concrete as a cement replacement for producing concrete that is friendlier to the environment than conventional concrete.
- Replacing up to 20% of cement with oil-well cutting material results in a decrease in both compressive and splitting tensile strengths for all mixes in a manner that the strength remains within the designed strength grade ranges for compressive strength.
- Replacement rates higher than 20% result in significant strength reduction.
- The strength in lower w/c ratios for the replacement percentages is more acceptable than the higher w/c ratios.

REFERENCES

ACI 211.1-91., 2019. Standard Practice for Selecting Proportions for Normal, Heavyweight, and Mass Concrete, no. 9. ACI, Unites States, pp. 120-121.

ASTM C143/ C143M-20., 2021. Standard Test Method for Slump of Hydraulic-Cement Concrete. ASTM, United States.

Al-Maqbali, A., Feroz, S., Ram, G., and Al-Dhamri, H., 2016. Feasibility study on spent pot lining (SPL) as raw material in cement manufacture process. *International Journal of Environmental Chemistry*, 2, pp.18-26.

Andrew, R.M., 2018. Global CO₂ emissions from cement production. *Earth System Science Data*, 10, pp. 195-217.

ASTM C143/ C143M-20., 2021. *Standard Test Method for Slump of Hydraulic-Cement Concrete*. ASTM, United States.

ASTM., 2015. C78, A. 04.15 *Standard Test Method for Flexural Strength of Concrete* (Using Simple Beam with Third-Points Loading. ASTM, United States, 2015.

Al Dhamri, H.S.R., and Rashid, H.S., 2019. *Oil-based Mud Cuttings as Additional Raw Material in Clinker and Cement Production*. University of Leeds, United Kingdom.

Benhelal, E., Zahedi, G., Shamsaei, E., and Bahadori, A., 2013. Global strategies and potentials to curb CO₂ emissions in cement industry. *Journal of Cleaner Production*, 51, pp.142-161.

BS-1881:120., 1984. Testing Concrete Part 120. *Method for Determination of the Compressive Strength of Concrete Cores*. British Standard Institution, London.

BS 1881: 105: 84., 1984. Testing Concrete. *Method for Determination of Flow*. British Standards Institution London, UK.

Chen, C., Habert, G., Bouzidi, Y. and Jullien, A., 2010. Environmental impact of cement production: Detail of the different processes and cement plant variability evaluation. *Journal of Cleaner Production*, 18, pp. 478-485.

Eldridge, R.B., 1996. Oil contaminant removal from drill cuttings by supercritical extraction. *Industrial and Engineering Chemistry Research*, 35(6), 1901-1905.

Ghazi, M., Quaranta, G., Duplay, J., Hadjamor, R., Khodja, M., Amar, H.A., and Kessaissia, Z., 2011. Life-cycle impact assessment of oil drilling mud system in Algerian arid area. *Resources, Conservation and Recycling*, 55, 1222-1231.

Hannesson, G., Kuder, K., Shogren, R. and Lehman, D., 2012. The influence of high volume of fly ash and slag on the compressive strength of self-consolidating concrete. *Construction and Building Materials*, 30, pp. 161-168.

Mahasanen, N., Smith, S., and Humphreys, K., 2003. *The Cement Industry and Global Climate Change: Current and Potential Future Cement Industry CO₂ Emissions*. *Greenhouse Gas Control Technologies-6th International Conference*, Elsevier, Netherlands, pp.995-1000.

MASSCOMPANY., 2021. *Physical and Chemical Properties of Ordinary Portland Cement*. Bazyan.

Mehta, P.K., 2001. Reducing the environmental impact of concrete. *Concrete International*, 23(10), pp.61-66.

Mohamed, O. A. and Najm, O. F., 2017. Compressive strength and stability of sustainable self-consolidating concrete containing fly ash, silica fume, and GGBS. *Frontiers of Structural and Civil Engineering*, 11, pp. 406-411.

Neville, A. M. and Brooks, J. J., 1987. *Concrete Technology*. Longman Scientific and Technical England, UK

Rubenstein, M., 2012. *Emissions from the Cement Industry*. State of the Planet,

United Kingdom.

Sata, V., Jaturapitakkul, C., and Kiattikomol, K., 2007. Influence of pozzolan from various by-product materials on mechanical properties of high-strength concrete. *Construction and Building Materials*, 21(7), pp.1589-1598.

Young, G., Growcock, F., Talbot, K., Lees, J., and Worrell, B., 1991. *Elements of Thermally Treating Oil-Base Mud Cuttings*. SPE/IADC Drilling Conference, OnePetro.

Zabihi-Samani, M., Mokhtari, S.P., and Raji, F., 2018. Effects of fly ash on mechanical properties of concrete. *Journal of Applied Engineering Sciences*, 8(2), pp.35-40.

Geomorphic Indicators of Folds Lateral Growth Using Satellite Images: Sulaimaniyah Vicinity in Kurdistan Region of Iraq

Varoujan K. Sissakian¹, Lanja H. Abdullah², and Balanbo N. Abdulkareem³

¹Department of Petroleum Engineering, Komar University of Science and Technology, Sulaymaniyah, Kurdistan region – F.R. Iraq

²Department of Geology, College of Science, University of Sulaimani, Sulaymaniyah, Kurdistan region – F.R. Iraq

³Department of Geological Survey, Kurdistan Regional Government, Ministry of Natural Resources, Sulaimanyah Oil and Mineral Directorate, Sulaymaniyah, Kurdistan region – F.R. Iraq

Abstract—Visual interpretation of satellite images is a very significant technique to recognize and interpret structural features, which indicate lateral growth of folds, the origin of folds, and dating of folds using the exposure dating method. In this study, Landsat 8 (ESSRI) and Google Earth images are used to recognize structural features at Pira Magroon, Surdash, and Azmar anticlines in the Sulaimaniyah vicinity, Kurdistan Region, north of Iraq. The mentioned anticlines are outstanding geomorphological and structural features in the Sulaimaniyah vicinity. The recognized and interpreted structural features include: en-echelon folding, domes, and Neotectonic indication. All these features are discussed in detail with many images to show the discussed cases, most of the interpreted data and presented figures are never mentioned previously.

Index Terms—Domes, En-echelon fold, Lateral growth, Neotectonic indications.

I. INTRODUCTION

The northeastern part of the Arabian Plate is occupied by the Kurdistan Region of Iraq (KRI). The plate is in collision with the Iranian Plate with convergent tectonic plate boundary (e.g., Alavi, 2004, Allen, et al., 2004; Fouad, 2015). In tectonically active areas, such as the KRI, the lateral growth of anticlines is a very common phenomenon (e.g., Blanc, et al., 2003, Bennett, et al., 2005, Ramsey, Walker and Jackson, 2008). The anticlines in this tectonically active area show different significant geomorphological and structural features which indicate the lateral growth of those folds.

The developed landscape and the drainage patterns provide indirect information on the tectonic activity (e.g., Bretis, Bartl and Grasemann, 2011; Burbank and Pinter, 1999; Burbank and Anderson, 2001; Keller, Gurrola and Tierney, 1999; Collignon, et al., 2016).

The mountain building and landscape evolution are controlled by interactions between river dynamics and tectonic forces (Collignon, et al., 2016). The described criteria by Keller, Gurrola and Tierney (1999); Ramsey, Walker and Jackson (2008), Fossen (2020), and Grasemann and Scholholz (2012) can be used to evaluate fold growth, among those criteria are: (1) The deformation of progressively younger deposits or landforms, (2) the development of characteristic asymmetric drainage patterns, (3) the development of domes within folds, and (4) the development of en-echelon plunges withing anticlines.

The Pira Magroon, Surdash–Sara, and Azmar are three main anticlines in the Sulaimaniyah vicinity, located around Sulaimaniyah city, in the northwest, north, and northeast of the city (Fig. 1).

We have reviewed many scientific reports and articles which were published concerning the studied area and the High Folded Zone. Those which dealt with the current work are mentioned briefly hereinafter. Colman-Saad (1978) showed that the simply folded belt of the Zagros Mountains has undergone folding from Miocene to recent time. He added that “Structures in the Competent group are typical of parallel folds formed by buckling and developed by a combination of flexural-slip and neutral-surface mechanisms.”

In the studied area, there is a main competent group formed by the rocks of the Kometan and Qamchuqa formations. Ameen (1991) implied the presence of a decollement horizon at or near the base of the sedimentary cover, the “Infra-Cambrian Hormuz Salt” and a passive role of the Precambrian basement in the tectonic evolution of the folded belt. Structural, stratigraphic, geophysical, and remote sensing evidence suggests that forced folding, due to faulting in the basement, has played a significant role in the development of

ARO-The Scientific Journal of Koya University
Vol. XI, No. 1 (2023), Article ID: ARO.11010. 9 pages
DOI: 10.14500/aro.11010

Received: 22 June 2022; Accepted: 22 February 2023
Regular research paper: Published: 23 March 2023

Corresponding author's e-mail: varoujan.sissakian@komar.edu.iq
Copyright © 2023 Varoujan K. Sissakian, Lanja H. Abdullah and Balanbo N. Abdulkareem. This is an open access article distributed under the Creative Commons Attribution License.



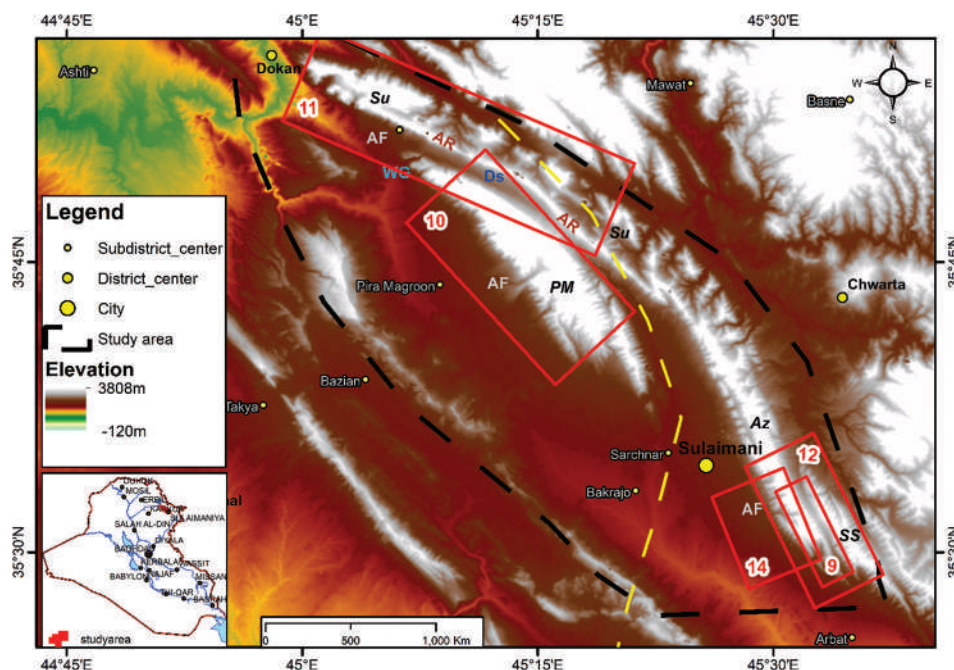


Fig. 1. Satellite image showing the location of the studied area; approximately limited by the black dashed line. Anticlines, PM=Pira Magroon, Su=Surdash, Az=Azmar, SS=Said Sadiq, AF=Alluvial fan, DS=Dissected slopes, AR=Anticlinal ridges, WG=Water gap, the yellow dashed line represents the approximate location of a paleo ridge.

many of the folds in this region. No comment can be added to this study since it is a surface study that mainly dealt with the acquired data from the interpretation of satellite images and field check. Blanc, et al. (2003) showed that the NW – SE-trending folds and thrusts in the Simple Folded Zone are shortened by right-lateral strike-slip fault on the NW – SE-trending main recent fault. The geometries of exposed structures suggest both basement thrusts and thin-skinned decollement levels, with major folds possibly nucleated above basement faults. Since the present study deals with the surface structural expressions; therefore, we cannot assure or otherwise the presented data. Bretis, Bartl and Grasmann (2011) focused on the interaction of the transient development of drainage patterns along growing antiforms, as this directly reflects the kinematics of progressive fold growth. We have interpreted many water and wind gaps along the studied anticlines, which confirm the growth of the anticlines under consideration. Omar (2011) studied the minor fold in the Azmar Anticlinorium and showed that the process involved both buckling and homogeneous flattening mechanisms. We also have interpreted such data, especially along the Azmar anticline, this is mainly due to the exposed homogeneous rocks of the Kometan and Balambo formations. A semi-detailed geological mapping was conducted for an area northwest of Sulaimaniyah covering Pira Magroon anticlines and part of the Surdash anticline (Sissakian and Al-Jiburi, 2014; Sissakian and Al-Jiburi, 2014). Zebari (2013) studied the geometry and evolution of the fold structures within the HFZ, he suggested that the folds are transitional between fault-bend folds and fault propagation folds. Karim, Bety and Khanaqa (2015) described the actual structural setting of the Azmar–Goizha anticline, they changed the previous piggy-

back thrust imbricated fan to a nearly isoclinal detachment fold. We have recognized many small double plunging folds with the en-echelon pattern within the main Azmar and Goizah anticlines, some of them are isoclinal. Burberry (2015) defined the relationship between the basement faults and surface structures, facies, and source-rock maturity through time. Omar, Lawa and Sulaiman (2015) found an imprint between tectonostratigraphic and structural with balanced sections in the studied area. Karim and Khanaqa (2017) studied the southeastern part of Pira Magroon anticline stratigraphically and structurally, they used nannofossils for the aging of intervals, and they showed that it is an asymmetrical anticline with a southwest plunge mainly in a few places, while it changes to overturned fold in others and is deformed by reverse fault. We also have recognized different fault types within the Pira Magroon anticline. Mohammed, Al-Kubaisi and Bety (2018) estimated the tectonic activity of the Pira Magroon anticline by calculating three geomorphic indices of three-sub-basins which were identified as very high, high, and moderate levels. Ahmed (2019) classified the anticlines in Zagros Fold Belt according to the orientation of compression stress, among these are Azmar, Pira Magroon, and Surdash anticlines. Karim, Khanaqa and Ismail (2020) mentioned the role of facies changes in shifting the trend of the anticlines in Zagros Fold-Thrust Belt (ZFTB).

The present study aims to describe the recognized significant structural features which are developed within the Pira Magroon, Surdash–Sara, and Azmar anticlines. Moreover, the present study aims to shed light on the relationship between the surface and subsurface tectonic and structural styles and the role of the basement depth and existing faults in the basement on the developed surface anticlines. The

visually interpreted and presented data can be used in similar studies, which use the visual interpretation of satellite images to recognize geomorphological and structural forms.

II. MATERIALS AND METHODS

The studied area is one of the most studied parts of the Iraqi Kurdistan Region; therefore, there are tens of published scientific articles, post graduate theses, which dealt with different geological aspects; some of those articles are reviewed and relevant data are acquired to confirm the visually interpreted data from the satellite images, some of them were confirmed by field check. Besides those articles, we have interpreted different satellite images (Google Earth, and Esri satellite image) to elucidate different geological features; mainly structural and some geomorphological. Most of the recently elucidated features were checked in the field by continuous field inspections through 2018–2021.

III. GEOLOGICAL SETTING

The geological setting of the studied area is briefly described. We have used the best available data in the description of Geomorphology, Structural geology, Tectonics, and Stratigraphy.

A. Geomorphology

The studied area is located physiographically in the High Mountainous Province which is characterized by rugged mountains and narrow valleys (Sissakian, Kadhum and Abdul Jab'bar, 2014). The main geomorphological units in the studied area are as follows:

Units of alluvial origin

Different types of alluvial fans were recognized, like old, and dormant (Fig. 2a), usually covered by a mantle of calcrete (Fig. 2b), others are small and still active; coalesced together forming bajada (Fig. 3). Valley fill and flood plain sediments (Fig. 4a) are well developed along the mainstream and valleys, such as Qash Qooly, Charmaga, Merga Pan (Shadala), Tabin, and Zewe, the size of the pebbles may reach 1 m or even more.

Units of structural

Denudational Origin: Among these units are anticlinal ridges (Fig. 1), which extend for a few kilometers. Flat Irons are well developed in Kometan and Qamchuqa formations, they reach a few hundred meters in height (Fig. 4b), and



Fig. 2. (a) Old alluvial fan at Jasana gorge in Surdash anticline and (b) calcrete cover of an old alluvial fan in Surdash anticline.

dissected slopes (Fig. 3) are developed in soft rocks, such as the Shiranish, Tanjero, Kolosh, and Gercus formations.

Units of karstification origin

The most common units are the caves (Fig. 5a) and solution holes (Fig. 5b). Both are developed in rocks of the Qamchuqa and Pila Spi formations.

B. Stratigraphy

The exposed geological formations in the studied area range in age from Jurassic to Eocene, they are presented in the geological map (Fig. 6) and a columnar stratigraphic section (Fig. 7), based on Sissakian and Al-Jiburi (2014).

C. Tectonic and Structural Geology

The studied area is located in the high folded zone of the outer platform which belongs to the Arabian Plate (Fouad, 2015). Moreover, it is part of the ZFTB which is developed within the Zagros Foreland Basin (Alavi, 2004, and Fouad, 2015).

The High Folded Zone is characterized by long anticlines and narrow synclines (Jassim and Goff, 2006). Three main anticlines exist in the studied area: Pera Magroon, Surdash (Sara), and Azmar. Although some local names are used by many researchers; however, we will call them as aforementioned. They all are oriented in NW – SE direction and the southwestern limb is steeper. Tens of faults of different types are developed along the three main anticlines with different displacements. The beds are highly deformed and crushed (Fig. 8). Among the faults are those which have formed Zewe gorge; in the Pera Magroon anticline and Jasana and Qamchuqa gorges in the Surdash anticline. The displacements are around a few tens of meters.

IV. RESULTS

From the interpretation of different types of satellite images, geological maps, and field investigations in the studied area, we found the following structural and Neotectonic forms. Besides the presence of anticlines, synclines, and different types of faults, we have recognized the following structural features, they all confirm the lateral growth of the anticlines in the study area.

A. Domes

The presence of dome(s) in an anticline is a good indication of its lateral growth (Blanc, et al., 2003; Bennett, et al., 2005). In the studied area, all anticlines show doming; some of them are already grouped due to the lateral growth of the anticline (Figs. 9-11). Grasemann and Schmalholz (2012) mentioned that growing folds can join each other forming one single fold, and this is the case in Pira Magroon and Surdash anticlines. In the Azmar anticline, the domes and successive anticlines and synclines are common (Fig. 9).

B. En-echelon Plunges

Anticlines showing en-echelon plunges are exhibiting lateral growth (Keller and Pinter, 2002; Ramsey, Walker

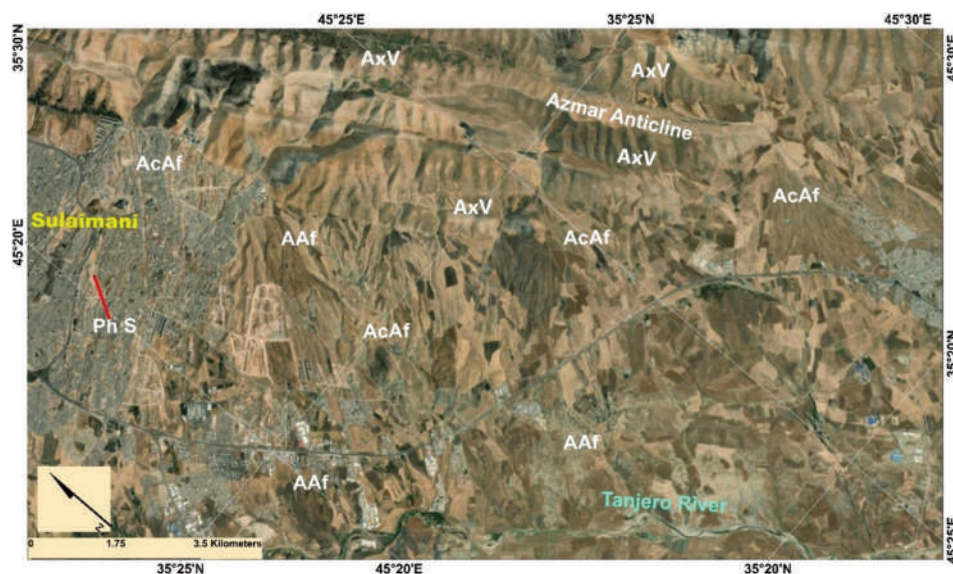


Fig. 3. Esri satellite image of alluvial fans in Azmar anticline for abandoned (AAf) and active (recent) fans (AcAf), AxV=Axial valley, PhS=Approximate site of the field photos (Fig. 15).

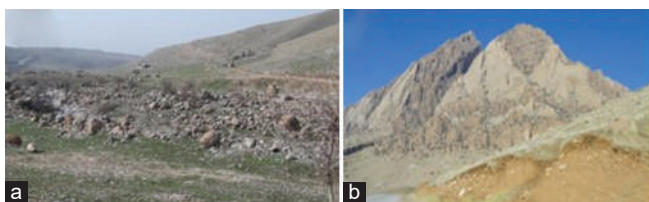


Fig. 4. (a) Valley fill sediments in Zewe Valley, Pira Magroon anticline and (b) Flat irons in the Qamchuqa Formation, Surdash anticline.



Fig. 5. (a) Jasana Cave, Surdash anticline, and (b) Solution holes in the carbonates of the Pila Spi Formation at the southwestern limb of Pera Magroon anticline.

and Jackson, 2008; Fossen, 2010). In the studied area, all anticlines exhibit en-echelon plunges; either totally separated from the neighboring anticline, as Pira Magroon and Sulaymaniyah anticlines (Fig. 6), Surdash and Khalakan anticlines, within the same anticline as in the Azmar anticline (Fig. 12), and within the same range; as Azmar and Surdash anticlines (Fig. 13).

C. Neotectonic Indications

Indications for neotectonic activities in the studied area are very common; however, we have selected a very clear indication from the east of Sulaymaniyah city within the old and recent alluvial fans (Fig. 14). The directions of old alluvial fans are different from the recent and active alluvial fans, and even they are dissecting indicating tilting of the slopes of the main foothills. Furthermore, the tilting of

old alluvial fans' sediments was seen at a construction site (Fig. 15).

The recent and abandoned old alluvial fans are distinguished based on the outcrop dating method (Burbank and Anderson, 2001). The feeder channels are used to distinguish between both types since the abandoned feeder channels (Fig. 14) are not following the regional gradient, which means that there is tilting in the area after the deposition of the old alluvial fans, accordingly, they were abandoned. In Fig. 12, the semestral fault is older than the developed alluvial fan. This is indicated by the location of the feeder channel which runs through the fault.

V. DISCUSSION

The anticlines in the Iraqi Kurdistan Region are still active and exhibit later growth (propagation) as witnessed by the presence of different geomorphological and structural forms; some of those indications are presented in the current research. The anticlines accompanied by synclines in the study area are developed due to the clockwise movement of the Arabian Plate and its collision with the Eurasian Plate forming a convergent tectonic plate boundary (Alavi, 2004, Allen, et al., 2004).

The exerted forces due to the collision of the plates have developed regional thrust faults and another local thrust, reverse, normal, and strike-slip faults. The structural style of the studied area and indications for the lateral growth mentioned in the present study is discussed hereinafter.

A. Structural Style

The studied area is a part of the High Folded Zone that belongs to the ZFTB; therefore, the folds are oriented generally in NW – SE trend with minor deviation to NWW – SEE trend (Figs. 1 and 6). Karim, Khanaqa and Ismail (2020) mentioned that the deviations in the folds

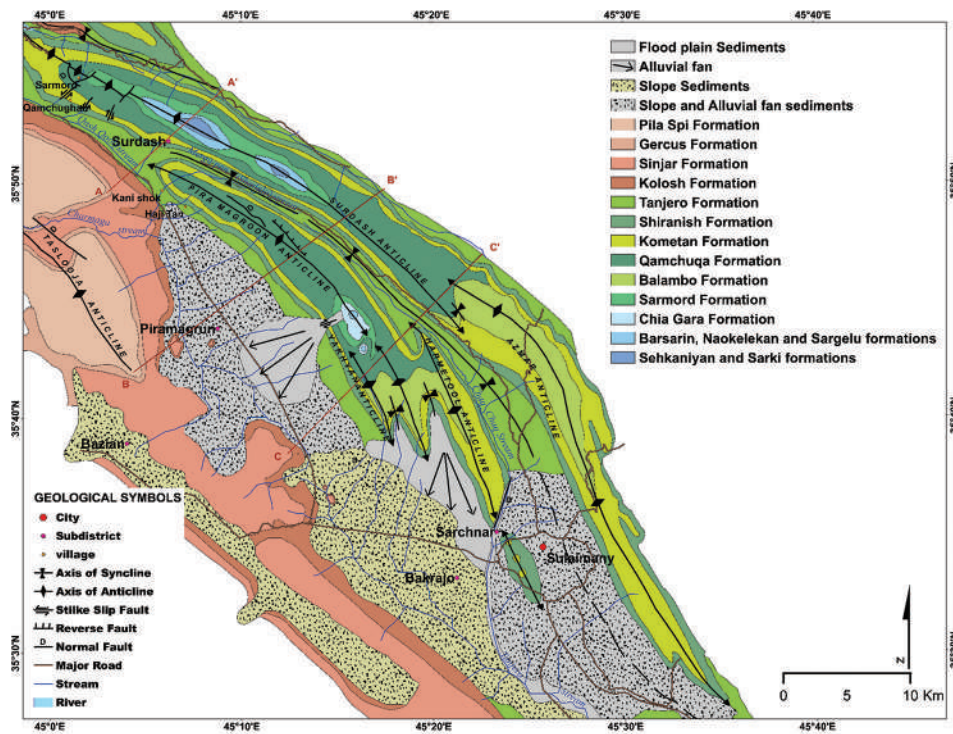


Fig. 6. Geological Map of the studied area (Modified from Sissakian and Fouad, 2015).

Formations	Age	Thickness (m)	Lithology	Lithologic description	
Pila Spi	U.Eocene	60		Well bedded limestone and dolostone with rare marl.	
Gercus	Eocene	110		Red elastic including clay stone, siltstone, sandstone and rare pebbles.	
Sinjar	L.Eocene L.Paleocene	80		Well bedded limestone and very rarely dolomitic.	
Kolosh	Paleocene	70		Black elastic including shale, sandstone and rare conglomerate.	
Tanjero	Upper Cretaceous	350		Olive green elastic including claystone, sandstone, shale and conglomerate occasionally with pillow like structure.	
Shiranish		200		Bluish grey soft papery marle underlain by thinly bedded of marly limestone.	
Kometan	Lower Cretaceous	170		Well thinly bedded marly limestone.	
Qamchuqa		650		Massive and thickly bedded limestone and dolostone.	
Balambo		330		Interbedding of crystalline limestone and dark blue papery shale.	
Sarmord		300		Interbedding of soft marl and hard limestone and dolostone.	
Chia Gara		L.Cretaceous U.Jurassic	160		Thinly bedded of limestone and dolostone with black bituminous shale.
Bersarin		Jurassic	16		Thickly bedded limestone and dolostone with stromatolite.

Fig. 7. Columnar stratigraphic section of the exposed formations in the study area (After Sissakian and Fouad, 2015).

are mainly due to facial changes. Although their study area is larger than the present study area and the minor folds are out of the studied area; however, we are in full accordance with them about the role of the facial changes in the deviations of the folds from the main trend. A good example is at the plunge area between Azmar and Surdash anticlines (Figs. 1, 6, 13), where the main facial change occurs between the Balambo (Basinal environment) and



Fig. 8. Disturbed beds due to folding and faulting, (a) Pira Magroon anticline and (b) Surdash anticline.

the Qamchuqa (Neritic environment) formations and the hardness of their rocks and thickness changes. However, the main deviation is slightly west of the concerned location. The type of the rocks also has contributed to the development of M-shaped parasitic Azmar anticline with many minor successive anticlines and synclines (Fig. 14) which have mainly very tight hinge lines (Points A and S, Fig. 14). The compressional forces exerted from the collision of the Arabian and Eurasian plates, besides the thrusting of the ophiolite bodies at Mawat Massif (20 km NE wards) have played a big role in the development of the parasitic fold system in the Azmar anticline, especially with the exposed monotonous ductile and incompetent rock types of marly limestone and marl.

The width of the anticlines of the studied area is also an interesting feature, especially the southwestern limb of the Pira Magroon anticline (Figs. 1, 6, 16). This is attributed to the minor folding within the Shiranish, Tanjero, Kolosh, Sinjar, and Gercus formations, besides the retreating of the main cliff of the Sinjar Formation due to continuous sliding (Fig. 17a).

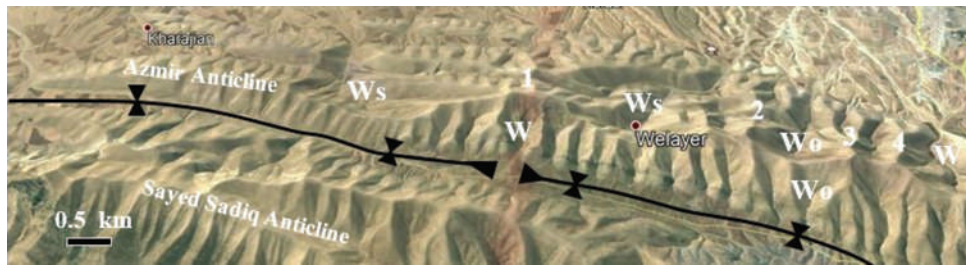


Fig. 9. Satellite images of Azmir anticline facing southeast showing possible domes at points 1, 2, 3, and 4 and many wine glasses (W), Wo=Opposite wine glass, and Ws=Successive wine glass, which are indications for the lateral growth of the anticline.



Fig. 10. Satellite image of Pira Magroon anticline facing SE. Note the domes of Pira Magroon anticline. Also note the absence of the Qamchuqa Formation left of point 1.



Fig. 11. Satellite image of Surdash anticline facing SE. Note the domes of the Surdash anticline. Also, note overturned beds at points 1 and 2.

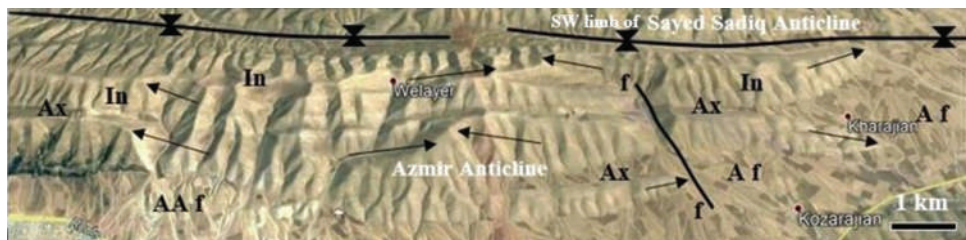


Fig. 12. Satellite image of Azmir anticline facing NE. The arrows point to plunges of minor folds, f – f is a sinistral fault. Different valleys: In=Inclined, Ax=Axial, AAf=Abandoned alluvial fan, Af=Active alluvial fan, all are indications of lateral growth of the anticline.



Fig. 13. Field photo, southeastern plunge of the Surdash anticline. Note the local syncline between the Surdash and Azmar anticlines. In the background is the Pira Magroon anticline.

The presence of isolated hills (which may attain 60 m in height) capped by the hard limestone of the Sinjar Formation (Fig. 6) is a good indication of the aforementioned two reasons for the widening of the Pira Magroon anticline. On contrary, the syncline between the Pira Magroon and Surdash anticlines is very narrow, although the rocks in the northeastern limb of the Pira Magroon anticline suffer from severe karstification (Fig. 17b) and many landslides (Fig. 10).

B. Domes

Domes are a good indication of the lateral growth of anticlines (Blanc, et al., 2003 and Bennett, et al., 2005). One dome form was interpreted in the Pira Magroon anticline

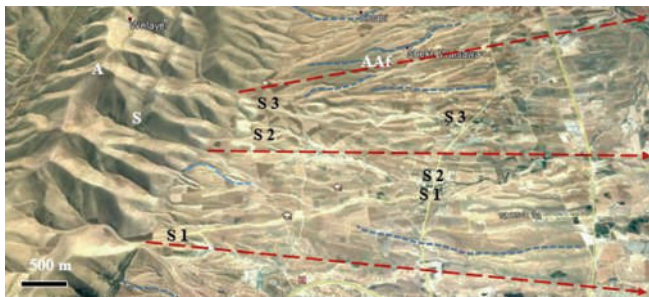


Fig. 14. Satellite image of Azmar anticline facing SW. The down arrows indicate the direction of old alluvial fans. Note the direction of the recent feeder channels (S1 – S1, S2 – S2, and S3 – S3) of active alluvial fans. Furthermore, note the very tight anticline (A) and syncline (S). AAf is an old alluvial fan. Blue dotted lines are scars of old feeder channels.

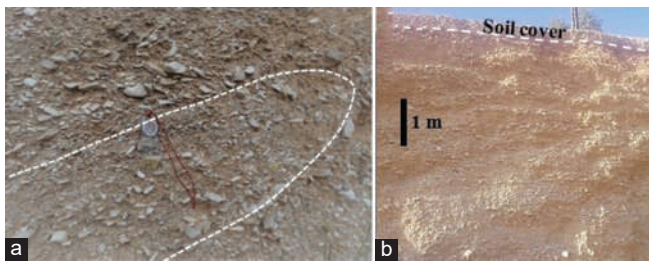


Fig. 15. Field photos for an old fan, (a) tilted sediments of old alluvial fan, note the tilted orientation of the pebbles and (b) hard soil cover. Both photos are toward SE.

(Fig. 10); it occupies a very large wine glass that is growing due to erosion and most probably due to lateral growth.

A good indication can be seen in point 1 (Fig. 10). This is most probably due to the absence of the exposures of the very hard and massive beds of the Qamchuqa Formation. In the Surdash anticline, five domes were interpreted, they also are occupied by wine glasses (Fig. 11), which are also growing due to erosion and lateral growth of the anticline. However, in the Surdash anticline, the shapes of the domes are thinner and shorter; as compared to those developed in the Pira Magroon anticline, this is attributed to the thinning of the Qamchuqa Formation eastwards; and accordingly, the core is occupied mainly by fairly hard rocks of the Sarmord Formation (Fig. 11), besides being subjected to more compressional forces; as can be seen from the overturned beds (Points 1 and 2, Fig. 11). In the Azmar anticline, however, no domes are developed. This can be attributed to the exposed monotonous rock types (marly limestone and marl) within the Kometan and Balambo formations (Figs. 12 and 14). Both marl and marly limestone are more incompetent and ductile as compared to the massive and very hard limestone and dolomite beds of the Qamchuqa Formation.

C. En-echelon Plunges

The presence of an en-echelon plunge within an anticline is also a good indication of the lateral growth of the

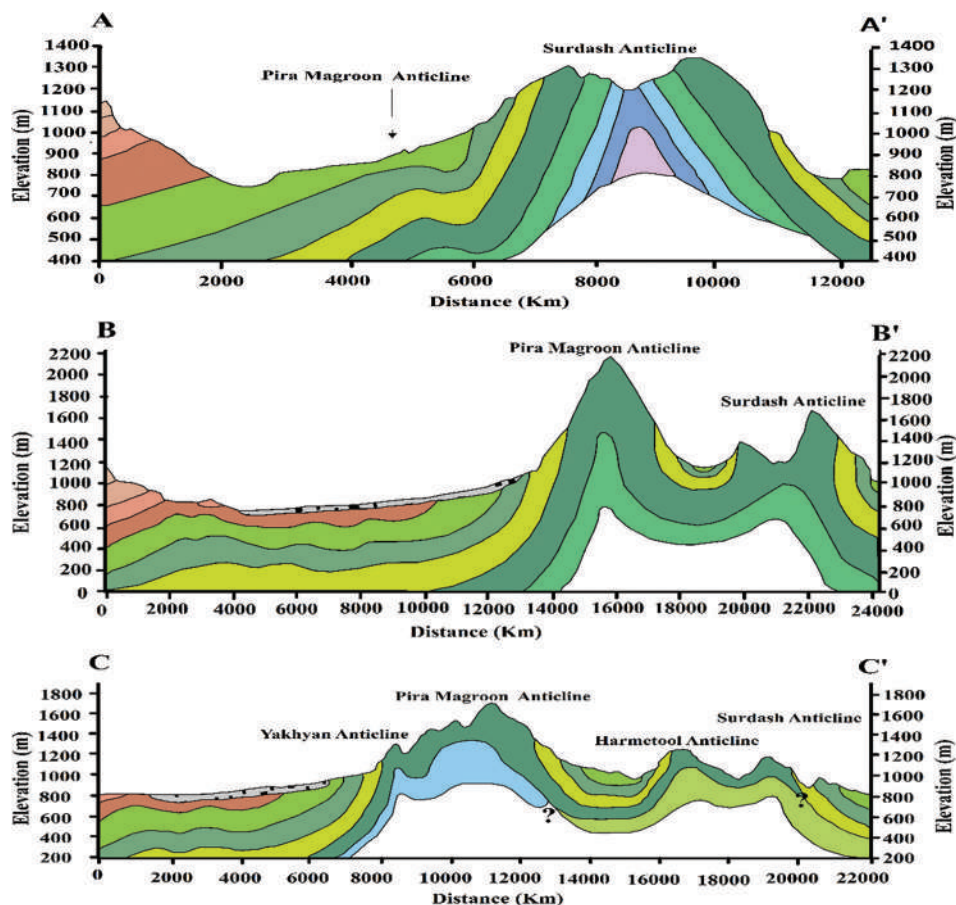


Fig. 16. Three cross-sections showing folding harmony in the studied anticlines (for the location of the cross-sections see Fig. 6).



Fig. 17. Pira Magroon anticline, (a) large landslide along the southwestern limb (The height is about 50 m) and (b) Karstified rocks along the northeastern limb (The height of the cliff is about 700 m).

anticline (Keller and Pinter, 2002; Ramsey, Walker and Jackson, 2008; Fossen, 2010). The Surdash and Azmar anticlines exhibit a right-hand en-echelon plunge (Fig. 13). The en-echelon plunge is developed at the areas where the Qamchuqa Formation pinches out; eastwards, the thickness of the formation at the plunge area is only 12 m (Sissakian and Al-Jiburi, 2014; Sissakian and Al-Jiburi, 2014), and at the type locality, which is at the northwestern part of the anticline is 792 m, whereas the thickness of the Balambo Formation is 320 m (Sissakian and Al-Jiburi, 2014; Sissakian and Al-Jiburi, 2014). This great change in the thickness is the reason for the change in the width of the Surdash anticline and its plunge area, as compared to that of the Azmar anticline (Fig. 13). Due to this big change in the thickness of the anticlines, and the difference in the hardness of the rocks on both plunge areas, the northwestern plunge of the Azmar anticline is moved out of the range; northwestwards (Fig. 6). The plunge area also coincides with a paleo-ridge (at NW – SE direction) that has separated the depositional basins of the Qamchuqa Formation (toward west) and that of the Balambo Formation (toward east) (Buday and Jassim, 1987; Jassim and Goff, 2006). The location of the paleo-high also coincides with the southeastern plunge of the Pira Magroon anticline (Fig. 1). In the Azmar anticline, however, many en-echelon plunges were interpreted within the anticline (Fig. 13), this is attributed to the presence of many minor anticlines successive to each other in both directions (NE – SW and EW), which form the main Azmar anticlines as M-shaped parasitic anticlines. The thick rock succession of the Balambo and Kometan formations (about 800 m of marly limestone and marl) has also contributed to the development of this type of anticline with the main Azmar anticline since they are ductile and incompetent.

VI. CONCLUSIONS

From the interpreted data and field investigations, the following can be concluded: The studied anticlines exhibit different structural features which indicate their lateral growth. Different structural features are recognized as an indication for the lateral growth of the anticlines in the study area, among them are domes, en-echelon plunges, and Neotectonic indications. Besides, geomorphological

indications of the lateral among them are different-shaped valleys (Radial, Fork-shaped, Axial, and Inclined), water and wind gaps, and abandoned alluvial fans. We also can conclude that the fold's thickness varies along its axis, some of the folds are parasitic types like the Azmar anticline. Some of the gorges in the Pira Magroon and Surdash anticlines are developed due to strike-slip faults.

ACKNOWLEDGMENTS

The authors would like to pass their sincere thanks to the authorities at the Komar University of Science and Technology, and the University of Sulaimani for their encouragement during this research work.

REFERENCES

- Ahmed, S.H., 2019. Designation and study of anticlines-Kurdistan region-NE Iraq. *Journal of Physics Conference Series*, 1294, p.082001.
- Alavi, M., 2004. Regional stratigraphy of the Zagros fold-Thrust Belt of Iran and its proforeland evolution. *American Journal of Science*, 304, pp.1-20.
- Allen, M., Jackson, J., and Walker, R., 2004. Late cenozoic reorganization of the Arabia-Eurasia collision and the comparison of short-term and long-term deformation rates. *Tectonics*, 23, p.TC2008.
- Ameen, M.S., 1991. Possible forced folding in the Taurus-Zagros Belt of Northern Iraq. *Geological Magazine*, 128(6), pp.561-584.
- Bennett, E.R., Youngson, J., Jackson, J.A., Norris, R.J., Raisbeck, G.M., Yiou, F. and Fielding, E.J., 2005. Growth of South Rough Ridge, Central Otago, New Zealand: Using *in situ* cosmogenic isotopes and geomorphology to study an active, blind reverse fault. *Journal of Geophysical Research Atmospheres*, 110, p.B02404.
- Blanc, E.J.P., Allen, M.B., Inger, S. and Hassani, H., 2003. Structural styles in the Zagros simple folded zone, Iran. *Journal of the Geological Society*, 160, pp.401-412.
- Bretis, B., Bartl, N. and Grasemann, B., 2011. Lateral fold growth and linkage in the Zagros fold and Thrust belt (Kurdistan, NE Iraq). *Basin Research*, 23, pp.615-630.
- Buday, T., and Jassim, S.Z., 1987. Tectonic Map of Iraq, scale 1:1000000. 1st ed. Iraq Geological Survey Publications, Baghdad, Iraq.
- Burbank, D.W. and Anderson, R.S., 2001. *Tectonic Geomorphology*. Blackwell Science Malden, United States of America.
- Burbank, D.W. and Pinter, N., 1999. Landscape evolution: The interactions of tectonics and surface processes. *Basin Research*, 11, pp.1-6.
- Burberry, C.M., 2015. The effect of basement fault reactivation on the Triassic-recent geology of Kurdistan, North Iraq. *Journal of Petroleum Geology*, 38(1), pp.37-58.
- Collignon, M., Yamato, P., Castellort, S. and Kaus, B.J.P., 2016. Modelling of wind gap formation and development of sedimentary basins during fold growth: Application to the Zagros fold belt, Iran. *Earth Surface Processes and Landforms*, 41(11), pp.1521-1535.
- Colman-Saad, S.P., 1978. Fold development in Zagros simply folded belt, Southwest Iran. *AAPG Bulletin*, 62, pp.984-1003.
- Fossen, H., 2010. *Structural Geology*. Cambridge University Press, United Kingdom, p.463.
- Fouad, S.F. 2015. Tectonic map of Iraq, scale 1: 1000 000, 3rd edition. *Iraqi Bulletin of Geology and Mining*, 11(1), pp.1-8.

- Grasemann, B. and Schmalholz, S.M., 2012. Lateral fold growth and fold lineage. *Geology*, 40(11), pp.1039-1042.
- Jassim, S.Z. and Goff, J.C., 2006. *Geology of Iraq*. Dolin, Prague and Moravian Museum, Brno, p.334.
- Karim, K.H. and Khanaqa, P.A., 2017. Stratigraphy and structure of the southeastern part of Piramagroon anticline, Sulaimani area, Northeast Iraq. *Bulletin of the Mineral Research and Exploration*, 154, pp.27-39.
- Karim, K.H., Bety, A. and Khanaqa, P.A., 2015. Geomorphology of the Piramagroon-Kanikhan valley, Sulaimani governorate, Kurdistan region, North Iraq. *International Journal of Geography and Geology*, 4(12), pp.183-195.
- Karim, K.H., Khanaqa, P.A. and Ismail, K.M., 2020. Role of facies changes in shifting trends of anticlines in the Zagros fold-Thrust belt: Examples from Sulaimaniyah area, Kurdistan Region, Northeastern Iraq. *Journal of Zankoy Sulaimani*, 22(1), pp.1-13.
- Keller, E.A., and Pinter N., 2002. *Active Tectonics: Earthquakes, Uplift, and Landscape*. 2nd ed., Prentice Hall, Upper Saddle River, New Jersey, p.359.
- Keller, E.A., Gurrola, L. and Tierney, T. E., 1999. Geomorphic criteria to determine direction of lateral propagation of reverse faulting and folding. *Geology*, 27(6), pp.515-518.
- Mohammed, S.K., Al-Kubaisi, M.S. and Bety, A.K., 2018. Geomorphic indices of tectonic activity through the analysis of the drainage systems in Pera Magroon anticline, Northeastern Iraq. *Iraq National Journal of Earth Sciences*, 18(2), pp.99-112.
- Omar, A.A., 2011. Analysis and interpretation of minor folds developed in the cretaceous formations within Azmar anticlinorium, in a part of Iraqi Zagros fold and Thrust belt, Suliyamania district, Northeastern Iraq. *Journal of Basic Applied Science Research*, 1(10), pp.1490-1497.
- Omar, A.A., Lawa, F.A. and Sulaiman, S.H., 2015. Tectonostratigraphic and structural imprints from balanced sections across the north-western Zagros fold-Thrust belt, Kurdistan region, NE Iraq. *Arabian Journal of Geosciences*, 8(10), pp.8107-8129.
- Ramsey, L.A, Walker, R.T., and Jackson, J., 2008. Fold evolution and drainage development in the Zagros mountains of Fars Province, SE Iran. *Basin Research*, 20, pp.23-48.
- Sissakian, V.K. and Al-Jiburi, B.S.M., 2014. Stratigraphy, geology of the high folded zone. *Iraqi Bulletin Geology and Mineral*, 6, pp.73-161.
- Sissakian, V.K. and Fouad, S.F., 2015. Geological map of Iraq, scale 1: 1000 000, 4th edition. *Iraqi Bulletin Geology and Mineral*, 11(1), pp. 9-18.
- Sissakian, V.K., Kadhun, T.H. and Abdul Jab'bar, M.F., 2014. Geomorphology. The geology of the high folded zone. *Iraqi Bulletin Geology and Mineral*, 6, pp.7-56.
- Zebari, M., 2013. *Geometry and Evolution of Fold Structures within the High Folded Zone: Zagros Fold-Thrust Belt, Kurdistan Region, Iraq*. Unpublished Master Thesis, Department of Earth and Atmospheric Sciences, University of Nebraska, Lincoln.

Deep Forest Based Internet of Medical Things System for Diagnosis of Heart Disease

Shavan K. Askar

Department of Information Systems Engineering, Erbil Technical Engineering College, Erbil Polytechnic University,
Erbil, 44001, Iraq

Abstract—Due to advancement in internet of medical things, the conventional health-care systems are transformed into smart health-care systems. The medical emergence services can be significantly enhanced by integration of IoMT and data analytic techniques. These technologies also examine the unexplored area of medical services that are still unseen and provide opportunity for investigation. Moreover, the concept of smart cities is not achievable without providing a smart connected healthcare scheme. Hence, the main purpose of this research is to come up with a smart healthcare system based on IoMT, Cloud and Fog computing and intelligent data analytic technique. The major objective of the proposed healthcare system is to develop a diagnostic model capable for earlier treatment of heart disease. The suggested scheme consists of distinct phases such as data acquisition, feature extraction, FogBus based edge/fog computing environment, classification, and evaluation. In data acquisition, different IoMT such as wearables and sensors devices are considered to acquire the data related to heart disease and the various features related to signal and data are extracted. Further, the deep forest technique is integrated into the proposed system for classification task and effective diagnosis capabilities of heart issues. The performance of the suggested scheme is evaluated through set of well-defined parameters. Comparison with other healthcare model was conducted for the purpose of performance evaluation. It is concluded that the proposed model has a superiority over other all other models in different aspects namely, the sensitivity measure, accuracy measure, and specificity.

Index Terms—Deep forest, Fog computing, Healthcare system, Heart disease, IoMT.

I. INTRODUCTION

Recently, cloud and fog computing environments gain wide popularity and can be acted as main pillar in the toady economy due to on demand services to users through global network (Mutlag, et al., 2019). These computing paradigms

have significant impact in industry as well as in academia. But due to delay response, cloud computing cannot be more appropriate in real time applications (Farahani, et al., 2018). Apparently, fog, IoT, edge, and big data have been exposed tremendously due to capability of less response time with respect to target applications (He, et al., 2017). These technologies provides better computations, communications, and storage for edge devices and also improved the variety of constraints such as latency, N/W bandwidth, mobility, privacy, and security. Through literature, it is identified that fog computing is more appropriate for latency sensitive and real time application (Rahmani, et al., 2018). At present, cloud computing frameworks also enhanced and provide more robust and reliable infrastructure and services for many applications (Gupta, Maharaj and Malekian, 2017). While, fog computing handles the issues such as energy consumption, n/w latency and response time through nodes, routers and gateways for offering better services. Other side, growth in IoT devices led to tremendous amount of data (Islam, et al., 2015). These devices are utilized into different domains such as transportation, healthcare, business, networks, industry, finance, and communication and having significant impact on users. In healthcare, these devices are widely adopted and deployed for obtaining the diverse data from users and further several techniques based on artificial intelligence, computer vision, deep learning, etc., are applied for analyzing the collected data (Gambhir, Malik and Kumar, 2016) (Singh and Kumar, 2019) (Kaur and Kumar, 2021) (Kumar, et al., 2019) (Gambhir, et al., 2019). This data analysis can be beneficial for designing and developing the efficient and robust healthcare model as well as earlier intervention, prevention and optimal management of health services. Fig. 1 illustrates the few applications of IoT devices. It is analyzed that collected data are in huge amount and existing tools are not capable to process and interpret such massive data (Srivastava, Kumar and Singh, 2022). IoT with data analytics, edge computing and fog computing are capable to provide state of art solutions for many healthcare applications such as health monitoring, diagnosis and prediction of diseases, emergence services, resource allocation, and elderly care. The objective of data analytics is to investigate the information of patients considering the medical tests and complications. Such information can be used for proper management of the disease and medication.

ARO-The Scientific Journal of Koya University
Vol. XI, No. 2 (2023), Article ID: ARO.11174. 11 pages
DOI: 10.14500/aro.11174

Received: 26 February 2023; Accepted: 13 March 2023

Regular research paper; Published: 01 April 2023

Corresponding author's e-mail: shavan.askar@epu.edu.iq

Copyright © 2023 Shavan K. Askar. This is an open access article distributed under the Creative Commons Attribution License.



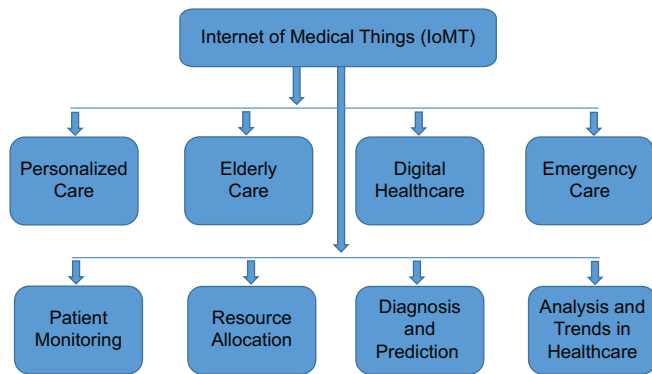


Fig. 1. Depicts the several applications of IoMT.

Further, the advance data management tools such as cloud computing, visualization can also facilitate to health organizations to develop platforms that can capture, store, and alter huge amount of data in effective manner. Other side, fog computing can be adopted in healthcare to get concise, precise and real time information for progressive improvements. Moreover, the incorporation of fog computing capabilities in the health-care application will improve the security as the resources will be close to users and this also helps to achieve minimum latency (*Machine Learning, Big Data, and IoT for Medical Informatics - Google Scholar*, no date). In turn, it can be beneficial to get earlier prediction and also enable essential and quick action for curing the critical disease patients. However, it provides the quick results, but has the challenge of complex data while at the same time it is required to provide precise results (Kumar, et al., 2018). Further, it is observed that several techniques have been considered for collecting the health-care data and it is acted in two ways:- (i) Get the data from input file and (ii) obtain the data from different IoMT devices (Kaur, Kumar and Kumar, 2019). It is noticed that more than 250 MB data/min is collected over the network (Satpathy, et al., 2020). However, the traditional techniques are not capable to capture and process the massive amount of data. This problem can be override by utilizing the fog computing capabilities. Data are collected and aggregated using smart devices over the IoMT network and it can be stored and processed either cloud server or edge nodes. Hence, the proposed system suggests to combine the IoMT, cloud and fog computing. The suggested scheme is summarized below.

To design a heart disease diagnosis system based on the IoMT, cloud and fog computing technologies, called decision support system (DSS).

The relevant information regarding the heart disease are gathered using the IoMT devices including signal data.

Signal features such as entropy, peak amplitude, and energy and data features, that is, mean, skewness, and kurtosis are extracted for accurate diagnosis of heart disease.

The diagnostic task is accomplished through optimized deep forest cascade technique.

The performance of proposed DSS is validated through a set of well-defined performance parameters.

II. RELATED WORKS

Mishra, et al., (2021) came up with a health-care monitoring system utilizing IoHT for detecting the lung cancer risk. The data are collected through patients using IoHT devices. The relevant attributes for lung cancer is identified using greedy best first search (GBFS) technique. Further, the symptoms of lung cancer are detected using the random forest technique. Simulation results indicated that GBFS-RF system obtains superior results in terms of accuracy (98.8%) and latency (1.16s) compared to other models. The suggested model is more sustainable in terms of energy sensitive and reduced overhead.

Khamparia, et al. (2021) presented an effective system for skin cancer classification\detecting. The proposed scheme is integrated IoHT, deep and transfer learning techniques to provide accurate skin cancer detection. The relevant features are extracted using the VGG19, Inception V3, ResNet50, and SqueezeNet techniques in automatic manner. These features are giving to the fully connected convolutional neural network (CNN) to determine the skin as benign and malignant. Moreover, the proposed framework is integrated with IoHT devices for assisting the specialist remotely to diagnosis the skin cancer. The efficacy of proposed framework is assessed through recall, precision, and accuracy parameters. The results stated that the proposed framework provides 99.20% of accuracy rate for detecting the skin cancer.

Vellameeran and Brindha (2022) designed the heart disease diagnosis system based deep belief network and wearable IoT medical devices. In the proposed diagnosis system, wearable devices are employed to get the relevant data from patient regarding the heart disease. Several features are extracted from the collected data such as skewness, kurtosis, and peak amplitude. Further, a hybrid algorithm called PS-GWO algorithm is utilized for computing the more relevant features from the extracted set of features. These relevant features are fed to the modified DBN to diagnosis of heart disease. The hyper parameters of DBN are also optimized using the PS-GWO technique. The performance of the heart disease diagnosis system is examined over three scenarios using accuracy parameter. It is reported that proposed diagnosis system achieves 88.8%, 87.1% and 83.8% accuracy rate with scenario 1, scenario 2, and scenario 3, respectively.

Mansour, et al. (2021) considered the artificial intelligence technique and IoT for designing the disease diagnosis model to achieve smart healthcare. The proposed model is utilized for accurate detection of heart and diabetes diseases. The working of model is described using four stages such as data acquisition, preprocessing, classification, and parameter tuning. The different IoT devices are employed to acquire the relevant data. The outlier data are identified using isolation forest technique. The cascade long short-term memory (LSTM) technique is adopted to perform the classification task, while crow search algorithm is applied for tuning the weight and bias parameters of aforementioned technique. The results are evaluated using accuracy, sensitivity, and specificity parameters. It is analyzed that CSO-CLSTM model provides superior results than exiting models in terms

of accuracy (96.16), sensitivity (96.38%), and specificity (94.30) rates.

Manogaran, et al. (2021) presented a smart healthcare system based on internet of things environment. The physiological symptoms of patients are collected through wearable devices and in turn, the collected data consists of heterogeneity. Hence, the aim of this work is to present the cognitive data processing technique for uncertainty analysis as well as enhancing the efficiency wearable sensor data management. The aggregation and dissemination uncertainties of sensor data are considered in this work and these are addressed through classification learning. Further, latency and overloaded interval are utilized for evaluating the simulation results and it is analyzed that the proposed cognitive method is more reliable and accurate for handling uncertainty of wearable sensor data.

Su, Ding and Chen (2021) presented the heart disease screening system based on deep learning and internet of things platform. The aim of this study is to measure the irregularities in context of heart and earlier detection of heart disease. This study considers the STM32 as IoMT controller and integrate it to IoT devices such as temperature sensor, pulse sensor, and sphygmomanometer cuff. Further, deep learning method is integrated into aforementioned architecture for detecting the heart irregularities and disease. The experiment results stated that proposed screening system is successfully detected the variation in heart signals.

Hossen, et al. (2022) developed the federated machine learning based model for detecting the skin disease as well as enhancing the security in IoMT environment. This work considers the CNN technique with federated learning for the detection of skin disease. The image augmentation technique is also adopted for enlarging the skin dataset and data privacy concern is addressed through federated learning. Further, the skin disease is divided into four classes such as acne, psoriasis, eczema, and rosacea with the help of dermatologist. The results are evaluated using precision, recall and accuracy. The accuracy rate of the proposed detection model is 81.21%, 86.57%, 91.15%, and 94.15% using 1000, 1500, 2000, and 2500 sample data.

Siddiqui, et al., designed an IoMT and cloud based intelligent prediction model for detection the breast cancer stages. The features are extracted from mammogram images using deep learning technique. The prediction of breast cancer and its stages is accomplished through two sub layer:- (i) Application layer and (ii) performance layer. The CNN technique is employed in application layer to classify the data. While, performance layer consists of parameter such as accuracy, precision, and miss rate. The training accuracy of the proposed model is 98.86%, while the validation accuracy of the model is 97.81%. It is also observed that proposed model considerably reduces the breast cancer mortality rate.

Ahmed, et al. (2021) demonstrated a health monitoring framework to predict and analyze the COVID-19. The proposed framework integrates the IoT platform and big data analytics. The big data analytics is adopted to perform descriptive, diagnostic, predictive, and prescriptive analysis for assessing the several symptoms of pandemic. The

diagnosis and prediction task is achieved through neural network based technique. The results stated that neural network model obtains superior accuracy (99%) than other ML models.

Abdellatif, et al. (2021) considered the edge computing and Blockchain for processing the medical data, called MEdge-Chain. The objective of work is to design a health-care system that aggregates the different health attributes under the national healthcare system which can enable swift, secure and storage of medical data. Further, the edge computing provides an automated patient monitoring system in remote manner as well as for critical medical emergence. The latency and computation cost of secure data exchange are handled through Blockchain technologies. It is summarized that proposed MEdge-Chain model is efficient model for data processing and achieved low latency.

Rhayem, et al. (2021) presented the patient monitoring system based on context aware, semantic information and internet of thing environment. The aim of this work is to describe the relationship among heterogeneous medical connected objects and its respective data. Further, SWRL rules are designed to interpret and manage the data into different contexts and these rules are also utilized for diagnosis and prediction of disease. The effectiveness of the monitoring system is evaluated using a case study based on gestational diabetes. The results are assessed using precision, recall and f-measure parameters. It is reported that proposed monitoring system obtains superior results than other models.

Dami and Yahaghizadeh (2021) predicted the cardiovascular event based on deep learning with respect to IoT environment. The deep belief network is utilized for extracting the relevant features from the collected dataset. The collected dataset contains the 5 min electrocardiogram (ECG) recording and demographic data. The time frequency features are extracted from the ECG signals. While, the demographic feature in context to heart is collected through wearable devices. The prediction task is executed using LSTM technique and predictive results are evaluated using various performance parameter, but accuracy is considered as more potential parameter. The performance of LSTM-DBN is compared with MLP, RF, support vector machine (SVM), and LR techniques and it's observed that LSTM-DBM attains 88.42% accuracy rate.

Madhavan, et al. (2021) demonstrated a Res-CovNet framework using IOHT and transfer learning for detection of COVID-19. This work considers the chest X-ray images for detection of COVID-19. The preprocessing task is accomplished through Res-CovNet, and the storage aspect is handled through MangoDB. The efficacy of proposed model is assessed over five thousand eight hundred fifty six images and simulation results are evaluated using accuracy parameter. It is noticed that proposed framework achieves 96.2% of accuracy rate.

Alqaralleh, et al. (2021) integrated the deep learning (DL) technique with Blockchain to design secure image transmission and diagnosis model in IoMT environment. The proposed diagnosis model contains data collection, secure transaction, hash value encryption, and data classification.

The data are collected through smart sensor devices. For the secure transmission, an optimal key is generated using ECC and the combination of grasshopper and fruit fly optimization is utilized for generation of optimal key. The hash encryption is done through NIS with BWT and finally, DBN is considered for diagnosis of disease. The performance of the proposed diagnosis model is validated using specificity, sensitivity and accuracy parameters. It is analyzed that proposed model provides higher specificity (96.73%), sensitivity (97.91%), and accuracy (98.96%) than other compared models.

Aitzaoui, et al. (2022) presented an intelligent platform based on WBN, IoT, and machine learning to predict the involuntary seizures. WBN and IoT devices are considered for collecting the data from the end users. The prediction task is completed through QuLRA, SeCA, and RT2CA. Moreover, IoT/WEB proxy security mechanism is adopted for secure transmission in between CoAP/DTLS protocol and hospital information system. The performance of proposed platform is evaluated using rand index and accuracy. Authors claimed that proposed platform outperforms than existing models and techniques in context of secure communication and classification results.

Raju, et al. (2022) developed a smart heart disease prediction system using IoT and Fog computing environments. The proposed prediction system integrates the cascaded deep learning model for predictive task. The patient's data are collected through IoT devices and optimized cascaded deep learning technique is utilized for prediction of heart disease. The hyper parameters of deep learning are optimized through galactic swarm optimization (GSO) technique. The performance of prediction system is evaluated using a set of well-defined performance parameters and it is found proposed heart disease prediction system obtains superior results with most of parameters as compared to similar existing models.

Ali, et al. (2021) designed a health-care monitoring framework to predict the abnormality. The proposed framework integrates the cloud computing and big data analytics to override the issues with traditional monitoring systems. The data analytics are performed using the ontology and Bi-LSTM, while cloud computing is utilized to store the data. Moreover, the dimensionality of data is reduced through information gain technique and aim of this process is to choose relevant features and improve the classification accuracy. The performance of proposed framework is investigated using blood pressure and diabetes prediction. The results showed that proposed framework effectively handles data heterogeneity and also enhances the classification accuracy of blood pressure and diabetes.

Kumar, Mandal and Kumar (2022) demonstrated the fog based framework for accurate prediction of diabetes disease using cloud environment. In this work, patient data are collected with the help of sensor in remote manner. Further, fog computing is utilized to collect and process the data end nodes, and also for immediate communication. The processed data are analyzed on the cloud layer using ANFIS-PSO-WOA technique. The results showed that proposed model

achieves more than 92% of accuracy rate than ANN, SVM, and ANFIS.

III. PROPOSED MODEL AND DESCRIPTION

In present era, IoT and cloud computing having significant impact for several applications. The issues associated with cloud are effectively handled through centralized IoT based platform. These issues are described in terms of lack of scalability and indulge requirements. These emerging technologies are widely adopted to design intelligent frameworks for health-care data analysis, disease diagnosis, surveillance system, precision agriculture, etc. It is observed that large amount of data is generated in healthcare field. To process such massive data, new computing techniques such as edge and fog computing are best when the application requires low delay and energy efficient system. However, issues such as less accuracy and response time are to be considered. However, it is seen that integration of fog, cloud, IoT, and edge computing obtains superior computation, communication, and storage solutions. This integration also superior in terms of n/w bandwidth, privacy, mobility, latency, and security. It is also found that combination of fog and cloud computing can be considered for real time and latency sensitive applications. It is also observed that existing heart disease system suffered with higher response time, workloads, resource usages, and energy consumption. Hence, the target is to have an intelligent DSS for heart disease based on fog computing in combination with IoT. The IoT devices and gadgets are used for collecting the heart disease related data from the patients. Different sensors are assumed for gathering the patient data in terms of activity level, blood pressure, electroencephalography (EEG), oxygen level, electromyography (EMG), respiration rate, and ECG. Further, fog nodes are assumed to process the heart disease data with high computing and less response time, delay, and latency compared to cloud scenario. Moreover, the collected data are transferred through the gateway devices to the worker/broker node for heart disease diagnosis. It is also mentioned that ECG signals are considered to extract the features for diagnosis of the heart disease and these features are separately extracted and processed. The possible features that are extracted for heart disease diagnosis are standard deviation, entropy, heart rate, peak amplitude, zero crossing, skewness, mean, median, kurtosis, and energy. Now, Fogbus is come into picture and having significant role for designing the DSS to heart disease diagnosis. Further, the preprocessed data is fed to the DSS and in DSS, deep forest cascading is implemented for the purpose of heart disease diagnosis. The deep forest technique predicts the data either heart disease or without heart disease while DSS will predict heart disease with maximum prediction accuracy. Fig. 2 depicts the proposed DSS for diagnosis of heart disease.

A. System Configuration

The proposed intelligent DSS can be described as light weight fog system that takes heart disease patients information

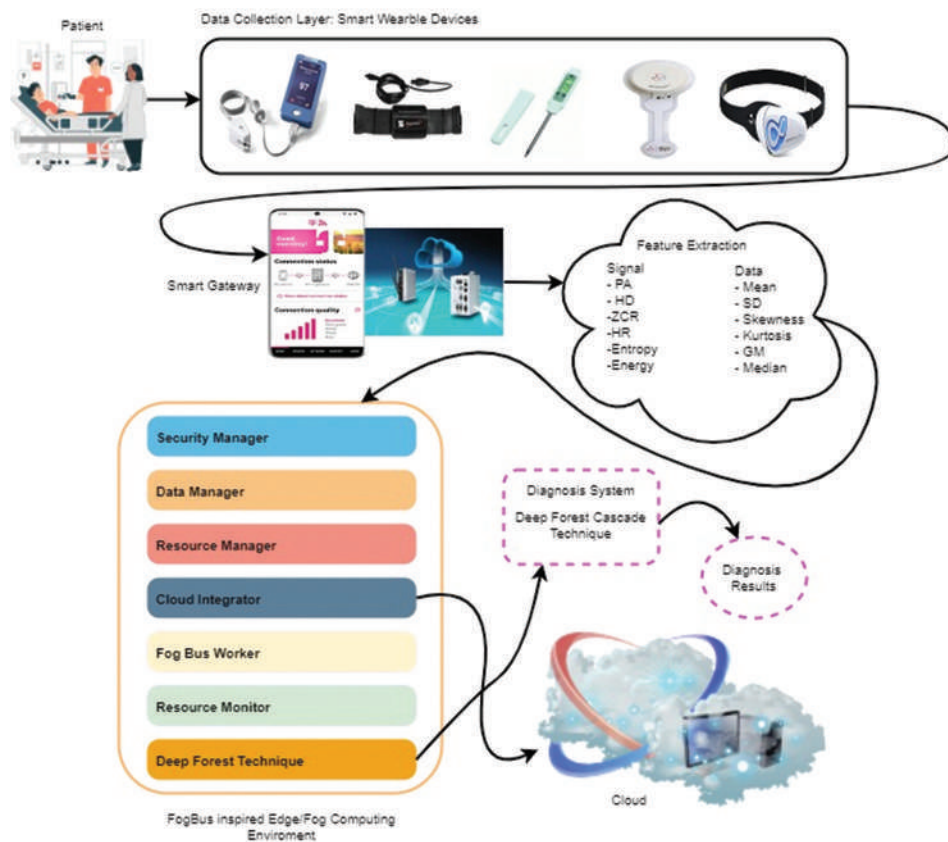


Fig. 2. Demonstrates the proposed decision support system for heart disease diagnosis.

through sensors and smart devices. FogBus is integrated into the proposed DSS and task of FogBus is to diagnosis of heart disease affected patients. Moreover, the Fogbus can be adopted for combining the Fog and cloud environments and it is also deliberated for deployment as well as development. It also provides structured communications and platform independent. The structured communications can be described as dedicated links with sensor devices and smart gadgets and another significance is to send data and task to worker nodes of fog system. While, the broker nodes manage the task initiation and resources. A security manager is also considered to ensure the robustness and dependability of proposed environment through encryption and authentication. Further, FogBus considers the HTTP RESTful APIs to integrate and communicate with the cloud layer.

B. IoT

The proposed intelligent DSS integrates several hardware devices (sensors and smart gadgets) and application software for smooth communication and integration of edge, fog, and cloud to obtain superior results. The proposed DSS contains environmental sensor, medical sensors and activity sensors as hardware devices. Few of sensors are described as ECG sensors, EEG sensors, glucose level sensors, EMG sensors, temperature sensors, respiration rate sensors, oxygen level sensors, and EMG sensors. The data regarding the patient health are collected through aforementioned sensors and collected data are transmitted through connected devices.

Data collection

The working of proposed DSS is tested on gathered data. This data are collected through different internet medical of things devices. These are the smart gadgets that are connected with patients to get the desired data. The details of the aforementioned medical sensors are listed as below.

- Glucose Sensor: This sensor measures the blood glucose level of the patients and can be significant one to manage the diabetes as monitoring of the glucose level is one of crucial activity to predict the heart disease. It is noticed that people with diabetes having higher chance for developing heart disease rather than people without diabetes.
- Respiration Sensor: The respiration sensor can be described through standard pulse oximeters and can be adopted for monitoring of respiratory rate. The outcome of respiration sensor can be defined in terms of flow rate in hundred per minute and it is important parameter to compute heart rate variability.
- Temperature sensor: Used to determine patient body temperature. The increased sensed temperature can also increase the heart beat rate. Hence, it is important to measure the temperature for diagnosis of heart disease.
- Oximeter: Used to measure the oxygen level in blood. Decrement in oxygen saturation level is related to faster heart rate and in turn variability in plus rate.
- EMG Sensor: It is used to evaluate and record the electrical signal resulted by skeletal muscles and adopted in clinical and biomedical applications. This sensor also determines

relationship among nerve cells and muscles in terms of health status. The range of the EMG signal is in between 0.1 and 0.5 mV.

- EEG Sensor: This sensor records the electrical signals of the brain. It is described in terms of waveform which reflects the cortical electrical activity.
- ECG Sensors: This sensor is utilized to determine the relationship among heart rate and rhythm.

Feature extraction

In this work, features are extracted from the signal as well as collected data for accurate prediction and diagnosis of heart disease.

Feature extraction form signal

This subsection presents the features that are extracted from the ECG signals for the purpose of heart disease diagnosis. Signals fed to feature extraction phase. In turn, several features are extracted which are listed in Table I. Through this process, redundant data is also reduced from the dataset and prediction process becomes more generalized.

Feature extraction form data

This subsection discusses the spectral features that are also extracted from the collected data for effective prediction and diagnosis of heart disease. These features are defined as mean, median, G-mean, standard deviation (SD), skewness, and kurtosis. The aim of these features is to minimize the resources for processing of data without loss of relevant

information. Further, the problem of over fitting of data is also resolved. Table II shows the spectral features extracted for heart disease.

C. Fog Computing

This subsection discusses the working of the fog nodes. In this work, the IoT devices can be severed as fog devices. These nodes process the collected data. It is conveyed that fog computing is implemented through FogBus and it contains several nodes such as worker, broker, and cloud data centers. The broker nodes receive the collected data from the gateway devices. It is also stated that prior to send the data, gateway devices send the job requests to the input module and the security module is responsible to transfer the data with secure communication to avoid data tempering and unauthorized access. In turn, system credibility and integrity can be improved. Further, it is said that arbitration module is one of the significant element of the resource scheduling especially the broker that computes the status of the load at the worker side in terms of input. It also identifies the subset of nodes that can perform the real time task. Moreover, the task can be allocated by worker node with the help of resource manager of broker node. However, these nodes can be characterized as stand-alone system and embedded devices that consist of deep forest cascading technique to analyze and process the input data and obtain the results. The main functions of worker node are summarized as filtering, preprocessing, data storage and analytics. To accomplish aforementioned task, data could be taken by the worker

TABLE I
DESCRIPTION OF THE FEATURES EXTRACTED FROM SIGNAL DATA

Features	Description
Peak amplitude	Max. positive\negative deviation from zero reference level
Harmonic distortion (HD)	$\frac{\sqrt{\sum_{v=2}^{N/2} h_v^2}}{h_1} \quad (1)$
Heart rate	Computed using interval for two successive QRS
Zero-crossing rate	$Zc_n = \sum_{t=-\infty}^{\infty} \left \text{sgn}[y(t)] - \text{sgn}[y(t-1)] \right ws(n-t)$
	$ws(n) = \begin{cases} \frac{1}{2N} & 0 \leq n \leq N-1, \\ 0 & \text{otherwise} \end{cases}$
	$\text{sgn}[y(t)] = \begin{cases} 1 & y(t) \geq 0 \\ -1 & y(t) < 0 \end{cases} \quad (2)$
Entropy	$e = p_i \log p_i \quad (3)$
Standard deviation	$\sigma^2 = \frac{1}{N} \sum_{j=0}^{N-1} (y_j - \mu)^2 \quad (4)$
Energy	$En = \int_{-\infty}^{\infty} y(t) ^2 dt \quad (5)$

TABLE II
ILLUSTRATES THE SPECTRAL FEATURES

Features	Description
Mean	$\mu = \frac{1}{N} \sum_{i=1}^N P_i, N \text{ denotes the total pixels presented in segmented region.}$
Median	$\text{Med}(P) = \begin{cases} P\left(\frac{N}{2}\right) & \text{if, } N \text{ is even} \\ \left(P\left(\frac{N-1}{2}\right) + P\left(\frac{N+1}{2}\right) \right) & \text{if, } N \text{ is odd} \end{cases} \quad (6)$
G-mean	$\text{GM} = \left(\prod_{i=1}^N P_i \right)^{\frac{1}{N}} = \sqrt[N]{P_1, P_2, P_3, \dots, P_N} \quad (7)$
SD	$\sigma = \sqrt{\frac{1}{N} \sum_{i=1}^N (P_i - \mu)^2} \quad (8)$
Skewness	$\text{sk} = \left(\frac{1}{N \times \sigma^3} \times \sum_{i=1}^N (P_i - \mu)^3 \right)^{1/3} \quad (9)$
Kurtosis	$\text{ku} = \left(\frac{1}{N \times \sigma^4} \times \sum_{i=1}^N (P_i - \mu)^4 \right)^{1/4} \quad (10)$

SD: Standard deviation

node from gateway nodes. The third part of the proposed DSS is cloud layer. It can be effectively used for processing of data and storage. If, size of data is higher than average, then latency can be increased and in turn fog layer will be overloaded. Hence, it is suggested that relevant features can be extracted from the data using efficient feature extraction algorithm and final decision can be taken on the basis of relevant features. The resource-manger consists of two main elements: Workload and arbitration module. Workload manager is designed to handle and process huge data. While arbitration module is responsible to schedule the fog and cloud resources as well as queued tasks processing and this module is integrated within broker node.

D. Deep Forest Cascade Technique

Finally, deep forest cascade technique is employed on the extracted dataset to obtain the desired outcome for prediction of heart disease. The prediction task is accomplished through resource manager as it is responsible to receive the data from gateway devices and task distribution to fog nodes. The final outcome can be recognized either heart disease or not. The deep forest is a new ensemble technique which consists of cascade structure. It is also reported that cascade structure contains more appropriate features than other techniques (Zhou and Feng, 2019) (Zhou and Feng, 2017). Further, it is two-step process:- (i) Multi-grained scanning and (ii) cascade forest. The high dimensional features are extracted using multi grained scanning while classification and prediction task are completed through cascade structure and it contains several forests with multiple trees. The selection of root node is done through Gini index method and it is calculated for each feature. Further, these features are arranged according the Gini index value and feature with lowest Gini index become root node. Final, tree is created on the basis of Gini Index. The computational procedure for computing the respective class of data is mentioned in Fig. 3.

Both scanning and cascade structure are utilized in this work. The relevant feature for classification are chosen using scanning procedure, while classification and prediction task is conducted using cascade structure. The cascade structure contains four forest with four random tree and further, fifty trees are considered in each forest. The parameters values are taken same as presented in (Kumar, Mandal and Kumar, 2022) (Zhou and Feng, 2019). The working of cascade structure is demonstrated in Fig. 4. The features are given

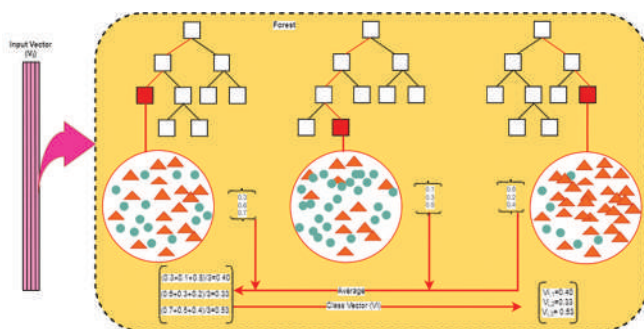


Fig. 3. Computational procedure for computing the class of data.

as input to cascade structure and input features are parsed through cascade structure. This parsed input is moved from 1st level to nth level. At each level, parsed input (previous output) is integrated with input data to produce optimal solutions. This process is continuing until cannot reach nth level. The class label is determined using the nth level. It is also seen that deep forest occurs less sensitivity to input parameters. The computational procedure of deep forest is listed in Algorithm 1.

IV. EXPERIMENTAL RESULTS

The suggested system is implemented in Python environment Intel core-i7 processor, RAM 8 GB, and 64-bit Windows OS. The different scenarios such as training-testing and cross validation are considered for evaluating the system. Simulation results of the suggested system are compared with recurrent neural network (RNN) (Choi, et al., 2017), CNN (Maragatham and Devi, 2019), LSTM (Dutta, et al., 2020), SVM (Ayon, Islam and Hossain, 2020), NN (Balakrishnan and Kumar, 2021), and RT (Balakrishnan and Kumar, 2021).

A. PERFORMANCE ANALYSIS AND DISCUSSION

The results are evaluated using the four different evaluation methods such as training-testing (70–30%), training-testing (80–20%), 5 cross-fold evaluation method, and 10 cross-fold evaluation method. Table I shows the experimental results according to accuracy and F1-score. It is clearly indicated

ALGORITHM 1: PROPOSED DEEP FOREST TECHNIQUE

Input: Heart Disease Dataset (DA), No. of Level (LE), No. of Forests (FO), Number of trees (TN).

Output: Either Heart Disease or Not Heart Disease

1. Initialize no. of forests, No. of trees (TN), No. of dimension in dataset (DIM), training data (TR) and In_Res.=0;
2. For i=1 to LE, do following/Start Training Phase
3. For j=1 to TR, do following
4. For k=1 to FO, do following
5. Construct decision tree for TR using DIM relevant features of heart disease (DA) and Init_Res.
6. Pick the optimal split node based on Gini Index.
7. Design tree at depth level (d).
8. Create TN number of tree for forest.
9. Endfor
10. Endfor
11. Endfor
12. For i=1 to L, do following/Start Testing Phase
13. For j=1 to N, do following
14. For k=1 to F, do following
15. Create decision tree for test data based on DIM relevant features using heart dataset (DA) and Init_Res.
16. Pick optimal split node based on Gini Index.
17. Design tree at depth level (d).
18. Construct TN number of tree for forest.
19. Endfor
20. Endfor
21. Endfor
22. Evaluate the class of heart data based on ensemble of decision trees.
23. Compute the efficiency of algorithm using performance parameters

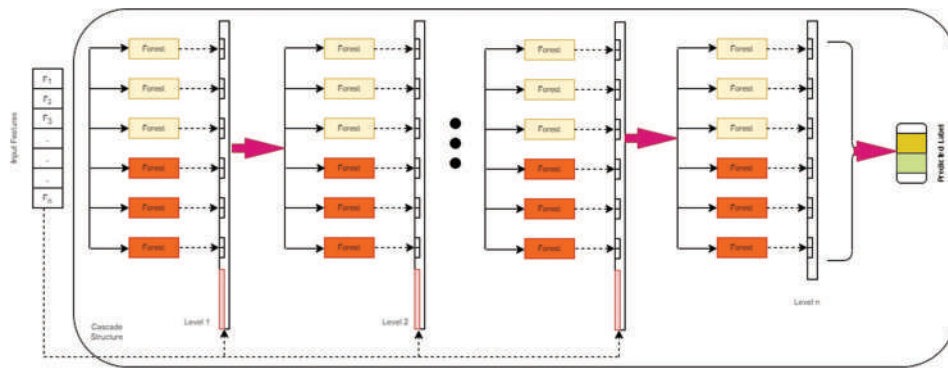


Fig. 4. Cascade forest structure using four forest.

that the suggested system has superior accuracy (95.64%) and F1-score (96.95%) rates using 10 cross fold method when compared to other schemes. Similarly, it is noticed that ANN exhibits less accurate results, that is, 88.08% and 91.92%, among all other techniques. On the analysis of evaluation methods, it is observed that 10-cross fold method having advantage over training-testing (70–30%), training-testing (80–20%), and 5 cross fold evaluation method. The results showed that proposed DSS achieves 95.64% and 96.95% of accuracy and F1-score rates, while F1-score accuracy rates with training-testing were (70–30%), training-testing (80–20%), and 5 cross fold evaluation method are (90.45% and 91.56%), (92.56% and 93.21), and (94.17 and 94.53), respectively. Similar, in case of ANN, the best performance is achieved using 10 cross fold method, that is, 88.08% (accuracy) and 91.92% (F1-score), while, the performance with training-testing (70–30%), training-testing (80–20%), and 5 cross fold evaluation method are (82.64% and 84.37%), (86.05% and 88.11%), and (87.15% and 90.46%). Hence, it is summarized that 10 cross fold validation method is significant evaluation method for the suggested system. The proposed DSS and other techniques obtain less accurate with training-testing (70–30%) method for diagnosis pf heart disease. However, proposed DSS also obtains better results than other techniques for heart disease diagnosis with training-testing (70–30%) evaluation method.

Table II shows the specificity and sensitivity results of the suggested model. It is analyzed that proposed DSS attains better sensitivity, that is, 96.39% and specificity, that is, 97.52% in comparison to other techniques. While, the performance of ANN technique is not so good in terms of sensitivity (92.24%) and specificity (91.60%) as compared other techniques like RT, SVM, RNN, LSTM and CNN. On analyzing the evaluation methods, it is found that 10 cross-fold technique improve the efficiency of the suggested system when compared to training-testing (70–30%), training-testing (80–20%), and 5 cross fold evaluation methods. While, training-testing (70–30%) method exhibits lower performance among all four evaluation methods. Similarly, it is noticed that ANN exhibits less accurate results i.e. 88.08% and 91.92%, among all other techniques. In addition, it is noticed that 10 cross-fold technique has superiority over training-testing (70–30%), training-testing (80–20%), and 5 cross fold

evaluation method. The results showed that proposed DSS provides 96.39% and 97.52% of sensitivity and specificity rates. Other side, training-testing (70–30%), training-testing (80–20%), and 5 cross fold evaluation method achieves (91.27% and 92.14%), (93.08% and 93.87%), and (94.56% and 95.31%) sensitivity and specificity rates using proposed DSS for heart disease diagnosis. Similarly, ANN obtains the best results using 10 cross fold method, that is, 92.24% of sensitivity and 91.60% of specificity rate, while with training-testing (70–30%), training-testing (80–20%), and 5 cross fold evaluation method ANN achieve (83.91% and 84.67%), (87.76% and 88.91%), and (89.29% and 90.17%) of specificity and sensitivity rates. It is shown that the suggested system hit significantly superior results than all other techniques using all aforementioned evaluation methods. Other side, ANN technique having less accurate results for diagnosis of heart disease using all evaluation methods. It is also noted that among all evaluation methods, training-testing (70–30%) method obtains less accurate results using all techniques.

Fig. 5 demonstrates the comparative analysis of accuracy parameter of proposed DSS and other techniques using all evaluation methods such as training-testing (70–30%), training-testing (80–20%), 5 cross-fold, and 10 cross-fold. The suggested system has higher accuracy rate using all evaluation methods and predicts the heart disease more accurately than other models. In addition, it was noticed that ANN having less accuracy rate among all techniques including proposed DSS for diagnosis of heart disease. In deep learning variants RNN, LSTM, and CNN, the CNN model achieves higher accuracy rate among all and also outperform than rest of techniques except proposed DSS.

Table III shows the DSS system accuracy simulation results when they are compared to other techniques while Table IV shows the simulation results of specificity and sensitivity of the proposed DSS system and other existing models for heart disease prediction. F1-score and sensitivity results of proposed DSS and other techniques for diagnosis of heart disease are reported into Figs. 6 to 8 using all evaluation methods. Fig. 6 shows that the suggested system having higher F1-score when compared to other models, while ANN technique having lower F1-score rate among all techniques using all evaluation model. In addition, the

TABLE III
THE DSS SYSTEM ACCURACY SIMULATION RESULTS COMPARED TO OTHER TECHNIQUES

Techniques	Training-Testing (70–30%)		Training-Testing (80–20%)		5 Cross Fold Validation		10 Cross Fold Validation	
	Accuracy	F1-Score	Accuracy	F1-Score	Accuracy	F1-Score	Accuracy	F1-Score
ANN	82.64	84.37	86.05	88.11	87.15	90.46	88.08	91.92
RT	84.51	85.57	87.34	88.53	88.41	91.23	89.44	92.73
SVM	85.74	87.58	88.2	89.24	89.54	92.11	90.34	93.34
RNN	86.93	87.95	89.41	90.76	90.83	92.76	91.58	94.17
LSTM	88.11	90.34	90.67	91.03	92.33	93.67	93.22	95.33
CNN	88.34	91.26	91.07	91.75	93.24	94.01	94.68	96.32
Proposed DSS	90.45	91.56	92.56	93.21	94.17	94.53	95.64	96.95

ANN: Artificial neural network, SVM: Support vector machine, RNN: Recurrent neural network, LSTM: Long short-term memory, CNN: Convolutional neural network, DSS: Decision support system

TABLE IV
SIMULATION RESULTS OF SPECIFICITY AND SENSITIVITY PROPOSED DSS AND OTHER EXITING MODELS/TECHNIQUES FOR HEART DISEASE PREDICTION

Techniques	Training-Testing (70–30%)		Training-Testing (80–20%)		5 Cross fold validation		10 Cross fold validation	
	Sens.	Spec.	Sens.	Spec.	Sens.	Spec.	Sens.	Spec.
ANN	83.91	84.67	87.76	88.91	89.79	90.17	92.24	91.6
RT	84.98	86.32	88.01	88.96	89.63	90.74	91.81	93.68
SVM	87.14	88.23	88.79	89.91	90.81	91.06	92.24	94.46
RNN	87.36	88.21	90.48	91.11	91.54	91.84	92.97	95.41
LSTM	89.71	91.02	91.53	91.89	92.78	93.12	94.8	95.86
CNN	90.08	91.77	91.38	92.54	93.41	94.04	95.8	96.84
Proposed DSS	91.27	92.14	93.08	93.87	94.56	95.31	96.39	97.52

ANN: Artificial neural network, SVM: Support vector machine, RNN: Recurrent neural network, LSTM: Long short-term memory, CNN: Convolutional neural network, DSS: Decision support system

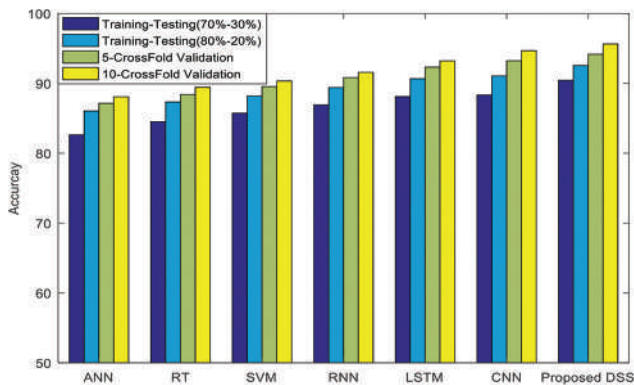


Fig. 5. Comparative analysis of different evaluation methods using accuracy parameter.

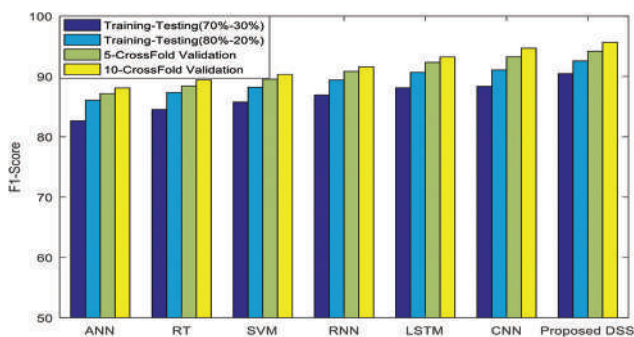


Fig. 6. Comparative analysis of different evaluation methods using F1-score parameter.

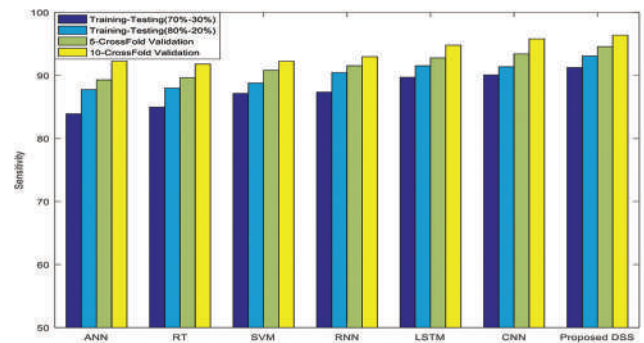


Fig. 7. Comparative analysis of different evaluation methods using sensitivity parameter.

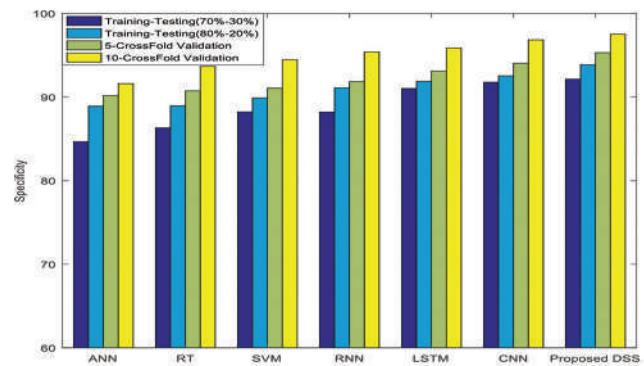


Fig. 8. Comparative analysis of different evaluation methods using specificity parameter.

10-cross evaluation produces considerably better outputs with all techniques including proposed DSS for heart

disease diagnosis. Fig. 8 shows the sensitivity results of the suggested system. Again, proposed DSS achieves superior

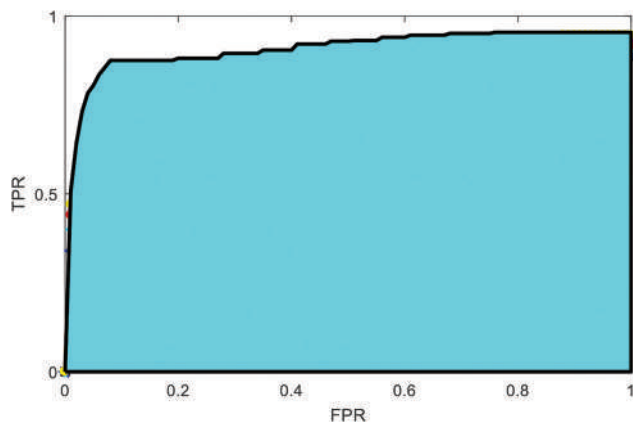


Fig. 9. The area under the curve results proposed decision support system for prediction of heart disease.

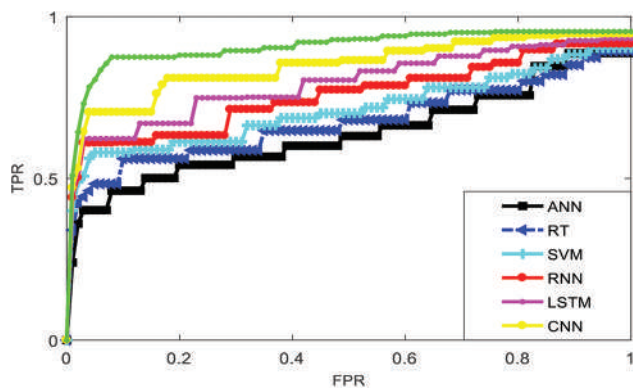


Fig. 10. The area under the curve results proposed decision support system and other existing techniques/models.

results for heart disease diagnosis than other techniques using all evaluation methods. It is also observed that RT technique having less accurate sensitive results using 5 cross fold and 10 cross fold evaluation methods, while ANN provides lower sensitivity results using training-testing (70–30%) and training-testing (80–20%) evaluation methods. Fig. 8 illustrates the specificity results of the proposed DSS and other technique using all evaluation methods. It is analyzed that proposed DSS outperforms than other techniques and provides higher specificity with each evaluation method. Other side, ANN shows less accurate performance in terms of specificity rate among rest of techniques using each evaluation. In addition, the 10 cross-fold evaluation is significant for evaluating the performance of the proposed DSS and other techniques. It is also observed that the performance of all techniques is substantially enhanced using 10 cross-fold method as compared to training-testing (70–30%), training-testing (80–20%) and 5 cross fold method.

Area under the curve (AUC) is also an important parameter for predicting the performance of the newly proposed models for diagnosis of diseases. This work also considers the AUC parameter for the evaluating purpose. AUC results of the proposed DSS are illustrated into Fig. 9. The AUC parameter result is described through relationship between TPR and FPR. The suggested model obtains significant AUC results

in earlier iterations. Fig. 10 demonstrates the AUC results compared to other models. The suggested system obtains superior AUC values compared to all other models. It is also stated that proposed DSS converges on optimized AUC results in earlier iteration than other techniques.

V. CONCLUSION

The proposed DSS is the combination of IMOT, edge, fog, and cloud computing technologies. Data are collected through different IMOT devices regarding the health status of heart. The signal data are also collected to evaluate the condition of heart and different features such as harmonic distortion, entropy, peak amplitude, SD, and heart rate are extracted from the signal data. Apart from above, some features such as mean, median, G-mean, SD, skewness, and kurtosis are also considered from the collected for accurate diagnosis of heart disease. Finally, data are fed to deep forest cascade structure for the purpose of heart disease prediction. In turn, the efficacy of the suggested system is evaluated using F1-score, accuracy, specificity, sensitivity, and AUC parameters. Further, different evaluation methods such as training-testing (70–30%), training-testing (80–20%), 5 cross-fold, and 10 cross-fold are utilized for the purpose of evaluating. Intensive experiments were conducted for the purpose of evaluation, the results was that the suggested system showed superiority in terms of the all above-mentioned parameters. AUC parameter is used for evaluation too, the suggested system having better AUC than RT, SVM, ANN, LSTM, RNN, and CNN. It is observed that proposed DSS with 10 cross-fold validation obtains higher accurate results than training testing (70–30%), training-testing (80–20%), and 5 cross fold method. Hence, it can be concluded that proposed DSS with IoMT, cloud, edge, and fog computing attains considerably better performance than existing models. In future, the proposed system can integrate feature selection techniques, learning strategy, and meta-heuristic algorithm for better classification and predictive accuracy for heart disease diagnosis.

REFERENCES

- Abdellatif, A.A., Samara, L., Mohamed, A., Erbad, A., Chiasserini, C.F., Guizani, M., O'Connor, M.D., and Laughton, J., 2021. MEdge-chain: Leveraging edge computing and blockchain for efficient medical data exchange. *IEEE Internet of Things Journal*, 8(21), pp.15762-15775.
- Ahmed, I., Ahmed, M., Jeon, G., and Piccialli, F., 2021. A framework for pandemic prediction using big data analytics. *Big Data Research*, 25, p.100190.
- Aitzaoui, C.E., Latif, A., Benslimane, A., and Chin, H.H., 2022. Machine learning based prediction and modeling in healthcare secured internet of things. *Mobile Networks and Applications*, 27(1), pp.84-95.
- Ali, F., El-Sappagh, S., Islam, S.M.R., Ali, A., Attique, M., Imran, M., and Kwak, K.S., 2021. An intelligent healthcare monitoring framework using wearable sensors and social networking data. *Future Generation Computer Systems*, 114, pp.23-43.
- Alqaralleh, B.A.Y., Vaiyapuri, T., Parvathy, V.S., Gupta, D., Khanna, A., and Shankar, K., 2021. Blockchain-assisted secure image transmission and diagnosis model on internet of medical things environment. *Personal and Ubiquitous*

Computing, 26, pp.1-11.

Ayon, S.I., Islam, M.M., and Hossain, M.R., 2020. Coronary artery heart disease prediction: A comparative study of computational intelligence techniques. *IETE Journal of Research*, 68(4), pp.2488-2507.

Balakrishnan, B., and Kumar, C.N.S.V., 2021. A comprehensive performance analysis of various classifier models for coronary artery disease prediction. *International Journal of Cognitive Informatics and Natural Intelligence*, 15(4), pp.1-14.

Choi, E., Schuetz, A., Stewart, W.F., and Sun, J., 2017. Using recurrent neural network models for early detection of heart failure onset. *Journal of the American Medical Informatics Association*, 24(2), pp.361-370.

Dami, S., and Yahaghizadeh, M., 2021. Predicting cardiovascular events with deep learning approach in the context of the internet of things. *Neural Computing and Applications*, 33(13), pp.7979-7996.

Dutta, A., Batabyal, T., Basu, M., and Acton, S.T., 2020. An efficient convolutional neural network for coronary heart disease prediction. *Expert Systems with Applications*, 159, p.113408.

Farahani, B., Firouzi, F., Chang, V., Badaroglu, M., Constant, N., and Mankodiya, K., 2018. Towards fog-driven IoT eHealth: Promises and challenges of IoT in medicine and healthcare. *Future Generation Computer Systems*, 78, pp.659-676.

Gambhir, S., Kumar, Y., Malik, S., Yadav, G., and Malik, A., 2019. Early diagnostics model for dengue disease using decision tree-based approaches. In: *Pre-screening Systems for Early Disease Prediction, Detection, and Prevention*. IGI Global, United States, pp.69-87.

Gambhir, S., Malik, S.K., and Kumar, Y., 2016. Role of soft computing approaches in healthcare domain: A mini review. *Journal of Medical Systems*, 40(12), p.287.

Gupta, P.K., Maharaj, B.T., and Malekian, R., 2017. A novel and secure IoT based cloud centric architecture to perform predictive analysis of users activities in sustainable health centres. *Multimedia Tools and Applications*, 76(18), pp.18489-18512.

He, S., Cheng, B., Wang, H., Huang, Y., and Chen, J., 2017. Proactive personalized services through fog-cloud computing in large-scale IoT-based healthcare application. *China Communications*, 14(11), pp.1-16.

Hossen, M.N., Panneerselvam, V., Koundal, D., Ahmed, K., Bui, F.M., and Ibrahim, S.M., 2022. Federated machine learning for detection of skin diseases and enhancement of internet of medical things (IoMT) security. *IEEE Journal of Biomedical and Health Informatics*, 27, pp.835-841.

Islam, S.M.R., Kwak, D., Kabir, M.H., Hossain, M., and Kwak, S.P., 2015. The internet of things for health care: A comprehensive survey. *IEEE Access*, 3, pp.678-708.

Kaur, A., and Kumar, Y., 2021. Healthcare data analysis using water wave optimization-based diagnostic model. *Journal of Information and Communication Technology*, 20(4), pp.457-488.

Kaur, P., Kumar, R., and Kumar, M., 2019. A healthcare monitoring system using random forest and internet of things (IoT). *Multimedia Tools and Applications*, 78(14), pp.19905-19916.

Khamparia, A., Singh, P.K., Rani, P., Samanta, D., Khanna, A., and Bhushan, B., 2021. An internet of health things-driven deep learning framework for detection and classification of skin cancer using transfer learning. *Transactions on Emerging Telecommunications Technologies*, 32(7), p.e3963.

Kumar, D., Mandal, N., and Kumar, Y., 2022. Fog-based framework for diabetes prediction using hybrid ANFIS model in cloud environment. *Personal and Ubiquitous Computing*, 26, pp.1-8.

Kumar, P.M., Lokesh, S., Varatharajan, R., Babu, G.C., and Parthasarathy, P., 2018. Cloud and IoT based disease prediction and diagnosis system for healthcare using Fuzzy neural classifier. *Future Generation Computer Systems*, 86, pp.527-534.

Kumar, Y., Yadav, G., Singh, P.K., and Arora, P., 2019. *A PHR-based System for Monitoring Diabetes in Mobile Environment*. Springer, Cham, pp.129-144.

Machine Learning, Big Data, and IoT for Medical Informatics. Available from: https://www.scholar.google.com/scholar?hl=en&andas_sdt=0%2c5andq=machine+learning%2c+big+data%2c+and+iot+for+medical+informatics&btnq [Last accessed on 2023 Feb 26].

Madhavan, M.V., Khamparia, A., Gupta, D., Pande, S., Tiwari, P., and Hossain, M.S., 2021. Res-CovNet: An internet of medical health things driven COVID-19 framework using transfer learning. *Neural Computing and Applications*, 26, pp.1-14.

Manogaran, G., Alazab, M., Song, H., and Kumar, N., 2021. CDP-UA: Cognitive data processing method wearable sensor data uncertainty analysis in the internet of things assisted smart medical healthcare systems. *IEEE Journal of Biomedical and Health Informatics*, 25(10), pp.3691-3699.

Mansour, R.F., El Amraoui, A., Nouaouri, I., Diaz, V.G., Gupta, D., and Kumar, S., 2021. Artificial intelligence and internet of things enabled disease diagnosis model for smart healthcare systems. *IEEE Access*, 9, pp.45137-45146.

Maragatham, G., and Devi, S., 2019. LSTM model for prediction of heart failure in big data. *Journal of Medical Systems*, 43(5), p.111.

Mishra, S., Thakkar, H.K., Mallick, P.M., Tiwari, P., and Alamri, A., 2021. A sustainable IoT based computationally intelligent healthcare monitoring system for lung cancer risk detection. *Sustainable Cities and Society*, 72, p.103079.

Mutlag, A.A., Abd Ghani, M.K., Arunkumar, N., Mohammed, M.A., and Mohd, O., 2019. Enabling technologies for fog computing in healthcare IoT systems. *Future Generation Computer Systems*, 90, pp.62-78.

Rahmani, A.M., Gia, T.N., Negash, B., Anzanpour, A., Azimi, I., Jiang, M., and Liljeberg, P., 2018. Exploiting smart e-Health gateways at the edge of healthcare internet-of-things: A fog computing approach. *Future Generation Computer Systems*, 78, pp.641-658.

Raju, K.B., Dara, S., Vidyarthi, A., Gupta, V.M., and Khan, B., 2022. Smart heart disease prediction system with IoT and fog computing sectors enabled by cascaded deep learning model. *Computational Intelligence and Neuroscience*, 2022, p.1070697.

Rhayem, A., Mhiri, M.B.A., Drira, K., Tazi, S., and Gargouri, F., 2021. A semantic-enabled and context-aware monitoring system for the internet of medical things. *Expert Systems*, 38(2), p.e12629.

Satpathy, S., Mohan, P., Das, S., and Debbarma, S., 2020. A new healthcare diagnosis system using an IoT-based fuzzy classifier with FPGA. *Journal of Supercomputing*, 76(8), pp.5849-5861.

Singh, H., and Kumar, Y., 2019. Cellular automata based model for e-healthcare data analysis. *International Journal of Information System Modeling and Design*, 10(3), pp.1-18.

Siddiqui SY, Haider A, Ghazal TM, MA Khan, Naseer I, Abbas S, 2021. IoMT cloud-based intelligent prediction of breast cancer stages empowered with deep learning. *IEEE Access*, 9, pp. 146478-146491.

Srivastava, A.K., Kumar, Y., and Singh, P.K., 2022. Hybrid diabetes disease prediction framework based on data imputation and outlier detection techniques. *Expert Systems*, 39(3), p.e12785.

Su, Y.S., Ding, T.J., and Chen, M.Y., 2021. Deep learning methods in internet of medical things for valvular heart disease screening system. *IEEE Internet of Things Journal*, 8(23), pp.16921-16932.

Vellameeran, F.A., and Brindha, T., 2022. A new variant of deep belief network assisted with optimal feature selection for heart disease diagnosis using IoT wearable medical devices. *Computer Methods in Biomechanics and Biomedical Engineering*, 25(4), pp.387-411.

Zhou, Z., and Feng, J., 2017. *Deep Forest: Towards An Alternative to Deep Neural Networks*. Available from: <https://www.cs.nju.edu.cn/zhouch/zhouch.files/publication/ijcai17gcforest.pdf> [Last accessed on 2023 Feb 26].

Zhou, Z.H., and Feng, J., 2019. Deep forest. *National Science Review*, 6(1), pp.74-86.

The Most Common Characteristics of Fragile Video Watermarking: A Review

Yasmin A. Hassan¹ and Abdul Monem S. Rahma²

¹Department of Computer Science, College of Science, University of Baghdad, Baghdad, Iraq

²Department of Computer science, College of Science, Al-Maarif University College, Al-Anbar, Iraq

Abstract—The progress of network and multimedia technologies has been phenomenal during the previous two decades. Unauthorized users will be able to copy, retransmit, modify reproduction, and upload the contents more easily as a result of this innovation. Malicious attackers are quite concerned about the development and widespread use of digital video. Digital watermarking technology gives solutions to the aforementioned problems. Watermarking methods can alleviate these issues by embedding a secret watermark in the original host data, allowing the genuine user or file owner to identify any manipulation. In this study, lots of papers have been analyzed and studied carefully, in the period 2011–2022. The historical basis of the subject should not be forgotten so studying old research will give a clear idea of the topic. To aid future researchers in this subject, we give a review of fragile watermarking approaches and some related papers presented in recent years. This paper presents a comparison of many relevant works in this field based on some of the outcomes and improvements gained in these studies, which focuses on the common characteristics that increase the effect of watermarking techniques such as invisibility, tamper detection, recovery, and security.

Index Terms—Fragile watermarking, Video watermarking, Tamper detection, Security, Invisibility.

I. INTRODUCTION

Digital videos, such as online movies, network TVs, and mobile videos, are becoming increasingly common due to the rapid growth of the internet and multimedia technologies (Yu, Wang and Zhou, 2018). Protecting the copyright ownership of original videos, as well as authenticating original works' material has become a pressing concern. As an effective technique to handle the problem of copyright protection and multimedia content authentication, digital

watermarking technology has become a study topic in the field of information security (Li, et al., 2020a).

Due to the availability of video content and modern video editing tools on the internet, however, accessing and manipulating video content has become a simple operation, compromising the process of authentication and copyright protection. As a result, it is more important than ever to create solutions that can protect copyrights, identify, and locate video modification (Elrowayati, et al., 2020). In most circumstances, a video editor is used to edit or change a digital video while a video that has been edited is no longer authentic. To solve this problem, additional information is added to this media to ensure authentication and copyright protection (Rahma, et al., 2016). The primary purpose of fragile watermarking is to determine whether or not the video has been tampered with by unauthorized users. Whenever the video has been altered, the algorithm should be capable to find the alteration place on the frames (Munir and Harlili, 2020).

Most watermarking systems are either robust or fragile, robust watermarking is for copyright protection and authentication while fragile watermarking is to detect modification (El Gamal, et al., 2013).

Intraframe and interframe tampering is the two forms of tampering. The insertion or removal of material within the frame is referred to as intraframe manipulation. Adding more frames, removing frames, changing the frame sequence, altering frames, and so on are all examples of interframe manipulation (Patil and Metkar, 2015).

Fragile watermarking may be classified into two kinds based on its purposes: Fragile watermarking for retrieving the original data (recovery) and fragile watermarking for manipulation detection capabilities. The tamper detection fragile watermarking can only detect and locate tampered zone, but it cannot recover the changed frame. Image recovery for tampered areas is essential in several instances (Wang, et al., 2018b).

The rest of this paper is organized as follows. Section II explains video watermarking and common types according to domains, cover media, and perception. In Section III, fragile watermarking has been presented as the core of this paper. In Section IV, the related works have been described;



Section V, summarizes the characteristics of the effective fragile watermarks, in Section VI presents conclusions of this work.

II. VIDEO WATERMARKING

Video watermarking is a relatively recent technology that has been proposed to address the issue of unauthorized digital video alteration and dissemination. Watermarking in videos embeds data for identification, intellectual property, and copyright protection (Hassan and Abbas, 2018).

Fragile, robust, and semi-fragile watermarks are the three most common types of video watermarks

- A. Fragile watermarking technique is employed to validate integrity authentication in the video when it is modified or tampered with high transparency and huge watermark capacities (Agarwal and Husain, 2021).
- B. Robust watermarking must withstand the majority of typical video processing operations, such as recompression and filtering, and may come at the expense of transparency and watermark capacity. It is mostly used to protect copyright.

- A. Semi-fragile watermarking is unaffected by conventional video processing procedures, but it is vulnerable to malicious assaults, making it ideal for tamper detection (Zhou, et al., 2022).

The digital watermarking systems may be further divided into spatial domain watermarking and transform domain watermarking based on the embedding domain as mentioned in Fig. 1 (Wang, et al., 2018a).

The watermarked message is inserted into the host image by directly modifying its pixel values in the spatial domain. The least significant bit (LSB) watermarking strategy is the most used method in the spatial domain.

For every potential alteration on the host frame, this embedding approach has a high level of fragility. It has been extensively employed for picture authentication and recovery due to its simplicity (Begum and Uddin, 2020). In the transform domain, the watermark is concealed in the host image through modulating transform domain coefficients (Yu, Wang and Zhou, 2019). The discrete cosine

transform (DCT), discrete wavelet transform (DWT), and singular value decomposition (SVD) are the most often utilized transformations (SVD). The robust and semi-fragile watermarking procedures are frequently conducted in the transform domain to ensure improved resilience against alterations (Wang, et al., 2018b)

III. FRAGILE WATERMARKING

Fragile watermarking is a type of watermarking that allows for precise authentication [5]. Watermarks are embedded in files that may be verified to see whether they are the same watermarked file. Fragile watermarking is rarely used in everyday situations since any modification made to the file, whether on purpose or by mistake, will be considered a new file (Gutub, 2022). Fragile watermarking has a few specific applications, such as checking for tampering or changes to works-in-progress. Fragile watermarking has a few specific applications, such as checking for tampering or changes to works-in-progress, even if it was just due to noise (Akhtar et al., 2022).

A fragile watermark includes three elements: watermark insertion, tamper detection, and tamper localization

- Watermark insertion is a process that editing a secret key to the original picture before it is spread. For a peripheral user, the watermarked image is nearly identical to the original image.
- Tamper detection is mainly based on statistical processes and it can be verified on a sample image that has been appropriately analyzed by measuring the true positive (TP) and false positive (FP) rates on the altered image, which are calculated by dividing the number of pixels detected as tampered by the number of pixels that have been really tampered.
- Tamper localization identifies the image's altered parts. As a result of the tamper localization technique, a two-level image exhibiting the ground of the modified areas can be generated (Di Martino and Sessa, 2012).

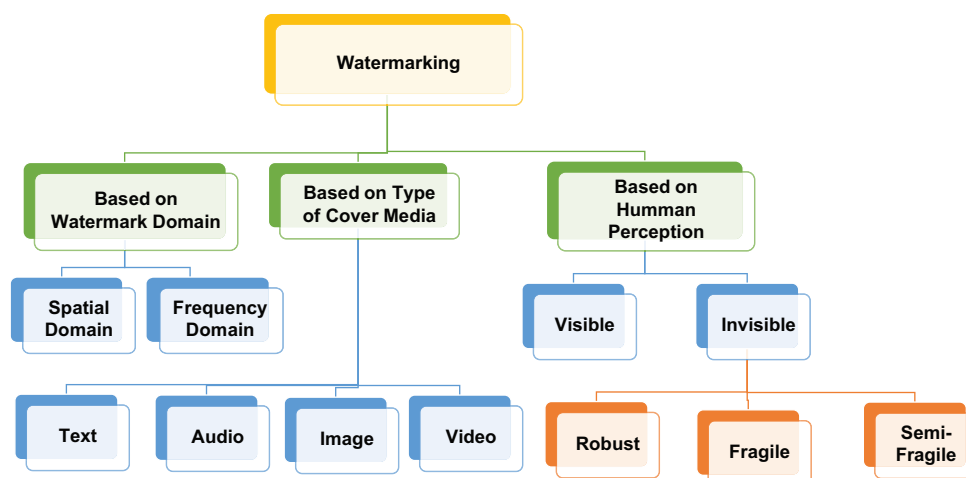


Fig. 1. General block diagram of watermarking.

IV. RELATED WORK

Fragile Watermarking for digital video has been a popular research topic. Commercial software has recently made it quite easy to change digital video, increasing the need to verify video material authenticity (Makhrib and Karim, 2022). In this study, the most common techniques for fragile watermarking have been collected to solve the current problems mentioned above. The search was done in Google scholar, research gate, and Google as a big library to us and takes only initial results of searching in time 2011–2022.

- Zhi-yu and Xiang-hong (2011) provide a fragile watermarking-based technique for color video integrity authentication. The RGB color mode is converted to YST, which is used to insert watermarking into the original video. The simulation results demonstrate that the technique is capable of maintaining video quality while also detecting tampering and attacks on the source material.
- El Gamal, et al. (2013) present a method of video watermarking (fragile) capable of detecting tampering in spatial domains. A mathematical method is used to incorporate the watermark bits for each block independently. The suggested technique successfully detects a large variety of tampering threats with a high detection rate at a low computation cost.
- Patil and Metkar (2015) designed a technique of fragile video watermarking to determine the tampered area. The watermark is generated from block numbers and frame numbers that are inserted into the frame as a watermark in the frequency domain. This method is really sensitive to changes, has a high capacity and transparency, and can also notice manipulation.
- Ait Sadi, et al. (2017) offer a technique for ensuring the integrity of the H.264/AVC video stream employing separate authentication of each Group of Pictures (GOPs) inside the video based on a content fragile video watermarking mechanism. While keeping the original bitrate and perceptual quality, the suggested approach delivers an accurate authentication mechanism with great fragility and fidelity. Its ability to detect tampered frames in the case of spatial, temporal, and color changes has also been shown.
- Bhattacharya and Palit (2018) provide a method for reducing the reference strategy by combining robust picture characteristics with fragile watermarking approaches. The technique does not require any other data other than the input image. The watermark is built from the picture to be sent using robust image characteristics and then placed as a fragile watermark in the image itself.
- Munir (2019) provides a spatial domain fragile watermarking technique for ensuring the integrity of video digital material. To boost security, the watermark is encrypted before embedding by XOR-ing it with a random image. A chaotic map, such as the Arnold Cat Map, is used to produce a random picture. The algorithm can recognize and pinpoint the changed region of video frames quite effectively, according to the results of the experiments.
- Munir and Harlili (2019) suggest a fragile video watermarking technique based on chaos is suggested in the spatial domain.

The watermark is a binary picture of the same size as the video frame size. To boost security, the watermark is coded using an XOR operation with a random picture before inserting. A cross-Coupled Chaotic Random Bit Generator (CCCBG) is used to create the random picture. The encrypted watermark is inserted into every RGB element of each frame.

- Hammami, et al. (2020b) offer a new semi-fragile frequency domain watermarking approach for surveillance video authentication. The system begins by producing a binary watermark using a unique watermark generation method. Regions of Interest (ROI) are recognized and employed as watermark holders throughout the embedding process. SVD and discrete wavelet transform (DWT) are used to decompose these areas into distinct frequency sub-bands.
- Li, et al. (2020a) present a semi-fragile video watermarking technique that can accomplish frame attack and video tamper detection at the same time performed by adding authentication code based on the numerical interaction of the DCT coefficients and the frame number as the watermark information.
- Munir and Harlili (2020) based on the chaotic map, a weak video watermarking was presented. The watermark is encrypted, watermark has been applied using an XOR operation with a random picture to boost security. “Cross-Coupled Chaotic Random Bit Generator is used to create the random picture (CCCBG)”. Every RGB element of each frame contains the coded watermark.
- Aminuddin and Ernawan (2022) present a color image authentication based on blind fragile image watermarking for tamper detection and self-recovery. The proposed technique utilizes an LSB shifting algorithm that can decrease the pixel intensity variation between the cover and watermarked images.

Table I present a comparison of previous works in this field including the used technique, used metrics main achievement that researchers accomplish in their papers with the limitations, and the accessed results concerning PSNR for the period (2011–2022). As a result of this comparison, the most used technique for fragile watermarking is the least significant bit (LSB). It is fast and easy to apply and does not consume much time compared to the use of transform algorithms but it is easy to crack, therefore, fragile watermarking with LSB is used for tamper detection in real-time video in addition to robust watermarking to obtain an efficient and secured system.

V. CHARACTERISTICS OF AN EFFECTIVE FRAGILE WATERMARK

Based on the purpose of the watermarking algorithm, there are several features used to evaluate the efficiency of a fragile watermarking method.

- Perceptibility: The inserted watermark should be completely invisible. It must be hard to notice it through human vision, and it should not affect the regular operation of the host image. In general, the stronger the watermark’s security,

TABLE I
A COMPARISON BASED ON PREVIOUS RELEVANT WORKS

References	Technique	Evaluation metrics	Achievements	Limitations	Results (PSNR)
Zhi-yu and Xiang-hong, 2011	YST color mode and DCT	PSNR	Good security after encryption, effective detection of video attacks, and localizing the position of tampering.	No recovery.	*33.64 **19.1
El Gamal, <i>et al.</i> , 2013	Spatial domain, block mean, and modulation factor.	PSNR	a minimal cost of computing and a high rate of detection against a variety of tampering attempts	Not all frames with watermarks can fully retrieve the watermark that is inserted.	*55.5 **49.2
Patil and Metkar, 2015	LSB and DCT	PSNR, SSIM	high capacity and transparency, and smaller video distortion.	not robust against compression.	*38.2 **19.4
Ait Sadi, <i>et al.</i> , 2017	DCT	PSNR, SSIM, and video quality metric	The system is sensitive enough to identify altered spatial, temporal, and color frames that are tampered with in videos.	To find the altered frames, the algorithm needs extra time.	*40.05 **34.91
Munir, 2019	Arnold Cat Map	NM	The algorithm does a great job of locating and detecting changed areas in video frames.	Don't use transform domain and compression.	NM
Hammami, <i>et al.</i> , 2020a	DWT and SVD	PSNR and BER	It effectively distinguishes between harmful and normal actions.	No recovery	*73.42 **48.74
Li, <i>et al.</i> , 2020b	DCT	PSNR	The technique displays high resilience, as the embedded watermarked video's visual quality is almost unaffected.	NM	*38.1 **33
Aminuddin and Ernawan, 2022	LSB	PSNR and SSIM	More security due to using two LSB for embedding watermark	The proposed scheme consumes a large time.	*43.63 **22.39
Makhrif and Karim, 2022	Modified LBP, LSB	PSNR and MSE	The suggested method provides improved robustness, greater imperceptibility, and good invisibility.	NM	*54.42
Al-Otun and Ellubani, 2022	DWT and LSB	PSNR and SSIM	Good security and effective self-restoration and tamper detection for color images	Consume more time	*44.52 **31.47

*Highest result. **Lowest result. NM: Not mentioned, DCT: Discrete cosine transform, DWT: Discrete wavelet transform, LSB: Least significant bit, PSNR: Peak signal-to-noise ratio, SVD: Singular value decomposition, SSIM: Structural SIMilarity index

TABLE II
A COMPARISON OF DIFFERENT WATERMARKING TECHNIQUES WITH THE MOST COMMON FACTORS

References	Used technique	Transform	Size of block	Watermark type	Invisibility	Tamper detection	Recovery	Robustness
Zhi-yu and Xiang-hong, 2011	Frequency domain	YST and DCT	4×4	Fragile	Yes	Yes	No	Yes*
Zigomitos, Papageorgiou and Patsakis, 2012	Watermarking in social network	No transform		Robust and semi-fragile	NM	Yes	NM	Yes
El Gamal, <i>et al.</i> , 2013	Spatial domain, modulation	No transform	B×B	Fragile	Yes	Yes	Yes	Yes
Patil and Metkar, 2015	Frequency domain	DCT	8×8	Fragile	Yes	Yes	No	No
Bhattacharya and Palit, 2018	Frequency domain	SVD		Fragile	NM	NM	NM	Yes
Ait Sadi, <i>et al.</i> , 2017	Motion vector	DCT		Fragile	NM	Yes	No	Yes
Wang, <i>et al.</i> , 2018b	Spatial domain and frequency domain	NM	NM	Fragile	Yes	Yes*	Yes*	Yes
Munir, 2019	Spatial domain and Arnold Cat Map	DCT		Fragile	NM	Yes	Yes	Yes
Rakhmawati, Wirawan and Suwadi, 2019	Frequency domain	DCT, DWT, DCT-DWT	8×8	Fragile	NM	Yes	Yes	Yes
Li, <i>et al.</i> , 2020a	Frequency domain	DCT	4×4	Semi-fragile	Yes	Yes	No	No
Munir and Harlili, 2020	Spatial domain based on chaos and cross-coupled chaotic random bit generator	No transform		Fragile	NM	Yes	Yes	Yes*
Hammami, Ben Hamida and Ben Amar, 2021	ROI, and QR	SVD and DWT		Semi-fragile	Yes	Yes	NM	Yes
Makhrif and Karim, 2022	Modified LBP, LSB	No transform		Fragile	Yes*	Yes	NM	NM
Al-Otun and Ellubani, 2022	LSB	DWT		Robust and fragile	Yes	Yes	Yes	Yes
Shukla, <i>et al.</i> , 2022	LSB	No transform		Fragile	NM	Yes	No	Yes
Aminuddin and Ernawan, 2022	LSB	No transform	2×2	Fragile	Yes*	Yes	Yes	Yes

*Intentional effect. NM: Not mentioned, DCT: Discrete cosine transform, DWT: Discrete wavelet transform, LSB: Least significant bit, SVD: Singular value decomposition

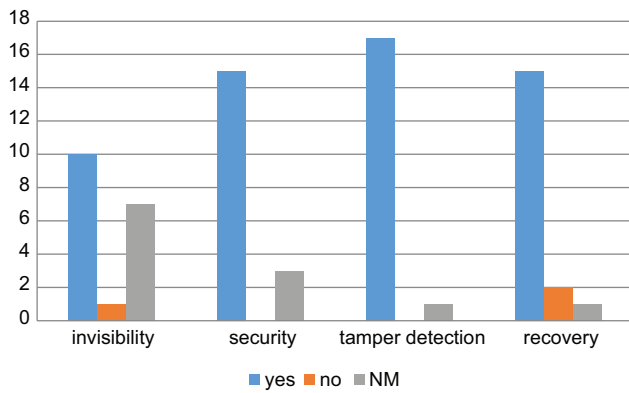


Fig. 2. The most common characteristics of this study.

the better the imperceptibility.

- B. Tamper detection: A fragile watermark should be able to locate where the tampering has been done to determine the directions of attackers to prevent such attacks in the future. The effect of picture recovery is determined by the tamper detection capability.
- C. Tamper recovery: The system must have the ability to detect unlawful picture alterations and recover photos from those that have been tampered with. The higher the tamper detection accuracy, the better the picture recovery outcome.
- D. Robust to known attacks: The design should be as resistant to well-known attacks as possible, such as the general, collage, and disturbing attacks (Wang, et al., 2018b, Rakhmawati, Wirawan and Suwadi, 2019).

In Table II, a comparison was presented between previous researchers and their achievements through a set of factors, including invisibility, which should be achieved in most watermarking techniques to thwart unauthorized users and cut the road to them when trying to know the watermark data. Detection of tampering, the main goal of the fragile watermarks, locating the tampered zone, and knowing the direction of the piracy when manipulating the content of video frames. Not all watermarking systems achieve recovery properties although it may be an essential point in some systems depending on the used application.

Fig. 2 visually summarizes the characteristics and shows that the most previous researches achieve these characteristics and it can be included that the feature of detecting manipulation is the most applied characteristic. As a result, whenever these factors combine, the watermark achieves the best effect when it is added to the video.

VI. CONCLUSION

Digital watermarking is a technique in which information is inserted in media for authentication, copyright protection, tamper detection, or modification area. Digital watermarking methods, in general, handle the problem of manipulating frames by inserting secret data directly in the image and identifying the changed area immediately. Based on the analysis, the fragile watermarking methods are effective in

real-time video processing in terms of finding the zone of tampering in the video in addition to robust watermarks to ensure copyright protection, the integrity of the video and, tamper detection in video. In this review, a comparison was presented between previous researchers and their achievements through a set of factors, including concealment, detection of change, retrieval, and safety, and as a result, whenever these factors combine, the watermark achieves the best effect when it is added to the video.

REFERENCES

- Agarwal, H. and Husain, F. 2021. Development of payload capacity enhanced robust video watermarking scheme based on the symmetry of circle using lifting wavelet transform and SURF. *Journal of Information Security and Applications*, 59, p. 102846.
- Ait Sadi, K., Guessoum, A., Bouridane, A. and Khelifi, F. 2017. Content fragile watermarking for H.264/AVC video authentication. *International Journal of Electronics*, 104, pp. 673-691.
- Akhtar, N., Saddique, M., Asghar, K., Bajwa, U.I., Hussain, M. and Habib, Z. 2022. Digital video tampering detection and localization: Review, representations, challenges and algorithm. *Mathematics*, 10, p. 168.
- Al-Otun, H.M. and Ellubani, A.A.A. 2022. Secure and effective color image tampering detection and self restoration using a dual watermarking approach. *Optik*, 262, p. 169280.
- Aminuddin, A. and Ernawan, F. 2022. AuSR1: Authentication and self-recovery using a new image inpainting technique with LSB shifting in fragile image watermarking. *Journal of King Saud University-Computer and Information Sciences*, 34, pp. 5822-5840.
- Begum, M. and Uddin, M.S. 2020. Digital image watermarking techniques: A review. *Information*, 11, p. 110.
- Bhattacharya, A. and Palit, S. 2018. Blind quality assessment of image and video based on fragile watermarking and robust features. *Multidimensional Systems and Signal Processing*, 29, pp. 1679-1709.
- Di Martino, F. and Sessa, S. 2012. Fragile watermarking tamper detection with images compressed by fuzzy transform. *Information Sciences*, 195, pp. 62-90.
- El Gamal, A., Mosa, N. and El Said, W. 2013. A fragile video watermarking algorithm for content authentication based on block mean and modulation factor. *International Journal of Computer Applications*, 80, pp. 21-28.
- Elrowayati, A.A., Alrshah, M.A., Abdullah, M.F.L. and Latip, R. 2020. Heve watermarking techniques for authentication and copyright applications: Challenges and opportunities. *IEEE Access*, 8, pp. 114172-114189.
- Gutub, A.A.A. 2022. Adopting counting-based secret-sharing for e-Video Watermarking allowing Fractional Invalidation. *Multimedia Tools and Applications*, 81, pp. 9527-9547.
- Hammami, A., Ben Hamida, A. and Ben Amar, C. 2021. Blind semi-fragile watermarking scheme for video authentication in video surveillance context. *Multimedia Tools and Applications*, 80, pp. 7479-7513.
- Hammami, A., Hamida, A.B., Amar, C.B. and Nicolas, H. 2020a. Regions based semi-fragile watermarking scheme for video authentication. *Journal of WSCG*, 28, pp. 96-104.
- Hammami, A., Hamida, A.B., Nicolas, H. and Amar, C.B. 2020b. Regions based semi-fragile watermarking scheme for video authentication. In: *International Conference in Central Europe on Computer Graphics, Visualization and Computer Vision*, pp. 96-104.
- Hassan, N.F. and Abbas, R.N. 2018. Proposed video watermarking algorithm based on edge or corner regions. *Engineering and Technology Journal*, 36, 25-32.
- Li, C., Yang, Y., Liu, K. and Tian, L. 2020a. A semi-fragile video watermarking

- algorithm based on H. 264/AVC. *Wireless Communications and Mobile Computing*, 2020, p. 8848553.
- Li, C., Yang, Y., Liu, K. and Tian, L. 2020b. A semi-fragile video watermarking algorithm based on H. 264/AVC. *Wireless Communications and Mobile Computing*, 2020, p. 8848553.
- Makhrib, Z.F. and Karim, A.A. 2022. Improved fragile watermarking technique using modified LBP operator. In: *2022 International Conference on Computer Science and Software Engineering (CSASE)*. IEEE, United States, pp. 132-137.
- Munir, R. 2019. A secure fragile video watermarking algorithm for content authentication based on arnold CAT map. In: *2019 4th International Conference on Information Technology (InCIT)*. IEEE, United States, pp. 32-37.
- Munir, R. and Harlili, H. 2020. Application of chaos-based fragile watermarking to authenticate digital video. In: *Digital Forensic Science*. IntechOpen, London.
- Munir, R. and Harlili, H. 2019. *Authentication of Digital Video Using Fragile Watermarking Algorithm Based on Chaotic Map*.
- Patil, R.D. and Metkar, S. 2015. Fragile video watermarking for tampering detection and localization. In: *2015 International Conference on Advances in Computing, Communications and Informatics (ICACCI)*. IEEE, United States. pp. 1661-1666.
- Rahma, A.M., Abdulmunim, M.E. and Al-Janabi, R.J. 2016. New Watermark Algorithm support Based on Watermark Designing. *Diyala Journal For Pure Science*, 12, 1-11.
- Rakhmawati, L., Wirawan, W. and Suwadi, S. 2019. A recent survey of self-embedding fragile watermarking scheme for image authentication with recovery capability. *EURASIP Journal on Image and Video Processing*, 2019, pp. 1-22.
- Shukla, A., Gupta, A., Jaglan, S. and Shivani, S. 2022. An efficient self-embedding fragile watermarking scheme based on neighborhood relationship. In: *Innovations in Computational Intelligence and Computer Vision*. Springer, Germany.
- Wang, C., Shan, R. and Zhou, X. 2018a. Anti-HEVC recompression video watermarking algorithm based on the all phase biorthogonal transform and SVD. *IETE Technical Review*, 35, pp. 42-58.
- Wang, C., Zhang, H. and Zhou, X. 2018b. Review on self-embedding fragile watermarking for image authentication and self-recovery. *Journal of Information Processing Systems*, 14, pp. 510-522.
- Yu, X., Wang, C. and Zhou, X. 2018. A survey on robust video watermarking algorithms for copyright protection. *Applied Sciences*, 8, p. 1891.
- Yu, X., Wang, C. and Zhou, X. 2019. A hybrid transforms-based robust video zero-watermarking algorithm for resisting high efficiency video coding compression. *IEEE Access*, 7, pp. 115708-115724.
- Zhi-Yu, H. and Xiang-Hong, T. 2011. Integrity authentication scheme of color video based on the fragile watermarking. In: *2011 International Conference on Electronics, Communications and Control (ICECC)*. IEEE, United States, pp. 4354-4358.
- Zhou, L., Zuo, M.J., Shi, H., Zhang, Y. and Gong, L.H. 2022. Robust watermarking algorithm against the geometric attacks based on non-subsampled shearlet transform and Harris-Laplace detector. *Security and Communication Networks*, 2022, p. 7605595.
- Zigomitos, A., Papageorgiou, A. and Patsakis, C. 2012. Social network content management through watermarking. In: *2012 IEEE 11th International Conference on Trust, Security and Privacy in Computing and Communications*. IEEE, United States, pp. 1381-1386.

Optical and Optoelectronic Studies of Binary and Ternary Films of Poly(L-Tryptophane), Poly(5-hydroxy-L-tryptophane), and P(TER-CO-TRI) Doped with Sudan Dye

Barham K. Rahim¹, Peshawa O. Amin², Fahmi F. Muhammadsharif³, Salah R. Saeed⁴, and Kamal A. Ketuly⁵

¹Department of Medical Physics, Faculty of Medicals and Applied Science, Charho University, 46023 Chamchamal, Sulaimania, Kurdistan Region - F.R. Iraq

²Charho Center for Research, Training and Consultancy, Charho University, 46023 Chamchamal, Kurdistan Region - F.R. Iraq

³Department of Physics, Faculty of Science and Health, Koya University, 44023 Koya, Kurdistan Region - F.R. Iraq

⁴Department of Physics, College of Science, University of Sulaimani, Qlyasan Street, Sulaimani 46001, Kurdistan Region - F.R. Iraq

⁵Department of Medical Chemistry, College of Medicine, University of Duhok, Duhok, Kurdistan Region - F.R. Iraq

Abstract—In this work, the optical properties and optoelectronics parameters of binary and ternary composite films made of two electron acceptors, poly(L-Tryptophane) and poly(5-hydroxy-L-Tryptophane), with an electron donor, P(TER-CO-TRI), doped with Sudan dyes, are comprehensively investigated. The films with different volumetric ratios of the components were deposited onto the glass substrates using spin coating technique. Results showed that with the help of dye doping into the binary systems of poly(L-Tryptophane):P(TRI-co-TER) (1:2) and poly(5-hydroxy-L-Tryptophane):P(TRI-co-TER) (1:2), the refractive index was increased from 2.01 to 2.32. The nature of the electronic transition in the studied films was found to be a direct allowed transition, which was derived from Tauc's equation. The combination of cyclic voltammetry technique and absorption spectroscopy was used to determine the molecular energy levels, HOMO and LUMO of the polymer samples. It was seen that the mixture of poly(L-Tryptophane):P(TRI-co-TER):Sudan dye (1:2:2) has led to increase the energy gap to 2.95 eV and the real optical conductivity (σ_r) to about 433.11 S.cm⁻¹. According to the findings, the investigated polymers can have a great potential for semitransparent organic solar cells.

Index Terms—Poly(L-Tryptophane), Poly(5-hydroxy-L-tryptophane), P(TER-CO-TRI), Sudan dye, Energy band gap, Refractive index, Dielectric constant.

I. INTRODUCTION

Since the emergence of organic-material-based electronic devices, a variety of organic materials have been the subject of investigation. This can be mainly due to the distinctive properties of organic materials such as solution processability, thermal stability, lightweight, flexibility, high emission yield, and energy gap tuneability (Rajeswaran, et al., 2009; Sajid, et al., 2015; Lewis, 2006; Kaltenbrunner, et al., 2013). However, performance and operation of organic devices necessitate exhaustive studies of organic semiconductors (Gather, Köhnen and Meerholz, 2011). As a result, obtaining sufficient information on the optoelectronic properties of the used organic materials under various doping situations is essential to fabricate an efficient optoelectronic device. The process of doping can be used to fine-tune the optical characteristics of a material to the preferred level, in which the doped material acts as a host for the dopant material (Basir, et al., 2021). Herein, the aim is to take advantage of the dopant's significant features while concurrently improving the host response. Consequently, tris(8-hydroxyquinoline) aluminum (Alq₃) and its counterpart, tris (8-hydroxyquinolate) Gallium Gaq₃, were broadly employed in the electronic devices based on organic materials such as light-emitting diodes. They are preferred due to their superior thermal stability, optical

ARO-The Scientific Journal of Koya University
Vol. XI, No. 1 (2023), Article ID: ARO.11103. 11 pages
Doi: 10.14500/aro.11103

Received: 31 October 2022; Accepted: 31 March 2023

Regular research paper: Published: 17 April 2023

Corresponding author's e-mail: fahmi.fariq@koyauniversity.org

Copyright © 2023 Barham K. Rahim, Peshawa O. Amin, Fahmi F. Muhammadsharif, Salah R. Saeed, and Kamal A. Ketuly. Rahmah.

This is an open access article distributed under the Creative Commons Attribution License.



performance, and optoelectronic response. In addition, Alq3 has been successfully engaged in the fabrication of organic solar cells as an electron transport layer (El Jouad, et al., 2016; Muhammad and Sulaiman, 2018). As a result, Alq3 is a potential dopant for tuning the optoelectronic characteristics of organic semiconductors. In addition, N, N' -Di [(1-naphthyl)-N, N' - diphenyl]-(1, 1' -biphenyl)-4, 4' -diamine was used as a donor material in ultraviolet (UV) photodiodes (Vickers, 2017). One of the characteristic features of organic semiconductors is the tunability of electronic energy levels, which consequently leads to the energy gap tailoring of the active layers, thereby realizing photodetectors for simultaneous sensing of UV and infrared light (Muhammad, et al., 2017; Omidvar, 2017; Yang, et al., 2019). Moreover, it was seen from the literature that a hybrid composition of inorganic and organic materials can also be utilized to improve UV detectors (Hu, et al., 2015; Bilgaiyan, et al., 2017; Garg, et al., 2019). As a result, finding a potential candidate for an organic composite to be used as the active layer of UV detectors is critical. Many researchers have made significant efforts to utilize inorganic-based semiconductors or their hybrid nanoarchitectures and have primarily undertaken research employing these materials (Hou, et al., 2011; Jheng, et al., 2020). Applications such as imaging, medical sensing, secure communication, and assessment of many surrounding surroundings are conceivable thanks to UV ray detection, and active research is underway (Zeng, et al., 2019).

To address organic materials and their viability for potential applications, in this current work the absorption response, optical energy gap, refractive index, dielectric constant, and optical conductivity of organic composite systems incorporating poly(L-tryptophane) and poly(L-Tryptophane):P(TRI-co-TER) with Sudan dye are investigated.

II. MATERIALS AND METHODS

Poly(5-hydroxy-L-Tryptophane) and poly(L-Tryptophane) are electron acceptors and P(TRI-co-TER) present an electron donor material. The molecular structures of the used materials are shown in Fig. 1. The organic materials were separately put inside vials and dissolved in chloroform solvent following their stirring overnight using a magnetic stirrer.

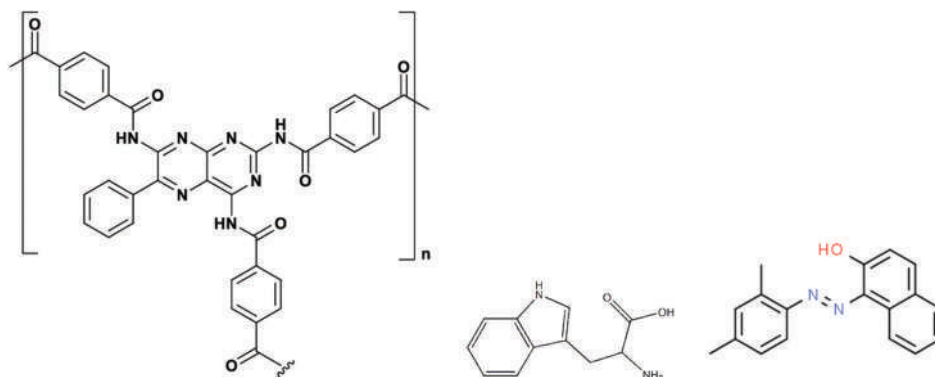


Fig. 1. Molecular structure of poly(triamterene-co-terephthalate), poly(L-tryptophan) and Sudan dye (left to right).

Later on, the solutions of poly(5-hydroxy-L-Tryptophane), poly(L-Tryptophane), and P(TRI-co-TER) were prepared with concentration of 30 mg/mL. The composite binary films were made by volumetric compositions of Acceptor: Donor through mixing poly(5-hydroxy-L-Tryptophane), and poly(L-Tryptophane) with P(TRI-co-TER). Then, Sudan dye was also used to form a ternary composite system. The area under the absorption curve was calculated for all volume ratios of binary systems, and it was determined that (1:2) is the optimal volume ratio. As a result, the optoelectronic properties of the composite at this ratio were thoroughly examined. The optimized system was then doped by Sudan dye to produce a ternary system with different ratios of the dye as follows 1:2:1, 1:2:2 and 1:2:3. The thickness of the grown films was measured using Field emission scanning electron microscopy (FE-SEM) technique (TESCAN MIRA3 FEG-SEM) and the calculated values are shown in Table I. Furthermore, the structural investigation of the single, binary, and ternary films was carried out using the X-ray diffraction (XRD) spectra (Malvern Panalytical's X'Pert, using CuK alpha radiation [1.5418]).

III. RESULTS AND DISCUSSION

A. Photophysical Properties

The optical properties of the polymers and their composite systems were assessed by UV-Vis absorption spectroscopy, as shown in Fig. 2. Despite the fact that intramolecular charge transfer (ICT) occurs at the main polymer chains between an electron deficient and an electron rich moiety due to visible absorption, it is also well known that the $\pi - \pi^*$ and $n - \pi^*$ transitions of delocalized excitons occur in the polymer chain due to UV absorption. (Wang, et al., 2018; Shim, et al., 2015; Kim, et al., 2018). The absorption coefficient spectra of the polymers were determined using the following equation (Alsoghier, et al., 2018; Amin, et al., 2021):

$$\alpha = \frac{2.303A}{t} \quad \alpha = \frac{2.303A}{t} \quad (1)$$

Where t is the thickness of the film, and A is the absorbance of the studied sample. Noticeably, as shown in Fig. 2a and b, the two acceptor polymers exhibited a sharp absorption band in the UV region and extended to the visible region. The absorption band for the acceptor, poly(L-

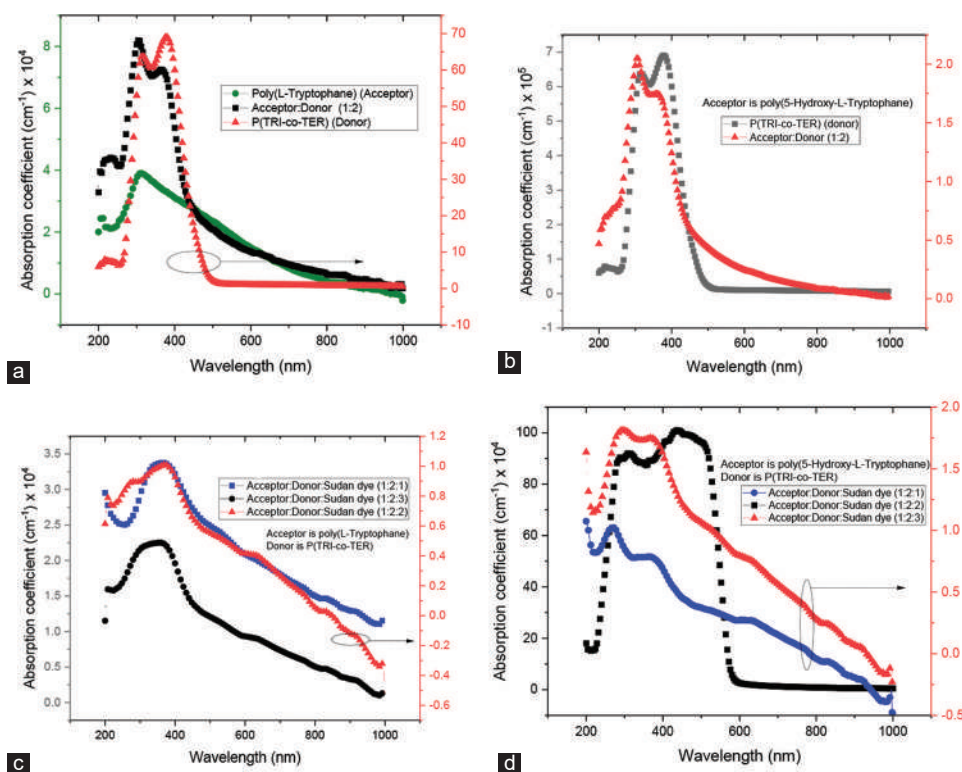


Fig. 2. Absorption coefficient spectra (a and b) of the studied polymers and binary films, and (c and d) ternary films.

TABLE I
THE MEASURED THICKNESS OF THE STUDIED ORGANIC FILMS

Film	Thickness (nm)
P (TRI-co-TER)	424
Poly (5-hydroxy-L-Tryptophane)	170
Poly (5-hydroxy-L-Tryptophane):P (TRI-co-TER) (1:2)	656
Poly (L-Tryptophane)	290
Poly (L-Tryptophane):P (TRI-co-TER) (1:2)	105
Poly (L-Tryptophane):P (TRI-co-TER):Sudan dye (1:2:1)	142
Poly (L-Tryptophane):P (TRI-co-TER):Sudan dye (1:2:2)	191
Poly (L-Tryptophane): P (TRI-co-TER):Sudan dye (1:2:3)	335
Poly (5-hydroxy-L-Tryptophane)	275
:P (TRI-co-TER):Sudan dye (1:2:1)	274
Poly (5-hydroxy-L-Tryptophane)	274
:P (TRI-co-TER):Sudan dye (1:2:2)	227
Poly (5-hydroxy-L-Tryptophane)	227
:P (TRI-co-TER):Sudan dye (1:2:3)	

Tryptophane) was prolonged to 424 nm, while that for poly(5-hydroxy-L-Tryptophane) was extended to 503 nm. The absorption band for the donor, P(TRI-co-TER) was continued till 468 nm, while the absorption band for the composite of poly(L-Tryptophane):P(TRI-co-TER) reached 474 nm. Noteworthy, on the addition of Sudan into the donor-acceptor system (Fig. 2c and d), the ternary composite structure has led to extending the absorption edge. This indicates that the strength of electronic transitions from $\pi - \pi^*$ has increased which is brought about by the addition of Sudan dye.

B. Optical Energy Gap and Transition Types

In optoelectronic applications, the measurements of the optical energy gap of the conjugated polymers and the type of electronic transitions are imperative. Hence, from the absorption spectra, it is plausible to measure the optical energy gap (Table II) and optical transition using Tauc's equation shown as Equation 3 (Muhammad and Sulaiman, 2011; Hamad, 2013). Alternately, the optical energy gap can be determined from the absorption spectrum by measuring the absorption edge of the spectrum, λ_{onset} as follows (Leonat, Sbârcea and Brañzoi, 2013):

$$E_g = \frac{1242}{\lambda_{onset}} \quad (2)$$

However, the nature of the transition can be assigned directly by Tauc's equations in addition to measuring the optical energy gap. Therefore, by taking the natural logarithm and derivation of Equation 3:

$$\alpha hv = \alpha_o (hv - E_g)^s \quad (3)$$

$$\frac{d \ln(\alpha hv)}{d(hv)} = \frac{s}{hv - E_g} \quad (4)$$

where α_o is an energy-independent constant, E_g is the energy gap, ν is the frequency of the incident wave, h is Planck's constant, and the value of s defines the type and nature of the transitions. If the value of $s = 2$, the transition is an indirectly allowed transition, $s = 3$ for indirectly forbidden transitions, $s = 1/2$ for directly allowed transitions and $s = 3/2$ for directly forbidden transitions. Fig. 3a depicts

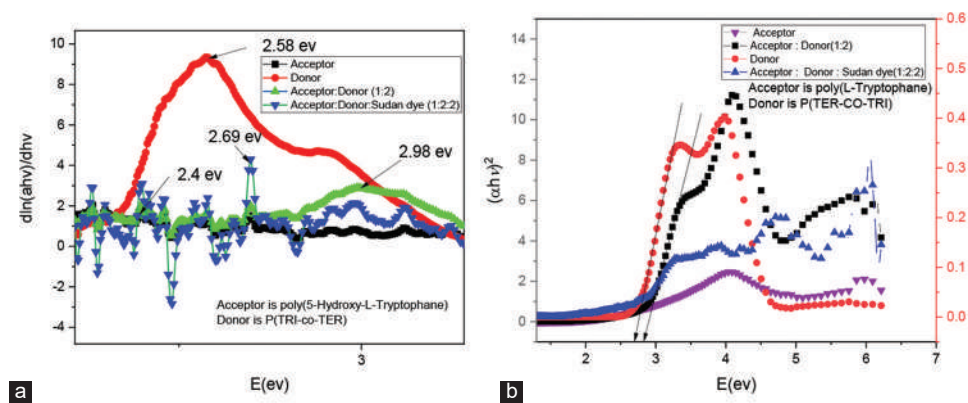


Fig. 3. Plot of $\frac{d\ln(ahv)}{d(hv)}$ versus hv (a), and $(ahv)^2$ versus E (b) for the representative films.

TABLE II
DETERMINED ENERGY GAP FOR THIN FILM OF THE POLYMERS AND TERNARY COMPOSITES

Materials	E_g^{Tauc} (eV)
P (TRI-co-TER)	2.66
Poly (L-Tryptophane)	2.61
Poly (L-Tryptophane):P (TRI-co-TER) (1:2)	2.85
Poly (L-Tryptophane):P (TRI-co-TER):Sudan dye (1:2:2)	2.95
Poly (5-hydroxy-L-Tryptophane)	2.34
Poly (5-hydroxy-L-Tryptophane):P (TRI-co-TER) (1:2)	2.89
Poly (5-hydroxy-L-Tryptophane):P (TRI-co-TER):Sudan dye (1:2:2)	2.60

the plots of $\frac{d\ln(ahv)}{d(hv)}$ versus hv for all the samples and from

which the approximate value of energy gap, $hv = E_g$ was taken at the peak value. Hereafter, the estimated value of E_g was employed for plotting $\ln(ahv)$ versus $\ln(hv - E_g)$ and from the slope of the curves the value of s was determined and it was found to be $\frac{1}{2}$, which is the evidence of the occurrence of a direct allowed transition between the intermolecular energy bands of the polymers. Henceforward, the accurate values of the energy gaps were determined by plotting $(ahv)^2$ as a function of (hv) and taking the extrapolation of the linear portion at $(ahv)^2 = 0$, as shown in Fig. 3b.

C. Electrochemical Properties

In designing and optimizing electronic devices based organic materials, several parameters should be revealed that define the nature of charge transfer and charge collection. To this end, the position of electronic energy levels (HOMO and LUMO) of organic semiconductor materials can be determined by electrochemical study before device fabrication. Therefore, cyclic voltammetry (CV) is a worthy technique to estimate energy levels for the relevant materials from the oxidation and reduction potentials. Hence, the oxidation and reduction potentials are infer from the onset potential, which is defined as the potential, where electrons

or holes are initially injected into the LUMO and HOMO levels, respectively, and the rise of anodic or cathodic current becomes obvious (Johansson, et al., 2003). Thus, the position of the HOMO and LUMO levels was first estimated by measuring the optical energy gaps from Tauc's equation, as was discussed previously. Then, from the equations below, the HOMO and LUMO levels were estimated using ferrocene as the reference couple (Cardona, et al., 2011) (Alqurashy, et al., 2020):

$$E_{\text{HOMO}} = -E(\text{onset,oxvs.Fc}^+/\text{Fc}) + 5.39 \text{ (eV)} \quad (5)$$

$$E_{\text{LUMO}} = -(E(\text{onset,redvs.Fc}^+/\text{Fc}) + 5.39) \text{ (eV)} \quad (6)$$

$$E_g^{Tauc} = E_{\text{HOMO}} - E_{\text{LUMO}} \quad (7)$$

Where $E(\text{onset,oxvs.Fc}^+/\text{Fc})$ and $E(\text{onset,redvs.Fc}^+/\text{Fc})$ represent the onset potential of the oxidation and reduction potential, respectively. The value of 5.39 represents the formal potential of the Fc^+/Fc redox couple versus vacuum. Fig. 4 shows the CV spectra of the polymers versus Fc/Fc^+ , while their corresponding electrochemical parameters are shown in Table III. The HOMO level is influenced by the type of substituents (whether electron withdrawing or electron donating species) and it can be seen that P(TRI-co-TER) experienced a high HOMO level compared to poly(L-Tryptophane) polymer. This could be due to the presence of the indole N-H group (Huang, et al., 2015). In addition, the LUMO level of P(TRI-co-TER) is 2.78 eV but LUMO levels of the acceptors, namely, poly(L-Tryptophane) and poly(5-hydroxy-L-Tryptophane), are 2.87 eV and 3.19 eV, respectively.

D. Optical Constants

Optical constants reveal the nature of interactions between organic materials and the electromagnetic spectrum. For instance, the loss of the incident photon due to scattering and absorption within the film is ascribed by the extinction coefficient (k). In addition, another constant entitled the optical dielectric constant (ϵ), which is a frequency dependent parameter, demonstrates the electronic response of the material when interacts with photons. Meanwhile, the dielectric constant is a complex function and its real part is assigned to polarization on the impact of an electromagnetic

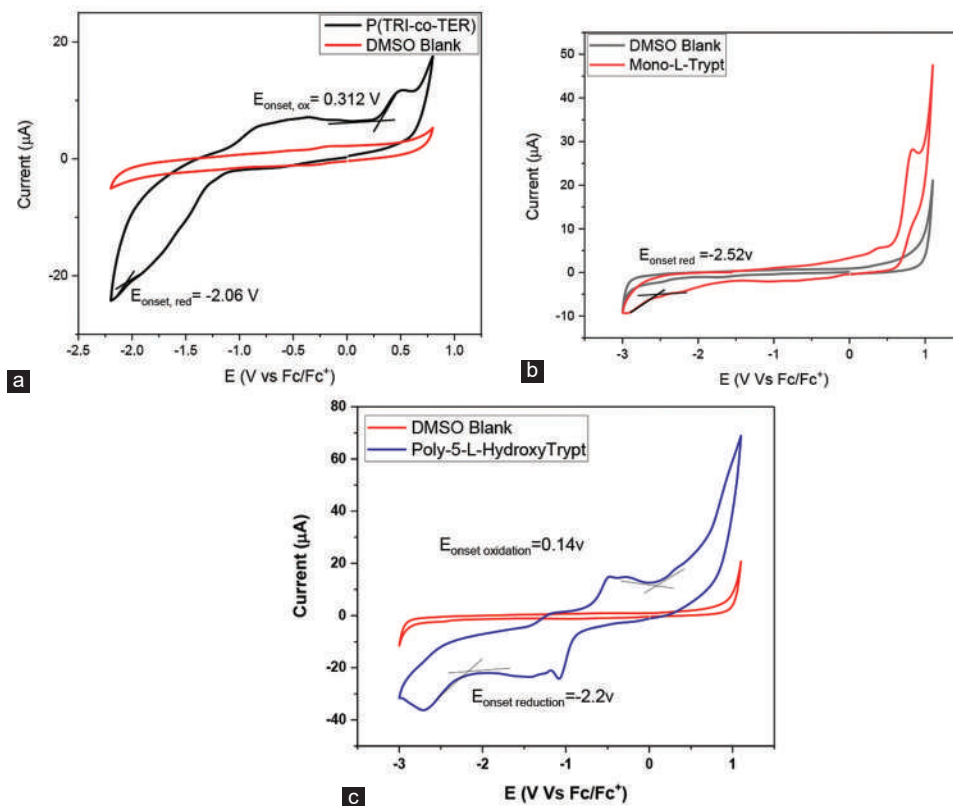


Fig. 4. The cyclic voltammetry of (a) P(TRI-co-TER), (b) poly(L-Tryptophane), and (c) poly(5-hydroxy-L-Tryptophane).

TABLE III

ELECTROCHEMICAL AND OPTICAL DATA FOR ALL SYNTHESIZED POLYMERS

Polymer	$E_{onset,ox}$ (V)	$E_{onset,red}$ (V)	E_{HOMO} (eV)	E_{LUMO} (eV)	E_g (eV)
P (TRI-co-TER)	0.312	-1.24	-5.70	-2.78	2.92
Poly (L-Tryptophane)	NA	-2.52	-5.39	-2.87	2.52
Poly (5-hydroxy-L-Tryptophane)	0.14	-2.20	-5.53	-3.19	2.34

field, while the imaginary part illustrates the optical loss. The following equations were sequentially used to calculate the optical parameters of the studied films (Fariq, Shujahdeen, and Hussein, 2015).

$$n = \frac{-2(R+1) - \sqrt{4k^2R^2 + 16R - 4k^2}}{2(R-1)} \quad (8)$$

$$k = \frac{\alpha\lambda}{4\pi} \quad (9)$$

$$\varepsilon = \varepsilon_r + i\varepsilon_i \quad (10)$$

$$\varepsilon_r = n^2 - k^2 \quad (11)$$

$$\varepsilon_i = 2nk \quad (12)$$

$$\text{Tan}\delta = \varepsilon_i / \varepsilon_r \quad (13)$$

Where ε_r represents the real part, ε_i is the imaginary part of the dielectric constant, n is the refractive index, k is the extinction coefficient, and R is the reflectance. Figs. 5 and 6 shows the real and imaginary dielectric constant spectra of the investigated films, while Fig. 7a and b shows the extinction coefficient in the wavelength range from 200

1000 nm for composite systems. Noticeably, it can be seen that the real part of the optical dielectric constant spectrum reflects the spectrum of refractive index (Fig. 8) because of the small value of k , while the spectrum of the imaginary part is essentially related to the spectrum of the absorption coefficient (see Eqs. 9, 11 and 12). Table IV shows that the real dielectric constant for the poly(L-Tryptophane), poly(5-hydroxy-L-Tryptophane), and P(TRI-co-TER) is lower than those of their mixed structures in the binary and ternary forms (Rahim, et al., 2022)

Fig. 8a and b shows the refractive index of the studied thin film in the wavelength range from 200 to 1000 nm. Therefore, it was perceived that refractive index follows an inconsistent dispersion in both UV and near visible region, while a non-dispersive response observed in the IR region (transparent region). In addition, the infinite refractive index (n_∞) can be experimentally extracted from the non-dispersive/flattened portion of the refractive index spectrum and its values for the investigated films were shown in Table IV. Hence, the refractive index values are shown in Table IV, which were obtained from the plateau region of the spectra shown in Fig. 8a and b. It was observed from Fig. 8a that the P(TRI-co-TER) ($n = 1.82$) and poly(L-Tryptophane) ($n = 1.62$) are lower than that of the mixed A: D (1:2) ($n = 2.01$) and A: D:Sudan dye (1:2:2) ($n = 2.32$). Interestingly, with the help of poly(L-Tryptophane) ($n = 1.62$) dopant, it is possible to increase the refractive index of P(TRI-co-TER) from 1.82 to 2.01 and to 2.32 in the binary and ternary systems, respectively. Similarly, as shown in Fig. 8b, with the help

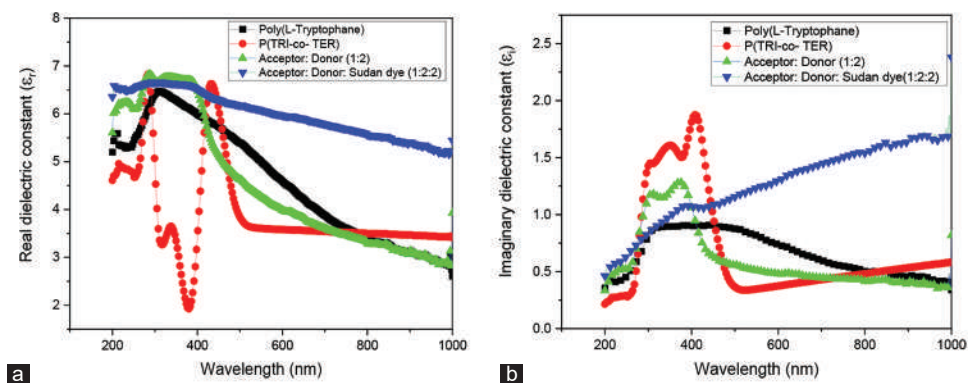


Fig. 5. Dielectric constant spectra, (a) real part and (b) imaginary part, for the poly(L-Tryptophane), P(TRI-co-TER), their binary and ternary systems.

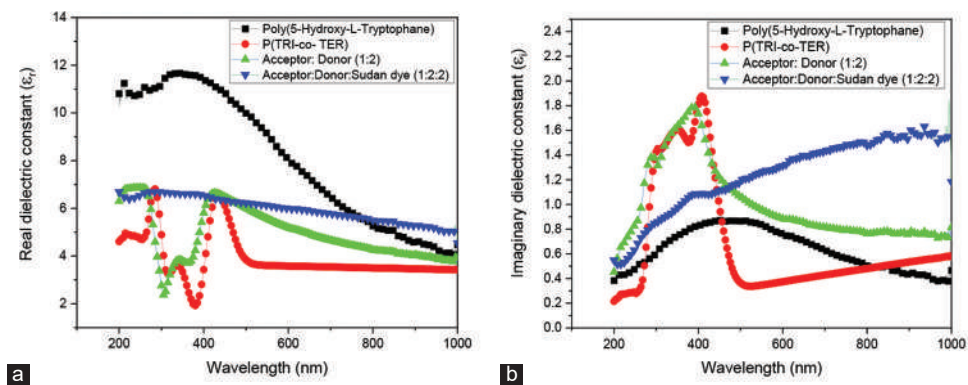


Fig. 6. Dielectric constant spectra, (a) real part and (b) imaginary part, for poly(5-hydroxy-L-Tryptophane), P(TRI-co-TER), their binary and ternary systems.

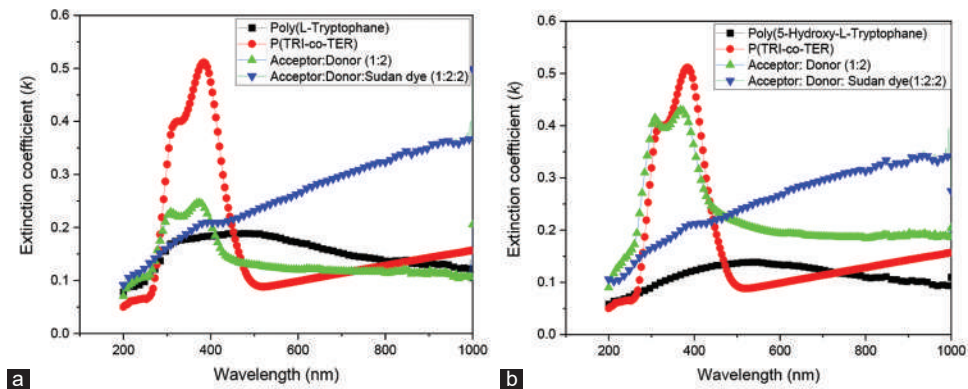


Fig. 7. Extinction coefficient spectra of poly(L-Tryptophane), poly(5-hydroxy-L-Tryptophane), P(TRI-co-TER), their binary and ternary systems.

TABLE IV

THE OPTOELECTRONIC PARAMETERS OF THE INVESTIGATED THIN FILMS

Materials	n	ϵ_r	σ_r (S.cm ⁻¹)
P (TRI-co-TER)	1.82	3.29	89.67
Poly (L-Tryptophane)	1.62	2.61	56.86
Acceptor: Donor (1:2)	2.01	3.99	145.19
Acceptor: Donor: Sudan dye (1:2:2)	2.32	5.02	433.11
Poly (5-hydroxy-L-Tryptophane)	1.79	3.19	36.09
Acceptor: Donor (1:2)	1.98	3.85	132.91
Acceptor: Donor: Sudan dye (1:2:2)	2.32	4.98	439.07

of dopant poly(5-hydroxy-L-Tryptophane) ($n = 1.79$), the refractive index was increased to 1.98 and 2.32, the binary

and ternary systems, respectively. This trend was found to be consistent with those described in the literature (Holzer, Penzkofer, and Hörhold, 2000). Consequently, it was found that the refractive index and real optical conductivity (Fig. 9) are increased with the addition of the second and third dopant components into the polymers. This can be ascribed to the increased conjugation bonds and better packing compact between the molecular arrangements of the structures, thereby reducing the speed of the incident light waves by a larger degree.

Furthermore, Figs. 9 and 10 exhibit the spectra of the optical conductivity of both composite systems and the real and imaginary components of optical conductivity

$(\sigma^* = \sigma_r + i\sigma_i) \sigma^* = \sigma_r + i\sigma_i$ can be investigated by means of the following formulas:

$$\sigma_r = \omega \epsilon_0 \epsilon_i \quad \sigma_r = \omega \epsilon_0 \epsilon_i \quad (14)$$

$$\sigma_i = \omega \epsilon_0 \epsilon_r \quad \sigma_i = \omega \epsilon_0 \epsilon_r \quad (15)$$

Where σ_r is the real optical conductivity, σ_i is the imaginary optical conductivity, ω is the angular frequency, and ϵ_0 is free space permittivity ($8.85 \times 10^{-12} F/m$). Figs. 9a and 10 reveal that, at long wavelengths, the values of real optical conductivity for both composite systems remain constant (non-dispersive). Figs. 9a and 10a reveal that, at long wavelengths, the values of real optical conductivity for both composite systems remain constant (non-dispersive). This indicates that the change in optical conductivity is directly related to the variation of excited electrons due to the absorption of photon energy by the thin film.

Therefore, the increment in the optical absorption of the obtained samples in the UV region is a consequence of increased optical conductivity and vice versa. Figs. 9b and 10b shows the imaginary optical conductivity for poly (L-Tryptophane), poly (5-hydroxy-L-Tryptophane), P (TRI-co-TER), along with the binary and ternary systems. In addition, the dissipation factor (DF) is a measure of loss-rate of energy of a mode of oscillation (mechanical, electrical, or electromechanical) in a dissipative system. It is the reciprocal

of quality factor, which represents the “quality” or durability of oscillation. It was seen from Fig. 11a and b that the DF for the donor system is larger than that of the other samples. Furthermore, a comparison between the major optoelectronic parameters of some polymers from literature and those achieved in the current study was carried out, as shown in Table V.

E. Morphological Properties

FE-SEM is a widely used technique to investigate the surface morphology, microstructure, grain size, and shape of the films. Fig. 12 depicts the FE-SEM images of the films, in which the shape of grains is found to be of different sizes and randomly distributed along the substrate surface. The average particle size on the surface of the acceptors and donor films was increased significantly compared to the binary and ternary films. It was seen that the number of pores increased when dopant concentration was increased (Trinh, et al., 2011).

F. Structural Properties

The X-ray diffraction patterns were used to characterize the structure of the studied films deposited on the glass substrate. Poly(L-Tryptophane) and poly(5-hydroxy-L-Tryptophane) acceptors and P(TER-CO-TRI) donor mixed with Sudan dye thin films were coated on the glass substrates and their XRD patterns were recorded in the

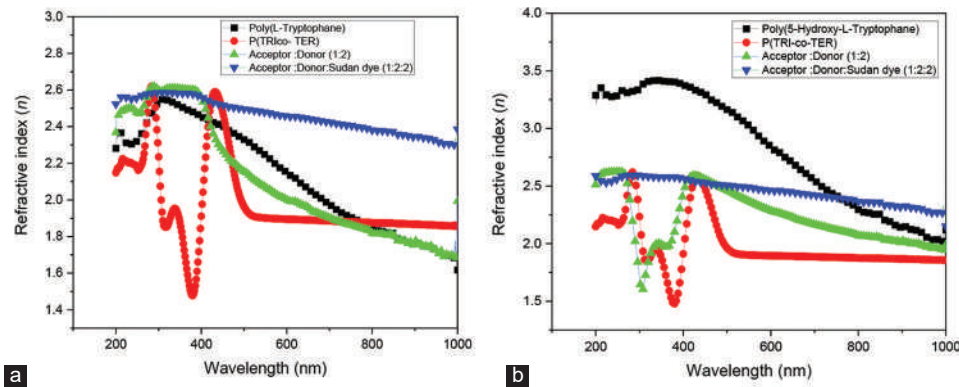


Fig. 8. (a and b) Refractive index spectra of poly(L-Tryptophane), poly(5-hydroxy-L-Tryptophane), P(TRI-co-TER), their binary and ternary systems.

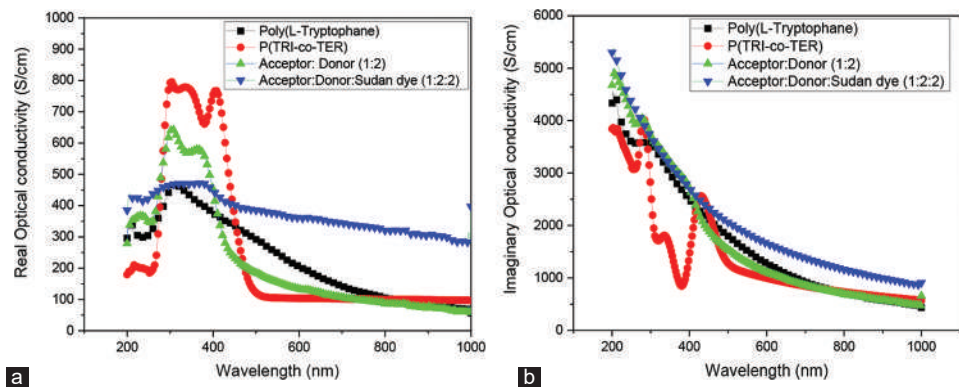


Fig. 9. Optical conductivity spectra of poly(L-Tryptophane) and its composite systems; (a) real part and (b) imaginary part.

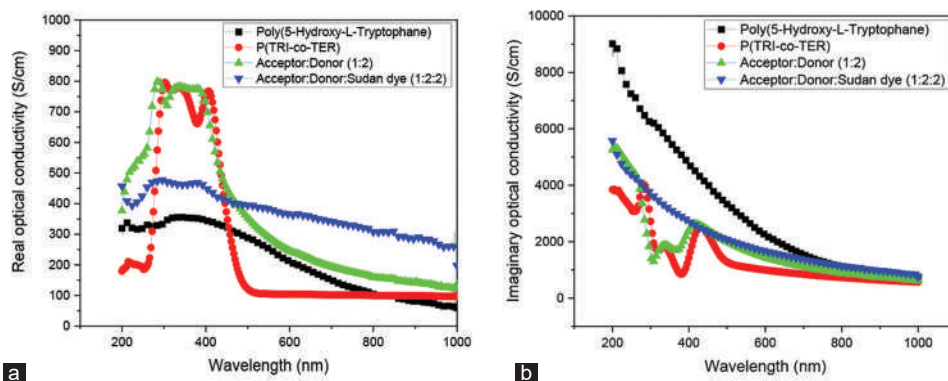


Fig. 10. Optical conductivity spectra of poly(5-hydroxy-L-Tryptophane) and its composite systems; (a) real part and (b) imaginary part.

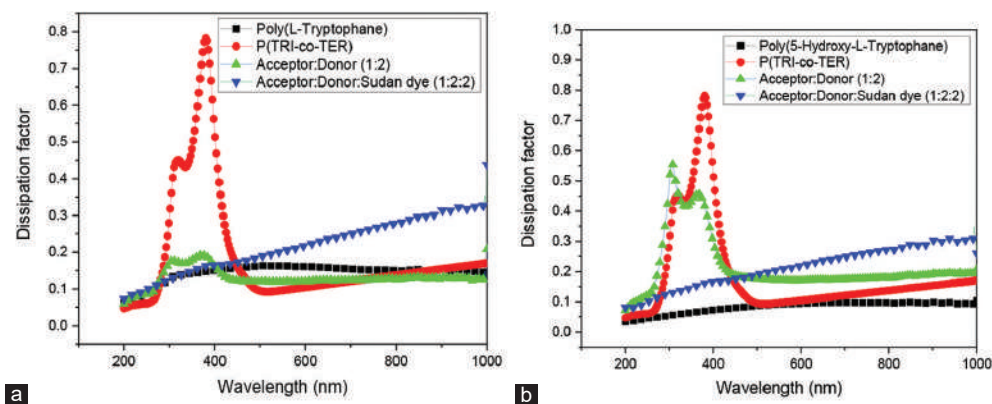


Fig. 11. Dielectric lost tangent (dissipation factor) spectra of poly(L-Tryptophane), poly(5-hydroxy-L-Tryptophane), P(TRI-co-TER), their binary and ternary systems.

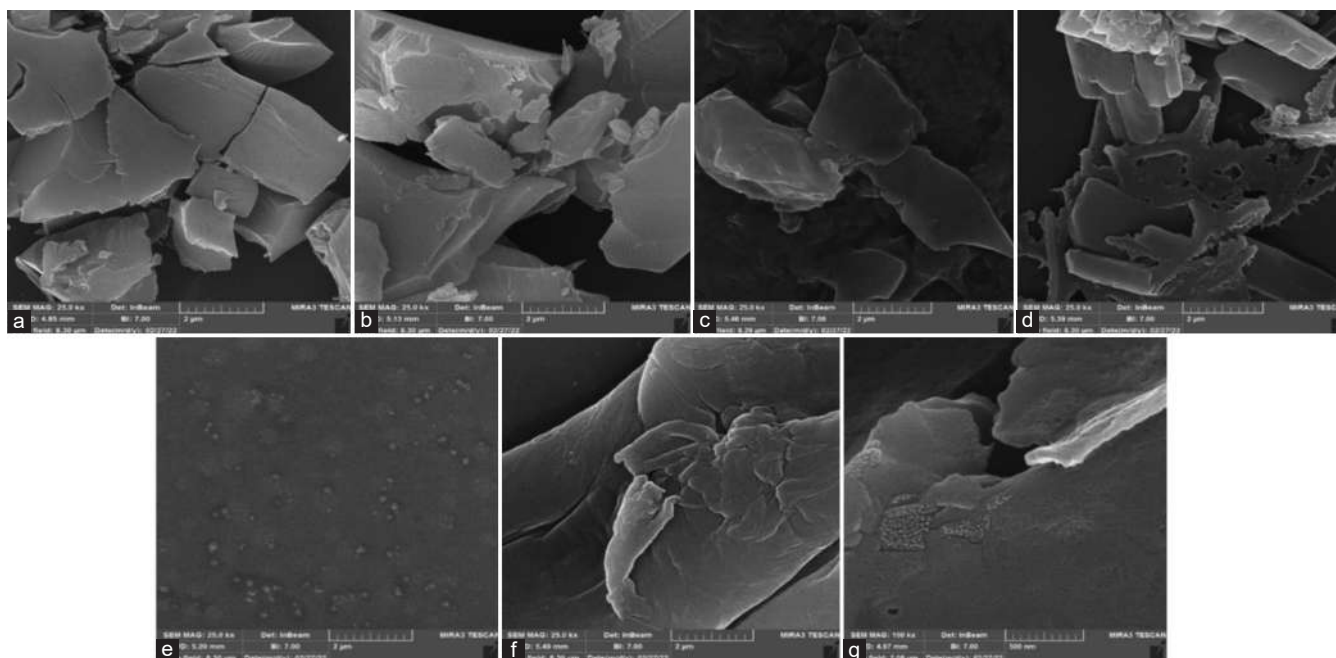


Fig. 12. The field emission-scanning electron microscopy image of (a) P(TER-co-TRI), (b) Poly(L-Tryptophane), (c) poly(L-Tryptophane):P(TER-co-TRI) (1:2), (d) Poly(L-Tryptophane):P(TER-co-TRI):Sudan dye (1:2:2), (e) Poly(5-hydroxy-L-Tryptophane), (f) Poly(5-hydroxy-L-Tryptophane):P(TER-co-TRI) (1:2) and (g) Poly(5-hydroxy-L-Tryptophane):P(TER-co-TRI):Sudan dye (1:2:2).

TABLE V

COMPARISON BETWEEN SOME POLYMERS AND THE INVESTIGATED THIN FILMS IN TERMS OF THE MAIN OPTOELECTRONIC PARAMETERS.

Materials	E_g (eV)	n	ϵ_r	References
P (TRI-co-TER)	2.92	1.82	3.29	This work
Poly (L-Tryptophane)	2.52	1.62	2.61	This work
Poly (5-hydroxy-L-Tryptophane)	2.34	1.79	3.19	This work
Polyvinylpyrrolidone (PVP)	2.40	1.49	3.60	Shubha, Manohara and Gerward, 2017
PHPMIVP	1.85	1.60	3.80	Barrillon, et al., 2023
Poly (ethylene oxide) PEO	2.60	1.45	2.20	Abd El-Kader and Elabbasy, 2020
Polysoprene	1.04	1.52	2.50	Fan, et al., 2020

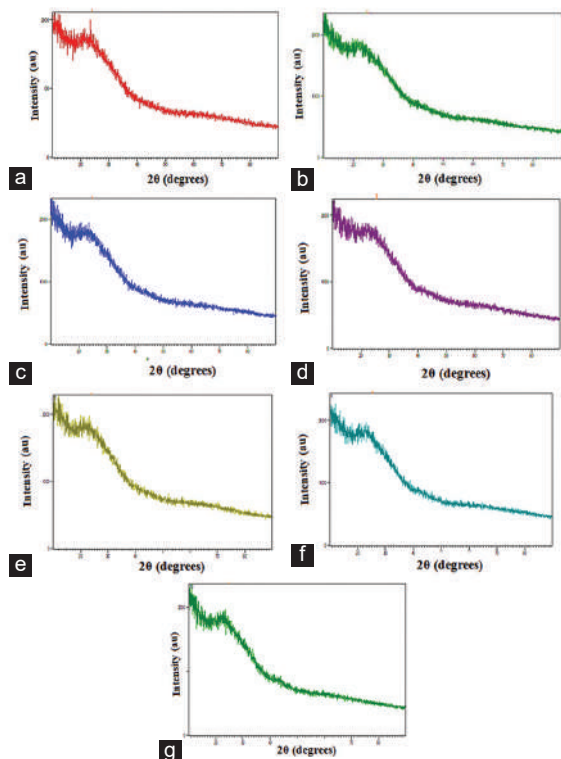


Fig. 13. The X-ray diffraction pattern of (a) P(TER-co-TRI), (b) Poly(L-Tryptophane), (c) poly(L-Tryptophane):P(TER-CO-TRI) (1:2), (d) Poly(L-Tryptophane):P(TER-co-TRI):Sudan dye (1:2:2), (e) Poly(5-hydroxy-L-Tryptophane), (f) Poly(5-hydroxy-L-Tryptophane):P(TER-co-TRI) (1:2) and (g) Poly(5-hydroxy-L-Tryptophane):P(TER-co-TRI):Sudan dye (1:2:2).

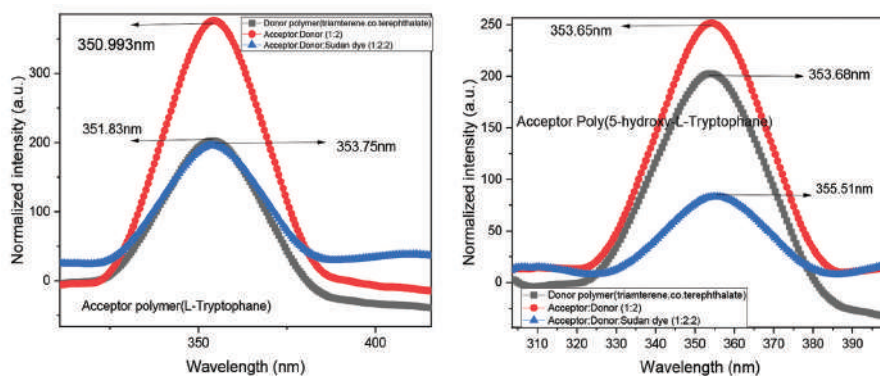


Fig. 14: Photoluminescence spectra of the investigated films in binary and ternary composite forms.

range of 2θ between 10° and 90° . Fig. 13 shows the XRD diffraction patterns of the films. The poly(L-Tryptophane) and poly(5-hydroxy-L-Tryptophane) along with the binary and ternary films they all showed a broad bump in the low angle of diffraction, which indicates their amorphous nature. However, the dopant P(TER-CO-TRI) films showed a single sharp diffraction peak at 24° , which corresponds to a d-spacing of 3.72 \AA . Furthermore, its low intensity could be used as an indicator for the small particle size (Al-Dulaimi, et al., 2017). Therefore, this peak indicates the intermolecular distance between two neighboring planes, which is obtained by Bragg's equation:

$$n \lambda = 2d \sin\theta \quad (16)$$

Where n (an integer) is the "order" of reflection, λ is the wavelength of the incident X-rays, d is the interplanar spacing of the crystal and θ is the angle of incidence (Kato, Ito and Hoshino, 2020).

G. Photoluminescence (PL) Properties

To investigate the PL spectrum of the films, they were excited by a 355 nm exciting laser. The PL spectra of Poly(L-Tryptophane), Poly(5-hydroxy-L-Tryptophane), binary and ternary films are illustrated in Fig. 14a and b. All films showed a typical UV emission peak centered at about 350 nm, near the band edge of binary and ternary. The charge transfer behavior of the acceptor and donor (A/D) between the layer and acceptor layer is examined by PL spectroscopy measurements. One can notice from Fig. 14a and b that the peak position of the emission is red-shifted for the binary system compared to that of the single film. Furthermore, the peak position for the ternary film is red-shifted compared to that of the binary film. This red-shifting is a clear evidence of the change in the electronic distribution of the system with the addition of the second and third components, implying the change in the energy band gaps, as was explained in the previous sections. Another feature of the PL peak is that its intensity has decreased in the ternary films compared to that of the binary ones. This indicates the more efficient charge transfer between the moieties of the acceptor and donor components on the absorption of light by the electronic states.

IV. CONCLUSIONS

In this work, a broad investigation on the optical properties and optoelectronic parameters of P(TER-CO-TRI), poly(L-Tryptophane), and poly(5-hydroxy-L-Tryptophane) along with their doping with Sudan dye was successfully performed. Optical spectroscopy was seen to be highly effective to measure the optoelectronic parameters of the binary and ternary composites made from the polymer materials and the dye. It was concluded that with the help of doping process, different values of energy band gap, refractive index, dielectric constant, and optical conductivity are achieved. This tuning achievement of the optoelectronic parameters plays a key role in shaping the possible applications of these materials in organic electronics, photodiodes, and photovoltaic devices. The nature of the electronic transition in the studied samples was confirmed to be a direct allowed transition, which was derived from the application of Tauc's equation. The combination of CV test and absorption spectroscopy was successfully used to determine the molecular energy levels, HOMO, and LUMO of the polymer samples.

V. ACKNOWLEDGMENT

Kamal A. Ketuly thanks the Erasmus + scheme for facilitating collaboration between the University of Duhok and the University of Glasgow.

VI. CONFLICTS OF INTEREST

The authors declare that there are no conflicts of interest regarding the publication of this paper.

VII. AUTHORS' CONTRIBUTIONS

Methodology: Barham Kamal Rahim; Conceptualization: Fahmi F. Muhammadsharif and Salah Raza Saeed; Writing - original draft preparation: Barham Kamal Rahim; Writing-review and editing: Fahmi F. Muhammadsharif, Salah Raza Saeed, Kamal Aziz Ketuly; Formal analysis and investigation: Fahmi F. Muhammadsharif, Salah Raza Saeed, Kamal Aziz Ketuly; Supervision: Fahmi F. Muhammadsharif, Salah Raza Saeed.

VIII. AVAILABILITY OF DATA AND MATERIALS

The data and material are available within the manuscript.

REFERENCES

Abd El-Kader, M.F.H. and Elabbasy, M.T. (2020). Gamma radiation modified the optical, electrical, and antibacterial characterization of CuONPs doped in polyethylene oxide/polyvinyl alcohol. *Journal of Materials Research and Technology*, 9(6), pp. 16179-16185.

Al-Dulaimi, N., Lewis, E.A., Savjani, N., McNaughten, P.D., Haigh, S.J., Malik, M.A., Lewis, D.J. and O'Brien, P. (2017). The influence of precursor on rhenium incorporation into Re-doped MoS₂ (Mo_{1-x}:XRe_xS₂) thin films by aerosol-assisted chemical vapour deposition (AACVD). *Journal of Materials*

Chemistry C, 5(35), pp. 9044-9052.

Alqurashy, B.A., Iraqi, A., Zhang, Y. and Lidzey, D.G. (2020). Pyrene-benzo[1,2,5]thiadiazole based conjugated polymers for application in BHJ solar cells. *Journal of Saudi Chemical Society*, 24(6), pp. 484-491.

Alsoghier, H.M., Selim, M.A., Salman, H.M.A., Rageh, H.M., Santos, M.A., Ibrahim, S.A., Dongol, M., Soga, T. and Abuelwafa, A.A. (2018). NMR spectroscopic, linear and non-linear optical properties of 1,3-benzothiazol-2-yl-(phenylhydrazono)acetonitrile (BTPA) azo dye. *Journal of Molecular Structure*, 1179, pp. 315-324.

Amin, P.O., Ketuly, K.A., Saeed, S.R., Muhammadsharif, F.F., Symes, M.D., Paul, A. and Sulaiman, K. (2021). Synthesis, spectroscopic, electrochemical and photophysical properties of high band gap polymers for potential applications in semi-transparent solar cells. *BMC Chemistry*, 15(1), p. 25.

Barrillon, S., Fuchs, R., Petrenko, A.A., Comby, C., Bosse, A., Yohia, C., Fuda, J.L., Bhairy, N., Cyr, F., Doglioli, A.M., Grégori, G., Tzortzis, R., d'Ovidio, F. and Thyssen, M. (2023). Phytoplankton reaction to an intense storm in the north-western Mediterranean Sea. *Biogeosciences*, 20(1), pp. 141-161.

Basir, A., Alzahrani, H., Sulaiman, K., Muhammadsharif, F.F., Mahmoud, A.Y., Bahabry, R.R., Alsoufi, M.S., Bawazeer, T.M. and Ab Sani, S.F. (2021). An investigation on the optical parameters of TPD: Alq₃ composite thin films. *Physica B: Condensed Matter*, 606, p. 412816.

Bilgaiyan, A., Dixit, T., Palani, I.A. and Singh, V. (2017). Performance improvement of ZnO/P3HT hybrid UV photo-detector by interfacial Au nanolayer. *Physica E: Low-Dimensional Systems and Nanostructures*, 86, pp. 136-141.

Cardona, C.M., Li, W., Kaifer, A.E., Stockdale, D. and Bazan, G.C. (2011). Electrochemical considerations for determining absolute frontier orbital energy levels of conjugated polymers for solar cell applications. *Advanced Materials*, 23(20), pp. 2367-2371.

Davis, E.A., Mott, N.F. (1970) Conduction in non-crystalline systems V. Conductivity, optical absorption and photoconductivity in amorphous semiconductors, *The Philosophical Magazine: A Journal of Theoretical Experimental and Applied Physics*, 22:179, 0903-0922, DOI: 10.1080/14786437008221061.

El Jouad, Z., Barkat, L., Stephant, N., Cattin, L., Hamzaoui, N., Khelil, A., Ghamnia, M., Addou, M., Morsli, M., Béchu, S., Cabanetos, C., Richard-Plouet, M., Blanchard, P. and Bernède, J.C. (2016). Ca/Alq₃ hybrid cathode buffer layer for the optimization of organic solar cells based on a planar heterojunction. *Journal of Physics and Chemistry of Solids*, 98, pp. 128-135.

Fan, X., Xu, H., Wu, C., Song, Y. and Zheng, Q. (2020). Influences of chemical crosslinking, physical associating, and filler filling on nonlinear rheological responses of polyisoprene. *Journal of Rheology*, 64(4), pp. 775-784.

Fariq, F., Shujahadeen, M. and Hussein, S.A. (2015). Effect of the dopant salt on the optical parameters of PVA : NaNO₃ solid polymer electrolyte. 26, pp. 521-529.

Garg, M., Tak, B.R., Rao, V.R. and Singh, R. (2019). Giant UV photoresponse of GaN-based photodetectors by surface modification using phenol-functionalized porphyrin organic molecules. *ACS Applied Materials and Interfaces*, 11(12), pp. 12017-12026.

Gather, M.C., Köhnen, A. and Meerholz, K. (2011). White organic light-emitting diodes. *Advanced Materials*, 23(2), pp. 233-248.

Hamad, T.K. (2013). Refractive index dispersion and analysis of the optical parameters of (PMMA/PVA) thin film. *Journal of Al-Nahrain University Science*, 16(3), pp. 164-170.

Holzer, W., Penzkofer, A. and Hörhold, H.H. (2000). Travelling-wave lasing of TPD solutions and neat films. *Synthetic Metals*, 113(3), pp. 281-287.

Hou, Y.N., Mei, Z.X., Liang, H.L., Ye, D., Liang, S., Gu, C. and Du, X.L. (2011). Comparative study of n-MgZnO/p-Si ultraviolet-B photodetector performance with different device structures. *Applied Physics Letters*, 98(26), p. 263501.

- Hu, Z.F., Huai-Hao, W., Yan-Wu, L. and Xi-Qing, Z. (2015). High response Schottky ultraviolet photodetector formed by PEDOT: PSS transparent electrode contacts to Mg_{0.1}Zn_{0.9}O. *Chinese Physics B*, 24(10), 107302.
- Huang, Y., Wu, F., Zhang, M., Mei, S., Shen, P. and Tan, S. (2015). Synthesis and photovoltaic properties of conjugated polymers with an asymmetric 4-(2-ethylhexyloxy)-8-(2-ethylhexylthio)benzo[1,2-b:4,5-b']dithiophene unit. *Dyes and Pigments*, 115, pp. 58-66.
- Jheng, J.S., Wang, C.K., Chiou, Y.Z., Chang, S.P. and Chang, S.J. (2020). Voltage-tunable uv-c-uvb dual-band metal-semiconductor-metal photodetector based on ga₂o₃/mgzno heterostructure by rf sputtering. *Coatings*, 10(10), p. 994.
- Johansson, T., Mammo, W., Svensson, M., Andersson, M.R. and Inganäs, O. (2003). Electrochemical bandgaps of substituted polythiophenes. *Journal of Materials Chemistry*, 13, pp. 1316-1323.
- Kaltenbrunner, M., Sekitani, T., Reeder, J., Yokota, T., Kuribara, K., Tokuhara, T., Drack, M., Schwödiauer, R., Graz, I., Bauer-Gogonea, S., Bauer, S. and Someya, T. (2013). An ultra-lightweight design for imperceptible plastic electronics. *Nature*, 499(7459), pp. 458-463.
- Kato, K., Ito, K. and Hoshino, T. (2020). Anisotropic amorphous X-ray diffraction attributed to the orientation of cyclodextrin. *Journal of Physical Chemistry Letters*, 11(15), pp. 6201-6205.
- Kim, J., Chae, S., Yi, A., Hong, S., Kim, H.J. and Suh, H. (2018). Characterization of push-pull type of conjugated polymers containing 8H-thieno[2,3-b]indole for organic photovoltaics. *Synthetic Metals*, 245, pp. 267-275.
- Leonat, L., Sbârcea, G. and Brañzoi, I.V. (2013). Cyclic voltammetry for energy levels estimation of organic materials. *UPB Scientific Bulletin, Series B: Chemistry and Materials Science*, 75(3), pp. 111-118.
- Lewis, J. (2006). Material challenge for flexible organic devices. *Materials Today*, 9(4), pp. 38-45.
- Muhammad, F.F. and Sulaiman, K. (2011). Utilizing a simple and reliable method to investigate the optical functions of small molecular organic films-Alq₃ and Gaq₃ as examples. *Measurement: Journal of the International Measurement Confederation*, 44(8), pp. 1468-1474.
- Muhammad, F.F. and Sulaiman, K. (2018). Thermal stability and reproducibility enhancement of organic solar cells by tris(hydroxyquinoline)gallium dopant forming a dual acceptor active layer. *Aro-the Scientific Journal of Koya University*, 6(2), p. 69.
- Muhammad, F.F., Yahya, M.Y., Aziz, F., Rasheed, M. and Sulaiman, K. (2017). Tuning the extinction coefficient, refractive index, dielectric constant and optical conductivity of Gaq₃ films for the application of OLED displays technology. *Journal of Materials Science: Materials in Electronics*, 28(19), pp. 14777-14786.
- Omidvar, A. (2017). Electronic structure tuning and band gap opening of nitrogen and boron doped holey graphene flake: The role of single/dual doping. *Materials Chemistry and Physics*, 202, 1-384.
- Rahim, B.K., Muhammadsharif, F.F., Saeed, S.R. and Ketuly, K.A. (2022). A study on the optical properties and optoelectronic parameters of Sudan dye doped poly (5-hydroxy-L-tryptophane) and P(TER-CO-TRI) polymers. *Modern Electronic Materials*, 8(3), pp. 85-96.
- Rajeswaran, M., Blanton, T.N., Tang, C.W., Lenhart, W.C., Switalski, S.C., Giesen, D.J., Antalek, B.J., Pawlik, T.D., Kondakov, D.Y., Zumbulyadis, N. and Young, R.H. (2009). Structural, thermal, and spectral characterization of the different crystalline forms of Alq₃, tris(quinolin-8-olato)aluminum(III), an electroluminescent material in OLED technology. *Polyhedron*, 28(4), pp. 835-843.
- Sajid, M., Zubair, M., Doh, Y.H., Na, K.H. and Choi, K.H. (2015). Flexible large area organic light emitting diode fabricated by electrohydrodynamics atomization technique. *Journal of Materials Science: Materials in Electronics*, 26(9), pp. 7192-7199.
- Shim, J.Y., Kim, T., Kim, J., Kim, J., Kim, I., Kim, J.Y. and Suh, H. (2015). Trifluoromethyl benzimidazole-based conjugated polymers with deep HOMO levels for organic photovoltaics. *Synthetic Metals*, 205, pp. 112-120.
- Shubha, A., Manohara, S.R. and Gerward, L. (2017). Influence of polyvinylpyrrolidone on optical, electrical, and dielectric properties of poly(2-ethyl-2-oxazoline)-polyvinylpyrrolidone blends. *Journal of Molecular Liquids*, 247, pp. 328-336.
- Trinh, T.T., Tu, H.N., Huy, H.L., Ryu, K.Y., Le, K.B., Pillai, K. and Yi, J. (2011). Improving the ethanol sensing of ZnO nano-particle thin films-the correlation between the grain size and the sensing mechanism. *Sensors and Actuators, B: Chemical*, 152(1), pp. 73-81.
- Vickers, N.J. (2017). Animal communication: When i'm calling you, will you answer too?. *Current Biology*, 27(14), pp. R713-R715.
- Wang, J., Yin, P., Wu, Y., Liu, G., Cui, C. and Shen, P. (2018). Synthesis and optoelectronic property manipulation of conjugated polymer photovoltaic materials based on benzo[d]-dithieno[3,2-b;2',3'-f]azepine. *Polymer*, 147, pp. 184-195.
- Yang, M., Wang, J., Yang, Y., Zhang, Q., Ji, C., Wu, G., Su, Y., Gou, Y., Wu, Z., Yuan, K., Xiu, F. and Jiang, Y. (2019). Ultraviolet to long-wave infrared photodetectors based on a three-dimensional dirac semimetal/organic thin film heterojunction. *Journal of Physical Chemistry Letters*, 10(14), pp. 3914-3921.
- Zeng, L.H., Chen, Q.M., Zhang, Z.H., Wu, D., Yuan, H., Li, Y.Y., Qarony, W., Lau, S.P., Luo, L.B. and Tsang, Y.H. (2019). Multilayered PdSe₂/perovskite schottky junction for fast, self-powered, polarization-sensitive, broadband photodetectors, and image sensor application. *Advanced Science*, 6(19), 1901134.

A Miniaturized wide Stopband Low-pass Filter using T and Modified L Shapes Resonators

Mani D. Fadaee, Farzin Shama, Mohammad S. Feali and Maryam S. Gilan

Department of Electrical Engineering, Kermanshah Branch, Islamic Azad University,
Kermanshah, Iran

Abstract—A new structure of microstrip-based low-pass filter with wide stopband and sharp roll-off is introduced, in this paper. In the proposed topology, resonators with T and modified L Shapes have been used. To improve the suppression factor and relative stopband bandwidth, the second resonator has been added to the first resonator. The designed filter has been fabricated on a 20 mm thickness RO4003 substrate, which has a loss tangent of 0.0021 and a relative dielectric constant equal to 3.38. All parameters including roll of rate, stopband, bandwidth, return loss, insertion loss, and figure of merit have significant coefficients. Simulation has been ran using advanced design system software. The 3dB cutoff frequency is appropriate. The value of the insertion loss parameter is <0.1 dB and the S_{11} parameter is -22 dB at this point. The stopband is extended from 2.42 up to 24 GHz, which shows an ultra-stopband. The results of the simulation and experiment are almost similar, which indicates a proper performance of the designed structure.

Index Terms—Low-pass filter, L-shaped, Microstrip, Resonator, Sharp roll off, T-shaped.

I. INTRODUCTION

Microstrip filters are one of the main components of telecommunication systems because, unlike passive and active circuits, they are much smaller in size and cost less. In recent years, researchers have developed microstrip filters using related structures. Each of these structures has strengths and weaknesses that can be combined to achieve a new structure with the improvement of all parameters (Chen, Li, and Chu, 2017; Du, Yang, Zhang, H., and Zhu, 2014; Imani, Shama, Alirezapoori, and Ekhteraei, 2018; Kolahi and Shama, 2018; Kumar and Parihar, 2016; Rekha, Abdulla, Jasmine, and Anu, 2020; Shama, Hayati, and Ekhteraei, 2018; Wang, Xu, Zhao, Guo, and Wu, 2010; Wei, Chen, and Shi, 2012).

In the design of microstrip low-pass filters (LPF), the small size of the filter always plays an important role. Semicircular structures in the filter design reduce the size of the circuit and follow the above rule. However, the suggested structures have a

problem such as inappropriate transition bands in the passband and very low stopband bandwidth (Hiedari and Shama, 2018).

Using a symmetrical parallel-coupled line structure, a new microstrip LPF has been designed (Jiang, et al. 2017). This structure has very low insertion loss, which is the biggest advantage of the introduced filter. In the stopband, the value of suppression is not enough, which leads to a quality reduction of the LPF (Jiang, et al. 2017).

Defected ground structure (DGS) is used to design an ultra-wide stopband bandwidth. Although the proposed structure produces an appropriate stopband bandwidth, the proposed double-layer architectural factor reduces the figure of merit. One of the most important parameters in the design of microstrip LPF is the appropriateness of the filter dimensions (Bhat, et al., 2018).

As mentioned, various structures including T-shaped, semicircular shapes, symmetric parallel coupled lines, and DGS have been proposed. Each of the above structures affected the value such as sharpness in the transition band, stopband bandwidth, return loss, insertion loss, and dimensions. However, each of these structures may improve one of the filter response properties, so achieving a response with various suitable properties may not be possible with just one structure.

In this research, a microstrip LPF with a T-shaped resonator and modified L-shaped resonator is simulated, fabricated, and measured. All response factors such as Roll of rate, stopband bandwidth, return loss, insertion loss, and figure of merit have significant values. All simulations are performed using advanced design system software. Using a RO4003 substrate with 20 mm thickness the proposed filter was implemented. RO4003 has a loss tangent of 0.0021 and a dielectric constant equal to 3.38.

II. MAIN RESONATOR

The proposed filter was designed using a T-shaped resonator. The suggested resonator has a good response with appropriate sharpness. The cutoff frequency is also appropriate. Calculated dimensions for the proposed resonator are: $L_1 = 7.2$ mm, $L_2 = 8$ mm, $L_3 = 7.3$ mm, $L_4 = 3$ mm, $W_1 = 5$ mm, $W_2 = 6.85$ mm, $W_3 = 3.15$ mm, $W_4 = 1.18$ mm, and $T_1 = 0.1$ mm and these dimensions are calculated using base resonators and then optimized (Blue arrows as the length, Green arrows as the width, and red arrows are considered as the Thickness). (Fig. 1a) shows the resonator structure.

ARO-The Scientific Journal of Koya University
Vol. XI, No. 1 (2023), Article ID: ARO.11157, 5 pages
DOI: 10.14500/aro.11157

Received 12 February 2023; Accepted 27 April 2023
Regular research paper: Published: 18 May 2023

Corresponding author's e-mail: f.shama@aut.ac.ir

Copyright © 2023 Mani D. Fadaee, Farzin Shama,
Mohammad S. Feali and Maryam S. Gilan This is an open access
article distributed under the Creative Commons Attribution License.



The proposed resonator frequency response from the simulation is shown in (Fig. 1b). The proposed resonator was able to create strong transmission zero at 2.41GHz. The measured value of transmission zero is -48 dB. By changing the value of L3, you can shift the cutoff frequency with transmission zero. However, it increases the insertion loss. The effect of changing parameter L3 is shown in Fig. 1.

The extracted equivalent circuit is depicted in Figs. 2 and 3. Methods discussed in (Hong and Lancaster, 2004; Pozar, 2011) can be used for extracting the values of parameters. (Fig. 2a) shows a low-impedance and high-impedance lossless line, in which both ends are terminated by low impedance-lines, which could also be introduced by a π -equivalent circuit, as shown in (Fig. 2b).

Inductors and capacitors will be obtained from the following equations:

$$L_S = \frac{1}{\omega} * z_S * \text{sinsin}\left(\frac{2\pi}{\lambda_g} l\right) \quad (1)$$

$$C_S = \frac{1}{\omega} * \frac{1}{Z_S} * \tan\left(\frac{\pi}{\lambda_g} l\right) \quad (2)$$

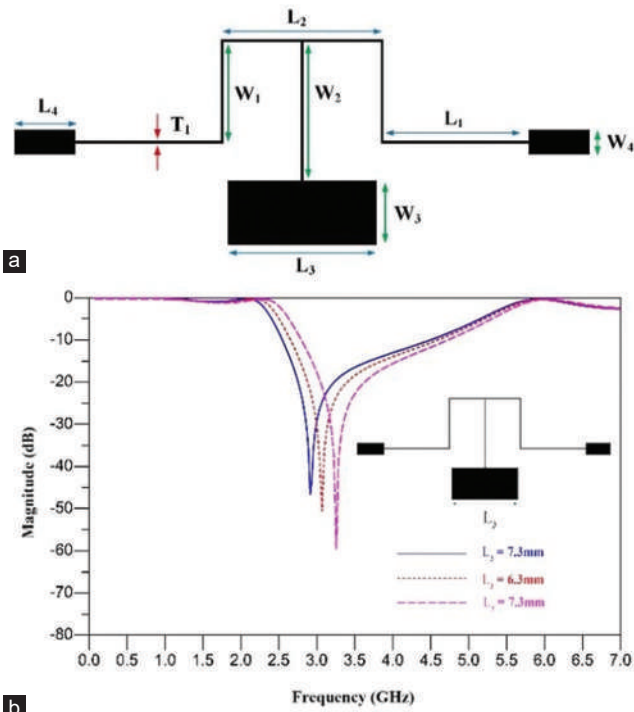


Fig. 1. (a) T-shaped resonator and (b) T-shaped resonator frequency response.

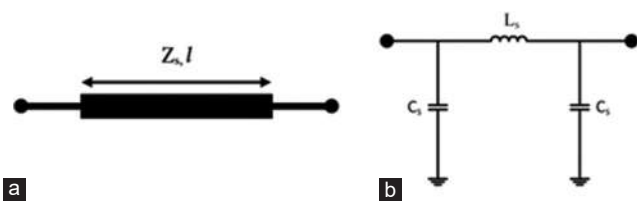


Fig. 2. (a) Low/high-impedance line and (b) LC model for a line.

In these equations, z_s , l , and λ_g represent the line characteristic impedance, the line length, and the guided wavelength, respectively. Open-end formulas were introduced in (Hong and Lancaster, 2004). In addition, (Fig. 3a and b) shows the structure and equivalent circuit.

For the T-shaped resonator, the LC equivalent circuit was extracted, considering the models introduced in Figs. 2 and 3. Equations 1 and 2 are used to calculate the values of the inductors and capacitors, respectively. (Fig. 4a) depicted the extracted LC equivalent circuit. Table I also shows the values of inductors and capacitors.

The transformation function can be expressed based on the proposed resonator equivalent LC circuit, represented in the following. By changing the parameters in the transformation function, the cutoff frequency can be shifted. The effect of this shifting appears on the insertion loss and increases it.

$$\frac{v_o}{v_i} = \frac{A \times ((B \times D \times c1S + E + L1S + L2S + 2 \times L4S + 2 \times L5S) \times c2S + F \times (R + L3S) \times c2S + 2 + G)}{(H \times ((B \times M \times c1S + N + O) \times c3S + P) \times U)} \quad (3)$$



Fig. 3. (a) The open-end structure and (b) equivalent circuit for LC.

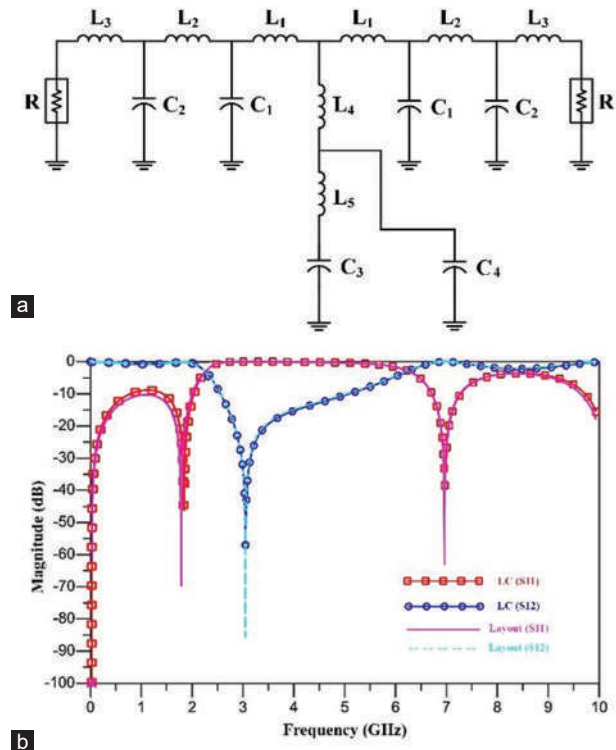


Fig. 4. (a) Resonator LC model and (b) frequency response diagram of the main resonator and LC equivalent circuit.

$$A = B \times L_1 S \times c_1 S + (L_1 S + L_2 S) \times (R + L_3 S) \times c_2 S + R + L_1 S + L_2 S + L_3 S \quad (4)$$

$$B = (L_2 S \times (R + L_3 S) \times c_2 S + R + L_2 S + L_3 S) \quad (5)$$

$$D = (L_5 S \times (L_1 S + 2 \times L_4 S) \times c_4 S + L_1 S + 2 \times L_4 S + 2 \times L_5 S) \quad (6)$$

$$E = (R + L_3 S) \times (L_5 S \times (L_1 S + L_2 S + 2 \times L_4 S) \times c_4 S) \quad (7)$$

$$F = (L_5 S \times (R + L_1 S + L_2 S + L_3 S + 2 \times L_4 S) \times c_4 S + R + L_1 S + L_2 S + L_3 S + 2 \times L_4 S + 2 \times L_5 S) \times c_3 S + (2 \times (L_1 S + 2 \times L_4 S) \times c_4 S) \times B \times c_1 S + (2 \times (L_1 S + L_2 S + 2 \times L_4 S) \times c_4 S) \quad (8)$$

$$G = (R + L_1 S + L_2 S + L_3 S + 2 \times L_4 S) \times c_4 S \quad (9)$$

$$H = B \times c_1 S + 1 + (R + L_3 S) \times c_2 S \quad (10)$$

$$M = (L_5 S \times (L_1 S + L_4 S) \times c_4 S + L_1 S + L_4 S + L_5 S) \quad (11)$$

$$N = (L_5 S \times (L_1 S + L_2 S + L_4 S) \times c_4 S + L_1 S + L_2 S + L_4 S + L_5 S) \times (R + L_3 S) \times c_2 S \quad (12)$$

$$O = L_5 S \times (R + L_1 S + L_2 S + L_3 S + L_4 S) \times c_4 S + R + L_1 S + L_2 S + L_3 S + L_4 S + L_5 S \quad (13)$$

$$P = B \times (1 + (L_1 S + L_4 S) \times c_4 S) \times c_1 S + (1 + (L_1 S + L_2 S + L_4 S) \times c_4 S) \quad (14)$$

$$U = (R + L_3 S) \times c_2 S + 1 + (R + L_1 S + L_2 S + L_3 S + L_4 S) \times c_4 S \quad (15)$$

Where, $R = 50\Omega$ is the matching impedance. The transmission zero is generated at the frequency of 2.41 GHz

TABLE I
COMPUTED PARAMETERS FOR THE FIRST RESONATOR

Inductors	L_1	L_2	L_3	L_4	L_5
Inductances	2.1nH	4.7nH	2.4nH	3.8nH	0.8nH
Capacitors	C_1	C_2	C_3	C_4	-
Capacitances	0.3pF	0.2pF	0.001pF	2.2pF	-

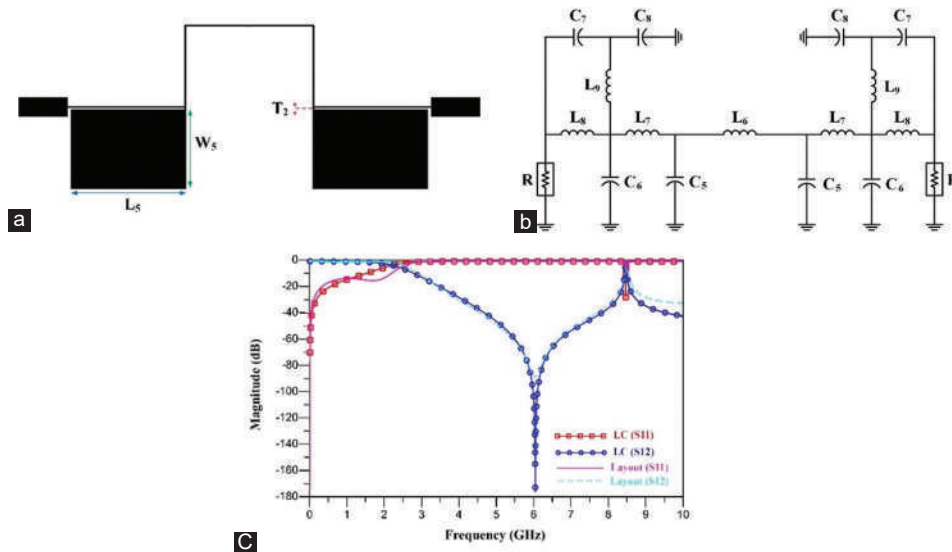


Fig. 5. (a) Structure of the second resonator, (b) LC model of the second resonator, and (c) simulated frequency response for the second resonator and LC model

with a magnitude of -48 dB. LC model and the designed layout are shown in (Fig. 4b). Good agreement between the LC and layout responses is obtained. However, this structure cannot be used alone. Because the suppression factor and relative stopband bandwidth (RSB) are not acceptable. To improve these parameters, the second resonator is inserted in the first resonator.

III. SECOND RESONATOR

The proposed second resonator is designed using a modified L-shaped resonator. This resonator has very good dimensions and is designed to provide transmission zeros for increasing stopband bandwidth. Dimensions calculated for the designed resonator are as follows: $T_2 = 0.1$ mm, $W_5 = 5.2$ mm, and $L_5 = 6.3$ mm. The structure of the second resonator is shown in (Fig. 5a). The LC equivalent circuit is extracted based on Figs. 2 and 3 and depicted in (Fig. 5b). Capacitor and inductor values are calculated based on Equations 1 and 2 and are shown in Table II.

The frequency responses of the LC circuit and the proposed layout are shown in (Fig. 5c). The transmission zeros of the second resonator are generated at a frequency of 6.1 GHz with a magnitude of -178 dB. The modified L-shaped resonator has a good response in the stopband, but the sharpness is not suitable. To improve the above parameter, two resonators are combined.

IV. COMBINATION OF THE FIRST AND SECOND RESONATORS

(Fig. 6a) shows the structure of the T-shaped and modified L-shaped resonators. The frequency response of the combination is just like a LPF, according to (Fig. 6b). The sharpness is very suitable, but the bandwidth is not a wide stopband. For improving the above parameter, the attenuator unit is used and added to the other resonator.

TABLE II
COMPUTED PARAMETERS FOR THE SECOND RESONATOR

Inductors	L_6	L_7	L_8	L_9
Inductances	3.71nH	5.7nH	3.2nH	0.2nH
Capacitors	C_5	C_6	C_7	C_8
Capacitances	0.175pF	0.26pF	0.4pF	2.8pF

TABLE III
FILTER PARAMETERS CALCULATION TABLE

1	$\epsilon = \frac{\alpha_{max} - \alpha_{min}}{F_s - F_c}$
2	$RSB = \frac{\text{Stopband bandwidth}}{\text{Stopband center frequency}}$
3	$SF = \frac{\text{Rejection level in stopband}}{10}$
4	$NCS = \frac{\text{Physical Size (Length * Width)}}{\lambda_g^2}$
5	$\lambda_g = \frac{300}{f_c \sqrt{\epsilon_{re}}}$
6	$FOM = \frac{\epsilon * RSB * SF}{NCS * AF}$

TABLE IV
COMPARISON CHART

Refs.	Roll-off	NCS (λ_g^2)	SF	AF	RSB	FOM
3	26	0.0180	2	1	1.34	3872
4	40.2	0.0117	1.5	1	1.60	8246
6	36.3	0.0062	1.5	2	1.32	11543
7	10.5	0.0324	2	1	1.46	949
8	81	0.0170	2	1	1.72	16400
9	100	0.0320	2	1	1.59	4968
10	44	0.0150	2	1	1.63	4723
11	45	0.0200	4	1	1.48	13320
12	103	0.0612	2	1	1.56	5269
13	81	0.0180	2.2	1	1.46	13140
14	56.7	0.0133	2	2	1.64	6983
15	35.4	0.0199	2	1	1.70	6051
16	62	0.0120	2	1	1.73	17876
17	100	0.0170	2	2	1.49	9030
18	148	0.0300	2	1	1.68	16576
Proposed filter	850	0.0420	2	1	1.64	66380

AF: Architectural factor, RSB: Relative stopband bandwidth, FOM: Figure of merit, NCS: Normalized circuit size

V. ATTENUATOR DESIGN

The modified L-shaped structure has been used in the design of the suppressor unit. The proposed suppressor unit and the frequency response of the final filter are depicted in (Fig. 7a and b), respectively. The dimensions of this suppressor unit are as follows:

According to the results presented in (Fig. 7b), all parameters have been significantly enhanced. The insertion loss parameter is <0.1dB and the return loss is -22 dB. The stopband is from 2.42GHz up to 24GHz. The roll-off rate is also very significant.

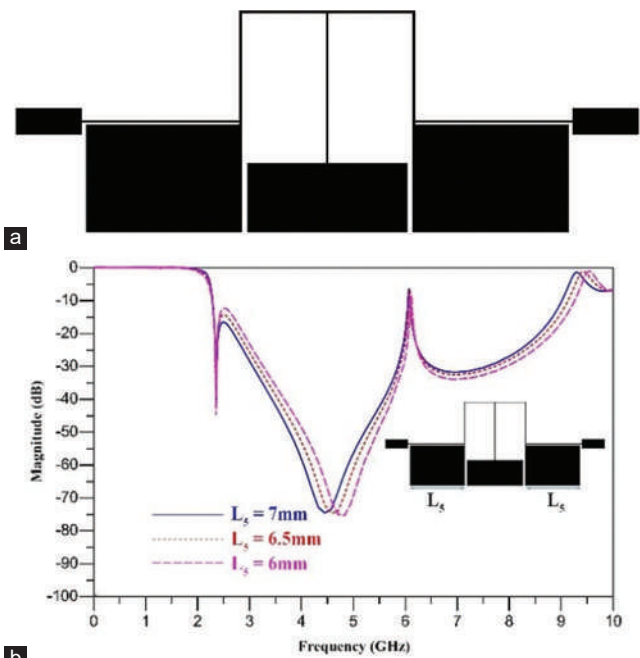


Fig. 6. (a) Structure of the main and second resonator and (b) the main and the second resonator comparison.

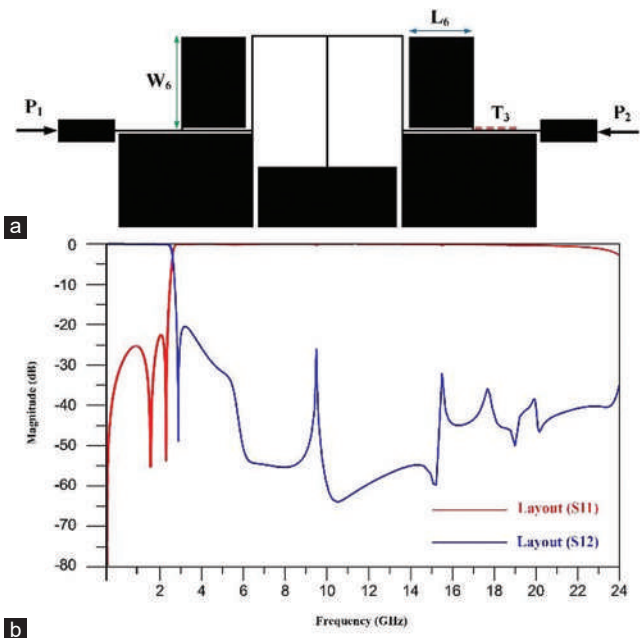


Fig. 7. (a) Structure of the proposed suppression unit with other resonators and (b) the final filter frequency response.

VI. RESULTS AND DISCUSSION

The filter is fabricated on a 20 mm thickness RO4003, (Fig. 8a). A comparison between the experimental and simulation results of the filter response is also depicted in (Fig. 8b). The filter dimension is 20.4 mm × 11 mm with an applicative cutoff at 2.4 GHz.

As seen in Table III, the most important factors in the filter response are defined and presented (Hayati, M., Abbasi, H., and Shama, F., 2014). It is clear from Table IV

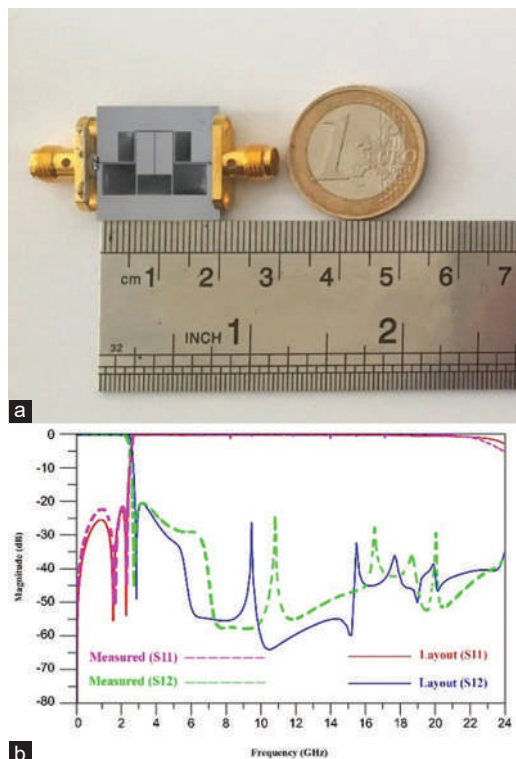


Fig. 8. (a) Fabricated circuit and (b) the final results for the fabricated filter.

that the designed LPF has the best roll-off rate between the mentioned works. In addition, with a high RSB, appropriate normalized circuit size (NCS), and good suppression factor (SF), it has a significant figure of merit (FOM) within these published works. Consequently, by considering these defined and conventional factors, besides having a smooth frequency response in the passband with minimum ripples (the insertion loss is significantly <0.1 dB, and the return loss is better than 20 dB in this band), the designed LPF is an appropriate candidate to attenuate the radiated n^{th} order harmonics on general wireless transmitters, which will be caused by non-linear blocks such as local oscillators, mixers, and power amplifiers. It is also ideal for reducing video transmitter interferences to nearby 2.4 GHz receivers and would be deposited between the transmitter and antenna.

VII. CONCLUSION

The steps of designing, simulating, fabricating, and measuring a microstrip LPF using a combination of T-shaped and modified L-shaped resonators are shown. The designed filter has a wide stopband from 2.42 GHz up to 24 GHz. The insertion loss is obtained <0.1 dB and the return loss is -22 dB.

REFERENCES

- Bhat, U.R., Jha, K.R., and Singh, G., 2018. Wide stopband harmonic suppressed low-pass filter with novel DGS. *International Journal of RF and Microwave Computer-Aided Engineering*, 28(5), p.e21235.
- Chen, F.C., Li, R.S., and Chu, Q.X., 2017. Ultra-wide stopband low-pass filter using multiple transmission zeros. *IEEE Access*, 5, pp.6437-6443.
- Du, Z., Yang, H., Zhang, H., and Zhu, M., 2014. Compact lowpass filter with high suppression level and wide stopband using stepped impedance m-shape units. *Microwave and Optical Technology Letters*, 56(12), pp.2947-2950.
- Hayati, M., Abbasi, H., and Fathabadi, O.S., 2015. A novel microstrip lowpass filter with sharp roll-off and ultra-wide stopband using SICMRC. *International Journal of Electronics*, 102(9), pp.1475-1485.
- Hayati, M., Abbasi, H., and Shama, F., 2014. Microstrip lowpass filter with ultrawide stopband and sharp roll-off. *Arabian Journal for Science and Engineering*, 39, pp.6249-6253.
- Hayati, M., and Shama, F., 2017. A compact lowpass filter with ultra wide stopband using stepped impedance resonator. *Radioengineering*, 26(1), pp.269-274.
- Hiedari, B., and Shama, F., 2018. A harmonics suppressed microstrip cell for integrated applications. *AEU-International Journal of Electronics and Communications*, 83, pp.519-22.
- Hong, J.S.G., and Lancaster, M.J., 2004. *Microstrip Filters for RF/Microwave Applications*. John Wiley and Sons, United States.
- Imani, M.A., Shama, F., Alirezapoori, M., and Ekhteraei, M., 2018. Miniaturized microstrip lowpass filter using cylindrical-shaped resonators for integrated applications. *Analog Integrated Circuits and Signal Processing*, 95, pp.223-229.
- Jiang, S., and Xu, J., 2017. Compact microstrip lowpass filter with ultra-wide stopband based on dual-plane structure. *Electronics Letters*, 53(9), pp.607-609.
- Jiang, Y., Wei, B., Heng, Y., Guo, X., Cao, B., and Jiang, L., 2017. Compact superconducting lowpass filter with wide stopband. *Electronics Letters*, 53(14), pp.931-933.
- Kolahi, A., and Shama, F., 2018. Compact microstrip low pass filter with flat group-delay using triangle-shaped resonators. *AEU-International Journal of Electronics and Communications*, 83, pp.433-438.
- Kumar, L., and Parihar, M.S., 2016. Compact hexagonal shape elliptical low pass filter with wide stop band. *IEEE Microwave and Wireless Components Letters*, 26(12), pp.978-980.
- Pozar, D.M., 2011. *Microwave Engineering*. John Wiley and Sons, United States.
- Rekha, T.K., Abdulla, P., Jasmine, P.M., and Anu, A.R., 2020. Compact microstrip lowpass filter with high harmonics suppression using defected structures. *AEU-International Journal of Electronics and Communications*, 115, p.153032.
- Shama, F., Hayati, M., and Ekhteraei, M., 2018. Compact microstrip lowpass filter using meandered unequal T-shaped resonator with ultra-wide rejection band. *AEU-International Journal of Electronics and Communications*, 85, pp.78-83.
- Wang, J., Xu, L.J., Zhao, S., Guo, Y.X., and Wu, W., 2010. Compact quasi-elliptic microstrip lowpass filter with wide stopband. *Electronics Letters*, 46(20), pp.1384-1385.
- Wei, F., Chen, L., and Shi, X.W., 2012. Compact lowpass filter based on coupled-line hairpin unit. *Electronics letters*, 48(7), p.1.

Radiation Detection and Heavy Metals Measurements in Powdered Blood Sample of Leukemia Patients

Zakariya A. Hussein

Department of Physics, Faculty of Science and Health, Koya University, Koya KOY45, Kurdistan Region - F.R. Iraq

Abstract—This research examines the measurements of radiation detection and heavy metals in blood samples of leukemia and health groups using CR-39 nuclear track detectors and X-ray fluorescence. The results show that the minimum and maximum values of uranium contents found in leukemia blood samples of male (18 years) and female (55 years) patients, respectively. The concentration of heavy metals (Pb, Cd, and Ni) and radium contents is higher in leukemia blood samples, as compared with their concentration in healthy blood samples.

Index Terms—Uranium concentration, Heavy element, leukemia, CR-39, X-ray fluorescence.

I. INTRODUCTION

Natural uranium consists of three radioactive isotopes in the following proportions ^{234}U , ^{235}U , and ^{238}U , all of which are decayed through alpha- and beta-emissions (Abdulwahid, et al., 2020).

Once uranium enters the human body, the soluble part will reach the blood and accumulate to some degree in all organs. The major health concerns related to the presence of elevated levels of uranium are radiation effects and toxicity effects. As a heavy, metal uranium is toxic to humans and animals and, in addition, poses a potential health risk from external and internal radiation exposure (Konishi, et al., 2019).

Uranium (U) is a naturally occurring radioactive element or as a result of human activities. Plus, it is the heaviest ingredient that occurs in large quantities. On the other hand, its concentration is higher than other toxic elements and it is present in varying amounts in the environment (Zou, et al., 2011).

Uranium has side effects when inhaled or ingested. Studies involving humans and animals have shown that inhaled insoluble uranium particles can cause serious respiratory effects. According to the World Health Organization (WHO),

approximately 2% of uranium that enters the body through ingestion is absorbed, but 98% is excreted through feces, and inhaled uranium can be absorbed into the blood by more than 20% (WHO, 2011).

Heavy metals enter the body through our food and beverages (ingestion), the air we breathe (inhalation), and less frequently through what we touch (absorption). Certain metals may pose health problems if they are present at high enough concentrations. Measuring heavy metals in the body may help to determine whether or not they are harmful (Kortei, et al., 2020; Hussein, 2019).

Toxic elements in the body could pose long-term health risks due to chemical toxicity and radioactivity, depending on the pathway and extent of exposure to toxic elements which are a serious threat to the human health (Buxton, et al., 2019). Exposure to toxic prolonged exposure to lead (Pb), chromium (Cr), cadmium (Cd), copper Cu, and nickel (Ni) can cause deleterious health effects in humans, namely, chronic inflammatory conditions and a higher risk for several cancers, cardiac, and pulmonary and neurological diseases. This scenario has been aggravated by erroneous human intervention that has significantly changed their natural cycle and balance, causing abnormal accumulation and environmental pollution (Isabel, Mariana and Mónica, 2016).

Heavy metals can be detected in human fluids such as blood. The most common samples used to test heavy metals are blood because they best represent the substance (Mohsen and Abojassim, 2019). Insoluble heavy metals build up toxins in the human body that affect human life. Metals such as Pb, Cd, Ni, and Cu are very venomous accumulative metals that pose serious risks to the environment (Jae, Jang and Yu, 2022; Tiange, et al., 2021). Heavy metals can be considered one of the main sources of many health problems, as some minerals replace others in the body and thus affect the organic process in the human body (Dler, et al., 2022; Mohammed and Ahmed, 2017).

Blood is the body fluid that is usually examined as far as trace elements are concerned. The amount of trace element entering the bloodstream after absorption into the gastrointestinal tract depends on how chemically bound it is in the food substance (Kim, et al., 2021; Basu and Kulkarni, 2014).



Heavy metals are metals that cannot be readily degraded and therefore build up in vital human organs. This condition causes different degrees of illness depending on acute and chronic exposure. Low condensation of weighty metals causes harm to humans and other living creatures. There is not yet an efficient mechanism to remove it from the body (Mahugija, Kasenya and Kiluiya, 2018; Nah, et al., 2018).

Environmental pollution from toxic elements and the resulting long-term health effects are a great global health interest over the previous three decades, concerns about the effects of environmental pollution on public health have increased globally. Many health problems are linked to exposure to toxic elements, as people are exposed to toxic elements such as revolution (Ghorani, Riahi and Balali, 2016; Hussein, Jaafar and Ismail, 2013).

This study aims to detection the concentration of uranium and heavy metals (Pb, Cd, and Ni) in blood samples for leukemia patients and health groups at Erbil Governorate.

II. MATERIALS AND METHODS

A. Samples Collection

The total number of blood samples for the leukemia patients and health group was 20 samples, female and male each one (ten samples). The blood samples for the leukemia patients group (ten samples) takes from the Nanakaly center of cancer in the Erbil governorate and the healthy group (ten samples) takes from the same governorate. The mean age of leukemia patients and health group is between 18 and 55 years. Blood specimens of 3 mL was taken from each leukemia patient and healthy groups were kept in the icebox (4°C) and then transfer to advance laboratories for heavy element analysis using the X-ray fluorescence (XRF) technique. Blood specimens were dried at 37°C for 5 h in an electrical laboratory oven (Adhraa, et al., 2019).

B. Reflection XRF

The spectrometry of XRF is the choice of generality petrologists and geochemists to obtain powder analysis (Ismail, Hussein and Sardar, 2020). This technique is intended for the speedy specific and specific investigation of great, minor, and trace components in a broad diversity of test types that do not require extensive training or experience on the part of the analyzer (Sergiusz, et al., 2021). To dry samples, the blood samples were heated with an electric heating incubator at 37°C for 6 h. The samples were placed in the chamber and measured with a 20 mm diaphragm under a vacuum (Rasha and Raghad, 2020). The spectrometer main unit consists of the sample chamber and the block unit. The chemical compositions of the samples were then measured from a computer program, as shown in Fig. 1.

C. CR-39 Nuclear Track Detectors

After collecting the blood samples from the patients and the healthy group, blood specimens were dried at 37°C for 5 h in an electrical laboratory oven (Hussein, 2015). The samples were put in the end of PVC tubes equipped with the

nuclear track detector type CR-39 (Hussein, et al., 2013b). All detectors were steady at the top end of PVC tubes with a diameter of 1.5 cm and a length of 6 cm, as shown in Fig. 2, all tubes were stored for about 90 days in the Research Center of Physics Laboratory. The chemical etching method contained 6.25N of Na OH, distilled water, and a water bath was used for warming the etching at 70°C for 8 h. The detector is hung in Na OH by fixing the attached wire, on the cover or at the edge of the beaker, keeping the detector for the requisite time and the solution was shacked regularly during the time of etching (Adhraa, et al., 2019).

D. Calculation

To estimation of uranium concentration (ppm). We can obtain the uranium concentration in the samples by dividing W_U on the weight of the dry samples

$$C_U (\text{ppm}) = \frac{W_U}{W_S} \quad (1)$$

Also, we calculate the weight of uranium by equation (Elzain, 2014).

$$W_U = \frac{N_U A_U}{N_{av}} \quad (2)$$

Where, (N_U) is number of the sample at secular equilibrium can be obtained according to Podgorsak, 2005, A_U is the mass number of ^{238}U , and N_{av} is Avogadro's number.

III. RESULTS AND DISCUSSION

Table I shows that the personal profile of patients, it is including location, age, and gender, also shows the results of uranium concentrations in blood samples for leukemia patients of Erbil governorate. The maximum and minimum uranium concentration in blood samples of leukemia patients was 1.15 ± 0.02 ppm for a female (55 years) and 0.12 ± 0.03 ppm for a male (18 years), respectively, and the average rate is 0.668 ± 0.28 ppm.

Table II shows the range value for uranium concentration of blood samples for the healthy group varied from 0.014 ± 0.002 ppm to 0.072 ± 0.008 ppm. The average value of uranium concentration in blood samples for leukemia patients is higher than the healthy group, as shown in Fig. 3, and this finding is in agreement with those of other researchers (Al-Hamzawi, Jaafar and Tawfiq, 2015).

Table III represents the average value of uranium concentration in the blood samples of male and female leukemia patients and healthy groups. From this table, the average value of uranium concentration of male and female leukemia patients group is 0.57 ± 0.03 ppm and 0.76 ± 0.02 ppm, respectively, while the average value of uranium concentration of male and female for the healthy group is 0.026 ± 0.08 ppm and 0.039 ± 0.05 ppm, respectively. The results showed that the average values of uranium concentration for female leukemia patients and healthy groups are higher than those for males. This is because the total blood volume in females is 4–5 L, while in

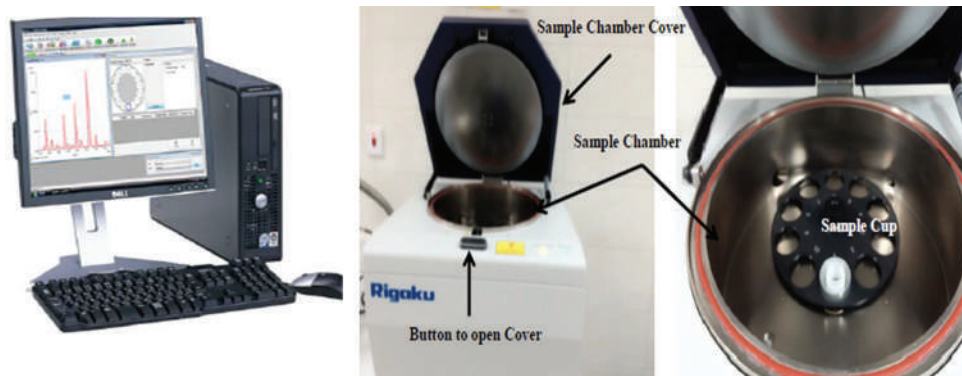


Fig. 1. X-ray fluorescence illustrates the sample chamber with their computer program.

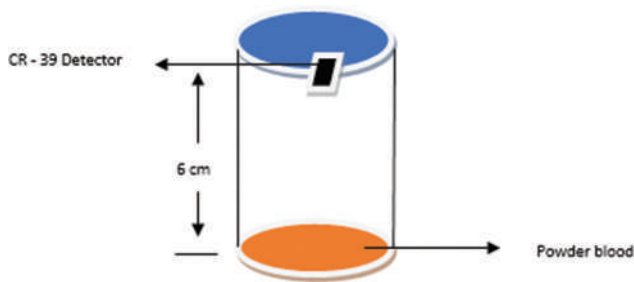


Fig. 2. Diagram of container for measuring uranium concentrations.

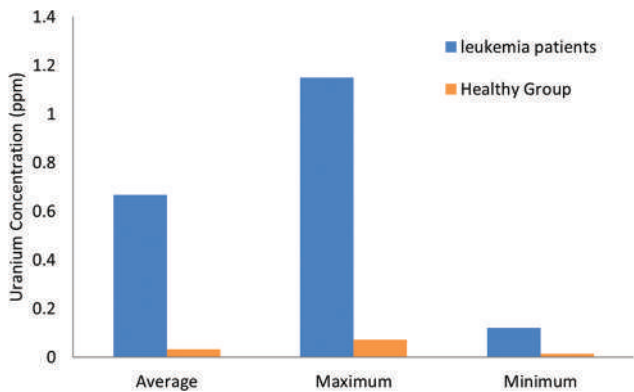


Fig. 3. Comparison of the uranium concentration between the leukemia patient and healthy groups.

males is 5–6 L (Basu, and Kulkarni, 2014). Results showed statistically significant in the uranium concentration with regard to gender in both groups ($p < 0.05$).

The heavy elements (Pb, Cd, and Ni) are investigated in the blood of 20 volunteers including ten samples for each leukemia patient and healthy group using the XRF technique. The heavy elements in blood samples for both groups are concise in Tables IV and V.

The average concentration of heavy elements of the leukemia patients (Pb, Cd, and Ni) was found 12.32 ± 1.2 ppm, 3.61 ± 0.2 ppm, and 5.17 ± 0.8 ppm, respectively. From Table V average concentration of heavy elements of the healthy groups (Pb, Cd, and Ni) was found 6.67 ± 0.26 ppm, 1.39 ± 0.04 ppm, and 2.04 ± 0.085 ppm, respectively.

The result shows that heavy elements (Pb, Cd, and Ni) are higher in the leukemia patients than in the healthy groups

TABLE I
URANIUM CONCENTRATION IN BLOOD SAMPLES OF THE LEUKEMIA PATIENTS

Sample	Gender	Age (year)	Location	Uranium concentration in (ppm)
1	Male	18	Daratu	0.12±0.03
2	Female	20	Kaznazan	0.32±0.04
3	Male	22	Shaqlawa	0.38±0.01
4	Female	23	Mergasor	0.56±0.02
5	Female	45	Hanara	0.88±0.05
6	Male	26	Soran	0.74±0.09
7	Female	54	Maxmur	0.92±0.02
8	Male	30	Choman	0.82±0.04
9	Male	28	Soran	0.79±0.03
10	Female	55	Heran	1.15±0.02
Average				0.668±0.28
Maximum				1.15±0.02
Minimum				0.12±0.03

TABLE II
URANIUM CONCENTRATION IN BLOOD SAMPLES FOR HEALTHY GROUP

Sample	Gender	Age (year)	Location	Uranium Concentration in (ppm)
1	Male	44	Daratu	0.034±0.004
2	Female	48	Kaznazan	0.018±0.007
3	Male	55	Shaqlawa	0.072±0.008
4	Female	36	Mergasor	0.026±0.004
5	Female	29	Hanara	0.024±0.005
6	Male	33	Soran	0.015±0.009
7	Female	25	Maxmur	0.022±0.006
8	Male	27	Choman	0.014±0.002
9	Male	52	Soran	0.064±0.008
10	Female	40	Heran	0.042±0.001
Average				0.033±0.006
Maximum				0.072±0.008
Minimum				0.014±0.002

TABLE III
THE AVERAGE URANIUM CONCENTRATION IN BLOOD SAMPLES FOR MALES AND FEMALES

Groups	Gender	Uranium concentration (ppm)	p-value
leukemia patients group	Male	0.57±0.03	0.001
	Female	0.76±0.02	
Healthy group	Male	0.026±0.08	0.001
	Female	0.039±0.05	

and element (Pb) value for leukemia patients and healthy groups is higher than (Cd and Ni) elements, as shown in

TABLE IV
HEAVY ELEMENTS CONCENTRATIONS IN BLOOD SAMPLES OF THE LEUKEMIA PATIENTS

Sample	Gender	Age (year)	Pb	Cd	Ni	Smoking Habited
1	Male	18	10.55	3.12	4.67	S
2	Female	20	11.28	3.24	4.86	N
3	Male	22	10.55	3.52	5.08	N
4	Female	23	11.78	3.65	5.12	S
5	Female	50	9.28	3.06	4.98	S
6	Male	26	8.92	2.66	3.88	N
7	Female	54	15.12	4.22	5.88	S
8	Male	30	14.92	3.98	5.78	S
9	Male	28	12.87	3.92	5.04	N
10	Female	55	18.82	4.78	6.42	S
Average			112.32±1.26	3.61±0.2	5.17±0.8	
Maximum			18.82	4.78	6.42	
Minimum			8.9	2.66	3.88	

TABLE V
HEAVY ELEMENTS CONCENTRATION IN BLOOD SAMPLES FOR HEALTHY GROUPS

Sample	Gender	Age (year)	Pb	Cd	Ni	Smoking habited
1	Male	44	4.92	0.84	0.98	N
2	Female	48	5.34	0.92	1.22	N
3	Male	55	5.84	1.61	2.42	N
4	Female	36	6.08	1.27	2.48	N
5	Female	29	7.94	2.12	2.82	N
6	Male	33	6.44	1.68	2.34	N
7	Female	25	10.12	2.22	2.78	N
8	Male	27	7.33	1.84	2.38	N
9	Male	52	8.62	1.12	1.92	N
10	Female	40	4.15	0.32	1.12	N
Average			6.67±0.26	1.39±0.04	2.04±0.085	
Maximum			10.12	2.22	2.82	
Minimum			4.15	0.32	0.98	

TABLE VI
HEAVY ELEMENT IN BLOOD FOR MALES AND FEMALES OF LEUKEMIA PATIENTS GROUP

Elements	Statistical rate	Male	Female
Pb	Minimum	8.9	18.28
	Maximum	14.92	28.9
	Mean±standard error	11.41±2.82	25.13±3.18
	p<0.05-(0.001)		
Cd	Minimum	2.66	3.06
	Maximum	3.98	4.78
	Mean±standard error	3.44±0.22	3.79±0.65
	p<0.05-(0.001)		
Ni	Minimum	3.88	4.67
	Maximum	5.78	6.42
	Mean±standard error	4.89±0.14	5.45±0.12

p<0.05

Fig. 4. The heavy elements concentrations in the blood of leukemia patients are increased by inhalation of airborne dust particles and exposure to radioactivity released and taking a radiation dose.

In addition, Fig. 5 appears that the rate of Pb in blood is 59% and is higher than that of Cd, and Ni, because the majority of lead concentrations found in the environment

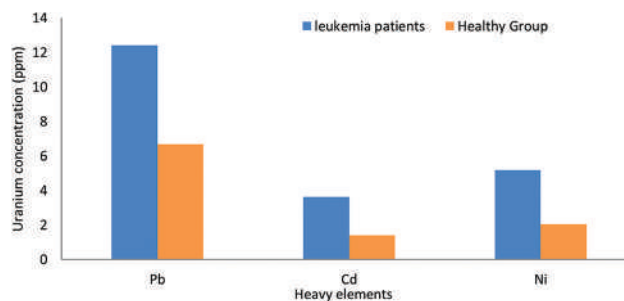


Fig. 4. Comparison heavy elements for leukemia patients and healthy groups.

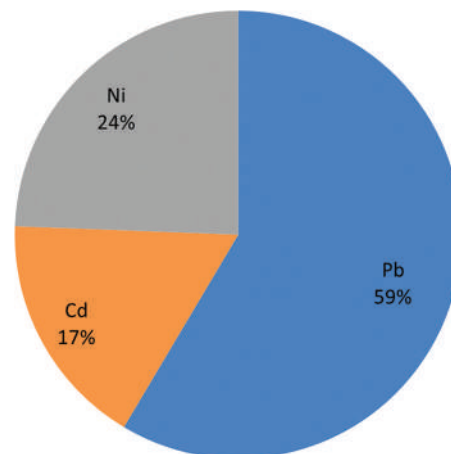


Fig. 5. The rate heavy element in leukemia patients.

are the result of human activities. Lead pollution at the local level results from emissions from cars using leaded gasoline, lead is still used in gasoline in many Middle Eastern countries, including Iraq. This result is consistent with another investigator in another country (Khoder, Al Ggamdi and Shiboob, 2012; Stojasavijevic, et al., 2020).

Table VI appears the average value of the heavy elements in the blood of male and female leukemia patients group, in this table, the average rate of heavy elements (Pb, Cd, and Ni) of the male leukemia patients group is 11.41 ± 2.82 ppm, 3.44 ± 0.22 ppm, and 4.89 ± 0.14 ppm, respectively. Furthermore, in this table, the average value of the heavy elements (Pb, Cd, and Ni) of the female leukemia patients group is 25.13 ± 3.18 ppm, 3.79 ± 0.65 ppm, and 5.45 ± 0.12 ppm, respectively. The results should compare with other articles obtained that the rate amount of heavy element for the male group is lower than for the female group. This is because the volume of the total blood in males is higher than, while in females, and also differences in red blood cell hemograms. Results showed statistically significant in the heavy metals concentration with regard to males and females in both groups $p < 0.05$.

IV. CONCLUSIONS

In this research, the uranium concentration and heavy elements (Pb, Cd, and Ni) were measured in blood samples of

leukemia patients and healthy groups in the Erbil governorate. The results obtained show that uranium concentrations in the blood samples of the leukemia patients group are higher than those of the healthy group. Heavy metals can be considered one of the main causes of many health problems. The result shows that the heavy elements rate in blood was higher in the leukemia patients than in the healthy groups. The result also obtained that the average rate of the heavy element (Pb, Cu, and Ni) in the blood samples from female leukemia patients is highest than males. The statistical results approved that the uranium concentration and heavy metals significantly changes ($p < 0.05$) with gender type in both groups.

ACKNOWLEDGMENT

The author is grateful to the blood donors that made possible this work and to the Nanakaly center of cancer hospitals for providing blood samples from leukemia patients.

REFERENCES

- Abdulwahid, T.A., Alsabari, I.K., Abojassim, A.A., Mraity, H.A. and Hassan, A.B. 2020. Assessment of concentrations of alpha emitters in cancer patients blood samples. *SYLWAN* 164, 183, pp. 242-246.
- Adhraa, B.H., Ahmed, A.M., Hussein, A.A. and Ali, A.A. 2019. Determination of alpha particles levels in blood samples of cancer patients at Karbala Governorate, Iraq. *Iranian Journal of Medical Physics*, 16(1), p. 41-47.
- Al-Hamzawi, A.A., Jaafar, M. and Tawfiq, N. 2015. Concentration of uranium in human cancerous tissues of Southern Iraqi patients using fission track analysis. *Journal of Radioanalytical and Nuclear Chemistry*, 303, 1703-1709.
- Basu, D. and Kulkarni, R. (2014). Overview of blood components and their preparation. *Indian Journal of Anaesthesia*, 58(5), p. 529.
- Buxton, S., Garman, E., Darton, T., Schlekot, E., Taylor, M. and Oller, A. 2019. Concise review of nickel human health toxicology and ecotoxicology. *Inorganics Journal*, 7(7), pp. 89-93.
- Dler, A., Ismail, A.H., Hashim, A.T. and Hussein, Z.A. 2022. Measurement of the trace element concentration in some livestock and poultry bone samples using X-ray fluorescence. *ZANCO Journal of Pure and Applied Sciences*, 24(12), pp. 67-73.
- Elzain, A. 2014. Measurement of Radon-222 concentration levels in water samples in Sudan. *Advances in Applied Science Research*, 5(2), pp. 229-234.
- Ghorani, A., Riahi, Z. and Balali, M. 2016. Effects of air pollution on human health and practical measures for prevention in Iran. *Journal of Research in Medical Sciences*, 21(4), pp. 1-12.
- Hussein, Z.A. 2015. Measurement of indoor radon concentration in dwellings of Koya using nuclear track detectors. *International Journal of Science and Research (IJSR)*, 4, pp. 2465-2467.
- Hussein, Z.A. 2019. Assessment of natural radioactivity levels and radiation hazards of soils from Erbil Governorate, Iraqi Kurdistan. *ARO-The Scientific Journal of Koya University*, 7(1), pp. 34-39.
- Hussein, Z.A., Jaafar, M.S. and Ismail, A.H. 2013. Measurements of indoor radon-222 concentration inside Iraqi Kurdistan: Case study in the summer season. *Nuclear Medicine and Radiation Therapy*, 4(1), pp. 1-4.
- Hussein, Z.A., Jaafar, M.S., Ismail, A.H. and Battawy, A.A. 2013. Radon exhalation rate from building materials using Passive Technique Nuclear Track Detectors. *International Journal of Scientific & Engineering Research*, 4(7), pp. 1276-1282.
- Isabel, S., Mariana, S. and Mónica, E. 2016. Kidney cancer. Heavy metals as a risk factor. *Porto Biomedical Journal*, 1(1), pp. 25-28.
- Ismail, H.A., Hussein, Z.A. and Sardar, P.Y. 2020. Investigation a relation between radioactivity concentrations of 40 Potassium (40K) in tooth and the various ethnic groups and its impacts on the rate of tooth damage. *Environmental Nanotechnology, Monitoring & Management*, 14, pp. 100385.
- Jae, M.L., Jang, S.S. and Yu, K.K. 2022. Red blood cell deformability and distribution width in patients with hematologic neoplasms. *Clinical Laboratory*, 68(10), pp. 11-14.
- Khoder, M., Al Ggamdi, M.A. and Shiboob, M.H. 2012. Heavy metal distribution in street dust of urban and industrial areas in Jeddah, Saudi Arabia. *Journal of King Abdulaziz University: Metrology, Environment and Arid Land Agricultural Sciences*, 142(588), p. 1-4.
- Kim, S.H., Yang, H.O., Hyun, C.A., Joo, H.S. & Chang, S.S. (2021). Levels of blood lead and urinary cadmium in industrial complex residents in Ulsan. *Annals of Occupational and Environmental Medicine*, 29(1), p. 26.
- Konishi, T., Kodaira, S., Itakura, Y., Ohsawa, D. and Homma S. 2019. Imaging uranium distribution on rat kidney sections through detection of alpha tracks using CR-39 plastic nuclear track detector. *Radiation Protection Dosimetry*, 183, pp. 242-246.
- Kortei, N., Korley, K., Alice, K., Papa, A., Nana, B. and Manaphraim, M. 2020. Potential health risk assessment of toxic metals contamination in clay eaten as pica (geophagia) among pregnant women of Ho in the Volta Region of Ghana. *BMC Pregnancy and Childbirth*, 20(1), p. 160.
- Mahugija, J., Kasenya, Z. and Kiluiya, K. 2018. Levels of heavy metals in urine samples of school children from selected industrial and non-industrial areas in Dar es Salaam, Tanzania. *African Health Sciences*, 18(4), pp. 1226-1235.
- Mohammed, R. and Ahmed, R., 2017. Estimation of excess lifetime cancer risk and radiation hazard indices in southern Iraq. *Environmental Earth Sciences Journal*, 76(3), pp. 76-80.
- Mohsen, A.A. and Abojassim, A.A. 2019. Determination of alpha particles levels in blood samples of cancer patients at Karbala Governorate, Iraq. *Iranian Journal of Medical Physics*, 16(1), pp. 41-47.
- Nah, E.H., Suyoung, K.S., Cho, M. and Han, I.C. 2018. Complete blood count reference intervals and patterns of changes across pediatric, adult, and geriatric ages in Korea. *Annals of Laboratory Medicine*, 38(6), pp. 503-511.
- Podgorsak, E. 2005. Basic radiation physics. In: *Radiation Oncology Physics: A Handbook for Teachers and Students*. IAEA, Vienna, pp. 1-7.
- Rasha, S.A. and Raghad, S.M. 2020. Assessment of uranium concentration in blood of Iraqi females diagnosed with breast cancer. *Radiation and Environmental Biophysics*, 60(6), pp. 96-201.
- Sergiusz, Ł., Marcin, C., Alicia, F., Jack, B., Robert, S. and Andrzej, S. 2021. Breast cancer-epidemiology, risk factors, classification, prognostic markers, and current treatment strategies-an updated review. *Cancers (Basel)*, 13(17), pp. 25-29.
- Stojavsijevic, A., Lilijana, V., Branislav, R., Slavica, B., Mariia, G. and Dragan, M. 2020. Assessment of trace metal alterations in the blood, cerebrospinal fluid and tissue samples of patients with malignant brain tumors. *Scientific Report*, 10(4), pp. 124-128.
- Tiange, L., Mingyu, Z., Mohammad, R., Xiaobin, W., Stefanie, H., Cuilin, Z. and Noel, T. 2021. Exposure to heavy metals and trace minerals in first trimester and maternal blood pressure change over gestation. *Environment International*. 53(6), pp. 72-76.
- WHO. (2001). Depleted Uranium Sources, Exposure and Health Effects. Technical Report, World Health Organization, Geneva.
- Zou, W., Bai, H., Zhao, L., Li, K. and Han, R. 2011. Characterization and properties of zeolite as adsorbent for removal of uranium (VI) from solution in fixed bed column. *Journal of Radioanalytical and Nuclear Chemistry*, 288, 779-788.

An Intelligent Intrusion Detection System for Internet of Things Attack Detection and Identification Using Machine Learning

Trifa S. Othman and Saman M. Abdullah

Department of Software Engineering, Faculty of Engineering, Koya University,
Koya KOY45, Kurdistan Region - F.R. Iraq

Abstract—The usability and scalability of Internet of things (IoT) technology are expanding in such a way that they facilitate human living standards. However, they increase the vulnerabilities and attack vectors over IoT networks as well. Thus, more security challenges could be expected and encountered, and more security services and solutions should be provided. Although many security techniques propose and promise good solutions for that intrusion detection systems (IDS)s still considered the best. Many research works proposed machine learning (ML)-based IDSs for IoT attack detection and classification. Nevertheless, they suffer from two main gaps. First, few of the works utilized or could analyze an up-to-date version of IoT-based attack behaviors. Second, few of the works can work as multi-class attack detection and classification. Therefore, this work proposes an intelligent IDS (IIDS) by exploiting the ability of ML algorithms to classify and identify malicious from benign behaviors among IoT network packets. The methodology of this work investigates the efficiency of three ML classifier algorithms, which are K-Nearest Neighbor, support vector machine, and artificial neural network. The developed models have been trained and tested as binary and multi-class classifiers against 15 types of attacks and benign. This work employs an up-to-date dataset known as IoT23, which covers millions of malicious and benign behaviors of IoT-connected devices. The process of developing the proposed IIDSs goes under different preprocessing phases and methods, such as null value solving, SMOTE method for the imbalanced datasets, data normalization, and feature selections. The results present IIDSs as good binary and multi-class classifiers even for zero-day attacks.

Index Terms—Internet of things networks, Intrusion detection system, Machine learning, Intelligent attack classification, and identification.

I. INTRODUCTION

Network technology has mostly oriented toward a new trend called the Internet of Things (IoT). Based on this

technology, connected devices can communicate with each other independently with or without human permission (Nagisetty and Gupta, 2019). Although the scalability indicator of networks has been improved with IoT, new challenges have been encountered and measured especially in the ones that are related to networks' security or connected devices' security. Some of the security challenges are related to energy consumption (Malik and Dutta, 2022) and others are related to the system environment of the IoT applications (Ho, 2022).

There are many reasons that make the devices connected over IoT networks be considered vulnerable more to attacks and intruders. Most devices are having resource limitations, such as power and memory limitations. With such limitations, the security tools could not work efficiently as they depend on complex algorithms. Another reason for vulnerability is the inability to build some security standards for connected objects among IoT vendors. IoT devices have been manufactured by many vendors and companies and each of them follow specific security standards. All these reasons increase the number of attacks and threats over IoT networks and expand the vulnerabilities and attack surfaces (Nawir, et al., 2016). Due to that most researchers are focusing on and addressing these open problems, and they are investigating machine learning (ML) techniques and tools for building classifier models to distinguish benign from malicious behaviors of packets that flow over IoT networks (Chen, et al., 2018; Saharkhizan, et al., 2020).

ML techniques have great abilities for detecting and classifying objects. They depend on analyzing some predefined behaviors or attributes, numerically, then mapping them to a class among some available classes (Radivilova, et al., 2019). To build any classifier models, all ML techniques should follow two phases, which are the training and testing phases. Although both phases are important for getting a perfect classifier model, the training phase needs more work and must be more focused. This is because the training phase teaches the ML model through a use of a training dataset, and when collected, such datasets need much preprocessing work that, if not done, it influences negatively on the accuracy rate of the ML classifiers (Sanmorino, 2019). Therefore, one of the questions that this work wants to investigate is about

ARO-The Scientific Journal of Koya University
Vol. XI, No. 1 (2023), Article ID: ARO.11124. 12 pages
DOI: 10.14500/aro.11124

Received: 26 December 2022; Accepted: 02 May 2023
Regular research paper: Published: 22 May 2023

Corresponding author's email: saman.mirza@koyauniversity.org
Copyright © 2023 Trifa S. Othman and Saman M. Abdullah. This is an open access article distributed under the Creative Commons Attribution License.



the possibility of improving the accuracy rate of classifier models through preprocessing steps. This question has been investigated in the security field of IoT networks, especially, using a new training dataset called (IoT-23) (Parmisano, Garcia and Erquiaga, 2020). Based on best knowledge of this work, the concept of the attack classification over IoT has been mentioned for the first time in the book (Giusto, et al., 2010). Since then, many works have been conducted and many investigations have been published (Kareem and Jasim 2022; Kumari and Mrunalini, 2022; Li, Rios and Trajković, 2021). Although the methodology that followed by those works and many other works depended on employing one of the ML techniques for training and evaluating the classifier model and then comparing the obtained results with results of some other works, many influenced parameters on the accuracy rate have not been investigated yet. Therefore, research projects in this field still not saturated. Besides that, most of the conducted research projects utilized some training datasets that were already collected through monitoring non-IoT networks (Tabassum, et al., 2021; Tabassum et al., 2022). Therefore, among the aims that this work wants to focus is, firstly, evolving a most recent collected dataset for attackers over IoT networks. Secondly, to investigate many preprocessing techniques against three ML algorithms to find out the best and more efficient classifier models that could be used for attack and malicious detection over IoT networks.

II. WORK CONTRIBUTIONS

As mentioned in Section 1, the main objective of this work is to build intelligent intrusion detection systems (IIDSs)-based classifier model that can detect and identify attacks by analyzing the packet behaviors of IoT-based networks. The main contributions of the work could be summarized as below:

- 1) The work focuses on the most recent dataset (IoT23) that is purely related to IoT-based attacks and benign behaviors excluding behaviors of the traditional networks.
- 2) The work focuses on analyzing fifteen types of attacks through training the proposed IIDS model on the dataset that mentioned in point (1). The focused type of attacks is up-to-date attacks and mostly related to behavior flow of the IoT-based network packets.
- 3) Few of works were conducted research projects on analyzing IoT-based behaviors using ML-based classifier models as IIDS binary and multiclass calcification.

III. RELATED WORKS

During the review process, it has been found that classifying attacks over IoT-networks depends on a variety of orientations, such as the type of the utilized ML techniques, dataset types and versions, types of the preprocessing techniques, and the performance indicators that used for evaluating the efficiency of the exploited ML algorithms. The orientation that covers the type of ML presents the

most important ML techniques that have been proposed by authors of the previous works as detection and classification models. The review presents, as well, the advantages and disadvantages of each technique in the viewpoint of the authors. Another focus of this study could be on the types of datasets used for training and testing ML models. More orientations are available, such as Feature selection, Data normalization, and/or data encoding. Finally, several studies could be categorized based on the utilized performance indicators to measure the efficiency of ML algorithm. In the subsequence sections, many articles have been reviewed based on these orientations.

Despite of diversity in investigating the ability of ML techniques in classifying IoT-based attacks, most researchers agree that expanding the scalability of networks makes connection of new devices to the internet or IoT-based networks becomes more vulnerable than before. It is true that such expansion makes networks be important for our daily life and increases the capability of connecting more devices. Nevertheless, the expansion increases the number of the cyber-attacks over the networks as well, especially over the IoT-based networks as they have limited resources and capabilities. The most important problem is detecting zero-day attacks, which means detecting new patterns or policies of attacks. To overcome this problem, most researchers investigated ML algorithms to build intelligent detection models that can classify new patterns of attacks through learning from known similar patterns. However, there is a disparity over the ability of the ML algorithms as each previous work has proposed a specific algorithm and has justified its ability. Therefore, reviewing those works is necessary.

In general, there are two types of ML algorithms. The first type of ML algorithm is known as classical or conventional algorithms; however, there are some other techniques known as deep learning algorithms (Picon Ruiz, et al., 2020; Sewak, Sahay and Rathore, 2018). The classical ML algorithms are less complex than the deep learning ones. Although, algorithms in both categories are utilized in different works as attacks classification or identification, this work focuses more on the classical ML algorithms as the second type of algorithms needs less resources than deep learning algorithms.

A. Artificial Neural Network (ANN)

The first ML algorithm that could be considered a most distinguished technique is ANN. The ANN algorithm has been utilized by (Soe, et al., 2019) to build an IDS. The author of that work argued that building an ANN model to detect different type of attacks is not sufficient. Instead, the work proposed sequential ANNs in which for each type of attacks an ANN has been designed and developed. Although the paper showed good and high accuracy rate, the structure of such model needs to be updated and a new ANN must be added to the sequence when a new type of attack or a zero-day attack comes to the live. ANN is considered as a supervised learning algorithm that could be utilized as

classifier model. This fact has been used in (Hanif, Ilyas and Zeeshan, 2019) to build an attack detection over IoT-based networks. The work showed that results of a 10-fold cross-validation reach to 84%, which somehow is not good enough. Moreover, the versions of the datasets that have been utilized for training the proposed ANN are going back to 1999 and 2015 which, somehow, are not up to date enough. Another work that focused on ANN to classify attacks over IoT-based networks has been proposed by (Fatayer and Azara, 2019). The work argued that IoT-based networks needs more security as different types of attacks can easily penetrated them. The work built an ANN model to detect many attack types and the work obtained a very good accuracy (97%). However, the work also utilized an old version of dataset (KDD CUP 99), in which, the behaviors of traditional networks have been analyzed and the ANN model cannot be evaluated with recent behaviors of IoT-based attacks. There are many recent works that focused on the ANN based attack classification (Gopi, et al., 2021; Churcher, et al., 2021; Mehmood, Khan and Elhadef, 2022) to classify attacks over IoT-based networks. However, a part of them focused only on one type of attack, other works focused on many types of attack through utilizing some outdated version datasets. Therefore, it is very necessary to investigate the efficiency of the ANN against classifying the most recent behaviors of the devices that connected to the IoT-based networks as binary or/and mutli-class based classifier models.

B. K-Nearest Neighbor (KNN)

Another type of the supervised learning algorithm is called KNN. This type is somehow considered as a lazy learner supervised algorithm as the training phase of this algorithm takes place while the prediction phase is started (Churcher, et al., 2021). Many recent works utilized KNN as classifier model for detecting attacks over IoT-based networks. However, based on the best of our knowledge, the work (Li, et al., 2014) was the first that utilized the KNN algorithm for attacks and penetrating detection over IoT-based networks. The work proposed the KNN to distinguish intruder sensors over the sensor networks through keeping the authorization of connected objects. One of the most recent works that utilized KNN for IoT-based network attacker is (Iman, 2022). The work proposed the KNN algorithm and argued detecting DDoS attacks over IoT-based networks with minimum consuming of energy. Although the work presented 99% as accuracy rate, the test of the work simulated in SDN environment and it focused only on one type of attack over IoT-based networks. Another recent work that utilized KNN for classifying IoT attacks has been trained with Bot-IoT dataset (Alfarshouti and Almutairi, 2022). The work also presented a taxonomy on the IoT-based attacks. The taxonomy work categorized the available attacks based on their relationship with each layer. Another recent work (Islam, et al., 2022) focused on the IoT-based attacks considering banking systems as an environment case. The work showed that KNN can detect malicious activities up to 98.7%. The work only focused on DDoS attack. Another

work that utilized KNN (Aslam, et al., 2022) was depended on adjusting some ML algorithms in the SDN environment and focused on the real-time sniffing packets. The work showed 99% of accuracy and concluded that using SDN controller could be more studied in the future for detection models. However, the work proposed a model to detect phishing attack as a future work. This means that single detection attack always needs to be updated when a new type of attacks comes to the live. Therefore, one of the objectives that addressed by this work is to propose a KNN that could be trained over classifying and detecting most recent type of attacks that penetrating IoT-based networks, not only one attack type.

C. Support Vector Machine (SVM)

SVM is another supervised ML algorithm that could be used for classification, regression, and outlier detection. In the field of IoT-based attack classification, SVM has more frequently used as a common ML algorithm. A recent work that utilized SVM to build an attack detection system over IoT-based networks has depended on Bot-IoT dataset (Alfarshouti and Almutairi, 2022). The work made a comparison between the results that have been obtained from their proposed SVM model with another type of detection model that designed using KNN classifier algorithm. More recent works have utilized SVM as detection method (Islam, et al., 2022). The work investigated one type of the IoT-based attacks, which is DDoS. The work argued that banking system is one of the important environments that should be kept more securable against IoT attacks, especially, DDoS attack which denies bank servers to serve authorized users. The work (Islam, et al., 2022) utilized banking dataset for training the suggested algorithms. Results of the work showed that 99% of the accuracy could be obtained with SVM. Most datasets that used for training the attack detection have complex dimensionality. Therefore, most works employed a process called feature selection for reducing the dimensionality size of the training dataset. A most recent work (Majeed Alhammadi, 2022) utilized principle component analysis (PCA) as a feature selection method to reduce the dimensionality of the training dataset to build a SVM-based attack detection model. The work depended on the outdated version of the intrusion behavior dataset, which known as NLS-KDD and contains 41 attributes. Another work compared the performance of the SVM with decision tree on two types of attacks (DDoS and Code Injection). The work proposed an intrusion detection system for attacks over IoT-based networks in smart city applications. They focused also on a comparison between two types of feature selection (constant removal and recursive feature elimination). The performance of SVM that obtained in that work was 98%. The summary of the research works that have been reviewed throughout sub-sections 3.1, 3.2, and 3.3 could be illustrated in Table I, which somehow summarizes the differences between the most reviewed works with this work.

Table I shows some differences that distinguish methodology of this work with methodology that followed

TABLE I
THE WORK REVIEW SUMMARY

Reference	ML tools	Datasets	Binary or multiclass	Number of attacks
Soe, et al., 2019	ANN	N-BaIoT	Multiclass	2
Hanif, Ilyas and Zeeshan, 2019	ANN	UNSW-15	Binary	1
Fatayer and Azara, 2019	ANN	KDD CUP 99	Binary	1
Iman, 2022	KNN	SDN simulation	Binary and DDoS	1
Islam et al., 2022	SVM	Bot-IoT	Binary and DDoS	1
Majeed Alhammadi, 2022	STV and DT	NLS-KDD	Multiclass	2
This work	ANN, KNN, and SVM	IoT-23	Binary and multiclass	8

ML: Machine learning, ANN: Artificial neural network, SVM: Support vector machine, DDoS: Distributed denial of service, KNN: K-nearest neighbor

by some previous works. The distinction of the work methodology of this work could be summarized as below:

This work investigates three common ML algorithms, which are ANN, KNN, and SVM. There are other works already employed these ML algorithms; however, based on the best knowledge of us, they have been utilized in different fields or for different topics.

1. Most of the reviewed works have utilized the ML algorithms that mentioned in (1) with outdated detests or with non-IoT based datasets. However, this work focused on the IoT23 dataset that could be considered as a most recent dataset for analyzing behaviors of IoT-connected devices.
2. Most reviewed works have been developed as binary classification, which means distinguishing behaviors of one type of attack with begin behaviors. However, this work develops binary classification and mutli-class classification.
3. With the present work, more than 15 types of attacks have been included for developing a multi-class classification model.
4. One of the major differences between this work and reviewed works is classifying zero-day-attacks as malicious behavior based on the behaviors of some known attacks.

It is important to consider all above-mentioned points together to highlight the differences between this work and most reviewed previous works. Because considering each difference individually decreases the difference and the gap between this work and previous works.

IV. MATERIALS AND METHODS

In this section and the subsequence sub-sections, the methodology and the materials that have been unitized by this work will be explained. Fig. 1 shows the framework of this project.

A. Dataset

This work utilizes the IoT23 dataset for training and testing the proposed IIDS. The work imports the dataset from (Garcia, Parmisano and Erquiaga, 2020), in which, records in this dataset represent benign and malicious behaviors of packets that flow over IoT-based networks. In the dataset, there are three groups or scenarios of benign behaviors and 20 groups or scenarios of malicious behaviors. Whether a behavior is benign or malicious, it consists of 21 features or attributes. The last feature is the label which represents the class of the correspondence behavior.

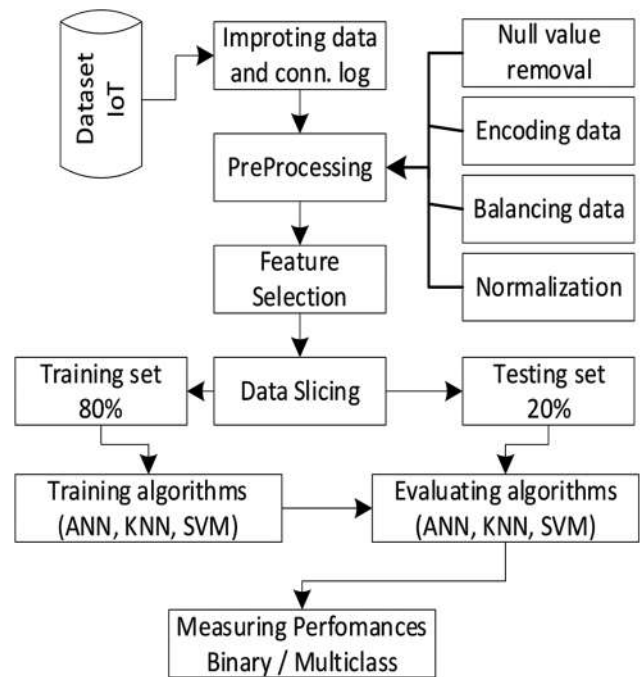


Fig. 1. The framework of the Internet of things attack classification and identification.

Behaviors in the IoT23 dataset could be labeled as benign or malicious when the goal is developing a binary classification. However, the dataset has been prepared for developing a multi-class classification as well, because a behavior in the dataset may has different attack classes. As an example, there are two different labels of attack (C&C and PartOfAHorizontalPortScan); however, a class of attack comes with label (C&C -PartOfAHorizontalPortScan), which means that this class is belong to a flow contains malicious activities from both type of attacks. Below are the description of each attack type and Table II shows the name of the available classes and the number of each class's observations.

1. Attack: This type of attack could be encountered when an infected device attacks another host, and it tries to take an advantage of a vulnerability.
2. Benign: Is a device which no suspicious or malicious activities detected from its flow over network
3. C&C: Is a command and controlled server that an infected device can connect to and control it. The infected device was connected to a CC server.

TABLE II
NUMBER OF FLOWS FOR EACH ATTACK CLASS IN THE DATASET

Serial number	Label	Flows
1	Benign	30,864,692
2	Attack	9,398
3	DDoS	19,538,713
4	Part of a horizontal port scan	213,852,924
5	Part of a horizontal port scan-attack	5
6	Okiru	60,990,708
7	Okiru-attack	3
8	File download	18
9	C and C	21,995
10	C and C-heart beat	33,673
11	C and C-file download	53
12	C and C-heart beat-attack	834
13	C and C-heart beat-file download	11
14	C and C-part of a horizontal port scan	888
15	C and C-Torii	30
16	C and C-Mirai	2
	Total	325,313,947

DDoS: Distributed denial of service

4. DDoS: Is a Distributed Denial of Service attack that an infected device launch a malicious activity to penetrate another device.
5. FileDownload: Is encountered when a file is being downloaded to an infected device.
6. HeartBeat: with this attack the track of the infected host by the C&C server will be sent through a packet.
7. Mirai: The connections have characteristics of a Mirai botnet.
8. Okiru: The connections have characteristics of a Okiru botnet.
9. PartOfAHorizontalPortScan: A horizontal port scan has been lunched by infected device to gather information for performing further attacks.
10. Torii: The connections have characteristics of a Torii botnet.

The imported dataset has a size of 20 GB. The dataset has been distributed over 23 folders; three of them are representing the benign datasets and the rest of 20 folders are representing the malicious activates over IoT-based networks. Inside each folder, there is a conn.log file (this is the Zeek conn.log file obtained by running the Zeek network analyzer using the original pcap file), and the file is containing the flow activities. Files in all folders focus on the same number of features, which are 23 features, including the target label feature, as shown in the Table III.

The flow activities in each file have not specified for a single type of attack, in the contrast, each file contains different malicious activities of IoT malwares.

B. Data Preprocessing

As shown in the Fig. 1, four main preprocessing activities have been utilized by this work and have been applied on the imported dataset. The pre-processes are:

1. Removing the null values and features with zero impact
2. Coding and encoding
3. Data balancing
4. Normalization.

For the first preprocessing, null values in the employed dataset have been handled. Three features in the imported dataset are empty and without any records, which means all cells in these three attributes have null value records. Those three features are local_orig, local_resp of connection types, and tunnel parents (No. 13, 14, and 21 in the Table III). These three features have been removed from the selected feature list, because null value methods cannot be applied on a feature that totally empty.

The process of feature selection will exclude other features as well. There are many features having zero impact on the classification process, which are feature no. 1 and feature no. 2 in the Table III. History is another feature which this work decided to delete it, as it describes only the history of conn_state. This work removes all these features as shown in Table IV.

IoT 23 dataset includes three numerical features that include missing value which are Duration, Origin Bytes and Respond Bytes (No. 9, 10 and 11). Although some categorical features also include missing value, they have not been dealt as missing value. For example, in Service variable the symbol (-) means no service is available and it has been replaced as (Nos) value as an indicator that this value shows that there is no service rather than considering it as a null or missing value. Class-based mean method is used to handle the null values in this method. The mean value of a variable is used to replace missing values, and missing values for benign and malicious observations within the same variable are computed separately (Lee and Zeng, 2008). Finally, the removing process also covered the duplicated observations. The output of this process reduces the dimensionality of the dataset. The number of features that remains in the dataset becomes 15 features.

The dataset needs Feature Encoding as it has six categorical features after applying the null value cleansing process on the dataset. Those categorical values should be changed to numerical variables. The process of encoding includes three steps (Label Encoding, Encoding categorical features, and IP Address Encoding). The labels of IoT 23 dataset are categorical values and must be encoded to numerical values for ML algorithms. As this study implements three classifiers (KNN, SVM, and ANN), the work requires two forms of Label-Encoding for identification. Ordinal encoding is used for (KNN and SVM) classifiers (as indicated in Table IV), while One Hot Encoding is used for (ANN) classifiers. Since in binary classification, the same label encoding is used for all classifiers, with 0 being assigned to benign label values and 1 to malicious values.

In Encoding Categorical Features, three categorical features of IoT 23 dataset (Protocol, Service and conn-state) encoded using frequency encoding, which according to this method, each value in a categorical feature must be modified with the total count or frequency of the value.

The two variables (id. orig_h Address, id. resp_h Address) of IoT 23 dataset are IP Address format, and they have been encoded to numerical format using IP Splitting method. According to this method, an IP address will be divided into four distinct octets number, in which each octet number will

TABLE III
NAME AND DESCRIPTION OF FEATURES

#	Feature	Description
1	Time	Time for flow starting
2	uid	Unique ID
3	id.orig-h	Source IP address
4	id.orig-p	Source port
5	id.resp-h	Destination IP address
6	id.resp-p	Destination port
7	Protocols	Transaction protocol: icmp, udp, tcp,
8	Service	dhcp, dns, http, irc, ssh, ssl
9	Duration	Total duration of flow
10	orig_bytes	Number of payload bytes the originator sent
11	resp_bytes	Number of payload bytes the responder sent
12	conn_state	Connection state. Possible values are found in Table III
13	local_orig	T if the connection originated locally and F if it originated remotely
14	local_resp	T if the connection is responded locally and F if it is responded remotely
15	missed_bytes	Number of bytes missed in content gaps, which is representative of packet loss
16	History	State history of connections as a string of letters. The letter is uppercase if it comes from the responder and lowercase if it comes from the originator. Possible letters can be seen in Table IV
17	orig_pkts	Number of packets that the originator sent
18	orig_ip_bytes	Number of IP level bytes that the originator sent
19	resp_pkts	Number of packets that the responder sent
20	resp_ip_bytes	Number of IP level bytes that the responder sent
21	Tunnel parents	The connection's ID, if it was tunneled
22	Label	Whether the capture was normal or malicious
23	Detailed_label	Identify the malicious capture type

TABLE IV
ORDINAL ENCODING OF THE LABELS OF INTERNET OF THINGS 23 DATASET FOR
K-NEAREST NEIGHBOR AND SUPPORT VECTOR MACHINE MODELS

Labels	Encoded label
C and C	1
C and C-heart beat-attack	2
C and C-Part of a horizontal port scan	3
Attack	4
C and C-heart beat	5
DDoS	6
Okiru	7
Part of a horizontal port scan	8
Part of a horizontal port scan-attack	9
Okiru-attack	10
File download	11
C and C-file download	12
C and C-heart beat-file download	13
C and C-Torri	14
C and C-Mirai	15

DDoS: Distributed denial of service

be assigned to a distinct variable. It means, the attribute of IP address will be converted to four distinct variables. In this way, this work encoded both the source and destination IP addresses, and as a result eight new variables have been added to the list of features. The two IP address variables in 32-bit address format were then removed, as shown in Fig. 2.

The third preprocessing step is balancing dataset. The IoT23 dataset is imbalanced in the number of the observations, it has in reference to each class. Based on the number of observations per classes, classes could be categorized into three main groups. The first group covers those classes that having millions of observations (number

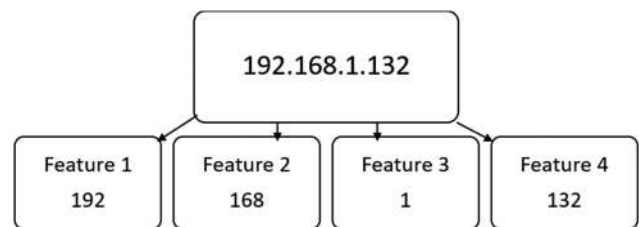


Fig. 2. IP splitting example.

1, 3, 4, 6 in the Table I). The second group is those classes that having thousands of observations (2, 9, and 10 in the Table I), and third group is those classes that having <1000 observations (5, 7, 8, 11, 12, 13, 14, 15, and 16 in the Table I). Fig. 3 clearly shows the imbalanced status of the dataset. This work achieves the process of balancing the IoT-23 dataset through two phases. At the first phase, the work reduces the gap that exists among the attack's classes in the number of observations that they have. To achieve that this work randomly picks 2000 samples from the first and second groups of attack's class in the IoT-23 dataset.

The second phase for illuminating the imbalances in the dataset is applying the SMOTE algorithm to the third group of attack's class to rise the number of the observations in all attack's classes up to 2000. The SMOTE method is a statistical technique, and it stands for Synthetic Minority Oversampling Techniques. According to recent research work (Wongvorachan, He, and Bulut, 2023), SMOTE uses for increasing the number of cases in a dataset for balancing purposes. It uses for increasing the number of cases in a dataset for balancing purposes. The technique works through generating new cases from the existing minority instances. The main condition that

SMOTE has is the implementation of the technique should not change number of the majority cases. The technique should inset just copies of the existing cases. Instead, the technique takes samples from the feature space of each targeted class and its nearest neighbors. Finally, the SMOTE will be applied to entire dataset; however, it only increases the percentage of minority cases.

Focusing on the IoT23 dataset, Fig. 3 shows the imbalanced status of the dataset before processing the dataset under the SMOTE algorithm, and Fig. 4 shows the output of the SOMT method.

Finally, this work applied the normalizing method on the dataset to put records in all remain features in the same range. This work uses the min-max normalization method. This process can speed up the training and testing phases of the classifier models.

C. Feature Selection

Feature selection is a method of reducing the number of attributes that utilized by the proposed model through selecting only relevant feature(s) and getting minimizing of noise in a dataset (Abdulla, Al-Dabagh and Zakaria, 2010). There are six features already have been excluded before feature selection process. Table IV presents these features and the reason of excluding each of them. For the rest of attributes, this work depends on computing the correlations coefficient among the attributes, first, then to compute the correlation coefficient

between each attribute and the target attribute. According to this method, the selection of the attributes (or features) in the dataset depends on the condition that states “Attributes should never have correlations among them. If any two correlated attributed found, the one that has less correlation with the target attribute will be excluded”(Weller-Fahy, Borghetti and Sodemann, 2014) (Abdulla, Al-Dabagh and Zakaria, 2010). After checking the correlations, the remaining features are (id. resp_h Address, id. resp_p port, Protocol, Service, Duration, Origin Bytes, Respond Bytes, conn_state, missed_bytes). Fig. 4 shows the correlation status among the attributes or features. Fig. 5 shows a sample of the dataset after the preprocessing steps, excluding the normalization process.

D. Data Slicing

This process is about splitting the dataset into two subsets, the training and the testing. Although the obtaining subsets will be directly used and fed to the ML classifier models, this process still be considered as a step of preprocessing activities. This work allocates 20% of the dataset as a testing subset and 80% of the dataset assigns for training phase. The process of extracting samples from the dataset for training and testing has been achieved randomly.

This work takes from the benign class 20% of records randomly, and the remain 80% will be used for training. However, taking the samples from the attack classes is slightly different for keeping the balance of the dataset in the viewpoint of attack participating. The work allocated from each attack class 20% for testing and 80% for training. Then, all 20% parts will be collected to form on testing subset and same is true for the training subsets.

E. Performance Indicators

Fig. 7 shows details of a typical confusion matrix (Bhandari, 2020). From the confusion matrix, all necessary accuracy indicators could be obtained. Although every index in the figure means something useful, rate of accuracy is most common that utilized to check the performance of detection and classification models.

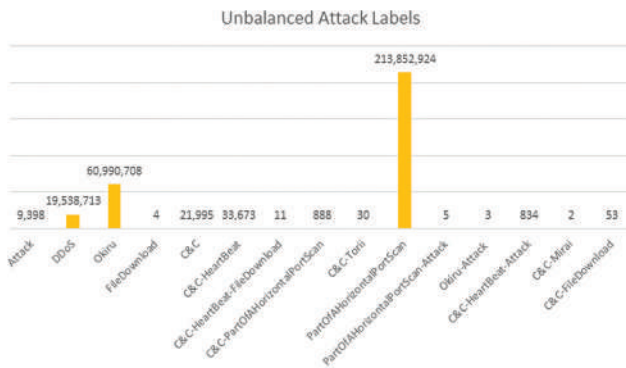


Fig. 3. The unbalanced Internet of things-23 structure.

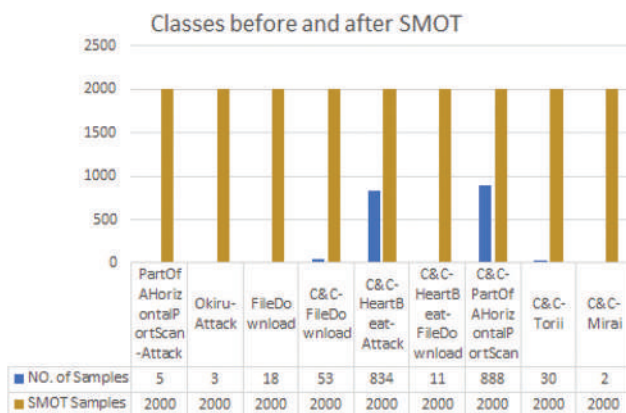


Fig. 4. Phase two output of unbalanced Internet of things-23 structure.

V. EXPERIMENTAL EVALUATION

This work utilized three major ML algorithms named ANN, SVM, and KNN. The aim of this work is building an intelligent binary and multi-class classification. The experimental evaluation in this work depends on k-fold method, by which, the dataset will be divided into five partitions, each time, a part will be used for testing and the remain nine parts used for training.

A. ANN Based Classification

ANN is a common ML-based model that functions based on how the human brain operates. It is a supervised learning algorithm that its structure consists of neurons or nodes. Those nodes are distributed over three main layers, namely, input layer, hidden layer, and output layer. Nodes at each layer have different functionalities. At the input layer, nodes take

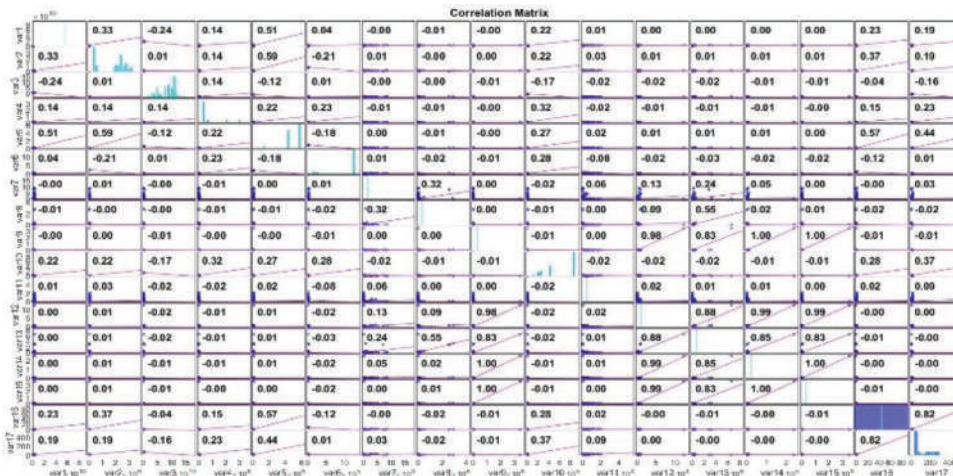


Fig. 5. Correlation coefficient graph of Internet of things 23 dataset features.

id_orig1	id_orig2	id_orig3	id_orig4	id_orig5	id_resp1	id_resp2	id_resp3	id_resp4	id_resp5	id_resp6	id_resp7	id_resp8	id_resp9	id_resp10	id_resp11	id_resp12	id_resp13	id_resp14	id_resp15	id_resp16	id_resp17	id_resp18	id_resp19	id_resp20	id_resp21	id_resp22	id_resp23	id_resp24	id_resp25	id_resp26	id_resp27	id_resp28	id_resp29	id_resp30	id_resp31	id_resp32	id_resp33	id_resp34	id_resp35	id_resp36	id_resp37	id_resp38	id_resp39	id_resp40	id_resp41	id_resp42	id_resp43	id_resp44	id_resp45	id_resp46	id_resp47	id_resp48	id_resp49	id_resp50	id_resp51	id_resp52	id_resp53	id_resp54	id_resp55	id_resp56	id_resp57	id_resp58	id_resp59	id_resp60	id_resp61	id_resp62	id_resp63	id_resp64	id_resp65	id_resp66	id_resp67	id_resp68	id_resp69	id_resp70	id_resp71	id_resp72	id_resp73	id_resp74	id_resp75	id_resp76	id_resp77	id_resp78	id_resp79	id_resp80	id_resp81	id_resp82	id_resp83	id_resp84	id_resp85	id_resp86	id_resp87	id_resp88	id_resp89	id_resp90	id_resp91	id_resp92	id_resp93	id_resp94	id_resp95	id_resp96	id_resp97	id_resp98	id_resp99	id_resp100	id_resp101	id_resp102	id_resp103	id_resp104	id_resp105	id_resp106	id_resp107	id_resp108	id_resp109	id_resp110	id_resp111	id_resp112	id_resp113	id_resp114	id_resp115	id_resp116	id_resp117	id_resp118	id_resp119	id_resp120	id_resp121	id_resp122	id_resp123	id_resp124	id_resp125	id_resp126	id_resp127	id_resp128	id_resp129	id_resp130	id_resp131	id_resp132	id_resp133	id_resp134	id_resp135	id_resp136	id_resp137	id_resp138	id_resp139	id_resp140	id_resp141	id_resp142	id_resp143	id_resp144	id_resp145	id_resp146	id_resp147	id_resp148	id_resp149	id_resp150	id_resp151	id_resp152	id_resp153	id_resp154	id_resp155	id_resp156	id_resp157	id_resp158	id_resp159	id_resp160	id_resp161	id_resp162	id_resp163	id_resp164	id_resp165	id_resp166	id_resp167	id_resp168	id_resp169	id_resp170	id_resp171	id_resp172	id_resp173	id_resp174	id_resp175	id_resp176	id_resp177	id_resp178	id_resp179	id_resp180	id_resp181	id_resp182	id_resp183	id_resp184	id_resp185	id_resp186	id_resp187	id_resp188	id_resp189	id_resp190	id_resp191	id_resp192	id_resp193	id_resp194	id_resp195	id_resp196	id_resp197	id_resp198	id_resp199	id_resp200	id_resp201	id_resp202	id_resp203	id_resp204	id_resp205	id_resp206	id_resp207	id_resp208	id_resp209	id_resp210	id_resp211	id_resp212	id_resp213	id_resp214	id_resp215	id_resp216	id_resp217	id_resp218	id_resp219	id_resp220	id_resp221	id_resp222	id_resp223	id_resp224	id_resp225	id_resp226	id_resp227	id_resp228	id_resp229	id_resp230	id_resp231	id_resp232	id_resp233	id_resp234	id_resp235	id_resp236	id_resp237	id_resp238	id_resp239	id_resp240	id_resp241	id_resp242	id_resp243	id_resp244	id_resp245	id_resp246	id_resp247	id_resp248	id_resp249	id_resp250	id_resp251	id_resp252	id_resp253	id_resp254	id_resp255	id_resp256	id_resp257	id_resp258	id_resp259	id_resp260	id_resp261	id_resp262	id_resp263	id_resp264	id_resp265	id_resp266	id_resp267	id_resp268	id_resp269	id_resp270	id_resp271	id_resp272	id_resp273	id_resp274	id_resp275	id_resp276	id_resp277	id_resp278	id_resp279	id_resp280	id_resp281	id_resp282	id_resp283	id_resp284	id_resp285	id_resp286	id_resp287	id_resp288	id_resp289	id_resp290	id_resp291	id_resp292	id_resp293	id_resp294	id_resp295	id_resp296	id_resp297	id_resp298	id_resp299	id_resp300	id_resp301	id_resp302	id_resp303	id_resp304	id_resp305	id_resp306	id_resp307	id_resp308	id_resp309	id_resp310	id_resp311	id_resp312	id_resp313	id_resp314	id_resp315	id_resp316	id_resp317	id_resp318	id_resp319	id_resp320	id_resp321	id_resp322	id_resp323	id_resp324	id_resp325	id_resp326	id_resp327	id_resp328	id_resp329	id_resp330	id_resp331	id_resp332	id_resp333	id_resp334	id_resp335	id_resp336	id_resp337	id_resp338	id_resp339	id_resp340	id_resp341	id_resp342	id_resp343	id_resp344	id_resp345	id_resp346	id_resp347	id_resp348	id_resp349	id_resp350	id_resp351	id_resp352	id_resp353	id_resp354	id_resp355	id_resp356	id_resp357	id_resp358	id_resp359	id_resp360	id_resp361	id_resp362	id_resp363	id_resp364	id_resp365	id_resp366	id_resp367	id_resp368	id_resp369	id_resp370	id_resp371	id_resp372	id_resp373	id_resp374	id_resp375	id_resp376	id_resp377	id_resp378	id_resp379	id_resp380	id_resp381	id_resp382	id_resp383	id_resp384	id_resp385	id_resp386	id_resp387	id_resp388	id_resp389	id_resp390	id_resp391	id_resp392	id_resp393	id_resp394	id_resp395	id_resp396	id_resp397	id_resp398	id_resp399	id_resp400	id_resp401	id_resp402	id_resp403	id_resp404	id_resp405	id_resp406	id_resp407	id_resp408	id_resp409	id_resp410	id_resp411	id_resp412	id_resp413	id_resp414	id_resp415	id_resp416	id_resp417	id_resp418	id_resp419	id_resp420	id_resp421	id_resp422	id_resp423	id_resp424	id_resp425	id_resp426	id_resp427	id_resp428	id_resp429	id_resp430	id_resp431	id_resp432	id_resp433	id_resp434	id_resp435	id_resp436	id_resp437	id_resp438	id_resp439	id_resp440	id_resp441	id_resp442	id_resp443	id_resp444	id_resp445	id_resp446	id_resp447	id_resp448	id_resp449	id_resp450	id_resp451	id_resp452	id_resp453	id_resp454	id_resp455	id_resp456	id_resp457	id_resp458	id_resp459	id_resp460	id_resp461	id_resp462	id_resp463	id_resp464	id_resp465	id_resp466	id_resp467	id_resp468	id_resp469	id_resp470	id_resp471	id_resp472	id_resp473	id_resp474	id_resp475	id_resp476	id_resp477	id_resp478	id_resp479	id_resp480	id_resp481	id_resp482	id_resp483	id_resp484	id_resp485	id_resp486	id_resp487	id_resp488	id_resp489	id_resp490	id_resp491	id_resp492	id_resp493	id_resp494	id_resp495	id_resp496	id_resp497	id_resp498	id_resp499	id_resp500	id_resp501	id_resp502	id_resp503	id_resp504	id_resp505	id_resp506	id_resp507	id_resp508	id_resp509	id_resp510	id_resp511	id_resp512	id_resp513	id_resp514	id_resp515	id_resp516	id_resp517	id_resp518	id_resp519	id_resp520	id_resp521	id_resp522	id_resp523	id_resp524	id_resp525	id_resp526	id_resp527	id_resp528	id_resp529	id_resp530	id_resp531	id_resp532	id_resp533	id_resp534	id_resp535	id_resp536	id_resp537	id_resp538	id_resp539	id_resp540	id_resp541	id_resp542	id_resp543	id_resp544	id_resp545	id_resp546	id_resp547	id_resp548	id_resp549	id_resp550	id_resp551	id_resp552	id_resp553	id_resp554	id_resp555	id_resp556	id_resp557	id_resp558	id_resp559	id_resp560	id_resp561	id_resp562	id_resp563	id_resp564	id_resp565	id_resp566	id_resp567	id_resp568	id_resp569	id_resp570	id_resp571	id_resp572	id_resp573	id_resp574	id_resp575	id_resp576	id_resp577	id_resp578	id_resp579	id_resp580	id_resp581	id_resp582	id_resp583	id_resp584	id_resp585	id_resp586	id_resp587	id_resp588	id_resp589	id_resp590	id_resp591	id_resp592	id_resp593	id_resp594	id_resp595	id_resp596	id_resp597	id_resp598	id_resp599	id_resp600	id_resp601	id_resp602	id_resp603	id_resp604	id_resp605	id_resp606	id_resp607	id_resp608	id_resp609	id_resp610	id_resp611	id_resp612	id_resp613	id_resp614	id_resp615	id_resp616	id_resp617	id_resp618	id_resp619	id_resp620	id_resp621	id_resp622	id_resp623	id_resp624	id_resp625	id_resp626	id_resp627	id_resp628	id_resp629	id_resp630	id_resp631	id_resp632	id_resp633	id_resp634	id_resp635	id_resp636	id_resp637	id_resp638	id_resp639	id_resp640	id_resp641	id_resp642	id_resp643	id_resp644	id_resp645	id_resp646	id_resp647	id_resp648	id_resp649	id_resp650	id_resp651	id_resp652	id_resp653	id_resp654	id_resp655	id_resp656	id_resp657	id_resp658	id_resp659	id_resp660	id_resp661	id_resp662	id_resp663	id_resp664	id_resp665	id_resp666	id_resp667	id_resp668	id_resp669	id_resp670	id_resp671	id_resp672	id_resp673	id_resp674	id_resp675	id_resp676	id_resp677	id_resp678	id_resp679	id_resp680	id_resp681	id_resp682	id_resp683	id_resp684	id_resp685	id_resp686	id_resp687	id_resp688	id_resp689	id_resp690	id_resp691	id_resp692	id_resp693	id_resp694	id_resp695	id_resp696	id_resp697	id_resp698	id_resp699	id_resp700	id_resp701	id_resp702	id_resp703	id_resp704	id_resp705	id_resp706	id_resp707	id_resp708	id_resp709	id_resp710	id_resp711	id_resp712	id_resp713	id_resp714	id_resp715	id_resp716	id_resp717	id_resp718	id_resp719	id_resp720	id_resp721	id_resp722	id_resp723	id_resp724	id_resp725	id_resp726	id_resp727	id_resp728	id_resp729	id_resp730	id_resp731	id_resp732	id_resp733	id_resp734	id_resp735	id_resp736	id_resp737	id_resp738	id_resp739	id_resp740	id_resp741	id_resp742	id_resp743	id_resp744	id_resp745	id_resp746	id_resp747	id_resp748	id_resp749	id_resp750	id_resp751	id_resp752	id_resp753	id_resp754	id_resp755	id_resp756	id_resp757	id_resp758	id_resp759	id_resp760	id_resp761	id_resp762	id_resp763	id_resp764	id_resp765	id_resp766	id_resp767	id_resp768	id_resp769	id_resp770	id_resp771	id_resp772	id_resp773	id_resp774	id_resp775	id_resp776	id_resp777	id_resp778	id_resp779	id_resp780	id_resp781	id_resp782	id_resp783	id_resp784	id_resp785	id_resp786	id_resp787	id_resp788	id_resp789	id_resp790	id_resp791	id_resp792	id_resp793	id_resp794	id_resp795	id_resp796	id_resp797	id_resp798	id_resp799	id_resp800	id_resp801	id_resp802	id_resp803	id_resp804	id_resp805	id_resp806	id_resp807	id_resp808	id_resp809	id_resp810	id_resp811	id_resp812	id_resp813	id_resp814	id_resp815	id_resp816	id_resp817	id_resp818	id_resp819	id_resp820	id_resp821	id_resp822	id_resp823	id_resp824	id_resp825	id_resp826	id_resp827	id_resp828	id_resp829	id_resp830	id_resp831	id_resp832	id_resp833	id_resp834	id_resp835	id_resp836	id_resp837	id_resp838	id_resp839	id_resp840	id_resp841	id_resp842	id_resp843	id_resp844	id_resp845	id_resp846	id_resp847	id_resp848	id_resp849	id_resp850	id_resp851	id_resp852	id_resp853	id_resp854	id_resp855	id_resp856	id_resp857	id_resp858	id_resp859	id_resp860	id_resp861	id_resp862	id_resp863	id_resp864	id_resp865	id_resp866	id_resp867	id_resp868	id_resp869	id_resp870	id_resp871	id_resp872	id_resp873	id_resp874	id_resp875	id_resp876	id_resp877	id_resp878	id_resp879	id_resp880	id_resp881	id_resp882	id_resp883	id_resp884	id_resp885	id_resp886	id_resp887	id_resp888	id_resp889	id_resp890	id_resp891	id_resp892	id_resp893	id_resp894	id_resp895	id_resp896	id_resp897	id_resp898	id_resp899	id_resp900	id_resp901	id_resp902	id_resp903	id_resp904	id_resp905	id_resp906	id_resp907	id_resp908	id_resp909	id_resp910	id_resp911	id_resp912	id_resp913	id_resp914	id_resp915	id_resp916	id_resp917	id_resp918	id_resp919	id_resp920	id_resp921	id_resp922	id_resp923	id_resp924	id_resp925	id_resp926	id_resp927	id_resp928	id_resp929	id_resp930	id_resp931	id_resp932	id_resp933	id_resp934	id_resp935	id_resp936	id_resp937	id_resp938	id_resp939	id_resp940	id_resp941	id_resp942	id_resp943	id_resp944	id_resp945	id_resp946	id_resp947	id_resp948	id_resp949	id_resp950	id_resp951	id_resp952	id_resp953	id_resp954	id_resp955	id_resp956	id_resp957	id_resp958	id_resp959	id_resp960	id_resp961	id_resp962	id_resp963	id_resp964	id_resp965	id_resp966	id_resp967	id_resp968	id_resp969	id_resp970	id_resp971	id_resp972	id_resp973	id_resp974	id_resp975	id_resp976	id_resp977	id_resp978	id_resp979	id_resp980	id_resp981	id_resp982	id_resp983	id_resp984	id_resp985	id_resp986	id_resp987	id_resp988	id_resp989	id_resp990	id_resp991	id_resp992	id_resp993	id_resp994	id_resp995	id_resp996	id_resp997	id_resp998	id_resp999	id_resp1000
----------	----------	----------	----------	----------	----------	----------	----------	----------	----------	----------	----------	----------	----------	-----------	-----------	-----------	-----------	-----------	-----------	-----------	-----------	-----------	-----------	-----------	-----------	-----------	-----------	-----------	-----------	-----------	-----------	-----------	-----------	-----------	-----------	-----------	-----------	-----------	-----------	-----------	-----------	-----------	-----------	-----------	-----------	-----------	-----------	-----------	-----------	-----------	-----------	-----------	-----------	-----------	-----------	-----------	-----------	-----------	-----------	-----------	-----------	-----------	-----------	-----------	-----------	-----------	-----------	-----------	-----------	-----------	-----------	-----------	-----------	-----------	-----------	-----------	-----------	-----------	-----------	-----------	-----------	-----------	-----------	-----------	-----------	-----------	-----------	-----------	-----------	-----------	-----------	-----------	-----------	-----------	-----------	-----------	-----------	-----------	-----------	-----------	-----------	-----------	-----------	------------	------------	------------	------------	------------	------------	------------	------------	------------	------------	------------	------------	------------	------------	------------	------------	------------	------------	------------	------------	------------	------------	------------	------------	------------	------------	------------	------------	------------	------------	------------	------------	------------	------------	------------	------------	------------	------------	------------	------------	------------	------------	------------	------------	------------	------------	------------	------------	------------	------------	------------	------------	------------	------------	------------	------------	------------	------------	------------	------------	------------	------------	------------	------------	------------	------------	------------	------------	------------	------------	------------	------------	------------	------------	------------	------------	------------	------------	------------	------------	------------	------------	------------	------------	------------	------------	------------	------------	------------	------------	------------	------------	------------	------------	------------	------------	------------	------------	------------	------------	------------	------------	------------	------------	------------	------------	------------	------------	------------	------------	------------	------------	------------	------------	------------	------------	------------	------------	------------	------------	------------	------------	------------	------------	------------	------------	------------	------------	------------	------------	------------	------------	------------	------------	------------	------------	------------	------------	------------	------------	------------	------------	------------	------------	------------	------------	------------	------------	------------	------------	------------	------------	------------	------------	------------	------------	------------	------------	------------	------------	------------	------------	------------	------------	------------	------------	------------	------------	------------	------------	------------	------------	------------	------------	------------	------------	------------	------------	------------	------------	------------	------------	------------	------------	------------	------------	------------	------------	------------	------------	------------	------------	------------	------------	------------	------------	------------	------------	------------	------------	------------	------------	------------	------------	------------	------------	------------	------------	------------	------------	------------	------------	------------	------------	------------	------------	------------	------------	------------	------------	------------	------------	------------	------------	------------	------------	------------	------------	------------	------------	------------	------------	------------	------------	------------	------------	------------	------------	------------	------------	------------	------------	------------	------------	------------	------------	------------	------------	------------	------------	------------	------------	------------	------------	------------	------------	------------	------------	------------	------------	------------	------------	------------	------------	------------	------------	------------	------------	------------	------------	------------	------------	------------	------------	------------	------------	------------	------------	------------	------------	------------	------------	------------	------------	------------	------------	------------	------------	------------	------------	------------	------------	------------	------------	------------	------------	------------	------------	------------	------------	------------	------------	------------	------------	------------	------------	------------	------------	------------	------------	------------	------------	------------	------------	------------	------------	------------	------------	------------	------------	------------	------------	------------	------------	------------	------------	------------	------------	------------	------------	------------	------------	------------	------------	------------	------------	------------	------------	------------	------------	------------	------------	------------	------------	------------	------------	------------	------------	------------	------------	------------	------------	------------	------------	------------	------------	------------	------------	------------	------------	------------	------------	------------	------------	------------	------------	------------	------------	------------	------------	------------	------------	------------	------------	------------	------------	------------	------------	------------	------------	------------	------------	------------	------------	------------	------------	------------	------------	------------	------------	------------	------------	------------	------------	------------	------------	------------	------------	------------	------------	------------	------------	------------	------------	------------	------------	------------	------------	------------	------------	------------	------------	------------	------------	------------	------------	------------	------------	------------	------------	------------	------------	------------	------------	------------	------------	------------	------------	------------	------------	------------	------------	------------	------------	------------	------------	------------	------------	------------	------------	------------	------------	------------	------------	------------	------------	------------	------------	------------	------------	------------	------------	------------	------------	------------	------------	------------	------------	------------	------------	------------	------------	------------	------------	------------	------------	------------	------------	------------	------------	------------	------------	------------	------------	------------	------------	------------	------------	------------	------------	------------	------------	------------	------------	------------	------------	------------	------------	------------	------------	------------	------------	------------	------------	------------	------------	------------	------------	------------	------------	------------	------------	------------	------------	------------	------------	------------	------------	------------	------------	------------	------------	------------	------------	------------	------------	------------	------------	------------	------------	------------	------------	------------	------------	------------	------------	------------	------------	------------	------------	------------	------------	------------	------------	------------	------------	------------	------------	------------	------------	------------	------------	------------	------------	------------	------------	------------	------------	------------	------------	------------	------------	------------	------------	------------	------------	------------	------------	------------	------------	------------	------------	------------	------------	------------	------------	------------	------------	------------	------------	------------	------------	------------	------------	------------	------------	------------	------------	------------	------------	------------	------------	------------	------------	------------	------------	------------	------------	------------	------------	------------	------------	------------	------------	------------	------------	------------	------------	------------	------------	------------	------------	------------	------------	------------	------------	------------	------------	------------	------------	------------	------------	------------	------------	------------	------------	------------	------------	------------	------------	------------	------------	------------	------------	------------	------------	------------	------------	------------	------------	------------	------------	------------	------------	------------	------------	------------	------------	------------	------------	------------	------------	------------	------------	------------	------------	------------	------------	------------	------------	------------	------------	------------	------------	------------	------------	------------	------------	------------	------------	------------	------------	------------	------------	------------	------------	------------	------------	------------	------------	------------	------------	------------	------------	------------	------------	------------	------------	------------	------------	------------	------------	------------	------------	------------	------------	------------	------------	------------	------------	------------	------------	------------	------------	------------	------------	------------	------------	------------	------------	------------	------------	------------	------------	------------	------------	------------	------------	------------	------------	------------	------------	------------	------------	------------	------------	------------	------------	------------	------------	------------	------------	------------	------------	------------	------------	------------	------------	------------	------------	------------	------------	------------	------------	------------	------------	------------	------------	------------	------------	------------	------------	------------	------------	------------	------------	------------	------------	------------	------------	------------	------------	------------	------------	------------	------------	------------	------------	------------	------------	------------	------------	------------	------------	------------	------------	------------	------------	------------	------------	------------	------------	------------	------------	------------	------------	------------	------------	------------	------------	------------	------------	------------	------------	------------	------------	------------	------------	------------	------------	------------	------------	------------	------------	------------	------------	------------	------------	------------	------------	------------	------------	------------	------------	------------	------------	------------	------------	------------	------------	------------	------------	------------	------------	------------	------------	------------	------------	------------	------------	------------	------------	------------	------------	------------	------------	------------	------------	------------	------------	------------	------------	------------	------------	------------	------------	------------	------------	------------	------------	------------	------------	------------	------------	------------	------------	------------	------------	------------	------------	------------	------------	------------	------------	------------	------------	------------	------------	------------	------------	------------	------------	------------	------------	------------	------------	------------	------------	------------	------------	------------	------------	------------	------------	------------	------------	------------	------------	------------	------------	------------	------------	------------	------------	------------	------------	------------	------------	------------	------------	------------	------------	------------	------------	------------	------------	------------	------------	------------	------------	-------------

Fig. 6. A sample of the obtained dataset through preprocessing.

		Predicted Class		
		Positive	Negative	
Actual Class	Positive	True Positive (TP)	False Negative (FN) Type II Error	Sensitivity $\frac{TP}{TP + FN}$
	Negative	False Positive (FP) Type I Error	True Negative (TN)	Specificity $\frac{TN}{TN + FP}$
		Precision $\frac{TP}{TP + FP}$	Negative Predictive Value $\frac{TN}{TN + FN}$	Accuracy $\frac{TP + TN}{TP + TN + FP + FN}$

Fig. 7. Typical Confusion Matrix with performance indicators.

the input information and pass them to hidden layer. The core computation of the ANN is occurred in the hidden layer, which in some cases, there are more than one layer. The results from the hidden layer(s) will be passed to the output layer. For the supervised ANN, the expected output and desired output will be involved in error computation which shows the accuracy rate of the training phase. When the obtained error is more the goal, ANN will start to modify the value of wights that exist between each two nodes in two different layers. This process will be repeated until minimum error will be obtained. The typical structure of an ANN is shown in the Fig. 5.

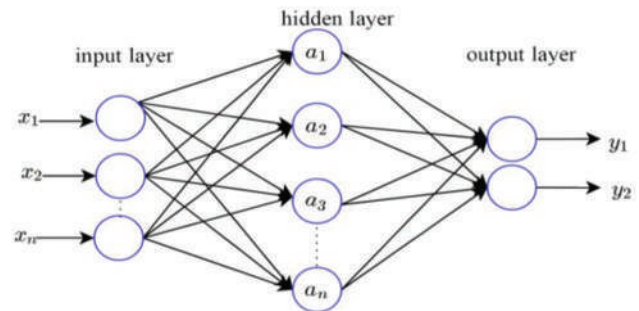


Fig. 8. Typical structure of artificial neural network.

For this work, the model has been designed and coded using Matlab-R2021a. It has been installed on a PC with intel CORE i7 (11th generation). The ANN that utilized by this work is called “Pattern Recognition Neural Network”. According to the dataset sample that shown in the Fig. 8, the number of the input feature in this work is (15). Therefore, the number of the input node of the proposed ANN for this work is 15. The work has tested the ANN to find out the best or the more efficient structure (number of hidden layer). The work set the number of hidden layers on one and the nodes in this layer on 10 nodes. Fig. 9 shows the ANN structure that designed by this wok for binary classification of attacks.

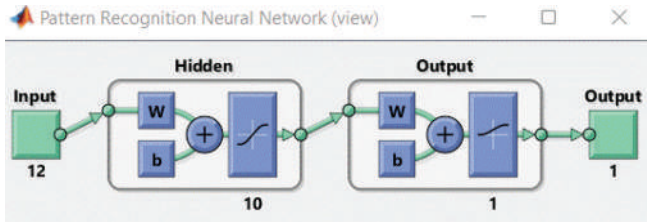


Fig. 9. The artificial neural network-based binary classification.

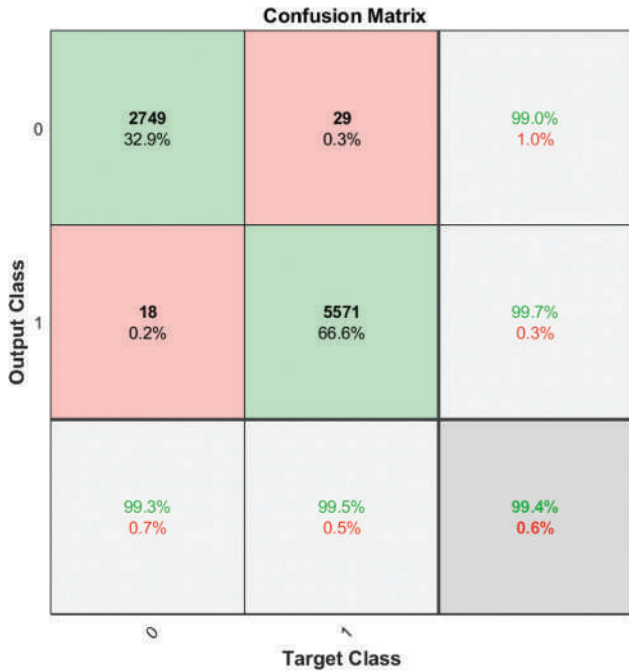


Fig. 10. Confusion Matrix for artificial neural network-based binary classification.

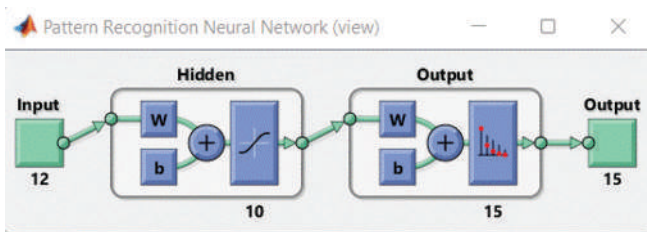


Fig. 11. The ANN based multi-class classification.

The proposed ANN just required 45 epochs for getting perfect training with error around 1.5%. To test the ANN, this work used 20% of the dataset and the result of testing is shown as confusion matrix for the binary in the Fig. 10. The result of the testing is 99%.

The next step of with ANN is to identify the type attacks after identifying a flow as attack. For this step, the name of the ANN is still “Pattern Recognition Neural Network”. However, the structure of ANN has not been changed as shown in Fig. 11 and with the same number of epochs.

The accuracy that obtained through the multi-class classification, as shown in the Fig. 12, is about 99.2%. Through both classifiers, it becomes clear that classifying benign from attacks and identifying the type of attacks

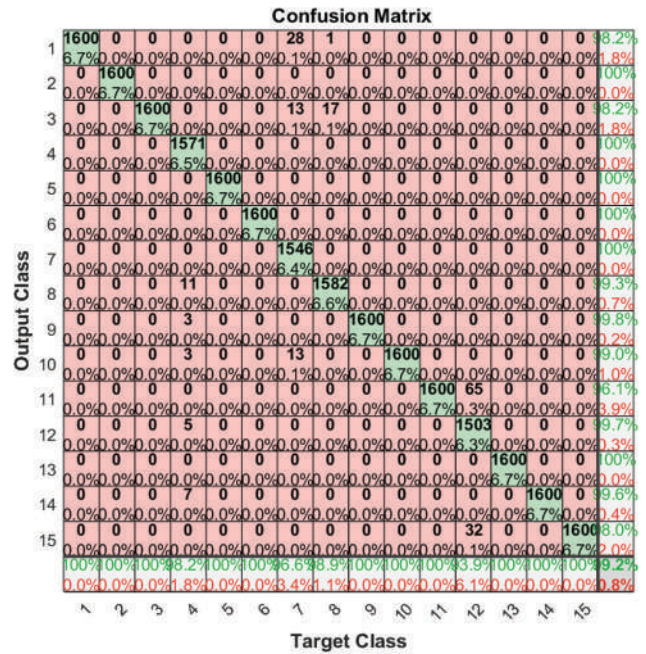


Fig. 12. The confusion Matrix of artificial neural network-based multi-class classifier (SMOTE).

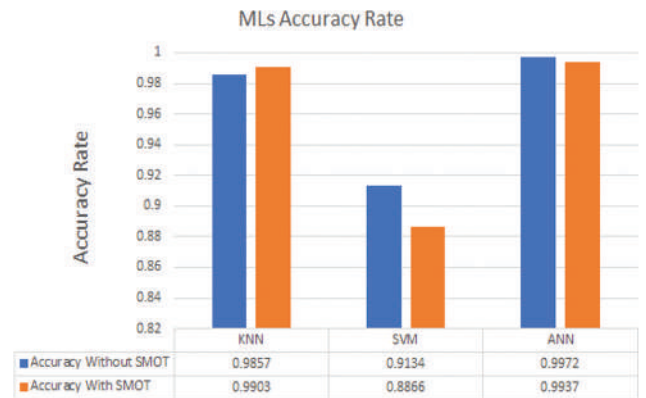


Fig. 13. Compression of the MLs accuracy.

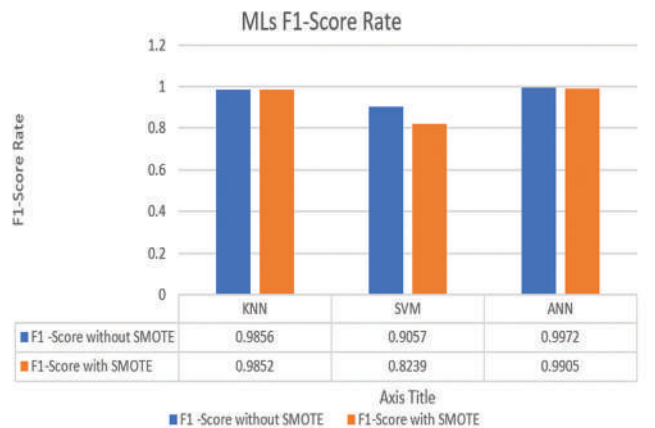


Fig. 14. Compression of the machine languages F1-score.

with ANN pattern recognition can reach up to 99% as an average.

VI. ML COMPARISON RESULTS

This work utilizes another two major ML techniques to evaluate their accuracy with the ANN based on attack classification and identification. These techniques are KNN and SVM. This work compared the ANN based model with both KNN and SVM when they work as binary classifiers

and work as multi-class classifiers. The comparisons result of the binary classification is shown in Figs. 13 and 14, and the results of multiclass classification are shown in the Tables VI and VII. The results also show the impact of the SMOTE technique on the accuracy and F1-score rates of the ML techniques. Moreover, the work compared the three ML techniques as the multi-classifiers. In general, the accuracy rate for ML techniques as binary classifiers ranged between 88.66% and 99.72%. SMOTE has a greater impact on multiclass classification than it has on binary classification.

There is one fact that should be presented at the beginning of this discussion, which is “The accuracy of any classification model that trained with unbalance dataset is useless even it has a very good rate”. This is because unbalanced dataset usually makes the training process to bias to a class that has more observations than other classes. Consequently, we tested the models using F1-Score as well, and the influence of SMOTE appeared significantly, as shown in Table VII. The results indicated that the labels (9, 10, 13, and 15) had 0% F1-score rate, which is due to the small number of observations in these labels, as shown in Fig. 15. The results of the SMOTE dataset then solved the problem, as illustrated in Fig. 12.

There are many arguments about SMOTE applying to the dataset. Much research works perusing applying the SMOTE only over the training part of the dataset. Others are focused on applying the SMOTE over all dataset. Therefore, this work investigates whether SMOTE overfits the model if applied on test part of the dataset or not. This work conducted another experiment to check that as shown in Table VIII. In this experiment SMOTE, only applied to Train set. The experimental results show that the models (KNN, SVM, and ANN) did not identify several attack classes, such as (10, 11, and 15). This is because the number of records in the test set data is quite low. In the test set, such attack classes (10 and 15) have only one record.

The classes (12, 13, and 14) have the same issue; however, in these classes, some methods produced at least some outcomes.

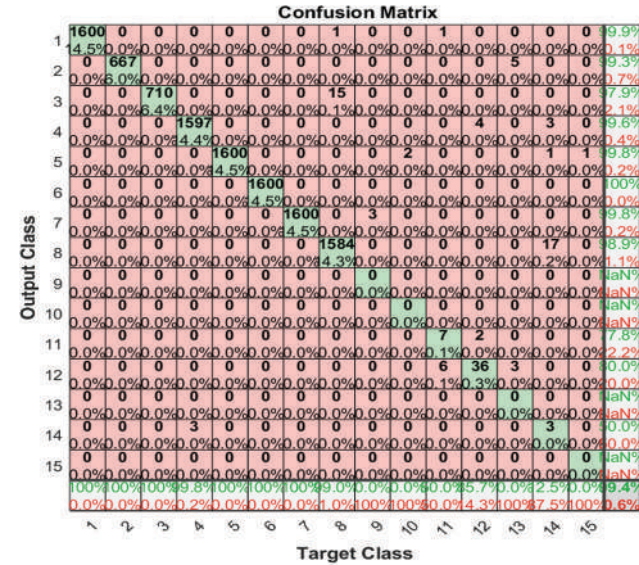


Fig. 15. The confusion Matrix of artificial neural network-based multi-class classifier (without SMOTE).

TABLE V
EXCLUDED FEATURES

Features	Reason of exclusion
Time	Not relevant to attack classification and identification
Uid	Not relevant to attack classification and identification
local_orig	All records are empty
local_resp	All records are empty
History	It is a description of another feature (conn state)
Tunnel parents	All records are empty

TABLE VI
THE IDENTIFICATION ACCURACY RATE OF MACHINE LEARNING TECHNIQUES FOR EACH ATTACK

Labels	KNN		SVM		ANN	
	Without SMOTE	With SMOTE	Without SMOTE	With SMOTE	Without SMOTE	With SMOTE
1	1	1	0.9999	1	0.9998	0.9988
2	0.9999	0.9999	0.9999	1	0.9995	1
3	0.9994	0.9998	0.9993	0.9994	0.9986	0.9988
4	0.9984	0.9993	0.9948	0.9809	0.9991	0.9988
5	1	1	1	1	0.9996	1
6	1	1	1	1	1	1
7	1	0.9998	0.9735	0.9853	0.9997	0.9977
8	0.9990	0.9998	0.9712	0.9872	0.9970	0.9988
9	0.9997	1	0.9997	1	0.9997	0.9999
10	0.9998	0.9998	0.9998	0.9975	0.9998	0.9993
11	0.9999	0.9991	0.9988	0.9837	0.9992	0.9973
12	0.9993	0.9989	0.9973	0.9946	0.9986	0.9957
13	1	1	0.9993	1	0.9993	1
14	0.9996	0.9998	0.9984	0.9999	0.9978	0.9997
15	0.9999	1	0.9997	1	0.9999	0.9987

ANN: Artificial neural network, SVM: Support vector machine, KNN: K-nearest neighbor

TABLE VII
THE IDENTIFICATION F1-SCORE RATE OF MACHINE LEARNING TECHNIQUES FOR EACH ATTACK

Labels	KNN		SVM		ANN	
	Without SMOTE	With SMOTE	Without SMOTE	With SMOTE	Without SMOTE	With SMOTE
1	1	1	0.9997	1	0.9994	0.9910
2	0.9993	0.9997	0.9993	1	0.9962	1
3	0.9951	0.9981	0.9944	0.9956	0.9895	0.9907
4	0.9944	0.9943	0.9822	0.8447	0.9968	0.9909
5	1	1	1	1	0.9987	1
6	1	1	1	1	1	1
7	1	0.9984	0.9161	0.8969	0.9990	0.9829
8	0.9966	0.9981	0.8905	0.8939	0.9897	0.9909
9	0	1	0	1	0	0.9990
10	0	0.9984	0	0.9813	0	0.9950
11	0.9630	0.9935	0	0.8881	0.6087	0.9801
12	0.8947	0.9922	0.4444	0.9587	0.8276	0.9672
13	1	1	0	1	0	1
14	0.8750	0.9978	0	0.9994	0.2000	0.9978
15	0	1	0.4000	1	0	0.9901

ANN: Artificial neural network, SVM: Support vector machine, KNN: K-nearest neighbor

TABLE VIII
THE IDENTIFICATION F1-SCORE AND ACCURACY RATE OF MACHINE LEARNING TECHNIQUES, WHICH SMOTE HAS NOT BEEN APPLIED TO TEST SET DATA

Labels	KNN		SVM		ANN	
	Accuracy	F score	Accuracy	F score	Accuracy	F score
1	1	1	1	1	0.9996	0.9989
2	0.9996	0.9970	1	1	0.9996	0.9969
3	1	1	0.9986	0.9889	0.9986	0.9889
4	0.9968	0.9886	0.9856	0.9476	0.9693	0.8803
5	1	1	1	1	1	1
6	1	1	1	1	1	1
7	0.9996	0.9988	0.9755	0.9217	0.9996	0.9989
8	0.9993	0.9975	0.9744	0.9026	0.9978	0.9925
9	1	1	1	1	1	1
10	0.9996	0	0.9996	0	0.9996	0
11	0.9986	0.3333	0.9859	0	0.9870	0
12	0.9982	0.8000	0.9986	0.8333	0.9913	0.4545
13	1	1	1	1	0.9935	0.2502
14	0.9982	0.7059	0.9986	0.7500	0.9960	0.5218
15	0.9993	0	0.9996	0	0.9996	0.6667

ANN: Artificial neural network, SVM: Support vector machine, KNN: K-nearest neighbor

So, their percentage within the dataset is the issue with the identification of smaller types of attacks. All algorithms were able to predict the major categories with at least 99% accuracy.

VII. CONCLUSION

This work proposes three major ML techniques as binary classifier and multi-class classifiers. The work utilizes these ML techniques as Intrusion Detection System for IoT based attacks detection and the attack's class identification. The work develops an IIDS through utilizing an up-to-date dataset, known as IoT 23. Through a systematic review of recent works, this work finds some gaps that still not addressed by previous works such as using up to date IoT-based dataset and building a multi-class classification for detecting zero-day attacks. Accordingly, this work addresses those gaps and addresses new objectives. To achieve the targeted objectives,

this work proposes a distinguished methodology that starts from data collection, preprocessing steps, training and testing phases, until evaluation of results.

Through implementing the work's methodology, it has been found that most classical ML algorithms could work perfectly as binary and multi-class classification for distinguishing malicious behaviors among IoT-based network packets. Therefore, no need to employ deep learning algorithms for developing IIDS as the structure of the deep learning algorithms is more complex than the classical ML algorithms. Consequently, the time complexity and the space complexity of the developed IIDS with deep learning algorithm expected be increased.

Another conclusion that has been ended through the work implementation is the impact of some preprocessing methods such as SMOTE on the accuracy rate of the developed IIDS. SMOTE method is usually applied on an imbalanced dataset to avoid under and/over fitting of the developed model, and maximizing the accuracy rate of the classifier models. The strange results that have been obtained in this work are the ineffectiveness of the SOMTE method in improving the accuracy rate of the proposed IIDS model as the security rate without SMOTE reached to an excellent level. Although the accuracy of the proposed IIDS showed extraordinary rates, this work suggests investigating more statistical and non-statistical properties of the IoT23 dataset to get more explanations on the ineffectiveness of the SMOTE method for improving the accuracy rate over imbalanced datasets.

REFERENCES

- Abdulla, S.M., Al-Dabagh, N.B., and Zakaria, O., 2010. Identify features and parameters to devise an accurate intrusion detection system using artificial neural network. *International Journal of Computer and Information Engineering*, 4, pp.1553-1557.
- Alfarshouti, A.M., and Almutairi, S.M., 2022. An intrusion detection system in IoT environment using KNN and SVM classifiers. *Webology*, 19, pp.130-143.
- Aslam, M., Ye, D., Tariq, A., Asad, M., Hanif, M., Ndzi, D., Chelloug, S.A.,

- Elaziz, M.A., Al-Qaness, M.A.A., and Jilani, S.F., 2022. Adaptive machine learning based distributed denial-of-services attacks detection and mitigation system for SDN-enabled IoT. *Sensors(Basel)*, 22, p.2697.
- Bhandari, A., 2020. *Everything you Should Know about Confusion Matrix for Machine Learning*, *Analytics Vidhya*. Available from: <https://www.analyticsvidhya.com/blog/2020/04/confusion-matrix-machine-learning/#:~:text=A%20Confusion%20matrix%20is%20an,by%20the%20machine%20learning%20model> [Last accessed on 2022 Aug 26].
- Chen, K., Zhang, S., Li, Z., Zhang, Y., Deng, Q., Ray, S., and Jin, Y., 2018. Internet-of-things security and vulnerabilities: Taxonomy, challenges, and practice. *Journal of Hardware and Systems Security*, 2, pp.97-110.
- Churcher, A., Ullah, R., Ahmad, J., Ur Rehman, S., Masood, F., Gogate, M., Alqahtani, F., Nour, B., and Buchanan, W.J., 2021. An experimental analysis of attack classification using machine learning in IoT networks. *Sensors (Base)*, 21, p.446.
- Fatayer, T.S., and Azara, M.N., 2019. IoT secure communication using ANN classification algorithms. In: *2019 International Conference on Promising Electronic Technologies (ICPET)*. IEEE, New Jersey, pp.142-146.
- Garcia, S., Parmisano, A., and Erquiaga, M.J., 2020. *IoT-23: A Labeled Dataset with Malicious and Benign IoT Network Traffic*. Stratosphere Lab., TechRep, Praha, Czech Republic.
- Giusto, D., Iera, A., Morabito, G., and Atzori, L., 2010. *The Internet of Things: 20th Tyrrhenian Workshop on Digital Communications*. Springer Science and Business Media, Berlin.
- Gopi, R., Sathiyamoorthi, V., Selvakumar, S., Manikandan, R., Chatterjee, P., Jhanjhi, N.Z., and Luhach, A.K., 2021. Enhanced method of ANN based model for detection of DDoS attacks on multimedia internet of things. *Multimedia Tools and Applications*, pp.1-19.
- Hanif, S., Ilyas, T., and Zeeshan, M., 2019. Intrusion Detection in IoT using Artificial Neural Networks on UNSW-15 Dataset. In: *2019 IEEE 16th International Conference on Smart Cities: Improving Quality of Life using ICT & IoT and AI (HONET-ICT)*. IEEE, New Jersey, pp.152-156.
- Ho, E.S.L., 2022. Data security challenges in deep neural network for healthcare IoT systems. In: *Security and Privacy Preserving for IoT and 5G Networks*. Springer, Berlin.
- Iman, A.I.N., 2022. *Low Rate DDOS attack Detection using KNN on SD-IOT*. Universitas Muhammadiyah Malang, Indonesia.
- Islam, U., Muhammad, A., Mansoor, R., Hossain, M.S., Ahmad, I., Eldin, E.T., Khan, J.A., Ur Rehman, A., and Shafiq, M., 2022. Detection of Distributed Denial of Service (DDoS) attacks in IOT based monitoring system of banking sector using machine learning models. *Sustainability*, 14, p.8374.
- Kareem, M.I., and Jasim, M.N., 2022. Fast and accurate classifying model for denial-of-service attacks by using machine learning. *Bulletin of Electrical Engineering and Informatics*, 11, pp.1742-1751.
- Kumari, K., and Mrunalini, M., 2022. Detecting denial of service attacks using machine learning algorithms. *Journal of Big Data*, 9, p.56.
- Lee, S.J., and Zeng, X., 2008. A Modular Method for Estimating Null Values in Relational Database Systems. In: *2008 Eighth International Conference on Intelligent Systems Design and Applications*. IEEE, New Jersey, pp.415-419.
- Li, W., Yi, P., Wu, Y., Pan, L., and Li, J., 2014. A new intrusion detection system based on KNN classification algorithm in wireless sensor network. *Journal of Electrical and Computer Engineering*, 2014, p.240217.
- Li, Z., Rios, A.L.G., and Trajković, L., 2021. Classifying Denial of Service Attacks Using Fast Machine Learning Algorithms. In: *2021 IEEE International Conference on Systems, Man, and Cybernetics (SMC)*. IEEE, New Jersey, pp.1221-1226.
- Majeed Alhammedi, N.A., 2022. Comparative study between (SVM) and (KNN) classifiers by using (PCA) to improve of intrusion detection system. *Iraqi Journal of Intelligent Computing and Informatics (IJICI)*, 1, pp.22-33.
- Malik, M., and Dutta, M., 2022. Security Challenges in Internet of Things (IoT) integrated power and energy (PaE) systems. In: *Intelligent Data Analytics for Power and Energy Systems*. Springer Nature, Berlin, pp.555-566.
- Mehmood, A., Khan, A.N., and Elhadeif, M., 2022. HeuCrip: A malware detection approach for internet of battlefield things. *Cluster Computing*, 26, pp.977-992.
- Nagisetty, A., and Gupta, G.P., 2019. Framework for Detection of Malicious Activities in IoT Networks using Keras Deep Learning Library. In: *2019 3rd International Conference on Computing Methodologies and Communication (ICCMC)*. IEEE, United States, pp.633-637.
- Nawir, M., Amir, A., Yaakob, N., and Bi Lynn, O., 2016. Internet of Things (IoT): Taxonomy of Security Attacks. In: *2016 3rd International Conference on Electronic Design (ICED)*. IEEE, United States, pp.321-326.
- Garcia, S., Parmisano, A. and Equiaga, M.J. (2020). *IoT-23: A Labeled Dataset with Malicious and Benign IoT Network Traffic (Version 1.0.0) [Data Set]*. Europe: Zenodo. <http://doi.org/10.5281/zenodo.4743746>
- Picon Ruiz, A., Gila, A.A., Irusta, U., and Huguet, J.E., 2020. Why deep learning performs better than classical machine learning? *Dyna Ingenieria E Industria*, 95, pp.119-122.
- Radivilova, T., Kirichenko, L., Ageiev, D., and Bulakh, V., 2019. Classification Methods of Machine Learning to Detect DDoS Attacks. In: *2019 10th IEEE International Conference on Intelligent Data Acquisition and Advanced Computing Systems: Technology and Applications (IDAACS)*. IEEE, United States, pp. 207-210.
- Saharkhizan, M., Azmoodeh, A., Dehghantanha, A., Choo, K.K.R., and Parizi, R.M., 2020. An ensemble of deep recurrent neural networks for detecting IoT cyber attacks using network traffic. *IEEE Internet of Things Journal*, 7, pp.8852-8859.
- Sanmorino, A., 2019. A study for DDOS attack classification method. *Journal of Physics: Conference Series*, 2019, p.012025.
- Sewak, M., Sahay, S.K., and Rathore, H., 2018. Comparison of Deep Learning and the Classical Machine Learning Algorithm for the Malware Detection. In: *2018 19th IEEE/ACIS International Conference on Software Engineering, Artificial Intelligence, Networking and Parallel/Distributed Computing (SNPD)*. IEEE, United States, pp.293-296.
- Soe, Y.N., Feng, Y., Santosa, P.I., Hartanto, R., and Sakurai, K., 2019. A Sequential Scheme for Detecting Cyber Attacks in IoT Environment. In: *2019 IEEE International Conference on Dependable, Autonomic and Secure Computing, International Conference on Pervasive Intelligence and Computing, International Conferenced on Cloud and Big Data Computing, International Conference on Cyber Science and Technology Congress (DASC/PiCom/CBDCom/CyberSciTech)*. IEEE, United States, pp.238-244.
- Tabassum, A., Erbad, A., Lebda, W., Mohamed, A., and Guizani, M., 2022. FEDGAN-IDS: Privacy-preserving IDS using GAN and federated learning. *Computer Communications*, 192, pp.299-310.
- Tabassum, A., Erbad, A., Mohamed, A., and Guizani, M., 2021. Privacy-preserving distributed IDS using incremental learning for IoT health systems. *IEEE Access*, 9, pp.14271-14283.
- Weller-Fahy, D.J., Borghetti, B.J., and Sodemann, A.A., 2014. A survey of distance and similarity measures used within network intrusion anomaly detection. *IEEE Communications Surveys and Tutorials*, 17, pp.70-91.
- Wongvorachan, T., He, S., and Bulut, O., 2023. A comparison of undersampling, oversampling, and SMOTE methods for dealing with imbalanced classification in educational data mining. *Information*, 14, p.54.

Drilling Pipe Corrosion Reduction Using Natural, Biodegradable, and Environmentally Friendly Additive to the Drilling Fluid

Pshtiwan T. Jaf¹, Jafar A. Ali¹, Ayad A. A. Razzaq²

¹Department of Petroleum Engineering, Faculty of Engineering, Koya University, Danielle Mitterrand Boulevard, Koya KOY45, Kurdistan Region – F.R. Iraq

²Department of Petroleum Engineering, College of Engineering, University of Baghdad, Baghdad – F.R. Iraq

Abstract—Corrosion is one of the disasters attacking the drilling tools, particularly the drill pipes. Drilling fluid is the corrosive that increase the rate of corrosion in the pipes. In this study, it is intended to reduce the corrosivity of drilling fluid using a *Prosopis farcta* powder material. A natural, biodegradable, and environmentally friendly additive is added to the fluid in different particle sizes and amounts to obtain the lowest corrosion rate. Experiments are conducted in a well-like environment (high pressure high temperature filter press) over a wide range of parameters including pressure, temperature, and properties of the drilling fluid under dynamic conditions. The aim is to eliminate or reduce the corrosivity of the mud as well as to control the losses. The results showed a lower corrosion rate, 0.0029 mm/year, using *P. farcta* material in comparison with those obtained by researchers in the previous studies.

Index Terms—Corrosion, Drilling fluid, Drilling pipe, pH, *Prosopis farcta*.

I. INTRODUCTION

Drilling is one of the oldest techniques in the world (Hossain and Al-Majed, 2005), it can be used to unlock crude oil and natural gas reserves (Hossain and Islam, 2018). The drilling rig can be classified to six systems, circulating is one of the main systems used to circulate drilling fluid (mud) down through the drill string and up the annulus, carrying the cuttings from the face of the bit to surface (Heriot Watt, 2005). The drilling fluid (mud) pumped from the tanks to the drill pipe, then to the bit for the purpose of cooling, lubricating, and so on (Guo and Liu, 2011). Most of the problems that occur during drilling are related to the type and the composition of the drilling fluid, so the appropriate

selection of drilling mud (type and composition) leads to the success of the drilling process. One of the technical problems that the drilling fluid cause is corrosion of the drilling pipes, Fig. 1. The types of corrosion attack the drill pipes are erosion, uniform, localized, and microbial corrosion Fig. 1. The main consequences of the corrosion in drilling pipes are drilling efficiency reduction, equipment failure, and safety hazards. The value of pH of the mud is playing an important role to control the uniform and localized corrosion. Many researchers in the field of drilling engineering were investigated different methods to obtain an optimum drilling fluid with acceptable pH value to control the corrosion in drilling pipes. Adebowale and Raji (2015) investigated the use of banana peel ash as an alternative additive to enhance pH to control corrosion. Okorie (2009) employed two local additives “Trona” powder and burnt palm powder as pH modifiers to increase the level from 7.0 to 13.0. The burnt palm head sponge powder gives a high mud pH impartation. There are some drilling fluid additives which seriously promote corrosion. The temperature and composition of make-up water can be a serious source of corrosion (Murray and Holman, 1967). This paper investigates the addition of a natural and environmentally friendly additive to the drilling fluid to reduce the corrosion in drilling pipes.

II. MATERIALS AND METHOD

A. Materials

Drilling fluid

Drilling fluid refers to the circulating continuum substance use to perform a successful drilling process with lowest cost (Azar and Samuel, 2007). They are divided to two general types: Water-based drilling muds (WBMs) and oil-based drilling muds (OBMs). Water based drilling fluid is the corrosive and its widely used in drilling purposes. Liquid part of the mud can be select based on the formation type (Fink, 2015). The properties of a drilling fluid can be analyzed by its physical and chemical attributes. The major properties of the fluid should be measured and reported daily

ARO-The Scientific Journal of Koya University
Vol. XI, No. 1 (2023), Article ID: ARO.11148. 5 pages
Doi: 10.14500/aro.11148

Received: 06 February 2023; Accepted: 06 May 2023
Regular research paper: Published: 01 June 2023

Corresponding author's e-mail: pshtiwan.jaf@koyauniversity.org
Copyright © 2023 Pshtiwan T. Jaf, Jafar A. Ali, Ayad A. A. Razzaq.
This is an open access article distributed under the Creative Commons Attribution License.





Fig. 1. Drilling Pipes.

in the drilling daily report (Rabia, 2002). The main properties involving in corrosion of drilling pipe are the pH of the drilling fluid. The pH, or hydrogen ion concentration, is a measure of the relative acidity or alkalinity. Except for salt muds, the pH of mud is seldom below 7 (Azar and Samuel, 2007). High downhole temperature will lead to the decrease of pH value, this will make the performance of drilling fluid deteriorate. It is of importance to monitor and keep the pH high as a decrease below the value of 7 will increase the acidity of the mud thereby aiding to increase the corrosion rate of down hole equipment's (Peretomode and Peretomode, 2021). In general, the pH of mud falls between 8 and 10.5, depending on the mud type (Okorie, 2009).

Prosopis farcta (PF)

The PF is a common plant Fig. 2 germinating in wide range area. It is a below ground tree. It looks like a shrub with a height of 20–100 cm (in rare cases up to 4 m high). PF is a small, pricking flower, and is found in Algeria, Egypt, Tunisia, Iran, Iraq, and Kazakhstan (Qasem, 2007). The shrubs grow noticeably in the warm summer months. The mesquite can survive difficult weather and soil conditions (including saline soil), but dislikes shadows (Patil, 2022). The chemical composition of the PF beans has been determined by Omid, Ansari Nik, and Ghazaghi (2012) as shown in Table I. The PF has a fibrous nature which is a type of the most common additives to drilling fluid.

Corrosion coupon

Corrosion coupons are usually used to measure the corrosion rate within a procedure in laboratories. In this study, corrosion coupons were prepared using the carbon steel API 5LX70 (Ismail, et al., 2014), the same material uses in manufacturing drilling pipes. The coupon size (30 mm × 12.5 mm × 1.25 mm) polished and cleaned with sand paper grade 60, 320, and 600 then degreased by ethanol, Fig. 3. Finally, the coupons dried, weighted, and the surface finish were recorded.

B. Methodology

The drilling fluid prepared at the laboratory according to the API standards. Additives (beans of PF) were collected from the outskirts of Koya district in Erbil province, Iraq, during the summer of 2021. The PF beans then being



Fig. 2. *Prosopis farcta*.

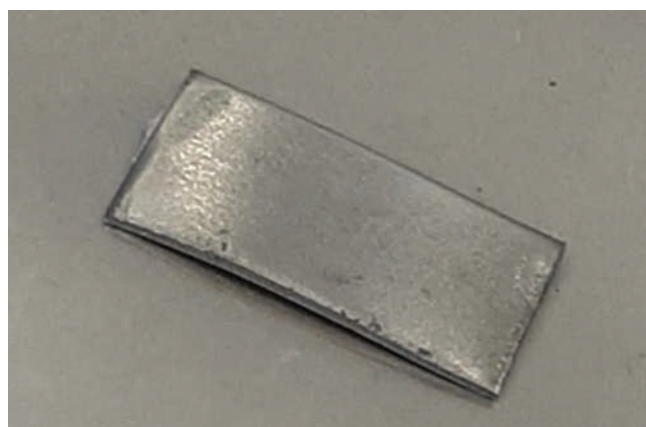


Fig. 3. Coupon Sample.

TABLE I
CHEMICAL COMPOSITION OF *PROSOPIS FARCTA* BEANS (OMIDI, ANSARI NIK, AND GHAZAGHI, 2012)

Variable	Amount (%)
Dry matter	97.45±0.18
Ash	3.15±0.20
Crude protein	9.97±0.45
Neutral detergent fiber	40.37±0.36
Acid detergent fiber	34.37±0.51
Crude fat	±0.09

dried in sun light and then being powdered by gridding. Moreover, to determine the effect of PF particle size distribution, the powdered PF beans were divided into three different sizes, fine, medium, and coarse through the use of API standard mesh sieves. Devices and measuring tools used throughout the experimental work. Corrosion coupon strips were used to measure the corrosion rate for different drilling.

III. EXPERIMENTAL WORK

A. Mud Sample Preparation

The reference mud RM with composition as shown in Table II has been prepared according to the API-SPEC-

13A-2010 standards. Once the mud is prepared, its pH and rheological properties were measured and recorded. The properties of the RM are summarized in Table III.

Different sizes (fine, medium, and coarse) of the prepared PF beans were added separately to the reference mud to find out the effect of the size distribution on drilling fluid. Moreover, for determining the effect of the PF concentration, various concentration of each size of the PF was added separately. The PF concentration was selected on the base of pounds of the PF per barrel of the drilling mud (ppb), the selected PF concentrations started from 5 ppb to 25 ppb with increment of 5 ppb. At the end, a blend of all PF sizes was added into the RM and various tests were conducted. The mud weight was conducted utilizing the mud balance.

B. Corrosion Test

pH

To determine the effect of the developed mud (with PF additive), various sizes and concentrations of the PF were added into the mud and the pH of each prepared mud has been measured using the pH meter as shown in Fig. 4. The pH of mud with most commercial additives such as CaCO_3 was measured also. As it is known that the best pH range for drilling mud is 8.5–10.5 (Asrar, 2010) but it was observed that the reference mud has pH of 12, higher than the recommended.

Surface morphology observation

Thermal imaging camera was used to determine any changes may occur to the surface of coupon. The property of the surface of the coupon was recorded before hanged

TABLE II
COMPOSITION OF REFERENCE MUD (RM)

Materials	Bentonite (gm)	Water (mL)	NaOH (gm)
Concentration	80	1400	2

TABLE III
PROPERTIES OF REFERENCE MUD (RM)

Density	8.61	ppg
Plastic viscosity	4	cp
Yield point	15.1	Ib/100 ft2
Gel strength (10 s)	9.3	Ib/100 ft2
Gel strength (10 min)	11.1	Ib/100 ft2
pH	12	---



Fig. 4. pH Meter.

in the mud and after. Infrared signal from the camera penetrates the surface of the coupon, any changes to the surface can be clearly observed. Fig. 5 shows the thermal and digital image of the coupon before insertion to the mud whilst Fig. 6 shows the surface images after used in the mud.

Corrosion rate measurement

Corrosion coupons are a simple yet effective tool for providing a quantitative estimation of corrosion rates occurring in an operating system. They also provide a visual indication of the type of corrosion which may be occurring in the monitored system. The drill-pipe coupons were suspended in the drilling mud at each specific temperature and high pressure set for at least 20 hours. The autoclave then after which was cooled at a rate of $2^\circ\text{C}/\text{min}$ to room temperature and the samples removed. At the end of each 20-h test, the samples were collected and thoroughly cleaned in a 10% HCl solution and rinsed in deionized water, and kept in a dry and well-sealed container immediately after collection before analysis (Mohammed, et al., 2021).

Oil-well steel coupon (N-80 steel) specimen of specification $30 \times 12.5 \times 1.25$ mm was used for the corrosion tests using the weight loss method. The weight of the coupon was

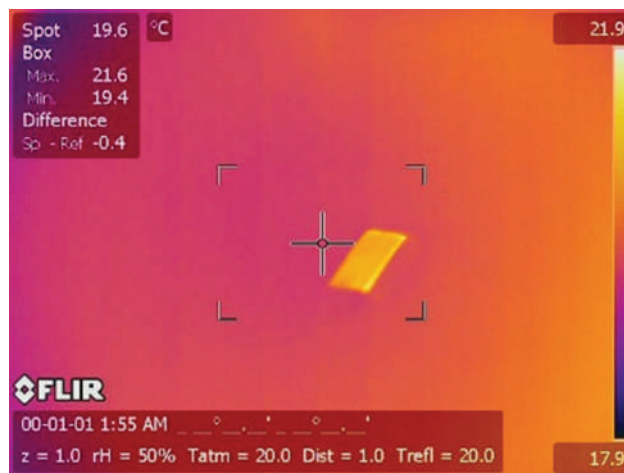


Fig. 5. Coupon surface before use in the mud.



Fig. 6. Coupon surface after use in the mud.

determined before it was subjected to the weight loss test Fig. 7a. The weight of the coupon was 3.355 g, in addition the surface of the coupon was recorded using thermal imaging camera Fig. 5. The tests were carried out using the high pressure, high temperature (HPHT) filter press machine Fig. 8. The HPHT dynamic filter press has overcome the limits of various traditional static filter presses and allows obtaining a new kind of results, much more representative of the borehole conditions. It can be used to measure the filtration property of drilling fluids and cement slurry accurately and safely under static and dynamic conditions. The usage of the instrument can provide the reliable data for realizing scientific, rapid, high quality, and safe drilling (Jaf, Razzaq and Ali, 2023). Then, an oil-well steel coupon which had been treated according to the API specifications (API RP-13 B-1) was hung in the mud (Jaf, Razzaq and Ali, 2023). When the pressure and temperature were stabilized. After 20 h from running the machine with the coupon inside, it is removed. Before the analysis, the coupons were scrubbed with a bristle brush to remove the corrosion products; and then kept in a dry and well-sealed container immediately after collection before analysis (Mohammed, et al., 2021). The corrosion products were carefully observed, the weight of the coupons was measured and recorded, the new weight of the coupon was 3.353 g, Fig. 7b.



Fig. 7. (a) Coupon on the weight scale before use. (b) Coupon on the weight scale after use.



Fig. 8. High Pressure High Temperature Filter Press.

IV. THEORETICAL WORK

The corrosion rates were calculated for each weight loss using the relation as shown in the Eq. (1) (Aremu, et al., 2017). This correlation has been widely used in the previous similar studies.

$$CPR = \frac{87.6 W}{\rho At} \tag{1}$$

Where: CPR = Corrosion penetration rate in (mm/year); W = Mass loss after the test (g); ρ = density of the specimen (g/cm^3); t = Time of exposure (h); and A = Area of exposure (cm^2). The density of iron is equal to $7.85 g/cm^3$.

$$W(\%) = (W_i - W_a) * 100 \tag{2}$$

Where W_i is the initial mass (g) before corrosion, W_a is the mass after corrosion.

V. RESULTS AND DISCUSSION

The pH for the reference mud RM was 12, this value is outside the desirable range. The widely used additive $CaCO_3$ was added to RM, the reduction of pH by $CaCO_3$ addition was not enough since the pHs were still above the optimum range. The present study additive PF then added to the RM. Best pH reduction could be achieved through the addition of various sizes and concentrations of PF, particularly the addition of 15 ppb of the fine sized PF (Fig. 9), which gives a mud with 9.5 pH. As a result, all PF sizes have the potential to be used as pH reducers, especially at high concentrations, suggesting their applicability in being used as a pH control agent. Moreover, for any additive to be added as a lost control material (LCM) should keep the pH of the mud within the optimum range, the usage of 15 ppb of fine sized PF will keep the value of the pH in that range.

As for corrosion rate, the coupon weight lost was 0.002 g in 20 h, the results obtained a corrosion rate of 0.0029 mm/year in drill pipes using the PF additive. This result is compared with the corrosion rate in the previous studies Fig. 10. Only one of the studies showed a corrosion rate lower than what is obtained in the present study.



Fig. 9. Fine size of *Prosopis farcta* additive.

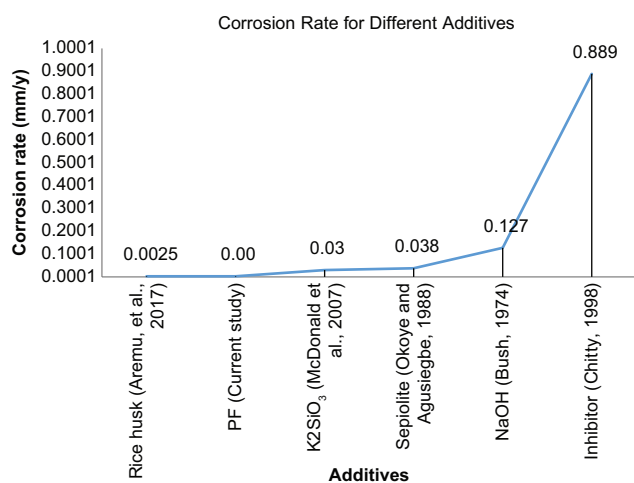


Fig. 10. Corrosion rate with *Prosopis farcta* in comparison with other additives.

VI. CONCLUSION

The research work is carried out to show the possibility of reducing the corrosivity of the drilling fluid and its effect on drill pipes. The additive used in this work reduced the corrosion rate in drill pipes. It is concluded that the PF is a good additive can be added to the drilling mud to reduce; it is corrosivity and the best size and concentration were fine sized and 15 ppb concentration. Furthermore, in addition to the overcome of the PF additive on the previous studies materials in term of pH control, it overcomes them in term of cost, availability, and environmentally as well. However, a blend of two or more sizes of the PF additive has not considered and recommended for future studies.

REFERENCES

- Adebowale, A., and Raji, J., 2015. Local content supplements as an alternative to imported corrosion control additives for drilling mud treatment (A case study of the use of burnt plantain and banana peels). In: *Proceedings of the International Academic Conference for Sub-Sahara African Transformation and Development*. University of Ilorin, Kwara State, Nigeria.
- Aremu, M.O., Arinkool, A.O., Salam, K.K., and Ogunmola, E.O., 2017. Potential of local pH control additives for corrosion inhibition in water base drilling fluids. *Petroleum and Coal*, 59(5), pp. 611-619.
- Asrar, N., 2010. *Corrosion Control of Drilling Tools Through Chemical Treatments-Effectiveness and Challenges*. SPE International Conference on Oilfield Corrosion, Aberdeen, UK.
- Azrar, J.J., and Samuel, G.R., 2007. *Drilling Engineering*. PennWell Corporation, Tulsa, Oklahoma.
- Bush, H.E., 1974. *Treatment of Drilling Fluid to Combat Corrosion*. Paper Presented at the Fall Meeting of the Society of Petroleum Engineers of AIME, Houston, Texas.

Chitty, H., 1998. *Corrosion Issues with Underbalanced Drilling in H₂S Reservoirs*. Paper Presented at the SPE/ICoTA Coiled Tubing Roundtable, Houston, Texas.

Fink, J., 2015. *Petroleum Engineer's Guide to Oil Field Chemicals and Fluids*. 2nd ed. Gulf Professional Publishing, Waltham.

Guo, B., and Liu, G., 2011. *Applied Drilling Circulation Systems: Hydraulics, Calculations and Models*. Gulf Professional Publishing, Texas.

Hossain, M.E., and Al-Majed, A.A., 2015. *Fundamentals of Sustainable Drilling Engineering*. John Wiley and Sons, Chichester, England.

Hossain, M.E., and Islam, M.R., 2018. *Drilling Engineering Problems and Solutions: A Field Guide for Engineers and Students*. John Wiley and Sons, Chichester, England.

Ismail, M., Noor, N.M., Yahaya, N., Abdullah, A., Rasol, R.M., and Rashid, A.S., 2014. Effect of pH and temperature on corrosion of steel subject to sulphate-reducing bacteria. *Journal of Environmental Science and Technology*, 7(4), pp. 209-217.

Jaf, P.T., Razzaq, A.A., and Ali, J.A., 2023. Effect of size and concentration of a new developed natural, biodegradable and environmentally friendly LCM on fluid losses characteristics. *Iraqi Geological Journal*, 56(1D) pp. 231-246.

Jaf, P.T., Razzaq, A.A., and Ali, J.A., 2023. The state-of-the-art review on the lost circulation phenomenon, its mechanisms, and the application of Nano and natural LCM in the water-based drilling fluid. *Arabian Journal of Geosciences*, 16(1), pp. 1-31.

McDonald, M., Barr, K., Dubberley, S.R., and Wadsworth, G., 2007. Use of *Silicate-Based Drilling Fluids to Mitigate Metal Corrosion*. Paper Presented at the International Symposium on Oilfield Chemistry, Houston, Texas, USA.

Mohammed, K.A., Okab, A.K., Hamad, H.S., Hashim, M., and Abdullhussain, R.K., 2021. Drilling and casing pipes corrosion investigation in water based drilling mud of Iraqi oil fields environment. *Journal of Mechanical Engineering Research and Developments*. 44(8), pp. 232-240.

Murray, A.S., and Holman, W.E., 1967. Drilling string corrosion-a major drilling problem. *Journal of Canadian Petroleum Technology*, 6(02), pp. 33-36.

Okorie, M.O., 2009. Modification of drilling fluid PH with local additives: Ash of burnt palm head sponge [BPHSP] and a rich potash mineral known as Trona. *Petroleum Technology Development Journal*, 1, pp. 1-16.

Okoye, C.U., and Agusiegbe, C.V., 1988. *Statistical Analysis of Factors That Promote Drilling Fluid Corrosion at Elevated Temperatures*. Paper Presented at the SPE Formation Damage Control Symposium, Bakersfield, California.

Omid, A., Ansari Nik, H., and Ghazaghi, M., 2013. *Prosopis farcta* beans increase HDL cholesterol and decrease LDL cholesterol in ostriches (*Struthio camelus*). *Tropical Animal Health and Production*, 45(2), pp. 431-434.

Patil, N., 2022. *Prosopis Farcta*. Available from: <https://alchetron.com/prosopis-farcta> [Last accessed on 2022 Mar 30].

Peretomode, E., and Peretomode, O., 2121. Temperature effects on the pH of water based drilling mud and mud ph Concerns on the environment. *FUTURE Journal of Scientific and Industrial Research*, 5(2), pp. 67-73.

Qasem, J.R., 2007. Chemical control of *Prosopis farcta* (Banks and Sol.) Macbride in the Jordan Valley. *Crop Protection (Guildford, Surrey)*, 26(4), pp. 572-575.

Rabia, H., 2002. *Well Engineering and Construction*. ENTRAC Consulting Limited, London.

Watt, H., 2005. *Drilling Engineering*. Heriot Watt University, Institute of Petroleum Engineering, UK.

The Overshot Gate as a Flow-Measuring Device

Jihan M. Qasim

Department of Water Resources Engineering, College of Engineering, University of Duhok,
Kurdistan Region – F.R. Iraq

Abstract—The overshot gate is a commonly used adjustable overflow weir for regulating the upstream water level in open channels. The amount of gate movement is proportional to the water level change. However, to effectively manage the water flow, it is also important for operators to accurately measure the flow rate in the channel. This study examines an overshot gate installed at the end of a laboratory flume to estimate the flow rate under various free flow conditions. This study investigates different gate angles ranging from 9.6° to 90° to evaluate their impact on the flow properties and the discharge coefficient. The analysis of the results indicates that the maximum flow rate values can be achieved with gate inclinations from 15.5° to 47.2° with relatively lower head; the inclined alignment of the gate decreases the effective gate height which consequently increases the gate efficiency. The use of the overshot gate is advantageous over the normal gate when channel depth is limited and higher discharge is required at relatively lower head. In this study, at the highest gate inclinations, the water surface is significantly stable having the lowest values of the approach Froude number. In addition, the head to gate height ratio decreases with raising the gate due to the reduced vertical contraction of the channel. Finally, this paper proposes an empirical equation for estimating the discharge coefficient based on the gate inclination, which demonstrates good accuracy in the specified range.

Index Terms—Overshot gate, Leaf gate, Inclined thin-plate weir, Pivot weir, Discharge coefficient, Discharge measurement.

I. INTRODUCTION

The overshot gate, also known as the leaf gate, or pivot weir, is an overflow adjustable weir that consists of a rectangular leaf hinged to the channel bed, and chained to a cable hoist that lowers and raises the gate to the desired height. The gate is popular for controlling the upstream water level in the channels and has been found very easy to operate and understand. The gate is raised to raise the water level and lowered to lower the water level. The amount of gate movement is proportional to the water level change (Stringam et al., 2012). In irrigation districts, the gate delivers nearly constant flow rates for the turnouts regardless of the flow rate in the main canal. It is known to handle surges in

the flow with limited depth changes (U. S. Department of the Interior Bureau of water, 2001).

The first overshot gate patent was granted to R.A. Lang in 1890, the device did not incorporate much of today's irrigation requirements, as cited in (Stringam et al., 2012; Stringam, 2010; Stringam and Gill, 2012). The overshot gate has been the subject of few studies and published works. The available published investigations agree on very few details of the discharge characteristics of this hydraulic structure due to the differences in experimental equipment and technique. Thin-plate weirs inclined toward downstream, similar to overshoot gates, were used in some research works. Wahlin and Replogle (1994) performed tests on a laboratory model gate and a prototype gate. Empirical equations were developed to determine the flow rate of a ventilated free-flow gate valid for gates angle between (16.2° – 63.4°) and for the upstream head to gate height less than unity. Weyer (2000; 2002), Qoi, Krutzen and Weyer et al. (2003), Eurén (2004), Mareels et al. (2005), Eurén and Weyer (2006), Ooi and Weyer (2007; 2008), Ooi, Foo and Weyer (2011), and Aleem, Muhammad, and Nasir (2014) studied the overshot gates located along irrigation channels, system identification models were presented to predict the head over the gates, and significant potential for substantial water savings was demonstrated. Prakash and Shivapur (2003; 2004), Shivapur, Mulangi and Swamy (2009), and Prakash, Ananthayya and Koor (2011) studied the variation of the discharge coefficient of an inclined rectangular sharp-crested weir with the normal position of the weir. They also analyzed the flow over inverted triangular, rectangular notch weirs, and compound notch-weir consisting of two triangular sections with different vertex angles inclined at (15° , 30° , 45° , and 60°) with the vertical plane. Discharge equations were established in terms of the head to crest height, and the inclination angle. Mohammed and Mohammed (2011) studied and compared the inclined side weir with crest angles (0° , 4° , 8° , and 12°) against and in the flow direction, and obtained an equation for the discharge coefficient. Nikou, Monem, and Safavi (2016) experimentally investigated the free and submerged flow over pivot weirs with angles between (20° – 90°) with different side contractions. Two discharge equations were used, the first one was Kindsvater-Carter's equation, and the second one was derived from energy and critical depth equations. For the free flow condition, the equations were accurate within ± 15 and $\pm 10\%$, respectively. For submerged flow condition, however, the accuracy was within $\pm 30\%$ and $\pm 20\%$. Bijankhan, Asce, and Ferro (2018) applied

ARO-The Scientific Journal of Koya University
Volume XI, No.1 (2023), Article ID: ARO.11170, 6 pages
DOI: 10.14500/aro.11170

Received: 23 February 2023; Accepted: 30 May 2023

Regular research paper: Published: 17 June 2023

Corresponding author's e-mail: jihan.mahmood@uod.ac

Copyright © 2023 Jihan M. Qasim. This is an open access article distributed under the Creative Commons Attribution License.



experimental and numerical simulations to study the effect of the inclination angles ranging within (30°–90°) on the stage-discharge formula of rectangular weir. It was found that the discharge capacity for 30° inclination increases by about 8.2% compared with that of the normal weir. In addition, the study concluded that flow through the normal weir is not sensitive to the inclination angle in the interval $54^\circ \leq \theta \leq 90^\circ$. Azimfar, Hosseini, and Khosrojerrdi (2018) proposed analytical equations to estimate the discharge coefficient of a pivot weir based on the Bernoulli and momentum equations with relative errors within $\pm 5\%$ and $\pm 10\%$ for the free and submerged flow conditions, respectively. Bijankhan and Ferro (2020) investigated the factors affecting submerged flow conditions for the pivot weir and proposed a stage-discharge formula with a mean absolute relative error of 6.4%.

In the present study, it is aimed to examine the reliability of the adjustable overshoot gate, which is usually used only to control the water level in a laboratory flume that is built-in with the gate at its downstream end, for estimating the flow rate. The present work differs from the earlier studies in that a greater number of inclination angles are experimentally investigated and, as a result, a greater amount of data are obtained that allows for a more comprehensive analysis of the hydraulic characteristics of the structure under different flow conditions.

II. METHODOLOGY

To achieve the objective of this study, an approach to the gate flow problem is found through using a combination of analysis of the underlying empirical laws and laboratory experiments. The experimental program is organized to measure the flow properties in the neighborhood of this hydraulic structure. The relationships between the various parameters are investigated.

For any flow-measuring device, the head-discharge equation has a discharge coefficient C_d and a velocity coefficient of the approach flow C_v , or their combination. The accuracy of the measurement depends to a great extent on the variation of these coefficients. The discharge over a vertical thin-plate weir can be calculated using a modified form of the Kindsvater-Carter equation which is also valid for a vertical overshoot gate (Wahlin and Replogle, 1994):

$$Q = C_e \frac{2}{3} \sqrt{2g} b_e h_e^{3/2} \tag{1}$$

$$b_e = b_c + K_b \tag{2}$$

$$h_e = h_1 + K_h \tag{3}$$

where Q = Discharge over the gate, C_e = Effective discharge coefficient, g = Acceleration due to gravity, b_e = Effective width of gate, b_c = Width of the control section, K_b = Empirical constant from Fig. 1 dependent on (b_c/B) that describe the boundary geometry, B = Width of the rectangular approach channel h_e = Effective head on the gate, h_1 = Piezometric head measured upstream from the gate, and

$K_h = 0.001$ m is constant regardless of the flow rate and the gate height where K_b and K_h have little effect on the flow rate at high heads.

By modifying the gate width and the head approaching the structure, the combined effects of viscous and surface tension forces are accounted for (Carter, 1956; Shen, 1981). An advantage of (1) is that the effect of approach velocity is incorporated and need not be included in the study. This procedure is valid for $h \geq 3$ cm, $h/p \leq 2$, $p \geq 10$ cm, and $b_c \geq 15$ cm (Kulin and Compton, 1975).

The overshoot gate is hydraulically similar to a sloping rectangular sharp-crested weir. To account for the inclination of the overshoot gate, C_a is introduced such that:

$$Q = C_a C_e \frac{2}{3} \sqrt{2g} b_e h_e^{1.5} \tag{4}$$

Setting the discharge coefficient $C_d = C_a C_e$, (1) becomes:

$$Q = C_d \frac{2}{3} \sqrt{2g} b_e h_e^{1.5} \tag{5}$$

The present study seeks establishment of an empirical formula for estimating C_d as a function of θ , the angle of gate inclination to the direction of flow, as shown in Fig. 2.

III. LABORATORY WORKS

The experimental tests are carried out in the Hydraulic Laboratory of the College of Engineering, University of Duhok using a horizontal rectangular flume having a working length of 500 cm, 30 cm width, and 45 cm depth. The tested

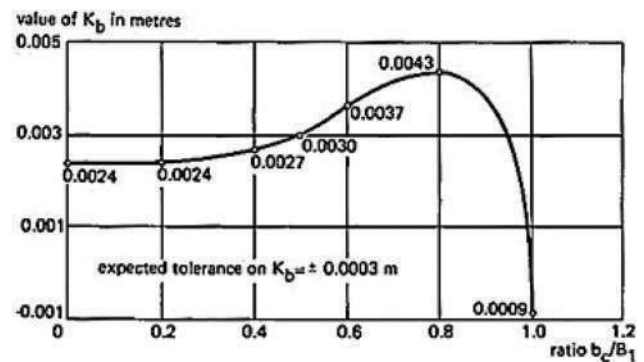


Fig. 1. Values of K_b versus b_c/B (Bos, 1989).

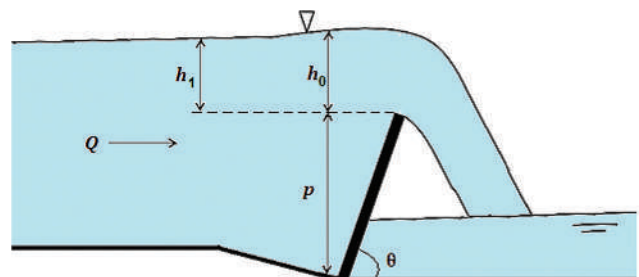


Fig. 2. Definition sketch of the overshoot gate.

overshot gate is located at the end of the flume. In the outlet of the flume, a part of the bed is sloping at an angle of 16.7° just upstream of the gate, as shown in Fig. 3. The gate is 29.7 cm wide, 60 cm high, and 0.6 cm thick.

For the purpose of flow ventilation, eight plastic hoses of 6 mm in diameter at space of 3 cm with their openings 24 cm below the top of the gate were fixed on the downstream face of the gate, as shown in Fig. 4. This precaution ensures that sufficient supply of air is maintained to the air pocket beneath the flow nappe so that the nappe is entirely free from the gate body after passing the gate. Otherwise, the pressure in the air pocket is reduced causing undesirable effects, such as, jet vibration resulting in an unsteady flow due to inconsistent air supply to the air pocket; and increased curvature of the overfalling jet resulting in increased discharge coefficient C_d values. If the discharge Q is fixed, the head h measured over the gate is reduced, and if the head h is fixed, the discharge is increased (Bos, 1989).

Different tilting angles of the gate θ were investigated ranging from 9.6° to 90° (normal position). Different flow rates were applied in free flow conditions, such that the top of gate is above the downstream water level. This is always the case for the laboratory channel we consider since the water drops out of the channel just after passing the gate. The flow rate and the head over the crest were recorded in each experiment. Ten experimental tests were accomplished for each value of θ , as shown in Table I. Thus, 260 experiments were made on the gate including flow rates from 0.00148 to 0.03318 m³/s with heads varying from 0.01645 up to 0.13725 m. The rate of flow was measured by an electromagnetic flow meter, and the water surface elevations were measured using point gauges.

IV. RESULTS AND DISCUSSION

For each gate height, the actual discharge against effective head h_e is drawn in Fig. 5 *a* through *f*. The smaller p is that



Fig. 3. Location of the overshot gate in the laboratory flume.



Fig. 4. Ventilation of the overshot gate.

the flatter is the gate which allows for more discharge to pass over it. At very small inclination angles such as when p is 10 and 12 cm (corresponding to θ values of 9.6 and 11.5°), the gate hydraulically behaves like a free overfall, which is also found by Bijankhan and Ferro, 2020. At this stage, the sloping part of the channel outlet accelerates the water flow until the gate is further raised. When p is between 14 and 44 cm, for a given head value, the discharge decreases with the increase of gate height with a small variation which could be due to measurement uncertainties. This observation also agrees with (Prakash and Shivapur, 2004).

However, when p is between 46 and 54 cm, Q_{act} increases with the increase of p which may be attributed to the fact that the increased gate inclination reduces the lower nappe. At p between 56 and 60 cm, lower flow rates can pass over the gate since raising the gate causes the water level to rise until the gate is completely vertical, and thus, the structure operates under minimum required head to avoid overflow of the approach channel.

It is worth mentioning that uncertainties in the head measurement in the present laboratory work may be attributed to the water surface fluctuations due to turbulent flow with Reynold's number Re ranging from 9000 to 72000, and the fact that the crest of the gate does not exactly resemble the crest of a sharp-crested weir. The percentage error in the head measurement for each gate inclination is presented in Fig. 6 with an average of 6.75% for the entire experimental program.

The relationship between inclination angle of the gate and the actual discharge is shown in Fig. 7. For each value of

TABLE I
SCOPE OF THE EXPERIMENTAL VARIATIONS

P (cm)	θ (°)	Number of tests	Range of Q (m ³ /s)	
			From	To
10	9.6	10	0.01465	0.02346
12	11.5	10	0.01484	0.02342
14	13.5	10	0.01536	0.03302
16	15.5	10	0.01537	0.03318
18	17.5	10	0.01536	0.03301
20	19.5	10	0.01542	0.03311
22	21.5	10	0.01525	0.03286
24	23.6	10	0.01535	0.03279
26	25.7	10	0.01528	0.03285
28	27.8	10	0.01504	0.03268
30	30	10	0.01537	0.03286
32	32.2	10	0.01523	0.03283
34	34.5	10	0.01524	0.03268
36	36.9	10	0.01516	0.03274
38	39.3	10	0.01522	0.03276
40	41.8	10	0.01502	0.03267
42	44.4	10	0.01499	0.03051
44	47.2	10	0.01019	0.01899
46	50.1	10	0.01026	0.01919
48	53.1	10	0.01028	0.01909
50	56.4	10	0.00522	0.01395
52	60.1	10	0.00521	0.01398
54	64.2	10	0.00420	0.00862
56	69	10	0.00207	0.00425
58	75.2	10	0.00148	0.00278
60	90	10	0.00142	0.002775

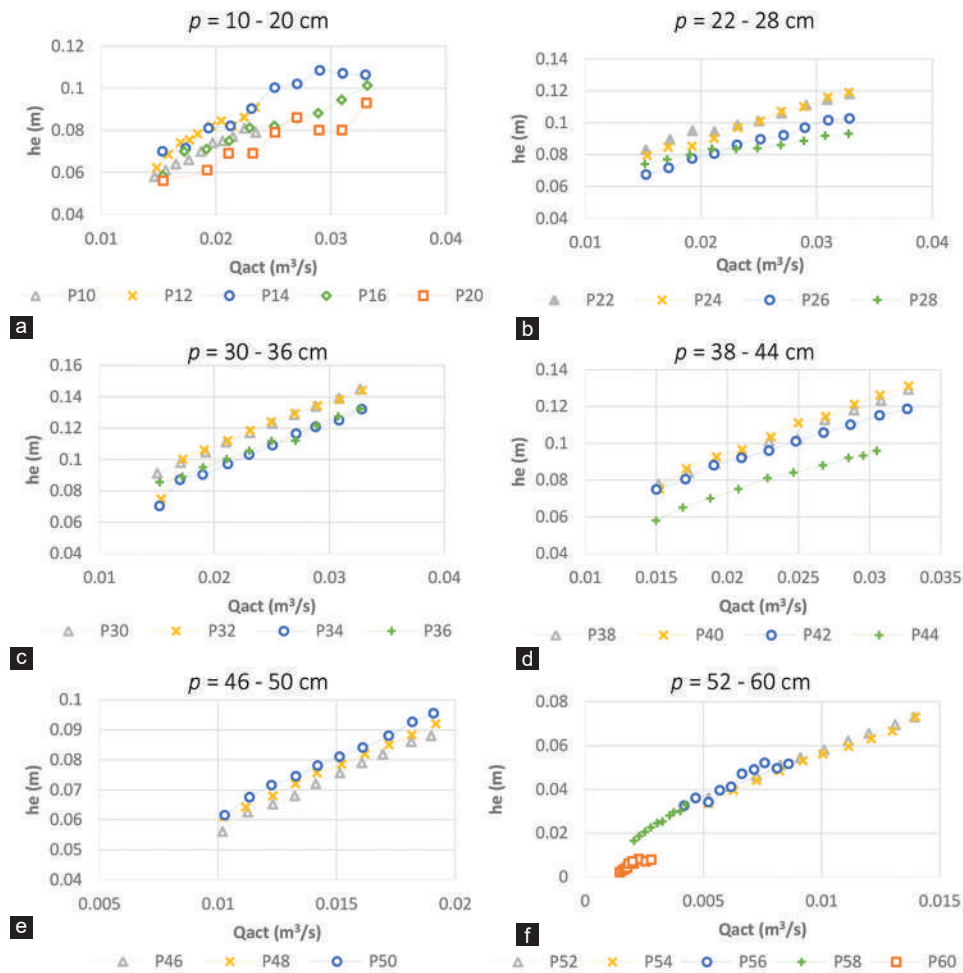


Fig. (a-f) 5. Variation of Q_{act} with h_e .

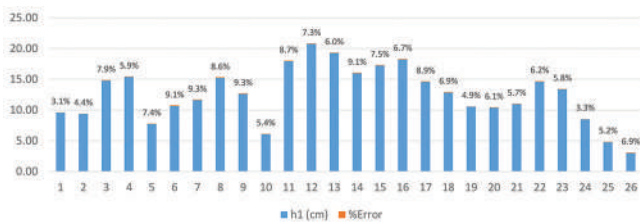


Fig. 6. Average percentage error in h_l for each θ .

θ , the value of Q_{act} is taken as the mean value of the whole range of the measured values of Q_{act} . Maximum values of flow rates are possible in the cases when θ is about 13.5° through 47.2° . Accordingly, the free board of the channel may be reduced in these cases for a more economical design (Shivapur, Mulangi and Swamy, 2009). The values of θ smaller than 13.5° exhibit characteristics of instability due to the intermittent clinging of the nappe to the gate surface. Similar behavior is observed at very low heads on almost all gate angles. This may be attributed to that the streamlines are no longer parallel and converge further when compared to the vertical gate. On the other hand, laboratory investigations show that for a given head value, the discharge decreases with the increase in gate inclination. It was also indicated in (Prakash and Shivapur, 2004) that lower gate angles allow

for higher discharges. Fig. 7 also shows that the discharge capacity of the gate decreases at the values of θ greater than 47.2° , as mentioned earlier, and reaches its minimum at $\theta = 90^\circ$.

The discharge coefficient is also a form of the Froude number (Kindsvater, 1964). Froude number is a dimensionless parameter that refers mainly to the amount of the velocity. From the laboratory data, Q_{act} can be plotted against the upstream Froude number, Fr_1 , for each gate inclination. There is a unique Fr_1 value for each flow state; this relation is given in Fig. 8. There is a clear trend for Fr_1 with each different discharge level. The result appears sensitive to the gate inclination, it indicates the water surface stability especially at the highest gate inclinations where the lowest values of Fr_1 are encountered.

The discharge coefficient C_d determines the ratio between the actual and the theoretical discharge. The variation of Q_{th} with Q_{act} for every value of θ is presented in Fig. 9 where it may be noticed that the values of C_d are high at the relatively smaller gate angles.

The ratio of the head to gate height h/p is a primary geometric ratio that describes the degree of vertical contraction of the channel. The upper and lower nappe profiles are a function of h/p (Carter, 1956). Its variation with the gate

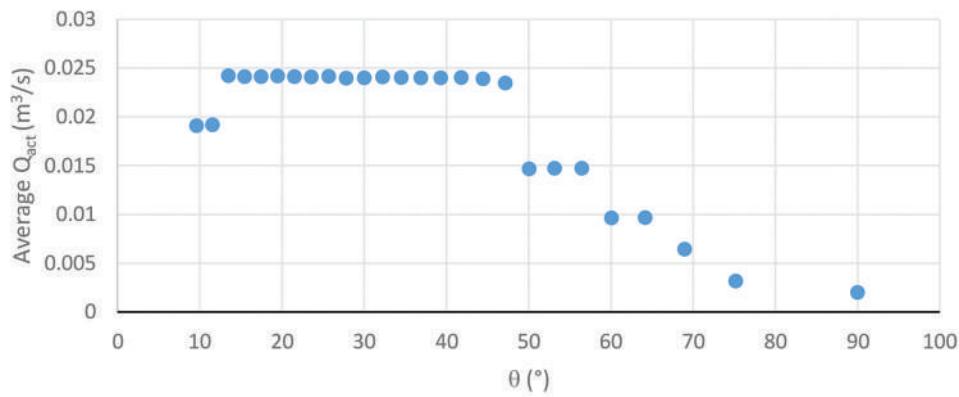


Fig. 7. Variation of Q_{act} with θ .

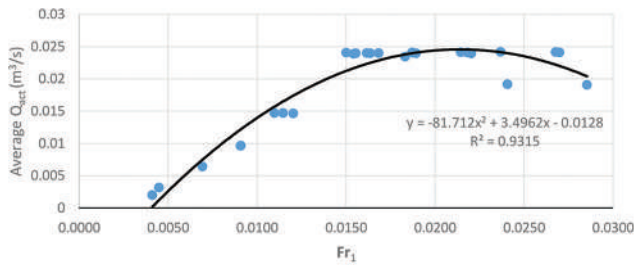


Fig. 8. Variation of Q_{act} with Fr_1 .

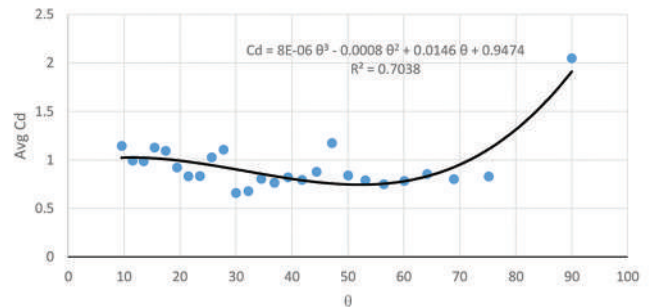


Fig. 11. Variation of C_d with θ .

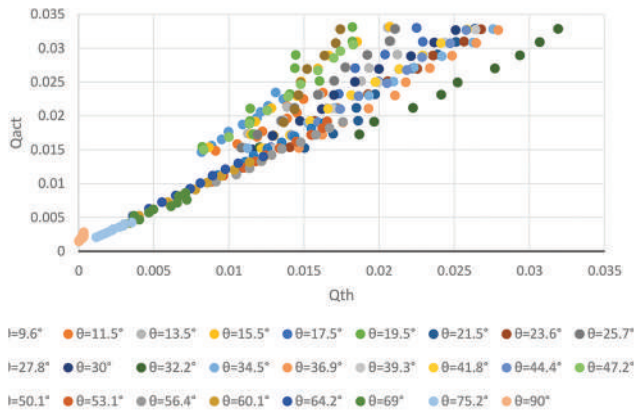


Fig. 9. Variation of Q_{th} with Q_{act} .

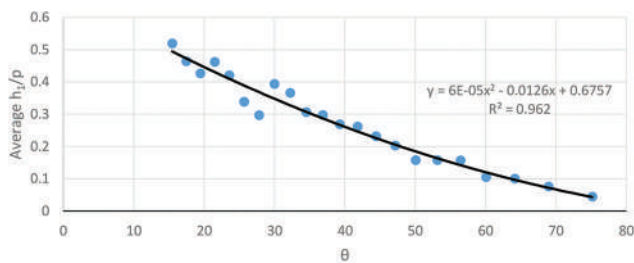


Fig. 10. Variation of h_r/p with θ .

inclination is shown in Fig. 10. The trend obviously declines with a considerable consistency as the vertical contraction of the channel decreases with raising the gate.

For estimating the C_d values, a cubic equation is proposed as the function of θ , such that:

$$C_d = 0.000008\theta^3 - 0.0008\theta^2 + 0.0146\theta + 0.9474 \quad (6)$$

The empirical formula is valid within the ranges of $\theta = (9.6^\circ-90^\circ)$, $Q = (0.00148-0.03413) \text{ m}^3/\text{s}$. As a result, the overshoot gate is reliable as a flow-measuring device. Fig. 11 displays this relation with the mean square error $MSE = 0.0287$ and the root mean square error, $RMSE = 0.17$.

V. CONCLUSION

With the increase in water demand and decrease in water resources, the issue of water measurement increasingly attains importance. In the present work, it is aimed to examine the measurement capability of the overshoot gate equipped at the downstream end of a laboratory flume. A wide range of gate angles are investigated under different free flow conditions. From analyzing the performance of the gate, the following conclusions may be drawn:

1. At the maximum gate inclination, the structure operates under minimal applicable heads and thus lower flow rates pass over the gate. In addition, the water surface is significantly stable having the lowest values of the approach Froude number.
2. At very small inclination angles, the gate behaves hydraulically like a free overfall. The flow exhibits characteristics of instability and the recurrent clinging to the gate surface, that is, the water nappe becomes in close contact with the downstream face of the gate and resists separation.
3. For a given discharge, the head over the crest increases with the increase in gate height, then it starts to decrease. The

head to gate height ratio decreases with raising the gate due to the reduced vertical contraction of the channel.

4. An empirical formula for estimating C_d is proposed for application within a broader range of θ than the formulae in the literature with acceptable accuracy, which makes the overshot gate reliable as a flow-measuring device.

For future research, there is potential for improvement in the gate performance using deeper laboratory channel than in the present study. This would allow for a wider range of discharges at the maximum gate inclination without causing the flow to overtop the channel sides.

ACKNOWLEDGMENT

The author owes recognition to the efforts of the lecturer Bshkoj S. Hussien and the engineers Alaa S. Abdolstar, Naz S. Salih, Roya K. Saeed, Sabrya Miroo, and Zilan M. Amin for their cooperation in the laboratory works at the Water Resources Engineering Department, College of Engineering, University of Duhok.

REFERENCES

- Aleem, S.A., Muhammad, A., and Nasir, H.A., 2014. System Identification of Distributory Canals in the Indus Basin. In: *IFAC Proceedings Volumes (IFAC-Papers Online)*. IFAC, United States.
- Azimfar, S.M., Hosseini, S.A., and Khosrojerrdi, A., 2018. Derivation of discharge coefficient of a pivot weir under free and submergence flow conditions. *Flow Measurement and Instrumentation*, 59, pp.45–51.
- Bijankhan, M., and Ferro, V., 2020. Experimental modeling of submerged pivot weir. *Journal of Irrigation and Drainage Engineering*, 146(3), pp.1-13.
- Bijankhan, M., Asce, A.M., and Ferro, V., 2018. Experimental study and numerical simulation of inclined rectangular weirs. *Journal of Irrigation and Drainage Engineering*, 144(1957), pp.1-8.
- Bos, M.G., 1989. *Discharge Measurement Structures*. 3rd ed. ILRI, Kenya.
- Carter, R.W., 1956. *A Comprehensive Discharge Equation for Rectangular-notch Weirs*, Master's Thesis, Georgia Institute of Technology.
- Eurén, K., 2004. *System Identification of Irrigation Channels with Overshot and Undershot Gates*. Department of Information Technology, Uppsala University, Sweden.
- Eurén, K., and Weyer, E., 2006. System identification of open water channels with undershot and overshot gates. *IFAC Proceedings Volumes*, 16, pp.638-643.
- Kindsvater, C.E., 1964. *Discharge Characteristics of Embankment-shaped Weirs*. United States Government Printing Office, Washington, D.C.
- Kulin, G., and Compton, P.R., 1975. *Guide to Methods and Standards for the Measurement of Water Flow*. National Bureau of Standards NBS, United States.
- Mareels, I.M.Y., Weyer, E., Ooi, S.K., Cantoni, M., Li, Y., and Nair, G., 2005. Systems engineering for irrigation systems: Successes and challenges. *Annual Reviews in Control*, 29, pp.191-204.
- Mohammed, M.Y., and Mohammed, A.Y., 2011. Discharge coefficient for an inclined side weir crest using a constant energy approach. *Flow Measurement and Instrumentation*, 22(6), pp.495-499.
- Nikou, N.S.R., Monem, M.J., and Safavi, K., 2016. Extraction of the flow rate equation under free and submerged flow conditions in pivot weirs with different side contractions. *Journal of Irrigation and Drainage Engineering*, 142(8), pp.1-8.
- Ooi, S.K., and Weyer, E., 2007. Control Design for an Irrigation Channel from Physical Data. In: *Proceedings of the IEEE International Conference on Control Applications*, pp.270-275.
- Ooi, S.K., and Weyer, E., 2008. Detection of Oscillatory Control Loops in Irrigation Channels. *IFAC Proceedings Volumes*, 41, pp.5500-5505.
- Ooi, S.K., Foo, M., and Weyer, E., 2011. Control of the Broken River. In: *IFAC Proceedings Volumes (IFAC-Papers Online)*. IFAC, United States, pp.627-632.
- Prakash, M.N.S., Ananthayya, M.B., and Kovoov, G.M., 2011. Inclined rectangular weir-flow modeling. *Earth Science India*, 4(I), pp.57-67.
- Prakash, M.N.S., and Shivapur, A.V., 2003. Flow over inclined sharp-crested triangular weir. *ISH Journal of Hydraulic Engineering*, 9(2), pp.80-88.
- Prakash, M.N.S., and Shivapur, A.V., 2004. Generalized head-discharge equation for flow over sharp-crested inclined inverted v-notch weir. *Journal of Irrigation and Drainage Engineering*, 130, pp.325-330.
- Qoi, S.K., Krutzen, M.P.M., and Weyer, E., 2003. *On Physical and Data Driven Modelling of Irrigation Channels*. IFAC, United States, pp.1939–1944.
- Shen, J., 1981. *Discharge Characteristics of Triangular-notch Thin-plate Weirs*. United States Government Printing Office, Washington, D.C.
- Shivapur, A.V., Mulangi, R.H., and Swamy, S.G., 2009. Use of inclined compound triangular notch-weir to improve discharge range. *ISH Journal of Hydraulic Engineering*, 15(3), pp.37-41.
- Stringam, B., 2010. Low Cost Linear Actuators for Canal Gate Control. In: *Meeting Irrigation Demands in a Water-Challenged Environment, USCID Conference*. Fort Collins, Colorado, USA, pp.275-285.
- Stringam, B., and Gill, T., 2012. Simplified overshot gate constructed and maintained by irrigation districts. *Irrigation and Drainage*, 61(5), pp.666-672.
- Stringam, B., Craig, K., McCaig, M., and Prozniak, J., 2012. Overshot Gate Development and History. In: *Managing Irrigation Systems in Today's Environment, USCID Water Management Conference*. Reno, Nevada, pp.249-261.
- U.S. Department of the Interior Bureau of Water, 2001. *Water Measurement Manual*. Available from: https://www.usbr.gov/pmts/hydraulics_lab/pubs/wmm [Last accessed on 2023 Feb 01].
- Wahlin, B.T., and Replogle, J.A., 1994. *Flow Measurement Using an Overshot Gate*. U.S. Department of the Interior Bureau of Reclamation, Denver.
- Weyer, E., 2000. System identification of an open water channel. *IFAC Proceedings Volumes*, 33(15), pp.265-270.
- Weyer, E., 2002. Decentralised PI Control of an Open Water Channel. In: *IFAC Proceedings Volumes*. IFAC, United States.

Seismic Fragility Curves for Reinforced Concrete Dual System Buildings: Pearl Tower as Case Study

Sarwar S. Ismael and Faris R. Ahmed

Department of Civil Engineering, Faculty of Engineering, Koya University,
Koya KOY45, Kurdistan Region – F.R. Iraq

Abstract—A seismic fragility curve is a visual representation that illustrates the likelihood of a structure surpassing a particular damage or performance limit state caused by an earthquake with a specific intensity or ground motion level. This curve is typically generated using probabilistic seismic hazard analysis and structural reliability analysis methods. It is based on statistical models that rely on past earthquake data and simulations of future earthquake scenarios to predict the structure or system's behavior under seismic forces. In this study, the seismic performance of 30 stories of 95 m height dual system reinforced concrete buildings located in Erbil is evaluated by analyzing three distinct ground motions. A non-linear platform is used to simulate and analyze data, followed by the generation of seismic inter-story drift fragility curves using Incremental Dynamic Analysis. The buildings' seismic structural performance is assessed based on five different performance levels, including operational phase, immediate occupancy, damage control, life safety, and collapse prevention (CP). Each level is associated with different levels of damage and corresponding degrees of functionality and safety. The fragility curves show that the building has a 50% chance of achieving or exceeding the (CP) level with highly intense ground vibrations with peak ground acceleration = 1.6 g. In addition, these curves can be beneficial in creating future local design codes and provide significant support in evaluating the seismic performance of existing buildings.

Index Terms—Dual system, Drift, Fragility curve, Incremental dynamic analysis, Seismic risk assessment, Vulnerability.

I. INTRODUCTION

Earthquakes are a natural phenomenon that can have catastrophic effects on buildings and human life. When an earthquake occurs, the ground shakes and the building responds to the resulting motion, which can lead to damage or collapse if the building is not properly designed and constructed to resist seismic forces. Building damage is the

main cause of seismic losses from earthquakes, and it is critical to assess the vulnerability of structures to seismic hazards, Fig. 1.

To this end, a key tool used in earthquake engineering is the seismic fragility curve (SFGC) technique. It is a graphical representation of the probability of a structure exceeding a given damage state, such as slight, moderate, extensive, or complete damage, as a function of the intensity of the ground motion. SFGCs are generated by analyzing the dynamic response of a structure to a set of ground motion records with increasing levels of intensity, using analytical models such as pushover or incremental dynamic analysis (IDA).

The output of the analysis is a set of curves that depict the probability of exceeding a damage state as a function of the peak ground acceleration (PGA), velocity, or displacement. These curves are then used to estimate the expected damage and loss for a structure under different levels of seismic hazard. The fragility curves used are unique to each building due to the specific fragility analysis carried out (Hancilar, et al., 2014; Vona, 2014).

SFGCs are extensively used in seismic risk analysis for designing and retrofitting buildings and other structures in seismically active regions. Provide a means of quantifying the risk of damage and collapse for various levels of seismic intensity, helping engineers and building owners to make informed decisions about the appropriate design, and retrofitting measures needed to ensure seismic safety and resilience.

Furthermore, SFGCs can be used to identify the most vulnerable components of a structure, allowing engineers to prioritize retrofitting measures and allocate resources efficiently. They can also be used to evaluate the effectiveness of different retrofitting strategies and to optimize the seismic design of new structures.

The fragility functions for different limit states (LSs) of the building are derived by combining the results of structural analysis with the probability distribution function (PDF) of the engineering demand parameter (EDP) given the intensity measure (IM) that represents the distribution. These functions are cumulative distribution functions expressing the seismic intensity in terms of the IM required to reach particular LS (Baker, et al., 2014).

Typically, one or more threshold capacities of the EDP's (i.e., EDPc) are associated with LS, and the fragility

ARO-The Scientific Journal of Koya University
Vol. XI, No. 1 (2023), Article ID: ARO.11172, 8 pages
DOI: 10.14500/aro.11172

Received: 23 February 2023; Accepted: 03 June 2023
Regular research paper; Published: 23 June 2023

Corresponding author's e-mail: sarwar.sadiq@koyauniversity.org
Copyright © 2023 Sarwar S. Ismael and Faris R. Ahmed. This is an open access article distributed under the Creative Commons Attribution License.



function is the probability of the seismic demand EDP exceeding the capacity EDP_c given the IM. The process of fragility assessment is computationally intensive, and non-linear dynamic analysis is a feasible method due to recent advancements in computer technology (Jalayer and Cornell, 2009). In addition, various methods for evaluating the distribution of EDP given IM and figuring out fragility functions utilizing non-linear dynamic analysis are discussed in this study. The requirements for performance-based seismic design are also discussed to evaluate structural performance. The degree of damage can be determined by using the maximum interstorey drift ratio (IDR), which is commonly used as the EDP.

Xue, et al., 2008 proposed five performance LSs (operational phase [OP], immediate occupancy [IO], damage control [DC], life safety [LS], and collapse prevention [CP]) with different probabilities of exceedance (0.5%, 1.0%, 1.5%, 2.0%, and 2.5%) to evaluate the building's seismic performance. These LSs are considered when developing fragility curves. Ultimately, SFGCs are crucial for ensuring the safety and resilience of structures in seismically active regions and are a critical tool in earthquake engineering (Xue, et al., 2008; FEMA 273, 1997).

In recent years, many high-rise building been built in Erbil, yet, there are limited amount of researches conducted on the seismic risk assessment of buildings. However, emerging studies have underscored the critical significance of evaluating the vulnerability of pre-seismic code buildings and emergency facilities, emphasizing the pressing need to mitigate their potential seismic losses. These investigations have shed light on the urgency of addressing the seismic resilience of structures in the region, particularly those constructed before the implementation of modern seismic design codes. By recognizing the inherent vulnerability of these buildings and facilities, researchers have highlighted the importance of comprehensive risk assessment methodologies to identify potential weaknesses, assess their performance under seismic loading, and propose effective strategies for minimizing the associated risks (Liel, et al., 2009; Abduljaleel, 2021). The findings of such research can provide crucial insights for policymakers, engineers, and stakeholders involved in enhancing the seismic resilience of the built environment in the city and similar contexts.

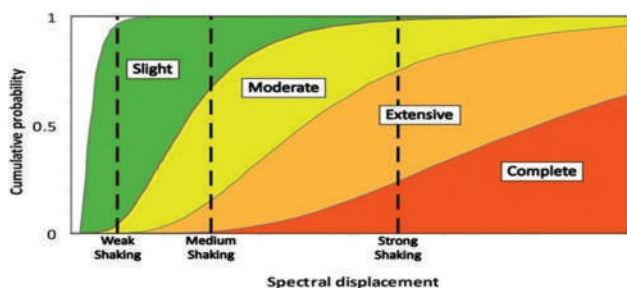


Fig. 1. Fragility curves for different limit states.

II. METHODOLOGY

Determining fragility required a thorough evaluation of structural response at various intensities. Nonlinear dynamic studies carried out in a variety of ways, with the primary differences being in the post-processing methods and the ground motion selection and scaling techniques that can be used. According to (Vamvatsikos and Cornell, 2004; Jalayer and Cornell, 2009), there are three primary methods for analyzing seismic performance: cloud analysis, stripe analysis, and IDA. Among these, cloud analysis is the least restrictive, as evidenced by the characteristic cloud pattern that emerges in the IM versus EDP plot, with each point representing a single analysis, as shown in Fig. 2 which shows an illustration of the findings from incremental dynamic analyses, which were utilized to determine the (IM) values linked with structural collapse for each of the ground motions.

The process of determining the fragility of a building, which is the likelihood that it will experience structural damage or collapse when subjected to seismic ground motions. To assess the building's performance under seismic loads, IDA technique is used. This technique is considered essential tool for determining a structure's safety margins.

The study develops fragility curves using a probabilistic approach based on five performance levels that are recommended for assessing building performance under seismic loads. These performance levels are defined by the IDR of the building, which is a widely used EDP that is used to assess the degree of damage in a building due to seismic loads. The maximum IDR is considered an excellent indicator for determining the degree of damage (Vamvatsikos and Cornell, 2002).

To generate the fragility curves, various scaling and record set selection strategies can be used. One option is to use a fixed record set that has been scaled to different levels of intensity, typically by multiplying all natural accelerograms by the same scale factor. Alternately, a distinct collection of natural records can be used for each level of IM, and scaling may be completely avoided. Fragility curves are the product

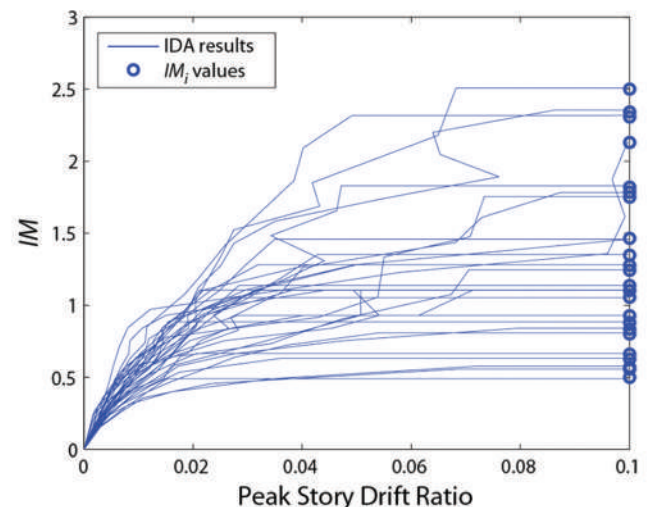


Fig. 2. Illustration of the findings from incremental dynamic analyses.

of seismic fragility analysis which clarify the probability of seismic demand (EDP) exceeding a certain LS at a specific ground motion IM as depicted in equation (1).

$$\text{Fragility} = P(\text{EDP} > \text{LS}/\text{IM}) \quad (1)$$

The fragility information can be extracted in several ways, such as using linear regression in logarithmic space to independently fit the non-collapsing IM-EDP points or using parametric or non-parametric regression (Ibrahim and El-Shami, 2011). Any statistical measure of EDP provided by the IM, such as the mean, 16/50/84 percentile, standard deviation, without the use of parametric or non-parametric regression, may be calculated directly from the relevant EDP data, greatly simplifying post-processing.

Also there are the different methods of analyzing seismic performance, which include cloud analysis, stripe analysis, and IDA. Cloud analysis is the least restrictive, and it produces a characteristic cloud pattern that emerges in the IM versus EDP plot, with each point representing a single analysis. Stripe analysis, on the other hand, uses any number of record sets, similar to cloud analysis, and it must use at least some scaling to ensure that all runs at a particular IM level truly exactly match the IM level requested, without any tolerance. The empirical distribution of the EDP findings taken from the relevant analyses directly represents the distribution of EDP given IM at each IM level. The sole basis for IDA is scaling. It focuses on individual recordings, which are scaled to various intensities until collapse is generally attained.

The decision to use any of the aforementioned methods ultimately rests on the analyst and their comprehension of the issue at hand. If other sources of uncertainty, such as the unpredictability of model parameters, must be taken into account, then more sophisticated (and complex) strategies should be used. Furthermore, the collapse margin ratio, which is recommended as a novel and effective seismic indicator by reference to the FEMA-P-695 methodology, is ultimately determined in this study based on the fragility search technique received from the (IDA). The methodological work for the case study is explained and summarized in the flow chart in Fig. 3.

A. Earthquake Records

The selection of ground motion recordings is an essential component of developing fragility curves. It is important to choose the appropriate ground motion and scale the ground motions correctly when creating the curves. Arbitrarily scaling ground motion to a specific spectral acceleration, S_a , at a period, T , may result in overly conservative structural response (Baker, et al., 2014). Ground motion should be

chosen from previously documented earthquake occurrences. Websites such as the Consortium of Organization for Strong Motion Observation System, K-NET, and the Pacific Earthquake Engineering Research NGA database website can be used to select ground motion. Other websites that provide ground motion data include the European Strong Motion database, the French Accelerometric Network, and the Swiss Earthquake Database (Pagani, et al., 2014).

The appropriate amount of ground motion is determined by the application and predicted structural response. Foreshocks are classified as either near-field site or far-field site ground motions, and the site-to-source distance, magnitude, spectral shape throughout the interest period range, and hazard curve at a period, T , are crucial variables for far-field sites. Near-field site considerations include spectral form and the potential for velocity pulses. Table I and Fig. 4 provide suggestions for selecting ground motion (Haselton, et al., 2012; SCEC, 2012; USGS Earthquake, n.d.).

Figs. 5-7 provide suggestions for scaling ground motion with recordings scaled to the elastic response spectrum. In an effort to align the previous records (Table I) with the building location and site class, SiesmoMatch software (SEISMOSOFT, 2023) used to match the chosen ground motion data in accordance with the intended target response spectrum using 5% damping, short periods spectral acceleration $S_s = 0.6$ g, and (1 s) period spectral acceleration $S_1 = 0.2$ g as per Iraqi seismic code 2017.

B. Simulations Methods

The NDA and time history analysis (THA) simulation methods have their unique advantages and limitations. The choice of simulation method depends on the specific characteristics of the structure, the level of accuracy required, and the available resources. These simulation methods are critical tools for engineers in assessing the seismic vulnerability of structures and developing strategies to enhance their seismic performance. Non-linear static analysis (NSA) has been employed in various studies such as those by Mosalam, et al. (1997), Di Ludovico, et al. (2013), Lee, et al. (2014), and Lee and Moon (2014). Other simulation methods such as non-linear THA (NL THA) have been utilized in studies by Aiswarya and Mohan (2014), Farsangi, et al. (2014), and Wang and Rosowsky (2014). IDA has also been employed in studies by Charalambos, et al. (2014), Raghunandan, et al. (2014), Dolsek (2009), Vamvatsikos and Fragiadakis (2010), and Sudret, et al. (2014).

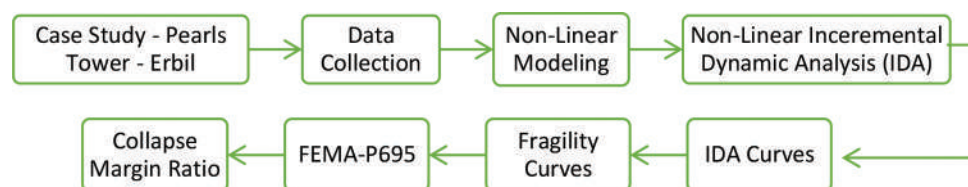


Fig. 3. Outlines and summarizes the methodology of current study.

TABLE I
GROUND MOTION RECORDS

Description	1940 El Centro earthquake (Imperial Valley-02)*	1995 Great Hanshin earthquake (Kobe Japan)*	1999 İzmit earthquake (Kocaeli, Turkey)*
UTC time	1940 May 19	1995 January 16	1999 August 17
Magnitude, Mw	6.9	7.3	7.6
Duration, s	39.48	20	37
Depth, km	16	17.6	15
Epicenter	32.733N 115.5W	34.59N 135.07E	40.748N 29.864W
Type	Strike-slip	Strike-slip	Strike-slip
Area affected	United State, Mexico	Japan	Turkey
Total damage	\$6 million	\$200 billion	\$3-8.5 billion
Maximum intensity	X (extreme) by Modified Mercalli Scale	XII (extreme) by Modified Mercalli Scale	X (extreme) by Modified Mercalli Scale
Causalities	9 dead 20 injured	6434 dead 43792 injured	18373 dead 48901 injured
PGA (g)	0.281	0.233	0.136

PGA: Peak ground acceleration

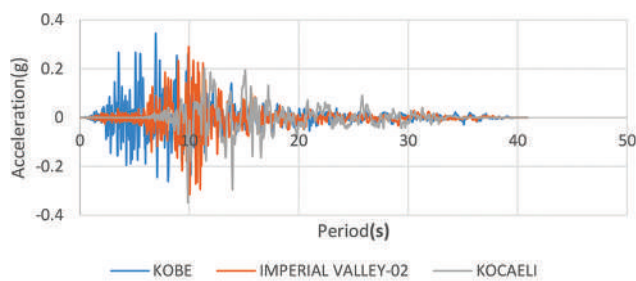


Fig. 4. Acceleration (g) of studied ground motions.

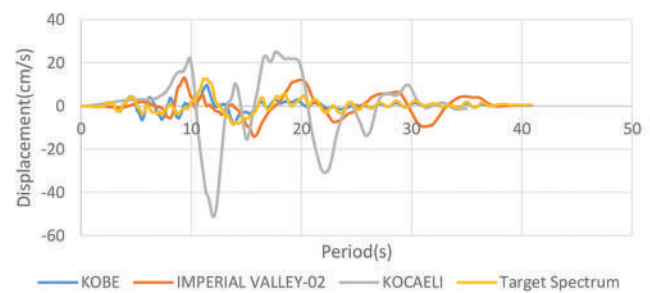


Fig. 7. Displacement (cm/s) of studied ground motions.

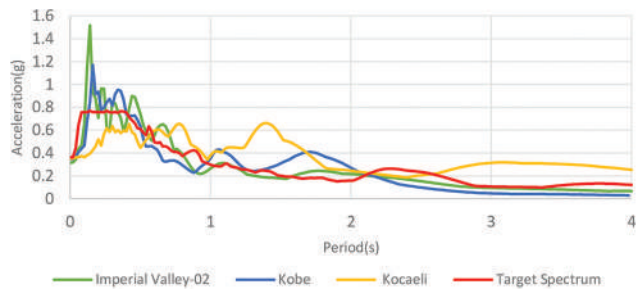


Fig. 5. Fourier transform spectra.

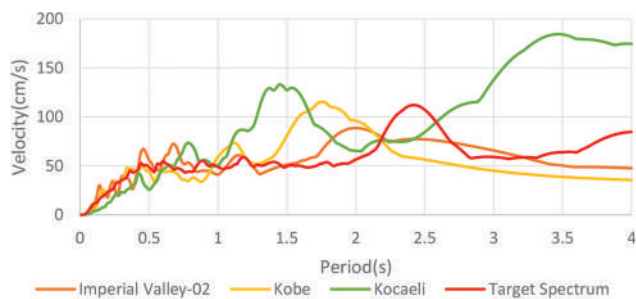


Fig. 6. Velocity (cm/s) of studied ground motions.

Non-linear IDA (NL-IDA)

The behavior of a given structure when subjected to seismic excitations of varying intensity, including expected structural response, failures, and losses, is examined through

IDA. The NL-THA (NL-IDA) approach provides more precise outcomes regarding how the structure would react to seismic activity. PGA, also known as PGA, is the most commonly utilized parameter. The relationship between the IDR and the intensity of the ground motion can be leveraged to produce IDA curves, which are referenced in many seismic codes (ASCE, 2016, FEMA 273, 1997) require a minimum of three or seven sets of ground motions. As a result, three sets of powerful ground movements for each model were employed in this work, and they were chosen from the NGA website of the (Berkeley, n.d.). Table II contains statistics on the ground motions which subsequently scaled from 0.1 g to 1.5 g in accordance with the intended target spectrum.

SFGC

A fragility curve is a mathematical function that depicts the probability of a structure exceeding a particular level of damage, given a specific ground motion intensity parameter such as PGA or spectral acceleration (SA). The curve provides an estimate of the probability of different levels of damage for a given ground motion intensity and it is often used in seismic risk analysis to evaluate the seismic vulnerability of structures. The maximum roof displacement can be divided by the overall height of the building (92 m) to determine the % drift, as specified in Eq. (1).

$$\% \text{ Drift} = \frac{\text{Roof displacement}}{\text{Building height}} \times 100 \quad (2)$$

The probability of damage ($P [D/PGA]$) is represented as a function of the logarithm of the ground motion intensity parameter (PGA), with mean (μ) and standard deviation (Φ) parameters determining the shape of the curve. The fragility curve equation can be written as follows:

$$P\left[\frac{D}{PGA}\right] = \Phi \frac{\ln(PGA) - \mu}{\sigma} \times 100 \quad (3)$$

Where: Φ is the standard normal cumulative distribution function, σ and μ are the mean value and standard deviation of logarithm PGA, and D is the damage state. The fragility curve is typically plotted on a graph, with the PGA values on the x-axis and the probability of exceeding a certain damage level on the y-axis. Damage levels are often expressed as a percentage of the structure's replacement cost, and several damage levels are typically evaluated, such as 0.5%, 1%, 1.5%, 2%, and 2.5% (Xue, et al., 2008; Ibrahim and El-Shami, 2011).

III. CASE STUDY

This study examines the Pearls Towers project, which is situated on the west side of the Empire World on a 100-m

TABLE II
SUMMARIZED FLOOR LOADS

Load description	Value
Dead load	
• Finishing	2.5 kPa
• Partition walls	2.0 kPa
• Mechanical, electrical and plumbing	0.5 kPa
Live load	
• Private rooms	1.92 kPa
• Balcony = 1.5*1.92	2.90 kPa
• Corridor	4.79 kPa
• Bathrooms	2.87 kPa
• Staircase	4.79 kPa
• Elevator access	4.79 kPa

road, Erbil, with a total area of 234,000 square meters. The building has a reinforced concrete structure with 30 floors, including 25 residential floors, two commercial floors, and three underground parking floors. The typical floors have an interstorey height of 3.0 m, while the basement and parking levels have a height of 4.0 m, resulting in a total building height of 95 m. The building columns have dimensions of C1 (60 × 170) cm reinforced with 24 ϕ 20 + 4 ϕ 25 corners, C2 (50 × 150) cm reinforced 24 ϕ 20 + ϕ 25 corners, and C3 (70 × 180) cm reinforced 28 ϕ 20 + ϕ 25 corners, while the beams are 50 × 55 cm, 50 × 75 cm, and 60 × 55 cm, with a slab thickness of 20 cm as shown in Fig. 8. The concrete has a compressive strength of 50 MPa for the entire structure, while the steel reinforcement has a yield stress of 420 MPa. A 3D model of the structure is created to perform structural analysis, including the effects of seismic and gravity loads, which include dead loads and live loads as shown in Table II per ASCE7-16. The findings are then utilized to establish the performance point of the building through control values.

IV. RESULTS AND DISCUSSION

A. IDA

To evaluate the seismic performance of the structure up to the point of collapse, three different earthquake records used to generate IDA curves as shown in Fig. 9. To do this, it is used NL-THA software to analyze each ground motion and plotted the IDA curves using PGA as the IM and interstorey drift % as the damage measure.

Gradually, it increased the IM of PGA in 0.1 g increments until it reached 1.5 g. At this point, the analysis was stopped due to the structures' dynamic instability. The tower's performance point was evaluated using five performance levels that were represented by vertical gridlines at drifts of 0.5%, 1%, 1.5%, 2%, and 2.5%.

To assess the structure, three cases with different ground motion intensities use as shown in Table I and Figs. 4-7. Refer to Fig. 9 in Case 1 had a strong ground motion intensity of 0.281 g PGA, Case 2 had an intermediate ground

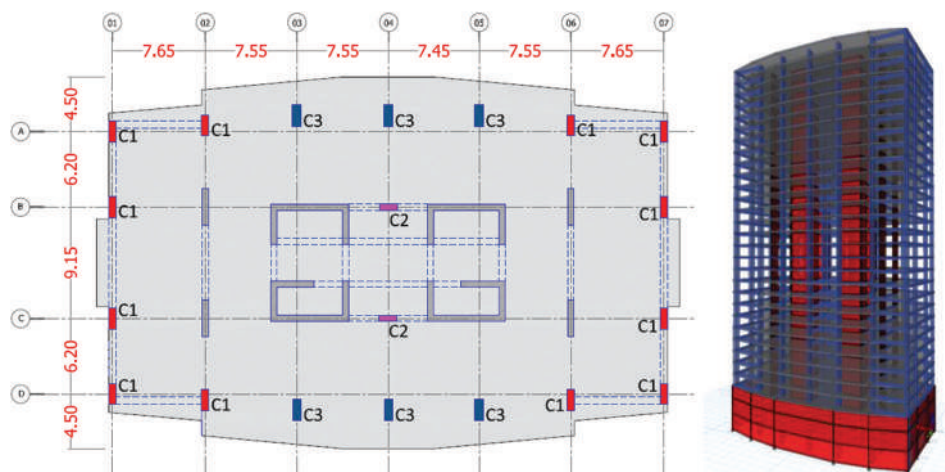


Fig. 8. Plan and isometric view of the building.

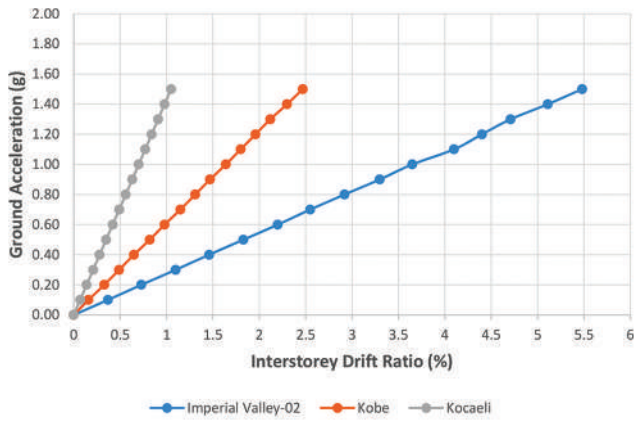


Fig. 9. Incremental dynamic analysis curve for the record data.

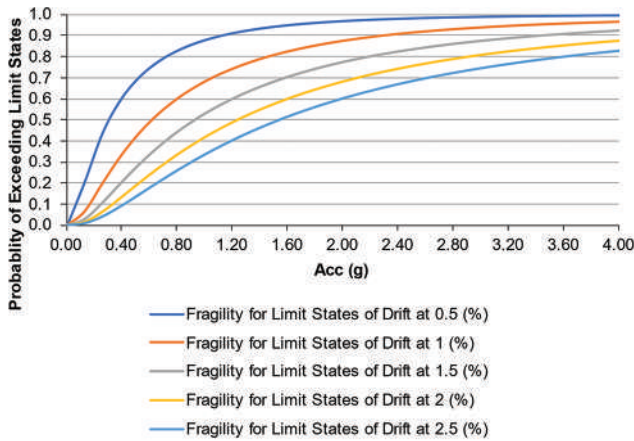


Fig. 10. Seismic fragility curve of the building considering 5 level of damages.

motion intensity of 0.233 g PGA, and Case 3 had a low ground motion intensity of 0.136 g PGA.

The analysis revealed that the building exceeded the DC performance limit of 1.5% and was close to the collapse limit margin for Cases 1 and 2, with IDRs of 1.8% and 1.64%, respectively. In other words, the building would experience significant structural damage in these scenarios.

However, in Case 3, the building was able to maintain its operational performance level during a low-intensity earthquake with an IDR of only 1.0% at a PGA of 1.4 g. This means that the building would experience little to no structural damage and would continue to function normally in this scenario. Overall, the IDA analysis revealed important information about the building’s seismic performance and helped to identify the performance limits of the structure.

B. SFGC

Fig. 10 presents that the study illustrates the outcomes of the simulation models used. The purpose of the study was to examine the performance of buildings under varying ground motion conditions. The performance levels considered in this study were IO, DC, and CP.

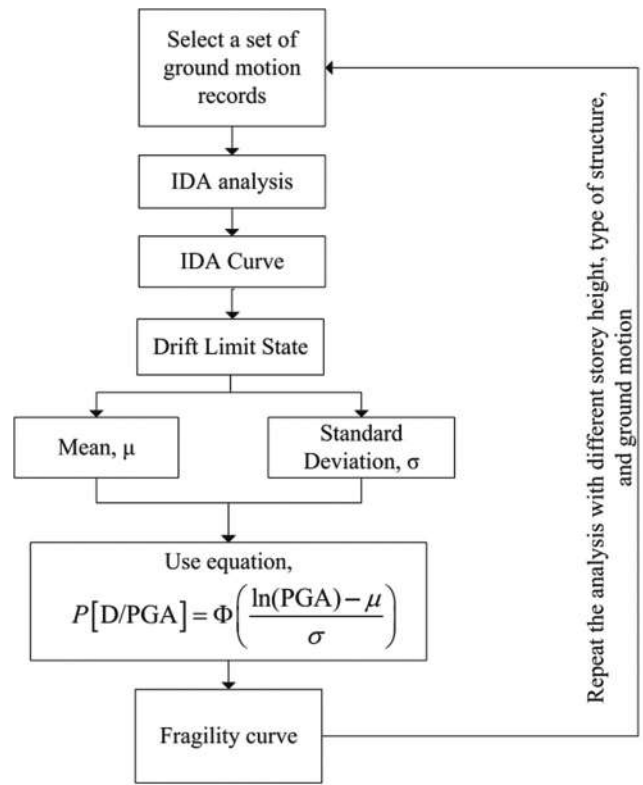


Fig. 11. Flow chart of generating fragility curve.

This study found that the probability of achieving the IO performance level during weak ground vibrations (PGA = 0.2 g) is only 5%. This indicates that the building’s occupants may experience discomfort and some non-structural damage during this level of ground motion.

However, for strong ground motion with PGA > 4.0 g, the probability of reaching or exceeding the IO performance level is 60%. This means that the building can accommodate its occupants with little to no damage during these high-intensity ground vibrations.

In terms of achieving the DC performance level, the study found that for a building equivalent to 1.2 g, the probability of reaching or exceeding the DC performance level is 70%. This suggests that some damage to non-structural elements may occur, but the building’s structural integrity remains intact. In addition, if the building is exposed to PGA = 2.5 g, there is an almost 80% probability of reaching or exceeding the DC performance level.

Furthermore, this study examined the CP performance level, which represents the highest level of performance that a building can achieve. The study found that there is a 60% chance of achieving or exceeding the CP level with highly intense ground vibrations with PGA = 1.6 g. This indicates that both the structural and non-structural components of the building are significantly deteriorating, and the building may be at risk of collapsing.

To summarize, the study provides insights into the performance of buildings under varying ground motion conditions. The fragility curve input and output generated

TABLE III
THE FRAGILITY CURVE INPUT

Total number of load intensities analyzed	15														
Intensity label	Acc														
Intensity unit	g														
Intensity No.	1	2	3	4	5	6	7	8	9	10	11	12	13	14	15
Acc (g)	0.1	0.2	0.3	0.4	0.5	0.6	0.7	0.8	0.9	1	1.1	1.2	1.3	1.4	1.5
Number of analysis performed in each intensity	3														
Engineering demand parameter (EDP) considered	Drift														
EDP unit	%														
Total number of performance levels considered	5														
Performance level	OP			IO			DC			LS			CP		
Drift limit (%)	0.5		1		1.5		2		2.5						
Acc (g)	Drift (%)				Ln (Drift)										
0.1	0.16				-1.832581										
0.1	0.37				-0.994252										
0.1	0.07				-2.65926										
0.2	0.33				-1.108663										
0.2	0.73				-0.314711										
0.2	0.14				-1.966113										
0.3	0.49				-0.71335										
0.3	1.1				0.09531										
0.3	0.21				-1.560648										
0.4	0.65				-0.430783										
0.4	1.46				0.378436										
0.4	0.28				-1.272966										
0.5	0.82				-0.198451										
0.5	1.83				0.604316										
0.5	0.35				-1.049822										
0.6	0.98				-0.020203										
0.6	2.2				0.788457										
0.6	0.42				-0.867501										
0.7	1.15				0.139762										
0.7	2.55				0.936093										
0.7	0.491				-0.711311										
0.8	1.31				0.270027										
0.8	2.92				1.071584										
0.8	0.561				-0.578034										
0.9	1.47				0.385262										
0.9	3.3				1.193922										
0.9	0.632				-0.458866										
1	1.64				0.494696										
1	3.65				1.294727										
1	0.701				-0.355247										
1.1	1.8				0.587787										
1.1	4.1				1.410987										
1.1	0.771				-0.260067										
1.2	1.96				0.672944										
1.2	4.4				1.481605										
1.2	0.841				-0.173164										
1.3	2.12				0.751416										
1.3	4.71				1.549688										
1.3	0.91				-0.094311										
1.4	2.3				0.832909										
1.4	5.11				1.631199										
1.4	0.98				-0.020203										
1.5	2.47				0.904218										
1.5	5.48				1.701105										
1.5	1.05				0.04879										
Standard deviation	1.4159														
Ln of standard deviation	1.0139														

OP: Operational phase, IO: Immediate occupancy, DC: Damage control, LS: Life safety, and CP: Collapse prevention

TABLE IV
THE FRAGILITY CURVE OUTPUT

Acc	Fragility for limit states of drift at				
	IO 0.5 (%)	OP 1 (%)	DC 1.5 (%)	LS 2 (%)	CP 2.5 (%)
0.0100	0.03	0	0	0	0
0.1333	20.21	6.45	2.76	1.39	0.77
0.2667	44.05	20.23	10.87	6.46	4.12
0.4000	59.90	33.25	20.25	13.21	9.07
0.5333	70.36	44.08	29.16	20.25	14.62
0.6667	77.49	52.85	37.13	27.02	20.26
0.8000	82.51	59.93	44.10	33.28	25.71
0.9333	86.16	65.68	50.15	38.97	30.85
1.0667	88.86	70.39	55.39	44.11	35.63
1.2000	90.91	74.27	59.94	48.73	40.05
1.3333	92.50	77.51	63.91	52.88	44.12
1.4667	93.74	80.23	67.37	56.60	47.86
1.6000	94.73	82.53	70.40	59.96	51.28
1.7333	95.53	84.49	73.07	62.98	54.43
1.8667	96.18	86.17	75.43	65.71	57.31
2.0000	96.71	87.62	77.53	68.17	59.97
2.1333	97.15	88.88	79.39	70.41	62.41
2.2667	97.52	89.97	81.05	72.45	64.66
2.4000	97.83	90.93	82.55	74.30	66.73
2.5333	98.09	91.77	83.88	75.99	68.65
2.6667	98.32	92.51	85.09	77.54	70.42
2.8000	98.51	93.17	86.18	78.95	72.06
2.9333	98.67	93.75	87.17	80.25	73.59
3.0667	98.82	94.28	88.07	81.45	75.00
3.2000	98.94	94.74	88.88	82.55	76.32
3.3333	99.05	95.16	89.63	83.57	77.54
3.4667	99.14	95.54	90.31	84.51	78.69
3.6000	99.22	95.88	90.93	85.38	79.75
3.7333	99.30	96.18	91.51	86.19	80.75
3.8667	99.36	96.46	92.03	86.94	81.68
4.0000	99.42	96.72	92.52	87.64	82.56

OP: Operational phase, IO: Immediate occupancy, DC: Damage control, LS: Life safety, and CP: Collapse prevention

from the simulation models is presented in the Tables III and IV that provided, which can be used to guide design decisions for buildings in areas with high seismic activity. Fig. 11 illustrates the finding of fragility curve.

V. CONCLUSION

SFGCs are essential tools for assessing the potential performance of structures under earthquake loading. In this study, the SFGCs were developed for dual system buildings in Erbil city using IDA. The fragility curves were developed for various LSs, including immediate occupancy, life safety, and CP, using the probability of exceedance of a given EDP given the level of an IM. It can be concluded that the building under Weak ground vibrations (PGA = 0.2g) have a low probability (5%) of achieving the maximum performance level, resulting in discomfort and some non-structural damage. Results from IDA show that walls fail at PGA values 5–6 times their design PGA in frame-equivalent systems. Strong ground motion (PGA > 4.0 g) has a higher probability (60%) of meeting the performance level, ensuring minimal damage and occupant safety. For the DC performance level, a building equivalent to

1.2g has a 70% chance of meeting the level, with some non-structural damage but overall structural integrity. Exposure to $PGA = 2.5g$ increases the probability to nearly 80%.

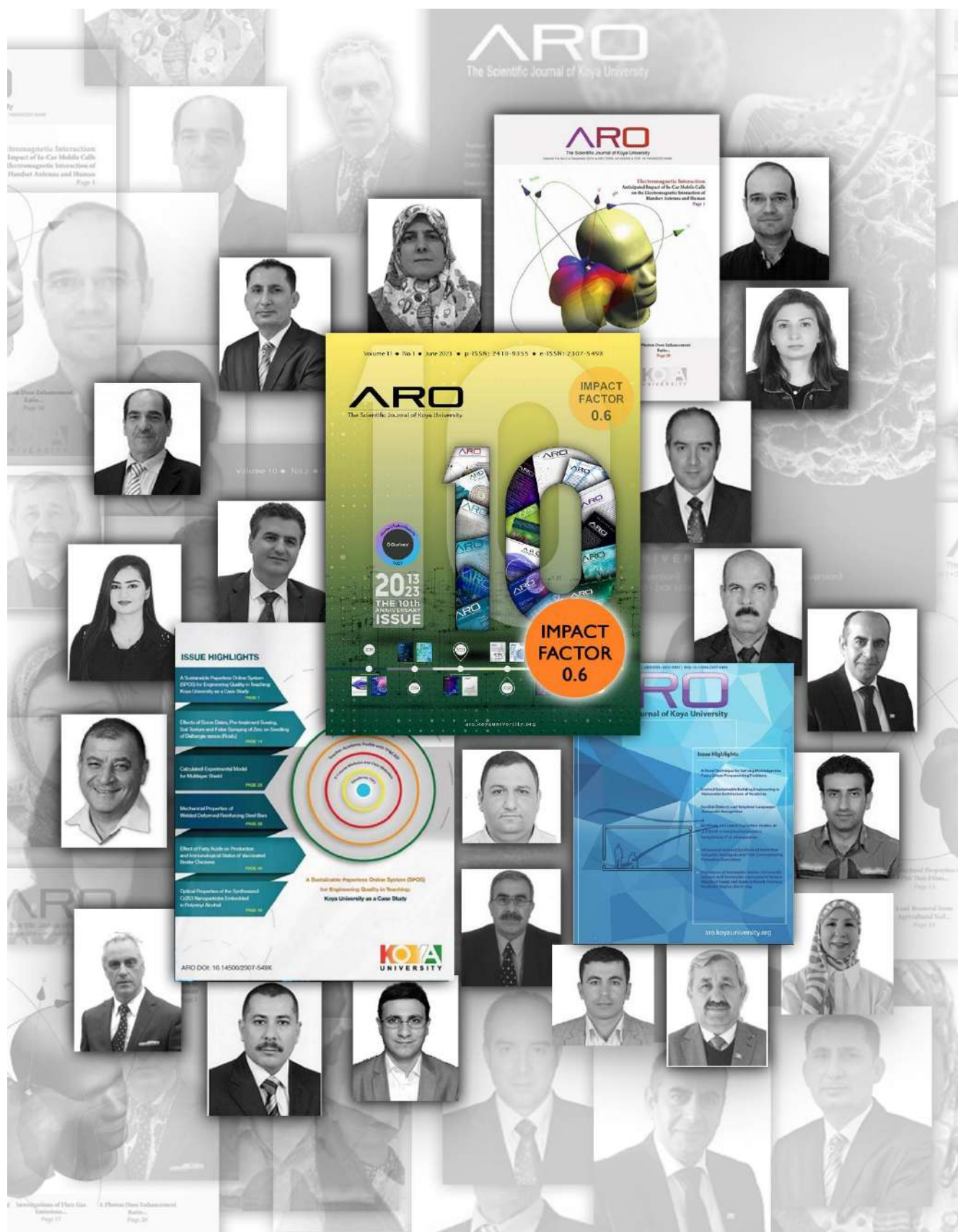
The CP performance level, representing the highest level, has a 50% chance of being met with $PGA = 1.6g$, indicating significant deterioration and collapse risk for both structural and non-structural components. This indicates that the structural components of the building are significantly strong enough to resist up to about 6 times of designed target spectrum. The developed fragility curves are unique to each building due to the specific fragility analysis carried out for each building. The results indicated that the seismic performance objectives of dual system buildings designed according to the current local codes can be achieved with good reliability. The fragility curves developed in this study provide valuable insights for improving the seismic performance of dual system buildings in Erbil city and can serve as a foundation for further research in this area.

REFERENCES

- Abduljaleel, Z.A., Taha, B.O., and Yaseen, A.A., 2021. Seismic vulnerability assessment of Rizgary hospital building in Erbil City, the capital city of KR of Iraq. *Journal of Engineering*, 27(8), pp. 59-79.
- Aishwarya, S., and Mohan, N., 2014. Vulnerability analysis by the development of fragility curves. *IOSR Journal of Mechanical and Civil Engineering (IOSR-JMCE)*, 11(2), pp. 33-40.
- ASCE, American Society of Civil Engineering., 2016. *Minimum Design Loads and Associated Criteria for Buildings and Other Structures*. ASCE/SEI, United States.
- Baker, S., Lesaux, N., Jayanthi, M., Dimino, J., Proctor, C.P., Morris, J., Gersten, R., Haymond, K., Kieffer, M.J., and Linan-Thompson, S. 2014. Teaching academic content and literacy to english learners in elementary and middle school. In: *IES Practice Guide, NCEE 2014-4012*. What Works Clearinghouse, United States.
- Berkeley, U.C., n.d. *Ground Motion Selection and Modification (GMSM) Program*. Available from: <https://apps.peer.berkeley.edu/gmsm/home> [Last accessed on 2023 Jun 10].
- Charalambos, G., Dimitrios, V., and Symeon., C., 2014. Damage assessment, cost estimating, and scheduling for post-earthquake building rehabilitation using BIM. In: *Computing in Civil and Building Engineering (2014)*. ASCE, United States, pp. 398-405.
- Di Ludovico, M., Polese, M., d'Aragona, M.G., Prota, A., and Manfredi, G., 2013. A proposal for plastic hinges modification factors for damaged RC columns. *Engineering Structures*, 51, pp. 99-112.
- Dolsek, M., 2009. Incremental dynamic analysis with consideration of modeling uncertainties. *Earthquake Engineering and Structural Dynamics*, 38, 805-825.
- Farsangi, E.N., Rezvani, F.H., Talebi, M., and Hashemi, S.A.H., 2014. Seismic risk analysis of steel-MRFs by means of fragility curves in high seismic zones. *Advances in Structural Engineering*, 17(9), pp. 1227-1240.
- FEMA 273, 1997. *NEHRP Guidelines for the Seismic Rehabilitation of Buildings, prepared by the Building Seismic Safety Council. (FEMA Publication No. 273)*. Federal Emergency Management Agency, Washington, D.C.
- Fragiadakis, M., and Vamvatsikos, D., 2010. Fast performance uncertainty estimation via pushover and approximate IDA. *Earthquake Engineering and Structural Dynamics*, 39(6), pp. 683-703.
- Hancilar, U., Cakti, E., Erdik, M., Franco, G., and Deodatis, G., 2014. Earthquake vulnerability of school buildings: Probabilistic structural fragility analyses. *Soil Dynamics and Earthquake Engineering*, 67, pp. 169-178.
- Haselton, C., Whittaker, A., Hortacsu, A., Baker, J., Bray, J., and Grant, D., 2012. *Selecting and Scaling Earthquake Ground Motions for Performing Response-history Analyses*. In: *Proceedings of the 15th World Conference on Earthquake Engineering, 2012*. Earthquake Engineering Research Institute, Oakland, CA, USA, pp. 4207-4217.
- Ibrahim, Y.E., and El-Shami, M.M., 2011. Seismic fragility curves for mid-rise reinforced concrete frames in Kingdom of Saudi Arabia. *The IES Journal Part A: Civil and Structural Engineering*, 4, pp. 213-223.
- Jalayer, F., and Cornell, C., 2009. Alternative non-linear demand estimation methods for probability-based seismic assessments. *Earthquake Engineering and Structural Dynamics*, 38, pp. 951-972.
- Lee, S.G., Kim, D.H., and Lee, I.K., 2014. Seismic fragility analysis of 5 MW offshore wind turbine. *Renewable Energy*, 65, pp. 250-256.
- Lee, Y.J., and Moon, D.S., 2014. A new methodology of the development of seismic fragility curves. *Smart Structures and Systems*, 14(5), pp. 847-867.
- Liel, A.B., Haselton, C.B., Deierlein, G.G., and Baker, J.W., 2009. Incorporating modeling uncertainties in the assessment of seismic collapse risk of buildings. *Structural Safety*, 31, pp. 197-211.
- Mosalam, K.M., White, R.N., and Gergely, P., 1997. Static response of infilled frames using quasi-static experimentation. *Journal of Structural Engineering*, 123(11), pp. 1462-4169.
- Pagani, M., Monelli, D., Weatherill, G., Danciu, L., Crowley, H., Silva, V., Henshaw, P., Butler, L., Nastasi, M., and Panzeri, L., 2014. OpenQuake engine: An open hazard (and risk) software for the global earthquake model. *Seismological Research Letters*, 85, pp. 692-702.
- Raghunandan, M., Liel, A.B., and Luco, N., 2014. Aftershock collapse vulnerability assessment of reinforced concrete frame structures. *Earthquake Engineering and Structural Dynamics*, 44(3), pp. 419-439.
- SCEC, 2012. *Report on the August 2012, Brawley Earthquake Swarm in Imperial Valley, Southern California*. Southern California Earthquake Center, USA. Available from: <https://www.scec.org/publication/1678> [Last accessed on 2023 Jun 10].
- SEISMOSOFT, 2023. *Earthquake Software for Response Spectrum Matching*. Earthquake Engineering Software Solutions.
- Sudret, B., Mai, C., and Konakli, K., 2014. Assessment of the lognormality assumption of seismic fragility curves using non-parametric representations. arXiv preprint arXiv:1403.5481.
- USGS Earthquake, n.d. *Earthquakes: U.S. Geological Survey*. Available from: <https://www.usgs.gov/programs/earthquake-hazards/earthquakes> [Last accessed on 2023 Jun 10].
- Vamvatsikos, D., and Cornell, C.A., 2002. Incremental dynamic analysis. *Earthquake Engineering and Structural Dynamics*, 31, pp. 491-514.
- Vamvatsikos, D., and Cornell, C.A., 2004. Applied incremental dynamic analysis. *Earthquake Spectra*, 20, pp. 523-553.
- Vamvatsikos, D., and Fragiadakis, M., 2010. Incremental dynamic analysis for estimating seismic performance sensitivity and uncertainty. *Earthquake Engineering and Structural Dynamics*, 39, pp. 141-163.
- Vona, M., 2014. Fragility curves of existing RC buildings based on specific structural performance levels. *Open Journal of Civil Engineering*, 4, 120.
- Wang, Y., and Rosowsky, D.V., 2014. Effects of earthquake ground motion selection and scaling method on performance-based engineering of wood-frame structures. *Journal of Structural Engineering*, 142(10), pp. 04014086-1-11.
- Xue, Q., Wu, C.W., Chen, C.C., and Chen, K.C., 2008. The draft code for performance-based seismic design of buildings in Taiwan. *Engineering Structures*, 30, 1535-1547.

The 10th Anniversary of ARO

2013-2023



This special issue commemorates the remarkable 10-year journey of Aro - The Scientific Journal of Koya University. Founded within the dynamic landscape of Koya University in 2003, nestled amidst the captivating scenery of the High Mountain in the Kurdistan Region of Iraq, Aro stands as a testament to the university's commitment to global scholarly discourse.

In early 2013, Aro was established with a forward-thinking vision, mission, and goals, driven by a dedicated small group of academics who volunteered their hard work to bring this endeavour to life. Today, Aro proudly represents Koya University's pursuit of knowledge advancement and interdisciplinary research.

As a biannual, peer-reviewed journal, Aro provides a platform for the dissemination of influential multidisciplinary scientific research, global news, and insightful commentary. Embracing the principles of open access, Aro ensures the free accessibility of its published articles worldwide, enabling the unrestricted dissemination of knowledge. With a CC-BY-NC-SA 4.0 license, Aro encourages content sharing and adaptation while upholding ethical practices and promoting responsible scholarship.

ARO Journal holds prestigious affiliations with ROAD and Crossref agencies, and it boasts ESCI indexing, an esteemed Impact Factor, the DOAJ seal, SHERPA/RoMEO deposit policy adherence, and LOCKSS archiving policy compliance.

ARO Journal's unwavering pursuit of excellence aims to showcase groundbreaking research that transcends disciplinary boundaries and creates a tangible impact on society. By providing a forum for scholarly discourse, Aro Journal aspires to shape scientific understanding and improve lives through the dissemination of knowledge.

ABOUT THE JOURNAL

Aro - The Scientific Journal of Koya University emerged in 2013 as a prestigious platform for researchers in the Kurdistan Region and beyond. Our dedication to academic excellence and groundbreaking research has made us a leading publication. At Aro, we prioritize quality and aim to advance knowledge across diverse disciplines, fostering interdisciplinary collaboration and innovative solutions to complex societal challenges.

Our esteemed editorial board brings expertise and meticulous review to ensure the acceptance of high-quality, original research. Through rigorous peer-review and editorial assessment, we guarantee the reliability, validity, and impact of published work. Aro is identified by the e-ISSN: 2307-549X, p-ISSN: 2410-9355, and DOI: 10.14500/2307-549X. As a peer-reviewed, open access journal, we aim to make valuable scientific contributions accessible to all.

Since February 2016, Aro has been listed by Clarivate Analytics, achieving a WoS-IF (Web of Science Impact Factor) of 0.6 on June 28, 2023. We invite researchers to join our esteemed community, contribute to global scientific discourse, and showcase their findings to a wide audience. Be a part of our journey towards advancing knowledge and making a significant impact in the academic world at Aro - The Scientific Journal of Koya University.

Vision:

The vision of Aro - The Scientific Journal of Koya University is to become a globally recognized and reputable journal, listed among esteemed publications. We aim to be a leading platform that scopes high-quality research, fosters academic ethics, and makes a significant impact through the generation of influential citations. Our vision is to provide researchers with a trusted publication venue that promotes academic excellence, innovation, and contributing significantly to the advancement of science and society.

Mission:

Our mission is to uphold the principles of academic ethics and integrity while providing an inclusive and accessible platform for researchers to publish their original works. Aro is committed to fostering interdisciplinary collaboration, encouraging innovative ideas, fostering intellectual growth and nurturing a vibrant research community. Our mission is to nurture a vibrant research community, encourage interdisciplinary collaboration, and promote the dissemination of research findings that have the potential to transform society.

Values:

At Aro, we are guided by a set of core values that shape our journal's ethos and operations:

- **Academic Ethics:** Aro upholds the highest standards of academic ethics, ensuring fairness, transparency, and integrity in all aspects of our publication process. We promote responsible research conduct and respect for intellectual property rights.
- **Open Access:** We strongly believe in the principles of Open Access, providing free and unrestricted access to knowledge. By removing barriers, we aim to maximize the global impact of research and foster collaboration among researchers worldwide.
- **Quality and Excellence:** Aro is dedicated to maintaining excellence in research publication. Our stringent peer-review process ensures the selection of high-quality, original research that contributes to the body of knowledge and advances scientific understanding.
- **Diversity and Interdisciplinary:** We embrace diversity across disciplines, encouraging interdisciplinary research to address complex challenges from multiple perspectives. Aro promotes cross-fertilization of ideas to foster innovation and creativity.
- **Global Outreach:** Aro aspires to have a global reach, facilitating the dissemination of research findings to a wide audience. We aim to connect researchers from different regions, promoting knowledge exchange and collaboration.
- **Supporting Researchers:** We are committed to supporting researchers in their scholarly endeavours. Aro provides constructive feedback to authors, guiding them in improving their work and enhancing its impact.
- **Accessibility:** Aro strives to be accessible to researchers from all backgrounds, offering a user-friendly platform that enables seamless submission and interaction with the journal.

By adhering to our vision, mission, and values, Aro - The Scientific Journal of Koya University is dedicated to making significant contributions to the academic community, enhancing the visibility of research, and contributing to the betterment of society as a whole.

AIMS AND SCOPE OF ARO JOURNAL

ARO Journal is dedicated to publishing influential papers that significantly advance scientific understanding within their respective fields or across interdisciplinary boundaries. As an Open Access, double-blind peer-reviewed scholarly journal, ARO Journal focuses on articles in the field of Sciences and Engineering, promoting the dissemination of high-quality research.

The journal accepts various types of submissions, including Original Research Articles, Review Articles, and Letters to the Editor, all of which undergo rigorous evaluation. ARO Journal evaluates articles based solely on objective criteria related to scientific and methodological soundness, without any subjective determinations.

ARO Journal adheres to the highest standards in all aspects of its operations. The publication places great emphasis on research integrity, maintaining high ethical standards, conducting constructive peer review, ensuring exemplary production quality, and utilizing cutting-edge online functionality for an enhanced reader experience.

Please note that ARO Journal does not accept pre-submission inquiries. However, if you have any doubts regarding whether your article aligns with our Scope, please feel free to contact us at aro.journal@koyauniversity.org. Our team will be happy to assist you.

ARO JOURNAL HISTORY

The journey of Aro is marked by transformative moments and the unwavering commitment of key individuals who have shaped its evolution. In 2012, under the visionary leadership of Dr. Dilan Majid Rostam, the Vice President for Scientific Affairs (Feb 2012 - Feb 2016), Koya University's publication policies underwent significant changes. Recognizing the need for specialized and targeted research dissemination, an innovative concept was introduced to the University Council: splitting the multidisciplinary journal into two distinct publications, one focused on humanities and social sciences and the other on multidisciplinary sciences and engineering. This strategic division aimed to elevate the quality and impact of research publications within the university and led to the birth of Aro - The Scientific Journal of Koya University.

Since its establishment in 2013, Aro has remained steadfast in its pursuit of a global influence within the academic community. Cognizant of past challenges faced in local academic publication, Aro took pioneering measures to align with international publication guidelines. Implementing frameworks like ISSN, DOI, DOAJ, OJS, and COPE, the journal ensured the utmost professionalism and ethical practices, raising its standards to meet the global expectations of scholarly publishing.

Guided by a passionate and proactive editorial board, Aro has flourished as a reputable platform for scientific discourse and knowledge dissemination. Their commitment to advancing scholarly contributions and upholding rigorous research practices has been instrumental in the journal's success. Aro attained indexing in the Emerging Sources Citation Index (ESCI) in 2016 and achieved an Impact Factor of 0.6 as of July 2023.

As we reflect on the history of Aro, we extend our profound appreciation to those who have led the journal, particularly Prof. Salah Ismaeel Yahya, a valued member of the Executive Editors and Head of the Management office. With their continued stewardship, Aro will remain at the forefront of scientific publishing, fostering a culture of excellence and innovation. We invite you to explore the archives of the journal and join us in celebrating the 10th Anniversary of Aro (2013-2023).

ARO EXECUTIVE EDITORS

Aro's Executive Editorial Board (EEB) consists of renowned experts within the relevant subject areas. With extensive experience, they uphold the highest standards of editorial excellence and integrity. Regularly convening, the EEB meticulously reviews submitted articles, evaluating scientific merit, relevance, and adherence to publication guidelines. Authors receive constructive feedback to enhance their manuscripts. Aro strictly follows the Guidelines for Editorial Board Participation, ensuring an independent and impartial EEB committed to editorial ethics. Transparency and fairness are integral to the decision-making process. The EEB's expertise and dedication play a vital role in maintaining Aro as a leading international journal in its field.



Mohammed H. S. Zangana (Executive Publisher) is an esteemed academic who holds a prominent position as the President of Koya University since June 2022. With a remarkable tenure as a member of the Petroleum Engineering Department's teaching staff since 2004, Dr. Zangana brings extensive expertise to his role. He completed his Ph.D. at the University of Nottingham, focusing on Multiphase Flow for oil and gas production, with his research project being part of the TMF funded by prestigious oil and gas companies like BP Exploration, Chevron, ExxonMobil, Petrobras, PETRONAS, Shell, Statoil, and TOTAL. During his M.Sc. studies at the University of Baghdad, Dr. Zangana specialized in Natural Gas processing, deepening his understanding of the field. Actively engaged in research, he has made significant contributions in multiphase flow, natural gas processing, renewable energy, and environmental studies, resulting in numerous publications in renowned journals and international conferences. His research endeavours have been recognized with several international grants, further highlighting his dedication to advancing knowledge in his areas of expertise. Dr. Zangana's outstanding leadership and academic achievements make him an invaluable asset to Koya University, driving its commitment to excellence and innovation in the realm of Petroleum Engineering and beyond.

[e-mail: mohammed.zangana@koyauniversity.org]



Dilan M. Rostam (Editor-in-Chief and Manager) feels deeply honoured to serve as the visionary Editor-in-Chief of this prestigious journal. His unwavering commitment to transforming higher education and fostering student-centred learning ignited the creation of Aro in 2013. Together with a dedicated editorial team, they aspired to establish Aro as a globally recognized publication dedicated to promoting quality and innovative research within the region and beyond. Driven by an insatiable curiosity for knowledge, Dilan pursued his educational journey at Chalmers University in Sweden, where he earned both his B.Sc. and M.Sc. in Civil Engineering/Structural. Fuelling his passion, he embarked on a Ph.D. in Civil/Structural Engineering at the University of Nottingham, United Kingdom, where he pioneered a revolutionary platform for virtual collaborative design in the AEC Industry. Throughout his illustrious career, he has held key positions, including Vice President for Scientific Affairs and Assistant Professor at Koya University's Department of Architectural Engineering. An ardent advocate of e-Smart and digital transformation concepts, he spearheaded the establishment of the ZankoLine nationwide system for student admission to universities in the Kurdistan Region of Iraq in 2011.

Dilan's relentless efforts in championing e-Smart campuses and digital literacy have played a pivotal role in elevating Koya University to the top-ranked University in the Region in 2016. Currently serving as a senior lecturer and esteemed researcher at the University of Duhok, he is steadfast in utilizing his vast knowledge and expertise to support and propel Aro in its ambitious endeavours. With Dilan M. Rostam at the helm, Aro stands poised to reach new heights, shaping the landscape of scientific publishing and driving impactful research in the academic world.

[e-mail: dilan.rostam@koyauniversity.org]



Salah I. Yahya (Executive Editor and Managing Director) is an esteemed Professor who joined the prestigious Department of Software Engineering at Koya University in 2010. With an impressive academic background, he holds a B.Sc. in Electrical Engineering, an M.Sc. in Electronics and Communication Engineering, and a Ph.D. in Communication and Microwave Engineering. His passion for research and scholarly excellence is evident through his active involvement in various professional organizations, including being a Senior member of the IEEE-USA, Consultant at the Iraqi Engineering Union, and a member of AMTA-USA and SDIWC-Hong Kong. Professor Yahya's expertise and reputation extend far beyond academia, as he serves as a regular reviewer for esteemed publications like the Electromagnetics Academy in Cambridge, USA, PIERs Journals, Science and Engineering of Composite Materials journal, and International Journal of Applied Electromagnetics and Mechanics. Additionally, he contributes significantly to the advancement of knowledge through over 100 ISI & Scopus published papers, solidifying his position as a distinguished researcher. At present, Salah I. Yahya's dedication to the field is further exemplified by his role as the Full-time Managing and Executive Editor of ARO Journal. His diverse research interests encompass a wide range of topics, including antennas, EM wave propagation, microwave passive components, electromagnetic compatibility, and artificial neural networks (ANN). His impactful contributions and commitment to academic excellence make him an invaluable asset to the Aro editorial team. [e-mail: salah.ismael@koyauniversity.org]



Fahmi F. Fariq (Executive Editor), an Assistant Professor at the esteemed Department of Physics, Koya University, is a leading expert in the realm of solar energy. His academic journey led him to earn a Ph.D. degree in Solar Energy from the prestigious University of Malaya, where he further honed his skills through postdoctoral research. With an unwavering passion for solar energy, Fahmi has left an indelible mark in the scientific community, publishing an impressive 82 research papers in esteemed international journals. Such prolific contributions have earned him a notable H-index of 22, a testament to his exceptional expertise and dedication. Fahmi's commitment to advancing scientific knowledge is evident through his active memberships in the International Solar Energy Society (ISES) and the International Association of Advanced Materials (IAAM). Embracing a multifaceted role, he has also been serving as an Executive Editor for ARO-The Scientific Journal of Koya University since 2014, where he continues to contribute significantly to the dissemination of cutting-edge research. Fahmi's research interests span a wide range of aspects within solar energy, particularly in the realms of solar cells and metamaterials. His innovative contributions and unwavering dedication to driving progress in the field make him an invaluable asset to the academic community at Koya University and beyond. [e-mail: fahmi.fariq@koyauniversity.org]



Wali M. Hamad (Executive Editor), an eminent and accomplished Professor in the department of Chemistry at Koya University, boasts a remarkable academic journey. His Ph.D. degree in physical chemistry, with a focus on liquid crystal research, was earned from the prestigious University of Baghdad in 2001. Dr. Hamad's exceptional leadership skills and dedication to education were evident during his tenure as the President of the Koya Technical Institute from May 2004 to November 2010, where he also led the Department of Oil Refinery for a year. Additionally, he served as the President of Koya University and Executive Publisher of Aro from 2015 to 2022, contributing significantly to the growth and development of both institutions. Dr. Hamad played a pivotal role in the establishment of the College of Science at Koya University, leaving

an enduring impact on the academic landscape. As an active member of the Teacher Federation and the Physics and Chemistry Society of Kurdistan, his commitment to the advancement of scientific knowledge is unwavering. Dr. Hamad's profound expertise is evident in his extensive research contributions, encompassing fields such as physical chemistry, advanced thermodynamics, and cultural science and politics. His scholarly works have been published in esteemed national and international journals and magazines. As a valued member of the Aro editorial team, Dr. Hamad's wealth of knowledge and expertise continues to enrich the journal's scientific discourse, leaving an indelible mark in the academic world. [e-mail: wali.hamad@koyauniversity.org]



Jorge Correia (Executive Editor), is a highly accomplished scholar with a profound dedication to the fields of architecture and urban studies. Holding a degree in Architecture and a Ph.D. from the University of Porto, Portugal, he has made significant contributions to research projects and scientific commissions. His extensive publication record includes impactful articles, book chapters, and conference papers. Prof. Correia's expertise has earned him invitations to deliver lectures and teach at renowned institutions worldwide, including UFRJ and UFES in Brazil, UJI in Spain, and Koya University in Kurdistan, Iraq. Currently serving as a Professor at the School of Architecture, Art and Design/University of Minho in Guimarães, he also acts as the Deputy Director of the Landscape, Heritage and Territory Lab (Lab2PT), overseeing various Master and Ph.D. theses. Prof. Correia's leadership was demonstrated during his presidency of the European Architectural History Network (EAHN) from 2020 to 2022. His research interests encompass the architectural and urban aspects of European colonial expansion, the cultural dimensions of heritage, and the study of traditional Islamic cities and their representation. With his extensive international experience and expertise, Prof. Correia is a valuable member of the Aro editorial team, bringing a unique perspective to the field of architecture and urban studies. [e-mail: jorge.correia@arquitectura.uminho.pt]



Nadhir Al-Ansari (Executive Editor), is a highly accomplished Professor at Luleå University of Technology in Sweden, where his expertise in Civil, Environmental, and Natural Resources Engineering shines. With an illustrious academic journey, he earned his B.Sc. and M.Sc. degrees from the esteemed University of Baghdad and went on to achieve a remarkable PhD in Water Resources Engineering from Dundee University. Throughout his distinguished career, Nadhir's contributions to the fields of Geology, Water Resources, and Environment have been truly exceptional. His extensive research portfolio boasts over 900 articles published in prestigious international and national journals, alongside 22 books and book chapters. His impact reaches far beyond borders, as he has successfully led more than 60 major research projects spanning Iraq, Jordan, Sweden, and the UK. Committed to nurturing the next generation of researchers, Nadhir has expertly supervised over 70 postgraduate students across various universities worldwide. His dedication to scientific and educational excellence has been recognized through numerous accolades, including the prestigious British Council's top 5 scientists in Cultural Relations award. As a distinguished member of renowned scientific societies, such as the International Association of Hydrological Sciences and Chartered Institution of Water and Environment Management, Nadhir serves on the editorial boards of 42 esteemed international journals. His boundless expertise and unwavering commitment continue to drive remarkable advancements in his field, making him a true trailblazer in the academic world. [email: nadhir.alansari@ltu.se]



Fouad Mohammad (Executive Editor), is an esteemed Senior Lecturer at the esteemed School of Architecture Design and the Built Environment, Nottingham Trent University, United Kingdom. His passion for education shines through as he imparts his vast knowledge in structural analysis to undergraduate Civil Engineering and Building Surveying students, and advanced-level courses for postgraduate Civil Engineering students. Moreover, his dedication to nurturing future scholars is evident in his active involvement in supervising the research work of B.Sc., M.Sc., and Ph.D. Civil Engineering students. Dr. Mohammad's exceptional teaching skills have earned him the prestigious Teacher of the Year award from his university in 2022, a testament to his outstanding commitment to education. His research expertise spans diverse areas, including the analysis and design of steel and reinforced concrete structures, finite element methods in structural and solid mechanics, railway track foundation, and soil-structure interaction. Through his invaluable contributions to academia and research, Dr. Mohammad significantly enhances the field of structural engineering and plays a vital role in the continued success of the esteemed Aro journal. [e-mail: fouad.mohammad@ntu.ac.uk]



Jacek Binda (Executive Editor), is an accomplished Associate Professor at the esteemed Bielsko-Biala School of Finance and Law in Poland. His academic journey is distinguished by a Ph.D. degree from the Department of Electronics and Information Technology at Warsaw University of Technology, coupled with an MD degree from the Department of Automatic Control, Electronics, and Computer Science at Silesian University of Technology. Dr. Binda's extensive expertise reaches far beyond the classroom, as he actively contributes to various European centres, commissions, and organizations. His dedication to advancing knowledge is evident in an impressive track record of scientific publications, reflecting his unwavering commitment to excellence. In recognition of his exceptional leadership and expertise, Dr. Binda currently serves as the esteemed Vice Rector at the Bielsko-Biala School of Finance and Law. Aro journal is privileged to have the valuable expertise of Dr. Jacek Binda as a valued member of its esteemed editorial team, contributing to the journal's pursuit of academic excellence and impactful research. [email: jbinda@wsfip.edu.pl]



Howri Mansurbeg (Executive Editor), an esteemed Professor in Petroleum Geoscientist, brings a wealth of expertise to the field, specializing in diagenesis, sequence stratigraphy, and reservoir characterization of siliciclastics and carbonates. With a Ph.D. from Uppsala University, Sweden, earned in 2007, Mansurbeg is deeply immersed in hydrocarbon exploration and exploitation, particularly in carbonate reservoirs within the Kurdistan Region of Iraq and the United Arab Emirates. Employing an integrated multidisciplinary approach in his research, he has left a profound impact on the industry, collaborating with various international oil companies in Europe and the US. Over the past 15 years, he has contributed significantly to numerous technical reports and research articles, showcasing his dedication to advancing the field. Mansurbeg's academic and managerial journey spans prestigious institutions in Europe and the Kurdistan Region of Iraq, a testament to his remarkable career trajectory. Currently serving as an Adjunct Professor at the School of the Environment in the University of Windsor, Canada, his passion for petroleum geoscience continues to drive groundbreaking discoveries. Aro is deeply honoured to have the distinguished presence of Prof. Howri Mansurbeg as a valued member of its esteemed editorial team. [email: howri.mansurbeg@uwindsor.ca]



Tara F. Tahir (Executive Editor), is a senior lecturer of Electroanalytical Chemistry at the Faculty of Science and Health, Koya University. She holds a Ph.D. in Environmental Electrochemistry from Universiti Sains Malaysia. With expertise in sensors, electrochemistry, and analytical techniques, Dr. Tahir's research focuses on developing innovative sensor technologies and applying electrochemical methods to environmental analysis. Her contributions to the field are evident through her extensive publication record and active participation in scientific conferences and collaborations. As an Editorial Board member of Aro, Dr. Tahir plays a vital role in upholding the journal's mission of promoting high-quality scientific research. Her dedication and expertise contribute to Aro's reputation as a leading platform for cutting-edge research. We are honored to have Dr. Tara F. Tahir as part of the Aro team, and we appreciate her invaluable contributions to the field of Electroanalytical Chemistry. [email: tara.fuad@koyauniversity.org].



Basim M. Fadhil (Executive Editor) is an esteemed Professor at the Department of Automotive Technology in Erbil Polytechnic University, located in the Kurdistan Region of Iraq. With a strong academic background, he holds a Ph.D. degree in Mechanical Engineering from the University of Technology (2000), an M.Sc. degree in Mechanical Engineering from the University of Technology (1993), and a B.Sc. degree in Mechanical Engineering from the University of Technology (1985). In addition to his impressive qualifications, Prof. Fadhil completed a Post-doctorate at the University of Nantes in France in 2018. Throughout his career, he has supervised numerous M.Sc. theses and has published a significant number of research articles in indexed international journals. Prof. Fadhil's research interests encompass a wide range of topics including the behaviour of composite materials under impact load, mechanical and thermal behaviour of materials, fracture mechanics of materials, and materials modelling and analysis using the finite element method (FEM). With his extensive expertise in these areas, Prof. Fadhil greatly contributes to the advancement of automotive technology and materials science. [e-mail: basim.fadhil@epu.edu.iq]



Yazan A. Khaleel (Executive Editor), is a distinguished member of the Aro team, serving as a Professor in the Department of Software Engineering at Koya University. With a strong educational background, he holds a B.Sc. degree in electrical and electronics engineering (1995), an M.Sc. degree in Signal processing, and a PhD degree in Electronics and Digital Signal processing. Dr. Khaleel's expertise and contributions to the academic community are evident through his nine published journal articles and three conference papers. As a member of the Iraqi Engineers syndicate and the Kurdistan Engineering Union, he actively engages in promoting engineering excellence. Dr. Khaleel's specialization in software engineering allows him to bring valuable insights and knowledge to the field, fostering research and innovation. Aro is privileged to have Prof. Yazan A. Khaleel as part of its distinguished team, enriching the journal's academic endeavours. [email: yazan.adnan@koyauniversity.org].

ARO ASSOCIATE EDITORS

The Associate Editorial Board (AEB) of Aro plays a crucial role in shaping the publication's editorial policy and reviewing manuscripts. Once a submission is received, the Editor assesses its quality and assigns an Associate Editor with expertise in the relevant field. The Associate Editor then seeks feedback from expert reviewers, formulating a recommendation for the manuscript. The final decision is made by the Editor, and the Associate Editor maintains communication with the author until publication. Additionally, the Associate Editor actively contributes to the journal's multidisciplinary approach, exploring innovative ways to connect papers and may be invited to write editorial introductions. An ideal candidate for the position possesses excellent communication skills and a commitment to enhancing their discipline's representation within Aro, thus contributing significantly to the journal's high standards and multidisciplinary collaboration. The following academics are the current AEB of Aro.



Hamed M. Jassim (Associate Editor), is a highly experienced academic and researcher in the field of natural resources engineering and management. Currently serving as a Professor at the Department of Natural Resources Engineering & Management at the University of Kurdistan Hewler in Erbil, he has held various leadership roles throughout his career. From 1995 to 2002, Dr. Jassim served as assistant dean of the College of Engineering at Baghdad University, and later as assistant dean and acting dean of Al-Khawarizmi Engineering College. During his tenure at Koya University, he served as the head of the School of Petroleum & Chemical Engineering from 2010 to 2013. Dr. Jassim holds a G.C.E. from Dudley Technical

College, a B.Sc. in Mining Engineering from Leeds University, and an M.Sc. and Ph.D. in Mining Engineering from Leeds University and Leoben School of Mines, respectively. He has published two textbooks and over 18 research papers and technical studies, both nationally and internationally. Dr. Jassim's expertise and contributions to the field make him a valuable member of the Aro editorial team. [e-mail: hamed.jassim@tiu.edu.iq]



Sahar B. Mahmood (Associate Editor), is an esteemed Assistant Professor at the Department of Architectural Engineering and the director of the Heritage Conservation Research Program (HCRP) at Koya University. Her outstanding contributions in the field of architectural conservation have been recognized through prestigious honours, including the Weinberg Fellowship in Architectural History and Preservation from the Italian Academy at Columbia University and the SAH-GETTY International Program Grant from the Society of Architectural Historians (SAH) and the Getty Foundation. With a Ph.D. in Architectural Engineering focused on Heritage Conservation from the University of Baghdad, Sahar's

research interests span various areas, such as conflict and post-conflict heritage, the preservation of religious and ethnic minority communities' heritage, Iraqi vernacular architecture, and the history of architecture. She has actively participated in international conferences, workshops, and initiatives dedicated to safeguarding endangered heritage in the Kurdistan Region. Sahar's commitment to architectural preservation extends beyond academia, as she serves as an editor for the Remembering Mosul website and has contributed to international teams working to protect threatened heritage. As a consultant architect, member of the Iraqi Engineers Union, and former councillor for the European Architectural History Network (EAHN), Sahar continues to make significant contributions to Aro's mission. [e-mail: sahar.basil@koyauniversity.org]



Ikbal M. Tahir (Associate Editor), is an accomplished academic with a strong background in agricultural research and teaching. With fifteen years of experience as a researcher at the State Board for Agricultural Research in Baghdad, followed by four academic years as a lecturer at the College of Agriculture in Koya University, Dr. Tahir currently holds the position of Assistant Professor in the Biology Department of the Faculty of Science and Health at Koya University since the 2012-2013 academic year. She earned her M.Sc. and Ph.D. degrees in Horticulture from Baghdad University, specializing in plant and post-harvest physiology. Dr. Tahir has made significant contributions to the field of agriculture through her extensive research work. With her expertise and dedication, she brings valuable insights and knowledge to the Aro journal, particularly in the realm of horticulture and plant physiology. [e-mail: ikbal.tahir@koyauniversity.org]



Layth I. Abd Ali Daabel (Associate Editor) is an esteemed member of the Aro editorial team, serving as an Assistant Professor of Analytical Chemistry in the Chemistry Department at the Faculty of Science and Health. With a strong academic background, he joined Koya University in 2010 as an Assistant Lecturer. Dr. Daabel holds a B.Sc. degree in Chemistry from the College of Science at Kufa University, an M.Sc. degree in Analytical Chemistry from Al-Mustansiriya University, and a Ph.D. degree in Analytical Chemistry from UTM in Malaysia. His notable contributions to the field include a patent and publications in renowned journals, as well as presentations at international conferences. Dr. Daabel's research interests lie in the areas of analytical chemistry, separation methods, trace metal analysis, magnetic nanoparticles, and pharmaceutical analysis. His expertise and commitment to advancing analytical chemistry make him an invaluable asset to the Aro editorial team. [e-mail: layth.imad@koyauniversity.org]



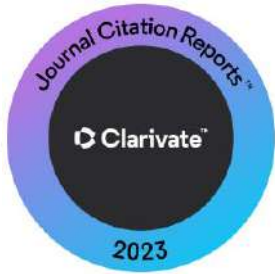
Saddon T. Ahmad (Associate Editor), is a highly dedicated Professor of Nuclear Physics at Koya University, where he has been an integral member since 2006. His academic journey began in 1979, and he holds a B.Sc. degree in Physics from Baghdad University and obtained his Ph.D. in Nuclear Physics from Sussex University, UK, in 1989. Throughout his illustrious career, Saddon has demonstrated exceptional commitment and expertise in nuclear structure and reactions. His contributions to the field are evident in numerous articles published in collaboration with his research group. As a seasoned researcher, he conducted experimental work at the prestigious ILL Institute in Grenoble, France, during his Ph.D. studies. Saddon's dedication extends to guiding and teaching postgraduate students, with an impressive record of supervising thirteen Ph.D. and twelve M.Sc. holders across various Iraqi universities. He has also published over 30 journal articles and presented at three international conferences, further solidifying his reputation as a respected authority in nuclear physics. As a scientific reviewer for reputable international journals indexed by Clarivate Analytics with WOS-IF (Web of Science Impact Factor), Saddon continues to contribute significantly to the academic community. [e-mail: saddon.taha@koyauniversity.org]



Mohammad G. Faraj (Associate Editor), is a Professor at the Department of Physics, Koya University. He holds a Ph.D. degree in solar energy from the School of Physics, Universiti Sains Malaysia (USM). With extensive research experience, including a Post-Doctorate Fellowship from the University of Santiago de Compostela (USC), Spain, Dr. Faraj has made significant contributions to the fields of solar cells, thin films, nanotechnology, polymers, and photodetectors Heterojunction. His research endeavors are showcased through his publications in prestigious ISI and Scopus journals, as well as his active participation in international conferences. As a respected member of the academic community, Dr. Faraj's expertise and commitment to advancing scientific knowledge enrich the research landscape at Koya University. We are honoured to have Dr. Mohammad Ghaffar Faraj as a distinguished member of our team at Aro. [e-mail: mohammad.ghaffar@koyauniversity.org]

University. We are honoured to have Dr. Mohammad Ghaffar Faraj as a distinguished member of our team at Aro. [e-mail: mohammad.ghaffar@koyauniversity.org]







UNIVERSITY

Koya University, established in 2003, stands as a vibrant institution in the heart of the Kurdistan Region of Iraq. Nestled amidst the captivating landscape of the High Mountain, its campus harmoniously blends with the natural surroundings, creating an inspiring environment for learning and research. With six faculties offering diverse programs, including Engineering, Science and Health, Humanities, and Social Sciences, Koya University provides a rich academic landscape encompassing fields such as Petroleum Engineering, Geotechnical Engineering, Software Engineering, Physics, Chemistry, Clinical Psychology, Social Science, Medical Microbiology, Medicine, and Sport Education.

ARO-The Scientific Journal of Koya University, proudly represents the university's commitment to advancing knowledge and fostering interdisciplinary research. As a peer-reviewed, biannual journal, ARO serves as a platform for disseminating original and influential multidisciplinary scientific research, global news, and insightful commentary. Embracing the principles of open access, ARO ensures that its published articles are freely accessible worldwide, facilitating unrestricted dissemination of knowledge. With a CC-BY-NC-SA 4.0 license, ARO encourages the sharing and adaptation of its content while upholding ethical practices and promoting responsible scholarship. ARO Journal holds prestigious affiliations with ROAD and Crossref agencies, boasting ESCI indexing and Impact Factor, DOAJ seal, SHERPA/RoMEO deposit policy, and LOCKSS archiving policy.

ARO Journal's unwavering pursuit of excellence aims to showcase pioneering research that transcends disciplinary boundaries and makes a tangible impact on society. By providing a forum for scholarly discourse, ARO Journal aspires to shape scientific understanding and improve lives through the dissemination of knowledge.

ARO

The Scientific Journal of Koya University

Koya University (KOU)
University Park
Danielle Mitterrand Boulevard
Koya KOY45, Kurdistan Region - Iraq

2013



2014

2015



2016

-Indexed by
WoS-ESCI



2017